P.C. Chu and J.C. Gascard
(editors)

DEEP CONVECTION AND DEEP WATER FORMATION IN THE OCEANS

ELSEVIER OCEANOGRAPHY SERIES

DEEP CONVECTION AND DEEP WATER FORMATION IN THE OCEANS

FURTHER TITLES IN THIS SERIES
Volumes 1–7, 11, 15, 16, 18, 19, 21, 23, 29 and 32 are out of print.

8 E. LISITZIN
SEA-LEVEL CHANGES
9 R.H. PARKER
THE STUDY OF BENTHIC COMMUNITIES
10 J.C.J. NIHOUL (Editor)
MODELLING OF MARINE SYSTEMS
12 E.J. FERGUSON WOOD and R.E. JOHANNES
TROPICAL MARINE POLLUTION
13 E. STEEMANN NIELSEN
MARINE PHOTOSYNTHESIS
14 N.G. JERLOV
MARINE OPTICS
17 R.A. GEYER (Editor)
SUBMERSIBLES AND THEIR USE IN OCEANOGRAPHY AND OCEAN ENGINEERING
20 P.H. LEBLOND and L.A. MYSAK
WAVES IN THE OCEAN
22 P. DEHLINGER
MARINE GRAVITY
24 F.T. BANNER, M.B. COLLINS and K.S. MASSIE (Editors)
THE NORTH-WEST EUROPEAN SHELF SEAS: THE SEA BED AND THE SEA IN MOTION
25 J.C.J. NIHOUL (Editor)
MARINE FORECASTING
26 H.G. RAMMING and Z. KOWALIK
NUMERICAL MODELLING MARINE HYDRODYNAMICS
27 R.A. GEYER (Editor)
MARINE ENVIRONMENTAL POLLUTION
28 J.C.J. NIHOUL (Editor)
MARINE TURBULENCE
30 A. VOIPIO (Editor)
THE BALTIC SEA
31 E.K. DUURSMA and R. DAWSON (Editors)
MARINE ORGANIC CHEMISTRY
33 R. HEKINIAN
PETROLOGY OF THE OCEAN FLOOR
34 J.C.J. NIHOUL (Editor)
HYDRODYNAMICS OF SEMI-ENCLOSED SEAS
35 B. JOHNS (Editor)
PHYSICAL OCEANOGRAPHY OF COASTAL AND SHELF SEAS
36 J.C.J. NIHOUL (Editor)
HYDRODYNAMICS OF THE EQUATORIAL OCEAN
37 W. LANGERAAR
SURVEYING AND CHARTING OF THE SEAS
38 J.C.J. NIHOUL (Editor)
REMOTE SENSING OF SHELF SEA HYDRODYNAMICS
39 T. ICHIYE (Editor)
OCEAN HYDRODYNAMICS OF THE JAPAN AND EAST CHINA SEAS
40 J.C.J. NIHOUL (Editor)
COUPLED OCEAN–ATMOSPHERE MODELS
41 H. KUNZENDORF (Editor)
MARINE MINERAL EXPLORATION
42 J.C.J. NIHOUL (Editor)
MARINE INTERFACES ECOHYDRODYNAMICS
43 P. LASSERRE and J.M. MARTIN (Editors)
BIOGEOCHEMICAL PROCESSES AT THE LAND-SEA BOUNDARY
44 I.P. MARTINI (Editor)
CANADIAN INLAND SEAS
45 J.C.J. NIHOUL and B.M. JAMART (Editors)
THREE-DIMENSIONAL MODELS OF MARINE AND ESTUARIN DYNAMICS
46 J.C.J. NIHOUL and B.M. JAMART (Editors)
SMALL-SCALE TURBULENCE AND MIXING IN THE OCEAN
47 M.R. LANDRY and B.M. HICKEY (Editors)
COASTAL OCEANOGRAPHY OF WASHINGTON AND OREGON
48 S.R. MASSEL
HYDRODYNAMICS OF COASTAL ZONES
49 V.C. LAKHAN and A.S. TRENHAILE (Editors)
APPLICATIONS IN COASTAL MODELING
50 J.C.J. NIHOUL and B.M. JAMART (Editors)
MESOSCALE SYNOPTIC COHERENT STRUCTURES IN GEOPHYSICAL TURBULENCE
51 G.P. GLASBY (Editor)
ANTARCTIC SECTOR OF THE PACIFIC
52 P.W. GLYNN (Editor)
GLOBAL ECOLOGICAL CONSEQUENCES OF THE 1982–83 EL NINO–SOUTHERN OSCILLATION
53 J. DERA (Editor)
MARINE PHYSICS
54 K. TAKANO (Editor)
OCEANOGRAPHY OF ASIAN MARGINAL SEAS
55 TAN WEIYAN
SHALLOW WATER HYDRODYNAMICS
56 R. CHARLIER and J. JUSTUS
OCEAN ENERGY. RESOURCES FOR THE FUTURE

Elsevier Oceanography Series, 57

DEEP CONVECTION AND DEEP WATER FORMATION IN THE OCEANS

PROCEEDINGS OF THE INTERNATIONAL MONTEREY COLLOQUIUM ON DEEP CONVECTION AND DEEP WATER FORMATION IN THE OCEANS

Edited by

P.C. Chu

Department of Oceanography, U.S. Naval Postgraduate School, Monterey, CA 93943, USA

and

J.C. Gascard

LODYC, Université P. et M. Curie (Paris 6), 4 place Jussieu, Tour 14 2e, 75252 Paris Cedex 05, France

ELSEVIER

Amsterdam — London — New York — Tokyo 1991

ELSEVIER SCIENCE PUBLISHERS B.V.
Sara Burgerhartstraat 25
P.O. Box 211, 1000 AE Amsterdam, The Netherlands

Distributors for the United States and Canada:

ELSEVIER SCIENCE PUBLISHING COMPANY INC.
655, Avenue of the Americas
New York, NY 10010, U.S.A.

Library of Congress Cataloging-in-Publication Data

International Monterey Colloquium on Deep Convection and Deep Water Formation in the Oceans (1990)
Deep convection and deep water formation in the oceans : proceedings of the International Monterey Colloquium on Deep Convection and Deep Water Formation in the Oceans / edited by P.C. Chu, J.C. Gascard.
p. cm. -- (Elsevier oceanography series ; 57)
Colloquium held at the Naval Postgraduate School in Monterey, Calif. March 26-30, 1990.
Includes bibliographical references and index.
ISBN 0-444-88764-4 (U.S. : alk. paper)
1. Convection (Oceanography)--Congresses. 2. Ocean circulation--Computer simulation--Congresses. I. Chu, P. C. II. Gascard, J. C. (Jean-Claude) III. Title. IV. Series.
GC228.5.I565 1990
551.47--dc20 91-27488
CIP

ISBN 0-444-88764-4

This book is printed on acid-free paper.

Printed in The Netherlands

FOREWORD

The International Monterey Colloquium was held at the US Naval Postgraduate School from 26 to 30 March 1990 to study "Deep Convection and Deep Water Formation in the Ocean". The papers were presented in the colloquium, followed by discussions among the approximately fifty attendees. More than half of the participants agreed to contribute their papers to this volume. All the manuscripts went through review process. The order of papers loosely follows the agenda of the colloquium, covering observations, experiments, theory, and numerical modeling.

We wish to express our gratitude to the U.S. Naval Postgraduate School and the U.S. Naval Oceanographer for the most valuable support. We thank all the referees for reviewing the papers published in the proceedings.

P.C. Chu

Jean-Claude Gascard

This Page Intentionally Left Blank

TABLE OF CONTENTS

LIST OF PARTICIPANTS

AAGAARD, K., NOAA/PMEL, 7600 Sand Point Way NE, Seattle, WA 98115, USA.
BOURKE, R.H., Department of Oceanography, U.S. Naval Postgraduate School, Monterey, CA 93943, USA.
BRUGGE, R., Space and Atmospheric Physics Group, Department of Physics, Imperial College, London SW7 2BZ, UK.
CARMACK, E., Institute of Ocean Sciences, P.O. Box 6000, Sidney, B.C., Canada V8L 4B2.
CARSEY, F., Jet Propulsion Laboratory, California Institute of Technology, Pasadena, CA 91109, USA.
CHU, P.C., Department of Oceanography, U.S. Naval Postgraduate School, Monterey, CA 93943, USA.
COLLINS, C., Department of Oceanography, U.S. Naval Postgraduate School, Monterey, CA 93943, USA.
CREPON, M., LODYC, Université P. et M. Curie (Paris 6), 4 place Jussieu, Tour 14 2e, 75252 Paris Cedex 05, France.
DAVIDSON, K.L., Department of Meteorology, U.S. Naval Postgraduate School, Monterey, CA 93943, USA.
DENBO, D.W., Battelle Pacific NW Laboratory, P.O. Box 999, Richland, WA 99352, USA.
DOWNING, J., Battelle Pacific NW Laboratory, P.O. Box 999, Richland, WA 99352, USA.
DEWAR, W.K., Department of Oceanography, Florida State University, Tallahassee, FL 32306, USA.
FOFONOFF, N.P., Woods Hole Oceanographic Institution, Woods Hole, MA 02543, USA.
FOLDVIK, A., Geophysical Institute, University of Bergen, Allegt 70, 5007 Bergen, Norway.
GARWOOD, R.W., Jr., Department of Oceanography, U.S. Naval Postgraduate School, Monterey, CA 93943, USA.
GASCARD, J.C., LODYC, Université P. et M. Curie (Paris 6), 4 place Jussieu, Tour 14 2e, 75252 Paris Cedex 05, France.
GORDON, A.L., LDGO, Columbia University, Palisades, NY 10964, USA.
GUEST, P.S., Department of Meteorology, U.S. Naval Postgraduate School, Monterey, CA 93943, USA.
HERMANN, A.J., Woods Hole Oceanographic Institution, Woods Hole, MA 02543, USA.
HUANG, R.X., Woods Hole Oceanographic Institution, Woods Hole, MA 02543, USA.

JOHANNESSEN, J.A., Nansen Environmental and Remote Sensing Center, Edv. Griegsvei 3a, 5037 Solheimsvik, Bergen, Norway.
JOHANNESSEN, O.M., Nansen Environmental and Remote Sensing Center Edv. Griegsvei 3a, 5037 Solheimsvik, Bergen, Norway.
JONES, H., Space and Atmospheric Physics Group, Department of Physics, Imperial College, London SW7 2BZ, UK
KILLWORTH, P.D., Robert Hooke Institute, Clarendon Laboratory, Parks Road, Oxford OX1 3PU, UK.
KOLTERMANN, K.P., WOCE International Project Office, IOS, Wormley, Surrey, GU8 5UB, UK.
MADEC, G., LODYC, Université P. et M. Curie (Paris 6), 4 place Jussieu, Tour 14 2e, 75252 Paris Cedex 05, France.
MARSHALL, H., Scientific Computation Group, University of Michigan, Ann Arbor, MI 48103, USA.
MARSHALL, J., Space and Atmospheric Physics Group, Department of Physics, Imperial College, London SW7 2BZ, UK.
MALANOTTE-RIZZOLI, P., Department of Earth, Atmospheric and Planetary Sciences, MIT, Cambridge, MA 02139, USA.
MARTINSON, D., LDGO and Department of Geological Sciences, Columbia University, Palisades, NY 10964, USA.
McPHEE, M., McPhee Research Co. 13335 Nile Road, Naches, WA 98937, USA.
MUENCH, R., SAIC, 13400B Northup Way, Suite 36, Bellevue, WA 98005, USA.
OWENS, W.B., Woods Hole Oceanographic Institution, Woods Hole, MA 02543, USA.
PAQUETTE, R.G., Department of Oceanography, U.S. Naval Postgraduate School, Monterey, CA 93943, USA.
PICKART, R., Graduate School of Oceanography, University of Rhode Island, Narragansett, RI 02882, USA.
PRICE, J., Woods Hole Oceanographic Institution, Woods Hole, MA 02543, USA.
QUADFASEL, D., Institut für Meereskunde, Universität Hamburg, D-2000 Hamburg 13, Germany.
ROACH, A., NOAA/PMEL, 7600 Sand Point Way, NE, Seattle, WA 98115, USA.
ROETHER, W., University of Bremen, FB1, P.O. Box 330440, D-2800 Bremen 33, Germany.
RUDELS, B., Institut für Meereskunde, Universität Hamburg, D-2000 Hamburg 13, Germany.
SANDVEN, S., Nansen Environmental and Remote Sensing Center, Edv. Griegsvei 3a, 5037 Solheimsvik, Bergen, Norway.
SCHOTT, F., Institut für Meereskunde, Universität Kiel, D-2300 Kiel 1, Germany.
SCOTT, J., Ocean Measurement Section, Admiralty Research Establishment, Portland, Dorset DT5 2JS, UK.

SEMTNER, A., Department of Oceanography, U.S. Naval Postgraduate School, Monterey, CA 93943, USA.
SKYLLINGSTAD, E., Battelle Pacific NW Laboratory, P.O. Box 999, Richland, WA 99352, USA.
SMETHIE, W., LDGO, Columbia University, Palisades, NY 10964, USA.
SMITH, S.D., Department of Fisheries and Oceans, Bedford Institute of Oceanography, P.O. Box 1006, Dartmouth, Nova Scotia, Canada B2Y 4A2.
VISBECK, M., Institut für Meereskunde, Duslernbrooker Weg 20, D-2300 Kiel, Germany.
WATTS, D.R., Graduate School of Oceanography, University of Rhode Island, Narragansett, RI 02882, USA.
WEISS, R.F., Scripps Institution of Oceanography, University of California - San Diego, La Jolla, CA 92093, USA.
WHITEHEAD, J.A., Woods Hole Oceanographic Institution, Woods Hole, MA 02543, USA.

This Page Intentionally Left Blank

INTRODUCTION

A workshop on deep convection and deep water formation was held at the Naval Postgraduate School in Monterey, California from March 26-30, 1990. Needless to say, the importance of the basic mechanisms leading to the formation of deep and bottom waters, has always been recognized for the general understanding of the world ocean, its dynamics and thermodynamics. In the recent past, focused interest in deep convection and deep water formation was evidenced as early as 1972 when an international colloquium entirely dedicated to this problem was convened by the Laboratoire d'Oceanographie Physique du Museum in Paris. At this colloquium, most of the presentations concentrated on mid-latitude regions. In contrast, 18 years later at the Monterey meeting, more observations were available at high latitudes.

Presentations and discussions were organized in 3 categories:
-- past and recent observations (description and analysis),
-- concepts and models, and
-- modern techniques for future observations

A clear distinction was established between open ocean deep convection and shelf processes, both leading to deep and bottom water formation. In the Weddell Sea, these two processes were recognized as equally important.

Dealing with open ocean convection, three kinds of problems were identified and discussed:
-- applicability of one-dimensional mixed layer theory to deep mixing including the production of turbulent kinetic energy (TKE) via tidal currents and thermobaric effects, in addition to the more classical wind generated TKE.
-- baroclinic instability acting very efficiently from the preconditioning to the final stage of the deep mixing in conjunction with the atmospheric forcing in order to reduce the vertical stratification.
-- small scale features acting during the violent mixing phase, characterized by similar horizontal and vertical scales (1 km) and speeds (10 cm/s). Even if those features are small, the Earth's rotation still has an effect on them since the internal radius of deformation is similar to the depth of the mixing.

Once again during the Monterey workshop, the limited areal extent of deep convection regions (chimneys) was presented as one of the more striking and challenging aspects of any study of processes leading to the oceanic deep water formation. Among the avenues of research explored on this problem during the last decade, it seems like the interaction between the general circulation and bottom topography via large scale baroclinic instability of the mean flow under atmospheric forcing, is one of the most promising.

A number of sophisticated numerical models were presented at the 1990 Monterey workshop, compared with only one in 1972 in Paris, thanks to spectacular advances realized in computing sciences over the last twenty years. It is quite obvious that in the very near future, high-resolution, three-dimensional numerical modeling will contribute significantly to the study of a complex problem such as deep water convection and deep water formation.

As co-chairmen of the 1990 Monterey workshop, we would like to thank all the 50 participants for their contributions. We wish also to thank the Naval Postgraduate School for hosting the meeting.

Jean C. GASCARD
Cochairman

Curt COLLINS
Cochairman

This Page Intentionally Left Blank

GEOPHYSICS OF DEEP CONVECTION AND DEEP WATER FORMATION IN OCEANS

P.C. CHU
Department of Oceanography, U.S. Naval Postgraduate School, Monterey, California 93943 (U.S.A.)

ABSTRACT

An important task for geophysicists studying deep convection and deep water formation in the ocean is to investigate various physical mechanisms generating vertical circulation. Two major types of such mechanisms are available so far, namely, thermodynamical instability, which generates convection and mixing due largely to surface buoyancy flux brought by net brine release or surface cooling, and dynamical instabilities, which also produce various vertical cells exchanging water masses at different depths. After reviewing various mechanisms, in this short note, symmetric instability is found to be very important for both near-boundary and open ocean deep convections. The symmetric instability is a combined inertial (or centrifugal) and baroclinic instability. Vertical cells driven by the symmetric instability are in planes perpendicular to the shear flow. However, vertical cells generated by the baroclinic instability are in the same plane as the shear flow. For the near-boundary deep convection, especially in off-shore wind prevailing regions (e.g., the Weddell Sea, the Ross Sea), where onshore Ekman flux is not available, the symmetric instability plays an important role in driving dense water off the shelf. For the open-ocean deep convection, the symmetric instability of a background cyclonic circulation generates vertical cells, exchanging water masses and reducing the stratification of the water column within the gyre. Therefore, the symmetric instability is a strong candidate for being a dominant mechanism for 'preconditioning' for open ocean deep convection.

INTRODUCTION

Deep convection in oceans is closely related to climate change on long time scales. Without deep convection in oceans, there is only a traditional positive radiation/climate feedback mechanism (Budyko, 1969; Sellers, 1969). A colder surface of the earth yields more ice, which increases the albedo, which leads to a decrease in net heat absorption and so a colder surface. With deep convection in oceans, a negative feedback mechanism becomes available (Killworth, 1983). A colder ocean surface does produce more ice, which by brine ejection gives a cold, saline surface layer. This leads to convection, bringing warmer water from deep layer; the warm water melts some of the ice and decreases the surface albedo, allowing more heat to be absorbed, warming the surface.

Since deep convection in oceans is a primary ingredient in the earth climate system, it becomes important to understand the basic mechanisms driving deep convection in

global warming and climate change before coupling this component (deep ocean convection) into climate models. From the geophysical point of view, the mechanisms driving vertical cells are treated as the main forcing for deep ocean convection and are classified into two categories: thermodynamical and dynamical.

Thermodynamical mechanisms driving deep convection invoke directly or indirectly to a convective instability. Any mechanisms that cause a denser water mass to lie over a lighter water mass belong to this category, e.g, convective instability, double diffusion, thermobaric instability, cabbeling instability, and potential instability.

Dynamical mechanisms contributing to deep convection are referred to as dynamical instabilities. Any dynamic instability generating vertical cells belongs to this category, e.g., Kelvin-Helmhotz instability, baroclinic instability, centrifugal instability, and symmetric instability. The vertical cells driven by dynamical instabilities not only exchange water mass in the vertical direction, which reduces the stratification and contributes to the preconditioning of open ocean deep convection, but also play important role in driving dense water mass off the continental shelves in near-boundary convection.

2. VERTICAL CELLS DRIVEN BY THERMODYNAMIC INSTABILITIES

This convection takes place inside the fluid, where the vertical gradient of the density ρ becomes positive, i.e.,

$$\frac{\partial \rho}{\partial z} > 0 \tag{1}$$

The equation of state of sea water is given by

$$\rho = \rho_0[1 - \alpha(\theta - \theta_0) + \beta(S - S_0)] \tag{2}$$

where θ, S are potential temperature and salinity, and θ_0, S_0, and ρ_0 are reference values. The thermal expansion coefficient (α) and saline contraction coefficient (β) are defined by (McDougall, 1987)

$$\alpha = -\frac{1}{\rho_0}\frac{\partial \rho}{\partial \theta}\Big|_{S,p} = -\frac{1}{\rho_0}\frac{\partial \rho}{\partial T}\Big|_{S,p}\Big[\frac{\partial \theta}{\partial T}\Big|_{S,p}\Big]^{-1}$$

$$\beta = \frac{1}{\rho_0}\frac{\partial \rho}{\partial S}\Big|_{\theta,p} = \frac{1}{\rho_0}\frac{\partial \rho}{\partial S}\Big|_{T,p} + \alpha\frac{\partial \theta}{\partial S}\Big|_{T,p} \tag{3}$$

Generally, α and β are functions of potential temperature, salinity, and pressure:

$$\alpha = \alpha(\theta, S, p), \qquad \beta = \beta(S, p) \tag{4}$$

which implies that the dependence of β on θ is very small. The Brunt-Vaisala frequency is

$$N^2 \equiv -\frac{g}{\rho_0}\frac{\partial \rho}{\partial z} = g\frac{\partial}{\partial z}\left[\alpha(\theta - \theta_0) - \beta(S - S_0)\right] \tag{5}$$

The convective instability takes place where the square of the Brunt-Vaisala frequency becomes negative, i.e.,

$$N^2 < 0, \tag{6}$$

which causes rapid overturning in the fluid.

Since the stratification of sea water is generally stable, convective instability does not occur very often in the deep ocean. Therefore, an important task for physical oceanographers is to investigate physical processes that cause the reduction of stratification, i.e.,

$$\frac{\partial}{\partial t}(g^{-1}N^2) < 0 \tag{7}$$

Substitution of (5) into (7) leads to

$$\frac{\partial}{\partial t}(g^{-1}N^2) = \frac{\partial}{\partial z}\left\{\left(\alpha\frac{\partial \theta}{\partial t} - \beta\frac{\partial S}{\partial t}\right) + (\theta - \theta_0)\left[\frac{\partial \alpha}{\partial \theta}\frac{\partial \theta}{\partial t} + \frac{\partial \alpha}{\partial S}\frac{\partial S}{\partial t} + \frac{\partial \alpha}{\partial p}\frac{\partial p}{\partial t}\right]\right.$$

$$\left. - (S - S_0)\left[+\frac{\partial \beta}{\partial S}\frac{\partial S}{\partial t} + \frac{\partial \beta}{\partial p}\frac{\partial p}{\partial t}\right]\right\} < 0 \tag{8}$$

From Gregg (1984) it can be shown that, for all practical purposes, the first law of thermodynamics can be regarded as a conservation equation for potential temperature θ. The conservation equations for heat and salt are

$$\frac{\partial \theta}{\partial t} = A_\theta + M_\theta - \frac{\partial D_T}{\partial z} \tag{9}$$

$$\frac{\partial S}{\partial t} = A_S + M_S - \frac{\partial D_S}{\partial z} \tag{10}$$

Here

$$A_\theta = -\vec{V}\cdot\nabla\theta, \quad A_S = -\vec{V}\cdot\nabla S$$

are advection of potential temperature and salinity, and

$$M_\theta = \nabla_2(K\nabla_2\theta) - \frac{\partial F_\theta}{\partial z}, \quad M_S = \nabla_2(K\nabla_2 S) - \frac{\partial F_S}{\partial z}$$

are the divergence of the fluxes of θ and S due to lateral mixing and small-scale turbulent mixing in the vertical direction, and F_θ and F_S are upward heat and salt turbulent fluxes. Horizontal eddy diffusivity is K. Heat and salt fluxes due to double diffusion are D_T and D_S. Substitution of (9) and (10) into (8) leads to

$$\frac{\partial}{\partial t}(g^{-1}N) = G_1 + G_2 + G_3 + G_4 + G_5 < 0 \tag{11}$$

where G_1, G_2, G_3, G_4, and G_5 are five terms representing different physical processes of thermodynamical destabilization: buoyancy flux induced instability, potential instability, double diffusion, thermobaric instability, and cabbeling instability.

The buoyancy induced instability arises from the condition

$$G_1 = \frac{\partial}{\partial z}(\alpha M_\theta - \beta M_S) < 0 \tag{12}$$

The effect of horizontal mixing on this instability has not been studied much, largely due to the uncertainty in the value of K. An approximate form of G_1, widely used by oceanographers, is

$$G_1 \simeq -\frac{(\alpha F_\theta - \beta F_S)|_{z=0}}{H^2} < 0 \tag{12a}$$

which indicates the convection generated by surface buoyancy loss (Fig.1).

Potential instability is primarily a result of differential flows at synoptic scale, causing

$$G_2 = \frac{\partial}{\partial z}(\alpha A_\theta - \beta A_S) < 0 \tag{13}$$

This mechanism is recognized by the meteorologists in explaining the meso-scale vertical circulations within extra-tropical cyclones due to a cool, dry flow moving over a warm, moist flow (Browning, 1974). However, the validity of this mechanism as it pertains to the deep convection in oceans is still an open question. This is mostly due to the lack of de-

tailed current measurements in the deep ocean. The generation of convection in deep currents by vertical-differential advection and mixing will be verified when good data sets become available.

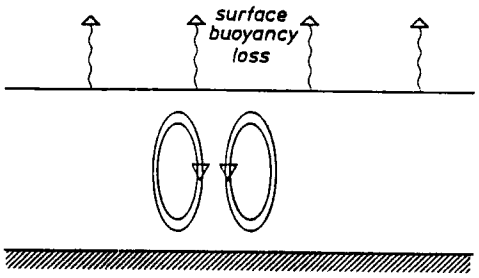

Fig. 1. Vertical circulation driven by the upward surface buoyancy flux.

Double diffusive convection takes place when

$$G_3 = \frac{\partial}{\partial z}\left(\beta \frac{\partial F_S}{\partial z} - \alpha \frac{\partial F_T}{\partial z}\right) < 0 \tag{14}$$

This type of convection is driven by the difference between heat diffusion (fast) and salt diffusion (slow). The idea of double diffusion of heat and salt was developed by Stern (1960) and Stommel (1962), and this gave rise to a series of theoretical and laboratory investigations of thermohaline convection. Laboratory experiments by Turner and Stommel (1964) and Turner (1965) showed that the occurrence of cold, and relatively fresh, water over dense, warm, and salty water results in a successive convective layers in which convection is induced by fast upward heat diffusion. The penetrative convection through the upper boundary of each layer is delayed by a density microjump created at this boundary by mixing in a stable gradient. There are two kinds of double diffusive convection, namely, diffusive staircases (in which relatively fresh, cold water overlies warmer, saltier water) and salt finger staircases (in which warm, salty water overlies cooler, fresher water). From the northwestern Weddell Sea during March 1986 (Muench et al., 1990), two typical vertical length-scales were found (1-5 m, and 100 m) in the layers in the staircases of the upper, steeper portion of the thermocline. This mechanism cannot explain the formation of extensive convective layers such as "chimneys".

Thermobaric instability appears when

$$G_4 = \frac{\partial}{\partial z}\{[(\theta-\theta_0)\frac{\partial \alpha}{\partial p} - (S-S_0)\frac{\partial \beta}{\partial p}]\frac{\partial p}{\partial t}\} < 0 \tag{15}$$

and cabbeling instability occurs when

$$G_5 = \frac{\partial}{\partial z}\{(\theta-\theta_0)\frac{\partial \alpha}{\partial \theta}\frac{\partial \theta}{\partial t} + [(\theta-\theta_0)\frac{\partial \alpha}{\partial S} - (S-S_0)\frac{\partial \beta}{\partial S}]\frac{\partial S}{\partial t}\} < 0 \tag{16}$$

Both instabilities are caused by nonlinearities in the equation of the state of seawater (McDougall, 1987).

3. VERTICAL CELLS DRIVEN BY DYNAMIC INSTABILITIES

The thermodynamic instabilities (buoyancy driven, potential, double diffusive, thermobaric, cabbeling) generally generate sporadic convection events. Only by being associated with some dynamical mechanism or some "preconditioning" may these thermodynamical instabilities take an active role in generating two main types of convection, namely, open-ocean deep convection and near ocean boundary convection (Killworth, 1983). It becomes necessary to review the different features of various dynamical instabilities, e.g., Kelvin-Helmholtz, baroclinic, symmetric, and centrifugal instabilities.

In a stably stratified ocean, Kelvin-Helmholtz instability takes place when the destabilizing influence of the shear flow overcomes the stabilizing effect of the buoyancy force. This can happen when the Richardson number is locally below its critical value of 0.25, i.e.,

$$Ri \equiv N^2/U_z^2 \ < \ 0.25 \tag{17}$$

where $U_z = \partial U/\partial z$. If the mean flow, U is geostrophically balanced, vertical shear (i.e., $U_z^2 > 0$) may cause baroclinic instability. The vertical cells generated by both Kelvin-Helmholtz and baroclinic instabilities are in the same plane of the shear flow (Fig.2), however, the horizontal scales are quite different. The vertical cells generated by the Kelvin-Helmholtz instability have a much smaller horizontal scale (comparable with the thermal convection scale) than that associated with baroclinic instability (Table 1).

Symmetric instability is known to occur as a series of two-dimensional rolls aligned with vertical shear flow (i.e., vertical cells are generally perpendicular to the flow, see

Fig.3) in a stably stratified ocean when the product of the Coriolis parameter f and the Ertel potential vorticity q becomes negative.

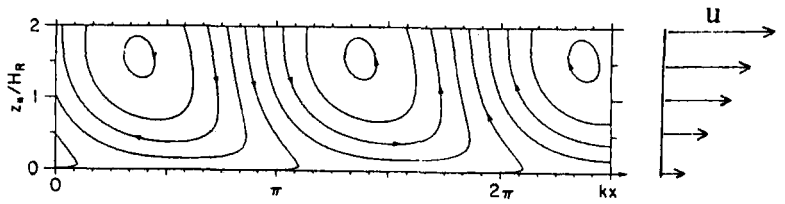

Fig. 2. Vertical circulation driven by the baroclinic instability and predicted by the Charney model, show that the vertical cells are in the same plane of the shear flow (Gill, 1982).

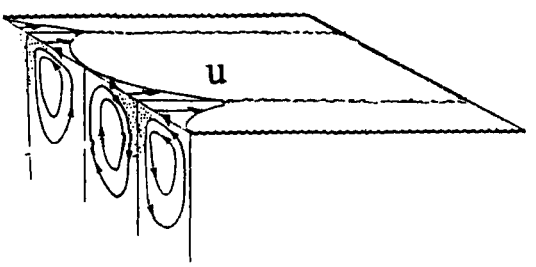

Fig. 3. The vertical circulation driven by the symmetric instability, show that the vertical cells are in planes perpendicular to the shear flow.

For a basic flow with thermal wind balance, q may be expressed in terms of the Richardson number, stratification, and vertical and horizontal shears (Emanuel, 1983):

$$q = \frac{fN^2}{g}\left(\frac{f+\bar{\zeta}}{f} - \frac{1}{Ri}\right), \quad \bar{\zeta} = -U_y \tag{18}$$

which leads to a necessary condition for the symmetric instability to occur (Table 1):

$$Ri + \frac{\bar{\zeta}}{f} Ri < 1 \tag{19}$$

Centrifugal instability, which is the symmetric instability in a vortex, was discovered by Rayleigh (1880). The vortex becomes unstable when the square of the angular momentum decreases outward (Rayleigh, 1916). Later, Taylor (1923) confirmed Rayleigh's discovery by his experimental and theoretical research on flow between coaxial rotating cylinders. When the outer cylinder rotates (with angular velocity Ω_2) in the same direction as the inner cylinder (with angular velocity Ω_1), but with a larger angular velocity that the square of the angular momentum increases outward, the flow is stable. When the outer cylinder rotates in the opposite direction ($\Omega_1 < 0, \Omega_2 > 0$), or rotates in the same direction with a smaller angular velocity ($\Omega_1 > \Omega_2 > 0$), the square of the angular momentum decreases with radius somewhere between the two cylinders, where the flow becomes unstable, and the vertical cells are intensified (Fig.4). Charney (1973) derived a general form for this instability. Chu (1991) discussed the formation of vertical cells inside the vortex. Analogous to the convection, the vertical cells generated inside the vortex can also transport heat and salt vertically and reduce the stratification. Therefore, this mechanism can be considered as another possible contributor to preconditioning.

TABLE 1
Criteria and horizontal scales for different types of instability.

Instability type	Criterion for instability	Horizontal scale
Baroclinic	$\lvert\overline{U}_z\rvert > 0$	NH/f
Kelvin-Helmholtz	$Ri < 1/4$	$\overline{U}_z/\overline{U}_{zz}$
Symmetric	$Ri + \overline{\zeta}Ri/f < 1$	$\overline{U}_z H/f$
Convective	$Ri < 0$	H

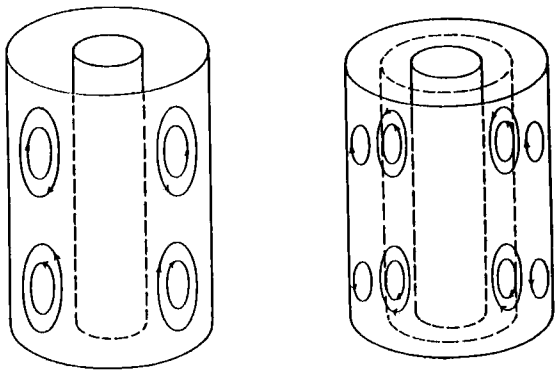

(*a*) $\Omega_1 > \Omega_2 > 0$ (*b*) $\Omega_1 < 0,\ \Omega_2 > 0$

Fig. 4. Vertical cells generated between coaxial rotating cylinders (after Charney, 1973).

4. IMPORTANCE OF SYMMETRIC INSTABILITY IN DEEP CONVECTION

4.1 Near-Boundary Convection

An important dynamical component for the near boundary convection, as mentioned by Killworth (1983), is the onshore surface Ekman transport by the prevailing winds. However, observation (Fig.5) shows that the prevailing coast-paralleling winds near Weddell Sea and Ross Sea ice edges are virtually across the ice edge. The climatological data collected by the Antarctic Automatic Weather Station also shows the cross ice edge winds prevailing in the Ross Sea (Stearns and Weidner, 1987). The Ekman transport generated by such a wind field is parallel to the coast, not cross-shelf. Therefore, we have to find other dynamical mechanisms for driving dense water off the shelf.

Vertical cells generated by the symmetric instability are in the plane perpendicular to the flow (Fig.3). The importance of this instability has been recognized by meteorologists for a long time (e.g., Solberg, 1933; Kuo, 1954). However, it has been given less attention by the oceanographic community. In order to investigate the structures of these cells, Emanuel (1979) formulated a equation for the streamfunction ψ for the disturbances generated by a mean flow U (in x-direction) with constant vertical and horizontal shears (U_z, U_y), and constant stratification. The mean flow, confined between two horizontal rigid boundaries, is in hydrostatic and geostrophic equilibrium. The disturbances are stationary overturning cells in the (y,z)-plane.

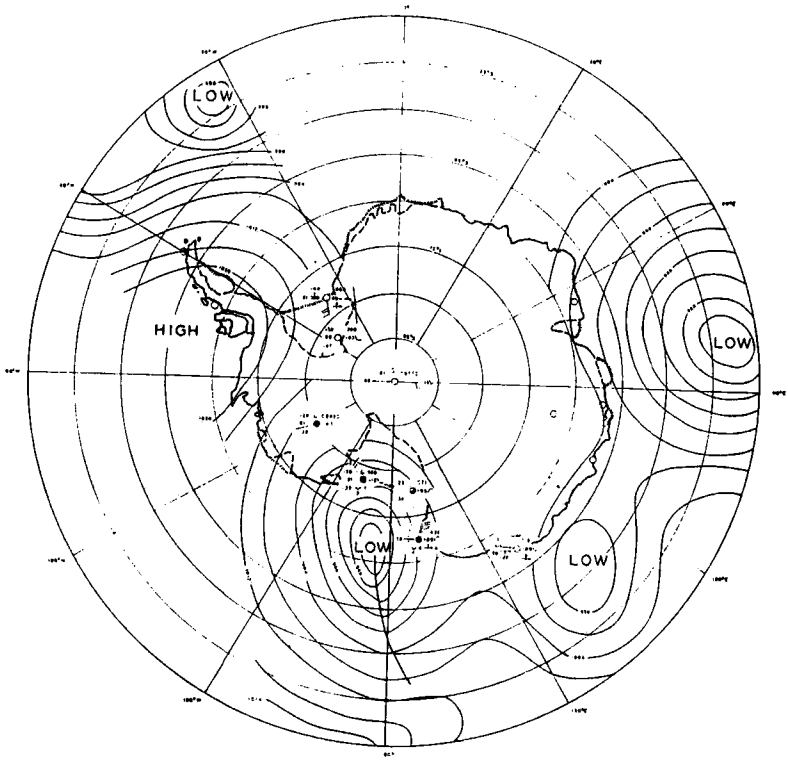

Fig. 5. Surface weather map at 1200, 11 August 1958 (after Vickers, 1966).

The streamfunction of the disturbances ψ satisfies the following equation as the growth rate is just zero (Emanuel, 1979)

$$P\frac{\partial^6\psi}{\partial z^6} + \chi\left(\frac{\partial^2\psi}{\partial y^2} + \frac{\partial^2\psi}{\partial y \partial z}\right) + \frac{\partial^2\psi}{\partial z^2} = 0 \tag{20}$$

where the viscosity and shear parameters P and χ are defined by

$$P = \frac{f}{f - U_y}\frac{\nu^2}{f^2 H^4}, \quad \chi = \frac{f}{f - U_y}\frac{(1 + Pr)^2}{RiPr} \tag{21}$$

Here ν is the eddy viscosity, H is the depth of the fluid, and Pr is the Prandtl number, ν/κ, where κ is the eddy diffusivity. The vertical and lateral coordinates in (20) have been normalized according to

$$z_* = H\,z, \quad y_* = H\frac{N^2 Pr}{fU_z(1+Pr)}y \tag{22}$$

where the asterisks denote dimensional quantities. An example of the structure of symmetric instability is shown in Fig.6. The streamlines take the form of sloped rolls. In the absence of onshore Ekman transport due to the cross-coastal winds (Fig.5), the current is virtually parallel to the ice edge. The overturning cells generated by the symmetric instability is a possible dynamical mechanism to drive the dense water off the shelf. The importance of this mechanism for the near boundary convection needs to be verified by a more sophisticated model with a complex topography.

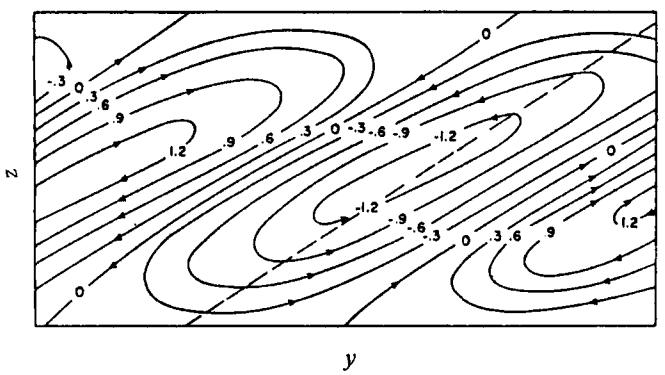

Fig. 6. Stream function in (y,z) plane (after Emanuel, 1982).

4.2 Open Ocean Deep Convection

There are two important requirements for open-ocean deep convection: background cyclonic circulation and preconditioning (Killworth, 1983). The main ideas are that the cyclonic circulation is necessary to form an upward "doming" of isopycnals in the center of the cyclonic gyre and so reduce the stratification of the water column within the gyre, and that the preconditioning (operating over a period of weeks) creates a region of very weak stratification within the cyclonic dome which then become suitable for convection

if the surface forcing is sufficiently intense. In the absence of baroclinic instability, Chu (1991) showed that vertical cells can also be generated by the vortex (Fig.7). The vertical circulation generated by the vortex exchanges the heat and salt at different levels and reduces the stratification. Therefore, this effect of the vortex on the secondary circulation, i.e., symmetric instability, should play an important role in the "preconditioning" for open ocean deep convection.

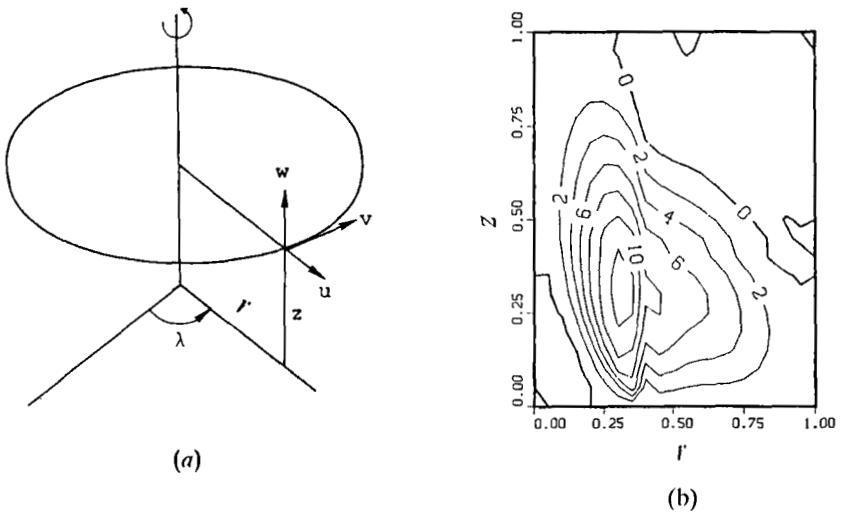

Fig. 7. (a) The cylindrical coordinates (r, λ, z) with the vertical axis at the center of the vortex. (b) The radial-vertical sectional streamfunction indicating the vertical cells generated by a barotropic Gaussian-type cyclonic vortex.

5. CONCLUSIONS

This short article is intended to bring the importance of the symmetric instability of currents or of vortices in the deep convection to the attention of the oceanographic community. In the near-boundary convection, the overturning cells generated by the symmetric instability of alongshore currents is a possible dynamical mechanism to drive dense water off the shelf. In the open ocean deep convection, the vertical cells generated inside a vortex by symmetric instability reduce stratification by the vertical exchange of heat and salt. It is reasonable to consider this mechanism as part of the "preconditioning".

6. ACKNOWLEDGEMENTS

The author is grateful to Prof. R.W. Garwood, Jr. and Ms. A. Bird of the Naval Postgraduate School for invaluable discussion and comments.

This research was sponsored by the U.S. Office of Naval Research, and the Naval Postgraduate School.

7. REFERENCES

Browning, K.A., 1974. Mesoscale structure of rain systems in the British Isles. J. Meteor. Soc. Jap., 52: 314-327.

Budyko, M.I., 1969. Effect of polar radiation variations on the climate of the earth. Tellus, 21: 611-619.

Charney, J.G., 1973. Planetary fluid dynamics. In: P. Morel (Editor), Dynamical Meteorology. Reidel, Dordrecht, 99-351.

Chu, P.C., 1991. Vertical cells driven by vortices- a possible mechanism for a preconditioning of deep convection. (in this volume).

Emanual, K.A., 1979. Inertial instability and mesoscale convective system, part I: linear theory of inertial instability in rotating viscous fluids. J. Atmos. Sci., 36: 2425-2449.

Emanual, K.A., 1983. Symmetric instability. In: D.K. Lilly and T. Gal-Chen (Editors), Mesoscale Meteorology - Theories, Observations, and Models. Reidel, Dordrecht, pp. 217-229.

Gill, A.E., 1982. Atmosphere-Ocean Dynamics. Academic, New York, 560-561.

Gregg, M.C., 1984. Entropy generation in the ocean by small-scale mixing. J. Phys. Oceanogr., 14: 688-711.

Killworth, P.D., 1983. Deep convection in the world ocean. Rev. Geophys. & Space Phys., 21: 1-26.

Kuo, H.L., 1954. Symmetric disturbances in a thin layer of fluid subject to a horizontal temperature gradient and rotation. J. Meteor., 11: 399-411.

McDougall, T.J., 1987. Thermobaricity, cabbeling, and water-mass conversion. J. Geophys. Res., 92: 5448-5464.

Muench, R.D., Fernando, H.J.S., and Stegen, G.R., 1990. Temperature and salinity staircases in the northwestern Weddell Sea. J. Phys. Oceanogr., 20:295-306.

Rayleigh, Lord, 1880. On the stability, or instability, of certain fluid motion. Scientific Papers, Cambridge University Press, 1: 474-487.

Rayleigh, Lord, 1916. On the dynamics of revolving fluids. Scientific Papers, Cambridge University Press, 6: 432-446.

Sellers, W.D., 1969. A global climatic model based on the energy balance of the earth-atmosphere system. J. Appl. Meteorol., 8: 392-400.

Solberg, H., 1936. Le mouvement d'inertie de l'atmosphere stable et son role dans la theorie des cyclones. Proc. -Verb. Assoc. Meteor. U.G.G.I. (Edinburgh), pt. 11: 66-82.

Stearns, C.R. and G.A. Weidner, 1987. Antarctic automatic weather stations, austral summer 1986-1987. Antarctic J. of the U.S., 22(5): 270-272.
Stern, M., 1960. The 'salt fountain' and thermohaline convection. Tellus, 12, 172-175.
Stommel,H., 1962. Examples of mixing and self-exciting convection on the T-S diagram. Oceanology, 2, 205-209.
Taylor, G.I., 1923. Stability of a viscous liquid contained between two rotating cylinders. Phil. Trans. Roy. Soc., A223: 289-343.
Turner, J.S., 1965. The coupled turbulent transport of salt and heat across a sharp density interface. Int. J. Heat & Mass Transfer, 8, 759-767.
Turner, J.S., and Stommel, H., 1964. A new case of convection in the presence of combined vertical salinity and temperature gradients. Proc. U.S. Acad. Sci., 52, 49-53.
Vickers, W.W., 1966. A study of ice accumulation and tropospheric circulation in western Antarctica. Antarctic Res. Series, 9: 135-176.

TWO STABLE MODES OF SOUTHERN OCEAN WINTER STRATIFICATION

ARNOLD L. GORDON
Lamont-Doherty Geological Observatory
of Columbia University
Palisades, New York, USA, 10964

ABSTRACT

The Southern Ocean is responsible for most of the world ocean's deep water characteristics. Cold Southern Ocean water masses are produced as buoyancy is removed by the polar atmosphere, usually in association with sea ice formation. Great amounts of sea ice formed within coastal polynyas are continually swept away by coastal winds, exposing the ocean surface to the cold antarctic atmosphere and further ice formation. Salt rejection forms dense shelf water masses, a key ingredient of Antarctic Bottom Water. In recent years a greater appreciation of winter processes over the deep ocean has developed. The extensive winter sea ice cover of the Southern Ocean is limited in its thickness by mixed layer entrainment of relatively warm and salty deep water. The same processes quickly disposes of the ice cover in the austral Spring. A network of negative feedbacks produces a relatively stable but thin veneer of sea ice. The sea ice cover and ocean static stability are maintained by salinity; this is referred to as the *saline mode*. The saline mode can be upset. The Weddell Polynya of the mid-1970's is a dramatic example of another stable mode. In the polynya condition the ocean stratification is destroyed and vigorous convection persists, eliminating the sea ice cover. This configuration is driven by the temperature instability and is referred to as the *thermal mode*. The conversion of the saline mode to the thermal mode requires the mixed layer salinity to become sufficiently high to force free convection with the deep water. It is unlikely that the Winter can be cold or long enough to force this conversion. Enhanced wind-induced sea ice divergence could accomplish this task, though that is difficult to reconcile a localized atmospheric effect with the repeated occurrences of small site specific polynyas. It is likely that the formation of offshore polynyas is driven by ocean processes, perhaps associated with circulation interaction with bottom topography. The persistent Weddell Polynya of the mid-1970s altered the thermohaline stratification of the water column to 3000 meters. Smaller, recurring polynyas observed since then are likely associated with sporadic convection events. These events slightly alter thermohaline stratification by injecting low salinity water into the mid-water column.

1 INTRODUCTION

Within the antarctic zone, stretching from the continental margins of Antarctica to the oceanic polar front (a span of roughly 35 million Km^2) the thermohaline stratification consists of cold surface water "floating", by virtue of its reduced salinity, over a much thicker stratum of warmer and saltier deep water (Bagriantsev et al. 1989). The top of the deep water is marked by temperature and salinity maxima and an oxygen minimum near 200 to 400 meters depth. The source of the warm/salty deep water mass is the circumpolar deep water, a blend of the world ocean's deep waters, including (but not exclusively composed of) the warm and salty North Atlantic Deep Water (NADW). The vigor of surface and deep water exchange within the antarctic

zone to a large measure determines the ventilating powers of the Southern Ocean, the characteristics of the seasonal sea ice cover and the coupling of the polar ocean with the atmosphere. The ventilation potential is strongly coupled to the frequency and size of polynyas, both of the coastal and offshore varieties (Gordon and Comiso, 1988). Polynyas are persistent breaks in an otherwise ice covered region; they are centers of extreme ocean atmosphere interaction (Smith et al. 1990).

Deep ocean vertical exchanges of ocean properties across the pycnocline during the winter are large enough to be a critical factor in sea-air heat exchange, the spring removal of the sea ice cover and in limiting winter sea ice thickness to substantially less than 1 meter (Gordon, 1981; Gordon and Huber, 1990). Static stability of the surface water depends for the most part on the fresh water budget, including the sea ice formation, melting and divergence rates. It is quite weak; small perturbations in the various factors which influence the surface salinity budget can overwhelm the pycnocline stability, inducing vigorous convection. However, it is likely that a powerful network of negative feedback mechanisms preserve the thin veneer of winter sea ice in a more-or-less stable configuration (Martinson, 1990). I refer to this type of stratification as the *saline mode.*

The Weddell Polynya of the mid-1970's (Carsey, 1980) is a dramatic example that another stratification mode can develop when the static stability of the saline mode is removed. The saline mode may be upset by additional salt (density) input to the surface mixed layer. Potential mechanisms for additional salt input are: increased wind induced sea ice divergence; decrease in the precipitation minus evaporation difference; stronger topographic induced oceanic upwelling; or perhaps by a colder and/or longer winter season (this topic discussed in section 4). Another stratification mode occurs within offshore polynyas. In this mode, increase of vertical heat flux accompanying persistent vigorous deep reaching convection, eliminates the sea ice cover, forming the polynya. The removal of the insulating sea ice cover permits enhanced ocean / atmospheric fluxes as the sea surface is exposed to the polar atmosphere. Continued convection ensues as relatively warm deep water carried to the sea surface is cooled by the atmosphere and sinks. I refer to this "polynya" condition as the *thermal mode.*

Vigorous modification of ocean water also occurs over the continental shelf of Antarctica. Satellite data reveal the frequent presence of coastal polynyas which are production centers for enormous quantities of sea ice which is transported seaward, leaving the coastal ocean exposed to the Antarctic air masses (Cavalieri and Martin, 1985; Zwally, et al. 1985). The heat flux into the atmosphere is supported by latent heat of fusion. Coastal polynyas are responsible for production of cold salty shelf water, dense enough to convect into the deep ocean. Thin sheets of dense shelf water are observed convecting down the slope (Foldvik, et al., 1985a,b), forming an essential ingredient of Antarctic Bottom Water (AABW; Carmack and Foster, 1975; Foster and Carmack, 1976; Foldvik, et al. 1985). Portions of shelf water temperatures are depressed by several tenths of a degree below the one atmosphere freezing point due to ocean / glacial ice exchanges (Ice Shelf

Water; Jacobs et al. 1985). This slight cooling may promote AABW formation as cold water is more compressible than warm water and therefore more susceptible to deep reaching convection (Killworth, 1979).

The link between the "ventilation potential" and frequency of the various polynyas types is being explored with observational and modelling methods. In this paper I first present a review of the impact of the Southern Ocean on global ocean characteristics and then discuss circumstances that might lead to offshore polynyas and deep ocean ventilation. Many ideas are offered that hopefully will encourage further consideration by oceanographers studying deep reaching ocean convection. For a complete discussion of the Southern Ocean circulation and water masses, the reader is referred to the review papers: Carmack 1986; Gordon, 1988; Patterson and Whitworth, 1990. Jacobs (1989) discusses the continental margin oceanography, specifically how it pertains to sedimentation. The companion papers of Gordon and Huber (1990) and Martinson (1990) present details of Southern Ocean Winter mixed layer characteristics with a quantitative treatment of observations and by model, respectively.

2. SOUTHERN OCEAN RELATION TO THE GLOBAL OCEAN

2.1 Water Masses

The Southern Ocean directly influences two strata within the global ocean (Fig. 1): there is the chilling effect of Antarctic Bottom Water, AABW and the the freshening influence of Antarctic Intermediate Water (AAIW). In the "classical" schematic of the Southern Ocean circulation and water masses developed by Deacon (1937) deep water drawn from the world ocean upwells to supply mass, heat and salt to the surface layer. The surface water migrates away from the Antarctic Divergence (average latitude of 65°S) towards Antarctica to the south and towards the Polar Front (often called the Antarctic Convergence; average latitude of 53°S) to the north, where it contributes to the sinking and northward spreading of the two basic Southern Ocean water masses- AABW and AAIW, respectively.

(i) Antarctic Bottom Water. The lower 2000 meters of the global ocean is dominated by AABW. About 57% of the deep ocean is colder than 2° C (determined from the temperature-salinity volumetric data supplied by Worthington, 1981). This is the percentage of ocean which must be influenced to some measure by AABW as the other major deep water mass, NADW, has a characteristic temperature near or above 2°C. The more intense influences of AABW occur below 1°C, which marks a stratum of stronger thermal gradients, a benthic thermocline (Fig. 1; and see

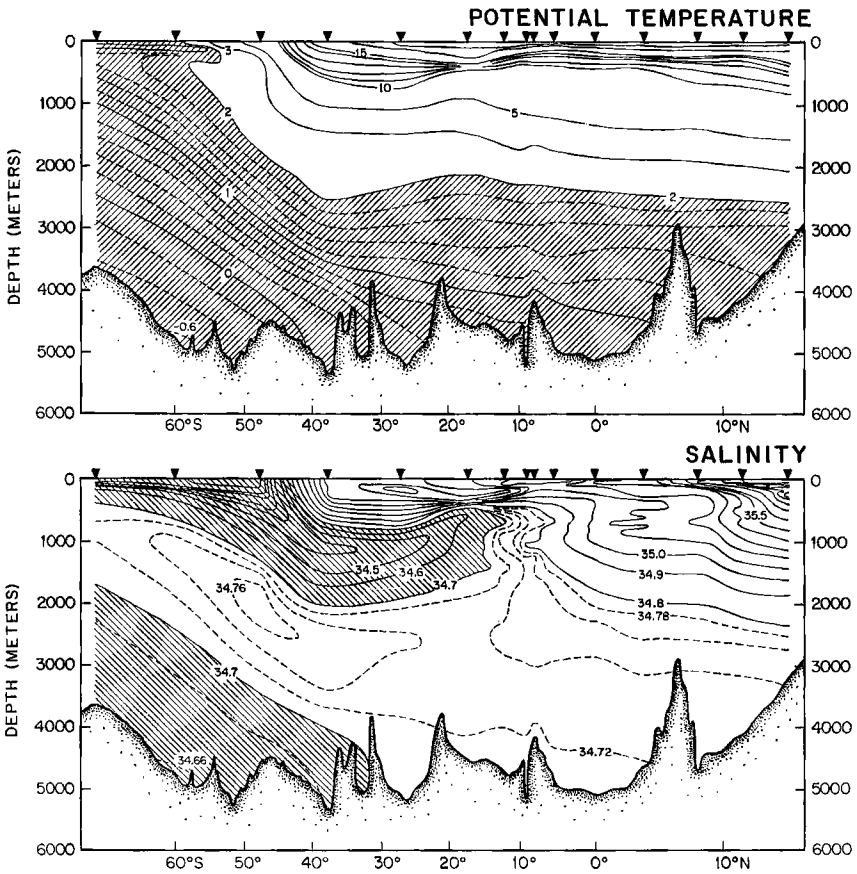

Fig.1. Potential temperature and salinity along the meridional plane in the western Indian Ocean, re-drawn from Spencer, et al., 1982. The hatched regions in each panel are vigorously influenced by Southern Ocean water masses. Southern Ocean water mass intrusion into the Indian Ocean is comparable to that of the Pacific and Atlantic Oceans.

the figures of Mantyla and Reid, 1983). Newly formed AABW is confined to temperatures well below 0°C, so its influence at higher temperatures requires mixing of purer forms of AABW into the overlying ocean. Mantyla and Reid (1983), who provide a review of the global spreading of AABW, conclude that the pure forms of AABW are hemmed in by circum-Antarctic ridges and it is

the mixtures of AABW with deep water that invade the global ocean. The most concentrated forms of AABW intrude into each ocean basin along specific routes (Fig. 2); eventually the cooling effects spread throughout the world ocean from these advective features.

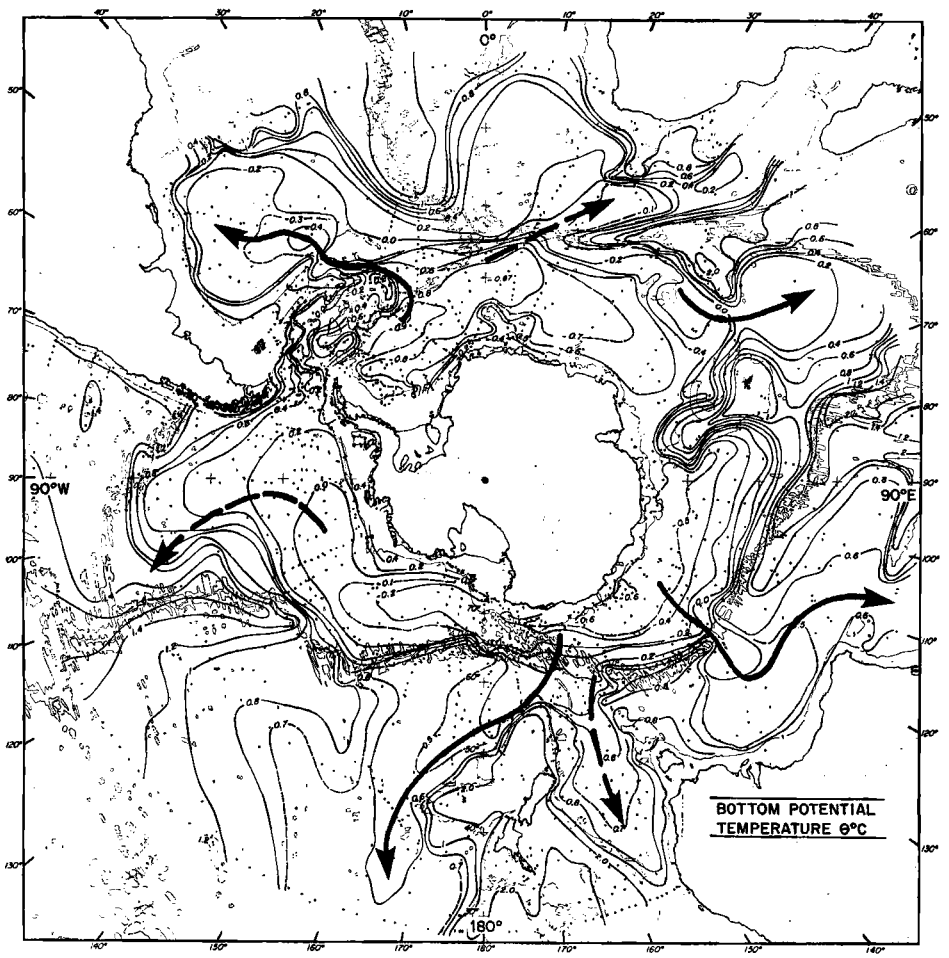

Fig. 2. Bottom potential temperature distribution of the Southern Ocean (Gordon and Molinelli, 1982, Plate 214). The primary escape routes of cold Antarctic Bottom Water into the global ocean are indicated by solid arrows. Northward flow into closed basins are shown with dashed lines.

There are two types of water mass formation leading to AABW: plume convection at the continental margins and open ocean convection.

The bulk of AABW is believed to be formed along the margins of Antarctica. The AABW formation process involves mixing of shelf and slope water across a well defined front, the Slope Front, in the vicinity of the shelf break (Foster and Carmack, 1976; Jacobs, in press). The Slope Front is observed around most of Antarctica, although the primary AABW production sites include the Weddell Sea whose output is a very cold variety of AABW and Ross Sea which contributes a somewhat warmer salty variety (Gordon, 1974; Jacobs et al. 1985). Other AABW formation sites along the continental margins of Antarctica are likely, including some where the convective plumes may not reach the sea floor, in what is called "not-quite-bottom water" by Carmack and Killworth, 1978.

Within the open ocean, there is an upper limit of mixed layer density imposed by the underlying deep water density. As this density is less than that achieved by continental shelf waters, open ocean convection cannot displace the products of the continental margins. On consideration of the cabbeling process, a mixed layer with salinity of 34.53 at the freezing point is sufficiently dense to initiate convection with the underlying deep water (Fofonoff, 1956; Carmack, 1986). Shelf water salinity above 34.7 at the freezing point is common (Gordon, 1974). The denser continental margin products spreading into the deep ocean, may be thought of as forming a "floor" for open ocean convection.

Water masses formed by open ocean convection have freer access to the north by isopycnal spreading and can pass above the ridge crests (Gordon, 1978, 1982). Perhaps it is the open ocean convective products that impose a greater constraint on deep ocean temperatures than continental margin produced AABW? The proportion of open ocean to margin water mass renewal determines the nature of Southern Ocean ventilation of the world ocean. Margin input may be quite steady as a reservoir of shelf water builds up over a period of years "behind" the confining walls of the Slope Front, while open ocean convection may be prone to more rapid changes (once the critical density is achieved convection quickly removes the anomalous surface water) and hence more sporadic in its occurrence. Open ocean convection most likely occurs every year but only in some years is it vigorous enough to massively cool the deep water. Formation of AABW may be strongly linked to the occurrence of coastal and offshore polynyas. Polynyas represent 'holes' in the insulating blanket of sea ice, with ocean/atmospheric heat flux 10 to 100 times that through the ice cover, which cool and elevate the salinity of the ocean (Smith et al. 1990).

(ii) Antarctic Intermediate Water. Salinity along the north-south plane within the western Indian Ocean (Fig. 1) reveals the freshening influence of polar surface water sinking and spreading near 1000-m (sigma-0 = 27.3) below the main thermocline. This is the AAIW (Deacon, 1937; Molinelli 1981; Piola and Georgi, 1982). Northward spreading of AAIW demarcates the lower boundary of the thermocline. The low salinity of AAIW allows cool water to be delivered to a low density stratum limiting the depth of the Southern Hemisphere's thermoclines, by limiting downward migration of low latitude heating. AAIW helps balance the global water budget by transferring polar excess precipitation into the evaporative subtropic regions. It also injects water of high oxygen into the lower thermocline, confining the subtropical oxygen minimum layer to the mid-thermocline.

A less dense variety of AAIW forms in the subpolar region just north of the polar front. It produces a water mass that invades the mid to lower thermocline, called Subantarctic Mode Water (SAMW, McCartney, 1977). It is drawn from deep winter mixed layer formed just north of the polar front zone and does not involve exchanges of water masses across the polar front zone. SAMW cools and freshens the thermoclines of the Southern Hemisphere at levels above that of the AAIW. SAMW injected into the Atlantic is relatively warm, near 14°C. SAMW of the Indian Ocean is about 10-12°C (its effect can be seen as a slight decrease in the vertical temperature gradient near 30°S on Fig. 1). In the Pacific SAMW is near 8°C in the west and 5°C in the east. Might AAIW represent the end-product of SAMW as suggested by McCartney? Georgi (1979) and Piola and Georgi (1982) consider this question, concluding that it is unlikely that the 5°C SAMW of the southeast Pacific flowing into the Atlantic could, with further modification by sea-air fluxes, account for AAIW. They find significant input of surface water from south of the Polar Front is required to achieve the conversion of SAMW into AAIW. However, the broad and multi-water type characteristic of the S-min in the southwestern Atlantic indicates a complex history for AAIW (Piola and Gordon, 1989) and the issue of the origin of the AAIW salinity minimum in the Atlantic and other oceans requires further research.

While the specific water types of AABW and AAIW are confined to a narrow density range, vertical mixing can carry their effects into other density strata. Additionally, the array of water masses of the Southern Ocean margins covers the full range of deep ocean density (Fig. 3), thus there is the potential for direct spreading of Southern Ocean water into the global ocean interior by isopycnal or neutral spreading surfaces, a point discussed in the next section.

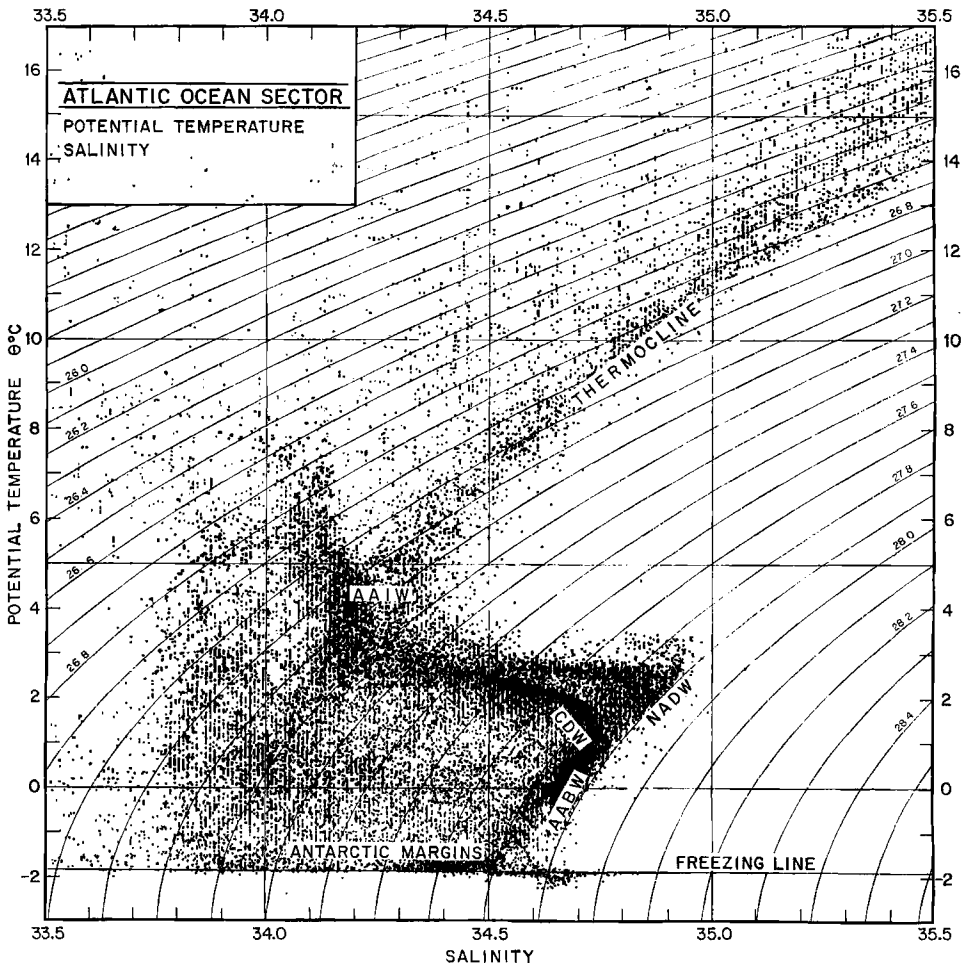

Fig. 3. Potential temperature versus salinity for the Atlantic sector of the Southern Ocean (south of 30°S). The deep waters of the ocean are labelled CDW-AABW (CDW- Circumpolar Deep Water; AABW- Antarctic Bottom Water). The coldest water represents the continental margin region, where waters dense enough to interact with the CDW-AABW density horizons are present.

2.2 Circumpolar Belt

Significant meridional advection of ocean water, outside of the Ekman Layer, requires a western boundary to supply the required vorticity. The lack of continuous western boundary

across the deep circum-Antarctic belt disallows advection of warm upper layer waters into the Southern Ocean. Establishment of the deep ocean band with the resident zonally flowing powerful Antarctic Circumpolar Current (ACC), inhibits meridional advection which tends to thermally isolate Antarctica. Sea ice and some continental glaciation probably began 38 million years ago as the circumpolar band was forming, with a persistent glacial ice sheet developing 11-14 million years ago (Kennett, 1977) as the circumpolar belt became fully established. With the cooling of the Southern polar regions came cooling of the deep ocean. Deep ocean temperatures at the end of the Eocene 38 million years ago were well above 10° C, falling below 5°C by mid-Miocene, 13 million years ago to the present day values of near 0°C (Shackleton and Kennett, 1975a, b).

The circumpolar oceanic belt has two competing effects: it isolates the Southern Ocean from the rest of the ocean, which limits its influence, but it also allows what does spread to the north to attain colder temperature increasing its chilling global impact. As the "completeness" of the circumpolar belt decreases with increasing depth, southern ocean water mass access to the ocean north of the circumpolar belt depends on depth or density horizon. At shallow depths meridional spreading may be limited to eddy processes and Ekman Layer transport. At deeper levels topographic channels guide deep and bottom currents across latitudes. At great depth, isolated pools of water without direct access to the north occur; their properties can spread northward only if they can mix vertically to shallower levels. Using a global ocean model, Cox (1989) concludes that establishment of the ACC limits northern penetration of cold antarctic water masses into the northern oceans. Of course, were there no ACC there probably would not be any cold polar water sufficiently dense to influence the deep global ocean. On balance it is likely that global spreading of cold Southern Ocean water masses, albeit hindered by the circumpolar belt, has a fundamental chilling effect on the global ocean.

It is likely that the present day circulation pattern with effective deep ocean cooling is related to the ice sheet reaching the coastal region (Hays, 1967). A fully glaciered Antarctica allows very cold air to reach the coastal ocean, forming cold shelf water that feeds formation of AABW (Gordon, 1971). An additional effect may be the depression of continental margins under the weight of the glacial ice sheet. The Antarctic continental shelf averages 500 m (Jacobs, 1989), significantly greater than the other continental blocks. This allows contact of the cold shelf water with the warmer open ocean deep water at elevated hydrostatic pressure across the base of the shelf-slope front, particularly within deeper shelf channels, such as the Filchner Depression of the Weddell Sea. The greater compressibility of cold water has an interesting effect in the Southern Ocean (Killworth, 1979): cold water not dense enough to convect into the deep ocean at one atmosphere pressure, can do so if it can be depressed in depth by a matter of a few hundred meters. Formation of very cold, dense shelf water coupled with a deep continental shelf may act together to encourage deep convection and cool the global ocean.

While warm upper layer water is prohibited from advecting into polar regions, the geostrophic balance of the ACC allows deep and bottom water to have isopycnal access to the cold polar atmosphere (Fig. 3). Density characteristic of the sea floor north of the ACC is found near the sea surface to the south of the ACC. Exposure of this dense water to the cold antarctic atmosphere produces cold water which can then mix along isopycnal (or more precisely, neutral surfaces as defined by McDougall, 1987 should be applied to the Southern Ocean condition) surfaces into the deep and bottom strata of the world ocean. It is interesting to note that with the present day density field, the baroclinic transport of the ACC, which amounts to about 90 x 10^6 m^3sec^{-1} (90 Sv) or 70% of the full transport (Whitworth, 1983; Whitworth and Peterson, 1985), is at a maximum. An increase in the ACC baroclinic component would require an increase in the strength of the stratification within the Southern Hemisphere subtropical water column. Without changing the baroclinic field of mass the ACC transport can increase only within the barotropic mode. The similarity of benthic density of the global ocean and the densest water exposed to the antarctic atmosphere represents coupling of the overall wind and buoyancy driven circulation.

3 ANTARCTIC ZONE STRATIFICATION AND POLYNYAS

The sea ice cover of the Southern Ocean acts to decouple the ocean from the atmosphere, limiting cooling of the ocean by the polar atmosphere. The insulating blanket of sea ice protects the ocean from the cold atmosphere. The extreme seasonality and rapid spring melting suggests an ocean heat role in Southern Ocean sea ice budget (Gordon, 1981): the build up of heat within the mixed layer induces melting even before the atmospheric radiation balance and temperatures warm sufficiently to melt ice directly. Ocean heat flux also limits sea ice thickness during the winter (Gordon and Huber, 1984, 1990).

As mixed layer / deep water exchange with associated vertical oceanic heat and salinity flux is responsible for the spring melt and limited winter sea ice thickness, we may consider that the vigor of Southern Ocean ventilation potential is directly related to sea ice seasonality, e.g. year-round constant sea ice cover is indicative of a strongly stratified ocean with small vertical heat flux, whereas a strongly seasonal ice cover is linked to substantial vertical oceanic fluxes, which melts the ice cover as the spring atmosphere heat budget cannot remove the oceanic heat flux. Variations in vertical heat flux are expected to yield interannual changes in ice cover extent and seasonality.

Extreme events do occur, such as the drastic cooling of the water column down to 3000-m within the Weddell Gyre (near Greenwich Meridian and 63°S) during the Weddell Polynya event of the mid-1970's (Fig 4; also see Bersch, 1988). Salinity and density profiles indicates the cooling was accomplished by deep reaching convection. While the large Weddell Polynya was observed only in the mid-1970's, small short lived polynya events are common (Comiso and Gordon,

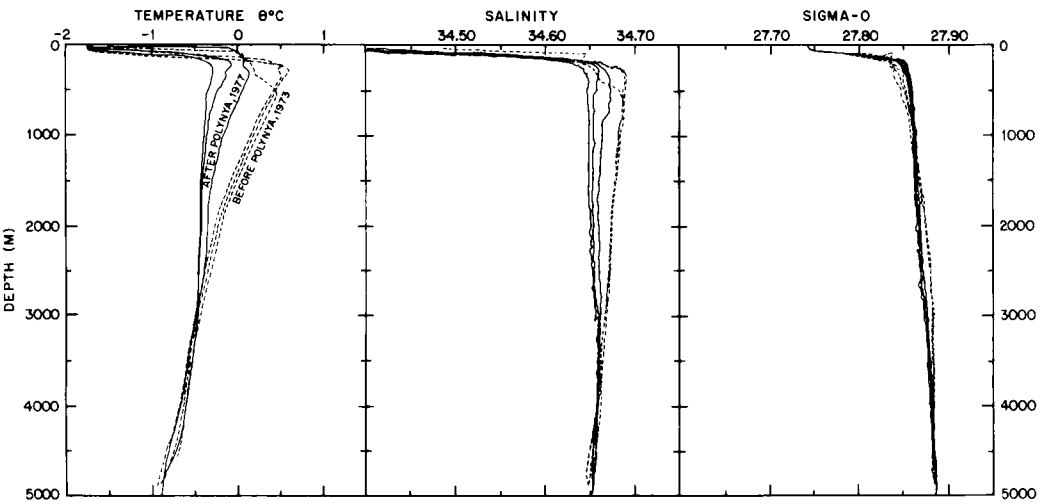

Fig. 4. Potential temperature, salinity and density profiles before and after the Weddell Polynya occurrence of 1974-1976 (data from the central region of the Weddell Gyre, redrawn from Gordon, 1982).

1987). It is likely that these transient polynyas are coupled to sporadic deep reaching convective cells .

There may be signs of sporadic convection in the details of the deep potential temperature (θ)/ salinity (S) relationship. The θ/S between the salinity maximum stratum of the Weddell Deep Water (WDW) and the AABW cold end-member while nearly linear within the Weddell Gyre, does display slight non-linear structure. The θ/S structure is slightly curved, with a salinity deficit

relative to a straight line (Fig. 5). The greatest negative salinity anomaly occurs near the -0.2°C level amounting to only 0.005 relative to the reference straight line between warm and cold end-

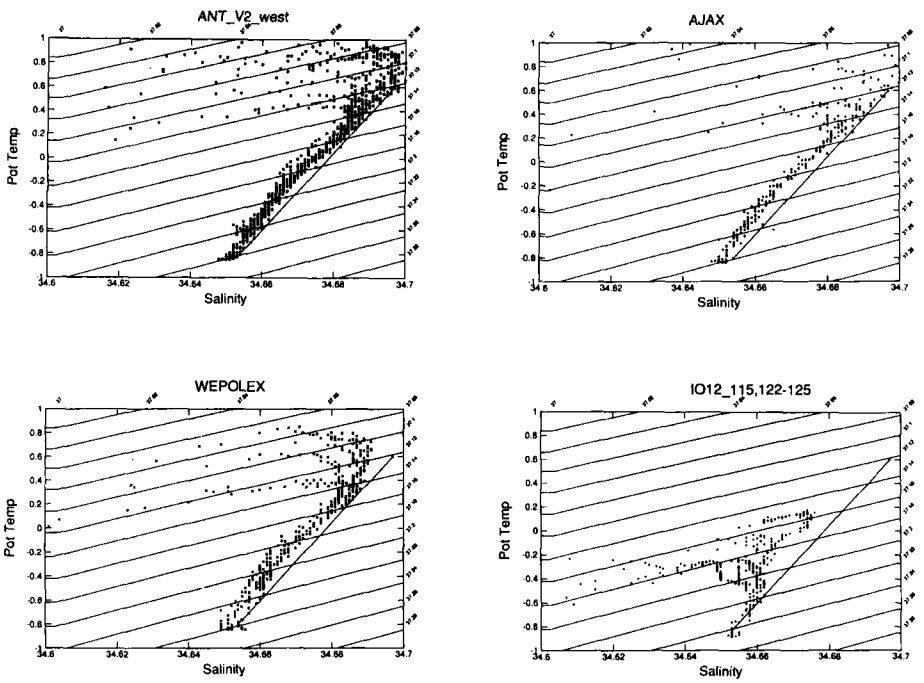

Fig. 5. Potential temperature versus salinity for the deep and bottom water of the central region of the Weddell Gyre. A reference straight line connecting the warmer and colder end-members along their saltier edge of scatter, is placed on the θ/S of representative stations from: ISLAS ORCADAS cruise 12-77 (1977) stations within the region cooled by the 1970's Weddell Polynya (same stations as shown in Fig. 4, with the addition of station 115, which was obtained within a remnant convective chimney of the previous Winter, Gordon, 1978); WEPOLEX, 1981 (Huber et al. 1983); Ajax, 1984 (Ajax Data Report, 1985); and the 1986 data set from POLARSTERN ANT V/2 (Huber et al. 1989).

members. The negative salinity anomaly is barely perceptible but it is present in all of the modern high precision CTD expeditions crossing the Weddell Gyre near the Greenwich Meridian. The ISLAS ORCADAS data set of 1977, obtained after the three year occurrence of the persistent Weddell Polynya, shows extreme low salinity within the deep water (also see Fig. 4). Station 115 was obtained within what was considered a remnant of a convective chimney associated with the Weddell Polynya (Gordon, 1978). The salinity anomaly of 1977 amounting to 0.01 is centered near -0.2°C.

Gordon (1978) suggested that the vigorous convective event of the mid-1970's associated with the Weddell Polynya, drastically modified the deep water, centered at the -0.2°C level, by injecting low salinity surface water into the deep water. In subsequent years, during which there were only brief, small polynyas near the Greenwich Meridian (Comiso and Gordon, 1987), sporadic convection only slightly modified the deep water from a simple straight line mixing curve between WDW and AABW end-members. It is hypothesized that the WDW/AABW θ/S structure is the product of three water types: 1- warmest is the WDW drawn into the Weddell Gyre from the circumpolar deep water; 2- the coldest is AABW formed along the margins of Antarctica; and 3- the middle layer is due to an injection of low salinity surface water by convection. The convection is usually too weak to greatly alter the deep water θ/S , except during persistent large Weddell Polynya events. This hypothesis of sporadic deep convection as the origin of the slight θ/S inflection must be evaluated with high precision data and perhaps with models. It should be evaluated against possible lateral injection of low salinity water, such as the "not-quite-bottom - water" concept of Carmack and Killworth (1978).

4 STAGES OF WINTER AND FORMATION OF OFFSHORE POLYNYAS

Winter observations from the POLARSTERN along the Greenwich Meridian from the ice edge to the Antarctic margin show the mixed layer beneath the winter sea ice cover is "contaminated" with WDW (Gordon and Huber, 1990). WDW introduces heat and salinity into the surface layer which strongly influences the mixed layer stability, sea-air exchanges and sea ice formation processes. The total WDW transfer into the mixed layer along the Greenwich Meridian from the ice edge to the margins of Antarctic averages 45 meters/year (40% of the mixed layer thickness), occurring mostly during the Winter season at a rate as high as 0.4 m/day. The winter heat flux of approximately 40 W/m^2 limits ice thickness to about 55 cm, agreeing quite well with observations (Wadhams et al. 1988). The air temperatures measured during the 1986 POLARSTERN cruise are just sufficient to remove the WDW heat input in the presence of observed ice thickness and concentration. This suggests that the sea ice cover and WDW heat input into the mixed layer are in approximate balance by mid-winter. Late winter measurements indicate that deep water entrainment into the mixed layer continues beyond mid-winter (Gordon and Huber,

1990). Can the WDW deliver enough heat and salt to eventually remove the ice and induce a polynya, i.e. a switch from the saline to the thermal mode?

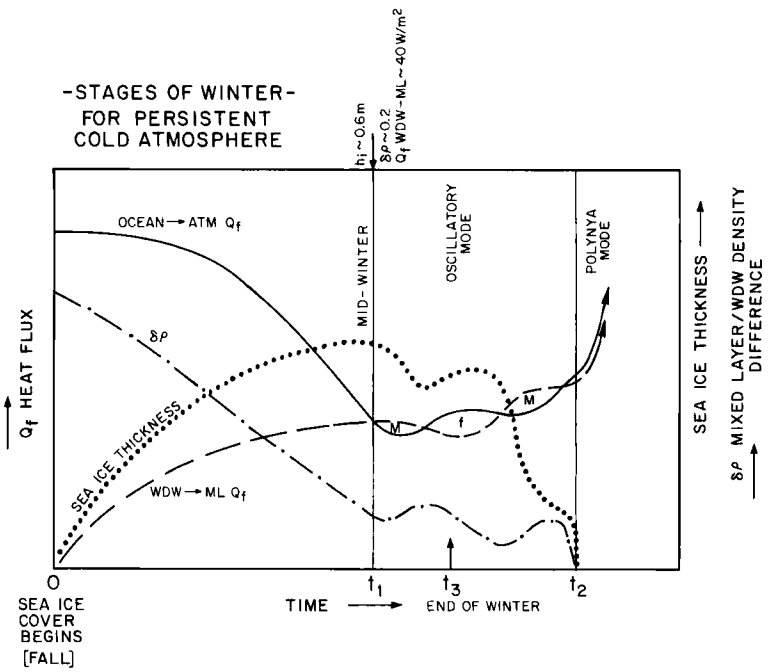

Fig. 6. Schematic of the possible fluxes during the winter period, see text. The schematic depicts expected trends of ice thickness, mixed layer static stability, and vertical heat fluxes for a constant atmosphere. Vertical scales are not shown, it is more the concept that is offered at this point. t_1= time (mid-Winter) when an equilibrium is reached between heat flux, sea ice thickness and air temperature. t_2 = start of an offshore polynya, the switch to a thermal mode of stratification. t_3 = the end of winter, when air temperatures warm.

A schematic representation of the events during winter which might trigger a switch from the saline to thermal mode is presented in Fig. 6. The schematic depicts expected trends of ice thickness, mixed layer static stability, and vertical heat fluxes for a constant atmosphere. Vertical scales are not shown, it is the concept that is offered at this point. Various mixed layer models deal with aspects of this process. See Martinson, 1990 for a model which described to the conditions encountered during the 1986 POLARSTERN expedition.

The 1986 data suggest that an equilibrium is reached between heat flux, sea ice thickness and air temperature by mid-winter (t_1). At this point heat transfer from WDW to the mixed layer balances heat loss to the atmosphere through leads and by conduction through the ice. After time t_1 as WDW to mixed layer transfer continues, the salt build up within the mixed layer decreases the density contrast across the pycnocline, allowing increased entrainment and inducing sea ice melt. Ice melt stabilizes the mixed layer, reducing WDW entrainment. If the air remains cold there can be a re-growth of sea ice, though not to its former thickness. Oscillation between ice growth and melt is expected to occur until the end of winter, t_3, when the air temperature increases, stopping further ice growth.

The point when the build up of mixed layer salt removes the pycnocline and a polynya ensues is marked by t_2. Does t_3 (the end of the winter cold) occur earlier or later than t_2 (start of an offshore polynya)? How long would it take to attain polynya state? A simple calculation based on the 1986 WDW entrainment rates indicates that with a daily entrainment of WDW into the mixed layer of approximately 0.4 m/day, many 100's of additional Winter days beyond the mid-Winter point of t_1 are required to substantially boost the mixed layer salinity and remove the pycnocline. This time is too long to attain a polynya thermal mode state within a single winter. Even with additional entrainment permitted by the diminishing pycnocline strength (mean of 1.0 m/day) and by sea ice divergence (half of the ice thickness is carried away and does not melt locally) it would still require three months of additional "Winter" months to reach convection. Clearly careful modelling of the coupled ocean / sea ice/ atmosphere system is needed, but it appears that unless: 1- the winter becomes much colder or longer, or 2- the wind field can spin-up the baroclinic flow sufficiently to shallow the pycnocline or increase sea ice divergences for specific regions, or 3- as Martinson, 1990 points out- WDW becomes saltier without a matching increase in temperature, the network of negative feedbacks which presently provide stability to the saline mode of stratification cannot easily be broken within the confines of a single winter. A multi-year build up of mixed layer salinity might be required to initiate a polynya condition.

While it seems unlikely that the present saline mode of stratification can be overcome with the present ocean / sea ice / atmosphere coupling, offshore polynyas do occur, so the thermal mode can be achieved (see Martinson, 1991, for further discussion).. Gordon and Huber (1990) suggest

that excess salt required to destabilize the stratification is derived from an external source. This source may be enhanced upwelling over topographic features, e.g. Maud Rise.

As a consequence of circulation/topography interaction, the Maud Rise water column stands out as an anomaly relative to the surrounding region, with a significantly more saline and dense mixed layer. The saline mixed layer probably represents a salt build up of more than a single Winter. The Maud Rise mixed layer salinity represents a balance between enhanced upwelling and exchanges with the surrounding region. Below the mixed layer the water column over the crest of the Rise is identical to that over the flanks if the latter water column is upwelled by 400 meters. This uplifting is believed to be a response of the upstream flow encountering the Rise. Increased upstream flow would be expected to increase Maud Rise upwelling and the dependent salinity (density) of the mixed layer (e.g. Hubbert and Bryan, 1978). Slight increases in the mixed layer density could trigger a convective thermal mode and generation of a polynya.

It is hypothesized that spin up of the Weddell Gyre's barotropic circulation induced by an increase of the regional wind stress curl would enhance the probability of polynya development over the flanks of Maud Rise. The Weddell Polynya of the mid-1970's and transient polynyas since then, form over the northern flank of Maud Rise, which is expected to be the primary route for westward flowing water encountering Maud Rise.

The sequence of events leading to a polynya may be as follows-

1- An increase of the regional wind stress curl spins up the barotropic circulation of the Weddell Gyre, with a response time on the order of months. A slower baroclinic response also works towards the thermal mode as gyre spin-up shoals the pycnocline, but with time scales of years or decades;

2- Upwelling over topographic features, such as Maud Rise, increases;

3- The vulnerability to a switch-over from the saline (sea ice covered) mode to the thermal convective (polynya) mode is enhanced as more salt is delivered to the overlying mixed layer by the topographic induced upwelling.

4- The thermal mode continues, until fresh water invades the convective region and damps out the convection (Martinson, et al. 1981). The temporary polynyas are small enough for large storms to 'blow' in enough of the surrounding ice to shut-down convection. For large polynyas individual storms may not be sufficient; the large Weddell Polynya was shut down as it drifted with the mean circulation into a convergent sea ice region of the western Weddell Gyre (Martinson, et al. 1981).

5 CONCLUSIONS

Southern Ocean water masses ventilate the global ocean. They have played this role since the establishment of the deep reaching circum-Antarctic oceanic belt. Formation of Southern Ocean water masses are associated with exposure of the ocean to the frigid Winter atmosphere within coastal and offshore polynyas. The coastal polynyas may be the primary feature responsible for

formation of the densest Southern Ocean water mass, the AABW. Offshore, the stratification is occasionally altered from the common salinity stabilized mode to the convectively active thermal mode. The thermal mode produces an offshore polynya. This is achieved by introduction of excess salt into the winter mixed layer. The most likely candidate to accomplish this task is eddy generation and upwelling induced by circulation and topography interaction. Deep reaching convection probably occurs each year, but massive overturning capable of greatly altering the deep water θ/S structure is reserved for the persistent offshore polynya events, represented by the Weddell Polynya of the mid-1970s.

Acknowledgements-

The author's Southern Ocean research is presently supported by the National Science Foundation Division of Polar Program grant DPP 90-08906. Additionally NASA grant NAGW 1752 covers study of polynya occurrences as seen in satellite microwave images. Lamont-Doherty Geological Contribution number 4721.

References-

Ajax Data Report, 1985. Physical, Chemical and In-Situ CTD Data from the Ajax Expedition in the South Atlantic Ocean, aboard RV KNORR Leg I: 7 October - 6 November 1983 Leg II: 11 January - 19 February 1984. University of California Scripps Inst. of Oceanography and Texas A&M Univ. Dept. of Oceanography. SI0 Reference 85-24, TAMU Reference 85-4-D.

Bersch, M. 1988. On Deep Convection in the Weddell Gyre, Deep-Sea Res., 35(8A): 1269-1296.

Bagriantsev, N. V., A. L. Gordon, and B. A. Huber, 1989. Weddell Gyre temperature maximum stratum. J. Geophys. Res., 94(C6): 8331-8334.

Carmack, E. C. 1986. Circulation and Mixing in Ice-Covered Waters. In: "The Geophysics of Sea Ice" ed. N. Untersteiner, Plenum Press, pages 641-712.

Carmack, E. C. and T. D. Foster, 1975. On the flow of water out of the Weddell Sea, Deep-Sea Res., 22: 711-724.

Carmack, E. C. and P. D. Killworth 1978. Formation and interleaving of abyssal water masses off Wilkes Land, Antarctica. Deep Sea Res. 25: 357-369.

Carsey, F. D., 1980. Microwave observations of the Weddell Polynya. Mon. Wea. Rev., 108: 2032-2044.

Cavalieri, D. J. and Martin, S., 1985. A passive microwave study of polynyas along the Antarctic Wilkes Land Coast. Oceanology of the Antarctic Continental Shelf, Ant. Res. Ser. 43, Am. Geophys. Un., Wash. D.C., pp. 227-252.

Comiso, J. C. and A. L. Gordon, 1987. Recurring polynyas over the Cosmonaut Sea and the Maud Rise. J. Geophys. Res., 92(C3): 2819-2833.

Cox, M. D. 1989. An idealized model of the world ocean. Part I: The global-scale water masses. Jour. Phys. Oceano. 19(11): 1730-1752.

Deacon, G.E.R. 1937. The Hydrology of the Southern Ocean. Discovery Reports XV:1-124.

Fofonoff, N. P. 1956. Some properties of sea water influencing the formation of antarctic bottom water. Deep Sea Res. 4: 32-35.

Foldvik, A., T. Gammelsrod, and T. Torresen, 1985a. Circulation and water masses on the southern Weddell Sea shelf. In: Oceanology of the Antarctic Continental Shelf, Ant. Res. Ser., 43, Am. Geop. Un., Wash. pp. 5-20.

Foldvik, A., T. Kvinge and T. Torresen, 1985b. Bottom currents near the continental shelf break in the Weddell Sea. In: Oceanology of the Antarctic Continental Shelf, Ant. Res. Ser., 43, Am. Geop. Un., Wash. pp. 21-34.

Foster, T. D. and E. C. Carmack, 1976. Frontal zone mixing and Antarctic Bottom Water formation in the southern Weddell Sea. Deep-Sea Res., 23: 301-317.

Georgi, D. T., 1979. Modal properties of Antarctic Intermediate Water in the southeast Pacific and the South Atlantic. J. Phys. Oceanogr., 9(3): 456-468.

Gordon, A. L. 1971. "Oceanography of Antarctic Waters". In: Antarctic Oceanology I, Vol. 15, AGU Antarctic Research Series, ed., J. L. Reid: pp. 169-203.

Gordon, A .L. , 1978. Deep Antarctic convection west of Maud Rise. J. Phys. Oceanogr., 8(4): 600-612.

Gordon, A. L. 1974. Varieties and variability of Antarctic bottom water, in: Processus de Formation des Eaux Oceaniques Profondes (en particulier en Mediterranee Occidentale). Editions du Centre National de la Recherche Scientifique, Paris, France, No. 215: pp. 33-47.

Gordon, A. L., 1981. Seasonality of Southern Ocean sea ice. J. Geophys. Res., 86: 4193-4197.

Gordon, A. L., 1982. Weddell deep water variability. J. Mar. Res., 40(suppl): 199-217.

Gordon, A. L., 1988 Southern oceans and global climate. Oceanus, 31(2): 39-46.

Gordon, A. L. and J. C. Comiso, 1988. Polynyas in the Southern Ocean. Sci. Am., 256(6): 90-97.

Gordon, A. L. and B. A. Huber, 1984. Thermohaline stratification below the Southern Ocean sea ice. J. Geophys. Res., 89(C1): 641-648.

Gordon, A. L. and B. A. Huber, 1990. Southern Ocean Winter mixed layer. Jour. Geop. Res. 95(C7): 11,655-11,672.

Gordon, A. L. and E. J. Molinelli, *Southern Ocean Atlas* . Columbia University, New York,1982.

Huppert, H. E. and K. Bryan, 1976. Topographically generated eddies. Deep-Sea Res., 23: 655-679.

Hays, J. D. (1967). Quaternary sediments of the Antarctic Ocean. Progress in Oceanography Vol 4: 117-131.

Huber, B.A., J. Jennings, C. Chen, J. Marra, S. Rennie, P. Mele and A. Gordon 1983 Reports of the US-USSR Weddell Polynya Expedition, October - November, 1981, Hydrographic Data. Lamont-Doherty report -83-1.

Huber, B. A., P. Mele and A. Gordon, Report of the Winter Weddell Sea Project, ANT V/2, Hydrographic data. L-DGO-89-1, Lamont-Doherty Geological Observatory, Palisades, N.Y., 1989.

Jacobs, S., R. Fairbanks and Y. Horibe, 1985. Origin and evolution of water masses near the Antarctic continental margin: Evidence from H_2 $^{18}O/H^2$ $^{16}0$ ratios in seawater. In: Oceanology of the Antarctic Continental Shelf, Ant. Res. Ser., 43, Am. Geop Un., Wash., pp. 59-85.

Jacobs, S. S. 1989. Marine controls on modern sedimentation on the Antarctic continental shelf. Marine Geol. 85: 121-153.

Jacobs, S. S. (submitted for publication) On the Nature and Significance of the Antarctic Slope Front. Proceedings Volume of the Brest Symposium, "The Biogeochemistry and the Circulation of Water Masses in the Southern Ocean".

Kennett, J. P. 1977. Cenozoic evolution of Antarctic glaciation, the circum-antarctic ocean, and their impact on global paleoceanography. Jour. Geop. Res. 82(27): 3843-3860.

Killworth, P. D., 1979. On "chimney" formations in the ocean. J. Phys. Oceanogr., 9(3): 531-554.

Mantyla, A. W. and J. L. Reid (1983). Abyssal characteristics of the World Ocean waters. Deep Sea Res. 30(8A): 805-833.

Martinson, D. G., 1991. Open ocean convection in the Southern Ocean. This Volume.

Martinson, D. G, 1990. Evolution of the Southern Ocean winter mixed layer and sea-ice: open ocean deepwater formation and ventilation. *Jour. Geop. Res.* 95(C7): 11,641-11,654

Martinson, D. G., P. D. Killworth, and A. L. Gordon, 1981. A convective model for the Weddell Polynya. J. Phys. Oceanogr., 11(4): 466-488.

McCartney, M. 1977. Subantarctic mode water. In: A Voyage of Discovery, M. Angel, editor, Supplement to Deep Sea Res. 24: 103-119.

McDougall, T. J. 1987. Neutral Surfaces. Jour. Phys. Oceano., 17: 1950-1964.

Molinelli, E. 1981. The Antarctic influence on Antarctic Intermediate Water. Jour. Mar. Res. 39: 267-293.

Patterson, S. L. and T. Whitworth, 1990. "Physical Oceanography" In: Antarctic Sector of the Pacific, ed. G.P.Glasby. Elsevier pages 55-93.

Piola, A. R. and A. L. Gordon, 1989. Intermediate waters in the southwest South Atlantic. Deep-Sea Res., 36: 1-16.

Piola, A. R. and D. T. Georgi, 1982. Circumpolar properties of Antarctic Intermediate Water and Subantarctic Mode Water. Deep-Sea Res., 29(6A): 687-711.

Shackleton, N. J. and J. P. Kennett, 1975a. Cenozoic oxygen and carbon isotope changes at DSDP site 284: Implications for glacial history of the northern hemisphere and Antarctica. In: Initial Reports of the Deep Sea Drilling Project, vol 29, p 801. US Government Printing Office, Washington, D.C.

Shackleton, N. J. and J. P. Kennett, 1975b. Paleotemperature history of the Cenozoic and the initiation of Antarctic glaciation: Oxygen and carbon isotope analysis in DSDP sites 277, 279 and 281. In: Initial Reports of the Deep Sea Drilling Project, vol 29, p 743. US Government Printing Office, Washington, D.C.

Smith, S., Muench, R. and C. Pease, 1990. Polynyas and Leads: an overview of physical processes and environment. Jour. Geop. Res. 95(C6): 9461- 9480.

Spencer, D., W. Broecker, H. Craig and R. Weiss, 1982. Geosecs Indian Ocean Expedition, Volume 6, sections and profiles. National Science Foundation, Wash D.C. 140 pages.

Wadhams, P., M. Lange, and S. Ackley, 1987. The ice thickness distribution across the Atlantic sector of the Antarctic Ocean in midwinter. J. Geophys. Res., 92(C13): 14,535-14,552.

Whitworth, T., III, 1983. Monitoring the transport of the Antarctic Circumpolar Current at Drake Passage. JPO, 13: 2045-2057.

Whitworth, T. III and R. G. Peterson, 1985. The volume transport of the Antarctic Circumpolar current from three-year bottom pressure measurements. J. Phys. Oceanogr., 15(6): 810-816.

Worthington, L.V., 1981. The water masses of the world ocean: Some result of a fine-scale census. Evolution of Physical Oceanography, Scientific Surveys in Honor of Henry Stommel, B.A. Warren and C. Wunsch, Eds., MIT Press, pp. 42-69.

Zwally, J., J. Comiso and A.L. Gordon, 1985. Antarctic offshore leads and polynyas and oceanographic effects. In: Oceanology of the Antarctic Continental Shelf, Ant. Res. Ser., 43, Am. Geop. Un., Wash. pp. 203-226.

This Page Intentionally Left Blank

OPEN OCEAN CONVECTION IN THE SOUTHERN OCEAN

D. G. MARTINSON
Lamont-Doherty Geological Observatory and Department of Geological Sciences, Columbia University, Palisades, New York 10964 (USA)

ABSTRACT

Observations and model studies suggest that the Weddell polynya was the surface manifestation of significant deep convection in the open ocean region of the Southern Ocean. The large polynya was only present throughout the austral winters of 1974-1976, though small short-lived versions were observed in 1973, 1977 and possibly 1980. Historical evidence suggests that there may have been an episode of convection in 1960 as well. The Cosmonaut Sea is also a region of potential convection as evidenced by an irregularly occurring polynya in that region. Recent model results and observational evidence suggest that the deep convection is initiated by a destabilization of the winter surface layer. The tendency toward destabilization is shown to be driven by any of the following changes in local conditions: (1) doming of the permanent pycnocline; (2) decreasing the static stability; (3) decreasing the ratio of heat to salt across the pycnocline; (4) increasing the heat loss from the ocean to the atmosphere; (5) decreasing the heat flux into the mixed layer from the deep ocean. Ice drift plays a key role in this problem since it represents the dominant term controlling the surface freshwater balance. A complementary relationship is suggested between shelf and open ocean mechanisms of deep water formation. Periods of enhanced divergence increase the exportation of shelf ice to the open ocean regions. The associated increase in coastal salinization aids deep water formation along the shelves while the exported ice acts to stabilize the open ocean region through additional meltwater. Given a reduction in the divergence, the opposite would occur.

1 INTRODUCTION

In 1921, Brennecke speculated that Antarctic Bottom Water (AABW) was formed along the Antarctic continental shelves, driven by intense cooling and salt rejection associated with sea ice formation. Wüst (1928), later speculated that this shelf mechanism was insufficient to account for the large volume of bottom water of Antarctic origin observed throughout the Southern Hemisphere. He suggested that open ocean deep convection, like that proposed by Nansen (1912) for deep water formation in the Arctic, must also occur in the Weddell region [specifically in the center of the cyclonic gyres noted by Meyer (1923) at 65° S, 30° W and 60° S, 30° E, though he later changed the location (Wüst, 1933) to the convergence region at the polar front]. While the shelf mechanism of Brennecke (1921) was accepted immediately, Mosby (1934) cast doubt on Wüst's open ocean deep convection mechanism, claiming it was impossible because of the stable stratification implied by the low salinity of the summer T_{min} water which represented the winter surface water.

Wüst was correct however, and it is ironic that the first solid evidence supporting his deep convection mechanism was not obtained until the year of his death (1977), nearly 50 years after he proposed it. The purpose of this paper is to review this evidence for open ocean convection in the Southern Ocean; describe the local processes and interactions controlling such convection; and, consider the likelihood of convection given changes in the regional setting and forcing.

2 EVIDENCE FOR DEEP CONVECTION

Throughout the austral winters of 1974-1976, microwave satellite imagery revealed a large area of ice free water (Figure 1) deep in the Antarctic pack ice (Zwally et al., 1976; Zwally and Gloersen, 1977). This ~350,000 km^2 open ocean polynya occurred near the center of the Weddell-Enderby gyre and occupied ~10% of its area. Smaller, short-lived versions of the polynya appeared in the winter of 1973 and at the end of the winter of 1977 (see Figure 1). The spatial position of the polynya shifted westward each year at a rate comparable to the estimated wind driven current speed (Carsey, 1980; Martinson et al., 1981) and the polynya's shape, elongated in the drift direction, was remarkably coherent from year to year (Carsey, 1980). Zwally et al. (1976) speculated that the polynya represented an area of anomalously high ocean heat flux due to the upwelling of warm deep water associated with the Antarctic divergence, and that this would likely "enhance the formation of Antarctic Bottom Water in this region".

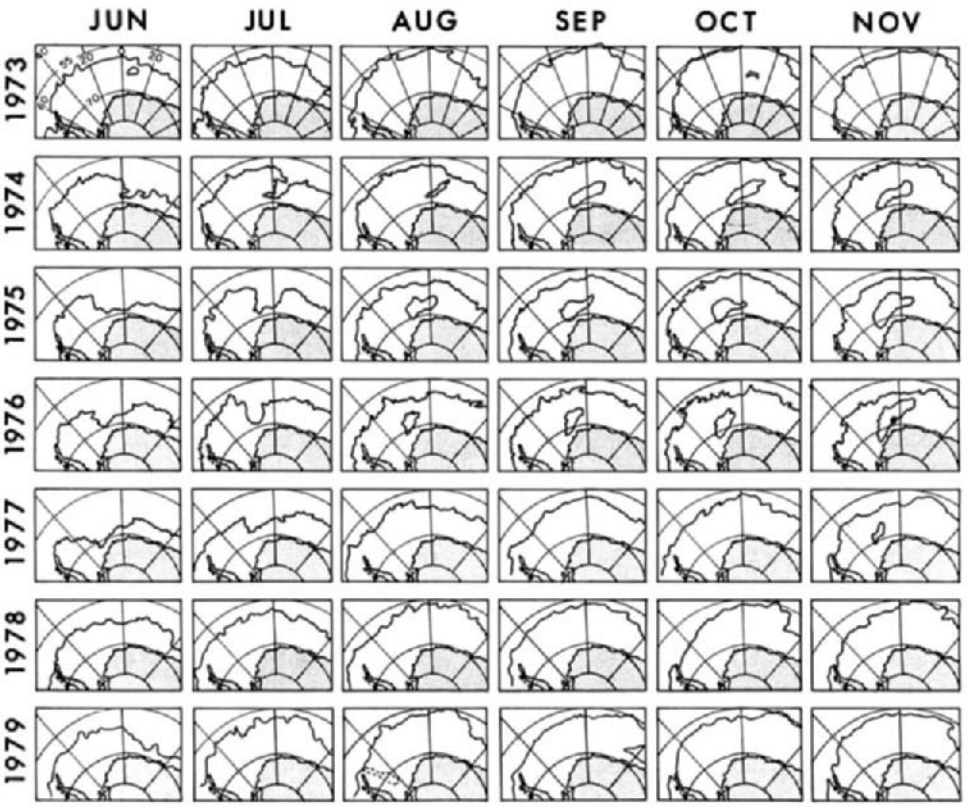

Figure 1. Average position of Weddell polynya within the seasonal sea ice field during the 1970's. Position of chimney observed by Gordon (1978) is indicated in November, 1976, as a solid dot. Figure from Martinson et al., 1981.

In the austral summer of 1977, immediately following the last large polynya occurrence, Gordon (1978) observed a deep chimney at ~67° S, 8° W (Figure 1). This cold, fresh, nearly homogeneous feature, overlain by a summer surface layer (~190 m thick), extended to ~3000 m depth and had a radius (~13 km) that was comparable to the Rossby radius of deformation (~11 km). Gordon (1978) speculated that the feature was one, of many, remnant convective cells associated with the polynya which had been present in the area two months earlier. Subsequent modeling work supported this idea.

In particular, Killworth (1979) showed that the entire Weddell region west of the Greenwich meridian was susceptible to convection; Martinson et al. (1981), using a two level convective model, produced results in good agreement with the observations; Parkinson (1983) showed that divergent winds may help to initiate the polynya, but its maintenance throughout winter required additional processes (e.g. convection); and, Motoi et al. (1987), using Japanese data collected in the polynya region in the austral summer of 1974, demonstrated the likelihood of convection given those observed conditions. As in the MEDOC region (MEDOC Group, 1970; Swallow and Caston, 1973), the Weddell region seems most susceptible to convection because of a preconditioning which elevates the pycnocline reducing the volume of surface water and increasing its sensitivity to buoyancy loss (Gordon, 1978; Killworth, 1979; Martinson et al., 1981; Killworth, 1983). The cause of the preconditioning is still unknown though the proximity of the polynya to the large topographic expression, Maud Rise, which rises to within a kilometer of the surface is a likely suspect (Martinson et al., 1981; Gordon and Huber, 1990; Gordon, 1991). The region is also one of reduced static stability (Martinson et al., 1981), which further increases its susceptibility and one of general doming of the pycnocline due to the cyclonic nature of the circulation (Gordon et al., 1978; Gordon et al., 1981).

Given this evidence of convection in the marginally stable Weddell region, Gordon (1982a) examined the historical data in an effort to establish the convection's impact on the deep water characteristics. Comparing data collected in the austral summer of 1973, preceding the first polynya appearance, to that from the summers of 1977 and 1978, following the last full polynya appearance, Gordon (1982a) showed that the Weddell Deep Water (WDW) in the vicinity of the polynya had decreased vertical stability and underwent a substantial cooling (~0.2° C averaged over 2500 meters of water; T_{max} decreased by ~0.4° C) and freshening (~0.02‰) between 1973 and 1977 (Figure 2). This modified portion of the WDW, referred to by Gordon (1982a) as the "cold spot", drifted westward from 1977 to 1978 with the polynya. Gordon (1982a) speculated that the intense cooling in the absence of sea ice, which can lead to a 10-100 fold increase in the air/sea heat exchange (Maykut, 1978), fueled the convection throughout the winters and cooled the WDW. The modifications observed were consistent with those predicted by the modeling (Martinson et al., 1981). By estimating the volume of modified WDW, Gordon (1982a) estimated that convection was contributing 1.6 to 3.2 Sverdrups (Sv; 1 Sv = 1×10^6 m^3/s) of surface water to deep water formation over each of the three polynya years. This is 3 - 6 times the estimated surface water contribution (0.5 - 1 Sv) to deep water formation above the continental margin (Weiss et al., 1979; Gordon, 1982a).

The WDW modifications, predominantly density compensating (a slight increase in density is

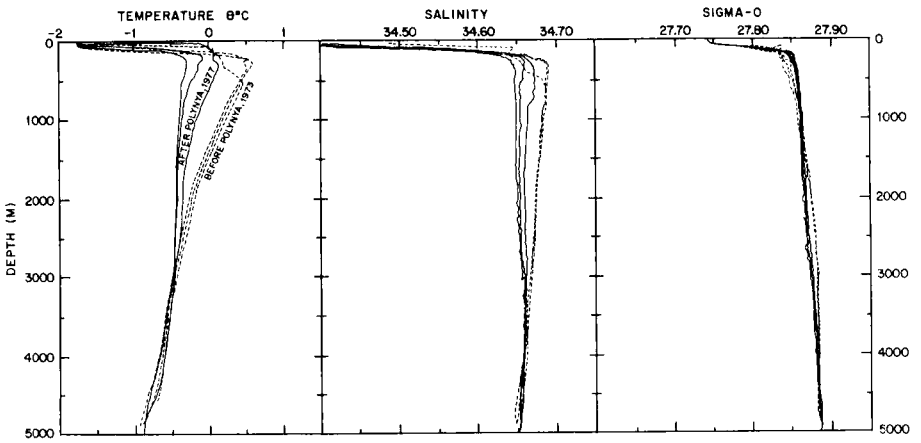

Figure 2. Comparison of average temperature, salinity and density profiles in the region of the Weddell polynya in 1973, before the polynya (solid lines) and in 1977 after occurrence of polynya (dotted lines) in the chimney. Note that water in the chimney is significantly colder and fresher down to 2700 m to 3000 m depth, and shows decreased vertical stability. Figure from Gordon (1991), adapted from Gordon (1982a).

realized due to the additional cooling through winter), extend to sigma-2 density levels of 37.21 - 37.23. Reid et al. (1977), who classified South Atlantic water masses lying between layers of increased vertical stability, indicated that the high oxygen, low salinity water lying between their stable layers 7 and 9 (Figure 6b of Reid et al., 1977) was Weddell Deep Water. Their layer 8, in the middle of this water mass (and for which they had no explanation as to its origin), falls near sigma-2 of 37.23 and is consistent with the lower depths of the convectively produced WDW. Layer 8 represents the deepest density surface to clear the Vema Channel which cuts through the Rio Grande Ridge separating the Argentine and Brazil Basins. Gordon (1978) suggests that the convectively modified deep water may thus be more successful in spreading, by isopycnal mixing, through the basins north of the Argentine Basin than the denser shelf-produced Antarctic Bottom Water (AABW) which is restricted by the Rio Grande Ridge. This is consistent with Reid et al. (1977) and Georgi (1981), who show that the denser shelf water has little influence north of the polar front, and with Hogg et al. (1982) who show that the main Antarctic waters flowing through the Vema Channel lie below stability layer 7 of Reid et al. (1977). From these observations it is clear that Weddell open ocean convection has the potential for ventilating and producing a significant amount of deep water (see Gordon, 1991 for further discussion).

Looking for evidence of convection prior to 1973 (the first year of passive microwave satellite coverage) Gordon (1982a) constructed a pseudo-time series showing T_{max} as a function of time using sparse historical data. A 1961 hydrographic station taken ~2° west of the 1977 chimney station, contained the distinct cold WDW signature suggesting an event in the austral winter of 1960. Prior to

the mid 1950's, T_{max} values were significantly higher than today (i.e. values ~0.7° C vs 0.4° C during non-polynya years and values of -0.2 to 0.2 following polynya years). Therefore it is not clear if the region is undergoing a gradual cooling (and associated destabilization) or whether the sparse data are merely giving a biased picture. Additional evidence of recent convection is suggested by the presence of relict convective features reported by Bersch (1988) and Muench et al. (1990), and discussed in more detail by Muench (1991).

Since 1977, the polynya has not re-appeared although a period of decreased concentration was observed in 1980 (Comiso and Gordon, 1987). As pointed out by Comiso and Gordon (1987), the polynya may need to attain a threshold size before it can remain open against the advection of in-drifting ice around its perimeter. Therefore, the decreased concentration in 1980 may represent open ocean convection on a smaller scale than what occurred in the mid-1970's. This is consistent with Gordon's (1991) suggestion that such convection may be responsible for a small nonlinear deviation in the potential temperature/salinity relationships present in Weddell region data sets (see Gordon's Figure 5). Also, it interesting to note that the region near Maud Rise where the polynya occurs is subject to early ice melt each year relative to the surrounding areas (Heap, 1964; Streten, 1973; Comiso and Gordon, 1987). That is, the ice melts back from the ice edge to the Maud Rise region forming a large open ocean embayment similar to that present during the months of July in 1974-1976 in Figure 1. This likely reflects an anomalously high oceanic heat flux in this region.

Elsewhere around Antarctica, away from the continental shelf regions, another fairly large polynya is sometimes seen in the vicinity of the Cosmonaut Sea (~66° S, 43° W). The Cosmonaut polynya has appeared for some portion of the winter months in 1973, 1975, 1979, 1980, 1982 and 1986 as either a full polynya or reduction in surface ice concentration (Martinson et al., 1981; Comiso and Gordon, 1987). Whether or not this polynya is also the surface manifestation of an open ocean convective event is yet to be determined. However, this region has a domed pycnocline and diminished stability which suggests that it may be properly preconditioned and susceptible to convection (Comiso and Gordon, 1987).

The fairly large Ross Shelf polynya occurs over the continental shelf and is most likely a wind produced, latent heat polynya (Zwally et al., 1985; Smith et al., 1990). That is, the heat loss from the water column is associated with the phase change as water at its freezing point turns to ice; the ice is then removed mechanically. In this case, no convection is associated with the polynya (though the salinization due to the ice growth may certainly lead to convection). This is in contrast to a sensible heat polynya in which case the water, warmer than its freezing point, so ice cannot form, is physically cooled. A sensible heat polynya is consistent with a convectively maintained polynya, since the convection driven by the cooling constantly replaces the cooled surface water with warmer (lighter) underlying water. Zwally et al. (1985) estimate that the ice growth rate in latent heat coastal polynyas is upward of 10 cm/day. It is unlikely that the marginally stable, thin surface layer of the open ocean region could survive the salinization associated with this growth rate over a sustained period without initiating deep convection (leading to a sensible heat polynya). Therefore, from this consideration alone, it is fair to assume that the presence of a full winter open ocean polynya in the Southern Ocean implies deep convection. That is, a sensible heat polynya can only be sustained if the

ocean heat flux to the surface layer exceeds the heat loss to the atmosphere so the water never reaches the freezing point - the tremendous heat loss to the atmosphere through an uninsulated sea surface in the Antarctic winter, can only be achieved in the open ocean by convection.

3 LOCAL PROCESSES CONTROLLING OPEN OCEAN CONVECTION

The general sequence leading to open ocean convection and the formation of an associated polynya is thought to be as follows (Martinson et al., 1981; Killworth, 1983). A seasonal sea ice cover develops over a marginally stable, preconditioned ocean surface layer. Haline rejection associated with the ice growth process weakens the stability. Too much ice growth, relative to the stability, destabilizes the water column inducing deep convection and eliminating the stratification. The convective heat flux is sufficient to eliminate the sea ice cover while the convective salt flux is sufficient to overwhelm the meltwater flux. Consequently, a polynya forms and the water column beneath it is destabilized so that cooling alone is sufficient to maintain the convection throughout the remainder of the winter. Furthermore, the convective salt flux upsets the annual freshwater balance so that deep convection is easily induced the following year, possibly by cooling alone. Given this process of destabilization and the marginal stability of the Southern Ocean water column, it is difficult to imagine why the water column doesn't actually overturn every year causing deep convection.

3.1 Observations

In 1986, observations were collected within the winter sea ice field over a 2-month period during the Winter Weddell Sea Project (WWSP-86; Schnack-Schiel, 1987). These winter data, supplement those collected under the ice in spring 1981 during the Weddell Polynya Expedition (WEPOLEX; Gordon, 1982b) and passive microwave satellite data (Zwally et al., 1983). Together, the descriptive analyses (Gordon et al., 1984; Gordon and Huber, 1984, 1990; Wadhams et al., 1987; Bagriantsev et al., 1989; Ackley et al., 1990) and related modeling work (Martinson, 1990) have allowed a more detailed understanding of the processes controlling open ocean deep convection. In particular, these reveal the following.

Oceanographically, the general (Weddell) region in which the convection has occurred is characterized by a cold and warm water regime (Figure 3; see also Gordon and Huber, 1984 and Bagriantsev et al., 1989). Lateral property gradients are essentially negligible within the regimes except in the vicinity of the front separating them and near Maud Rise where topographic influences are significant (Gordon and Huber, 1990). Key features of the 1986 winter property profiles include a deep surface mixed layer, O(100 m) deep, underlain by a pycnocline ~20-40 m thick and a nearly homogeneous deep water (WDW) to the bottom, ~5 km deep (Huber et al., 1989). WDW temperatures below the pycnocline are ~1°C in the warm regime and ≤0.4°C in the cold regime. In both regimes this represents a strong source of heat isolated from the surface by a very thin and weak pycnocline - the Brunt-Vaisala frequency across the pycnocline is typical of values in the deep ocean elsewhere (Gordon, 1981). Sea ice undergoes rapid initial growth, ~40 - 50 cm within the first weeks, followed by slow to no thermodynamic growth throughout the remainder of winter (Wadhams et al. 1987). The ice thickness observed in late October during WEPOLEX was ~75 cm

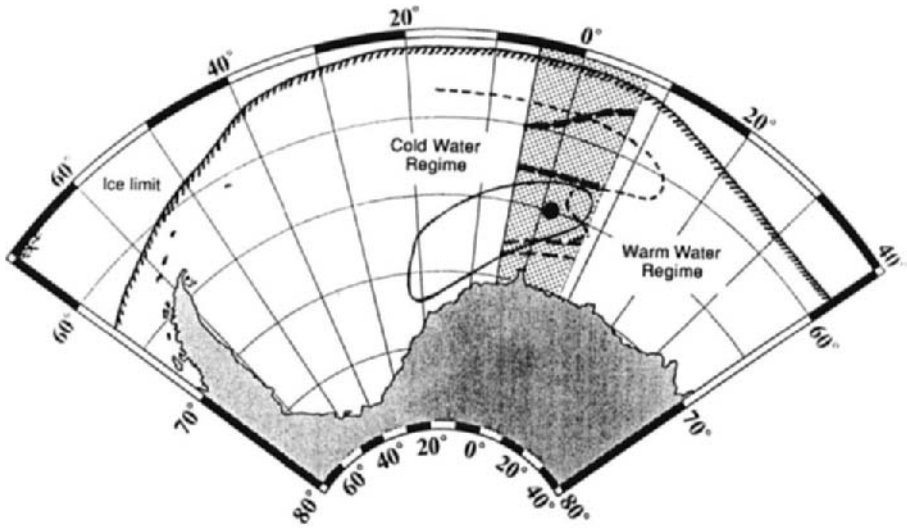

Figure 3. The Weddell regional setting. Deep convection has occurred within the area enclosed by the solid line (this is the area in which the polynya has appeared). Positions of ice edge, cold and warm regimes (separated by thin dashed line), and Maud Rise (large seamount rising to within a kilometer of the surface; large solid dot) are also shown. Winter data collected by POLARSTERN during WWSP-86 was collected within stippled region. Cold and warm regimes are characterized by negligible horizontal property gradients which also occur (between the bold dashed lines) approaching Maud Rise and the front separating these regimes.

thick (Ackley et al., 1982) and in 1934, Mosby (1934) estimated that the average thickness was 80 cm. Lead area was consistently ~5% throughout the 1986 winter (Wadhams et al. 1987) and 1981 early spring (Ackley et al., 1982).

3.2 Modeling the Local Interactions

The nature of the winter air/sea/ice interactions which determine whether the water column will overturn or not have been evaluated in a local process model (Martinson, 1990) which clearly reveals the system parameter dependence. The model is one dimensional in the vertical. This is justified by the negligible horizontal property gradients (away from the rare major fronts and topographic features such as Maud Rise and continental shelves) which imply insignificant lateral fluxes. Figure 4 presents a schematic representation of the modeled interactions and processes which control the winter system. Turbulent mixing (wind stirring) maintains a steady surface mixed layer depth and a sharp interface between the mixed layer and pycnocline by mixing downward any positive buoyancy introduced at the surface, such as meltwater, and mixing upward properties that are fluxed across the mixed layer base. This latter mixing works against the rising of the pycnocline due to upwelling and the smearing of the pycnocline/mixed layer interface by diffusion. For simplicity, these basal fluxes (advective and diffusive) are parameterized as a single turbulent diffusive flux (F_D). This flux is large

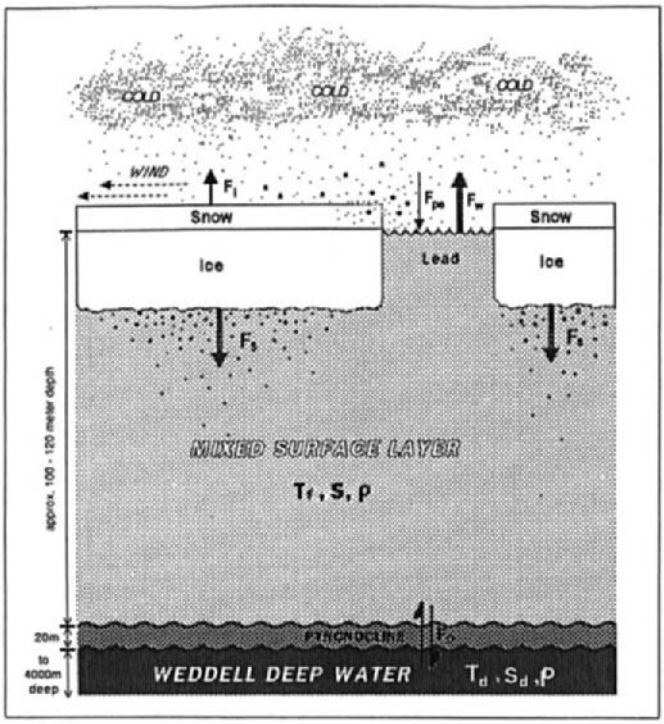

Figure 4. Schematic of dominant processes controlling the winter evolution of the ocean/sea-ice system. Heat is lost from the ocean to the atmosphere: through leads (F_w) this loss is uninhibited; through the ice and snow (F_i) it is by slow conduction. Mechanical mixing, driven by the wind, maintains a well mixed surface layer. The surface layer expands by free convection - sinking of dense (heavy) surface water, made dense by the injection of salt (F_S) into the water column as ice grows. The surface layer gains heat and salt from the deep water by diffusion (F_D) across the thin pycnocline, this supplies much of the heat lost to the atmosphere and significantly reduces the amount of ice growth. Snow enters through leads (F_{pe}; a negligible amount) which tends to stabilize the system slightly.

because of the strong thermal and salt gradients through the pycnocline; the deep water is significantly warmer, 2.5-3° C, and saltier than the surface mixed layer water and the transition zone separating these two water masses is only 20-40 m thick. Typically, the diffusive heat flux (F_{DT}) contributes ~25-30 W/m^2 to the mixed layer (of which ≤10 W/m^2 is actually attributed to the upwelling flux). This heat gain tends to supply most of the heat loss to the atmosphere which is uninhibited through leads (F_w) and by conduction through the ice and snow (F_i). If the flux through leads is only 20 times larger than that through the ice/snow, an area of 5% leads vents approximately as much heat to the atmosphere as a 95% ice covered area. In this respect, the area and distribution of leads is extremely important.

Given the observed 5% lead area, the atmospheric heat loss is ~35 W/m^2, and while this is

largely supplied by the strong oceanic heat flux, it still results in a net heat loss. This drives ice growth which introduces a salt flux (F_s) due to haline rejection associated with the ice growth process. This salt flux destabilizes the mixed layer and the resulting static instability is relieved by vertical mixing to a depth at which point the water column is again stable. The mixing process, or entrainment, deepens the mixed layer by eroding into the pycnocline. If the entrainment is sufficient to completely erode away the pycnocline, deep convection will ensue since the underlying water column is nearly neutrally stable. However, erosion of the pycnocline releases the heat contained within the entrained water (representing a "thermal barrier") into the mixed layer introducing an additional entrainment heat flux which reduces the net heat loss of the system and which thus serves as a negative feedback.

So, despite a weak pycnocline, stability of the upper water column is usually maintained and open ocean convection avoided due to the strong oceanic heat flux and entrainment heat flux. That is, the ocean heat flux minimizes the net heat loss and therefore reduces the net ice growth minimizing the salt buildup needed to destabilize the system. Furthermore, as ice does grow, it drives the negative feedback which contributes additional heat reducing ice growth further. Without these oceanic heat fluxes, the wintertime atmospheric cooling of the Southern Ocean region is sufficient to grow ~3 m of ice (similar to what grows in the Arctic regions where the oceanic heat is minimal). As it is, the 60 - 75 cm of ice growth observed at the end of winter occurs in a region where calculations show that only 90 - 100 cm of ice growth would often be enough to eliminate the pycnocline and induce deep convection. Therefore, the oceanic heat flux is presently just sufficient to prevent overturn.

The above interactions are described by a system of equations for entrainment, mixed layer salinity and ice growth, which are solved analytically (see Martinson, 1990, for details). The solutions give the evolution of the mixed layer as a function of time and are shown in Figure 5. As seen in the figure, entrainment, salinity and ice growth continue to increase throughout winter but the rate of increase drops off as the negative feedback works to slow down the system and drive it toward steady state. While the solutions themselves offer a complete description of the system evolution, they are algebraically tedious and not presented here. Instead, the model scaling for entrainment is given. This scaling approximates the full solution to within 15% (Figure 5) over a wide range of parameter values and provides a clear indication of the external parameter dependence. It also indicates whether the system is tending toward deep convection (destabilization indicated by increased entrainment) or stabilization (decreased entrainment).

Explicitly, the magnitude of entrainment, Δh_e, is approximated by:

$$\Delta h_e \approx \beta^{*2} \overline{\Delta h}_e [1 - (\overline{\Delta h}_e / h_o)^{1/2}] \qquad (1)$$

where β^* is a constant (converting salinities to densities as a function of thermocline strength), and $\overline{\Delta h}_e$ is the amount of entrainment due to free convection induced by increasing the salinity of the mixed layer by a net external salt flux, $\mathcal{F}_S$, consisting of the oceanic salt flux, surface freshwater input (nearly negligible in winter) and salinization due to ice growth.

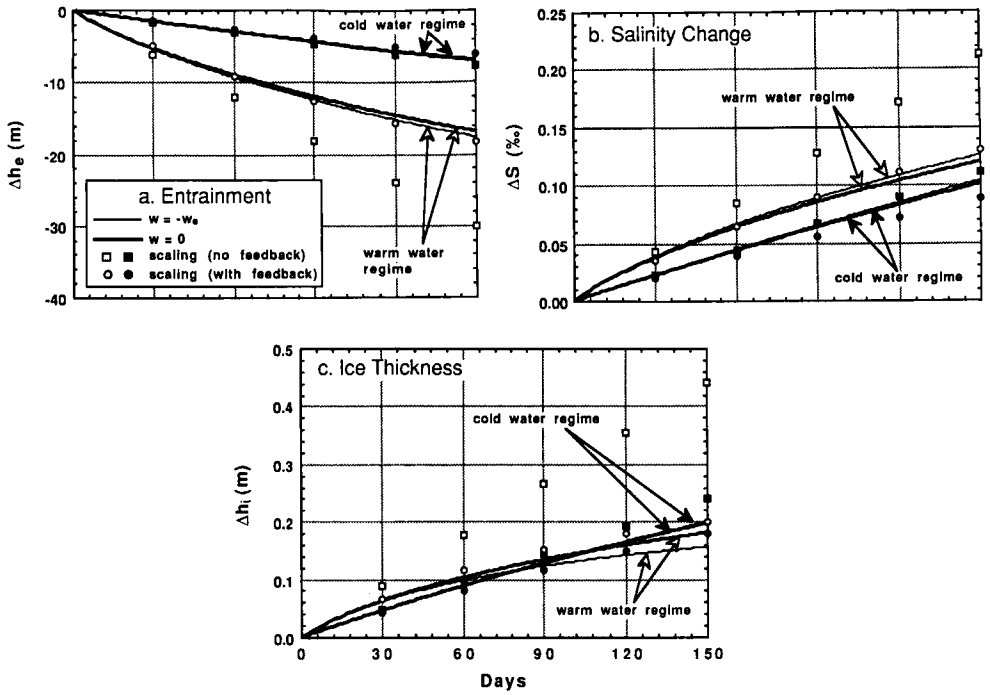

Figure 5. Net amount of: (a) entrainment (Δh_e); (b) salinity increase (ΔS) and (c) ice growth (Δh_i) as a function of time. Results are given using parameters representative of the warm and cold regimes (indicated) and for four different model formulations. The light solid line indicates the case where upwelling is assumed to balance entrainment, so the net mixed layer thickness doesn't change; the bold solid line is for the case in which upwelling is ignored, so the mixed layer depth increases directly with entrainment; squares represent the evolution ignoring the negative feedback at monthly intervals and circles represent the model scalings which include the negative feedback effect. Solid symbols represent the cold regime; open symbols represent the warm regime. From Martinson, 1990.

Specifically, $\overline{\Delta h_e} = \mathcal{F}_S t/(h_o \nabla S)$, where t is time, h_o is the initial winter mixed layer depth (top of the permanent pycnocline), and ∇S is the salinity gradient through the pycnocline. $\overline{\Delta h_e}$ represents the direct response of the system to the external forcing and simply states that the destabilization due to the buoyancy loss attributed to the salt input $\mathcal{F}_S t$ mixed over a layer of thickness h_o, is resisted by the stabilizing influence of the pycnocline, given by ∇S. The terms in brackets in equation (1) reveal the importance of this direct destabilization relative to the stabilizing influence of the negative feedback. So, the magnitude of $(\overline{\Delta h_e}/h_o)^{1/2}$ relative to 1 reveals the relative importance of the negative feedback to entrainment. Its influence ranges from ~10% in the cold regime to ~40% in the warm regime.

The sensitivity of the magnitude of entrainment to changes in the external parameters is shown in Figure 6. For example, Figure 6a shows that in the present day, the pycnocline depth is typically 100 m and after 5 months of winter, ~7 m of the pycnocline has been eroded away and incorporated

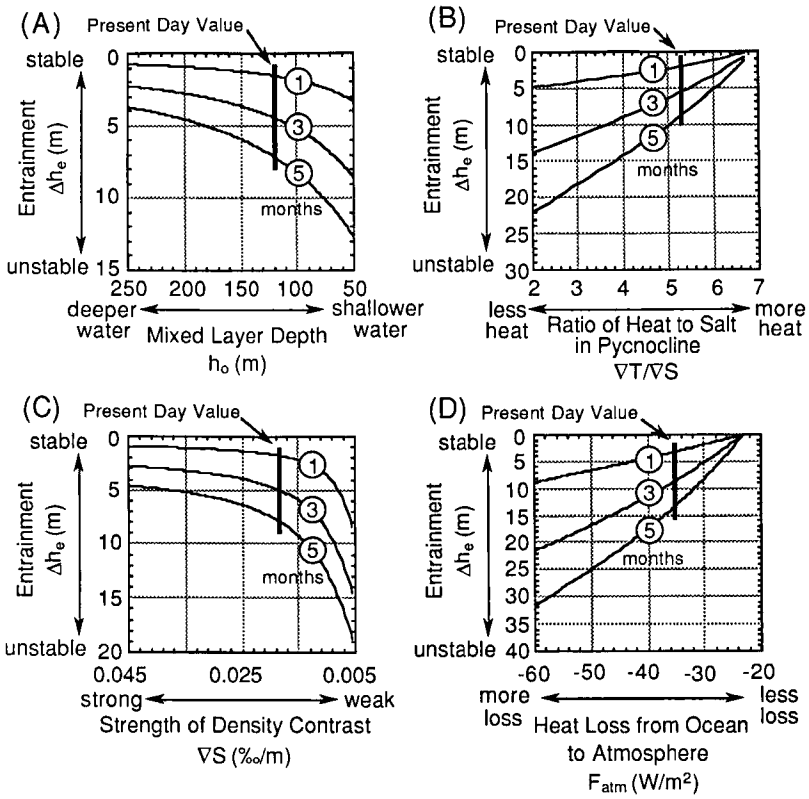

Figure 6. Change in system stability (indicated by change in entrainment) as a function of changes in external parameters. Decreasing stability coincides with increased entrainment (Δh_e; erosion of the pycnocline). The numbers 1, 3 and 5 on the lines indicate the amount of entrainment after 1 month time, 3 months, and 5 months (for the cold water regime). The vertical bars mark the location of the present day values of the parameters. Panels show amount of entrainment as a function of: a) h_o - the initial winter mixed layer thickness which corresponds to the upper level of the permanent pycnocline; b) γ - essentially the ratio of heat to salt in the pycnocline; c) ∇S - the pycnocline strength; and d) F_{atm} - the atmospheric heat loss. Adapted from Martinson, 1990.

into the mixed layer. For a 20 m thick pycnocline, an additional 13 m of entrainment will overturn the system causing deep convection. If the system changes so that the pycnocline is shallowed to only 50 m depth, then after 5 months of winter ~15 m of the pycnocline is eroded. While this may not be enough to overturn the system, it is a clear indication that if the pycnocline is made shallower, the system is more likely to overturn [this is also apparent by examination of equation (1)]. Whether this explicit change alone can induce overturn depends upon the exact pycnocline thickness and what effect other changes have on the system.

In general, as seen from Figure 5, the shallowing of the pycnocline, the decrease in the ratio of

heat to salt within the pycnocline, the direct weakening of the pycnocline strength and the cooling of the atmosphere all tend to destabilize the system and drive it toward deep convection. Changes in the opposite direction tend to stabilize the system. In terms of ice growth, in some regions an additional 15 cm of ice growth may be sufficient to destabilize the system; a change which can be induced by upsetting the present heat balance by 3 W/m^2 over winter. This suggests that the Southern Ocean stability and susceptibility to open ocean deep convection today is in a very delicate balance between the atmosphere and ocean. Full year modeling (work in progress), reveals additional feedbacks which also contribute to maintaining this balance. For example, if the forcing or environmental setting changes from one year to the next in a manner that tends to destabilize the system, the ocean stability will adjust through a system of inter-seasonal feedbacks to achieve a more stable configuration the following year. This makes system more robust relative to gradual climatic changes.

4. SENSITIVITY OF CONVECTION TO REGIONAL SCALE PROCESSES

The model scalings and sensitivity studies reveal the likelihood of overturn given changes in the external parameters relative to their present day values. The values of the external parameters, h_o, ∇S, ∇T (thermal gradient through the pycnocline), F_{atm} (atmospheric heat loss), and k (turbulent diffusion coefficient and magnitude of upwelling) however, reflect regional scale processes. Therefore, consideration of how the regional scale processes influence the external parameters links the local and regional scales. In general, the wind fields, thermohaline circulation and regional climate control the regional setting suggesting the following scenario and speculation.

Stronger cyclonic winds will increase the vigor of the cyclonic polar gyres. This will: (1) increase upwelling (larger k, increased stability); (2) decrease the pycnocline depth (smaller h_o, decreased stability), though increased turbulent mixing will offset this to some degree; (3) increase sea ice divergence, thus increasing lead area and heat loss to the atmosphere (larger F_{atm}, decreased stability), though stronger heat loss will drive faster ice growth leading to more rapid filling of leads, reducing this effect; (4) increase the magnitude of ice drift leading to more ice, formed near the shelf, melting in the open ocean which will tend to decrease the open ocean surface salinity (larger ∇S, increased stability) while destabilizing the shelf regions; and (5) increased turbulent mixing may lead to increased energy available for turbulent mixing across the pycnocline (larger k, increased stability). Also, increased wind forcing can influence the rate at which deep waters cross the Antarctic Circumpolar Current (ACC), raise the isopycnals to shallower depths, and potentially effect the degree of mixing as the waters move across the ACC in their route around the Antarctic thus altering the temperature and salinity characteristics of the WDW. However, the impact that these effects will have on the local gradients and pycnocline properties is not known. Decreased cyclonic winds would lead to the opposite of above changes.

Increased atmospheric cooling will: (1) increase F_{atm} directly (decreased stability); (2) increase ice growth rate filling leads more rapidly (smaller F_{atm}, increased stability); and (3) increase ice volume leading to farther drift of ice before melting [the ice drifts, on average, ~26 km/day (Martinson and Wamser, 1990)] possibly stabilizing the open ocean region while destabilizing the

coastal region, as discussed in point (4) above. Atmospheric warming would lead to the opposite effects.

Changes in the thermohaline circulation will influence the pycnocline strength, and gradients of heat and salt across the pycnocline. These will have a strong influence on the stability but cannot be predicted in any general manner without additional information regarding changes in the northern source deep water properties and circulation paths.

The net outcome of the above effects depends upon the relative magnitude of the individual components which cannot be easily estimated in the absence of a large scale model. However, the system is most sensitive to changes in the ocean heat flux, and the surface freshwater balance, dominated by ice drift. Thus changes affecting these parameters are likely to dominate the net effect. Given the influence of Maud Rise on the ocean heat flux (Gordon and Huber, 1990; Gordon, 1991), this sensitivity may make the water column over Maud Rise most susceptible to destabilization (see Gordon, 1991), though the additional influence of the lateral fluxes in this vicinity has not been treated in any quantitative manner. Also, intrusion of eddies from the warm regime into the cold regime act to strongly destabilize the system (Gordon and Huber, 1984; Lemke et al., 1990; Martinson, 1990).

Finally, Gordon (1982a) suggests that there may be a tradeoff between open ocean production of deep water and shelf production. Given the sensitivity of the system to the surface freshwater balance, the above scenarios suggest such a linkage. That is, the divergent system drives ice formed along the shelves to the open ocean region where it melts. This acts to destabilize the shelf region while simultaneously stabilizing the open ocean region. Changes in the vigor of the circulation which lead to increased stabilization in one region (e.g. increased export of ice to the open ocean) will automatically lead to destabilization in the other. Therefore, in the mid-1970's when open ocean convection was active, it is possible that this coincided with decreased export of shelf ice, stabilization of the shelf regions and reduced deep and bottom water production in those regions. In this respect, the formation of Antarctic deep and bottom waters may be self regulating, though the impact on the deep water properties as a function of their formation area is not considered here and may introduce a further feedback or linkage.

5. CONCLUSIONS

Deep open ocean convection in the Southern Ocean appears to occur episodically, the last such event, which persisted for several years, occurred in the mid-1970's at ~65° S near the Greenwich Meridian. Historical observations provide evidence suggesting a prior event in 1960. The deep convection appears to influence properties down to ~3000 m depth, and the associated vertical heat and salt fluxes lead to the formation of a polynya in the seasonal sea ice field. Strong cooling through the polynya drives the convection throughout the winter period leading to substantial ventilation/formation of modified Weddell Sea Deep Water. Water of this density and from the Weddell represents the dominant deep water component north of the polar front in the South Atlantic. Open ocean convection may therefore play a significant role in Antarctic Bottom Water formation.

The marginal stability of the Southern Ocean water column suggests that the water column is

relatively susceptible to overturn each year, but the strong ocean heat flux directly supplies most of the heat lost to the atmosphere, limiting ice growth and minimizing the destabilizing salinization associated with the ice growth process. Further, any entrainment of the warm pycnocline waters by winter expansion of the mixed layer introduces an additional source of heat into the mixed layer which acts as a negative feedback to the system reducing further destabilization. In this manner, the water column manages to avoid destabilization in nonconvective years. However, in the least stable regions, a relatively small perturbation to the forcing or regional setting would be sufficient to induce overturn (e.g. increase the atmospheric cooling or reduce the ocean heat flux by ~3 W/m^2 over the winter). In general, additional atmospheric cooling, doming of the pycnocline, decreasing the ratio of heat to salt in the pycnocline, decreasing the pycnocline strength or decreasing the oceanic heat flux all tend to drive the system toward destabilization in winter. Perturbations of this nature are driven by changes in the regional scale processes (e.g. wind stress field, thermohaline circulation and regional climate). Most notable of the regional influences is the connection between the stability of the open ocean and shelf regions. Since ice drift dominates the freshwater balance of the region, changes in the vigor of the wind stress field will influence the extent with which ice grown over the shelf regions is melted in the open ocean region. With increased divergence, more ice will melt in the open ocean tending to stabilize that region while destabilizing the shelf region. Decreased divergence will lead to the opposite. In this manner, conditions favoring open ocean convection coincide with unfavorable conditions on the shelves and vice versa.

Acknowledgements. This work was supported by National Science Foundation research grant DPP 85-01976. Lamont-Doherty Geological Observatory contribution number 4727.

6. REFERENCES

Ackley, S.F., Clarke, D.B. and Smith, S.J., 1982. Weddell Polynya Expedition preliminary data report: Physical, chemical and biological properties of ice cores. Technical note, U.S. Army Cold Water Regions Res. and Eng. Lab., Hanover, N.H.

Ackley, S.F., Lange, M. and Wadhams, P., 1990. Snow cover effects on Antarctic sea ice thickness. In: Sea Ice Properties and Processes: Proc. of the W.F. Weeks Symposium, S.F. Ackley and W.F. Weeks, (Editors), CRREL Monograph 90-1, 300 pp.

Bagriantsev, N.V., Gordon, A.L. and Huber, B.A., 1989. Weddell Gyre: Temperature maximum stratum. J. Geophys. Res., 94: 8331-8334.

Bersch, M., 1988. On deep convection in the Weddell Gyre. Deep-Sea Res., 35: 1269-1296.

Brennecke, W., 1921. Die ozeanographischen Arbeiten der deutschen antarkischen Expedition 1911-1912 ("Deutschland"). Arkiv. der Deutschen Seewarte, 39: 1-216.

Carsey, F. D., 1980. Microwave observations of the Weddell Polynya. Mon. Weather Rev., 108: 2032-2044.

Comiso, J. and Gordon, A.L., 1987. Recurring polynyas over the Cosmonaut Sea and the Maud Rise. J. Geophys. Res., 92: 2819-2834.

Georgi, D.T., 1981. Circulation of bottom waters in the southwestern South Atlantic. Deep-Sea Res., 9: 959-979.

Gordon, A.L., 1978. Deep Antarctic convection of Maud Rise. J. Phys. Oceanogr., 8: 600-612.

Gordon, A.L., 1981. Seasonality of Southern Ocean sea ice. J. Geophys. Res., 85: 4193-4197.

Gordon, A.L., 1982a. Weddell Deep Water variability. J. Marine Res., 40: 199-217.

Gordon, A.L., 1982b. The US-USSR Weddell Polynya Expedition. Antarctic J., 17: 96-98.

Gordon, A.L., 1991. Two stable modes of Southern Ocean winter stratification. This volume.

Gordon, A.L. and Huber, B.A., 1984. Thermohaline stratification below the Southern Ocean sea ice. J. Geophys. Res., 89: 641-648.

Gordon, A.L. and Huber, B.A., 1990. Southern Ocean winter mixed layer. J. Geophys. Res., 95: 11655-11683.
Gordon, A.L., Molinelli, E., and Baker, T.N., 1978. Large-scale relative dynamic topography of the Southern Ocean. J. Geophys. Res., 83: 3023-3032.
Gordon, A.L., Martinson, D.G. and Taylor, H.W., 1981. The wind-driven circulation in the Weddell-Enderby Basin. Deep-Sea Res., 28A: 151-163.
Gordon, A.L., Chen, C.T.A. and Metcalf, W.G., 1984. Winter mixed layer entrainment of Weddell Deep Water. J. Geophys. Res., 89: 637-640.
Heap, J.A. 1964. Pack ice. Antarct. Res., R. Priestley, R.J. Adie and G. De Q Robin (Editors), Butterworth, 360 pp.
Huber, B.A., Mele, P. and Gordon, A.L., 1989. Report of the Winter Weddell Sea Project, ANT V/II, Hydrographic data, L-DGO-89-1, Lamont-Doherty Geol. Observ., Palisades, N.Y.
Killworth, P.D., 1979. On "chimney" formations in the ocean. J. Phys. Oceanogr., 9: 531-554.
Killworth, P.D., 1983. Deep convection in the world ocean. Rev.Geophys. and Space Phys., 21(1): 1-26.
Hogg, N., Biscaye, P., Gardner, W. and Schmitz Jr., W.J., 1982. On the transport and modification of Antarctic Bottom Water in the Vema Channel. Jour., Marine Res., 40: 231-263.
Lemke, P., Owens, W.B., and Hibler III, W.D., 1990. A coupled sea ice-mixed layer-pycnocline model for the Weddell Sea. J. Geophys. Res., 95: 9513-9525.
Martinson, D.G., 1990. Evolution of the Southern Ocean winter mixed layer and sea ice; open ocean deep water formation and ventilation. J. Geophys. Res., 95: 11641-11654.
Martinson, D.G. and Wamser, C., 1990. Winter Antarctic pack ice drift and momentum exchange. J. Geophys. Res., 95: 1741-1755.
Martinson, D.G., Killworth, P.D. and Gordon, A.L., 1981. A convective model for the Weddell Polynya. J. Phys. Oceanogr., ll: 466-488.
Maykut, G.A., 1978. Energy exchange over young sea ice in the central Arctic. J. Geophys. Res., 83: 3646-3658.
Motoi, T., Ono, N. and Wakatsuchi, M., 1987. A. Mechanism for the formation of the Weddell Polynya in 1974. J. Phys. Oceanogr., 92: 2241-2247.
MEDOC Group, 1970. Observation of formation of deep water in the Mediterranean Sea. Nature, 227: 1037-1040.
Meyer, H.H.F., 1923. Die Oberflachenstromungen des Atlanrischen Ozeans im Februar, Veroffentlichungen de Instituts fur Meereskunde, Berlin, Neue Folge. A. Geographisch-naturwissenschaftliche Reihe. Heft 11., Berlin.
Mosby, H., 1934. The waters of the Atlantic Antarctic Ocean. Scientific Results of the Norwegian Antarctic Expeditions 1927-1928, I, 117 pp.
Muench, R.D., Fernando, H.J.S. and Stegen, G.R., 1990. Temperature and salinity staircases in the northwestern Weddell Sea. J. Phys. Oceanogr., 20: 295-306.
Muench, R.D., 1991. Relict convective features in the Weddell Sea. This volume.
Nansen, F., 1912. Das Bodenwasser und die Abkuhlung des Meeres. Int. Rev., ges. hydrobiol., Hydrogr., Bd. v, 1-32.
Parkinson, C.L., 1983. On the development and cause of the Weddell polynya in a sea ice simulation. J. Phys. Oceanogr., 13: 501-511.
Reid, J.L., Nowlin, Jr., W.D. and Patzert, W.C., 1977. On the characteristics and circulation of the Southwestern Atlantic Ocean. J. Phys. Oceanogr., 7: 62-91.
Schnack-Schiel, H., 1987. The winter expedition of RV POLARSTERN to the Antarctic (Ant V/1-3). Berichte zur Polarforschung 39: 1-259.
Smith, S.D., Muench, R.D. and Pease, C.H., 1990. Polynyas and leads: An overview of physical processes and environment. J. Geophys. Res., 95: 9461-9479.
Streten, N. A., 1973. Satellite observations of the summer decay of the Antarctic sea-ice. Arch. Met. Geoph. Biokl., Ser. A22: ll9-l34.
Swallow, J.C. and Caston, G.F., 1973. The preconditioning phase of MEDOC 1969 - I. Observations. Deep-Sea Res., 20: 429-448.
Wadhams, P., Lange, M. A. and Ackley, S. F., 1987. The ice thickness distribution across the Atlantic sector of the Antarctic Ocean in midwinter. J. Geophys. Res., 92: 14535-14552.
Weiss, R.F., H.G. Ostlund and H. Craig, 1979. Geochemical studies of the Weddell Sea. Deep-Sea Res., 26: 1093-1120.
Wüst, G., 1928. Der Ursprung fer Atlantischen Tiefenwasser, (Aus den Ergebenissen der Deutscen Atlantischen Expedition), Jubilaums-Sonderband 1928 der Zeitschrift der Gesellschaft fur Ewrdkunde zu Berlin, Berlin.

Wüst, G., 1933. Das bodenwasser und die Gliederung der Atlantischen Tiefsee. Wissenschaftliche Ergebnisse der Deutschen Atlantischen Expedition auf dem Forschungs- und Vormessungsschiff "Meteor" 1925-1927, 6(1), 106 pp. (English translation #340, by M. Slesser, U.S. Naval Oceanogr. Office, 1967).

Zwally, H.J. and Gloersen, P., 1977. Passive microwave images of the polar regions and research application. Polar Rec., 18: 431-450.

Zwally, H.J., Wilheit, T.T., Gloersen, P. and Mueller, J.L., 1976. Characteristics of Antarctic sea ice as determined by satellite-borne microwave imagers, Proceedings of the Symposium on Meteorological Observations from Space: Their Contributions to the First GARP Experiment, 1976, Boulder CO., National Center for Atmospheric Research, 94-97.

Zwally, H.J., Comiso, J.C. and Gordon, A.L., 1985. Antarctic offshore leads and polynyas and oceanographic effects. In: Oceanology of the Antarctic Continental Shelf, S. Jacobs (Editor), Ant. Res. Ser., 43, Am Geophys. Un., Wash. D.C., 203-226.

Zwally, H.J., Comiso, J.C., Parkinson, C.L., Campbell, W.J., Carsey, F.D. and Gloersen, P., 1983. Antarctic sea ice, 1973-1976: Satellite passive-microwave observations, NASA Scientific and Technical Information Branch, Washington, D.C. 206 pp..

RELICT CONVECTIVE FEATURES IN THE WEDDELL SEA

R.D. MUENCH
Science Applications International Corporation, 13400B Northup Way, Suite 36, Bellevue, WA, 98005 (USA)

ABSTRACT

The Weddell Sea is characterized by a weak, primarily barotropic, cyclonic circulation. The water column is characterized by low static stability which, coupled with annual winter ice formation over all but the westernmost Weddell which is permanently ice-covered, facilitates deep convection. The eastern Weddell is the most likely site of deep convection, probably in the form of mesoscale convective cells with associated cyclonic circulation. These cells can migrate westward under the influences of the regional circulation and the interaction between the cell circulation and planetary vorticity (the beta effect), evolving and decaying through a variety of processes during this migration. They can provide a means to advect lower temperature mid-depth water into the central and western Weddell gyre, and provide possible explanations for a variety of features which have been found there.

1. INTRODUCTION, AND GOALS OF THIS PAPER

Deep ocean convection through formation of mesoscale features, such as so-called "chimneys" (e.g. Killworth, 1979, and papers by Martinson, Dewar, Herman and Jones elsewhere in this volume) is believed to play a significant role in vertical heat transport and conditioning of deep waters. In a relatively quiescent environment, such features can be assumed to persist for considerable lengths of time. The Weddell Sea, known to be a site for convective events, is an extremely low energy regime wherein convectively formed features might accordingly persist over long periods after cessation of active convection.

This paper utilizes a phenomenological approach to summarize and discuss past field observations from the Weddell Sea within the context of convective processes. It focusses upon observed features having mesoscale to sub-gyral scales, and develops qualitatively the hypothesis that they are remnants of winter convective features which either formed *in situ* or formed elsewhere and then either were advected to or migrated to the observed locations. Some aspects are discussed of the behaviour of such features and their possible impacts on the regional oceanography.

2. SOME POSSIBLE REMNANT CONVECTIVE FEATURES

Ideally, in order to test conjectures concerning the fates of convective

features in the Weddell Sea, we would like to have time series observations of one or more discrete features. These observations would trace their evolutions from newly-formed and easily identifiable convection cells through periods of decay to the point where they were no longer distinct from the ambient water. We do not, however, have such time series. We have, instead, observations of individual features, which may or may not be convective in origin, scattered throughout the Weddell gyre. These observations are assumed to be, for purposes of hypothesis development, "snapshots" taken during the evolution (or, alternately, the decay) of convective features. A

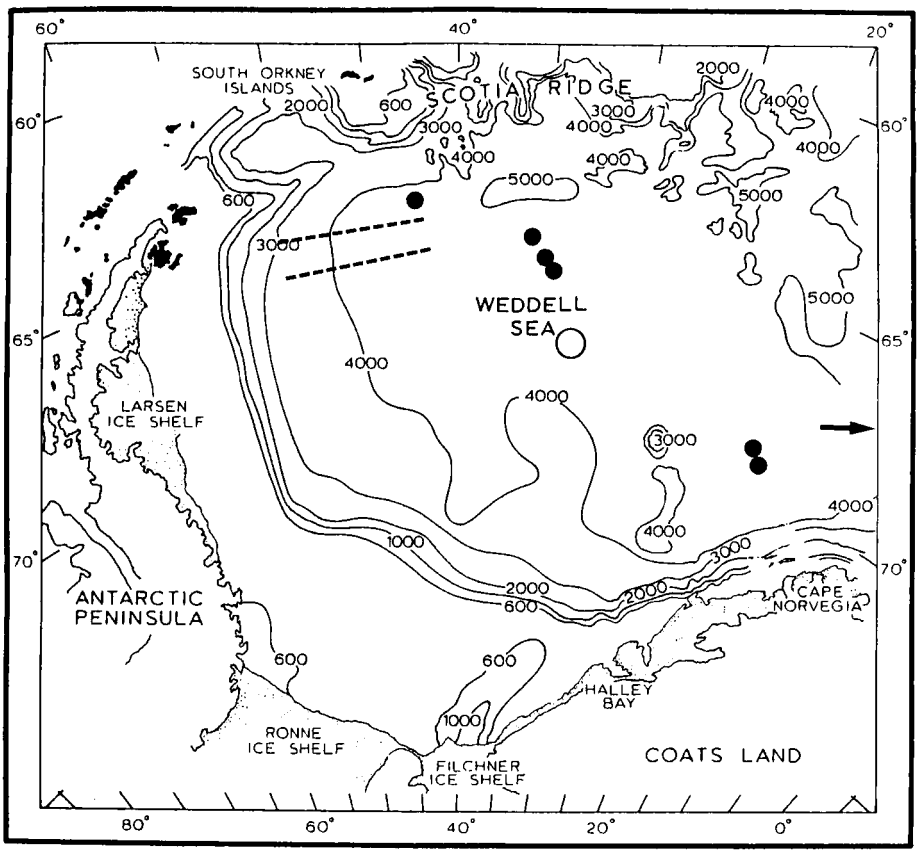

Figure 1. Geographical locations in the Weddell Sea, showing approximate sites of some of the features described in the text. Arrow points to site of convective cell observed by Gordon (1978) (just off chart). Open circle is site of feature reported by Bersch (1988). Dashed lines show two transects along which Muench et al. (1990) reported large thermohaline staircases, and solid circles show other sightings of these staircases.

representative sequence is summarized below, where the sites of the described features are shown on Figure 1.

A mesoscale eddy which was clearly a recent remnant winter convective feature was observed in summer 1977 and reported by Gordon (1978) (Figure 2). This feature was observed just west of Maud Rise in the eastern Weddell Sea. It was cyclonic, about 30 km in diameter, had maximum associated surface current speeds of order 50 cm/s, and extended downward to at least 3000 m. The core of the eddy was more uniform and colder than the surrounding water. Gordon (1978) hypothesized that the eddy may have formed during the preceding winter through vertical convection followed by subsequent baroclinic readjustment. Alternately, the eddy may have been advected into the region from elsewhere. Winter convection would then have occurred at the center of the eddy where upward doming isopycnals led to reduced vertical stability, and created a chimney.

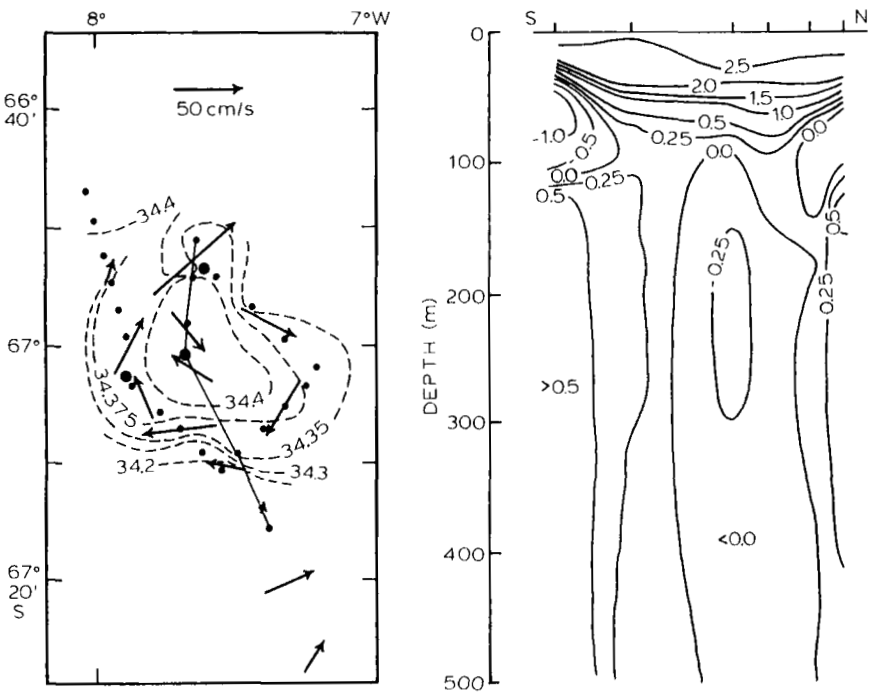

Figure 2. Convection cell observed in the eastern Weddell Sea by Gordon (1978). Left panel shows surface circulation, and right panel shows distribution of T with depth (from Gordon, 1978). Approximate location is indicated on Figure 1.

Bersch (1988) identified a feature in the central Weddell Sea which had anomalous T and S properties and was less than 200 km across (Figure 3). He suggested on the basis of T-S properties that this feature was the evolving remnant of a convective cell which had been advected to its observed location from a formation site to the southeast in the Antarctic Coastal Current.

Bagriantsev et al. (1989) identified, using field data obtained during 1980-1988, two minimum temperature regions in the maximum temperature strata which is present 300-500 m deep within the central Weddell Gyre. They speculate that this structure might have reflected secondary circulation features within the Weddell Gyre. They do not speculate on the origins of these features, however, the presence of anomalously low temperature water at depth would be consistent with past convective activity.

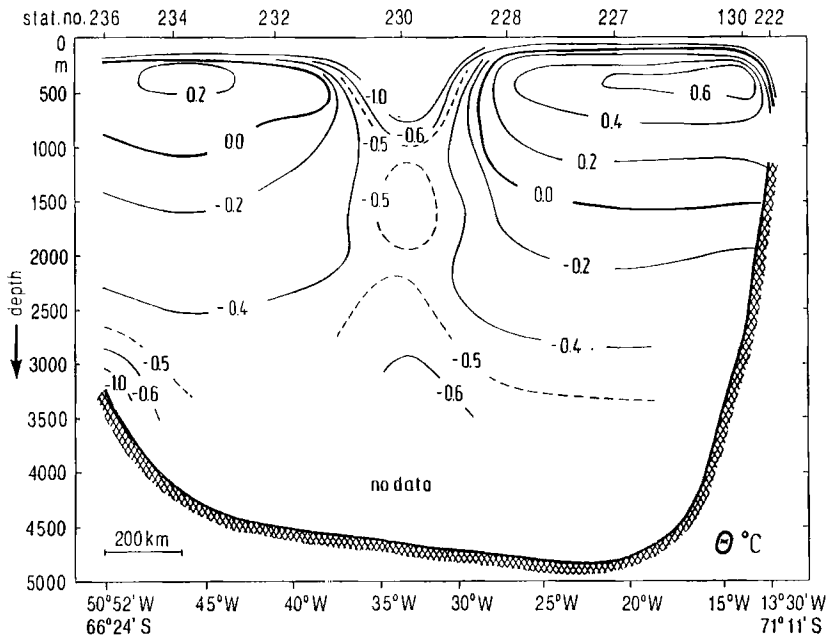

Figure 3. Thermal signature of feature reported by Bersch (1988) and suggested by him to be a remnant convective cell (from Bersch, 1988). Approximate site is indicated on Figure 1.

Muench et al. (1990) documented a field of unusually large thermohaline staircases some 200 km across at intermediate depths in the western Weddell Sea, near the ice edge, during late summer 1986. The steps were imbedded in a region at least 40,000 km^2 in extent wherein upper ocean T was slightly lower than in the ambient waters (Figure 4). They demonstrated through field data

analyses and results from laboratory experiments that these staircases were consistent with past convective activity. A more thorough discussion of their hypothesized mechanism is given in section 3.3.

Muench et al.'s (1990) hypothesis suggests that the presence of unusually large thermohaline steps might be indicative of past convective activity. Such steps have been observed in other parts of the Weddell Sea (Figure 1). Foster and Carmack (1976) observed them in the northern central Weddell at a site several hundred kilometers east of Muench et al.'s (1990) observations. Middleton and Foster (1980) reported their presence at a single station some 300 km east of this site. Huber et al. (1981) documented them at an isolated group of three stations near 10° E within about 100 km of the Antarctic coast. Foldvik et al. (1985) observed them south and east of Muench et al.'s (1990) study area. Foster (1986 and 1988 personal communications) observed them east, but not west, of about 50° W during summer 1980, but noted that none were observed in this same region during November 1987. These features are apparently widespread. If they do in fact represent remnants of convective features, then convection may exert an influence over Weddell Sea hydrography over a region far greater than just the eastern portion which is supposed most susceptible to active vertical convection.

3. A HYPOTHESIS CONCERNING EVOLUTION OF WEDDELL SEA CONVECTION CELLS

It is hypothesized that winter convection, primarily in the eastern Weddell Sea, leads to formation of features which persist for considerable lengths of time. These features evolve in time, primarily through molecular processes because of the very quiescent interior of the Weddell gyre. They migrate westward, while evolving, in response to the mean circulation and to interaction between their intrinsic circulation and the planetary vorticity. The hypothetical evolution of a single feature is illustrated in Figure 5, while Figure 6 illustrates in plan view the migration of such features.

3.1. *Formation of Convective Features*

Central to the hypothesis presented here is the concept of a convective cell. These may form in two ways. In one, upper layer water density is increased through cooling and/or brine rejection sufficiently that it erodes the pycnocline and mixes ever deeper, limited primarily by the extent to which the upper layer density increase can overcome the ambient static stability. Once such a cell has formed, baroclinic readjustment occurs and a cyclonic eddy forms which contains uniform, cold, dense water at its center. Such a feature may also form when a cyclonic eddy is advected into a region where severe surface cooling or ice formation occurs. In this case, the eddy is

said to be "preconditioned" because its circulation causes upward doming, which decreases vertical stability, in the center of the eddy. The upper layer density increase due to cooling and ice formation subsequently leads to deep convection and a cold, dense, uniform core at the eddy center. This latter case is that of so-called "chimneys" as discussed by Killworth (1979).

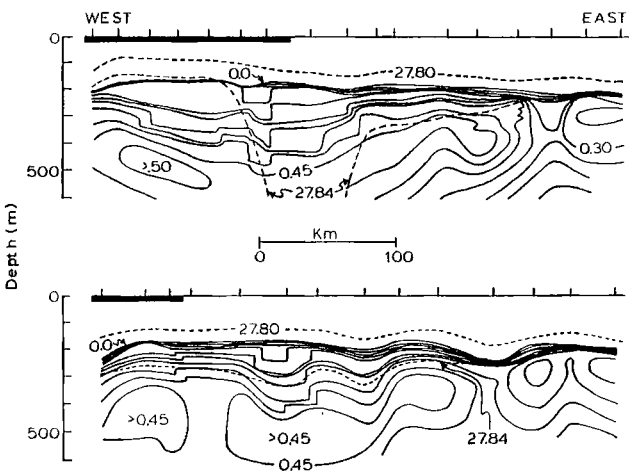

Figure 4. Vertical distribution of T, contoured at 0.05° C, through the region of large thermohaline staircases reported by Muench et al. (1990), from Muench et al. (1990). Upper layer contours were omitted for clarity. Site of transects is indicated on Figure 1.

The entire Weddell Sea is characterized by very low static stability, as a consequence of small vertical T and S gradients and an upward doming, interior to the gyre, due to Ekman upwelling. Because of this low stability, the region is subject to vertical convective events during the winter months, when cooling or brine from freezing ice can increase upper layer density to the point where deep convective mixing can occur (Martinson, 1990). This tendency toward convection is most pronounced in the eastern Weddell Sea, where convection associated with pre-existing cyclonic eddies (chimneys) is more probable than farther west. Such eddies presumably originate farther north in the energetic Polar Frontal zone and are advected south into the eastern Weddell. Other than the convective cell observed by Gordon (1978), which may have evolved from such an eddy, there are however no observations of such features. It is impossible to estimate how many such eddies might be advected into the Weddell Sea. The best-known instance of a presumed convective event was the Weddell Polynya of the mid-to-late 1970's, when convection transported

enough heat upward so that ice was prevented from forming (Martinson et al., 1981). Gordon (1978) estimated that from 10 to 100 individual mesoscale convective features may have been present in the eastern Weddell in association with the polynya. There were however no observations obtained from the polynya during winter, so that these conjectures could not be verified through field observations.

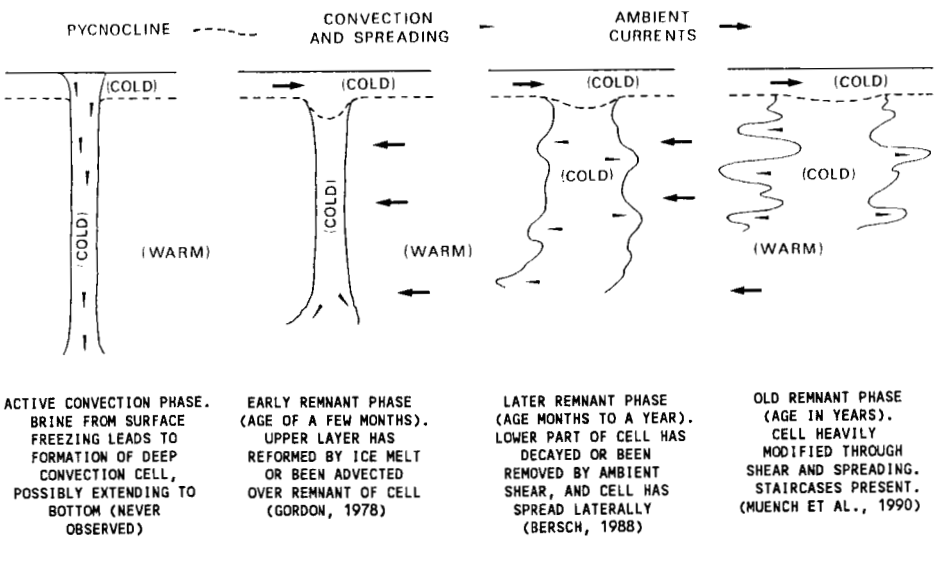

Figure 5. Conceptualization showing hypothetical evolution of a newly-formed convection cell (left) through intermediate to final stages, where at the last large thermohaline staircases and a mid-depth T deficit are all that remain of the initial feature. Arrows are meant to suggest sense of spreading, which broadens the feature, and ambient shear which decouples the feature from the surface.

It is uncertain to what extent convection might occur in other portions of the Weddell sea. Bersch (1988) hypothesized, based on observed low static stability, that the Antarctic Coastal Current might be a region of convection. This region is, moreover, impacted by high winds and low air temperatures from the Antarctic continent which might induce greater ice formation than farther north, hence, contributing to convection. Simple salt balance arguments dictate that more than 1.5 m of ice must form in the central and western Weddell in order for convection to penetrate the pycnocline and impact the deep, warm water layers. The presence of a permanent pack ice cover in the

westernmost Weddell dictates against significant new ice cover, however, and the limited available observations suggest that ice formed just east of the summer ice edge does not exceed about 0.5 m in thickness (S. Ackley, CRREL, 1990 personal communication). It therefore is unlikely that convection will occur over a significant area of the western to central Weddell, although isolated incidents associated with locally divergent ice or localized ocean preconditioning cannot be ruled out. In fact, as suggested below, such preconditioning might be provided by remnants of previous convection cells; this is probably the mechanism which allowed the Weddell Polynya to persist for several years in the 1970's.

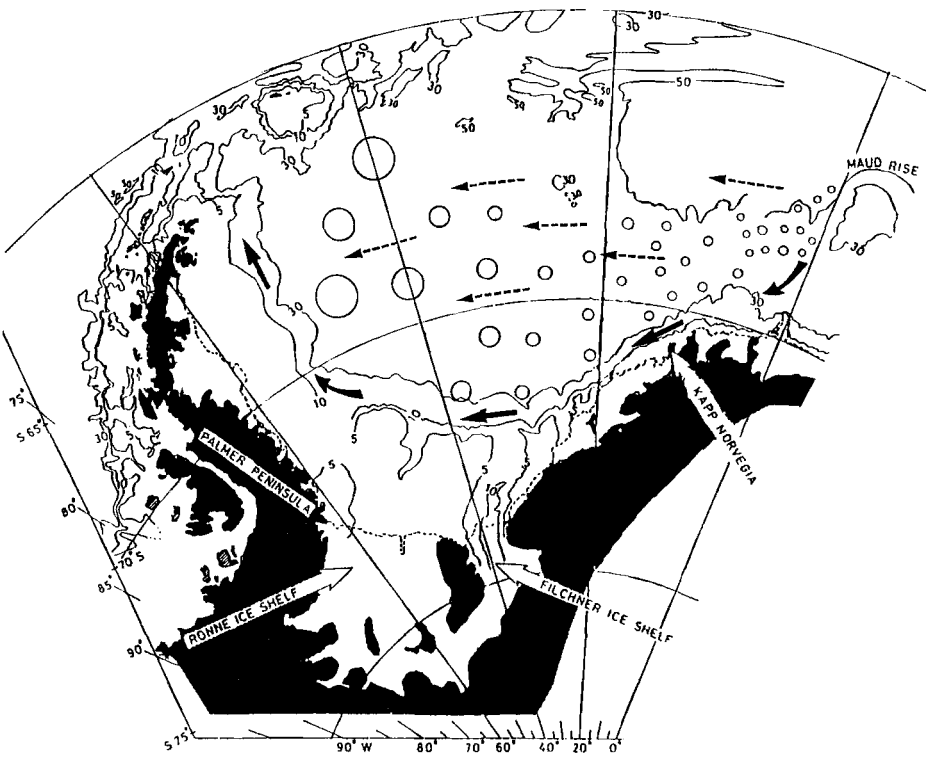

Figure 6. Conceptualization showing possible migration routes for remnant convective features in the Weddell Sea. Increasing diameters of cells suggest increase in lateral scales, through spreading, as they migrate westward. Solid arrows indicate ocean currents, whereas dashed arrows indicate migration pathways.

In view of the foregoing, it is assumed that the eastern Weddell will be the primary site of convective activity. At the onset of winter ice

formation, brine rejection leads to formation of deep convective features. It is hypothesized that these features have horizontal scales of the same order as the internal radius of deformation (typically, 20 km), strong associated cyclonic circulation (current speeds of several tens of cm/s), and are deep (3000-4000 m).

There is no reason to expect convective activity to occur on an annual basis. Though such activity probably occurred in association with the Weddell Polynya, it has not been demonstrated that significant deep convection has occurred since that time. It is impossible, conversely, to rule out development of convective features in localized areas of ice divergence or in cases where preconditioning occurs due to migration into a potentially convective region of a cyclonic eddy. It can be safely assumed that such processes are subject to wide interannual variability.

3.2. *Migration of The Features*

Once formed, convection cells are not likely to remain in place at their sites of formation. They will, rather, move about under the influence of the mean ocean circulation, through interaction (in the case of very deep features) with bottom topography, and through interaction with planetary vorticity (the beta effect).

The Weddell Sea is occupied by a basin-wide, primarily barotropic, cyclonic gyre. The dominant mean southward circulation in the eastern Weddell is associated with this gyre. It is probable that topographically influenced circulation modes are associated with Maud Rise, given the highly barotropic nature of the flow, but these will influence primarily the currents directly over Maud Rise and will be ignored here. Outside the Antarctic Coastal Current, which is constrained by the coastline to flow westward, there is considerable uncertainty regarding the circulation pattern. The possibility exists (Bagriantsev et al., 1989) of multiple sub-gyre circulations within the basin.

The field data are adequate for estimation of current speeds only in the western Weddell. While vertically integrated horizontal transports are believed to be large, baroclinic upper layer circulation is sluggish when compared to other ocean basin scale gyres. Early estimates based on wind stress curl calculations for the whole Weddell gyre yielded northward transports in the western Weddell, necessary to close the gyre, of 76 x 10^6 m^3 /s (Gordon et al., 1981). Given a barotropic flow and 250 km current width, this transport would be consistent with a northward current in the western Weddell of about 8 cm/s. Published dynamic topographies based on large-scale, historical data indicate that the baroclinic circulation is

nearly negligible (Gordon et al., 1978), and more closely spaced data recently obtained from the northwestern Weddell Sea are consistent with this view (Nelson et al., 1989).

Ice and ship drift data from the western Weddell suggest northward mean surface speeds there of 4-5 cm/s (Ackley, 1979; Ackley and Holt, 1984; Limbert et al., 1989), about half that which would be expected based solely on wind stress curl derived estimates. Nelson et al. (1989) reported that an ice floe instrumented for drift observation along the eastern edge of the multiyear pack ice cover showed virtually no motion from March-April 1986. This observation was interpreted by them to mean that the region fell east of the boundary current regime.

If convective features are formed primarily, as seems likely, in the eastern Weddell, then the effect of the mean circulation will be to advect them southward to southeastward with the mean flow. Features attaining the westward Antarctic Coastal Current might continue westward in that flow. Existing data are inadequate to estimate advection rates in these regions. If the greatest gyre-associated speeds are in the western boundary region, however, then speeds in the eastern and southern regions are less than the 4-8 cm/s western boundary speeds. Eddy advection rates due to the mean flow are, in this case, a few cm/s.

Eddies, of which convection cells are a special case, can migrate through dynamic interactions with bottom topography (see, e.g., Smith and O'Brien, 1983). This is perhaps not important in the case of eastern Weddell Sea convective features, within the context of this paper, for several reasons. Effective interaction between a circulating convective cell and bottom topography supposes that the feature extends to the bottom. While this may be true initially, we have no evidence supporting this (Gordon's 1978 observations showed the convective feature extending to about 3000 m, but did not demonstrate that it extended to the bottom). Assuming that such a feature initially penetrates to the bottom, there is a natural tendency for isolated eddies to evolve into upper layer, baroclinic features through combined deep dispersion and vortex stretching effects (Mied and Lindemann, 1979; McWilliams and Flierl, 1979). Hence migration through bottom topographic interaction might occur only during the earliest part of the feature's lifetime. While such interactions might be expected over Maud Rise, the bottom is relatively featureless west of Maud Rise. It is concluded that topographic interactions are not likely to exert a major control over cell migration once away from the immediate vicinity of Maud Rise.

Interactions between the cell circulation and planetary vorticity will always impart a westward movement to the cells. At the latitude of the

Weddell Sea, planetary vorticity can be represented reasonably by a beta plane. Cushman-Roisin et'al. (1990) have summarized and extended earlier work and have shown that eddies will propagate westward in a beta plane irrespective of their rotation direction. They provide an equation which can be used to compute migration speeds for eddies, provided that we know something of their structures (i.e. diameters, eddy current speeds, vertical structure and ambient stratification). Speeds of a few cm/s, of the same order as the presumed mean current speeds in the eastern Weddell, are typical for lenticular, cyclonic eddies. Though the basic principles are universally valid, quantitative extension of Cushman et al.'s (1990) results to convection cells is not straightforward. Part of the difficulty stems from the small diameter, deep nature of the cells. Modification of the Cushman-Roisin et al. (1990) work to the case of Weddell Sea convection cells is the subject of ongoing work and is beyond the scope of this present paper.

Unless the above speculations concerning mean circulation speeds in the interior of the Weddell Gyre are significantly in error, a significant portion of convection cell movement away from Maud Rise and the Antarctic Coastal Current will be westward propagation due to the beta-effect. Away from the immediate vicinity of Maud Rise, then (so that we may discount eddy-bottom topography interactions), the cells can be expected to migrate south to west in response to mean currents or simply west in response to the beta effect (Figure 6). Speeds are expected to be a few cm/s. At a speed of 2 cm/s, about three years would be required for a convection cell/eddy to migrate from a formation site near Maud Rise (say, at the Greenwich meridian) to the westernmost Weddell.

3.3. *And Evolution of The Features*

Isolated convective features such as those observed by Gordon (1978) and depicted schematically in Figure 5 can be expected to evolve through two sets of mechanisms which are probably mostly decoupled because they involve greatly differing time and length scales. One involves the mesoscale dynamical processes through which an eddy interacts with its environment. The other involves small-scale processes, down to and including molecular, which become relatively more important as the eddy decays and loses its energy and identity. Detailed discussions of these processes occupy entire books (e.g. Robinson, 1983 in the case of eddy dynamics and Turner, 1973 in the case of small-scale processes), and no attempt will be made here at complete discussions. It will be attempted, rather, to suggest those few processes which may be of most importance.

Subsequent to their formation, convection cells will commence to

"spin-down" as they lose energy through lateral friction throughout their vertical extent and frictional loss to the bottom (assuming they were initially barotropic and extended to the seafloor). Following Mied and Lindemann (1979) and McWilliams and Flierl (1979), we assume that the deeper parts will decay first such that the eddy-like circulation evolves from an initially barotropic feature to an upper layer, baroclinic feature. The cell may then, with time, become more of a lenticular baroclinic eddy. The convective nature of the feature makes it subject, in addition, to spreading which will dissipate the feature over time (Hermann and Owens, this volume). The spreading process can, under certain conditions, result in baroclinic instability which convolutes a single eddy into three or more smaller eddies, with the nature of the instability depending upon such features as the size of the initial convective cell (e.g., Madec et al., 1990; Hermann and Owens, this volume; Jones et al., this volume).

Upper layer shear, due possibly to winds, might isolate the eddy circulation from the surface, leaving an undisturbed upper layer overlying the eddy as observed by Gordon (1978). Summer ice melt might, additionally, restratify the upper layer overlying the eddy and mask its surface signature. While mean circulation in the Weddell Sea is primarily barotropic, it can be expected that sufficient deep vertical shear is present to vertically decouple a convection cell over periods up to years. Isolated from the surface and the bottom, the persisting remnant of the convection cell would be subject to attenuation through drag forces and loss of its baroclinic signature as heat and salt exchanged with the ambient water.

Toward the end of the convection cell as an identifiable feature, molecular processes such as double diffusion could become relatively important. Muench at al. (1990) demonstrated using laboratory results that upward double diffusive heat fluxes through large thermohaline staircases, which they hypothesized were remnant convective features, were of order 15 W/m^2 . They demonstrated using field data that the intermediate depth waters were unstable relative to double diffusive convection. They then showed by laboratory experiments that similar staircases form when a uniform water column is heated from below. One possible geophysical analog would be an initially uniform convection cell which, over a period of time, becomes underlain by warm water. From these results, they hypothesized that the Weddell Sea feature was a remnant convective cell which had been evolving through double diffusion while drifting about the Weddell Gyre.

For the foregoing argument to be credible, it is necessary that a mechanism exist by which heat can be input to the bottom of the cold, uniform convective layer. Warm water is present at intermediate depths in the Weddell Warm Water

layer, and there are several mechanisms through which the uniformly cold center of an eddy might eventually overlie this warm water. One is through the above-referenced initial decay, wherein a deep eddy evolves into an upper layer lenticular feature so that the cold eddy core can then overlie warmer water. A second means might be through even weak vertical ambient shear, given the probable slow speeds and long lifetimes of the features. Finally, lateral mixing of heat into the eddy at the depth of the Warm Water layer might have the same effect. In the absence of supporting data, the precise mechanism remains speculative.

As in the case of migration speeds, we have few data upon which to base numerical estimates of what might be considered realistic lifetimes of decaying convective features. Work on eddies elsewhere has suggested that lifetimes of years are not uncommon (cf. Robinson, 1983). Ou and Gordon (1986) estimated that small anticyclonic subsurface eddies in the Arctic Ocean might have lifetimes of several years. Isolated from the sea surface by the upper pycnocline and mixed layer, and enclosed within the very low energy ambient environment provided by the interior Weddell Gyre, lifetimes of order years seem reasonable for the convective features. This is of the same order as the time scales suggested above required for westward migration across the Weddell gyre.

4. DISCUSSION

Migrating, decaying convective features, such as described above, might have a number of effects on the ambient waters. Perhaps most significant, westward migration of these features can provide a means for transporting cold, vertically uniform water into the central and western Weddell gyre. Without this mechanism, the convective features would follow the mean circulation which tends to be appreciable only near the basin boundaries as the Antarctic Coastal Current and the western boundary current. It is possible, though not provable, that anomalously low T regions such as observed by Bagriantsev et al. (1989) are due to westward migration of cold convective features. These would have been blurred through vertical mixing and lateral spreading so that they would no longer have been identifiable as convective features. Only the heat deficit resulting from their low core T would have survived.

Migration of convective features might provide a means for westward transport of water having anomalously low (compared to the ambient water into which it moves) vertical stability. If present in large enough numbers, they might lead to significant lowering of the stability in the central and western Weddell, effectively preconditioning the water for convection. In such low

stability regions, ice formation can lead to deep convection and upward heat transport adequate to prevent new ice formation. It is interesting to note, with this in mind, that Martinson et al. (1981) reported on a region where little or no ice cover was present in the northwestern Weddell during August 1979. One way in which such a feature might occur would be through advection to this region, presumably via the western boundary current, of a low stability water parcel which had previously been conditioned through deep convection. Comiso and Zwally (1989) show anomalously low ice cover during November 1980 and November 1981 in the area just east of the summer ice edge location. This feature, also, might be explained by the presence of a low stability, remnant convective cell which allows sufficiently great upward heat transport to cause localized early decay of the ice cover. Alternatively, it might reflect the presence there of *in situ* convection associated with some physical discontinuity, such as air-sea drag coefficient differences leading to localized ice divergence and heavy freezing and brine production, offered by the ice edge.

ACKNOWLEDGEMENTS

Helpful comments have been provided on this manuscript by two anonymous reviewers. The work reported here has been carried out with support from NSF grants DPP-8420646 and DPP-8715979 to Science Applications International Corporation (SAIC), and ONR contract N00014-82-C-0064 with SAIC.

REFERENCES

Ackley, S.F., 1979. Mass balance aspects of Weddell Sea pack ice. J. Glaciol., 24: 391-405.

Ackley, S.F. and Holt, E.T., 1984. Sea ice data buoys in the Weddell Sea. CRREL Report No. 84-11, CRREL, Hanover, NH, USA.

Bagriantsev, N.V., Gordon, A.L. and Huber, B.A., 1989. Weddell gyre temperature maximum stratum. J. Geophys. Res., 94: 8331-8334.

Bersch, M., 1988. On deep convection in the Weddell Gyre. Deep-Sea Res., 35: 1269-1296.

Comiso, J.C., and Zwally, H.J., 1979. Polar microwave brightness temperatures from Nimbus-7 SMMR: time series of daily and monthly maps. NASA Spec. Rept. SP-1223, NASA, Washington, DC, USA.

Cushman-Roisin, B., Chassignet, E.P. and Tang, B., 1990. Westward motion of mesoscale eddies. J. Phys. Oceanog., 20: 758-768.

Foldvik, A., Gammelsrod, T. and Torresen, T., 1985. Hydrographic observations from the Weddell Sea during the Norwegian Antarctic Research Expedition 1976/77. Polar Res., 3: 177-193.

Foster, T.D. and Carmack, E.C., 1976. Tamperature and salinity structure in the Weddell Sea. J. Phys. Oceanog., 6: 36-44.

Gordon, A.L., 1978. Deep Antarctic convection west of Maud Rise. J. Phys. Oceanogr., 8: 600-612.

Gordon, A.L., Molinelli, E. and Baker, T., 1978. Large-scale relative dynamic topography of the Southern Ocean. J. Geophys. Res., 83: 3023-3032.

Gordon, A.L., Martinson, D.G. and Taylor, H.W., 1981. The wind-driven

circulation in the Weddell-Enderby Basin. Deep-Sea Res., 28: 151-163.
Gordon, A.L. and Huber, B.A., 1990. Southern Ocean winter mixed layer. J. Geophys. Res., 95: 11655-11672.
Huber, B.A., Rennie, S.E., Georgi, D.T., Jacobs, S.S. and Gordon, A.L., 1981. Islas Orcadas Cruise 12 Jan.-Feb. 1977; Hydrographic stations 53-126. Tech. Rept. CU-2-81-TR2, Lamont-Doherty Geological Observatory, Palisades, NY.
Killworth, P.D., 1979. On "chimney" formations in the ocean. J. Phys. Oceanog., 9: 531-554.
Limbert, D.W.S., Morrison, S.J. and Sear, C.B., 1989. Pack-ice motion in the Weddell Sea in relation to weather systems and determination of a Weddell Sea sea-ice budget. Ann. Glaciol., 12: 104-112.
Madec, G., Chartier, M., Delecluse, P. and Crepon, M., 1990. A three-dimensional numerical study of deep water formation in the northwestern Mediterranean Sea. J. Phys. Oceanog., 20: in press.
Martinson, D.G., 1990. Evolution of the Southern Ocean winter mixed layer and sea ice: open ocean deepwater formation and ventilation. J. Geophys. Res., 95: 11641-11654.
Martinson, D.G., Killworth, P.D. and Gordon, A.L., 1981. A convective model for the Weddell Polynya. J. Phys. Oceanog., 11: 466-488.
McWilliams, J.C. and Flierl, G.R., 1979. On the evolution of isolated nonlinear vortices. J. Phys. Oceanog., 9: 1155-1182.
Middleton, J.H. and Foster, T.D., 1980. Fine structure measurements in a temperature-compensated halocline. J. Geophys. Res., 85: 1107-1122.
Mied, R.P. and Lindemann, G.J., 1979. The propagation and evolution of cyclonic Gulf Stream rings. J. Phys. Oceanog., 9: 1183-1206.
Muench, R.D., Fernando, H.J.S. and Stegen, G.R., 1990. Temperature and salinity staircases in the northwestern Weddell Sea. J. Phys. Oceanog., 20: 295-306.
Nelson, D.M., Smith, W.O., Jr., Muench, R.D., Gordon, L.I., Sullivan, C.W. and Husby, D.M., 1989. Particulate matter and nutrient distributions in the ice edge zone of the Weddell Sea: Relationship to hydrography during late summer. Deep-Sea Res., 36: 191-209.
Ou, H.-W. and Gordon, A.L., 1986. Spin-down of baroclinic eddies under sea ice. J. Geophys. Res., 91: 7623-7630.
Robinson, A.R. (Editor), 1983. Eddies in Marine Science. Springer-Verlag, New York.
Smith, D.C., IV and O'Brien, J.J., 1983. The interaction of a two-layer isolated mesoscale eddy with bottom topography. J. Phys. Oceanog., 13: 1681-1697.
Turner, J.S., 1973. Buoyancy effects in fluids. Cambridge Univ. Press, Cambridge, UK, 368 pp.

This Page Intentionally Left Blank

Forced Convection in the Upper Ocean near Fram Strait in Late Winter

Miles G. McPhee
McPhee Research Company
Naches, WA 98937 USA

ABSTRACT

Measurements of mean flow and turbulence in the boundary layer under drifting Arctic pack ice during the 1989 CEAREX O Camp experiment support the hypothesis that turbulence derived from internal waves and other flow features in the underlying pycnocline was an important factor in maintaining a deep mixed layer. Turbulent stress measurements in the upper 30 m of the boundary layer showed less attenuation with depth than previous experiments, implying existence of a source of turbulence in addition to shear at the ice/ocean interface. Although wind is usually the main source of shear between ice and ocean in the Arctic, in the O Camp region it was secondary to tidal currents apparently amplified by interaction with the Yermak Plateau. A packet of energetic internal waves impinging on the mixed layer/pycnocline interface at about 100 m depth is investigated, and appears to lose much of its energy to smaller scale motion there. It is suggested that similar phenomena may help account for the relative depth of the mixed layer in the central Weddell Sea, where deep convection has occurred in the past.

1. Introduction

Away from the continental slopes and marginal seas, the upper Arctic Ocean typically exhibits a strong pycnocline overlain by a relatively fresh mixed layer less than 60 m thick. The upper part of the pycnocline is cold, often near freezing, and strongly stratified by salinity; thus a very effective barrier exists between turbulent processes at the air-ice-sea interface and the warm Atlantic water at depth, and there is little possibility of deep convection and "catastrophic" overturn. The perennial ice pack in the Arctic provides a strong negative feedback to enhanced oceanic heat flux by its stabilizing effect on the boundary layer. In the Antarctic, the situation is different. Recent wintertime expeditions to the Weddell Sea (see, e.g., Gordon and Huber, 1990) have shown that the mixed layer there is relatively deep (>100 m) and stability is marginal. Martinson (1990; this volume) demonstrates that minor changes in a few key variables could nudge the present day Weddell into overturn, and the presence of a vast, all season polynya (the Weddell Polynya) during the 1970s shows that, once established, deep convection can apparently persist for years.

One of the more puzzling aspects of deep mixed layers in ice covered water is what keeps them mixed. The picture emerging from recent winter Antarctic work (Gordon and Huber, 1990) is one in which ice grows rapidly during the first few weeks of winter until it reaches a thickness of about 60 cm, after which heat conducted through the ice is roughly balanced by upward heat flux at the base of the mixed layer, and to first order, the system approaches a steady state with an upward heat flux estimated to be around 40 W m^{-2}. This is at least an order of magnitude larger than oceanic

heat flux typically found under multi-year Arctic ice during the winter (McPhee and Untersteiner, 1982), but still much smaller than heat lost by open water in direct contact with the polar atmosphere. In terms of ocean boundary layer (OBL) physics, there is an important distinction between heat lost through conduction and heat lost directly to freezing. The thermal expansion coefficient is so small at temperatures near freezing that surface buoyancy flux is controlled almost exclusively by salinity, thus freezing produces a strong destabilizing buoyancy flux while heat loss through conduction has little effect on stability.

When forced convection at the surface is aided by destabilizing buoyancy flux, either from strong surface cooling in the open ocean, or from rapid ice growth when the mixed layer is at freezing, deep mixing is expected. However, when surface cooling is not accompanied by buoyancy flux, two factors work to limit the depth of mixing in polar boundary layers: (1) Coriolis attenuation of surface driven turbulent stress is large at high latitudes, consequently shear production of turbulent kinetic energy (TKE) falls off more rapidly and the rotational length scale (Ekman depth) for the boundary layer is smaller than at lower latitudes (an extreme example is presented by McPhee [1990, Fig. 6.9] where much of the stress attenuation and rotation occurs in the upper 10 m beneath a hydraulically smooth surface). (2) Processes that transport heat and salt into the boundary layer from below (the most likely candidates are direct upwelling and turbulent diffusion) also tend to reduce mixed layer depth, unless there is active entrainment at the top of the pycnocline.

During the *Coordinated Eastern Arctic Experiment* (CEAREX) *Oceanography Camp (*O Camp*)* drift in March and April of 1989, we encountered conditions that may bear on the question of what maintains deep, ice-covered mixed layers. In the region where the ice camp drifted (a southwest trajectory, centered at about 82°30' N, 8° E) the mixed layer was atypical of the Arctic in that it was salty (typically 34.1 psu), often about 100 m thick, and the halocline and thermocline coincided, so that the underlying warm (Atlantic) water was potentially in direct contact with the ice-covered surface. Since the ice cover was relatively compact and thick, convection driven by brine rejection was minor. The O Camp mixed layer was thus similar in some respects to the "cold" Weddell regime of Gordon and Huber (1990, see their Fig. 7c) except that the change in density across the pycnocline separating the mixed layer from the warm layer below was about twice as large in the Arctic, and the vertical extent of the pycnocline was much greater.

The intent of this paper is to explore characteristics of turbulence and other high frequency motions measured in the upper ocean under O Camp. Previous observations of turbulence under pack ice have underlined the importance of wind forcing: when the winds stops blowing, the ice/ocean shear and associated turbulence vanish. It is tempting to assume that the turbulent OBL set up by wind-driven drift across a quiescent ocean is similar to the OBL that would occur if the ocean flowed past stationary ice with the opposite velocity— this is the basis, e.g., of comparing the under-ice OBL with the atmospheric boundary layer (McPhee and Smith, 1976). The tacit assumption is that the only source of turbulence is shear at the ice-ocean interface. During much of the drift of O Camp we experienced strong diurnal currents relative to the ice that had little if any direct relation to the wind. The O Camp results suggest instead that turbulence generated by internal wave

breaking near the mixed layer/pycnocline interface may have boosted overall turbulence levels in the mixed layer, and helped keep the mixed layer deep.

2. Turbulence Measurements

During O Camp, we deployed two instrument systems for measuring both mean and high frequency flow characteristics, using "turbulence clusters" (TC's) comprising three small current meters mounted along orthogonal axes near a Sea-Bird temperature/conductivity pair. The first system consisted of two rigid masts suspended through hydroholes with TC's at several levels down to 12 m below the ice, i.e., the upper part of the OBL. The second system (Fig. 1), newly developed for the O Camp experiment, is a rigid frame with 6 TC's spanning 11 m in the vertical, all interfaced to a Sea-Bird CTD unit equipped with compass and tiltmeters. Over the course of the experiment, the topmost cluster was eliminated, and one of the remaining temperature sensors failed, leaving 5 velocity turbulence clusters, with 4 including temperature and salinity. The whole "super CTD" can be lowered by a small winch to depths of 100 m or more. This system was intended mainly for studying internal waves and other small scale motions in the upper part of the pycnocline, but could also be positioned for boundary layer measurements nearer the surface.

From late on April 11, 1989 (day 101) through April 14 (day 104) a small storm was observed at O Camp with sustained easterly winds of 6-8 m/s (Guest and Davidson, 1989). For part of that period, the mobile CTVD frame was raised so that its topmost cluster was at approximately the same depth as the lowest cluster on the fixed mast, i.e., 12 m below the depth of the ice/ocean interface at 2.4 m. This provided a comparison between two clusters separated horizontally by about 6 m, and extended the turbulence measurements 9 m deeper in the boundary layer.

Turbulence statistics were extracted from the raw data as follows. The system samples velocity of each rotor six times per second, with these samples averaged for 1 s in the interface deck units and recorded digitally. For each cluster, sums of the data and data products and cross products are accumulated for 15 min periods, from which average velocities and zero lag covariances are calculated. Components of the Reynolds stress tensor are defined by

$$\tau_{ij} \equiv \langle (u_i - U_i)\ (u_j - U_j) \rangle$$

where angle brackets denote the ensemble spatial average, u_i is the instantaneous velocity component in the ith direction, and $U_i = \langle u_i \rangle$,. The true Reynolds stress is approximated by the covariance matrix under the assumption that a horizontally homogeneous field is advected past the probes in a steady flow. Obviously, these conditions are rarely encountered in nature, and our hope is that there is a "spectral gap" between the frequencies of the dominant turbulent eddies and other flow features. We have found from past measurements in the OBL (McPhee and Smith, 1976; McPhee, et. al, 1987) that an averaging interval of 15-20 minutes represents a suitable compromise between sampling the entire turbulent spectrum and having lower frequency, nonturbulent flow variations contaminate the statistics. Since the time scale of the most energetic turbulence eddies is of order minutes, there is much variability from one 15-min realization to another, especially in the off-diagonal (shear stress) components of the Reynolds stress tensor. Thus several 15-min realizations must

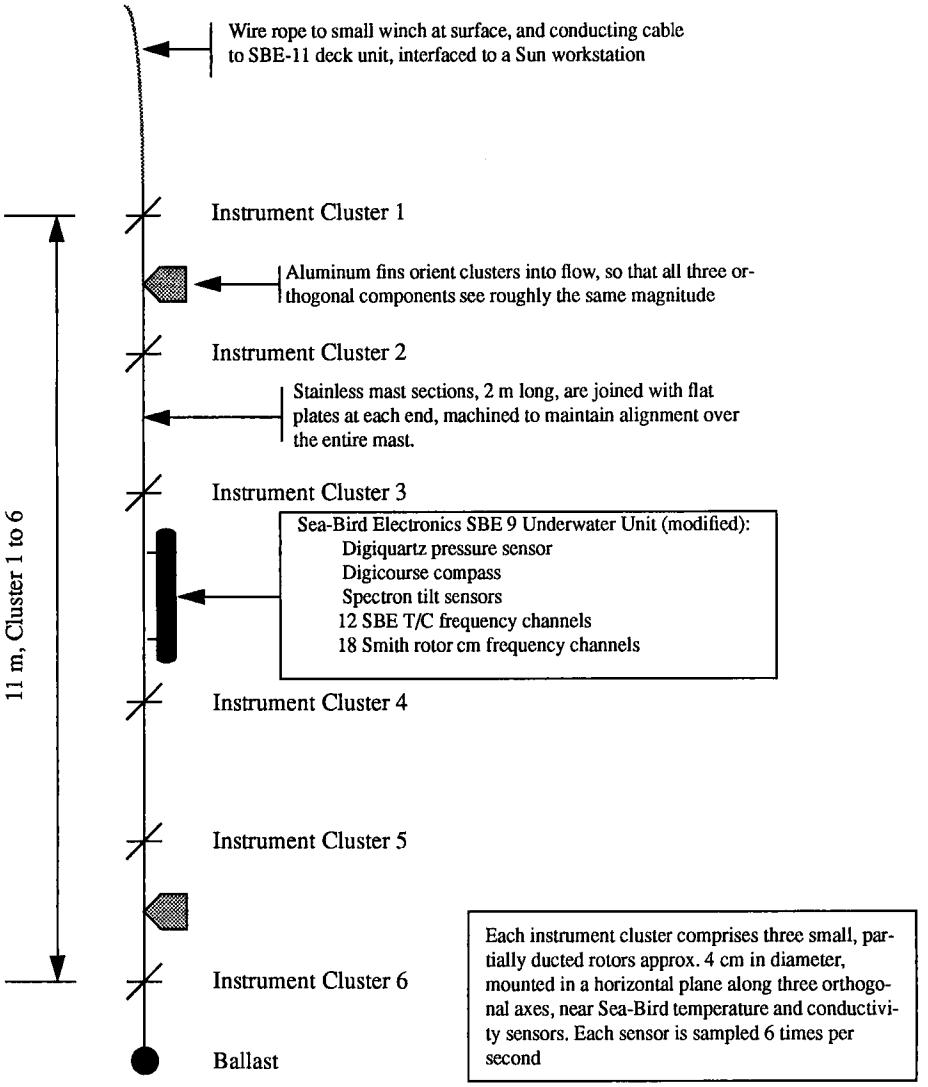

A Multi-level CTDV System on a Rigid Mast

Fig. 1. Schematic of the mobile Conductivity-Temperature-Velocity-Depth (CTVD) frame developed for the CEAREX O Camp experiment. The frame could be lowered to about 110 m depth.

be averaged before the Reynolds stress statistics "settle down."

Fig. 2a shows a 5.25-hr average (i.e., the average of 21, 15-min realizations of the Reynolds stress tensor), beginning at 103:10:08 UT, of mean velocity (relative to the ice) and Reynolds stress for three clusters on the main fixed TC frame. This may be compared with a 6-hr average starting at 103:10:15 UT of 5 clusters on the mobile CTDV frame (Fig. 2b). Although the times are not exactly the same, there is reasonably close correspondence between both velocity and turbulent stress where the depths overlap. Fig. 2c shows velocity and stress measurements from an earlier time when the mobile CTVD frame was lower in the OBL, and the flow was less energetic: the mean velocity at 22.9 m is 12.0 cm/s vs. 19.9 cm/s at 23.2 m in Fig. 2b.

The variability in stress in the upper part of the OBL, especially the decrease in stress 2 m from the interface (Fig. 2a), probably results from variation in the under-ice topography surrounding the experiment site. A side-looking sonar survey of the ice undersurface showed that the ice was relatively smooth near the deployment site, but that there here were sizable pressure ridge keels within 100 m (R. Colony, personal comm., 1989). If the roughness of the undersurface were uniform, stress would increase monotonically toward the interface; however, as the turbulence frames are usually sited under smooth ice, it is common for the stress to decrease near the surface (see, e.g., McPhee, et. al., 1987).

The profiles of Fig. 2 exhibit characteristics which distinguish these data from previous studies under sea ice.The main feature is the lack of angular shear (turning) in both vector fields. In most previous OBL measurements, the turning occurred within the upper 30 m of the water column (McPhee and Smith, 1976; McPhee, et. al., 1987); however, those data were from mixed layers that were 40 m or less thick. At the time of the present measurements, the mixed layer under O Camp was about 70 m deep (J. Morison and R. Andersen, personal comm., 1990). In order to quantify how this would affect theoretical velocity and stress profiles, we adapted a steady state, quasi-analytic OBL model (McPhee, 1990; 1991) so that it matched the modeled stress to the measured stress at a particular level (14.2 m in Fig. 3a), then reconstructed the entire stress profile, including the inferred stress at the interface, shown as the dashed vectors in Fig. 3. The model velocity profile relative to an observer on the ice was then constructed from the stress profile, with the surface layer shear specified by finding a surface roughness ($z_o = 0.1$ m) which gave close agreement with velocity measured at the same 14.2 m depth. Results are shown in Fig. 3a, in a format chosen to facilitate comparison with the measurements. The dotted curves around the topmost vectors show theoretical hodographs (plan views) for velocity and stress for a logarithmic grid across the upper 100 m, and are included to indicate the total expected turning in both vector fields. Note that in the reference frame attached to the ice there is little angular shear in the velocity field in the upper 20 m, but that the Reynolds stress vector exhibits substantial turning.

The model includes the effect of buoyancy flux at the pycnocline on the turbulence structure, and the results show that the lack of turning in the velocity profile is not unexpected (although the angle between velocity and stress is less in the model than in the data). The modeled stress shows more turning than observed, but generally approximates a smoothed rendition of the ob-

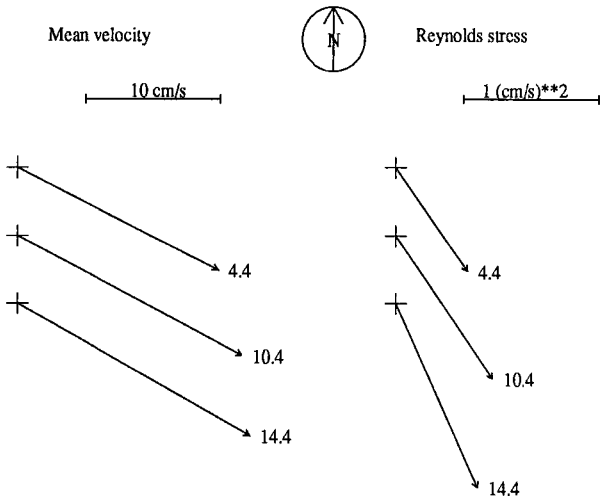

Fig. 2a. Mean velocity (relative to observer on the ice) and Reynolds stress for three clusters of the fixed frame, averaged for 5.25 hrs beginning at 103:10:14 UT. Numbers to the right of each vector are depth in m (subtract 2.4 for distance from ice underside)

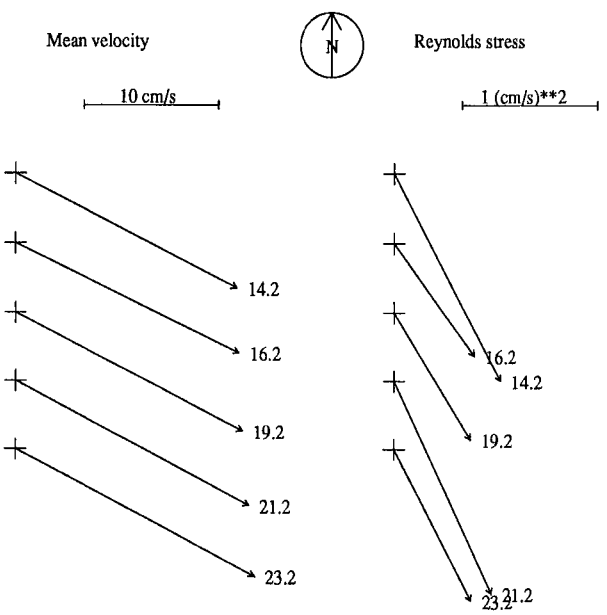

Fig. 2b. Mean velocity and Reynolds stress for the mobile CTVD frame, averaged for 6 hrs beginning at 103:10:15.

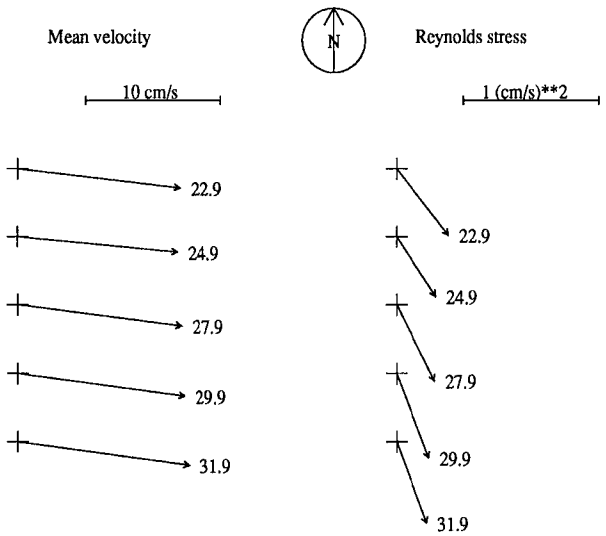

Fig. 2c. Same as Fig. 2b, except 1.75 hr average starting at 102:14:15

served stress.

For the model to have validity, it should apply as well to different conditions. This was tested by forcing the modeled stress at 22.9 m to match data from the earlier observations of Fig. 2c. Results are shown in Fig. 3b, and discrepancies are readily apparent. In order to match the observed stress at 22.9 m, the model finds a fairly high value of surface (interface) stress, which produces enough shear through the logarithmic surface layer (using the same 0.1 m for z_0) that the modeled velocity at 22.9 m is roughly 40% higher than observed. In addition, the modeled stress 9 m below the reference level is noticeably smaller and rotated farther clockwise than observed. Thus the measured velocity implies that the actual interfacial stress is smaller, and that the model overestimates attenuation of stress with depth.

While uncertainties in the model and data are large, the theoretical results suggest that stress is more uniform, and penetrates farther into, the O Camp mixed layer than we would expect based on the behavior of previously measured boundary layers. Aside from the depth of the mixed layer, a major difference between the O Camp and previous mixed layers is the strength of oceanic flow not driven directly by the wind. Recalling the discussion in Section 1, in most of the Arctic, wind is the prime mover of ice, and the *absolute* (i.e., in a frame of reference fixed to earth) velocity in the lower part of the boundary layer approaches the geostrophic current in the ocean, typically a few centimeters per second. Our impression at O Camp was that currents in the boundary layer had little

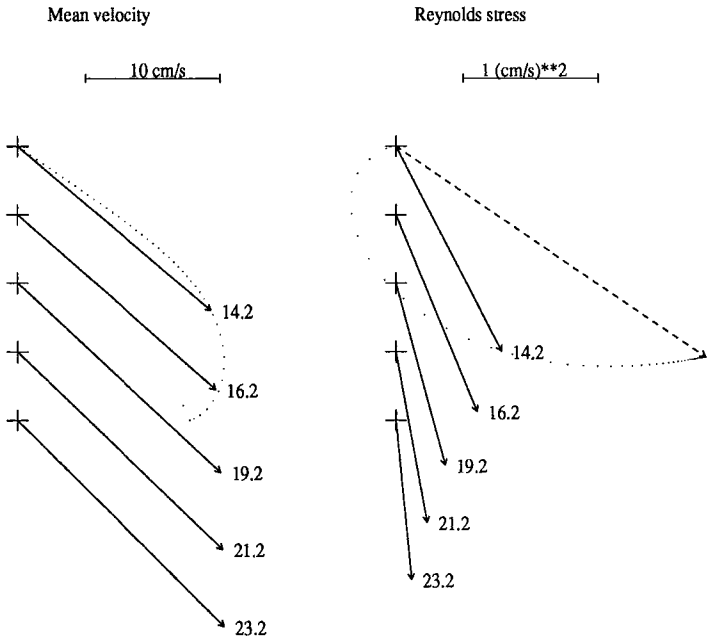

Fig. 3a. Analytic model of relative velocity and Reynolds stress, forced to match the observed stress at 14.2 m (Fig. 2b). Solid vectors are drawn offset downward to coincide with the measurement levels. The dashed stress vector is the required ice/ocean stress and hodographs of stress and velocity are shown as dotted curves emanating from the uppermost level.

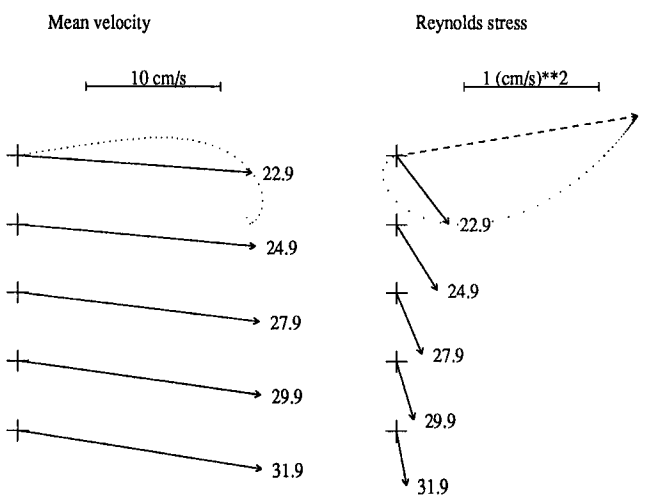

Fig. 3b. Same as Fig. 3a, except the model was forced to match the stress at 22.9 m to simulate the upper ocean structure of Fig. 2c.

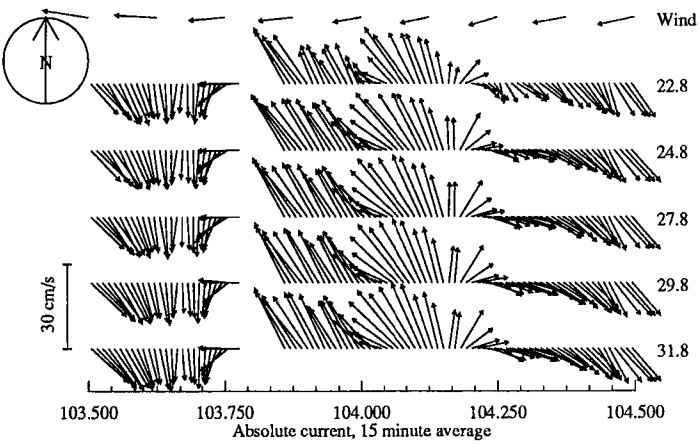

Fig. 4. Fifteen minute averages of absolute horizontal velocity at 5 levels of the mobile CTVD frame. Numbers at right indicate average depth in m. Absolute velocity is the vector sum of the measured water velocity and the ice velocity determined from satellite navigation. The row of vectors labeled "Wind" indicates surface wind velocity divided by 50, so that the scale bar at the left is equivalent to a wind magnitude of 15 m/s.

direct connection with the wind, which is substantiated by Fig. 4, showing the absolute horizontal currents at each level on the mobile frame for the period 103:12:00 to 104:12:00 UT and 3-hr averages of the surface wind. The frame was occasionally moved in the vertical during the interval shown, but remained relatively shallow until the last few hours, when it was lowered into the pycnocline. While the wind remains relatively steady from the east, there is a strong south to north and back again reversal in the flow. Shortly after midnight on day 104, there is a significant flow event superimposed on the northward part of the diurnal cycle. It may be that this energetic flow, which will be discussed further in the next section, is instrumental in increasing turbulence levels in the entire mixed layer and thus smearing the momentum exchange between the ice and ocean across a larger vertical extent.

3. Deep Boundary Layer Measurements

Results presented above are from a time with the mobile CTVD frame positioned near the surface, when it was in effect an extension of the near surface, fixed frame. Four days later, both systems measured a remarkably similar flow regime, but this time the mobile frame was near the bottom of the mixed layer. Fig. 5a shows horizontal current in the same format as Fig. 4, with the frame spanning levels from about 93 to 102 m. The deeper flow has many features of the earlier record, including the dominant diurnal reversal, a dramatic direction swing shortly after midnight, and little apparent connection with the wind. The temperature record (Fig. 5b) illustrates that strong

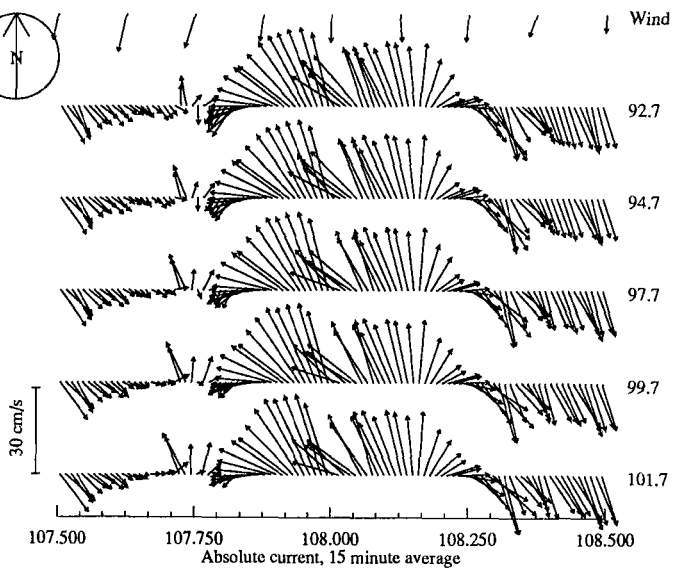

Fig. 5a. Same as Fig. 4, except for time 107:12:00 to 108:12:00, with the mobile CTVD frame deep in the mixed layer/upper pycnocline.

thermal signatures accompany both the velocity reversals and mid-cycle disturbances at intervals of slightly over 6 hrs. Salinity is not shown but follows temperature closely with a maximum excursion of about 0.4 psu. A plausible interpretation is that the recurring thermal features are some type of internal bore associated with amplification of internal tides by the Yermak Plateau to the south, as discussed in the context of a dominant diurnal component in current meter records from the region by Hunkins (1986). The disturbances are also apparent in Fig. 5c, which shows q^2 (i.e., the sum of the diagonal components of the Reynolds stress tensor), based on two-minute averages of the deviation of velocity components (measured at 1 sec intervals) from their means. The short averaging time was chosen to separate the small scale effects from variance associated with irrotational internal waves, and thus may not represent the entire turbulent spectrum; nevertheless, "patches" of intense q^2 most likely indicate active turbulent transfer down the energy cascade from larger to smaller scales. There is a period of relatively high turbulence in the afternoon of day 107 without the dramatic temperature/salinity signal, but it appears in this case that the disturbance existed deeper in the water column (L. Padman, personal comm., 1990).

The midnight event was accompanied by a packet of energetic internal waves, as illustrated most clearly in the vertical velocity records of Fig. 6. These waves were also evident in data from tiltmeters embedded in the ice (Czipott, et. al., 1990). The average spectrum of vertical velocity for the entire 24-hour period is shown in Fig. 7. Spectra were calculated for each cluster by smoothing

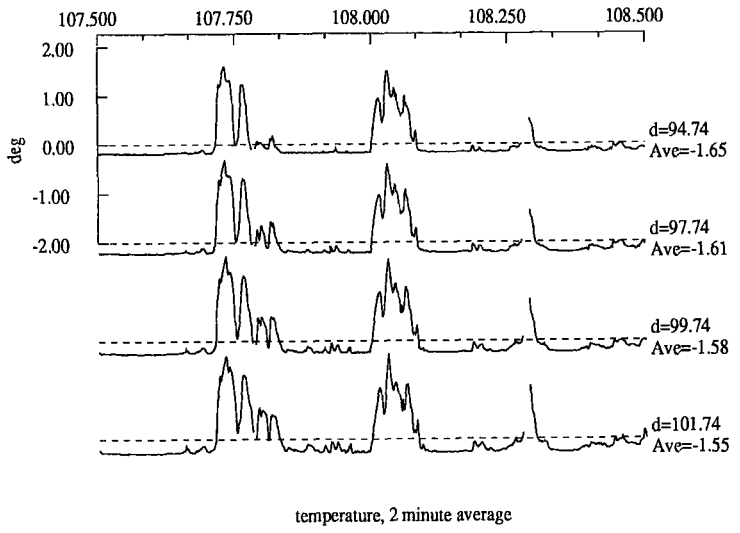

Fig. 5b. Deviations of temperature from mean values for 4 mobile frame clusters, for the period 107:12:00 to 108:12:00. Numbers at right indicate cluster depth and average temperature for the time series, in deg C.

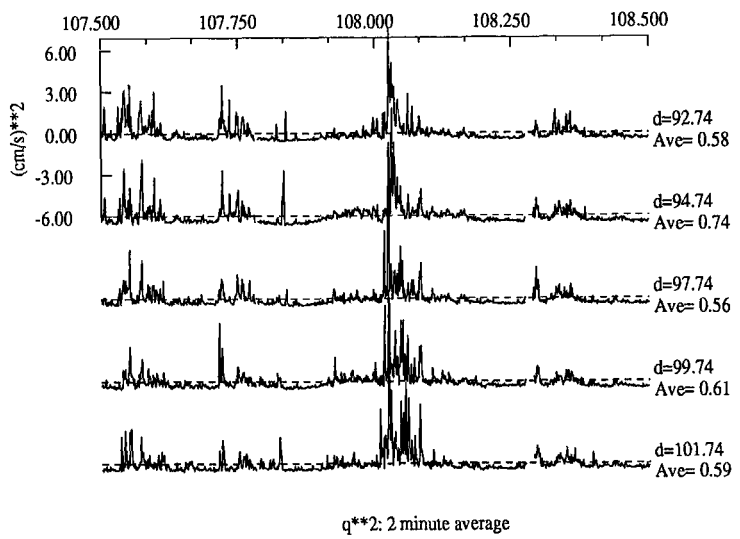

Fig. 5c. $q^2 = \langle u'u' \rangle + \langle v'v' \rangle + \langle w'w' \rangle$ averaged for two minutes, shown as deviations from the mean at 5 levels on the mobile frame.

the periodogram (proportional to the squared amplitude of the discrete Fourier transform of one minute averages of vertical velocity) with one pass of a modified Daniell filter of halfwidth 4 min^{-1} (Bloomfield, 1976). The spectra from all 5 clusters were then averaged for Fig. 7. A peak with a frequency of approximately 0.04 cpm (25 minute period) stands out, which agrees within a minute of the period reported by Czipott, et. al. (1990) in ice flexure.

A number of interesting events occur during the first 6 hrs of day 108, which may illustrate how deep mixing is enhanced in the Yermak Plateau region. A salinity profile just prior to the onset of the bore event at about midnight is shown in Fig. 8a, along with 10-min average salinities from the lower 4 clusters. The instrument frame started out near the base of the mixed layer, then apparently entered and exited the pycnocline as the interface followed the internal waves, as indicated by the difference in salinity across the instrument frame as a function of time (Fig. 8b). After the main thermal anomaly passed in about 2 hrs, the stratification reverted to its former small value. The 25-min period internal waves continued until about 05:00. The abrupt rise in q^2 lags the passage of the bore temperature front by about half an hour, then seems to die away more or less exponentially over the next 5 hrs. A picture thus emerges of an internal bore, which is itself highly turbulent, traversing the lower part of the mixed layer, leaving energetic internal waves and elevated turbulence levels in its wake.

A detail of the spectra of vertical velocity for the first 6 hrs of day 108 is shown in Fig. 9. The solid line is the average spectrum for the upper three clusters on the mobile frame, with symbols indicating individual spectra for the same three clusters (the lower two clusters are not shown in order to keep the graph legible, but are quite similar to cluster 3, marked by pluses). Near the 25-minute peak [log(f)= -1.4], there is a substantial difference in energy density across the 5 m span of the clusters. There is a plateau in the frequency range from log(f)= -1.1 (1/12 min) to -0.8 (1/6 min) which may indicate harmonics of the dominant internal waves, or the dominant turbulent eddy size, or perhaps a combination of both. At the higher frequencies, the energy levels of the higher cluster (asterisks) are no longer discernibly smaller, in fact may be larger.

Similar velocity measurements are available from two, 3-hr records of the fixed-mast turbulence system near the surface, spanning the period from 107:23:56 to 108:06:14. Fig. 10 shows power spectra of 1-min averages of vertical velocity for clusters at 4, 8, and 12 m below the ice/water interface in the same format and to the same scale as Fig. 9. Calculation of the spectra is the same as before, except that the individual cluster spectra are the average of spectra from two 3-hr segments instead of one 6-hr segment. There is essentially no indication in the shallower data of the 25-min waves, even 12 m below the ice. In fact, the spectra begin to fall off near the peak of the lower spectra. This was somewhat surprising in view of the tiltmeter results mentioned above; on the other hand, the actual displacement of the ice is very small, and if there is energy at 25 min, it is masked by the turbulence levels at higher frequencies. The lack of a spectral peak in the cluster at 12 m is important because it shows that the 25-min waves are not losing their energy only when they encounter the high stress and shear near the interface, but that much of the energy transfer to turbulence is happening near the base of the mixed layer.

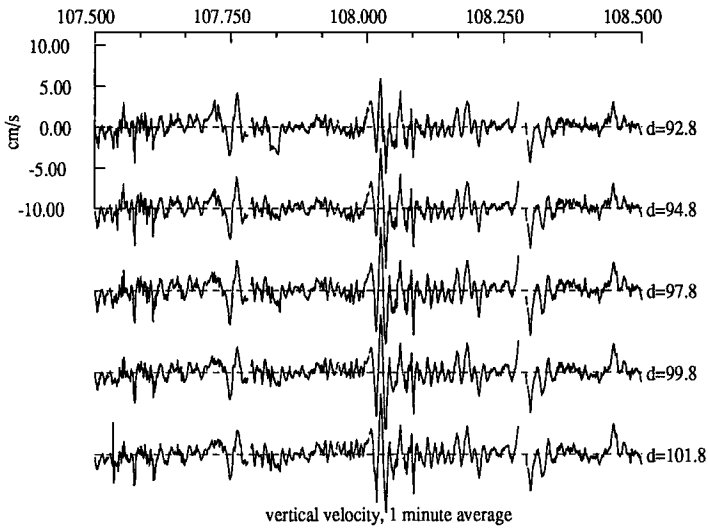

Fig. 6. Time series of vertical velocity at 5 levels on the mobile frame. Each small time division is 2 hrs.

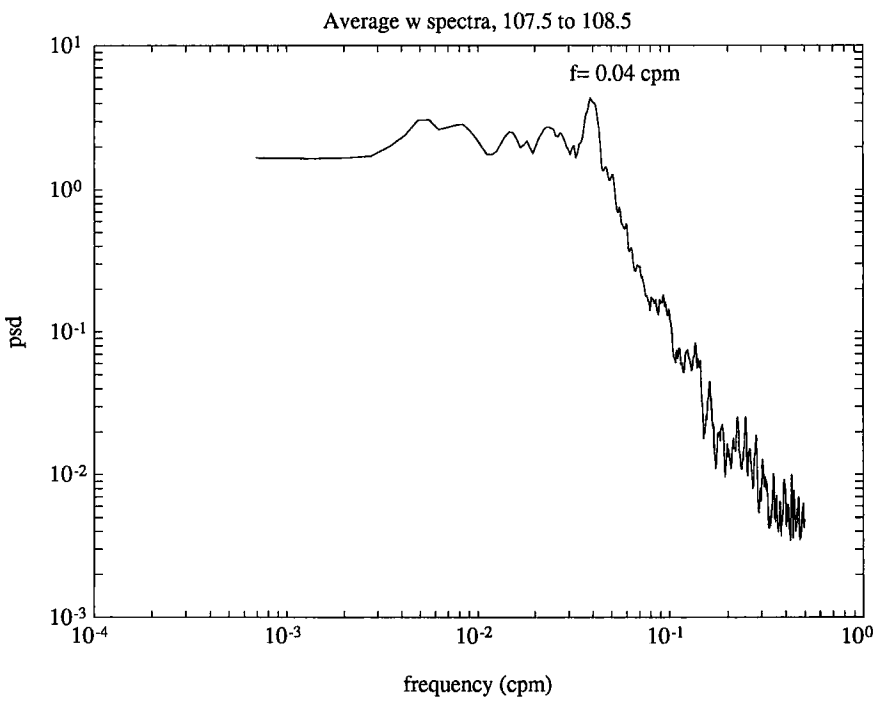

Fig. 7. Average power spectrum of vertical velocity for 5 clusters of the mobile frame for the period 107:12:00 to 108:12:00 UT. Spectra for each cluster are calculated by smoothing the periodogram of 1-min velocity averages with one pass of a modified Daniell filter of halfwidth 4 min^{-1}.

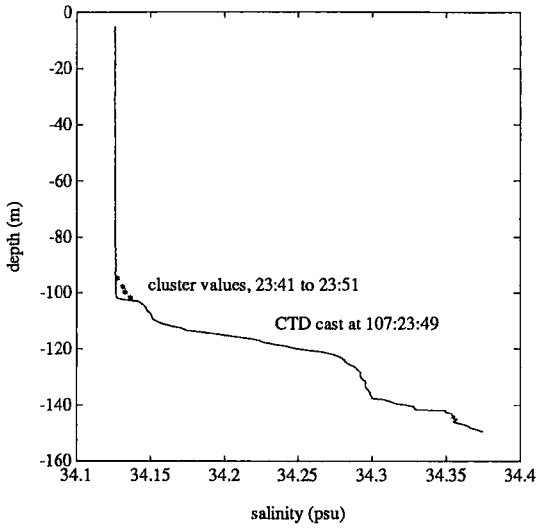

Fig. 8a. Salinity profile (courtesy J. Morison and R. Andersen) just prior to the onset of the anomalous event starting at midnight. Asterisks mark the 10-min average of mobile frame salinities at approximately the same time.

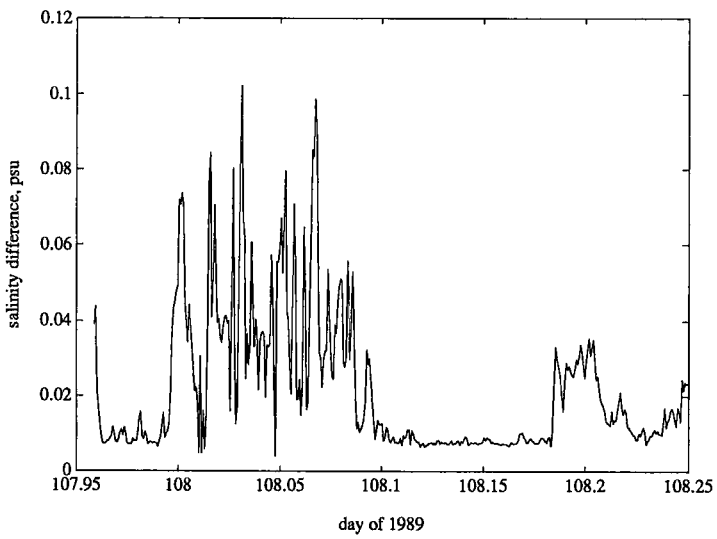

Fig. 8b. Time series of the difference in salinities between mobile frame cluster 4 (at 101.7 m) and cluster 2 (at 94.7 m) for the period 107:23:00 to 108:06:00 UT.

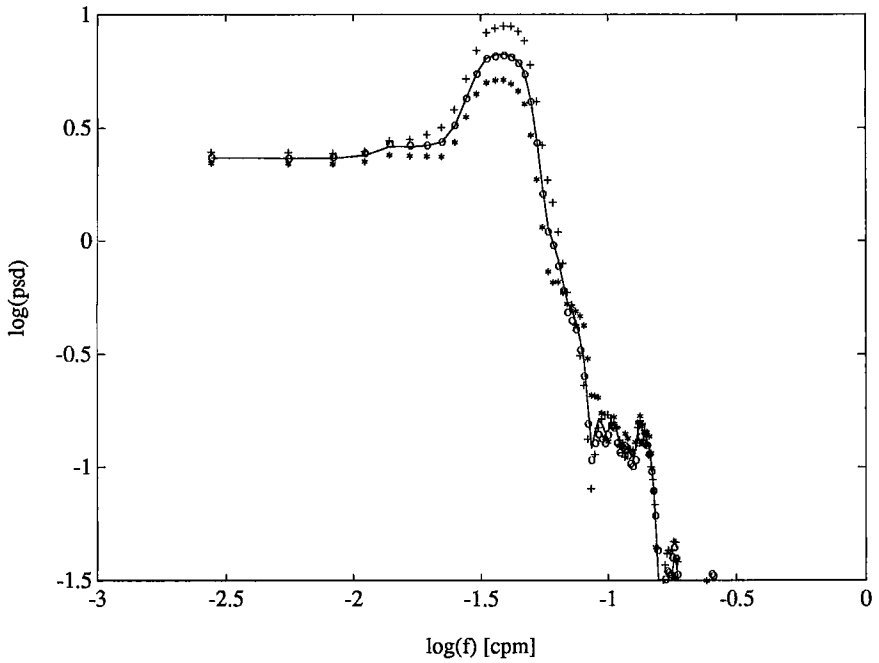

Fig. 9. Power spectra of vertical velocity from three clusters on the mobile frame for the period 108:00:00 to 108:06:00. Symbols mark spectra from individual clusters: cluster 1 at 92.7 m (*), cluster 2 at 94.7m (o), and cluster 3 at 97.7 m (+). The solid curve is the average. Spectra from deeper clusters are similar to cluster 3.

A reasonable interpretation of the spectra of vertical velocity from both deep in the mixed layer and near the surface, is that energetic internal waves are propagating into the system from below, and losing their energy as they encounter the low stability and existing turbulence in the lower part of the mixed layer. Fig. 9 is provocative in that if it truly represents a transfer of energy from the frequency of the dominant internal waves to smaller scales across the 5 m separation of the three clusters, then it shows that the main source of TKE just above the main pycnocline comes from below.

4. Summary

While the upper ocean under O Camp was never close to overturn and subsequent deep convection, the regime there may be the closest Arctic analog yet studied of the ice covered winter mixed layer of the Weddell Gyre, where overturn is possible with slight variation of the forcing parameters (Martinson, this volume). The question posed for each region is how the upper ocean remains mixed to deep levels (by polar standards) when destabilizing surface buoyancy is cut off by the ice cover, and when upwelling and diffusion across the pycnocline tend to reduce the mixed layer depth. Results of the present study suggest that activity in the pycnocline below the mixed layer may have significant impact on the turbulence and momentum flux in the OBL. A source of OBL turbulence other than direct shear at the ice/ocean interface would mimic some aspects of an unsta-

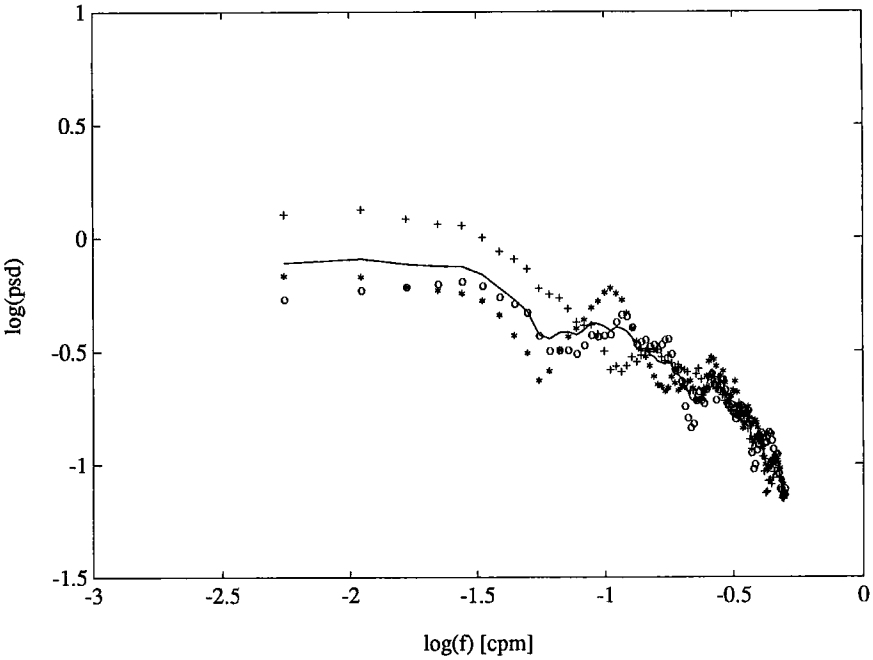

Fig. 10. Power spectra of vertical velocity from three clusters on the main fixed frame for the period 107:23:56 to 108:06:14. The format, including plot scales for direct comparison, is the same as Fig. 9, except: cluster 1 at 6.4 m (4 m below the ice) (*); cluster 2 at 10. 4 m (o); cluster 3 at 14.4 m (+). Note the lack of a discernible peak at 25 min [log(f)= -1.4].

ble, convective boundary layer: i.e., just as stable stratification reduces the size of turbulent eddies, and confines the OBL momentum (deficit, in this case) to smaller depths with more angular shear (see, e.g., McPhee, 1983; Mellor, et.al., 1986), an agent that increases eddy size would conversely increase the scale of the OBL and reduce the turning. The near surface measurements in Section 2 showed that stress levels were higher in the range from 15-30 m than we had come to expect from previous studies of neutral boundary layers under sea ice, implying some enhancement of turbulence levels. The ice cover in the vicinity of O Camp was relatively thick and compact, thus it is unlikely that unstable buoyancy flux had much influence on OBL dynamics.

A case study of an energetic packet of internal waves superimposed on what appears to be a fairly regular tidal bore that traverses the O Camp region, may indicate where the enhanced turbulence originates. Fig. 5c shows that small scale velocity fluctuations (most likely turbulence) near the base of the mixed layer are strongly intermittent and related to the larger scale flow features. Fig. 9 shows a steep vertical gradient in power spectral density in the vertical velocity components near the mixed layer/pycnocline interface. The vertical displacement associated with a simple internal wave with the vertical velocity amplitude observed shortly after midnight on day 108 (Fig. 6) is about 20 m, yet 80 m higher in the boundary layer (and still 12 m from the interface), there was virtually no evidence of the 25-min waves in the vertical velocity spectrum (Fig. 10). The clear impli-

cation is that quite a lot of energy has been transferred from lower to higher wavenumber scales, and that as the internal waves impinge on the mixed layer from below, the process takes place preferentially at depth. A source of turbulence for maintaining a sharp interface deep in the mixed layer is thus identified.

What created the oceanic conditions responsible for the activity below the OBL at O Camp is beyond the scope of this work, yet it may be germane to point out the geometric similarities between the Arctic Ocean floor around the Yermak Plateau, and the Weddell Sea in the vicinity of Maud Rise. While the proximity of Maud Rise to the initial location of the Weddell Polynya of the 1970s may be coincidental, one can speculate that an increase in internal wave activity in the pycnocline, say from the interaction of an oceanic eddy with Maud Rise, might have raised turbulence levels in the mixed layer, and entrainment at its base, enough to initiate deep convection, and then to prevent re-establishment of the stable winter regime now dominant. Further research, both observational and theoretical, seems warranted.

5. Acknowledgment

Support for this work by the Office of Naval Research, Contract N00014-84-C-0028 is gratefully acknowledged, as is help in the field from the CEAREX logistics staff and fellow O Camp scientists. I thank R. Andersen, K. Davidson, P. Guest, and J. Morison for providing data. Comments on the manuscript by P. Czipott, L. Padman, and an anonymous reviewer are appreciated.

6. References

Bloomfield, P. 1976. *Fourier Analysis of Time Series: An Introduction.* John Wiley and Sons, New York, 258 pp.

Czipott, P.V., W. Podney, M.D. Levine, C.A. Paulson, and R. Williams. 1990. Ice flexure forced by an internal wave packet in the Arctic Ocean. *Eos, Transactions of the Am. Geophys. Union, 71,* p. 130 (abstract).

Guest, P.S., and K.L. Davidson. 1989. CEAREX "O" and "A" Camp meteorology atlas, Naval Postgraduate School data report (unpubl.), Monterey, CA

Gordon, A.L., and B. Huber. 1990. Southern Ocean winter mixed layer, *J. Geophys. Res. 95,* 11,655-11,672.

Hunkins, K. 1986. Anomalous diurnal tidal currents on the Yermak Plateau, *J. Mar. Res., 44,* 51-69.

McPhee, M.G. 1990. Small scale processes, in: *Polar Oceanography,* ed. W. Smith, 287-334, Academic Press, San Diego, CA.

McPhee, M.G. 1991. A quasi-analytic model for the under-ice boundary layer, in press, *Annals of Glaciology.*

McPhee, M.G., G.A. Maykut, and J.H. Morison, 1987. Dynamics and thermodynamics of the ice/upper ocean system in the marginal ice zone of the Greenland Sea. *J. Geophys. Res., 92,* 7017-7031.

McPhee, M.G., and J.D. Smith. 1976. Measurements of the turbulent boundary layer under pack ice, *J. Phys. Oceanogr., 6,* 696-711.

McPhee, M.G., and N. Untersteiner, 1982. Using sea ice to measure vertical heat flux in the ocean. *J. Geophys. Res., 87,* 2071-2074.

Martinson, D.G. 1990. Evolution of the Southern Ocean winter mixed layer and sea ice: Open ocean deepwater formation and ventilation. *J. Geophys. Res. 95,* 11,641-11,654.

Mellor, G.M., M.G. McPhee, and M. Steele. 1986. Ice-seawater turbulent boundary layer interaction with melting or freezing. *J. Phys. Oceanogr., 16,* 1829-1846.

EDDY-RELATED WINTER CONVECTION IN THE BOREAS BASIN

O. M. JOHANNESSEN, S. SANDVEN AND J. A. JOHANNESSEN
Nansen Environmental and Remote Sensing Center, Edv. Griegsvei 3a, 5037 Solheimsvik, Bergen (Norway)

ABSTRACT

In March 1989 a weakly stratified chimney containing Deep Water with temperature of - 0.41° C and salinity of 34.91 ppt (parts per thousand) at the surface was observed outside the ice edge in the northern Greenland Sea. The chimney was about 20 km in diameter and had fairly uniform potential density (sigma-theta ≈ 28.056) from the surface to at least 500 m. Below this depth the potential density only increased to 28.077 near the bottom of 2800 m. Surface cooling of only a few tenths centigrades is sufficient to initiate vertical convection in the chimney. We propose that the mechanism responsible for exposing deep water masses to the surface in this case is a cyclonic eddy characterized by strong doming of the isopycnals. This mechanism can occur in areas where the layer of surface and intermediate water masses, which usually reside in the upper few hundred meters in winter, is thin and weakly stratified. At the surface the water is cooled by the heat flux due to air temperatures of about -20° C and 10 - 15 ms^{-1} northerly winds which is typical for winter conditions in the northern Greenland Sea. Surface cooling can then drive the convection to several hundred meters in order of 10 days, the characteristic life-time of mesoscale eddies in the area.

1. INTRODUCTION

The classical model for deep water formation in the Greenland Sea was first suggested by Mohn (1887) and further developed by Nansen (1902, 1906) and Helland-Hansen and Nansen (1909). They suggested deep water to be formed by cooling of surface water during late winter primarily in the Greenland Gyre where weak vertical stratification is observed in early winter. The cooled surface water sinks and is replaced by warmer water from below. As cooling continues the entire water column is gradually mixed with new water masses from the surface. The amount of deep water formed in a given year depends on the severity of winter cooling.

As the first good winter observations from the area were obtained in the 1950's no clear evidence for deep water formation was found, and the classical theory was considered to be unproven. However, the "G. O. Sars" from the Institute of Marine Research in Norway obtained an almost completely uniform hydrographical station

station in the Greenland Basin in April 1958 (Blindheim, personal commun.). The potential density increased by only one hundredth of sigma-theta from surface to bottom (approximately from 28.08 to 28.09).

A likely mechanism for sinking of dense surface water to deeper layers was suggested to be flow along sloping isopycnal surfaces (Metcalf, 1955). Carmack and Aagaard (1973) carried out a volumetric census using 58 hydrographical stations, all available pre-1967 winter data, in the Greenland Sea. Their analysis indicated that Deep Water constituted at least 85% of the total volume of water in the Greenland Basin and that about 30 x 10^3 km^3 new Deep Water is produced each year. They found no occurrences of vertical homogeneity, nor any evidence for slanted sinking along isopycnal surfaces. This led them to propose that bottom water was formed by large-scale convective regimes coupled to double-diffusive processes.

Swift and Aagaard (1981) studied the seasonal variation in water masses and pointed out that deep water formation could be a more complicated process where Atlantic Water and intermediate water masses play an important role. They concluded that mixing of intermediate water along isopycnal surfaces produces water which needs only to undergo a final cooling stage to be transformed into new deep and bottom water. Some of these intermediate water masses have a very short residence time (a few years) in their formation areas and are therefore able to rapidly transmit surface-induced signals into the deep North Atlantic (Aagaard et al., 1985). In his review article Swift (1986) pointed out that a number of mechanisms may play a role in the production and modification of the deep water masses. Cooling and sinking of intermediate water masses in subsurface chimneys is one possibility.

By use of geochemical tracers the formation and exchange of deep water masses in the Greenland Sea has been quantified by Peterson and Rooth (1976) and Smethie et al. (1986). Both studies indicate a residence time for the Greenland Sea Deep Water of about 30 years. This means that an average of 20 x 10^3 km^3 new deep water is produced each year, which agrees well with the findings of Carmack and Aagaard (1973). During the first extensive survey of the Greenland Sea, carried out by the USSR State Committee for Hydrometeorology in March and April 1984, winter convection was observed over a 100 km wide area centered at 74° 45'N and 2°W. It was found that surface cooling and convective mixing of surface waters penetrate deeper and deeper and eventually overturn the entire water column in the center of the Greenland Sea Gyre. Evidence of deep convection was not observed in later surveys. The process is therefore considered to be sporadic and attributable to the intensity of northerly winds and the cyclonic circulation (Dikarev, 1990). In the same area Rudels et al. (1989) found a narrow column of almost uniform water between 100 and 1200 m in February 1988. They indicated that this observation was an intermediate stage of deep water renewal and that convection occurs in steps during the winter.

A theoretical study on the possibilities of formation of chimneys in the ocean was reported by Killworth (1979). He presented two models; one quasi-steady and one time-dependent model, where chimneys can be produced by deep convection in narrow regions of intense mixing. A preconditioning process, where a reduction of the vertical stratification takes place, is necessary to produce a chimney. This process can be caused by baroclinic instability of the mean flow producing eddies with horizontal length scale exceeding the width of the chimneys. At the center of the cyclonic eddies the vertical stratification is greatly reduced in the top 300m, thus acting as an efficient preconditioning mechanism at the onset of winter cooling.

The important area for deep water formation in the Greenland Sea is considered to be the 3500 m deep Greenland Basin centered at 75° N and 2° W. Therefore several attempts to investigate the process have been carried out in this area. Little attention has been given to the study of the process in the Boreas Basin, located further north, at about 77° N. Winter conditions in this area was investigated during the MIZEX 87 program, when several upper ocean chimneys were observed. These chimneys were 10 - 20 km in diameter and consisted of relatively warm (1.0° C), saline (34.96 ppt) Lower Arctic Intermediate Water from the surface down to about 600 m (MIZEX Group, 1989). The density at the surface of these chimneys was 28.02 - 28.03 in sigma-theta units, only 0.03 - 0.04 less than the deep water in the area. Surface cooling of these chimneys, caused by characteristic heat flux in winter time (> 500 Wm^{-2}), can overturn the water column in less than 10 days (Häkkinen, 1988).

In the SIZEX 89 program one of the objectives was to study chimneys in order to improve our knowledge of their temporal and spatial distribution, horizontal and vertical scale, and their role in deep water formation. First, a general description of the SIZEX program is presented. Then observation of circulation and water masses in the Boreas Basin in wintertime is described, and finally the occurrence of Deep Water at the surface of cyclonic eddies and consequences for deep water formation is discussed.

2. THE SIZEX 89 EXPERIMENT

The Seasonal Ice Zone Experiment (SIZEX) was an international, multi-disciplinary oceanographic, ocean acoustical, remote sensing, meteorologic and sea ice experiment which was carried out in the Barents and Greenland Seas in February and March 1989. Data were collected from various platforms: one ice-strengthened vessel, R/V "Polarbjørn"; one open ocean ship, R/V "Håkon Mosby"; helicopter, drifting buoys, bottom-moored buoys, aircraft and satellites. A CTD program was carried out jointly by the two ships in the period between March 10 and 31. R/V "Polarbjørn"

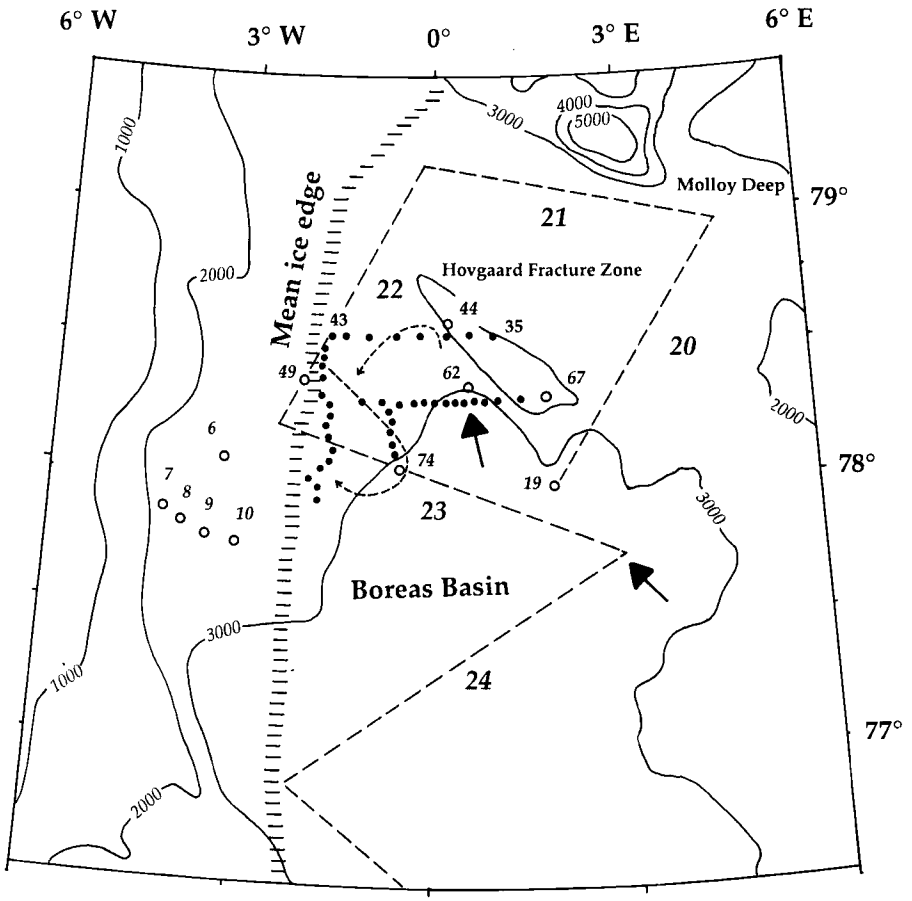

Fig. 1. Topographic map of the Boreas Basin in the northern Greenland Sea. Bottom depth is in meter. Dashed lines indicate Seasoar sections (20, 21, 22, 23 and 24) obtained by R/V "Håkon Mosby" 11-12 March 1989. Open circles mark deep CTD stations and bold dots mark shallower CTD stations (500 - 1000 m) taken by R/V "Polarbjørn" between 18 and 28 March. Curved, dashed arrows indicate the track of two drifting Argos buoys caught in a cyclonic eddy. Bold arrows show the location of two deep water chimneys.

obtained 75 CTD casts, 13 of which were deeper than 2000 m, while R/V Håkon Mosby" took 13 deep CTD cast in between 17 sections of towed Seasoar data. Water bottle samples from both ships were obtained for salinity calibration and dissolved oxygen measurements. The accuracy of the salinity was estimated to $\pm$ 0.006 ppt for the

deep CTD casts and ± 0.01 ppt for the Seasoar data which were obtained between the surface and 250 m.

The investigations were done in the marginal ice zone and in open water outside the ice edge. In the Boreas Basin the mean ice edge was directed north-south along 2° W (Fig. 1). East of this meridian it was mostly open water with some scattered patches of new-frozen pancake ice. During the eddy investigations several drifting buoys with Argos positioning system were deployed on ice floes to document the eddy velocity field. Most of the time the wind conditions were dominated by northerly winds 5 - 10 ms^{-1} and air temperature was between - 10 ° C and - 20 ° C. The eddy activity along the ice edge was monitored by images from airborne SAR and NOAA AVHRR.

TABLE 1

Water masses in the Greenland Sea

Water Type	Abbreviation	Salinity (ppt)	Temperature (°C)
Polar Water	PW	S < 34.4	T < 0
Polar Intermediate Water	PIW	34.4 < S < 34.7	T < 0
Atlantic Water	AW	35.0 < S	2 < T
Arctic Surface Water	ASW	34.4 < S < 34.7	0 < T
		34.7 < S < 34.9	0 < T < 2
Upper Arctic Interm. Water	UAIW	34.7 < S < 34.9	0 < T < 2
		34.7 < S < 34.85	-2 < T < 0
Lower Arctic Interm. Water	LAIW	34.9 < S	0 < T < 2
Deep Water	DW	34.85 < S < 34.95	T* < 0
Greenland Sea Deep Water	GSDW	34.88 < S < 34.92	-1.3 < T* < -1.1
Norwegian Sea Deep Water	NSDW	34.90 < S < 34.94	-1.1 < T* < -0.5
Arctic Ocean Deep Water	AODW	34.92 < S < 34.93	-0.9 < T* < -0.6

* Potential temperature

3. CIRCULATION AND WATER MASSES

3.1 Upper ocean water mass distribution.

The water mass definition used in this study is adopted from Carmack and Aagaard (1973) and Swift and Aagaard (1981), and is presented in table 1. A closed box of Seasoar data was obtained by R/V Håkon Mosby around the Hovgaard Fracture Zone in the northern Boreas Basin (Fig. 1). These data indicated that the upper ocean circulation was characterized by rich mesoscale structure. The northern section (21) shows that Polar Water (PW) and Polar Intermediate Water (PIW) are present in the upper 100 m in the western part close to the ice edge (Fig. 2). A branch of PIW is also found in the eastern part of the section. These water masses are transported southwards by the East Greenland Current, and filaments are branched off from the

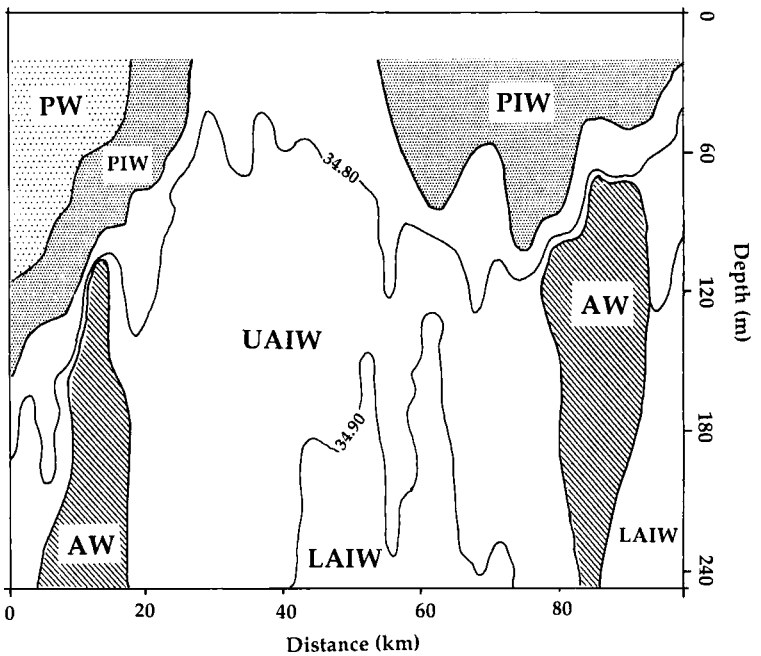

Fig. 2. Distribution of water masses in Seasoar section 21 as defined in table 1. Two isohalines (34.80 and 34.90) are drawn. The western end of the section is to the left.

main current by eddies in the Molloy Deep area, located upstream. In addition Upper Arctic Intermediate Water (UAIW) and Lower Arctic Intermediate Water (LAIW) dominate the upper 500 m of the water column. UAIW resides on top of LAIW and reaches the surface where the Polar waters are absent. In the eastern section of the box, not shown here, the upper 250 m consists almost exclusively of LAIW. This water mass is assumed to be produced by cooling of Atlantic Water (AW) off Spitzbergen mainly in winter time (Swift, 1986). Two cores of AW are found below 100 m in figure 2 and document the recirculation of AW in the Fram Strait (Quadfasel et al., 1987). The most pronounced core of recirculated AW, with $T > 3.0$ ° C and $S > 35.00$ ppt, was observed close to the ice edge below 200 m in the western section (22), not shown here. In the southern section (23) PIW, associated with the East Greenland Current, and UAIW are only present in the western part (Fig. 3). LAIW constitutes a large part of the section, but the most interesting feature is two chimneys of

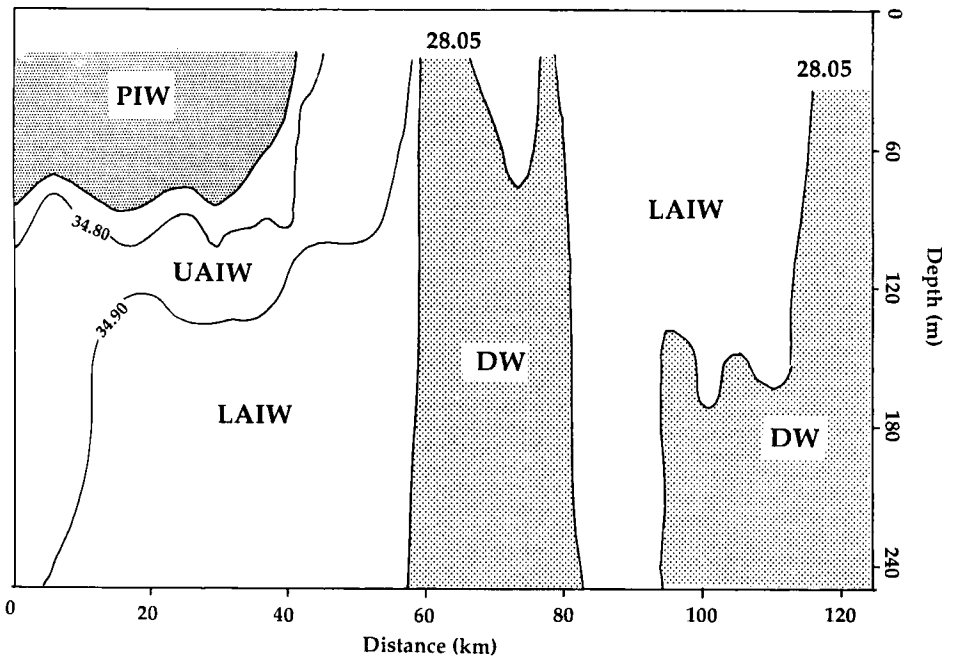

Fig. 3. Distribution of water masses in Seasoar section 23, as defined in table 1. The near-surface density (< 28.05) of the deep water chimneys is indicated.

Deep Water ($T < 0.0°$ C, $S > 34.90$ ppt, $\sigma_t > 28.04$) which are elevated to the surface. The chimneys are vertically uniform at least down to 250 m, the deepest observations obtained by the Seasoar. The easternmost observations showed a near-surface density of 28.055 at 20 m. Neither in the remaining Seasoar sections obtained in this experiment nor in the MIZEX 87 observations were deep water observed in chimneys near the surface. Although the scales of the chimneys are similar to the 87 observations, the noteworthy difference is the water mass composition of the chimneys. In 1987 the chimneys consisted of relatively warm, saline LAIW with density between 28.02 and 28.03 (MIZEX Group 1989), while the two chimneys in Fig.3 consisted of Deep Water.

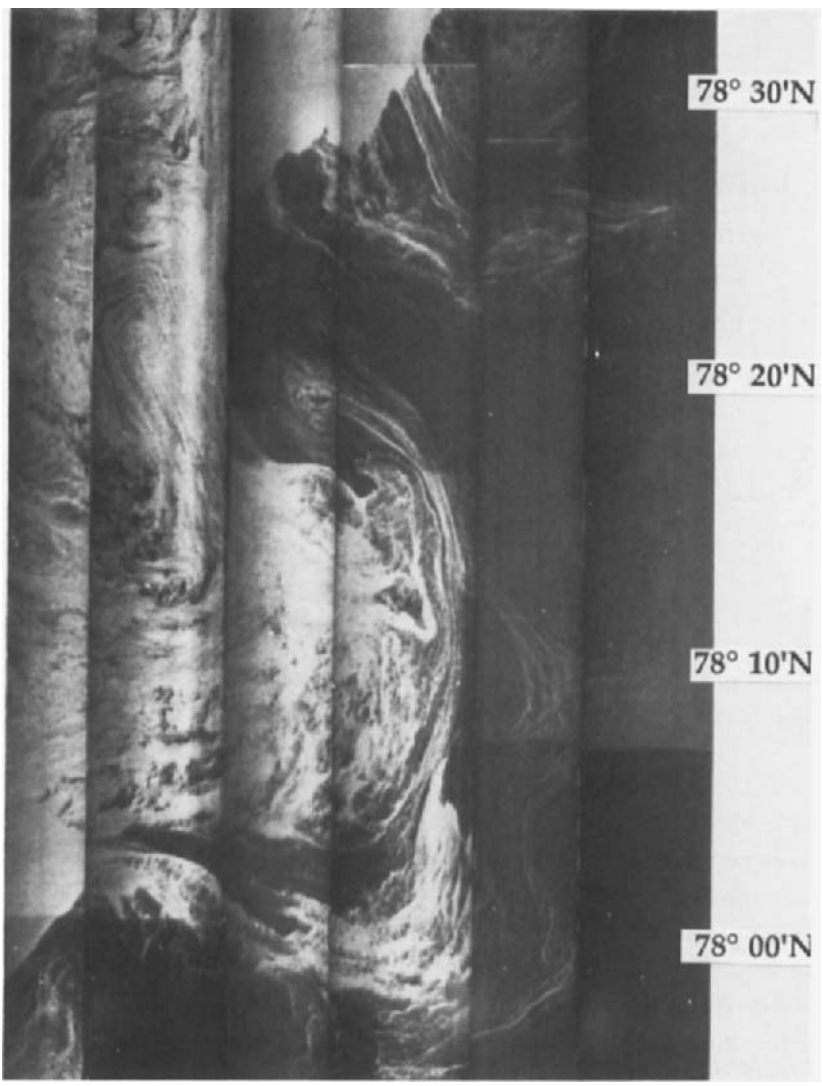

Fig. 4 SAR image from the Greenland Sea obtained on March 26 1989. Bright signature indicates ice while dark is open ocean (Courtesy R. A. Shuchman).

3.2 CTD sections across a cyclonic eddy

The area centered around the Hovgaard Fracture Zone is characterized by numerous mesoscale eddies. Investigations during summer conditions (Johannessen et al., 1987) show that cyclonic eddies with characteristic vertical scale of 1000 m and typical diameter of 30 km dominate the area. Drifting buoys indicate that these eddies can have orbital velocities up to 0.40 ms^{-1}. In SIZEX 89 such eddies were also observed during a dedicated investigation from March 24 to 28. By use of remote sensing data (images from airborne SAR and the NOAA satellites) and helicopter surveys a well-defined cyclonic eddy was located near 78° 20' N and 0° E. The SAR image of March 26 showed a tongue of ice which advected out from the main ice edge and turned into cyclonic rotation (Fig. 4). Drifting buoys were deployed in the eddy region in order to quantify the velocity field, and two CTD sections through the eddy were completed.

The first CTD section was obtained from west to east at 78° 30' N. The casts were taken to 1000 m and the section shows the characteristic doming of deep water near the eddy center at station 38 (Fig. 5). Here the 28.05 σ_t surface, which corresponds to T ≈ - 0.25° C and S ≈ 34.92 ppt, is elevated to about 100 m. At all other stations the 28.05 σ_t surface is deeper than about 500 m. Around the eddy center relatively warm and saline LAIW is present between 50 and 150 m. The eddy extends deeper than 1000 m, has a characteristic diameter of 40 km, and shows a geostrophic velocity near the surface of 0.10 - 0.15 ms^{-1}. The trajectories of the drifting buoys are shown in Fig. 1 and document the cyclonic rotation of this eddy. One buoy was deployed east of the eddy center and drifted to the north and then west at 0.15 ms^{-1}. The other buoys were deployed west of the eddy center and drifted in a southeasterly direction at 0.30 - 0.40 ms^{-1}.

Previous studies suggest that the eddies in this area tend to propagate southwards with the East Greenland Current at 1-5 km per day (Johannessen et al., 1987). In order to repeat the section three days later and hopefully cut through the eddy center again, a second section was therefore obtained 15 km further south (Fig. 1). Most of the CTD casts in this section, which is presented in Figure 6, extended to 500 m. Only station 49 and 62 were obtained to depths of about 2800 m. The most pronounced feature is a 20 km wide chimney of near homogeneous deep water which rises to the surface. The chimney is located in the center of the cyclonic eddy where T = - 0.4° C, S = 34.92 ppt and $\sigma_t \approx 28.05$. The chimney can be defined as enveloped by the 28.05 σ_t surface which forms a vertical cylinder in the upper 400 m (Fig. 6 c). Below 400 - 500 m the chimney vanishes because the σ_t surfaces turn horizontally. The vertical structure of the chimney is characterized by a weak decrease in both temperature and salinity with increasing depth. The chimney is presumably the result of strong doming of deep water in the center of an energetic cyclonic eddy. In winter time, when the stability and thickness of the surface layer is smaller than in the summer, this dome

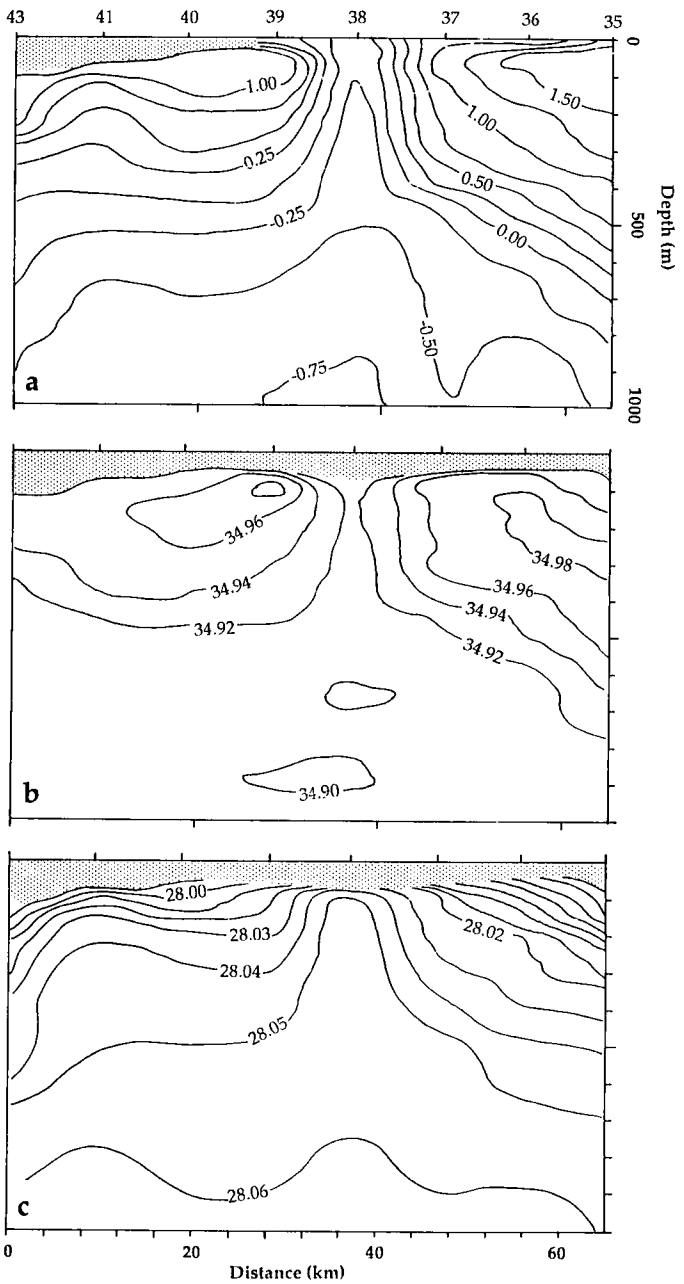

Fig. 5. CTD section obtained in east-west direction outside the ice edge at 78° 30'N. (a): temperature (°C), (b); salinity (ppt) and (c): sigma-t. The stratified layer in the upper 100 m is shaded.

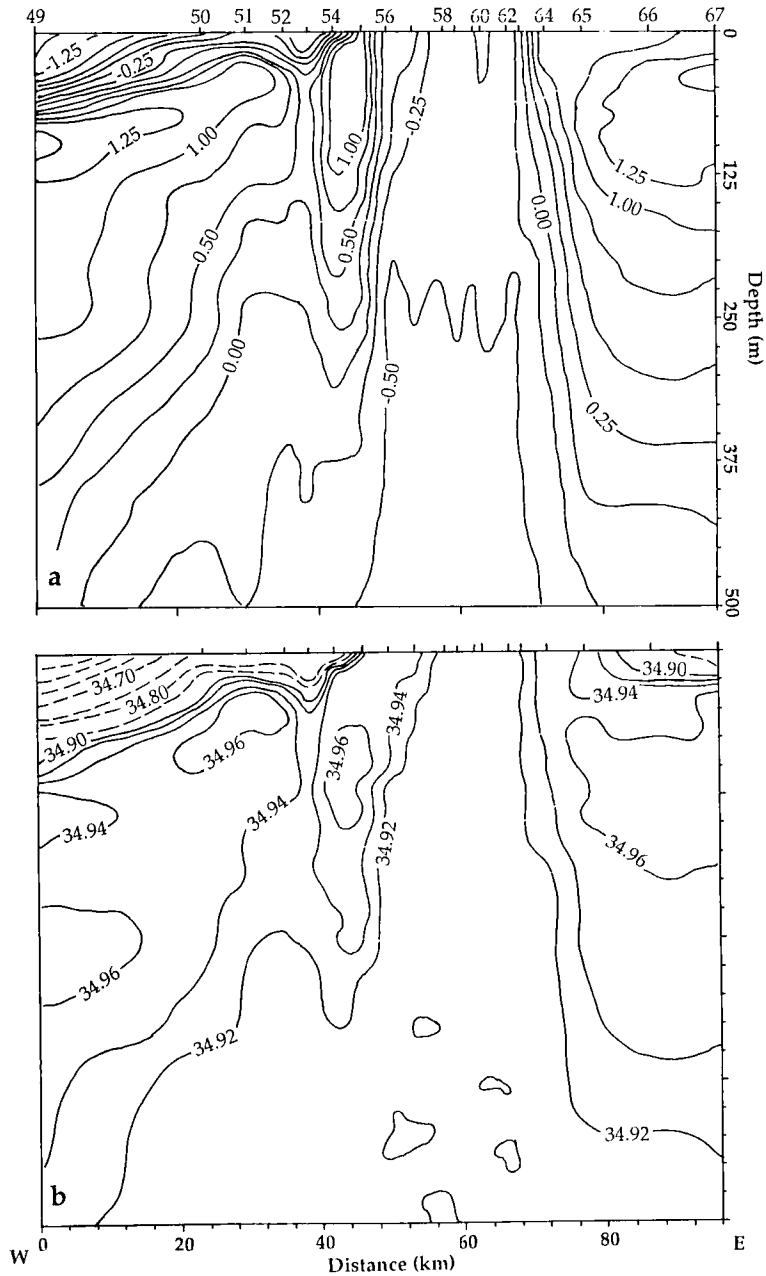

Fig. 6. CTD section obtained in east-west direction at 78° 17'N on March 27, 1989. (a): Temperature (°C), (b): Salinity (ppt), (c) Density (sigma-t) and (d) Geostrophic velocity relative to 500 m (cm/s) where dashed lines indicate flow towards south. The sections show the presence of a 20 km wide chimney of deep water which is elevated to the surface in the center of a cyclonic eddy.

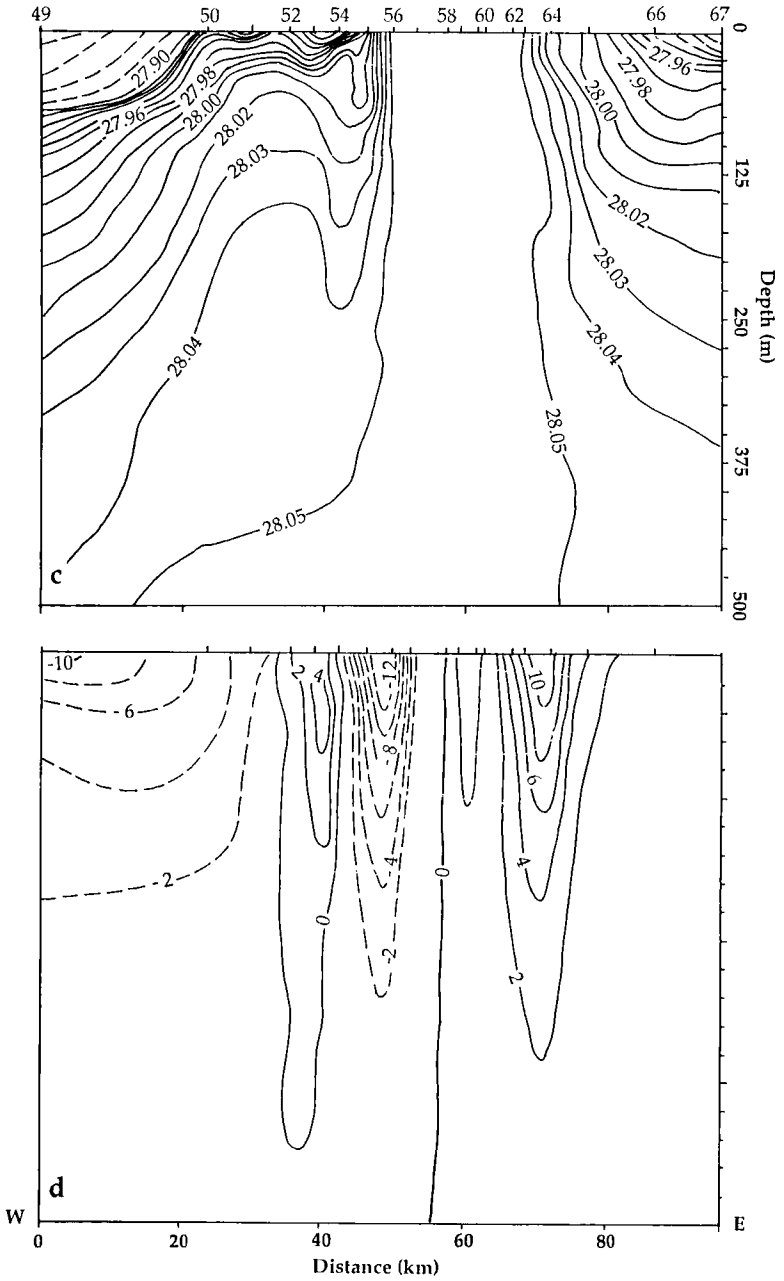

Fig. 6. continue

can reach the surface and form a chimney as seen in Fig. 6. The ice edge is located near station 49 and the whole area east of station 50 was ice-free. The section also shows a thin surface layer of PW on the western side and two cores of LAIW on both sides of the eddy center. The geostrophic velocity at the surface of the eddy, computed relative to 500 m, is about 0.10 ms^{-1}. Drifting buoys indicated that the real surface velocity is 0.30 - 0.40 ms^{-1} southwards on the western side and 0.10 - 0.15 ms^{-1} northwards on the eastern side of the eddy center.

The second CTD section can be interpreted to lie closer to the eddy center than the first section since it cuts through more deep water in the upper layer. The eddy is therefore probably elongated towards southeast. An alternative interpretation is that both sections were obtained near the eddy center, and that the eddy had propagated southwards and was more fully developed when the second section was obtained three days after the first section. The location of the eddy is east of the main ice edge and the core of the East Greenland Current, and south of Hovgaard Fracture Zone. Therefore the eddy can be generated by barotropic and baroclinic instabilities of the East Greenland Current combined with topographical effects.

3.3 Deep CTD stations

During the two-week investigation of the Boreas Basin ten deep CTD stations were obtained. The westernmost stations were located in ice-covered area and one of these stations (6) is plotted in the TS-diagram in Fig. 7. The water column is characterized by PW and PIW in the upper 100, with UAIW below. A core of cooled AW (2° C < T < 3 ° C) was found at about 200 m, and LAIW was confined between 200 and 800 m. In the easternmost stations, located in open water, LAIW was higher in the water column, typically from 400 m and up to the surface (station 19). The deep water characteristics differ somewhat between the western and eastern stations. Below 2000 m the potential temperature and salinity is close to -1.10 °C and 34.90 ppt, respectively, at stations 19 and 62 south of Hovgaard Fracture Zone. This water is typical Greenland Sea Deep Water. Station 6, on the other hand, has a temperature of -0.89 ° C and a salinity of 34.925 ppt at 2300 m. These values indicate that the water mass is Arctic Ocean Deep Water from the Eurasian Basin (Swift et al., 1983) which presumable flows southwards near bottom along the slope of Greenland continental shelf.

The most homogeneous water column observed was at station 62, where the bottom depth was close to 3000 m. Data from this station, presented in table 2, are plotted as bold dots in Fig. 7, and shows that Deep Water is present in the entire water column. At the surface temperature and salinity is -0.410° C and 34.912 ppt, respectively, which is characteristic for NSDW slightly mixed with LAIW. At 2800 m

the corresponding values are -1.190° C (potential temperature) and 34.896 ppt, which is defined as GSDW (Table 1). The potential density ranges from 28.056 at the surface to 28.077 near bottom. Within the accuracy of the measurements it is the same at the surface as at 500 m. In the upper 500 m small instabilities are observed, while the water column below 500 m is weakly stratified.

Dissolved oxygen was measured at selected depths at several deep stations. The general oxygen level in the upper 500 m varied from 7.40 to 7.60 ml/l, a rather high level indicating water masses which have been in contact with the surface recently. Below 1000 m the values were lower, 7.0 - 7.20 ml/l, which is characteristic for deep water typically 30 years old. Within the chimney (station 62) there is a considerable vertical variability in the oxygen values. From 500 to 1500 m the oxygen contents decreases from 7.52 to 7.02 ml/l, and beyond 2000 m it increases slightly. These observations show that there has been no vertical exchange of water masses throughout the water column at station 62. However, at 1000 m the oxygen level is higher at station 62 (7.30 ml/l) than outside the chimney where values of 7.05, 7.12 and 7.21 ml/l were found. One would expect a lower level at station 62 compared to the stations outside the chimney because deep water with lower oxygen content is elevated in the eddy center. This suggests that some oxygen has been added to the deep water at 1000 m, perhaps by vertical mixing in the chimney. The upper 500 m is well mixed since it is fairly homogeneous both in salinity, density and oxygen. From 500 to 1000 m less mixing is possible because of the stratification. The low oxygen content at 1500 and 2000 m indicates that the water at these depths is not influenced by convection higher in the water column.

TABLE 2

Selected data from CTD station 62 obtained by R/V Polarbjørn March 27 1989 at 78° 18' N 0° 40' E.

Depth (m)	Potential temp. (°C)	Salinity (ppt)	Dissolved oxygen (ml/l)	Potential density (sigma-theta)
10	- 0.410	34.912	-	28.056
50	- 0.402	34.913	-	28.057
100	- 0.423	34.908	7.48[1)]	28.054
250	- 0.499	34.905	-	28.055
500	- 0.548	34.904	7.52[1)]	28.056
1000	- 0.878	34.895	7.30	28.062
1500	- 1.013	34.895	7.02	28.069
2000	- 1.072	34.894	7.03	28.070
2800	- 1.190	34.896	7.15	28.077

[1)] obtained at station 56

4. DISCUSSION

Observations from SIZEX 89 show that deep water with T = -0.5°C and S = 34.91 ppt can be lifted to the surface in chimneys located in the center of cyclonic eddies and be exposed to low air temperatures. Cooling and sinking of surface water can occur as proposed in the classical theory by Helland-Hansen and Nansen (1909). When a cooled particle of water sinks it will be replaced by warmer particles from below which in turn is cooled. A continuous supply of warmer water from below is necessary to keep the surface ice-free and maintain effective surface cooling. The chimney observed in SIZEX 89 was ice-free throughout the investigation period. Mesoscale cyclonic eddies, which are frequently observed along the ice edge of the Greenland Sea, can play an important role as a preconditioning mechanism for deep water formation by lifting relatively dense water to the surface. Necessary conditions for deep convection to occur in the eddy center are low air temperature and high winds allowing sufficient heat flux into the atmosphere to rapidly cool the surface water. As the surface water cools it eventually reaches a temperature where density is equal to the underlying water mass and convection will start. However, at greater depths the pressure effect causes the isolines for *in situ* density in the TS-diagram to be tilted more horizontally. This means that the surface water which has reached a certain depth, needs to be further cooled to sink to greater depths. Hence the water column will be ventilated by progressive deepening of the convection (Aagaard and Carmack, 1989). The longer the cooling lasts the deeper will the convection reach. Surface heat fluxes in the Greenland, Norwegian and Barents Seas for the year 1979 have been estimated by Häkkinen and Cavalieri (1989). Their study shows that the monthly mean heat flux in the Boreas Basin was more than 600 Wm^{-2} in January and about 400 Wm^{-2} in March. Characteristic sensible heat flux estimates obtained from the "Polarbjørn" was up to 500 Wm^{-2} during the operations in the Boreas Basin. During extreme conditions, such as when strong northerly winds blows from the Arctic out in open water, the total heat flux can be more than 1000 Wm^{-2} (Buckley et al., 1978), however such conditions were not observed during SIZEX 89.

Estimates of the time needed to cool a given water column (Johannessen et al., 1989) shows that it takes about 10 days for a 200 m thick column to be cooled 0.5 °C. In reality, when cooling acts on the surface deep convection penetrates to greater and greater depths and the temperature of the mixed water column decreases gradually. At station 62 it is sufficient to cool a particle at the surface 0.1° C to attain the same density as at 500 m. A renewal of the water masses down to this depth can therefore be completed in less than a week. Because of the stratification and the gradients in salinity and oxygen below 500 no vertical convection seems to have occurred beyond this depth. It is noteworthy that the deep water mass observed in a uniform

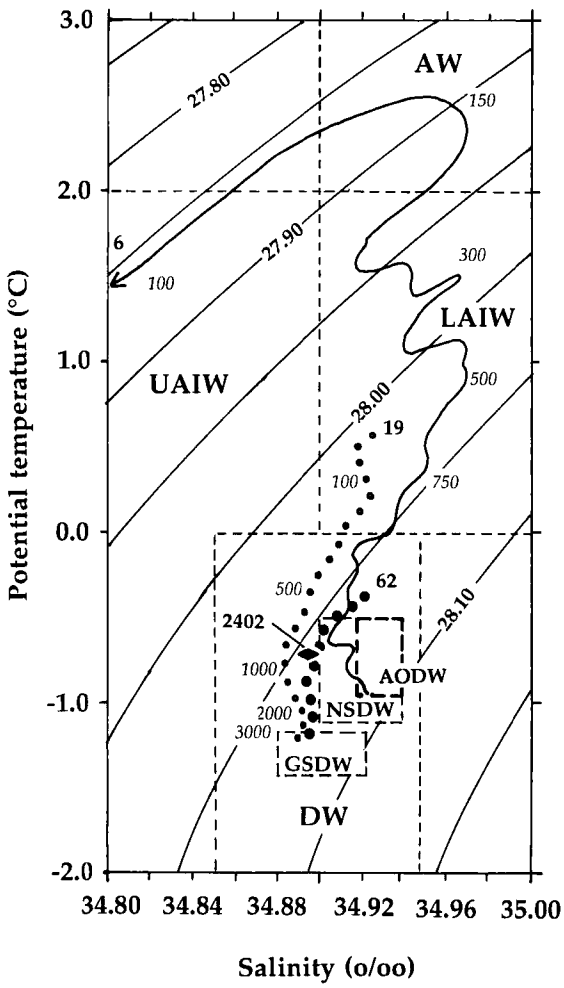

Fig. 7. TS-diagram of selected CTD stations in the Boreas Basin. Water masses as defined in table 1 are indicated. Full line: station # 6; dotted line: station # 19; bold dots: station # 62. Homogeneous deep water observed in the upper 250 m of Seasoar station # 2402 at the eastern end of section 23 is also indicated. The location of the stations are shown in fig. 1. Italic numbers indicate depths along some of the TS curves. Contour lines for density is calculated relative to the surface.

chimney in the upper 250 m (Fig. 3) was also found at about 800 m at station 62. This suggests that renewal of water masses can occur at least down to 800 m in other chimneys located south of the Hovgaard Fracture Zone.

The SIZEX 89 investigations show that a well-defined chimney can occur in the center of a cyclonic eddy. The chimney was well mixed down to 500 m indicating that vertical convection had occurred. In order to quantify deep water formation it is first of all necessary to estimate the amount of deep water which can be renewed in one eddy. To do this the eddy has to be monitored throughout its life time. Secondly, it is necessary to estimate number of eddies present in areas of low stratification where deep water potentially can reach the surface. The amount of deep water which can be produced in one eddy depends on parameters such as cooling rate, stratification, lifetime and width of the eddies. If sufficient amount of upper ocean water masses of lower density are present in an eddy, the stratification increases and the deeper water masses may not be able to reach the surface in spite of a strong doming of the isopycnals. Eddies is only one among many possible mechanisms by which deep water may be formed. The Seasoar section in Fig. 3 shows two chimneys of deep water which reached the surface in an area where no eddies were observed. Upwelling is another process which can lift a dense water mass towards the surface and expose it to cooling (Häkkinen, 1987). As pointed out by Aagaard and Carmack (1989), the amount of fresh water produced each year, which plays an important role to determine the structure of upper ocean water masses, is a crucial factor for deep water formation at high latitudes. This determines for example if there are thick layers of LAIW and UAIW which inhibit deep water to penetrate to the surface. If the water mass structure is favorable for deep water formation, the SIZEX 89 observations indicate that the mesoscale eddies act as a localizing mechanism which determines where and when deep convection can occur. This mechanism is recommended to be taken into account in climate models, where deep water formation is among the least known processes.

ACKNOWLEDGEMENT

We acknowledge, with thanks, the Office of Naval Research, under grant N00014-80-J-1003, and the University of Bergen for their support which made the SIZEX 89 field experiment possible. We are indebted to Kathleen Geiger for careful data processing after the experiment. A special thanks goes to the crews onboard R/V "Polarbjørn" and R/V "Håkon Mosby" for excellent cooperation during the field experiment.

REFERENCES

Aagaard, K., Swift, J. H. and Carmack, E. C., 1985. Thermohaline Circulation in the Arctic Mediterranean Seas. J. Geophys. Res., 90: 4833-4846.

Aagaard, K. and Carmack, E. C., 1989. The role of sea ice and other fresh water in the Arctic circulation. J. Geophys. Res., 94: 14485-14498.

Buckley, J. R., Gammelsrød, T., Johannessen, J. A., Johannessen, O. M. and Røed, L. P., 1978. Upwelling: Oceanic structure at the edge of the Arctic ice pack in winter. Science, 203: 165-167.

Carmack, E. and Aagaard, K., 1973. On the deep water of the Greenland Sea. Deep Sea Res., 20: 687-715.

Dikarev, S. N., 1990. Best places for deep convection in ice-covered seas. Presented at 22nd International Liege Colloquium On Ocean Hydrodynamics, Liege, May 7-11, 1990.

Häkkinen, S., 1987. Upwelling at the ice edge: A mechanism for deep water formation? J. Geophys. Res., 92: 5031-5034.

Häkkinen, S., 1988. A note on chimney formation in the ice edge region. J. Geophys. Res., 93: 8279-8282.

Häkkinen, S. and Cavalieri, D. J., 1989. A study of oceanic surface heat fluxes in the Greenland, Norwegian and Barents Seas, J. Geophys. Res., 94: 6145-6157.

Helland-Hansen, B. and Nansen, F., 1909. The Norwegian Sea. Its physical Oceanography based upon the Norwegian researches 1900-1904. Rep. Norw. Fishery Mar. Invest., 2(1), (2), 390 pp.

Johannessen, J.A., Johannessen, O. M., Svendsen, E., Shuchman, R. A., Manley, T., Campbell, W. J., Josberger, E. J., Sandven, S., Gascard, J-C., Olaussen, T., Davidson K. and Van Leer, J., 1987. Mesoscale eddies in the Fram Strait marginal ice zone during 1983 and 1984 Marginal Ice Zone Experiments. J. Geophys. Res., 97: 6754-6772.

Johannessen, J. A., O. M. Johannessen and S. Sandven, 1989. Chimneys in the Marginal Ice Zone. Proceedings from the workshop "Regional and Mesoscale Modeling of Ice Covered Oceans", 23-27 Oct. 1989, Bergen Norway. Nansen Environmental and Remote Sensing Center conference Report No. 3, pp. 48-54.

Killworth, P. D., 1979. On 'chimney' formation in the ocean. J. Phys. Ocean. 9: 531-554.

Metcalf, W. G., 1955. On the formation of bottom water in the Norwegian Basin. EOS, Trans. Amer. Geophys. Union, 36: 595-600.

MIZEX Group, 1989. MIZEX East 1987: The winter Marginal Ice Zone Program in the Fram Strait/Greenland Sea. EOS, Trans. Amer. Geophys. Union, 70: 545-555.

Mohn H., 1887. Nordhavets dybder, temperatur og strømninger. Den norske nordhavs-Exped. 1876-1878., 212 pp.

Nansen, F., 1902. The oceanography of the North Polar Basin. The Norwegian North Polar Expedition 1893-1896, Scient. Results 3(9), 427 pp.

Nansen, F., 1906. Northern waters: Captain Roald Amundsen's oceanographic observations in the Arctic seas in 1901. Vid. Selskap. Skrifter, I. Matem-Naturv. Kl., 1(3), 145 pp.

Peterson, W. H., and Rooth, C. G. H., 1976. Formation and exchange of deep water in the Greenland and Norwegian seas. Deep Sea Res., 23: 273-283.

Quadfasel, D., Gascard, J-C. and Koltermann, K-P., 1987. Large-scale oceanography in Fram Strait during the 1984 Marginal Ice Zone Experiment. J. Geophys. Res., 92: 6719-6728.

Rudels, B., Quadfasel, D., Friedrich, H. and Houssais, M-N., 1989. Greenland Sea convection in the winter of 1987-1988. J. Geophys. Res., 94: 3223-3227.

Smethie, W. M. Jr., Østlund, H. G. and Loosli, H. H., 1986. Ventilation of the deep Greenland and Norwegian seas: evidence from krypton-85, tritium, carbon-14 and argon-39. Deep Sea Res., 33: 675-703.

Swift, J.H., and Aagaard, K., 1981. Seasonal transitions and water mass formation in the Iceland and Greenland seas. Deep Sea Res., 27: 29-42.

Swift, J. H., Takahashi, T. and Livingstone, H. D., 1983. The contribution of the Greenland and Barents Seas to the deep water of the Arctic Ocean. J. Geophys. Res., 88: 5981-5986.

Swift, J. H., 1986. The arctic waters. In: B. Hurdle (Editor), The Nordic Seas, Springer Verlag, New York, 777 pp.

This Page Intentionally Left Blank

UPPER OCEAN STRUCTURES IN THE SOUTH-WESTERN ICELAND SEA - A PRELIMINARY REPORT

JOHN C SCOTT[1] and PETER D KILLWORTH[2]
(1) Ocean Measurement Section, Admiralty Research Establishment, Portland, Dorset DT5 2JS; (2) Robert Hooke Institute, Clarendon Laboratory, Parks Road, Oxford OX1 3PU (UK)

ABSTRACT
Scott, John C. and Killworth, Peter D., 1990. Upper ocean structures in the South-Western Iceland Sea - A preliminary report.

Results are presented from a single 200km straight-line tow of a 400m long thermistor chain North of Iceland (near 69 degrees North, 18 degrees West) in Summer 1987. The track was near the Eastern edge of the East Greenland Current. Vertical structures were observed in the temperature distribution throughout the track, and in one place these were sufficiently regular to be called chimneys. In these, cold water was passing from just below the very cold, fresh sub-layer, through the warmer, more saline underlayer. A series of CTD stations, measured in about the same location two weeks earlier, give information about the probable thermohaline structure of the chimneys seen in the chain data. The mechanism of formation is not yet clear, and this paper summarizes the available evidence.

1. INTRODUCTION

This paper presents a set of experimental measurements from a thermistor chain tow North of Iceland in August 1987, in the vicinity of 69^{o}N, 18^{o}W. A series of CTD casts, made along essentially the same track about two weeks earlier, are also presented.

Section 2 describes the datasets included here, and section 3 presents a summary of the data. Preliminary conclusions drawn from the observations are given in section 4.

1.1 The Location of the Data

Figure 1 shows the 200km tow track, indicating the region in which the data shown in the subsequent figures were taken. The track is in two sections, with a turn at 69^{o}N, 18^{o}W. This track was covered from 8-10 August 1987 by MV SEA SEARCHER, travelling at a fairly steady four knots, in calm weather.

The track lies North of Iceland, near the eastern edge of the East Greenland Current, which flows South-Westwards along the East Greenland Shelf and leaves the Iceland Sea via the Denmark Strait, West of Iceland (Swift, Aagaard &

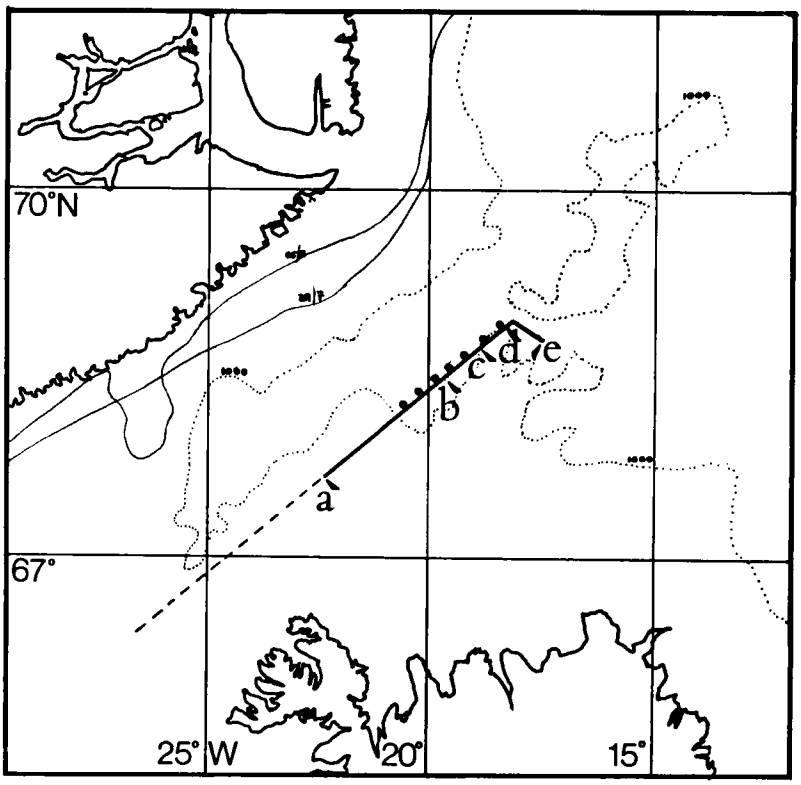

Fig. 1. The track along which the thermistor chain data were taken. The two land masses shown are Greenland (top left) and Iceland (bottom), and the 1000m depth contour is shown as a dotted line. The mean ice edge positions for 29 July and 5 August are indicated by continuous lines. Positions marked a-e along the track line refer to the start and end positions of the chain data shown in figures 2-4; figure 3 shows the Northerly end, b-e, and the region in which regular 'chimneys' were found is shown in figures 4 & 5. The large dots show the locations of the CTD casts presented in figures 5-7.

Malmberg, 1980). At its Southern end, as the East Greenland Current approaches the Denmark Strait along the Western boundary, it starts to interact with warm saline waters flowing Northwards along the Eastern boundary of the Strait. This is the Irminger Current, of basically Atlantic origin, which subsequently joins the Iceland Current North of Iceland. The boundary between the two water masses is particularly sharp, and highly variable within the Denmark Strait. Although its position is approximately fixed by the Ridge in the centre of the Strait, its influence stretches at least to the Southern end of the track shown in figure 1.

The East Greenland Current here is characterized by a 50m thick, cold, low salinity layer, which in the Summer is influenced by the cold, fresh input from the receding ice edge. This cold layer rests above a warmer, more saline layer.

Note that the data were taken in the middle of Summer, and the cold layer is well covered by the seasonal warm upper boundary layer. Since the East Greenland ice sheet might be considered to have an influence we have included an impression of the ice edge position in figure 1, derived from data provided by the US Naval Polar Oceanography Center. The retreating ice edge was more than 120km away from the chain data track, to the North-West, at the time of the thermistor chain measurements. Bergy bits and growlers had been encountered much further South-West, on the approach track through the Denmark Strait, and it is possible that these had been in the data track area at some time. However, no ice was observed in this area, either during the chain data track or during the earlier CTD measurements.

The weather had been very mild during the three-week period leading up to the chain data. Winds had normally been less than 10 knots, exceptionally rising to 20 knots, but not in a sustained manner. Skies had been generally overcast, but with significant periods of sunshine. This is consistent with the shallow warm upper boundary layer observed in the water column.

2. THE DATA

2.1 Thermistor Chain Data

The ARE digital thermistor chain was used for the observations (Lane & Scott, 1986). For the results shown here 100 sensor pods were arranged along a 380m length of chain, and at a towing speed of 4 knots they sampled a vertical

aperture of about 300m. The chain was sampled every 0.9s, giving a temperature profile about every 2m horizontally. Each sensor pod along the chain measured temperature, and about one in five also measured pressure, allowing the depth distribution of the data to be deduced. Relative precision in the temperature measurements is estimated as +/-5m^{o}C, twice the digital resolution, and relative precision in depth measurement overall is estimated as +/-2%.

Figure 2 shows a subsection of the Northerly end of the track, marked b-e in figure 1, and figure 3 shows an expansion of the central part of this track, labelled c-d. Both figures show 0.2C isotherms over the range -2^{o}C to +8^{o}C. To aid interpretation, we have also included figure 4 which shows the vertical structure more clearly in a sub-sampled version of the data using a 'washing-line' presentation.

One feature of the structure immediately apparent from figure 2 is its highly irregular nature. The 'amplitude' of the 'noise' in many ocean regions is frequently similar to that of the 'significant' structure, although filtering throws away much valuable information about the structure itself. This is a characteristic of the Denmark Strait region; indeed it is likely that the small-scale events described here are one of the causes of the irregularity.

It can also be noted that much of the horizontal variability involves very steep boundaries, approaching the vertical, with thicknesses of the order of a few hundred metres.

Figure 3 shows two very regular vertical cold structures, about 3km wide. Comparison of this figure with the two preceding figures shows their overall location in the track covered. It is these structures, which we will call 'chimneys' which are the subject of this preliminary report. These structures can be seen below the characteristic cold sub-layer of the region, starting at about 70m depth. The water within the chimneys is about 1.2C cooler than that outside them, and they continue to the maximum depth of the chain data, here about 270-280m. They contain water of temperature down to about 0.0C, and they appear to punch cleanly through the warmer water, maximum about +1.2C, which is present below the sub-layer.

Figure 2 suggests that similar chimneys are also present near the two ends of the cold sub-layer. These are less regular than those chosen for our particular attention here, possibly a result of the influence of the strong horizontal variation near the ends. Their thermal structure is very similar to

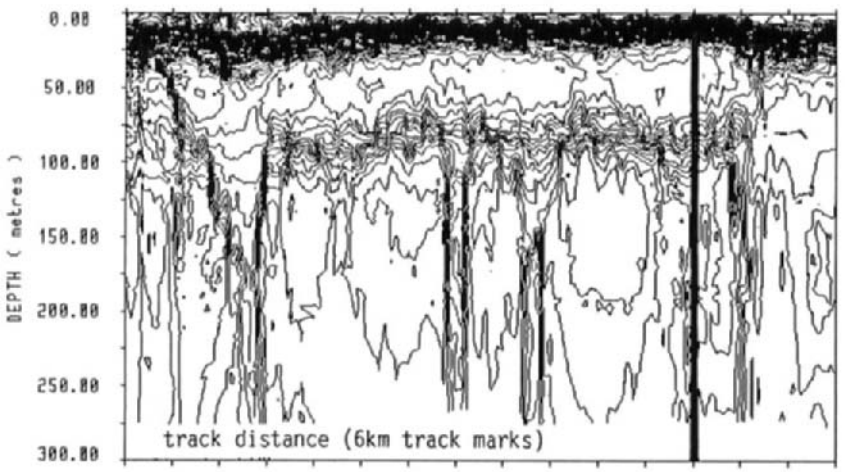

Fig. 2. Thermistor chain data from the section of track marked b-e in figure 1, in the form of 0.2C isotherms from -2C to +8C; the Northern corner of the track is marked by a thick vertical line towards the right-hand end. The track length shown is about 110km, and the tick marks are 6km apart. The surface layer is at about +7.5C; the cold sublayer from 25m to 100m reached a minimum near -1.5C, and the warmer layer beneath this decreases downwards from about +1.2C.

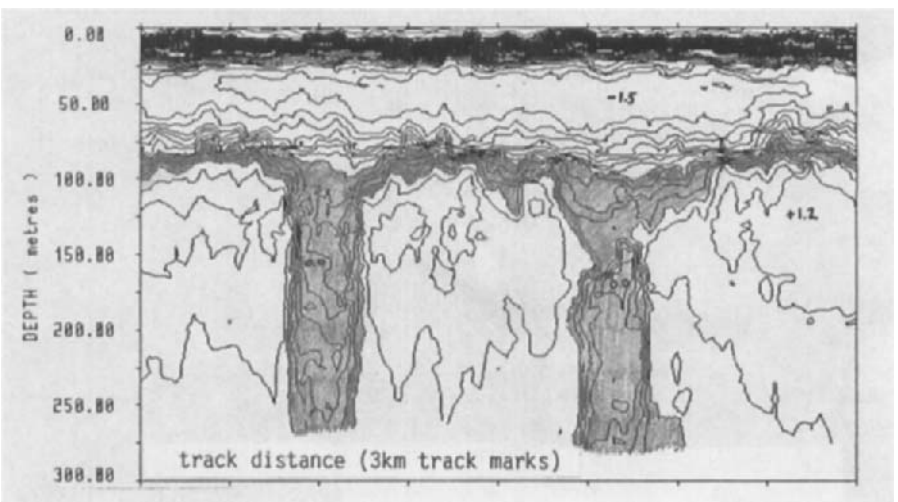

Fig. 3. An expansion of the central part of figure 2, showing just the 30km section c-d, again in the form of 0.2C isotherms from -2C to +8C. 3km marks are given along the top and bottom. The surface layer is at around +7.5C, the cold sublayer reaches a minimum of about -1.5C around 30-40m depth, and there is a local maximum temperature of about +1.2C around 130-140m. A horizontal section at 150m encounters temperatures changing from about +1.2C outside the chimneys to about 0.0C inside the chimneys. The shaded region denotes the temperature range 0.0C to 0.8C.

the two described in detail here, and it is likely that they have the same cause.

It appears from the sections that the water present in the chimneys has been drawn from layers that are beneath the cold layer, but above the temperature maximum.

The situation differs significantly from many others involving exchange of water between layers in that the atmospheric boundary layer plays no role. Here, the surface layer is at around +7.5C, and is completely de-coupled from the chimneys by the cold sublayer, which reaches a minimum of about -1.5C at around 30-40m depth. Apart from some weak horizontal structure within the cold layer, there appears to be very little influence of the chimneys upwards from this; none is detectable in the very warm surface layer. It is possible, however, that the cold layer might play a part analogous to a cooling atmosphere, if the effect of upwards heat transport is greater than that of upwards salt transport.

The chimneys clearly arise in one of the least complex parts of the track shown in figure 2, but it is not possible from the present data to deduce whether this is a requirement for their formation; if the structures seen at the two ends of the cold sub-layer have the same cause then this is unlikely.

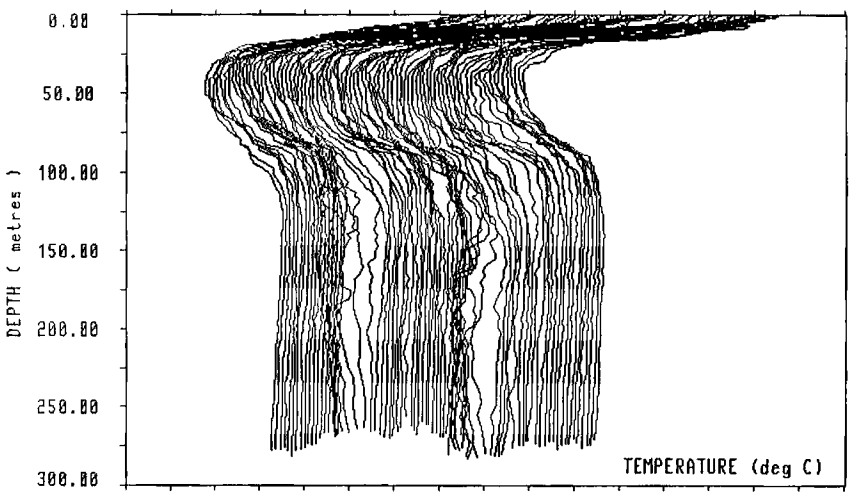

Fig.4 The series of offset thermistor chain profiles for the region shown in figure 3 (c-d in figure 1). Profile locations along the track are separated by about 400m. The bunching of the profiles shows the relatively lower temperature within the chimneys.

However, the closer the track approaches the Denmark Strait, the more the situation might be influenced by the warmer, more saline Irminger Current or Iceland Current waters.

It is clearly not possible to draw conclusions about the mechanism of formation of the chimneys without good salinity data to go with the detailed temperature data. The limited amount of conductivity data available from the chain is unfortunately not adequate for this purpose. However, we have managed to locate a series of CTD dips made about 14 days before the chain tow, very close to where we subsequently found the chimneys; these data will be considered next.

2.2 CTD Data

The absence of reliable salinity data has been compensated to some extent because seven closely spaced CTD dips have been identified from almost exactly the same region, only about 14 days earlier than the chain tow along the track. The approximate positions of the CTD dips are shown in figure 1. These dips were about 18km apart.

Inspection of figures 1 & 3 suggests that, unless the oceanographic conditions had changed significantly during the two-week interval, the 18km separation CTD casts might have been expected to encounter one of the chimneys. We believe that this did in fact happen. One of the seven casts does indeed differ significantly from the other six, the difference being mainly in the reduction of the maximum temperature found below the cold layer. This closely matches the relative change in characteristics of the chimneys as indicated by the 280m depth chain data.

The relevant portion of the temperature-depth variation in the top 500m is shown in figure 5 for the seven CTD dips. Figure 6 shows the salinities, and figure 7 the densities. The thin dotted line (labelled 'A') shows a profile we believe comes from within a chimney. The firm line (labelled 'B') probably comes from a cast at the edge of a chimney. The remainder of the temperature profiles, although 'noisy', with layered temperature inversions of the order of 0.2C, are all fairly similar and represent the "environment" around the chimneys. Note the clear temperature maximum between 100 and 200m in all of the environment profiles. All the profiles are consistent with the thermistor chain data (figures 3 & 4).

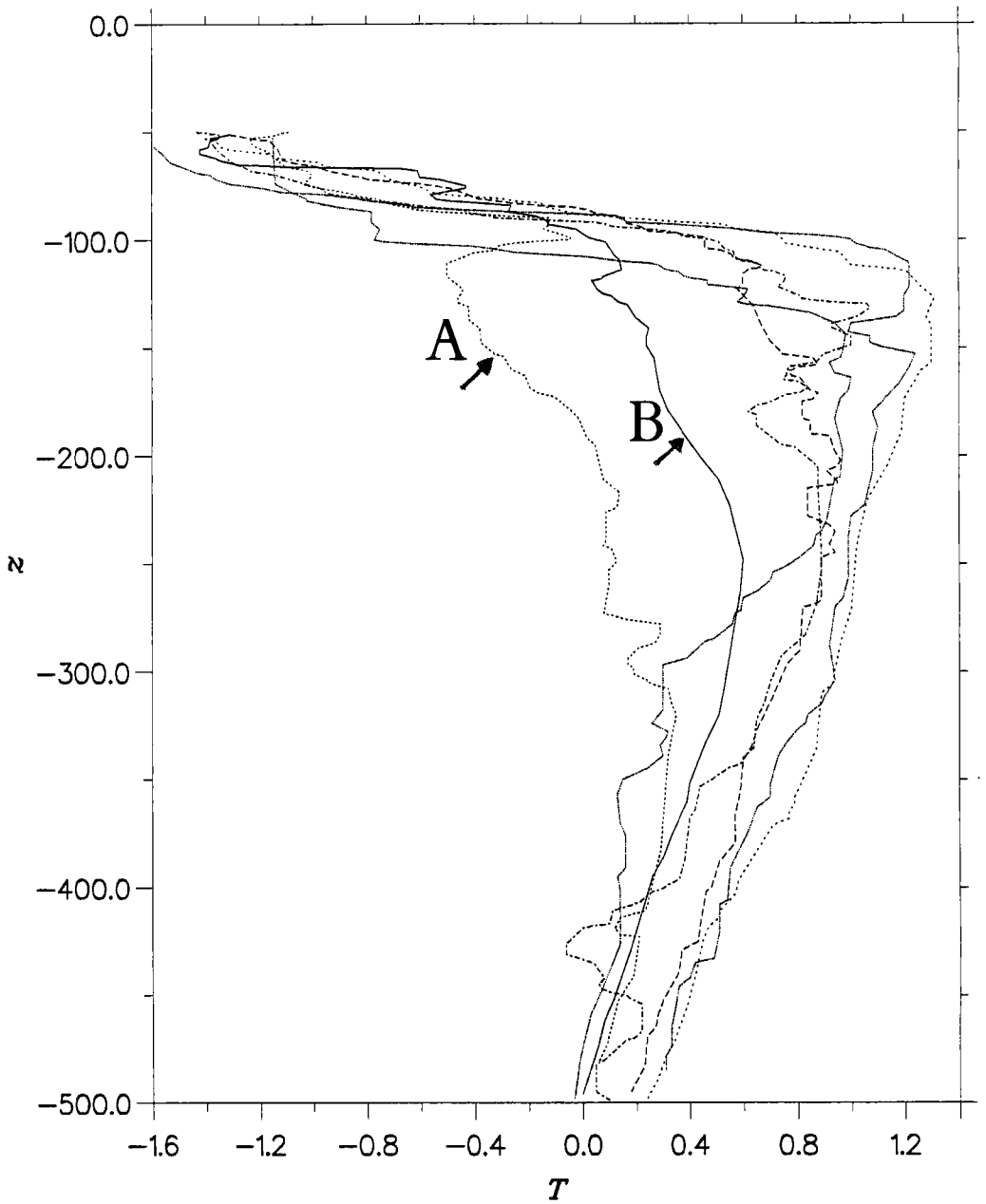

Fig. 5. The ensemble of temperature-depth profiles from the CTD casts taken at the positions indicated in figure 1. The profile marked 'A' is believed to come from a chimney; that marked 'B' probably comes from near the edge of a chimney.

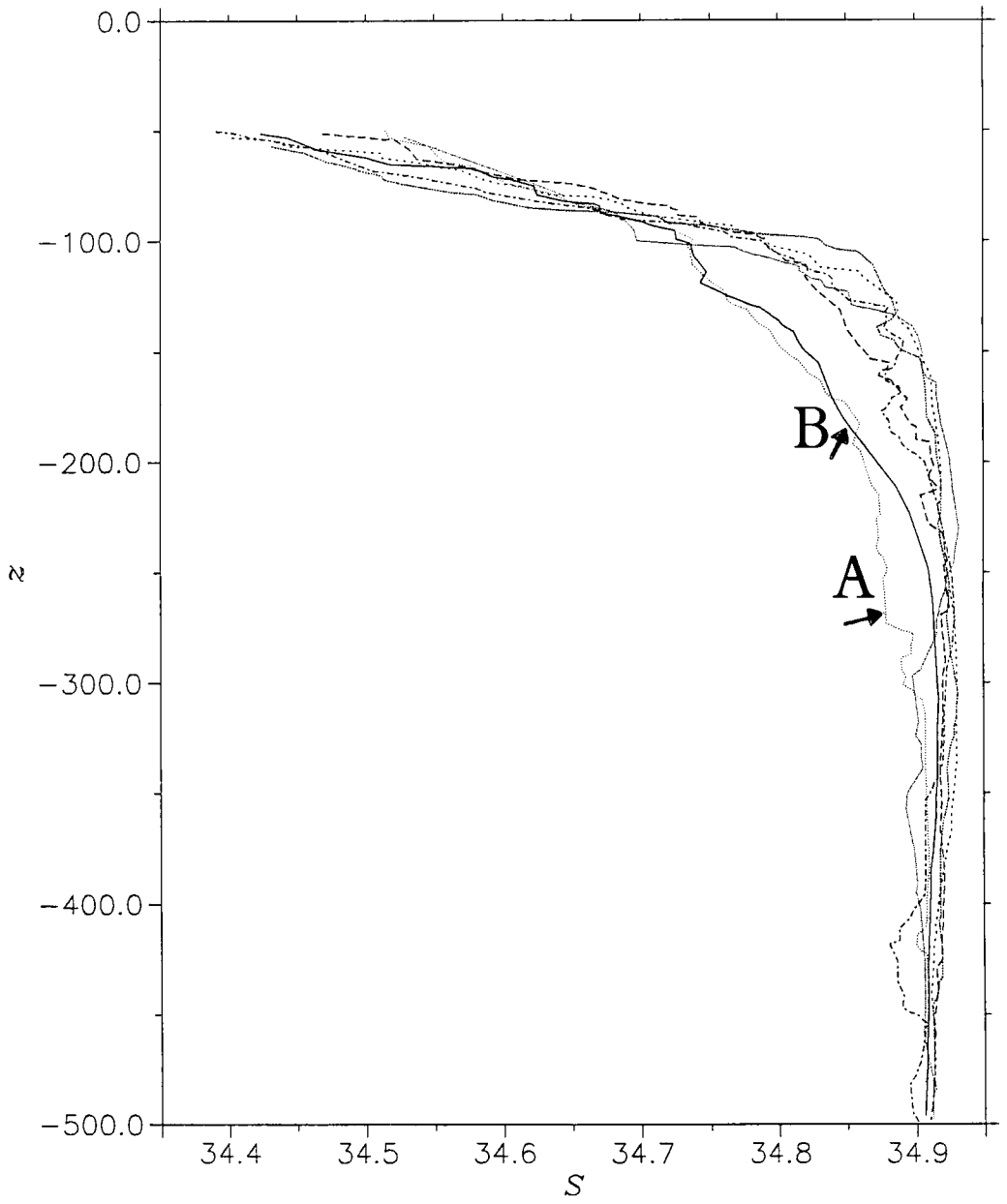

Fig. 6. The ensemble of salinity-depth profiles from the CTD casts taken at the positions indicated in figure 1. The profile marked 'A' is believed to come from a chimney; that marked 'B' probably comes from near the edge of a chimney.

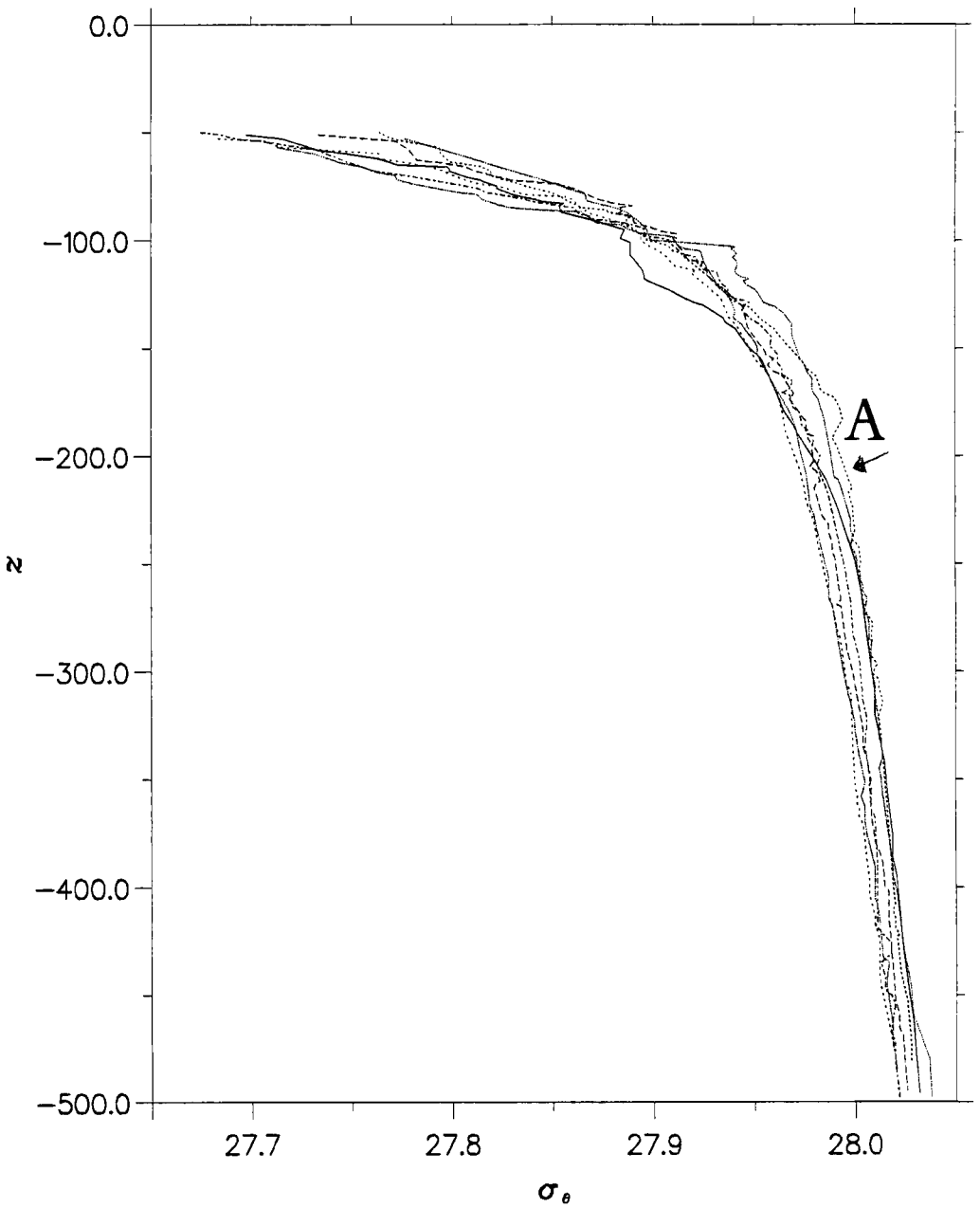

Fig. 7. The ensemble of density-depth profiles from the CTD casts taken at the positions indicated in figure 1. The profile marked 'A' is believed to come from a chimney; that marked 'B' probably comes from near the edge of a chimney.

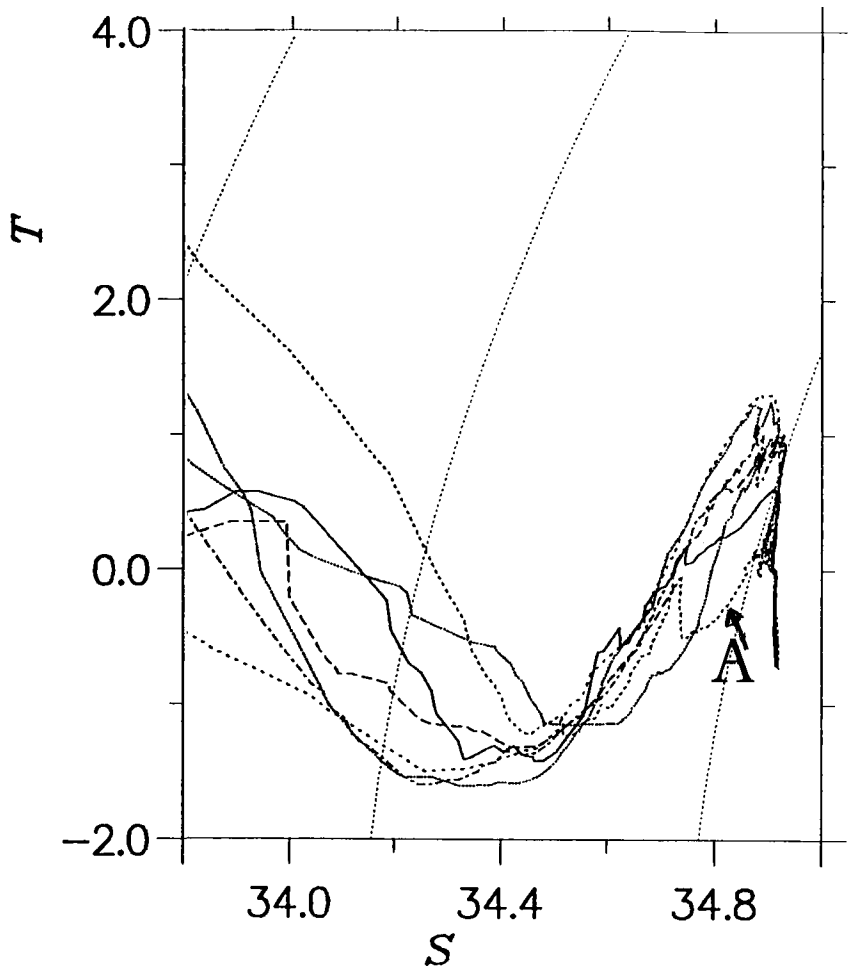

Fig. 8. Temperature-salinity (T-S) relations for the CTD casts taken at the positions shown in figure 1.

The difference between cast A and the environment is most marked in the depth range 100-200m, again consistent with the chain data. The maximum difference between the profiles in this depth range is about 1.8C, which also matches the chain data. The salinity variation in all casts is sufficient to make the density statically stable almost everywhere, even in the temperature inversions. However, very small regions of density inversion were found.

The T-S relations of the casts are shown in figure 8. The environment T-S relation shows the peaked shape typical of the region, with a maximum in salinity just deeper than the maximum temperature. This temperature peak is missing in the 'chimney' T-S relation (profile A) however, and in its place are two much smaller peaks, both approximately aligned with the sides of the environment peaks.

The deeper (higher-salinity) side of all the T-S curves tend to coincide. In the five 'normal' profiles this includes the salinity maximum; in the chimney case and the intermediate case the T-S curves do not reach the temperatures at which this maximum is normally found.

The shallower (low-salinity) side of the curves is less uniform, as might be expected as a result of variations in the lateral input of melt-water into the cold layer during the summer. The 18km spacing between dips is not negligible compared with the distance from the retreating ice edge. The upper warm layer is very stably stratified, with temperature steadily increasing upwards and salinity steadily decreasing upwards, down to values between 32.2 and 32.8 psu.

The observed salinity maximum contains the highest salinities observed in the water column, around 34.93 psu.

Several of the T-S curves also show very small, sharp peaks on the sides of the central maximum, similar in appearance to the peaks in profile A; in all of these sharp T-S peaks the density stratification locally approaches zero, and in a few cases the CTD data indicate weak density inversion. This may be evidence for the mechanism of formation of the chimneys.

3. CONSIDERATIONS ON MECHANISMS

It is not clear how the chimneys shown here are produced. It seems unlikely that they are steady, free features, because a very small horizontal diffusivity (say 10 m^2/s) would erase a 3km wide feature within 10 days. Two possibilities remain. First, the process may be spasmodic and short-lived

(like larger-scale open-ocean convection, cf. Killworth, 1983). The number of chimneys observed would then imply that the process must be ubiquitous. Second, the process may be fairly stationary at the locations observed, and maintained presumably from above (the static stability of all the casts would seem to prohibit influence from below). Note, however, that the surface is essentially "capped" by the warm surface layer, so that air-sea interaction is very unlikely to be involved.

In either case, it is difficult to discover the energy source for the chimneys. All the density profiles are stable (apart from localised inversions), so that driving water downwards would involve doing work on the fluid. However, note that profile A is denser than all others below about 160m, and denser than most others below about 125m.

We have considered various candidates for the energy source.

The chimneys we have observed are cold and fresh (as noted in section 2.1, presumably drawn from water above the temperature maximum), and appear to satisfy little in the way of traditional plume dynamics. The lateral density contrast between a chimney and its environment is around 0.01, yet the change in ambient stratification through which the chimney water apparently sinks is well over 0.1. In other words, the water in the chimney, left to itself, could only sink a fraction of the vertical distance we observe before becoming neutrally stable. Turbulent entrainment could only lessen this distance, not increase it (indeed, the vertical T-S variation is in rough agreement with a simple entraining plume model, provided dynamics are neglected).

It is this difficulty that seems to set our chimneys apart from other convective situations; they are simply not dense enough to sink to the observed depths, and the surroundings are too stably stratified. The possibility that profile A is not, after all, within a chimney (so that our estimates of chimney density are erroneous) seems negated by the good agreement in temperature between A and the thermistor chain data.

We are forced to examine other candidates to maintain the chimneys.

Double diffusion effects are a potential candidate. The position of the temperature maximum, above the salinity maximum, suggests that asymmetric cooling at the temperature maximum could produce locally denser water. However, even a cooling by 0.2C at the temperature maximum (say 1C) would involve only a density increase of 0.01, which is clearly insufficient to generate vertical motions on the scales we assume. Perhaps, though, double

diffusion may act through a staircase-like sequence; but in such a case we might expect to see far more density inversions than were observed.

Cabelling (Foster, 1972) is another possibility. However, we have tested this with presumed mixtures of cold fresh waters from around 50-70m with the warm salty waters at 100-125m, and no mixture was denser than the latter warm salty waters.

Lateral double diffusion is another possibility. Suppose a horizontal layer of hot salty water has a blob of cold fresh water inserted into it. Then the more rapid heat diffusion would convert this blob into hot fresh, which would be too buoyant to sink. Reversing this situation (injecting hot salt into cold fresh) would create a dense layer of cold salty water; but this is not observed in the chimneys, which are fresh, not salty.

We are thus led to wonder whether the chimneys we observed are slices through some three-dimensional process which may have its origins some way from the area under observation. (Note, though, that the linear potential vorticity within the chimney shows little change from that in the environment, suggesting that similar water masses must be involved.) In this case, vertical movements, which were difficult to produce by a convective process because of the stable stratification, might not be required (except as a necessary requirement of continuity and movement on isopycnal surfaces: Pollard and Regier, 1990). Geostrophic flows, though dubious to estimate with such small length scales, are of the order of a few cm/s, in agreement with the readings from the acoustic Doppler current profiler on board the ship. Thus the features could only be advecting at a few km/day from their source. We noted above that lateral diffusion would wipe out such features within around ten days, which would suggest that the lateral movement of the features is limited to a few tens of kilometres. Certainly it would seem difficult for a lateral swirl from an ice-edge eddy (for example) to reach the area of observation without gross modification by mixing.

At this stage, then, we still have no clear perception of how the chimneys are produced. Assuming that strong vertical motions are involved, these chimneys clearly form an important link between the surface and deeper ocean. More research is necessary to understand the phenomenon, and to find out how widespread such chimney events are in the rest of the ocean.

4. CONCLUSIONS

Detailed thermistor chain data have been presented showing vertical structures near the Eastern edge of the East Greenland Current, which appear to represent downwards transfer of cooled, relatively saline water. These thermal data have been supplemented with CTD data. Various potential candidates for the mechanism inducing the chimneys have been discussed, but no clear mechanism has emerged.

5. ACKNOWLEDGEMENTS

The results reported here were obtained on the ARE IF'87 Measurement Trial, and thanks are due to the trials team, led by Nichola Lane, and to the ship's officers and crew, led by Lindsey Wigmore. We are also grateful to LtCdr Rod Davis for meteorological data.

6. REFERENCES

Foster, T.D. (1972) 'An analysis of the cabelling instability in seawater', Journal of Physical Oceanography, **2**, 29-30

Killworth, P.D. (1983) 'Deep convection in the world ocean', Reviews of Geophysics and Space Physics, **21**, 1-26

Lane, N.M., and Scott, J.C. (1986) 'The ARE digital thermistor chain', Proceedings, Marine Data Symposium, New Orleans, pp.127-132, ISBN 0-933957-03-3

Pollard, R.T., and Regier, L. (1990) 'Large variations in potential vorticity at small spatial scales in the upper ocean', Nature **348**, 227-229

Swift, J.H., Aagaard, K., and Malmberg, S.A., (1980), The contribution of the Denmark Strait overflow to the deep North Atlantic', Deep-Sea Research, **27**, 29-42

This Page Intentionally Left Blank

AN APPROACH TO BRINE AND FRESHWATER FLUXES INTERPRETED FROM RADAR AND MICROWAVE RADIOMETER DATA

F. D. CARSEY, Earth and Space Sciences, Jet Propulsion Laboratory, California Institute of Technology, Pasadena CA 91109 (USA)

ABSTRACT

Carsey, F. D., 1990, An approach to brine and freshwater fluxes interpreted from SAR and microwave radiometer data.

Methods are discussed for the estimation of fluxes of brine and freshwater from sea ice formation and melt in ice-covered seas. These estimates will be drawn from a combination of Synthetic aperture Radar (SAR) data, Special Sensor Microwave Imager (SSM/I) microwave brightnesses and environmental analyses. The approach is to use SAR data to generate ice motion and divergence fields to both track the ice and to provide open-water production while using the SSM/I data to monitor the development of the ice in time.

INTRODUCTION

Brine production due to ice formation and growth in the Greenland Sea has been suggested as a key driving term for the local wintertime ventilation that produces most of the world's Atlantic Deep Water. In addition, ice fluxes from the central Arctic have been shown to be the largest input of freshwater to the Greenland-Iceland-Norwegian (GIN) Seas and the greatest export of freshwater from the Arctic Ocean (Aagaard and Carmack, 1989). Ice-ocean interactions in the Fram Strait area have also been suggested as controlling terms in the local surface-water fluxes and in maintaining Arctic mixed-layer properties (Untersteiner, 1988). Years with heavy ice in this area have been correlated with salinity changes in the North Atlantic with the suggestion that the ice cover and the salinity have enjoyed a positive feedback (Mysak and Manak, 1989). In the Weddell Sea there is an additional body of information pointing to ice formation in this area being responsible for the formation of intermediate and deep waters of the world oceans. In the shelf regions of the Arctic basin, ice formation in dynamically produced flaw leads generates cold brine that flows into the

Atlantic layer of the Arctic Ocean. In short, ice surface fluxes, motion and type observations in a number os seas are known to be quite interesting with respect to a number of phenomena and processes.

2 THE SATELLITE SIGNAL

There is good reason to be optimistic that a combination of satellite radiometer and imaging radar data can be used to estimate these fluxes with some accuracy. The satellite radiometer under discussion of the Special Sensor Microwave Imager (SSM/I) (see Hollinger et al, 1987) and the imaging radar is the Synthetic aperture Radar (SAR) (see Fu and Holt, 1982). The SSM/I is operational now; the SAR will be from mid 1991 on. In this paper the approaches to using this data will be outlined.

In the Greenland Sea ventilation, the excess ice production required to drive convection to overturn the Greenland Gyre water (located in the region of 0E, 74N) has been estimated at about 30 cm (Aagaard and Carmack, 1989), and resolving changes of this amount in thin first-year ice is a challenging prospect. There is at present neither an accepted algorithm nor a widely held conceptual model for the separation of new and thin ice species in microwave observations, but there are indications that such identifications may be possible (see Comiso et al, 1989; Steffen and Maslanik, 1988; Cavalieri et al, 1986; Grenfell, 1986; scatterometer preliminary results from Onstott, private communication, 1990). Also, preliminary examination of NOAA-AVHRR data (P. Gudmandsen, private communication, 1990) has indicated that the ice cover of the Greenland Gyre, probably the new ice extent, has a basic variation period of 10-14 days; this time scale is readily observed by satellite sensors. When a ventilation event occurs there is upwelling of warmer water from depth (see, e.g., Killworth, 1979), and this warm water should influence thin ice conditions sufficiently to give a microwave signal. The observation of these warm-water events from space would be an advance in itself and would supply milestones for the microwave data set.

A key aspect of the interpretation of the microwave brightness change as ice thickness is the removal of the part of the change caused by ice deformation. Ice deformation influences the observation in two ways; it produces open water, which drives the observed brightness down, and/or thicker ice, which drives the brightness up. In both cases the brightness changes are irrespective of changes in brightness caused by ice thickening from thermodynamic growth. Ice deformation is measured to adequate accuracy, as nearly as can be anticipated in the absence of real experience,

by interpretation of SAR images (Kwok et al, 1990). Given cloud-free conditions IR images, such as from AVHRR, could be used, but cloud-free conditions cannot be relied upon. Thus, the corrections required in SSM/I observed microwave brightness caused by deformation are, in principle, determinable by ice motion information derived from SAR observations.

3 THE METHODS

From the above it seems clear that the time is ripe to utilize spacecraft microwave data with in situ information to examine processes at work at the surface of those ice covered seas where deep water formation is taking place, e.g. the GIN and Weddell Seas. The approach that suggests itself is to use both SSM/I data and SAR data in the determination of ice growth and melt in the Gyre area.

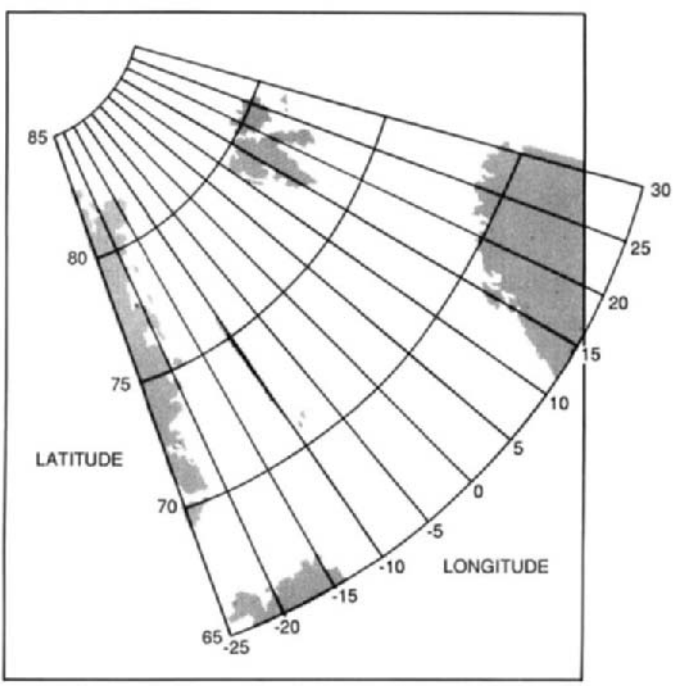

Fig. 1. The SSM/I data grid. The land masses are, from top left, Greenland, Iceland, Norway and, at upper right, Spitzbergen. The area of greatest interest, the Greenland Gyre, is in the vicinity of 74N, 0E. The meridians at -25 and +30 are the borders of the GIN Sea zone of interest.

SSM/I data for the GIN Sea for the winter of 1989, the first Greenland Sea Project intensive period were acquired and are being processed into a data set. Fig. 1 shows the area of interest, the Greenland-Iceland-Norwegian Seas. The SSM/I extraction is indicated in Fig. 2 which shows a a typical SSM/I swath where each dot is an observation of the coarse resolution (25 km) radiances. One channel, 19 GHz H, of microwave brightness temperature data for this swath is shown in Fig. 3. The SSM/I data set must eventually be expressed on a 5 km grid for 2 purposes, ready integration with the SAR data set (see below) and optimization of the microwave brightness data which is of coarse resolution (25 km) but is temporally dense (there are 8-10 observations per day in the Greenland Sea). Care must be taken with respect to 2 issues, atmospheric corrections to the data prior to averaging and averaging times, probably 12 or 24 hours.

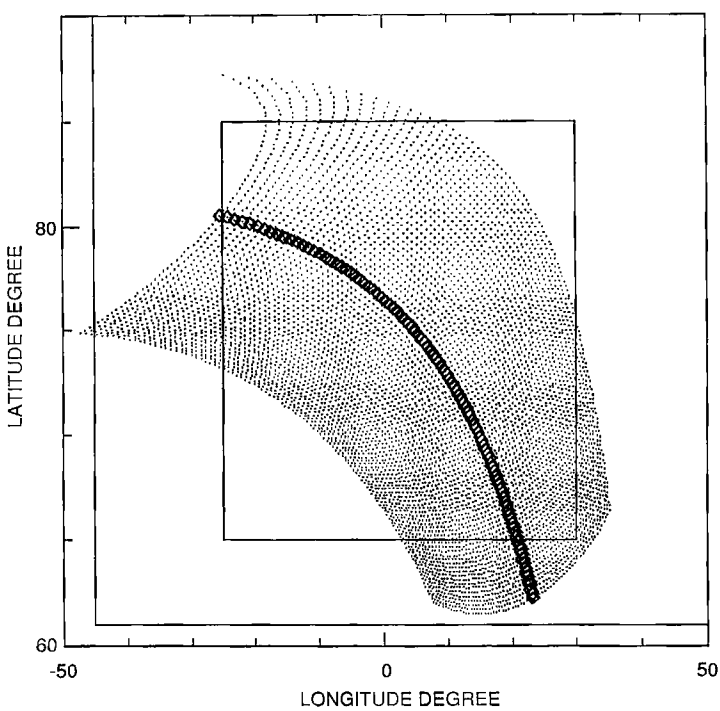

Fig. 2. A location trace of a single SSM/I swath taken at 2 am Jan 1, 1989. Each observation from one of the low frequency channels, (19 GHz, 22 GHz or 37 GHz) is indicated by a dot. Note that this figure is not on the same projection as Fig. 1. The inner box is the zone of interest shown in Fig.1.

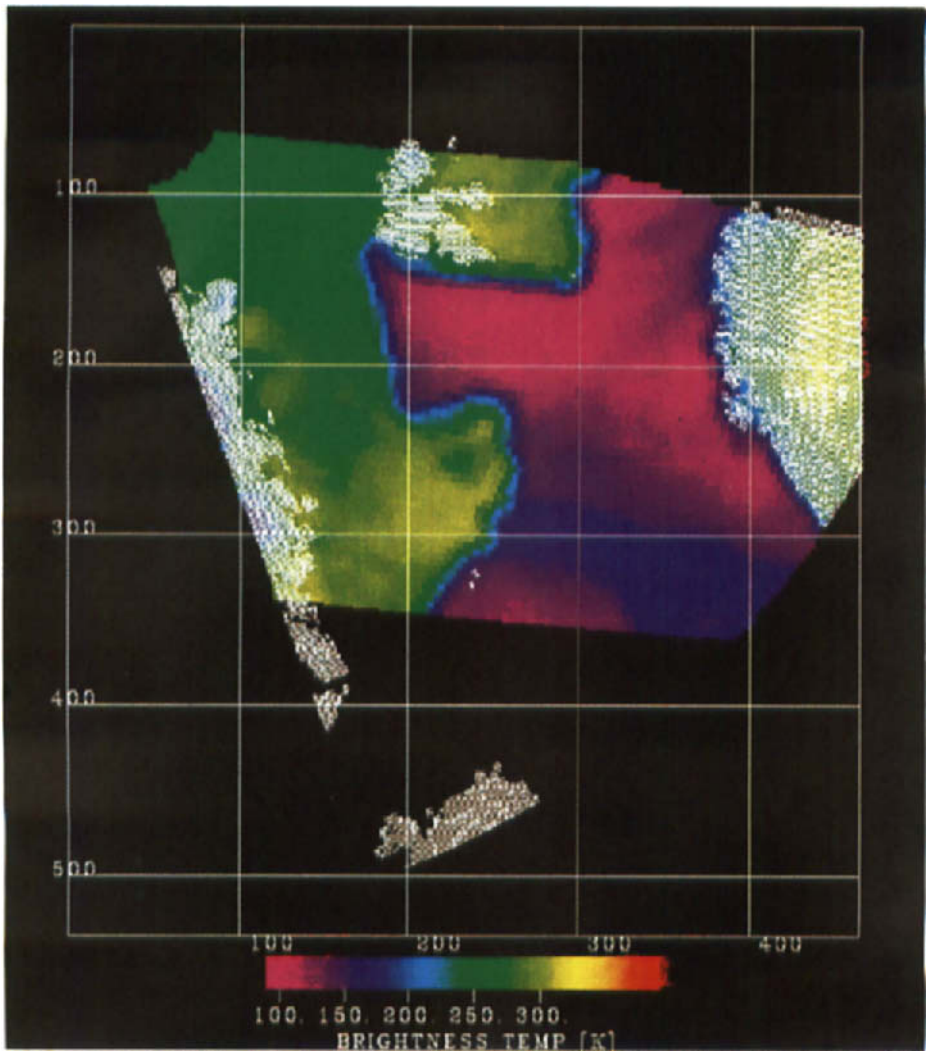

Fig. 3. The 19 GHz horizontal polarization brightness data for the swath shown in Fig. 2. In this figure the ocean is shown in red and blue, and the ice is in yellow, green and turquoise. The dark blue feature in the ocean just off the Icelandic Plateau area is due to atmospheric water vapor and droplets. The numbers refer to the SSM/I data grid.

A significant component of this kind of analysis is access to SAR data and data products. One resource for these data sets is the Alaska SAR Facility (ASF) (Carsey et al, 1987; Holt et al, 1989) which will process the ERS-1 SAR data to images, another is the Alaska SAR Facility Geophysical Processor System (ASF-GPS) which ingests the SAR images and generates a record of ice motion (Kwok et al, 1990) and ice type. These determinations are made on a 5 km earth-fixed grid. The ice motion data is rather good, having an error of only a few 100 m per interval (3 days), but the ice type information is subject to various sorts of confusion, e.g., of pancake ice and open water with old ice as well as open-water and thin ice (Holt et al, 1989). This confusion may be inherent to the use of SAR data for ice work, or it may be significantly diminished by the use of the next generation of polarimetric SAR systems.

4 PHYSICAL BASIS FOR BRINE FLUX DETERMINATION

The microwave behavior of the thin ice species, those ice types less than about half a meter thickness, is such that some data on ice thickness is available. The backscatter signal change for thin ice is complex and depends on the history of the ice. For example surface roughening through pancake formation when the ice is a centimeter or less thick can result in a backscatter magnitudes similar to old ice. In some cases the areal coverage of thin ice can, however, be estimated quite accurately. The microwave brightness situation is more useful to this calculation as thin ice goes through a continuous increase in brightness from open water to a thickness of perhaps a meter. This variation is shown for the Greenland Sea in Fig 4.

To utilize this information the ice must be tracked and its brightness monitored in a Lagrangian fashion; this will be done using SSM/I brightness with SAR motion data. There is a fundamental problem in interpreting these brightness changes: the rate of brightness increase is a function of growth rate, and possibly other variables such as snowcover, so that the inversion of brightness to compute thickness is not unique. This picture is further complicated by areal changes through opening and closing of the ice as these processes change the coverage of the thinner species, including open water, with consequent brightness changes that are not related to thickness changes driven by growth. While the errors in this active-passive approach will clearly be large there is a good starting-out prospect of getting the sign correct.

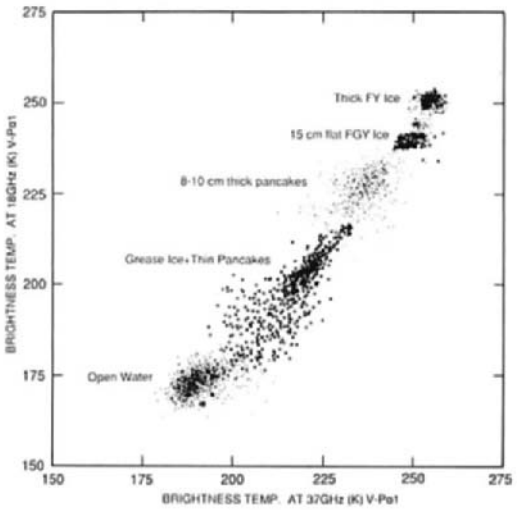

Fig. 4. 37 GHz vertical polarization data taken on the surface by Grenfell (private communication, 1990) in the Greenland Sea in 1987. The change in brightness as the ice thickens is the key to the use of this data for brine production estimation.

Specifically, the microwave brightness Tb at the surface can be expressed in terms of the previous brightness Tb', the change due to open water production of δA, the change due to closing, δTbd, and the change due to growth, δTbg.

$$Tb = Tb' - \frac{\delta A\ (\ Tb' - Tti)}{A} + \delta Tbd + \delta Tbg \qquad .....(1)$$

Where all the terms except δTbg can be evaluated from SAR and SSM/I data sets. There is additionally an atmospheric contribution which is wavelength dependent; is routinely 10% of the total, and may dominate the signal received (NORSEX Group, 1983). Thus the change in brightness due to ice growth is estimable. while the local errors may be substantial, the errors on larger, 25 km or more, regions should be better behaved as many of the error sources arise from uncertainty as to exactly how the ice has moved--the areas are conservative.

In the analysis of Wadhams (1981), shown in Fig. 5, the amount of thin ice in and to the north of Fram Strait is about 10%. This coverage of open-water and thinner ice species contributes about 5% of the brightness signal. The analysis of changes in this 5% is the basis of the brine production estimation. Clearly it is a challenging task.

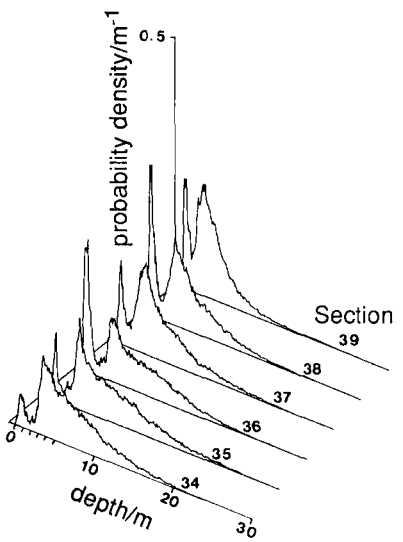

Fig. 5. Submarine sonar derived ice thickness distributions from Wadhams, 1981, for the Fram Strait area. Profile 39 is from Fram Strain and the smaller numbered samples are from 100 km long track elements located consecutively northwestward. The stretching of the ice pack as it leaves the Nansen Basin is apparent in the change in population in the thinnest, 1 m, thickness category.

5 TECHNICAL APPROACH TO BRINE FLUX ESTIMATION.

The fluxes are generated through a multipath data analysis scheme, depicted in block diagram in Figure 6. The steps involved are:

A. Form initial thickness distribution consistent with Tb and SAR data.
B. Monitor positions of monitored ice areas with SAR and buoy data
C Form time series of brightness-change and SAR-derived ice type
D. Estimate deformation with SAR ice-motion information
E. Compute heat flux for new thickness distribution,interpret as growth
F. Estimate grow-rate induced changes in Tb
G. Interpret Tb as thickness change
H. Observe changes in ice-type distribution in SAR images
I. Interpret changed first-year and new-ice areas as growth
J. Compare calculated fluxes (Thomas and Rothrock, 1989)

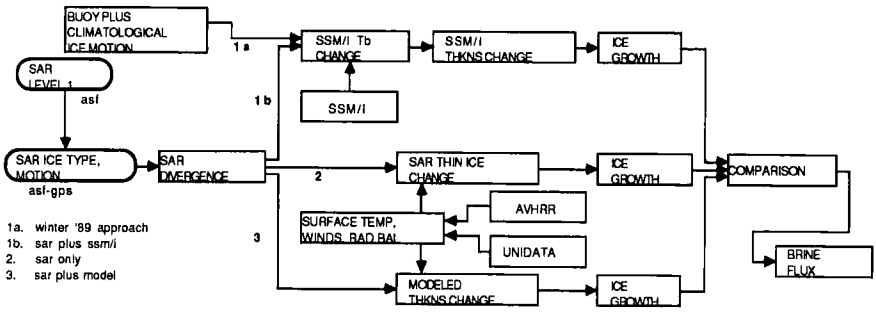

Fig. 6. A flow chart for SAR-SSM/I analysis for brine production estimation. The SAR data will be available from late 1991 through the remainder of the decade from European, Japanese and Canadian satellites.

6 ICE MOTION.

Fine scale ice motion is clearly key to these calculations. In the years prior to the availability of SAR observations, only buoy data will be available, and this data, smoothed in space and time, can be used to estimate ice advection for Tb changes in time. Ice deformation is not directly addressable, but the stretching of the flow in the region of the Greenland Gyre should be present in the buoy motion analysis. In 1992 when ERS-1 SAR data will be available, but it will be restricted to a 100 km wide band oriented approximately parallel to the Greenland coast. Only with RADARSAT data, starting in 1995, will adequate observations be available to monitor the fluxes of the GIN Sea. The situation in the Weddell Sea is not as clear as the size of the zone of deep water formation is not known, but it is likely that RADARSAT coverage will also be required there.

7 THE PHYSICAL BASIS FOR CALCULATING FRESH WATER FLUXES.

Fresh water flux estimation is characterized by extensive use of assumptions and proxy data at this time. It is important because of its role in shutting down convection and because similar data sets are to be employed to those for brine flux. It will be possible to sample with ERS-1 SAR data the flux of ice area through Fram Strait and to complement this data with ice thickness data to be generated by upward-looking sonar to obtain an ice flux.

The fresh water flux is dominated by old ice and thick first-year ice being ablated on the bottom surface; this process was recently discussed by Steele et al (1989). Slicks observed in SAR data for the Chukchi Sea (Fu and Holt, 1982) may be a good indication that melt is taking place. To better evaluate the processes of melt it will be necessary to extend the Arctic Basin warm season analyses of Carsey (1985) and Holt and Digby (1985) to determine the onset of melting conditions and to characterize the state of melt through warm periods. Examination of simultaneous SAR and SSM/I data will extend understanding the processes of this area.

8 ACKNOWLEDGMENT.

The author is indebted to Ben Holt, Mark Drinkwater, Dale Winebrenner, Tom Grenfell and Don Cavalieri for useful discussions. This work was supported by NASA under contract to the California Institute of Technology.

9 REFERENCES

Aagaard, K. and Carmack, E., 1989, The role of sea ice and other fresh water in the Arctic circulation, *J. Geophys. Res., 94*, 14485-14498.

Carsey, F., 1985, Summer arctic sea ice character from satellite microwave data, *J. Geophys. Res., 90*, 5010-5034.

Carsey, F., Jezek, K., Miller, J., Weeks, W.,and Weller, G., 1987, The Alaska Synthetic aperture Radar (SAR) Facility Project, *EOS 68*, 593, 596.

Cavalieri, D. Gloersen, P., and Wilheit, T., 1986, Aircraft and satellite passive microwave observations of the Bering Sea ice cover during MIZEX west, *IEEE Trans Geosci. and Remote Sens., GE-24*, 368-377.

Comiso, J., Grenfell, T., Bell, D., Lange, M., and Ackley, S., 1989, Passive microwave observations of winter Weddell Sea ice, *J. Geophys. Res., 9 4*, 10891-10905.

Drinkwater, M R. and Crocker, G., 1988, Modeling changes in the dielectric and scattering properties of young snowcovered sea ice at GHz frequencies, *J. Glac., 34*, 274-282.

Fu, L.-L. and Holt, B., 1982, *Seasat views oceans and sea ice with synthetic-aperture radar*, JPL Pub 81-120,200p.

Gloersen, P., and Cavalieri, D. J., 1986, Reduction of weather effects in calculation of sea ice concentration from microwave radiances. *Journal of Geophysical Research, 91*, 3913-3919.

Grenfell, T., 1986, Surface-based passive microwave observations of sea ice in the Bering and Greenland Seas, *IEEE Trans. Geosci and Remote Sens., 3*, 378-382.

Hollinger, J., Lo, R., Poe, G., Savage, R., and Pierce, J., 1987, *Special Sensor Microwave Imager user's Guide*, Naval Research Laboratory, Washington DC, 76p.

Holt, B. and Digby, S., 1985, Processes and imagery of first-year fast sea ice during the melt season, *J. Geophys. Res. 90*, 5045-6062.

Holt, B., Kwok, R., and Rignot, E., 1989, Ice classification algorithm development and verification for the Alaska SAR Facility using aircraft imagery, *Proc. IGARSS'89*, 751-754.

Killworth, P. D., 1979, On "chimney" formations in the ocean, *J. Phys. Oceanography, 9*, 531-553.

Kwok, R., Curlander, J., McConnell, R., and Pang, S.,1990, An ice-motion tracking system at the Alaska SAR Facility, *IEEE J. Ocean Eng., 15*, 44-54.

Norwegian Remote Sensing Experiment Group, 1983, The Norwegian remote sensing experiment in a marginal ice zone. *Science, 220*, 781-794.

Mysak, L. and Manak, D.,1989, Arctic sea ice extent and anomalies, 1953-1984, *Atmos. Ocean, 27*, 376-405.

Steele, M., Mellor, G. and McPhee, M, 1989, Role of the molecular sublayer in the melting or freezing of sea ice. *J. Geophys. Res., 19*, 139-147.

Steffen, K., and Maslanik, J., 1988, Comparison of Nimbus 7 Scanning Multichannel Microwave Radiometer radiance and derived sea ice concentrations with Landsat imagery for the North Water area of Baffin Bay. *J. Geophys. Res., 93*, 10769-10781.

Thomas, D., and Rothrock, D., 1989, Blending sequential Scanning Multichannel Microwave Radiometer and buoy data in a sea ice model. *J. Geophys. Res., 94*, 109007-10920.

Untersteiner, N, 1988, On the ice and heat balance in Fram Strait. *J. Geophys. Res., 3*, 527-531.

Wadhams, P., 1981, Sea-ice topography of the Arctic Ocean in the region 70W to 25E. *Phil. Trans. of the Royal Soc. of London, 302*, 45-85.

This Page Intentionally Left Blank

FORMATION OF BAFFIN BAY BOTTOM AND DEEP WATERS

R. H. BOURKE and R. G. PAQUETTE
Department of Oceanography, Naval Postgraduate School Monterey, CA 93943, U. S. A.

ABSTRACT
Bourke, R. H. and Paquette, R. G., 1990. Formation of Baffin Bay bottom and deep waters.

Evidence is presented for the formation of Baffin Bay bottom and deep waters from an Arctic Intermediate Water issuing from Nares Strait, cooled and made more saline by admixture with winter shelf water. The latter water is produced in the shallows of eastern Smith Sound and southeastern Kane Basin in winter under the partially open water of the North Water. The calculated volume of potential bottom water draining into the basin of Baffin Bay is far higher than age measurements in the bottom water would indicate. Hence, mixing of the descending plume of potential bottom water with ambient waters must involve drastic shedding or "shaving" of the outer layers of the plume.

1 INTRODUCTION

Baffin Bay contains in its west central portion a depression of depth greater than 2200 m. This depression is filled with Baffin Bay Bottom Water (BBBW) overlain by Baffin Bay Deep Water (BBDW). The deep basin of Baffin Bay is isolated from the surrounding oceans by shallower water. To the north the water is of the order of 200 m deep in Nares Strait and the channels through the Canadian Archipelago. To the south at the sill of Davis Strait, 750 km distant, it is of the order of 600 m deep. This sill separates the deep water of Baffin Bay from the Labrador Sea. The bathymetry of the region may be seen in Figure 1.

The characteristics of the waters of Baffin Bay are illustrated in the temperature-salinity diagram of Figure 2 which shows old historical data as well as the SIR JOHN FRANKLIN data of September 1986 (Bourke et al., 1989). On this diagram the bottom

water is taken to be that deeper than 1800 m and the deep water that between 1400 and 1800 m, following Muench (1971a). The bottom water has a potential temperature of -0.46 to -0.50°C and a salinity of 34.49 - 34.50 PSU. The deep water is about 0.01 PSU less saline and ranges in temperature from -0.23° to -0.46°C. The deep and bottom waters have been relatively non-varying in the few times they have been sampled during the period 1928 to 1966. Above the BBDW lies a transition zone rising to a maximum temperature at about 500 m depth. This temperature maximum is the manifestation of the Atlantic Intermediate Water (AIW) of the West Greenland Current. At shallower depths the AIW changes gradually into a cold, dilute water termed Baffin Bay Arctic Water (BBArW). The minimum temperature visible in Figure 2 at about 100 m depth is a residue of the previous winter's haline convection. This temperature minimum has not been seen deeper than 150 m in its area of prevalence, northern Baffin Bay and Smith Sound.

The present reexamination of the mechanisms of formation of the BBDW and the BBBW stems from the results of the September 1986 cruise of the CCGS SIR JOHN FRANKLIN (Bourke et al.,1989). In that cruise, CTD stations were occupied along the length of Nares Strait from about 76° 20'N to 82° 10'N and in northeastern and northwestern Baffin Bay. Lateral sections were made routinely with station spacings of about 40 km. In northeastern Baffin Bay, Melville Sound, three sections were made which were orthogonal to the flow of the West Greenland Current. The stations in southern Nares Strait and Smith Sound showed that the Arctic Intermediate Water (ArIW), flowing southward from Kane Basin, is so rapidly diluted in its trip southward that, even in winter, it is unlikely to be sufficiently cold and saline to reach the level of the BBDW, in disagreement with Muench (1971a). It was shown that this deficiency could be overcome by mixing cold, saline winter shelf water with the ArIW. The present paper extends the calculations of Bourke et al. (1989).

2 EARLIER THEORIES

2.1 Labrador Sea Deep Water as a source

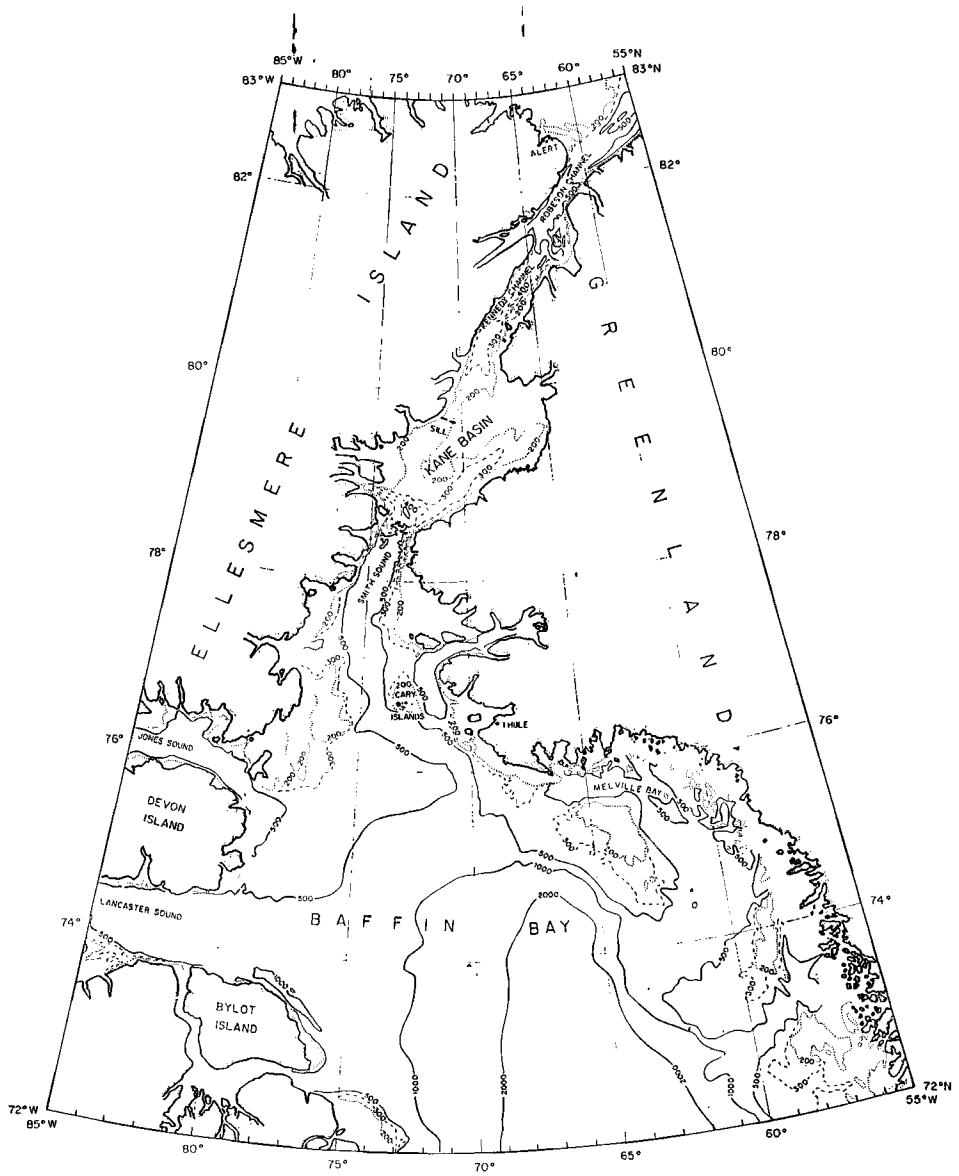

Figure 1. Bathymetry of Nares Strait and northern Baffin Bay. The entire passage, including Smith Sound, Kane Basin and Kennedy and Robeson Channels, bears the name Nares Strait. A sill of about 230 m depth in Kane Basin restricts the southward flow of the saltier (denser) components of ArIW, a blockage which minimizes its capability to modify the deep and bottom waters of Baffin Bay. Contours are in meters. From Canadian Hydrographic Service (1980).

Sverdrup et al.(1942) placed the origin of the BBDW and BBBW in the Labrador Sea Deep Water (LSDW). Their conclusion was based on the MARION and GENERAL GREENE cruises of 1928 - 1935 as reported by Smith et al. (1937). The latter data show Labrador Sea water with salinity of 34.6 PSU and temperature 1°C protruding 60 km north of the sill in Davis Strait in summer. Five hundred kilometers to the south the LSDW at sill depth was at 34.9 PSU and 4°C, indicating that in summer the LSDW is propagating northward rather slowly. Because of its high temperature, the density anomaly, sigma-theta, for the LSDW north of the sill is nearly the same as that of the BBBW, 27.712 kg m^{-3} as compared to 27.719 for BBBW. Cooling in winter, as Sverdrup et al. suggest, conceptually could cause the requisite density increase. For example, cooling the above LSDW to -1.8°C would increase sigma-theta to 28.100 and make propagation of LSDW northward into the depths a possibility.

However, one winter data set indicates that northward propagation of appropriately cooled LSDW does not occur. Garrison (1977) reported the results from two lines of stations sampled to 186 m depth in and near Davis Strait in February-March 1977. One line, centered on the axis of the strait, extended from about 58°N to 68°N. The other was an east-west transect roughly along the 64th parallel near the shallowest part of the sill. Cold water,the result of recent brine convection, was observed to only about 80 m depth; the 0°C isotherm was at about 100 m depth north of the sill and at an average of about 50 m depth over the sill, indicating that any earlier convection had not penetrated deeply. Deeper than 50 m, the water increased in temperature uniformly with depth to 4°C, giving no evidence of deep convection in the past. The weak surficial cooling which must have brought about these conditions is in accord with what would be expected for so southerly a latitude.

Formation of bottom water here seems even more unlikely if one considers the added fact that the density difference, surface to 180 m depth, was 0.7 kg m^{-3}. This represents a much greater obstacle to deep convection than the gradients in regions where such convection is known to occur. For example, the density

difference in the upper 200 m of the central Greenland Sea in winter, where deep convection due to one or more of several mechanisms is considered likely to produce bottom water (Carmack and Aagaard, 1973; Killworth, 1977), is only 0.045 kg m^{-3}. Thus, the requisite cooling of the LSDW in winter does not seem to occur and it is highly unlikely that generation of BBBW by brine-driven convection from the surface in Davis Strait can occur.

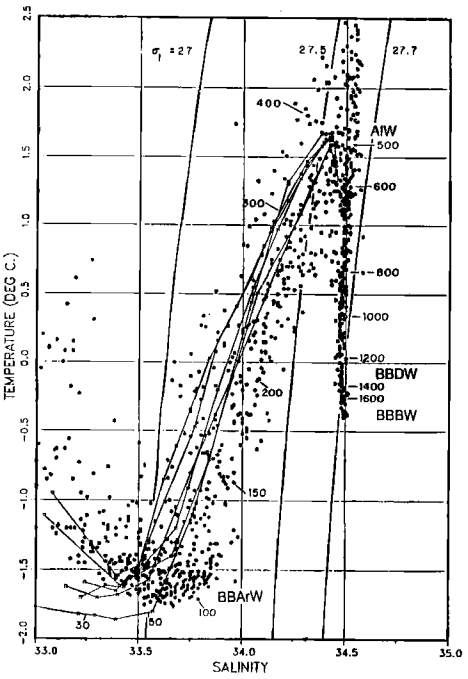

Figure 2. Waters in the West Greenland Current between 74°N and 76°N. Historical data are shown as dots, 1986 data as curves. Average depth bands are shown.

2.2 Summer waters from Nares Strait

The only likely source of BBDW and BBBW then must be in the extreme north of Baffin Bay in winter where sufficiently dense and cold ArIW may issue from Nares Strait in winter or, alternatively, surface water may be increased in density by surficial cooling and brine convection. Muench (1971a, p. 62ff) argues the first hypothesis and notes that water of properties similar to upper BBDW have been seen in Nares Strait in summer. Water of the properties of BBBW have not been observed in Nares Strait, but he postulates that they may periodically pass through the strait in winter because they exist at a level of about 200 m in the Eurasian Basin of the Arctic Ocean. We shall call water approximating the above properties Arctic Intermediate Water (ArIW), if its source is the Arctic Ocean. Unfortunately, the only cold-weather data from Nares Strait were obtained in May 1969 when

the waters were beginning to warm. Muench (1971b) recorded the results of a 14-day time-series measuring temperature and salinity at a location just south of the sill in Kane Basin. Near-bottom (235 m) properties of the water under maximum salinity conditions were T = -0.08°C, S = 34.68 PSU, more saline than BBBW but substantially warmer. Who can say what might happen sporadically in mid-winter? The gravest weakness in Muench's argument lies in concluding that an ArIW that is so close in characteristics to BBBW could survive the effects of dilution unchanged while descending to the depths of Baffin Bay from Nares Strait.

Bourke et al. (1989), in the absence of winter data, were unable to deny the possibility that ArIW or denser water could flow sporadically through Nares Strait in winter in sufficient volume to reach the bottom of Baffin Bay. However, they did show that under the late summer conditions of SIR JOHN FRANKLIN 86 the intermediate waters of Nares Strait which passed over the sill in Kane Basin were rapidly diluted on their trip southward through Kane Basin and Smith Sound. It is doubtful that the diluting waters could be substantially more saline in winter because ArIW, at its shallowest in Smith Sound is deeper than the maximum depth of generalized haline convection previously mentioned in connection with Figure 2. Hence, it is highly improbable that a hypothetical winter ArIW, even though slightly more saline and slightly colder than BBBW, could survive the dilution processes and reach the bottom of Baffin Bay. This suggests that a candidate source water for the BBBW or BBDW must be substantially more saline and colder than the destination waters, if it is to survive dilution effects during the several hundred kilometers of down-slope flow enroute to the depths. No such candidate is readily apparent in Nares Strait nor the Arctic Ocean.

2.3 Age of bottom water.

In the process of computing the volume of water potentially able to reach the bottom of Baffin Bay, we shall need to know the age of the bottom water. The age or replacement time of BBBW has been computed by Top et al. (1980) in three ways. They do not

distinguish between age and replacement time, but when the new water mixes thoroughly with the old water, a reasonably likely situation, the two quantities are substantially the same. From the oxygen concentration near the bottom of Baffin Bay (ca. 3.21 ml l^{-1}) they computed two replacement times or ages. They used the Riley (1951) oxygen utilization rate for the deep north Atlantic, 0.002 ml l^{-1} y^{-1}, to obtain an age of 1500+ years and Munk's (1966) utilization rates of 0.0027 - 0.0053 ml l^{-1} y^{-1} to obtain a range of 570 - 1100 years. From their own ^{3}H-^{3}He measurements they computed a replacement time of 77 - 455 years for the waters deeper than 1200 m. The lowest value above is certainly suspect in view of the general agreement of the values derived from the oxygen concentrations. Therefore, we choose a reasonable mean age of 750 years.

3 ENHANCED BRINE GENERATION IN SHALLOW WATER

3.1 Necessity for both thin ice and short water columns

If ArIW, coming along the bottom of Nares Strait in winter is to form BBBW, it must be cooled and probably made more saline so that it can withstand the effects of dilution during the long trip to the bottom of Baffin Bay. The likely component water to accomplish this is a surface water formed in eastern Smith Sound in winter by continual freezing in the North Water area (Bourke et al., 1989). The North Water is an area of thin ice and open water filling Smith Sound and part of Kane Basin in winter. It appears to be maintained by northerly winds that export ice southwestward inasmuch as insufficient sensible heat is available in the water to melt the ice (Muench, 1971a). In spite of accelerated freezing under the thin ice, the summer data show no evidence of general winter haline convection to depths greater than 150 m, as mentioned above. Therefore, one turns to the possibility of forming a cold, saline water by freezing and brine rejection over the short water columns of shallow water. When the depth of the water column with which the brine can mix is limited by the bottom, high salinities may be reached with plausible heat losses. The occurrences of such

processes are becoming more widely accepted since their invocation by Aagaard et al. (1981) to explain the formation of the upper deep waters of the Arctic Ocean and the modelling of the same process by Melling and Lewis (1982).

To come to quantitative conclusions, it is necessary to identify shallow water areas in Smith Sound and form an estimate of the thickness of ice to be found over the shallows in order to estimate the heat losses to be expected. We have estimated the area of shallow water more conservatively than Bourke et al. (1989), including only the northeastern part of Smith Sound north of 77° 30'N, the area where open water and thin ice are most prevalent. Here 800 km^2 of water 50 m or less deep are present. Additional small areas of possible brine generation occur in Lady Ann Strait near the southern part of Jones Sound (Steffen, 1985) and in southeastern Kane Basin (Muench, Steffen, personal communications). These have been neglected.

3.2 Thin-ice statistics for the North Water

A measure of the prevalence of thin ice and open water may be had from the results of 14 airborne radiation thermometer surveys of the North Water in the periods November 1978 to March 1979 and December 1980 to March 1981. These were reported by Steffen (1985, 1986) and Steffen and Lewis (1988). A portion of each flight was along the eastern side of Smith Sound and into the extreme southerly part of Kane Basin, returning down the middle of Smith Sound. These results were tabulated in Steffen's (1986) Table III.

Of more direct interest for our purposes were statistics for the part of the flight paths showing the greatest frequency of open water, a 50-km section southwest and west of Cape Alexander and close to shore, which were tabulated separately in Steffen's (1986) Table IV, but only for 7 of the 14 flights. These data are of particular interest because they may be taken to be representative of the relatively large fraction of near-shore shallow area which was not covered by the flights. We extrapolated these frequencies to a data base of 14 flights by a simple proportion, assuming that seven sets of near-shore frequencies changed with time in the same

way as did the frequencies for all of the wider-based eastern Smith Sound data segments. The results of the extrapolation are shown in Table 1.

Approximately 35% of the near-shore area is open water or covered by ice less than 0.05 m thick; 45% less than 0.1 m. Hence, a sizeable fraction of the shallow North Water region possesses an ice cover capable of generating significant quantities of cold, brine-enhanced, saline water. In a following section we estimate the volume of brine produced in this region, assuming typical wintertime conditions. But first we address the possibility that heat rising from below significantly reduces ice formation and consequent brine generation.

3.3 Heat upwelling not a major factor in the heat balance

Steffen detected conditions which he classed as open water by a measurement of apparent surface temperature warmer than -1.8°C; in some instances his temperatures were considerably warmer than this. They were warm enough that, even if his estimated uncertainty of ±0.15°C is negative, some cells of surface water must have been warmer than the freezing temperature. One must ask if enough heat is being supplied from below the ice to vitiate our calculations of ice production.

Both Muench (1971a) and Steffen (1985) compute upwelled heat fluxes based on a computation of Ekman transports and an assumed temperature of the upwelled water. The two authors differ markedly in their assumptions and results. Muench assumes that the source water for the upwelling is the AIW of the West Greenland Current with a temperature of 1°C, a water that has a depth of 500-600 m in its area of prevalence, south of Smith Sound. He finds an Ekman transport of 200 kg m^{-1} s^{-1} and an upwelled heat flux of 0.837×10^{12} W over the entire area of the North Water. Steffen gives the upwelled water a temperature of 0.1°C, a more common temperature for the intermediate waters of upper Smith Sound, and finds an Ekman transport of 1000 kg m^{-1} s^{-1} and an

TABLE 1
Statistics on various ice types in northeastern Smith Sound.

Ice Type	Thickness m	Frequency[a] 14 Flights %	Standard[a] Deviation	Frequency[b] Near Shore %
Ice-Free	0	2.91	4.61	13.81
Dark Nilas	<0.05	6.71	4.60	20.86
Light Nilas	0.05 - 0.10	5.96	4.14	9.49
Grey	0.10 - 0.15	9.54	8.36	18.18
Grey-White	0.15 - 0.30	29.31	13.66	24.39
White	>0.30	45.56	23.41	17.00

[a] From Steffen's (1986) Table III
[b] Extrapolated from Table III using ratios from Steffen's (1986) Table IV.

upwelled heat flux of 3×10^{12} W. Both their water temperatures are higher than we would estimate. Noting that the maximum depth from which upwelled water is likely to reach the surface is 300 m, the warmest temperature of upwelled water would be about -0.6°C, judging from FRANKLIN 86, Station 41 (to be seen in Figure 3). Using -0.6°C as the temperature of the source water, Muench's heat upwelling would become 0.367×10^{12} W and Steffen's 1.92×10^{12} W. A further cause of discrepancy between the two is the length of coast considered. Muench used 100 km, Steffen used 350 km. Adjusting Muench's value to 350 km yields 1.28×10^{12} W, bringing them into agreement within a factor of 1.5. To obtain the heat flux per unit area one must know the width of the upwelling zone. A width of 250 km would not be extraordinary, as may be seen in the example of upwelling along the southwestern African coast in Dietrich et al. (1980, p.509). However, since the entire width of Smith Sound averages less than 200 km, we choose a conservative 100 km width of upwelling zone. Then, using Steffen's heat flux, the upwelling heat flux per unit area becomes $(1.92 \times 10^{12})/(3.5 \times 10^{10}) = 54.8$ W m^{-2}. Not only is this small compared to the soon-to-be-computed heat loss to the atmosphere of 266 W m^{-2} but it is this large only because of the assumption that

all of the upwelled water comes from 300 m depth and that all of the shallower waters which also upwell are products of the -0.6° water and cooling within the upwelling area. This is likely to be only partly true and the computed upwelling heat flux therefore is too high.

With upwelling heat relatively so small, how can Steffen's observations of "warm water" at the surface be brought into perspective? We suggest that Steffen's warm water cells were probably not due to upwelling. If the error levels of his measurements are considered, a substantial fraction of his warm cells were merely water at the freezing point swept free of ice by the wind. The rest, in their sporadic nature, suggest the possibility of deeply penetrating adjacent chimneys of down-going brine and up-going replacement water, as illustrated by Gordon (1988).

4 WINTER SHELF-WATER PROPERTIES

We will assume that the open water and thin ice frequencies found along Steffen's (1986) 50-km track are typical of all of the northeastern shore of Smith Sound and its shallow areas. From these ice frequencies we next proceed to calculate the ice and salt production and the resultant water column salinities.

4.1 Heat loss and salt production

The estimation of heat loss in the shallow water of north-eastern Smith Sound is based on Maykut's (1986) heat fluxes over several different thicknesses of ice in the "central" Arctic. Examination of the Marine Climatic Atlas for the World (Superintendent of Documents, 1963) indicates that the average winter temperatures and cloud frequencies in Smith Sound are quite similar to those north of Alaska, the region from which Maykut's data come. Thus, his results may be regarded as a reasonable estimate.

Table 2 is modified slightly from Table 2 of Bourke et al. (1989). The latter authors took a too conservative view of the heat losses from the water by averaging over the period October to

May. Here, we shall use Maykut's heat losses, averaged from December to April. Table 2 shows the increased salinities of water column due to the brine drainage resulting from applying these heat losses to water columns of five lengths under four different thicknesses of overlying ice. The initial salinities, S_0, are from WESTWIND 69 Station 50 in late September at 76° 51'N, 71° 58'W in southeastern Smith Sound, south of the Carey Islands, in 800 m of water. The integrated mean salinities within the specified column depth are used. The appreciable initial cooling normally necessary to bring the water columns to the freezing temperature is neglected because cooling prior to December will already have brought the columns to freezing, or nearly so. The down-slope flow of brine away from the generating area is assumed to be negligible compared to the rate of brine generation. This assumption is reasonable because brine is being generated over a large area while flow away from the area is taking place only along some portion of the outer periphery. The heat of fusion of salty ice is from Zubov (1945, p.154) and the salinity of the ice is from Cox and Weeks (1974). The temperatures of the resultant water are not given because they will be at the freezing point, about -2°C.

TABLE 2.
Effects of one month's cooling

	Overlying Ice Thickness, m			
	0.00	0.05	0.10	0.20
Avg. cooling, W/m^2	848.0	452.2	324.0	208.2
Ice salinity, PSU	14.2	13.3	12.3	10.4
Heat of fusion, kJ/kg	193.8	213.9	243.6	271.6
Ice formed, m	12.3	6.0	4.5	2.2
Resultant salinity				
125-m column, S_0=33.33	35.02	34.18	33.89	33.68
100-m column, S_0=33.26	35.36	34.32	33.96	33.70
50-m column, S_0=33.04	37.20	35.15	34.43	33.92
25-m column, S_0=32.88	41.13	37.06	35.64	34.62
10-m column, S_0=32.88	53.51	43.33	39.79	37.23

4.2 Brine production.

The mass of salt produced in one month was computed by numerical integration of a product of salinity excess, water volume and probability of an ice thickness summed with respect to ice thickness probability and distance from shore. The salinity excess was with respect to a mean column salinity of 32.92 PSU. The water volume was computed as a function of depth, assuming that the entire brine-generating area was a rectangular block with triangular section and having a plane, slanted bottom. For this purpose, Table 2 was expanded to higher resolution and shallower depths. The integration was carried from 3 m depth to four different depths with the results shown in Table 3.

TABLE 3
Brine produced in one month after applying ice thickness probabilities.

Maximum depth of area, m	25.0	50.0	100.0	125.0
Salinity of brine, PSU	38.78	36.16	34.75	34.46
Volume of brine, km^3	4.93	19.93	79.93	124.9
Excess salt, 10^{10} kg	2.97	6.64	15.05	19.72
Total salt, 10^{10} kg	19.63	74.01	285.3	442.1

In this table, "Volume of brine" is the geometric volume from 3 m depth out to the depth shown, "Salinity of brine" is the mean resulting salinity if all the salt produced is mixed into the tabulated volume. "Excess salt" is the salt resulting only from ice formation and "Total salt" contains not only the excess salt but also the salt in the original water. The latter two numbers will not be used further in our discussion but are provided for those accustomed to think in terms of the salt transport into the depths.

It is not proper to count the volume of brine as a contribution of saline water to the depths if the water that contains it is not saline enough to sink to bottom. In Table 3, water columns up

to nearly 125 m depth will be above salinity 34.5 and thus potentially saline enough to sink to the bottom of Baffin Bay.

4.3 Replacement time

The volumes of water potentially able to reach the bottom of Baffin Bay in Table 3 are highly sensitive to the replacement time. If the replacement time is halved, the volume of potential bottom water is reduced to about one-sixth. The results of the Melling and Lewis (1982) model tend to justify our choice of 30 days as the residence time. We extrapolated their mean brine plume speeds to the relatively flat shelf conditions of northeastern Smith Sound and, using their mean plume buoyancy and thickness, computed the time to drain the shelf area out to the 50 m contour to be 48.5 days.

5 CANDIDATE BOTTOM WATER

Let us provisionally accept for the volume of brine generated during winter a middle value from Table 3, 19.93 x 5 or 99.65 km^3 of water with salinity about 36.0 PSU during the 5 months of winter. The next questions are: How much of it reaches bottom? With what waters does it mix? How much water does it entrain and how much becomes so diluted that it is shed from the descending plume of salty water at intermediate depths? At the core of the discussion will be a comparison of the time required to replace the 23,300 km^3 of BBBW with the age of 750 years discussed in Section 2.3.

5.1 Component waters

The winter shelf water will flow down into the Smith Sound canyon, interacting first with the winter mixed layer and then consecutively with waters very similar to a summer water column, finally encountering a narrowly fractionated portion of the ArIW water mass near bottom. This water column (FRANKLIN 86, station 41 augmented with a winter surface layer) is shown with solid circles in Figure 3.

As a matter of interest, a segment of the ArIW water mass of

the Arctic Ocean (ARLIS II, Sta. 55) is shown marked with triangles. The Smith Sound water column is extended speculatively to the Muench (1971b) near-bottom time-series properties mentioned in Section 2.2. This point lies on the ArIW curve and shows that ArIW from depths near 230 m manages to pass over the sill. The parts of the ArIW that would be candidates to form BBBW directly, those around 170 m depth, apparently do not reach the sill and, instead, are replaced by lighter water.

The second step in the trip to the deep bottom of Baffin Bay involves a passage for a distance of about 200 km along the bottom

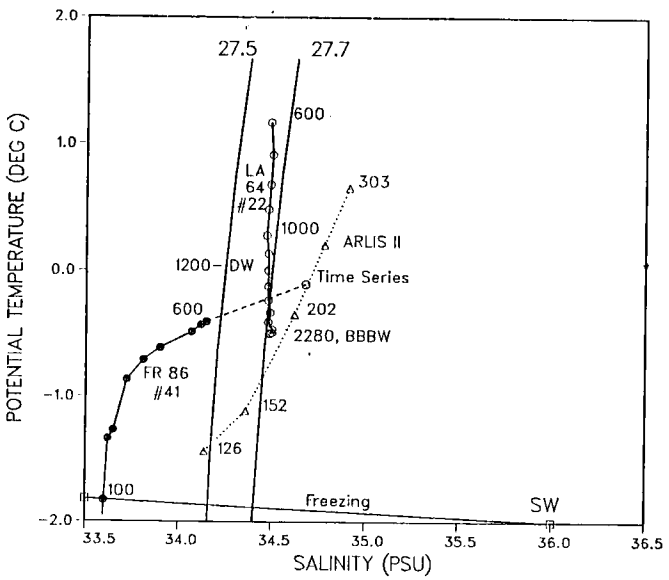

Fig. 3. Potential temperature-salinity correlations for several waters involved in the formation of BBBW. Solid circles are from FRANKLIN 1986, Station 41 in the southern mouth of Kane Basin. The surface data have been altered for the first 100 m to represent a brine-convected mixed layer. The open circles are from LABRADOR 1964, Station 22. They show the central Baffin Bay basin properties including the deep and bottom waters. The dotted curve is a portion of ARLIS II Station 55 showing a plausible parent water of the deepest waters flowing through Nares Strait. The dashed curve is a hypothetical extension of Station 41 to the properties of the most saline water found near bottom during a time series in May 1969, indicating possible bottom properties at Station 41 in winter.

of the sightly sloping Smith Sound canyon, mixing with an ArIW

which is increasingly diluted by warmer AIW until, at the end of that traverse, it begins the third step, a steeper descent into the main basin through the AIW water mass and into the deep and bottom waters, a course marked with circles in Figure 3.

5.2 Dilution and entrainment

To continue with the discussion of the formation of BBBW, let us use Figure 4, a simplified version of Figure 3, in conjunction with Figure 3 and note the restrictions which must be placed on the properties of the candidate bottom water (CBW), the water which will travel down the slope of the main basin of Baffin Bay and, however modified on the way, become BBBW. The CBW, after it reaches the southern end of the Smith Sound Canyon at about 600 m depth, will encounter only waters like those in the LABRADOR 64

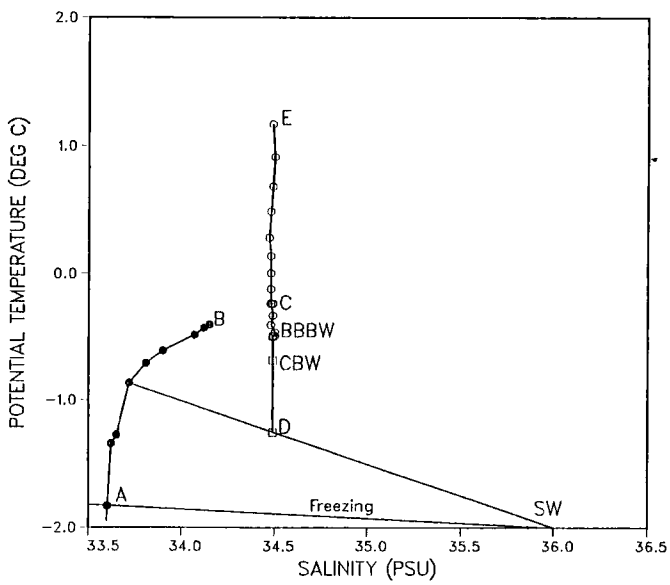

Figure 4. Potential temperature-salinity diagram illustrating first the mixing taking place between a cold, saline shelf water, SW, and an average of the waters present in Smith Sound down to 600 m at the end of the Smith Sound canyon, the arc AB. This produces a mixture D. D then travels for 200 km down the canyon, mixing with an ArIW conceived to have the properties shown at C to make CBW. CBW then descends into the main basin of Baffin Bay, mixing with waters from E on down to BBBW, if it gets that far. Mixing products that are less dense than the environment are shed at intermediate depths. CBW, at the core of the descending plume, gradually changes in properties toward BBBW.

curve, beginning at the shallow, high-temperature end. These waters are at a salinity of 34.485 ± 0.015 PSU all the way down to 2280 m depth. The upper portion of this water column down to perhaps 1000 m may be considered to have its properties stabilized and maintained by the continual flow of the WGC. The deeper part, which is not flushed by the WGC, must be maintained by water descending from the surface. On the average, any water which starts at 600 m depth and is to form bottom water after mixing with the waters along the way must have a salinity very near 34.5 PSU and a temperature lower than that of BBBW because the only waters with which the CBW can mix have a salinity very near 34.5 PSU and a temperature warmer than BBBW.

The descending plume will be stratified, as suggested by Aagaard et al. (1985) and illustrated by Foldvik and Gammelsrød (1988) for a plume on the continental slope of the Weddell Sea. Stratification is to be expected because mixing of the plume with ambient water will be more thorough near the outer fringes than near the core. The outer fringes of the plume are the first waters to be diluted. Their reduced density forces these outer fringe waters to be shed at a density horizon at intermediate depth. This is a process called "shaving" by Aagaard et al. (1985) and would contribute water to the BBDW as well as to the intermediate waters. The greater the supply of the CBW the thicker the descending plume will be, the more isolated the core of the plume will be from the diluting effects of the ambient water and the closer CBW may be to the properties of BBBW and be expected to penetrate to bottom. Conversely, if there is only a small supply of CBW, it must be substantially colder than BBBW to eventually reach bottom.

5.3 Multi-stage mixing to form BBBW

Continuing with Figure 4, the processes that are likely to take place are as follows. Shelf Water (SW) mixes successively with waters of Types A through B during the first descent into the Smith Sound Canyon to produce water of Type D, conceived to be on a line between SW and the middle of the arc AB. Any mixtures less saline than D will be shed at shallower depths into the upper layers of

Smith Sound. Mixtures more saline than D are conceptually possible and would result in a CBW potentially capable of slightly increasing the salinity of BBBW, as has been discussed above. Near the bottom of Smith Sound, Water D interacts for about 200 km of travel with ArIW of approximate composition C. Here, the probability that ArIW will have a salinity as high as 34.68, the one-time late winter maximum, is considered to be small. The product of this mixing is CBW. We are led to place CBW relatively close to the composition of BBBW because otherwise there would be too much tendency to continually lower the temperature of BBBW. By scaling on Figure 3 it is found that composition D will contain 0.335 of SW and CBW will contain 0.46 of D. Thus CBW will contain 0.154 of SW, resulting in an increase to 6.5 times the volume of the original shelf water, assuming that only entrainment of diluting water takes place in the first 600 m of depth.

One can see that forming a CBW that can reach bottom is a rather critical process. A little too much ArIW and the CBW will be too warm and insufficiently dense. If there is too little ArIW, either there will be too little volume of water to reach bottom or there will be an episode in which the temperature of BBBW is slightly lowered and its salinity slightly increased.

The CBW starts at about 600 m depth and must descend to 1800 m depth, if it is to become a part of the BBBW. Attrition of the plume of CBW during its descent through waters with compositions from E to BBBW will occur by mixing of ambient waters into the outer layers of the plume, producing waters no longer dense enough to continue on down with the core. These outer layers will be continually shed into the intermediate depths and even into the BBDW at appropriate density levels. The core will also suffer dilution but at a slower rate than the outer fringes of the plume. The diluted core water, insofar as it remains more dense than the environment, will increase in volume. Thus, the composition of the core will shift slowly toward the composition of BBBW while the outer layers of the original plume will be left behind at a continuity of levels from E to BBBW.

While the resultant diminution in volume due to shedding of

water from the plume cannot be calculated directly, one may estimate what it should be from the known age of the BBBW. Taking the volume of the BBBW as 23,300 km^3, using the previously estimated production of shelf water of 99.6 km^3 yr^{-1} and correcting that mass with the entrainment factor of 6.57, the number of years to replace the BBBW would be 23,300/(99.6 x 6.57) or 36.0. Then the CBW must be diminished in mass by a factor of 750/36.0 or 21 times during its descent from 600 m depth to 1800 m, the top of the BBBW layer.

5.4 Apparent long-term constancy of BBBW

In the long term, the salinity of the bottom water remains remarkably stable at 34.5 PSU. The major reason for this constraint lies in the opposing effects of two processes on the waters supplying the BBBW.

1) The sill in Kane Basin cuts off the high-salinity end of the ArIW water mass and permits salinities only slightly higher than 34.5 PSU to pass.
2) The long water column through which the CBW must pass enroute to bottom is very near 34.5 PSU in salinity. Fractions of the CBW having lower salinity also generally have lower density and hence are shed into the mid-depths.

Thus, lower salinities are completely excluded from the BBBW and it is only higher salinities resulting from particularly saline shelf water that have the potential for increasing the salinity of BBBW. Because the shelf water volume is only about one-sixth of the CBW, this effect must be small.

We must not ignore the possibility that the BBBW is replaced only extremely infrequently in massive surges. There is no way of detecting such a history, using existing data. In opposition, we note that the probability of forming moderate amounts of sufficiently saline water on the shallow shelf is high and with it the probability of continual replacement.

6 SUMMARY

It has been shown in more detail than previously that Baffin Bay Bottom Water is quite unlikely to have its origin in Labrador Sea Deep Water and must have its source in the north of Baffin Bay. Two waters mix to form the source water for Baffin Bay Bottom Water: 1) a cold, saline water produced by freezing in winter in the shallow waters of eastern Smith Sound and 2) a typical winter water column in Smith Sound terminated by a narrowly selected fraction of Arctic Intermediate Water flowing along the bottom of Nares Strait and fractionated in properties by the action of a sill in Nares Strait.

A plausible salinity and production rate for the cold shelf water was computed. This production rate was computed to be increased by entrainment during the first 200 km of flow of the descending plume of dense water by a maximum factor of 6.6. Thereafter, the volume of the plume must decrease by a factor of 21 before reaching the bottom water, if the replacement rate deduced from the measured age of the bottom water is to be satisfied.

7 ACKNOWLEDGMENTS

This work was conducted in conjunction with work sponsored by the Arctic Submarine Laboratory, Naval Ocean Systems Center, San Diego, California and funded by the Naval Postgraduate School. We are particularly appreciative of the careful criticisms of one of the reviewers.

8 LITERATURE CITED

Aagaard, K., Coachman, L. K. and Carmack, E., 1981. On the halocline of the Arctic Ocean, Deep-Sea Res., Part A, **28**(6): 529-546.

Aagaard, K., Swift, J. H. and Carmack, D. C., 1985. Thermohaline circulation in the Arctic Mediterranean Seas, J. Geophys. Res., **90**(C3): 4833-4846.

Bourke, R. H., Addison, V. G. and Paquette, R. G., 1989. Oceanography of Nares Strait and northern Baffin Bay in 1986 with emphasis on deep and bottom water formation, J. Geophys. Res., **94**(C6): 8289-8302.

Bucca, P. J., 1990. A compendium of environmental data collected during the Iceshelf-88 exercise, Naval Oceanographic and

Atmospheric Research Laboratory Technical Note 32, Stennis Space Center, Mississippi, 54 pp.
Canadian Hydrographic Service, 1980. Baffin Bay bathymetry, Dept. of Fish. and Oceans, Map 817A, Ottawa.
Carmack, E. C. and Aagaard, K., 1973. On the deep water of the Norwegian Sea, Deep-Sea Res., **20**: 687-715.
Cox, G. F. N. and Weeks, W. F., 1974. Salinity variations in sea ice, J. Glaciol., **13**(67): 109-120.
Dietrich, G., Kalle, K., Krauss, W. and Siedler, G., 1980. General Oceanography, an Introduction, 2nd ed., transl. from Allgemeine Meereskunde, 1963, N. Y., Wiley, 626 pp.
Foldvik, A. and Gammelsrød, T., 1988. Notes on Southern Ocean hydrography, sea ice and bottom water formation, Paleogeography, Paleoclimatology, Paleoecology, **67**: 3-17.
Garrison, G. R., 1977, Oceanographic measurements in the Chukchi Sea and Baffin Bay - 1976, Report APL-UW 7710, University of Washington Applied Physics Laboratory, Seattle, 95 pp.
Gordon, A. L., 1988, The Southern Ocean and Global Climate, Oceanus, **31**(2): 39-46.
Killworth, P. D., 1977, On "chimney" formations in the ocean, J. Phys. Oceanogr., **9**: 531-554.
Maykut, G. A., 1986, The surface heat and mass balance, in The geophysics of sea ice, N. Untersteiner (ed.), Plenum, New York, 395-463.
Melling, H. and Lewis, E. L., 1982. Shelf drainage flows in the Beaufoft Sea and their effect on the Arctic Ocean pycnocline, Deep Sea Res., Part A, **29**(8): 967-985.
Muench, R. D., 1971a. The physical oceanography of the northern Baffin Bay region, Scientific Report No. 1, Arctic Inst. N. Amer., Washington, D. C., 150 pp.
Muench, R. D., 1971b. Oceanographic conditions at a fixed location in western Kane Basin, May 1969, Oceanogr. Rep. CG 373-54, 1-5, U. S. Coast Guard, Washington, D. C.
Munk, W., 1966. Abyssal recipes, Deep-Sea Res. **13**, 707-730.
Riley, G. A., 1951. Oxygen, phosphate and nitrate in the Atlantic Ocean, Bull. Bingham Oceanog. Coll., **13**, 1-26.
Steffen, K., 1985. Warm water cells in the North Water, northern Baffin Bay during winter, J. Geophys. Res., **90**(C5): 9129-9136.
Steffen, K., 1986. Ice conditions of an Arctic polynya: North Water in winter, J. Glaciol., **32**: 383-390.
Steffen, K., and Lewis, J. E., 1988. Surface temperatures and sea-ice typing for northern Baffin Bay, Int. J. Remote Sens. **9**(3): 409-422.
Sverdrup, H. U., Johnson, M. W. and Fleming, R. H., 1942. The Oceans, Their Physics, Chemistry and General Biology, Prentice-Hall, Englewood Cliffs, N. J., 1087 pp.
Timofeyev, V. T.,1957, Atlanticheskiye vodi v arkticheskom basseine, Probl. Arkt., **2**: 41-51.
Top, Z., Clarke, W. B., Eismont, C. and Jones, E. P., 1980. Radiogenic helium in Baffin Bay Bottom Water, J. Mar. Res., **38**(3), 435-452.

This Page Intentionally Left Blank

OPEN OCEAN CONVECTION AND DEEP WATER FORMATION REVISITED IN THE MEDITERRANEAN, LABRADOR, GREENLAND AND WEDDELL SEAS

JEAN-CLAUDE GASCARD
Laboratoire d'Oceanographie Dynamique et de Climatologie, Université Pierre et Marie Curie, Tour 14, 2e, 4 Place Jussieu, 75252 Paris Cedex 05 (France)

ABSTRACT
A number of different scales of organization are believed to be important in the deep convection and deep water formation processes. Among them we clearly identify two scales: the so called chimney and the mesoscale eddies resulting from a baroclinic instability of the chimney. Based on past and recent observations in the Mediterranean, Greenland, Labrador and Weddell Seas, we are discussing the chimney-eddy structure in detail in each of these four distinct areas. Then we analyze the dynamics of this complex structure in order to infer its importance in the context of deep convection and deep water formation in the ocean. Some elements related to bottom topography are presented dealing with the preconditioning state of the chimney-eddy structure formation.

1 INTRODUCTION

The basic mechanism leading to the formation of oceanic deep and bottom waters is still an area of active research. The importance of this problem for the general understanding of the world ocean, its dynamics and thermodynamics, the general circulation as well as the thermohaline circulation, is recognized unanimously. The first international colloquium entirely dedicated to the problem of the formation of oceanic deep waters took place in Paris in October 1972 (CNRS, 1972). Three years before, the first international campaign was organized in the northwest Mediterranean Sea, the so called Medoc, to study the formation of the deep and bottom water of the western Mediterranean Sea. The Paris meeting took place in the middle of a series of six Medoc campaigns. Although many new and interesting aspects of the problem were presented and discussed in Paris, many more were to come in the following years. The last Medoc campaign occurred in 1975, followed shortly in 1976 and 1978 by two winter cruises in the central Labrador Sea.

In this paper, based on similarities and differences resulting from past and recent observations taken mainly in the Mediterranean and Labrador Seas but also in the Weddell and Greenland Seas, we will focus the discussion on two scales of organization: the so-called chimneys and

mesoscale eddies that had been observed in those regions during deep convection. These scales (mesoscale) can be presented under the generic name of baroclinic instability which appears more and more likely to play a central role in the whole process of deep convection and deep water formation in the world ocean. As a matter of fact, it is the only mechanism able to explain why deep convection is occurring in very restricted areas representing between 1/1000 and 1/100 of the total surface of the global ocean according to recent estimations (Gascard, 1990). This is indeed a very small surface considering that at least 3/4 of the total volume of the world ocean has to go through it, in order to renew deep waters during an entire geophysical cycle (approx. 1000 years) (Broecker and Peng, 1982).

In the following, we will present the facts which are relevant to the baroclinic instability and its role in the deep convection leading to the deep water formation in the frame of quasi-geostrophic and hydrostatic approximations. Small scale features characterized by very high vertical velocities (10 $cm.s^{-1}$), the highest ever measured in the deep ocean, will be left out of this discussion since, non-hydrostatic assumptions are more relevant in this case.

2 DEEP CONVECTION AND CHIMNEYS

The concept of the chimney was first introduced by the Medoc group (1970) to define an area where deep convection was very active, leading to the formation of well mixed waters from the surface to great depths and eventually down to the bottom as in the case of the Medoc area in the northwest Mediterranean Sea. Nothing was really specified at that time, from a dynamical point of view. The chimney was characterized by an hydrological structure made of very homogeneous waters embedded in more stratified waters.

Killworth (1976), in studying the mixing and spreading phases of the Medoc phenomenon, presented the chimney as a narrow and unstable region where intense vertical mixing occurred under atmospheric cooling acting on the surface. Most of the mixing was interpreted in terms of non-penetrative convection, and advection from the side was considered quite negligible. A (baroclinic) instability of the chimney would start as soon as the surface cooling would stop and then the instability would generate eddies during the following spreading phase. The early preconditioning phase was not taken into account in this first approach and the fact that deep convection was observed in very restricted areas, was not explained. Based on the whole series of Medoc experiments taken

from 1969 to 1975 and in particular, the last one, Medoc 1975, Gascard (1977,1978) demonstrated the importance of baroclinic instability not only during the final stage of the deep water formation (the sinking and spreading) but at any other instant including the preconditioning stage.

Following the discovery of a chimney in 1977 by Gordon (1978) in the Weddell Sea, Killworth (1979) paid more attention to the preconditioning phase than in his 1976 paper, in order to explain why the deep convective overturning was so localized in space. Indeed, he realized that an application of classical 2D mixing models to a real case study, like the Weddell Sea for instance, would trigger deep convection on a scale much bigger than reality. Then, he proposed that a baroclinic instability of the mean flow was occurring and that this large scale instability was generating eddies of the same width as the observed chimneys. The chimneys would develop in large cyclonic eddies preferentially, because cyclonic eddies are quite sensitive to the atmospheric surface cooling which tends to erode their upper stratification more efficiently and, consequently, weaken their stability more than anticyclonic eddies. In summary, eddies generated during the preconditioning phase by a large scale baroclinic instability of the mean flow, would contribute to the formation of chimneys later on, under the action of the atmospheric cooling. Ultimately, these chimneys, containing well mixed waters, will spread out under another baroclinic instability phenomenon occurring at a smaller scale, after the cooling had stopped at the surface. This small scale instability would also generate small scale eddies, smaller than the chimneys anyway.

The concepts of eddies and chimneys have been largely used in a rather confusing manner. At this stage, it is worth making an attempt to clarify the situation. We propose to re-examine the observations which are particularly relevant to this problem. Besides the Medoc chimneys observed from 1969 until 1975, and the 1977 Weddell chimney, other chimneys have been reported in the literature: in the Labrador Sea in 1976 by Clarke and Gascard (1983), (Gascard and Clarke, 1983), and more recently in 1989 in the Boreas Basin by Johannessen, et al. (1991). Let us examine them all successively.

2.1 *The 1969 Medoc Chimney*

The first chimney was observed in the northwest Mediterranean Sea during Medoc 1969 and was reported by several authors (Anati and Stommel, 1970), (Tchernia and Fieux, 1971) and J. Swallow (personal communication). During February 10-28, 1969, they observed the chimney

on three occasions from three different ships: RV Atlantis II; RV Jean Charcot; and RV Discovery II, respectively. On these occasions the chimney was observed approximately between the same latitudes 41°50N-42°10N, and along three different meridional sections: 5°E (Discovery II); 5°30E

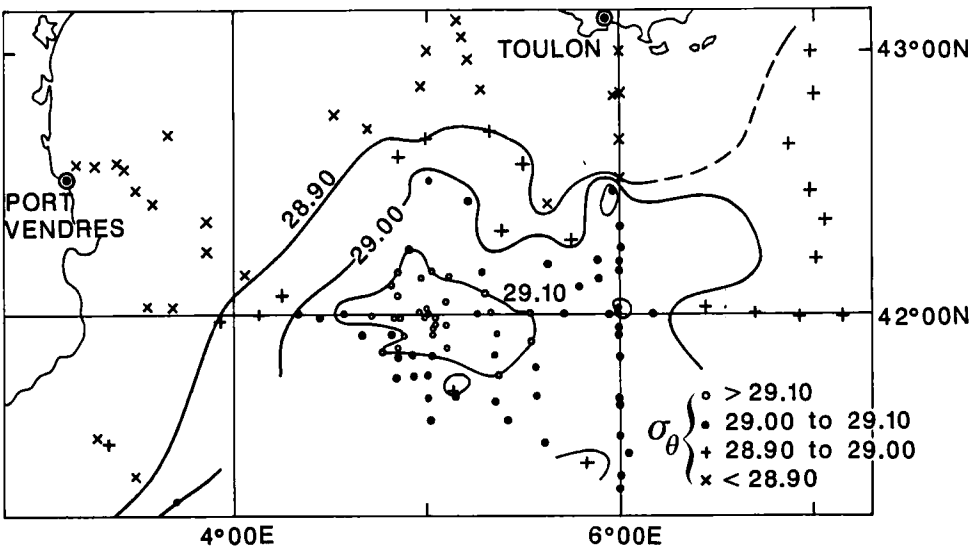

Fig. 1. Surface isopycnals (σ_θ) deduced from temperature and salinity measurements taken on February 10-28, 1969, during Medoc 69.

Atlantis II sections intersected the chimney near the center. The Jean Charcot section was already a little too far east. The chimney had a rather E-W elongated shape (Fig. 1). In the three cases the hydrological structure looked identical and was characterized by a very distinct breakthrough in the entire water column stratification. This was quite visible on all parameters: temperature, salinity, density, and oxygen. Figure 2 shows the vertical density structure along a meridional section. It is not obvious to map the size of the chimney precisely. This is strongly dependent on the parameter we select. The potential density ρ_θ of the northwest Mediterranean bottom water is typically 1.02911-1.02912; we arbitrarily chose 1.02910 as the surface density characteristic of the chimney at least during the final stage (i.e. at the time there is a complete breakthrough in the entire water column stratification). Accordingly, one can estimate the size of the Medoc chimney at about 20 miles in the

north-south direction (Figures 1 and 2). The corresponding values for temperature and salinity are within the range 12.85°C-12.90°C and 38.42-38.45 psu respectively, and the vertical gradient of potential density estimated over H = 2000m of water is $5.10^{-9}m^{-1}$, from which we can deduce an internal radius of deformation R_d of approximately 4.5km (Table 1). This is quite close to the critical gradient of $1.10^{-9}\ m^{-1}$, obtained when R_d = H, that is for N = f (N, Brunt-Vaisala frequency, and f is the Coriolis parameter).

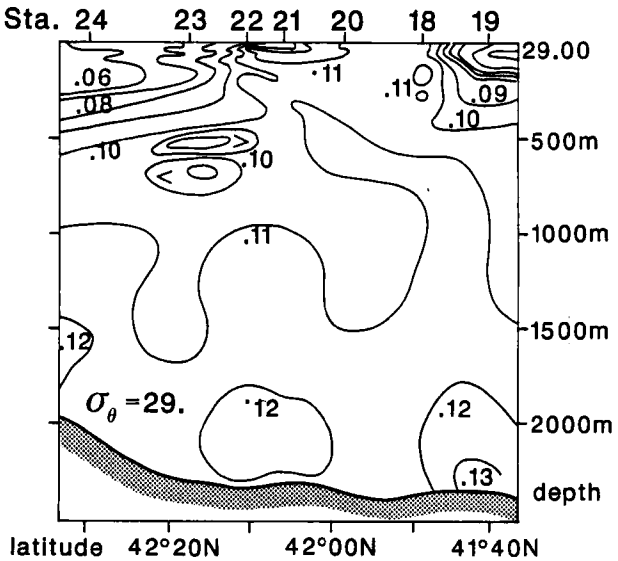

Fig. 2. North-South vertical section of density (σ_θ) taken on February 10,1969, along 5°30E during Medoc 69.

The 4.5km internal radius of deformation was significantly smaller than the size of the chimney. Also, one could say that the three observations of the chimney made successively during February 1969 in the Medoc area, tended to prove that the size of the chimney was fairly stable during this whole period. It did not move nor did it grow significantly. It was also interesting to observe the hydrological situation within the same area, before the chimney appeared fully developed, i.e. during the preconditioning stage. An hydrological meridional section on 5°10E (Fig. 3) was taken from the Atlantis II by Anati and Stommel on February 1, 1969

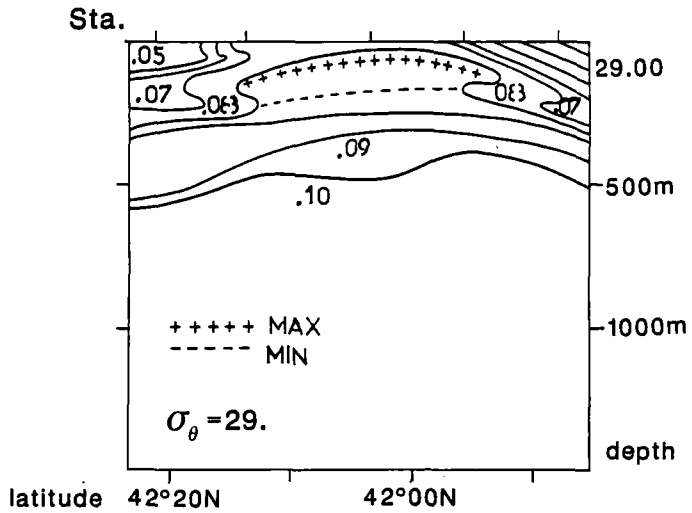

Fig. 3. North-South vertical section of density (σ_θ) taken on February 1, 1969, along 5°10E during Medoc 69.

(1970). In this section, one could already see a perturbation of the isopycnals between 1.02895 and 1.02910 from the surface down to 500m at least, and extending over 20 miles in latitude from 41°55N-42°15N, i.e. at about the same location the chimney was observed 10 days later. So it is important to note that the size and the location of the chimney remained constant from the preconditioning phase until the homogenisation phase.

2.2 *The 1976 Labrador Sea Chimney*

The chimney identified by Clarke and Gascard (Clarke and Gascard, 1983) (Gascard and Clarke, 1983) in the central Labrador Sea at about 57°N and 54°W, in March 1976, is one of the best examples of a deep convective chimney ever observed, both from an hydrological and kinematical point of view. As a result, we will refer to it extensively in the following. It was described as a circular pool 50-60km in diameter, composed of cold (T=2.90°C) and relatively fresh (S=34.84 psu) very homogeneous water (the new 1976 vintage Labrador Sea Deep Water, LSDW) extending from the surface down to a 2200m depth and surrounded

by slightly lighter and stratified waters. Underneath, one could find the North Atlantic Deep Water (NADW) much denser than the LSDW and extending down to the bottom located at about 3300-3400m in this region. A remarkable fact was that, underneath the Labrador chimney, the NADW was found at a 2200m depth, while elsewhere it was found at about a 1500m depth. As we will see in the next chapter, this explains why horizontal circulation (including eddies), observed inside the Labrador chimney, was anticyclonic.

Eddies observed inside the chimney and having a radius ($\approx$10km) close to the internal Rossby radius of deformation (7.5km), computed from the vertical stratification inside the chimney (Table 1), were interpreted by Gascard and Clarke (1983) as resulting from a baroclinic instability of the chimney itself, and in a way similar to what Saunders (1973) observed in an experiment he performed in a tank on a rotating table. The instability of the chimney, when it occurred, was able to incorporate into the "melting pot" not only some of the lighter stratified waters found outside the chimney in the upper layer, as in the case of the Mediterranean Sea, but also some of the NADW found down below and across the main pycnocline to form the new LSDW. At this point it is important to note that the 50-60km chimney is a much bigger structure than the 15-20km mesoscale eddies embedded within it.

2.3 *The 1977 Weddell Sea Chimney*

In February 1977, Gordon (1978) discovered a chimney in the central Weddell Sea, west of Maud Rise. The chimney was described as a cyclonic eddy with a 14km radius, made of cold and low saline water extending down to a 4000m depth. Surface currents reached 1 knot within the eddy with a corresponding two days period by revolution. The internal Rossby radius of deformation was estimated at about 11km (Table 1), slightly less than the eddy radius but, due to uncertainty, both were considered to be of the same scale. This is quite comparable to the Labrador 76 eddy with a 9-10km radius related to a 7.5km internal radius of deformation. But this Weddell feature cannot be at all compared to the 50-60km diameter Labrador chimney. In fact, we believe that Gordon's observation only corresponds to an eddy feature rather than a chimney. As for the Labrador 1976 eddy, it is quite probable that this Weddell eddy was embedded in a much larger structure, a chimney, that Gordon had not observed due to lack of time. Bear in mind that it took 10 days for Clarke and Gascard in 1976, to observe the eddy-chimney feature in the Labrador Sea, compared with the 12 hours for Gordon in 1977 to observe the

Weddell sea eddy. According to Gordon (1978), it is quite interesting to note that Foldvik observed a similar feature (if not the same one) 30 nautical miles southwest of where it was observed by Gordon two weeks earlier. This is once again, strikingly comparable with the situation described by Gascard and Clarke (1983) for the Labrador Sea where they observed in 1976, an eddy 20 nautical miles northeast of its position a week earlier. In this last case, it has been proven that eddies remained embedded in the same chimney structure for the entire time.

Based on these facts, one can estimate that the 1977 Weddell chimney could have been approximately 40 nautical miles in diameter, significantly bigger than the 1976 Labrador chimney (30 miles in diameter) and even twice as big as the 1969 Medoc chimney (20 miles in diameter). In these three cases, the chimney radius was approximately three times bigger than the internal radius of deformation typical of the interior structure of the chimney: 11km, 7.5km and 5km respectively (Table 1).

TABLE 1

Chimney characteristics observed in 4 different deep ocean convection regions

	MEDITERRANEAN SEA (MEDOC)			LABRADOR SEA			GREENLAND SEA (BOREAS)			WEDDELL SEA		
TIME	February 1969			March 1976			March 1989			February 1977		
Latitude	42°N			57°N			78°18N			67°S		
Longitude	5°E			54°W			0°40E			7°40W		
f (10^{-4})	1 s^{-1}			1.22 s^{-1}			1.43 s^{-1}			1.33 s^{-1}		
Depth	θ	S	σ_θ	θ	S	σ_θ	θ	S	σ_θ	θ	S	σ_θ
0	12.90	38.45	29.10	2.91	34.83	27.78	-0.41	34.91	28.05	-0.2	34.66	27.87
1000	12.80	38.43	29.11	2.90	38.84	27.79	-0.88	34.89	28.06	-0.3	34.66	27.88
									37.43*			37.22*
2000	12.70	38.42	29.12	2.89	34.84	27.79	-1.07	34.89	37.45*	-0.4	34.66	37.23*
3000				2.0	34.92	27.93	-1.19	34.90	37.46*	-0.5	34.66	37.24*
Mixed Layer Depth	2000m			2200m			500m			4000m		
Bottom	2500m			3500m			3000m			5000m		
N(s^{-1})	2 10^{-4}			2.6 10^{-4}			4.2 10^{-4}			3.8 10^{-4}		
Rd	4.5 km			7.5km			9km			11km		

* σ_{2000}

This seems to be a fairly typical condition for a chimney to be baroclinically unstable and consequently to generate eddies with a radius equal to or close to the internal radius of deformation. According to Saunders' experiment (1973), one could predict between 3 and 4 eddies in these conditions (Gascard and Clarke, 1983).

2.4 *The 1989 Greenland Sea Chimney*

(Johannessen, et al., in press) recently described deep and homogenous hydrological structures approximately 10 miles in diameter, observed in the Boreas Basin of the northern Greenland Sea in March 1989. These structures separated by about 20-30 miles were characterised by a potential density, sigma-theta 28.056, constant from the surface to a 500m depth and then increasing to 28.077 at a depth of 2800m near the bottom. One could estimate the internal radius of deformation (approx. 9km), from a vertical potential density gradient of 8.10^{-9} m^{-1} (Table 1).

Again, this closely resembled the situation observed in the Labrador Sea and Weddell Sea. Once more, one could admit that the chimney-eddy features identified by Johannessen, et al. (1991) were more likely to be eddies resulting from the instability of a chimney, and that these Boreas eddies could have very well been embedded in a larger chimney-like structure comparable in size to the Labrador chimney.

3 DEEP CONVECTION AND MESOSCALE EDDIES

Obviously, both the Weddell and the Greenland Sea chimneys need further investigation to confirm our hypothesis. A big issue is to understand how these chimneys had been initialized in the first place. Is it as Killworth (1979) suggested that they result from a large scale baroclinic instability of the mean flow? Are chimneys large scale unstable eddies (large compared with the internal radius of deformation in the deep convective areas)? Consequently, there would be two very distinct scales of instability. This is still a matter of speculation and we will return to this very important subject in Section 7. Before then, we would like to more carefully examine the eddy structures embedded within the chimney structure in the case of the Mediterranean and Labrador Seas in particular, in order to understand how they can be related to each other.

3.1 *The 1975 Medoc Eddy*

During the last Medoc experiment in 1975 (Gascard, 1978), an eddy-like feature was observed nearby a frontal region separating

well-mixed from stratified waters. This is the best example of an eddy ever observed, directly related to a deep convection event. We believe that this kind of eddy is really important for the general understanding of the complex phenomenon associated with deep convection. In particular, one wants, first to understand its meaning in the whole process and within the context of the baroclinic instability theory and, second to define its role within the deep mixing processes. For that it is necessary to describe this kind of eddy very precisely and to analyze its dynamics carefully.

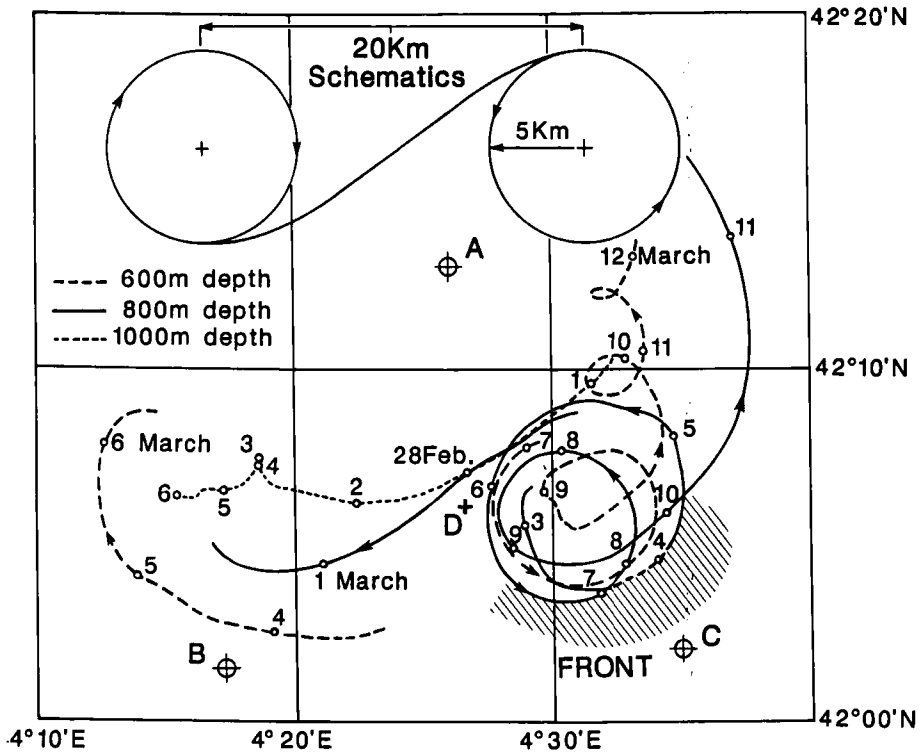

Fig. 4. Horizontal trajectories of floats drifting at depths of 600m, 800m and 1000m from February 28 until March 12, 1975, during Medoc 75. A, B and C are moored radioacoustic buoys for float positioning. D represents a currentmeters mooring.

Figure 4 represents the Medoc 75 eddy. This observation was made by tracking acoustically neutrally buoyant floats drifting at mid depths in about 2400m of water. Being neutrally buoyant and because they are less compressible than sea water, the floats followed isobars in a first

approximation. The three floats in Figure 4 were drifting at a 600m, 800m and 1000m depth respectively, within a quiescent barotropic layer located just underneath an upper baroclinic layer in the first 100m. With a good approximation, one can assume the shear was negligible between 600m and 1000m, as shown in Figure 5.

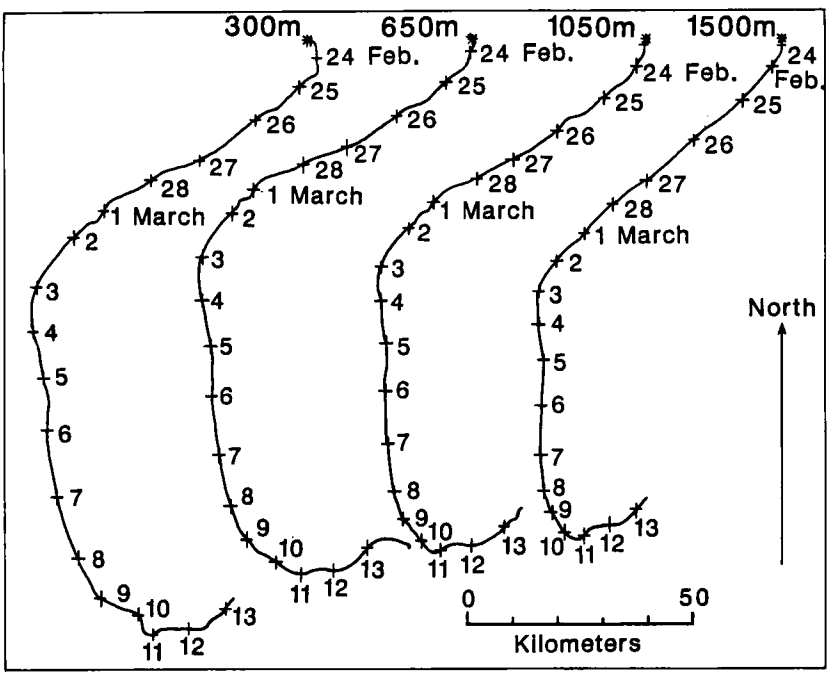

Fig. 5. Progressive vector diagrams computed from horizontal currents measured at depths of 300m, 650m, 1050m and 1500m respectively, from February 22 until March 13, 1975, at D (Fig. 4).

Consequently, each float could be considered a good indicator of fluid trajectories not only at its own level but also at the two other float levels. Let us then group the floats by pairs, ignoring their depths. From each pair, one can virtually define a vector joining two floats at the same instant. In the following, we will only consider the horizontal projection of this vector. Each horizontal vector can then be defined by its orientation $\propto$ (relative to any arbitrary references) and its length L. Figures 6a and 6b represent variations of L and $\propto$ as a function of time for two pairs of floats (600m and 800m; 800m and 1000m).

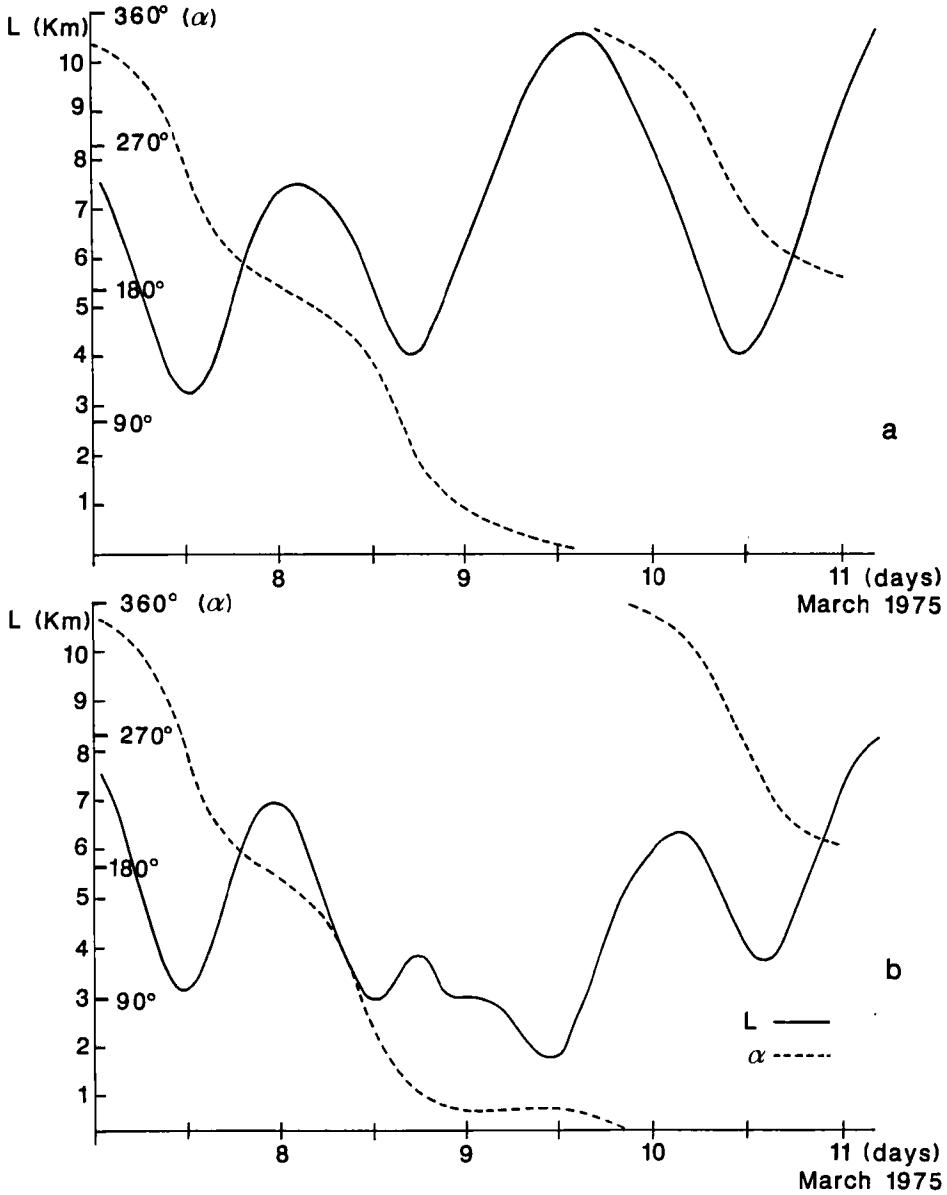

Fig. 6 Horizontal separation L and course $\propto$ between floats drifting from March 7 until March 10, 1975 (Fig. 4).

a. 800m and 1000m floats - b. 600m and 800m floats.

From this representation, one can precisely determine the main characteristics of the Medoc eddy (Jeannin, 1980). Its period of rotation is typically 2.5 days and the maximum horizontal distance L (approx. 10 km) is, in a good approximation, equivalent to its diameter.

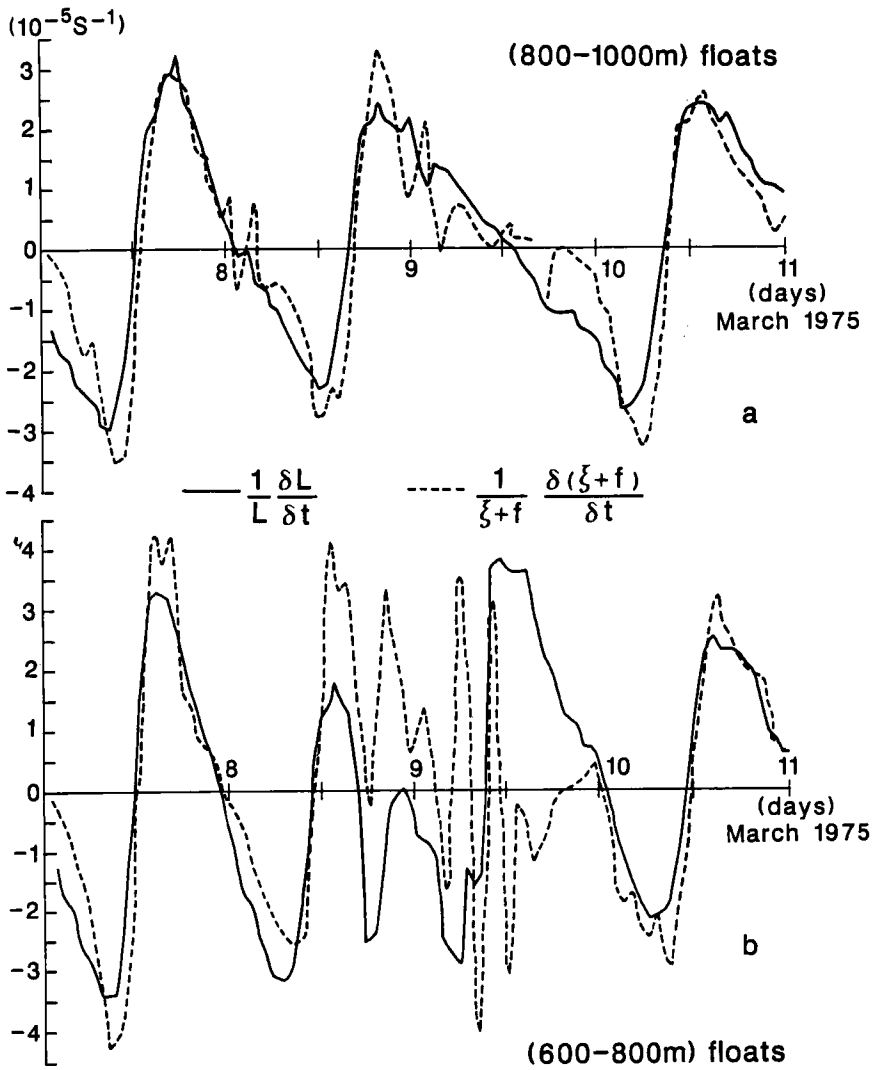

Fig. 7 First order derivatives $\partial L/\partial t$ and $\partial(\zeta+f)/\partial t$ calculated from floats separation L and course $\propto$ (Fig. 6), for the period March 7-10, 1975.

a. 800m and 1000m floats - b. 600m and 800m floats.

It is also important to note that the radius of this eddy is close to the internal Rossby radius of deformation which we estimated to be about 4.5km.

Next, one can proceed to a dynamical study of the Medoc 75 eddy by computing the first time derivative of L and the second time derivative of $\propto$. In a solid body rotation, the first time derivative of $\propto$ represents exactly the relative vorticity ζ divided by 2. Consequently, in our calculation we will estimate the relative vorticity within the eddy as the first time derivative of $\propto$ multiplied by 2. The factor 2 comes from the fact that the relative vorticity is the sum of the shear vorticity and of the curvature vorticity. Figure 7 shows a striking similarity between these first $\partial L/\partial t$ and second derivatives $\partial^2 \propto / \partial t^2$ computed for the Medoc 75 eddy, both scaled by L and by the absolute vorticity $(\zeta+f)$, respectively. As demonstrated in the case of the Labrador Sea (Gascard and Clarke, 1983), this resemblance comes from a balance between the vorticity term and the divergence term :

$$\frac{\partial}{\partial t}(\zeta + f) = - (\zeta + f) \nabla.V$$

This balance validates the quasi-geostrophic approximation used in the next section to calculate the proper unstable wave solutions from the vorticity equation for a two-layer fluid which represents to a good approximation, the Medoc and the Labrador Sea structures.

3.2 *The 1976 Labrador Eddy*

The same type of analysis applied to the study of the Labrador 76 eddy gave the following results (Gascard and Clarke, 1983) : a three day rotation period and a diameter of approximately 18km, so it was significantly bigger than the Medoc eddy. The internal Rossby radius of deformation was also significantly bigger than the Medoc one. For the first baroclinic mode, it was estimated to be 7.5km, according to (Gascard and Clarke, 1983). This corresponds to a more pronounced stratification which was mainly due to the presence of a strong deep pycnocline situated at about a 1500m depth in the central Labrador Sea and which separated the upper well mixed deep convective layer from the lower stratified North Atlantic deep water. Both layer thicknesses are approximately equal to 1500m. This situation cannot exist in the Mediterranean Sea where deep convection can extend all the way from the surface down to the bottom.

In the central Labrador Sea, this deep pycnocline underneath the well mixed layer, where deep convection did occur, also explains why the Labrador eddy rotation was anticyclonic instead of cyclonic as in the Medoc eddy. The main pycnocline, found at a 1500m depth away from the eddy, was found at a 2200m depth just underneath the eddy, i.e., 700m deeper than its average depth! So, although the geostrophic velocity relative to the surface was slightly cyclonic within the upper layer, (because upper layer waters inside the eddy were still slightly heavier than surrounding waters), there was a strong reversal between 1500m and 2200m producing a strong anticyclonic geostrophic circulation decreasing slowly up to the surface. Consequently, the strong anticyclonic geostrophic circulation generated at depth is still overwhelming the slight upper layer cyclonic circulation at the surface. Although the Labrador Sea situation was much more complicated than the Medoc one, it gave us the opportunity to test the validity of the wave solutions given by the same analytical model for two different situations, as described in the next chapter.

4 DEEP CONVECTION AND BAROCLINIC INSTABILITY

Having justified the quasi-geostrophic approximation, we can apply it analytically to find wave-like solutions to the vorticity equation for two-layer models adapted to the Medoc and Labrador chimneys respectively. These models, similar to one proposed by Tang (1975), for instance, usually provide analytical solutions in terms of unstable waves which can be interpreted as resulting from a baroclinic instability theory. Characteristics of these waves (wavelength, phase speed, and growth rate) correspond to most of the observed features associated with the Medoc 75 eddy as well as the Labrador 76 eddy. The success of this analytical model is a direct consequence of the validity of the quasi-geostrophic approximation applied to the Medoc and Labrador situations. The models used, gave the following important results :

- The nondimensional wavenumber of the most unstable wave appeared to be close to 1 in the Medoc case and close to 1.2 in the Labrador case. This is nondimensionalized relative to the internal radius of deformation. That means that the wavelength of the most unstable wave would be 2π times the internal radius of deformation and that would correspond to about 30km for the Medoc case, 50km for the Labrador case, 60km for the Greenland Sea and 70km for the Weddell case. The proper features associated with this phenomenon are particularly difficult to observe simply because they correspond to an unsteady state. How can we compare

these model results with observations? At an early stage of the instability, the undulating trajectory of a float drifting at an 800m depth (Fig. 8), was the best manifestation of the growing unstable wave and that gave a clear indication of its scale.

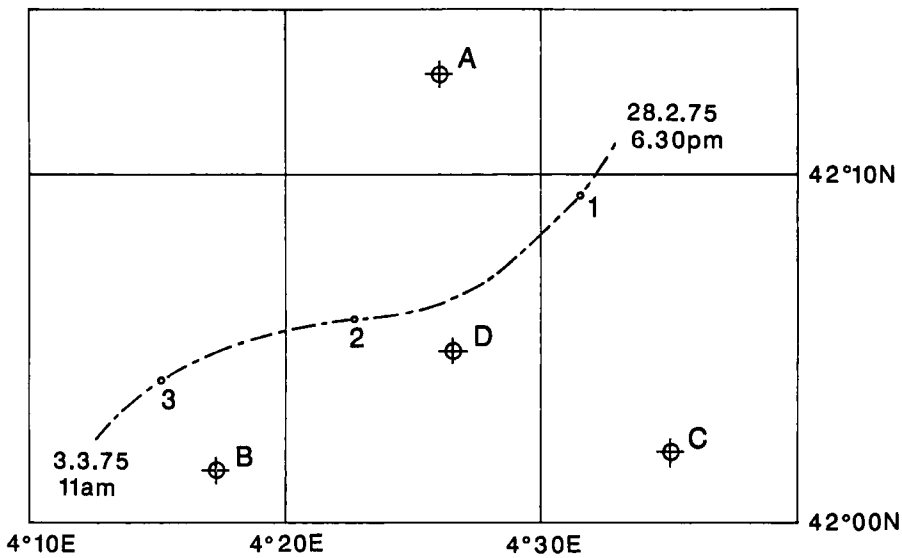

Fig. 8. Horizontal trajectory of a float drifting at an 800m depth from February 28 to March 3, 1975, during Medoc 75.

At a later stage this kind of instability will give rise to a fully developed eddy (like the Medoc 75 eddy). Then, one can also estimate the wavelength of the unstable wave from the distance which separates eddy centers.

Another strong validation of the baroclinic instability theory and of its applicability to the Medoc and Labrador chimneys, is provided by the calculation of the phase speed of the most unstable wave. In the Medoc case, the waves traveled at about 6cm/s in theory, four times slower than in the Labrador case. In each case the results of the calculation are in fairly good agreement with the observations. The phase speed can be deduced from the translation speed of the eddies which moved along the front inside the unstable chimney feature characterized by well mixed waters.

A very important issue is to understand the coupling between eddies and chimneys and in particular, of all the mesoscale structures identified during a deep convective event. Of upmost importance is the size of the chimneys compared to the size of the eddies versus the internal radius of deformation. Johannessen et al. (1991), following Killworth (1979), describes chimney-like features characterized by scales smaller than mesoscale eddies. According to these authors, eddies would be the preconditioning phase for chimneys. Are they considering the same type of eddies as the ones we clearly identified in the Mediterranean and Labrador Seas? Are there different types of eddies involved in deep convection resulting from different scales of instability?

5 DEEP CONVECTION AND TOPOGRAPHIC EFFECTS

A very instructive point, in the case of the Labrador Sea, was the discovery in March 1976, by Allen (1979) of topographic Rossby waves generated within the continental slope region, propagating offshore and interacting with the chimney-eddy structure observed in the central Labrador Sea at the same time. They were described as waves of eight to ten day periods and with a 12cm/s amplitude, superimposed on a mean current of about the same magnitude. They were mainly barotropic but they could interact with the upper stratification. Gascard and Clarke (1983) noted that the last waves packet, among three observed in March 1976, reached the Labrador 76 Chimney exactly at the same time the three floats moved anticyclonically at 25cm/s inside the chimney and along its periphery. We previously mentioned that the two layer quasi-geostrophic baroclinic instability model adapted to the Labrador Sea chimney conditions by Gascard and Clarke (1983), allowed them to calculate a phase speed for the most unstable wave in very good agreement with the float speeds. Is the time and space correlation between Allen's topographic waves propagating offshore and floats propagating offshore inside the 1976 Labrador Sea chimney pure coincidence?

More recently, the same kind of waves have been observed by Millot (1985) in the northwest Mediterranean Sea along the continental shelf in winter. Like Allen waves, they have approximately the same period (eight days) and are also interpreted as topographic Rossby waves generated in the vicinity of the continental slope and propagating offshore. Up until now we have not been able to establish any link between these waves and the baroclinic instabilities observed in the Medoc deep convective region. However, the question of unstable baroclinic features like a chimney having a typical dimension of 2π times the internal radius of deformation

generated by topographic Rossby waves and having a period of eight days and an amplitude of 10-20cm/s should now be addressed quite seriously. There is a strong need, however, to get more information about the characteristics of these waves and their mode of propagation and interaction with a baroclinic field.

(Hogg, 1973) was the first to address the question of convection and deep water formation related to a topographic effect. His study concerned the Medoc region in the vicinity of the Deep Sea Rhone fan. The nature (and the solution) to Hogg's problem was conceived in the context of a Taylor column which meant that the preconditioning to trigger a deep convection was inevitably related to the presence of a topographic feature at the same place the convection was going to happen. Although this condition seemed to be partly fulfilled in the Medoc case, it was not in the Labrador case since deep convection was observed in the central Labrador Sea over a flat bottom and far away from any kind of peculiar topographic features.

It is interesting to mention several cases where bottom topography had been suggested as a preconditioning element to deep convection. Gordon (1978), for instance, mentioned a probable relationship between Maud Rise and the presence of open ocean convection observed in the Weddell Sea west of Maud Rise. Martinson et al. (1981) also mentioned that topographical features may quantitatively affect both the movement and occurence of the Weddell polynia, constituting one of the largest area of deep ocean convection. Recently, Johannessen et al. (1991) discovered the presence of a chimney-eddy like feature in the Boreas Basin in the vicinity of the Hovgaard Fracture zone. So it looks like bottom topography might play a remote role as well as having a direct local effect.

What is quite puzzling, is the fact that a model such as the one developed by Madec (1990) even with no topography, is able to generate the 40km unstable wavelength we observed in the Medoc area! Obviously, these important questions need further investigation both from a theoretical and observational point of view.

6 VERTICAL MOTIONS AND DEEP CONVECTION

Being equipped with vanes which forced them to rotate about their vertical axes, the neutrally buoyant floats used during Medoc and Labrador cruises could detect the vertical component of the velocity as they were drifting horizontally.

Unfortunately, none of the floats (VCM) used during the Medoc 75 experiment were recovered and the information concerning the vertical velocities measured in situ and recorded internally in each float, has been

lost. However, such measurements were obtained by (Voorhis and Webb, 1970) as early as Medoc 69 but without any accurate fixing of the floats at the same time. What did these measurements reveal? First of all, they showed that vertical velocities in an area where deep water was forming, were covering a very broad spectrum from a few hours and vertical speeds up to $10cm.s^{-1}$, to quasi-steady motions with a vertical speed of $1\text{-}2mm.s^{-1}$. This was confirmed by similar measurements obtained in the Labrador Sea in 1976 (Gascard and Clarke, 1983). It is quite obvious that only the quasi steady slow vertical motions can be related to a baroclinic instability process, at least within the context of the theory we have used and considering the quasi-geostrophy and hydrostatic approximations we made a priori. Still, the relationship between the quasi steady slow vertical motions and the baroclinic instability has to be explained. We know from the theory that this instability process converts potential energy into kinetic energy by moving particles across a frontal system within a so called "wedge of instability". The wedge of instability is defined by the slope γ (Fig. 9) of the isopycnals above the horizontal and across the front. In fact, the "wedge" is the region located within γ and only particles moving into this region convert potential into kinetic energy.

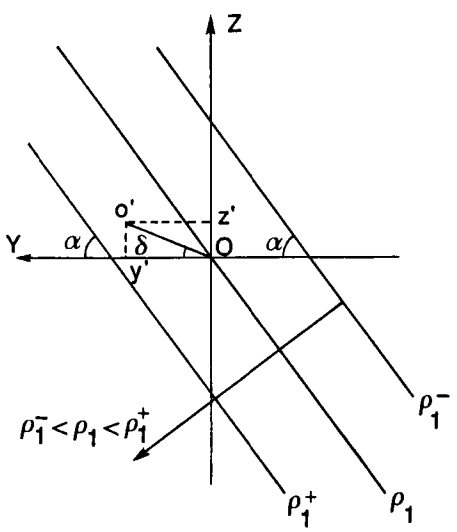

Fig. 9. Vertical density section across a frontal structure (idealized situation) showing baroclinic unstable motions at an angle δ within a wedge of instability γ .

Let us suppose that one of these particles of density ρ_1 is displaced from O to O' within time dt. The density perturbation in O' is then

$$\rho' = - y' \frac{\partial \rho(y)}{\partial y} - z' \frac{\partial \rho_0(z)}{\partial z}$$

with

$$v' = \frac{dy'}{dt}, \quad w' = \frac{dz'}{dt}, \quad \frac{w'}{v'} = \frac{z'}{y'} = \delta$$

$$\rho' = - y' \frac{\partial \rho(y)}{\partial y} - y'\delta \frac{\partial \rho_0(z)}{\partial z}$$

$$\rho' = y' (\gamma - \delta) \frac{\partial \rho_0(z)}{\partial z}$$

$$\rho' w' = y' \frac{dy'}{dt} (\delta\gamma - \delta^2) \frac{\partial \rho_0(z)}{\partial z}$$

Considering v' constant, the maximum value for $\rho'w'$ is achieved when

$$\frac{\partial(\rho'w')}{\partial\delta} = (\gamma - 2\delta)y'\frac{dy'}{dt}.\frac{\partial \rho_0(z)}{\partial z} = 0$$

that is for

$$\delta = \frac{\gamma}{2}$$

Usually, the slope of the isopycnals across the front which separates well mixed and dense waters from lighter stratified waters is of the order of 1%. For particles moving typically at horizontal speeds of v' = 10 to 20cm.s^{-1} at an angle δ above the horizontal for an optimal conversion of potential into kinetic energy, w' is 0.5-1mm.s^{-1}. So we believe that the steady vertical speeds within the range of a fraction of a mm.s^{-1} to a few

$mm.s^{-1}$ detected by the VCM resulted from a baroclinic instability mechanism. Of course, such vertical speeds should be detected upwards and downwards as well. Up until now, we do not have enough information on that matter to draw reliable conclusions. It would be very valuable in the near future to have much more data about vertical motion measured by the VCM in a convective region.

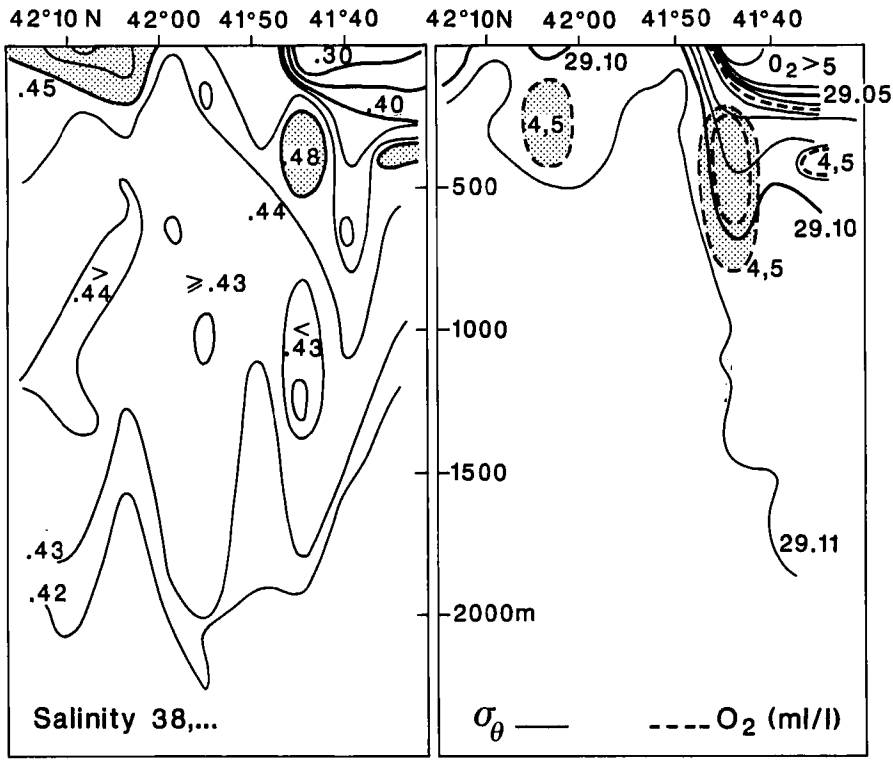

Fig. 10. North-South vertical sections of salinity, density σ_θ and oxygen taken on February 25-28, 1969, along 5°E during Medoc 69.

Hydrological sections across frontal regions can also provide valuable information. In Figure 10 we are presenting such a section taken during Medoc 69 (February 25-28, 1969) by the Discovery which shows quite clearly the upwards motion of the so called intermediate water, warm and salty, across a frontal region. The intermediate water (of Levantine origin) can be followed from its nominal depth at about 300m (T=13.08°C, S=38.48) in the stratified region, up to the surface in the well mixed

region where this water still conserved its almost original T,S characteristics (T=12.95°C, S=38.47). In fact, the salinity remained unchanged in this instance. It had not yet been affected; only the temperature is already decreasing because of the exchanges with the atmosphere. Assuming this intermediate water moved in a straight line across this section, it would correspond to an upward motion at an angle of about 300m/20 miles, i.e. 1/120, the core being 300m deep at about 41°45N and on the surface at about 42°05N. In fact, there is no reason to believe that this water was moving along in this particular section. More than likely, there is good reason to believe that it was circulating around an eddy (similar to the Medoc 75 eddy) centered at 41°55N between stations 13 and 14 as indicated by the trajectories of some floats drifting at a depth of 500m at the same time the section was taken. The implication is that the distance the intermediate water traveled along a spiral to reach the surface from its initial depth located at 300m, had been multiplied by 3. Consequently, the slope of its ascending motion has been divided by 3, i.e. instead of 1/120 it is more like 3/1000. Still, the corresponding vertical velocity relative to an horizontal speed of 20cm/s, is 0.6mm/s. This fact is essential to understand the role of the baroclinic instability in the complex process of the deep water formation in the ocean.

7 DISCUSSION AND CONCLUSION

The formation of a chimney is the basic problem in understanding the oceanic deep convection process and, consequently, the formation of deep waters. If we were able to describe how this formation does occur, then we could predict where and when it would happen. The question, "*How is a chimney formed?*"", is not yet easy to answer. "*How is a chimney preconditioned?* ", is an even harder question.

Chimney Formation

Based on all observations made about chimneys one can say that they only appear at places where the overall stratification can be destabilized and destroyed from the interior rather than from the surface. This gives also the basic explanation for the limited extent over which deep convection and consequently deep water formation is actually observed. The vertical mixing by turbulent entrainment triggered from the surface, is a very inefficient mechanism for mixing water over great depth. A much more efficient way, as we observed it, is when a subsurface layer (an intermediate water, warm and salty), is injected from below into the

surface layer by a baroclinic instability process. We observed that this injection did occur across a frontal system where and when it becomes baroclinically unstable, that is where and when isopycnals outcrop to the surface at a fairly steep angle. The frontal system separates stratified waters on one side to weakly stratified waters on the other side of the front.

The baroclinic instability of the frontal system has a tendency to weaken the steepness of the front in transferring stratified waters from one side of the front into the weakly stratified region of the other side. The first direct consequence is to restabilize the whole frontal system. But this system cannot stay in equilibrium since the warm and salty intermediate water (stratified water) is now exposed at the surface to the atmospheric forcing (cooling and evaporation). Quite rapidly this intermediate water will lose heat and gain salt and consequently will become quite dense. This increase in density occurring at the surface, will intensify the vertical mixing and will build up a new unstable frontal system with dense homogeneous waters and lighter stratified waters located side by side. In fact, by the time the intermediate water reaches the surface, it is already mixing up with the surface water, colder and fresher. So both waters are participating in the formation of the deep dense patch which will ultimately represent a chimney-like feature. How can we generate initially a frontal system which will precondition a region to become a chimney at a later time?

Chimney Preconditioning

Such a frontal system could be produced by a large scale baroclinic instability of a large scale gyre or a boundary current. The instability could be triggered by an interaction with bottom topography either locally or remotely. Such an instability will produce a perturbation of the general circulation pattern. This could be an eddy feature or a Rossby wave (topographic Rossby wave), scaled by the internal radius of deformation proper to the general circulation or a slope parameter in case of a topographic influence. Then this perturbation will interact with a baroclinic structure containing warm and salty water at an intermediate depth and will start to build up a front. The intermediate water is the basic potential ingredient we need to form a chimney as described earlier.

Although this scenario is supported by observations taken in all regions of deep water formation this is still a very critical area under active research. At this stage one must admit there is still too much speculation and preconditioning in the chimney formation needs much more

work.

Chimney Decay

The mesoscale eddies observed in a chimney (eddy radius equal or close to the internal radius of deformation), such as the 1975 Medoc or 1976 Labrador eddies, are only a manifestation of a baroclinic instability of a chimney, leading consequently to a break-up of the chimney. They coincide with the active sinking and spreading phase of the newly formed deep water. Most of the eddies reported in regions where deep convection did occur, belonged to this category. We believe that the 1977 Weddell Sea eddy observed by Gordon (and by Foldvik) also enter into this category. We have collected a great deal of information about these eddies as they are the easiest part to observe in the entire process. The main reason is that, being stable, they are much easier to observe than those having a large scale compared to the internal radius of deformation and which correspond to an unstable situation.

REFERENCES

Allen, A. A., 1979. Current variability at the offshore edge of the Labrador current, Master of Science Thesis, Dalhousie.

Anati, D. and Stommel, H., 1970. The initial phase of deep water formation in the northwest Mediterranean Sea, during MEDOC 69, on the basis of observations made by "Atlantis II" (January 25-February 12, 1969). Cah. Océanogr. 22(4): 343-351.

Broecker, W. S. and Peng, T.-H., 1982. Tracers in the Sea., L.-D. G. Observatory, Palisades, New York, Eldigio Press, 690 pp.

Clarke, A. R. and Gascard, J.-C., 1983. The Formation of Labrador Sea Water. Part I: Large-Scale Processes. J. Phys. Oceanogr. 13(10): 1764-1778.

CNRS, 1972. Processus de formation des eaux océaniques profondes en particulier en Méditerranée Occidentale, La formation des Eaux Océaniques Profondes, Paris, CNRS, 215: 278.

Gascard, J.-C., 1977. Quelques elements de la dynamique de formation des eaux profondes mediterraneennes., Phd. Thesis, Paris 6.

Gascard, J.-C., 1978. Mediterranean deep water formation, baroclinic instability and oceanic eddies. Oceanologica Acta 1(3): 315-330.

Gascard, J.-C. and Clarke, A. R., 1983. The Formation of Labrador Sea Water. Part II: Mesoscale and Smaller-Scale Processes. J. Phys. Oceanogr. 13(10): 1779-1797.

Gascard, J. C., 1990. Deep Convection and Deep Water Formation: Progress and Directions. EOS 71(49): 1837-1839.

Gordon, A. L., 1978. Deep Antarctic Convection West of Maud Rise. J. Phys. Oceanogr. 8(4): 600-612.

Hogg, N. G., 1973. The preconditioning phase of MEDOC 1969-II. Topographic effects. Deep-Sea Res. 20(449-459).

Jeannin, P. F., 1980. Structure de tourbillons océaniques associés à l'instabilité barocline au cours de la formation des eaux profondes, Master Thesis, Université PARIS 6.

Johannessen, O. M., Sandven, S. and Johannessen, J.A., 1991. Eddy-related winter convection in the Boreas basin. In: J.-C. Gascard and P.-C. Chu, Deep Convection and Deep Water Formation in the Ocean, Elsevier. E. O. Series (in press).

Killworth, P. D., 1976. The mixing and spreading phases of Medoc. Prog. Oceanog. 7(59-90).

Killworth, P. D., 1979. On "Chimney" formations in the ocean. J. Phys. Oceanogr. 9(3):531-554.

Madec, G., 1990. La formation d'eau profonde et son impact sur la circulation regionale en Méditerranée Occidentale: Une approche numérique., Phd. Thesis, Paris.

Martinson, D. G., Killworth, P.D. and Gordon, A.L., 1981. A convective model for the Weddell Polynia. J. Phys. Oceanogr. 11(4): 466-488.

Medoc Group, 1970. Observation of formation of deep water in the Mediterranean sea. Nature 227(5262): 1037-1040.

Millot, C., 1985. Evidence of a Several-Day Propagating Wave. J. Phys. Oceanogr. 15(3): 258-272.

Saunders, P., 1973. The instability of a baroclinic vortex. J. Phys. Oceanogr. 3(1): 61-65.

Tang, C. M., 1975. Baroclinic instability of stratified shear flows in the Ocean and Atmosphere. J. Geophys. Res. 80(9): 1168-1175.

Tchernia, P. and Fieux, M., 1971. Résultats des observations hydrologiques exécutées à bord du N/O "Jean Charcot" pendant la campagne MEDOC 69 (30 Janvier-28 Février, 18-31 Mars 1969). Cah. Océanogr. 23(1): 1-91.

Voorhis, A. D. and Webb, D. C., 1970. Large vertical currents observed in a winter sinking region of the northwestern Mediterranean Sea. Cah. Oceanogr. 22(6): 571-580.

This Page Intentionally Left Blank

EQUATORWARD CURRENTS IN TEMPERATURES 1.8 - 6.0°C ON THE CONTINENTAL SLOPE IN THE MID-ATLANTIC BIGHT

D. RANDOLPH WATTS
Graduate School of Oceanography, University of Rhode Island, Narragansett, RI 02882-1197

ABSTRACT

A large historical set of near-bottom current meter measurements along the continental slope and rise off the northeastern US coast between Cape Hatteras and Georges Banks is used to determine the mean Deep Western Boundary Current (DWBC) velocity and temperature structure and to estimate transports of several water types. While essentially all the mean flow is equatorward in the depth range 800 to 4000 m, there are three distinctly higher speed bands imbedded within a surrounding mean flow of lower speed. The banding can best be categorized according to the mean potential temperature, θ, as follows: Near bottom on the continental rise in 3400–4500 m, there is a thin relatively swift (6 cm s^{-1}) cold ($\theta \leq 2.0$°C) band of flow. From $\theta = 2.1$ to 2.7°C the flow is weak (3 cm s^{-1}). Above this, near 2500 m depth and $\theta = 2.9$ to 3.0°C is another band of swifter flow (7 cm s^{-1}). Shallower and warmer yet, from $\theta = 3.1$ to 3.9°C, the mean equatorward flow is again weak (3 cm s^{-1}). The warmest ($\theta = 4.0$ to 4.3°C) and shallowest (1100 to 800 m) waters included in this study are in another relatively swift band of equatorward flow (6 to 10 cm s^{-1}).

There are three striking points to note about this structure, that differ from traditional concepts regarding the equatorward flow of DWBC waters. Firstly, the "deep" western boundary current extends up to as shallow as 800 m in the Mid-Atlantic Bight. Secondly, water of "traditional" Labrador Sea Water (LSW) characteristics ($\theta = 3.3$ to 3.9°C) is relatively absent (*i.e.*, has weak flow) here, but is flanked above and below by swifter bands of flow. Other water-mass tracer properties are quoted from the literature to support this banded nature of the flow, the absence of LSW, and predominance of older North Atlantic Deep Water (NADW) in its place. Thirdly, the observed speeds would imply a remarkably short transit time from a northern source (4000 km) of about 2 to 4 years. Thus the evidence suggests that some components of the DWBC, at least within the Mid-Atlantic Bight, arrive there by some longer indirect route rather than a continuous ribbon hugging the western boundary. Approximate transports are presented for the various temperature bands and water types.

INTRODUCTION

In the North Atlantic the Deep Western Boundary Current (DWBC) flows equatorward, roughly following bathymetric contours along the continental slope and rise. The water-mass components that would be expected in a Stommel-Arons (1960) idealization of the DWBC would come south directly from northern sources along the western boundary and would traditionally include the North Atlantic Deep Water (NADW) and Labrador Sea Water (LSW). Observations summarized below contradict that idealization in important ways. The water-mass properties, source strengths, and flow paths of the deep North Atlantic Basin waters are summarized well in Worthington (1976). Much updated information on DWBC properties is given in a companion article by Smethie (1990) in this volume.

The study reported here began as an attempt to determine the mean flow speeds and transit

times, and to estimate the transports within the DWBC. The study was based upon combining new and historical current meter data off the northeastern US coast that by now cover the region in enough detail to make such a summary possible. However, interesting velocity/temperature structure was found that contradicts the traditional "textbook" description to some extent, particularly with regard to waters within the potential temperature range θ = 2.9 to 4.3°C. While the focus of this paper is on the results from the current meter data, I will also discuss and attempt to explain these contradictions. To do so requires further introductory background.

The characteristics and spreading paths of traditional LSW have been discussed in detail by Lazier (1973) and in a pair of excellent papers by McCartney and Talley (1982) and Talley and McCartney (1982). The formation processes for LSW are summarized by Clarke and Gascard (1983) and Gascard and Clarke (1983), who observed renewal events in 1972 and 1976 in which severe wintertime cooling converted the central waters of the Labrador Sea to a large deep pool of θ = 2.9°C water.

The Labrador Sea between Labrador and Greenland, and particularly the Labrador Basin to the east and northeast of Newfoundland are regions of intense air-sea interaction and heat exchange. For example, Budyko (1974) shows a strong peak in the annual mean loss of heat from the surface waters to the atmosphere of 60 to 80 kcal cm^{-2} yr^{-1}. This peak extends throughout much of the Labrador Basin and is most intense between Newfoundland and the Mid-Atlantic Ridge, associated with cold dry winds coming off the North American continent. In that area late winter formation of Sub-Polar Mode Water (SPMW) occurs, as detailed by McCartney and Talley (1982).

2 OBSERVATIONS AND METHODS

In the past two decades many experiments have deployed current meters in the near-bottom waters along the continental slope and rise of the Mid-Atlantic Bight off the northeastern U.S. coast between Cape Hatteras and Georges Banks. There are now archived over 100 deep current meter records in this region; many are from repeated deployments at various sites, and most come from the time period 1974–1986. I had been involved in several experiments that moored deep current meters in this region; in particular the Mid-Atlantic Slope and Rise (MASAR) experiment produced many of the records. I must also thank Nelson Hogg, who shared with me a "SYNOP Archive" data set that he assembled to include many additional records from other experiments. For this study I have selected sites at bathymetric depths between 800 to 4000 m with current meters moored between 50–300 m off the bottom so as to be within the DWBC but out of the bottom boundary layer. The key selection criterion has been to find record lengths sufficient to produce statistically significant estimates of the mean currents; the statistical test of significance is described briefly in the next paragraph. For 40 such sites the mean current has been determined, in many cases by linking together records from different deployments at the same site. My purpose was to chart and

summarize the mean circulation in this region and to characterize the strengths of the equatorward currents according to their temperature and associated water-mass properties.

Deep current records along this continental slope and rise region can be highly variable with time, with principal axes of variance nearly parallel to the bathymetry and the flow often reversing in direction. The standard deviation in the north or east component often exceeds the mean flow by several fold, and thus current records at each site must be long enough to average over the variability with sufficient degrees of freedom to determine a statistically significant mean flow. The uncertainty of each mean component is estimated by calculating the autocovariance function (which determines the degrees of freedom for a given record length) and using the procedure of Bendat and Piersol (1971) and Dewar and Bane (1989). The mean current vector was calculated by combining records from separate deployment time periods, and the standard error of the mean was calculated accounting for their combined degrees of freedom. Because the deep variability in this region is mainly associated with topographic Rossby waves (Johns and Watts, 1986; Schultz, 1988) that have considerably shorter correlation time scales (10–12 days) than mid-ocean eddies, statistically significant mean currents can be determined from records as short as six months in many cases. At most of the sites selected the duration from combined deployments was 12 to 24 months. The standard error of the mean is consistently plotted on all the following figures.

The measured currents are also classified according to temperature in order to relate them to the structure of the various water-masses that constitute the DWBC. The measured *in situ* mean temperature, T, for each record has been approximately converted to potential temperature, θ, for this purpose using $\theta = T - \overline{\Gamma} \cdot Z$, *i.e.*, by simply subtracting an approximate adiabatic temperature gradient $\overline{\Gamma} = 0.1°\text{C km}^{-1}$ times the current meter depth, Z. This simplification is consistent with the desired accuracy to distinguish large temperature classes and with the typical calibration accuracy of current meter thermistors ($\pm 0.1°$C). The statistical error of the mean T due to record variability is typically only a few hundredths °C in these deep records and thus does not spoil the above classification scheme.

3 DEEP CURRENT MAPS

The mean-flow vectors between 50–300 m off the bottom are shown in Figure 1, revealing avery consistent pattern throughout the bathymetry range 800–4000 m. The mean current is southwestward following bathymetric contours with mean speeds of 2 to 10 cm s^{-1}. Shoreward of the 4000 m isobath the mean flow field is well defined because the boxes indicating the standard error of the mean (SEM) are generally much smaller than the mean vectors themselves. This is mainly a propitious result of long record lengths and relatively short time scales of variability at these sites, not necessarily an indication of small variance. For reference, the mean surface path of the "north wall" of the Gulf Stream and its meander envelope are indicated respectively as the solid and two dashed lines arcing

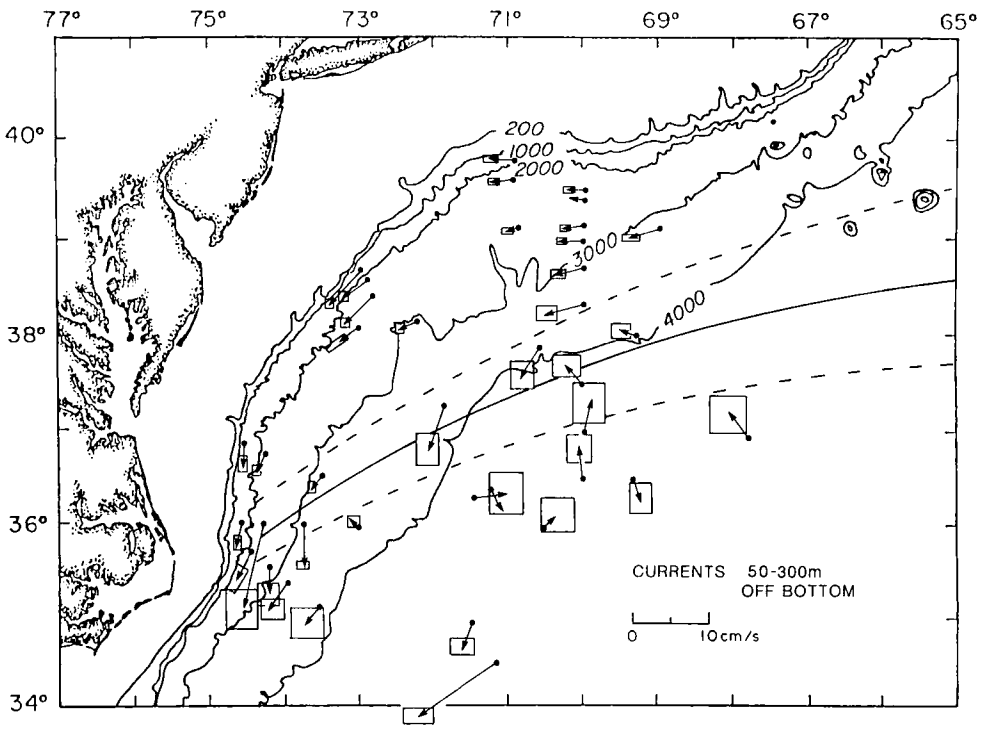

Fig. 1. Mean current vectors 50–300 m above the ocean bottom. Speed key is given at lower right. Boxes indicate standard error of the mean in u,v directions, as described in text.

east-northeastward from Cape Hatteras. An equatorward mean flow crossing under the Gulf Stream is clearly defined. Its offshore limit is suggested by the skewed vector near 36N 73W for which the mean is of marginal significance.

Offshore of the 4000 m isobath the mean currents vary in direction with a hint of a cyclonic gyre centered at 37N 71W. The SEM boxes show this feature to be of marginal statistical significance, primarily because those records were only 8 months long and the variability in this deeper offshore water under the Gulf Stream has longer time scales resembling mid-ocean mesoscale eddies; records much longer than 8 months would be required to define this feature well.

For comparison, in Figure 2, I have similarly summarized the mean currents within 300–1500 m above the bottom. The currents are somewhat stronger, but the pattern is very similar to the near-bottom currents just described, except near Cape Hatteras, where the mean vectors turn eastward to join the Gulf Stream, rather than cross under it.

The Deep Western Boundary Current south of New England has components as shallow as 800 m crossing under the Gulf Stream at Cape Hatteras. Pickart and Watts (1990) show from an observational and dynamical viewpoint that as the DWBC crosses under the Gulf Stream it also

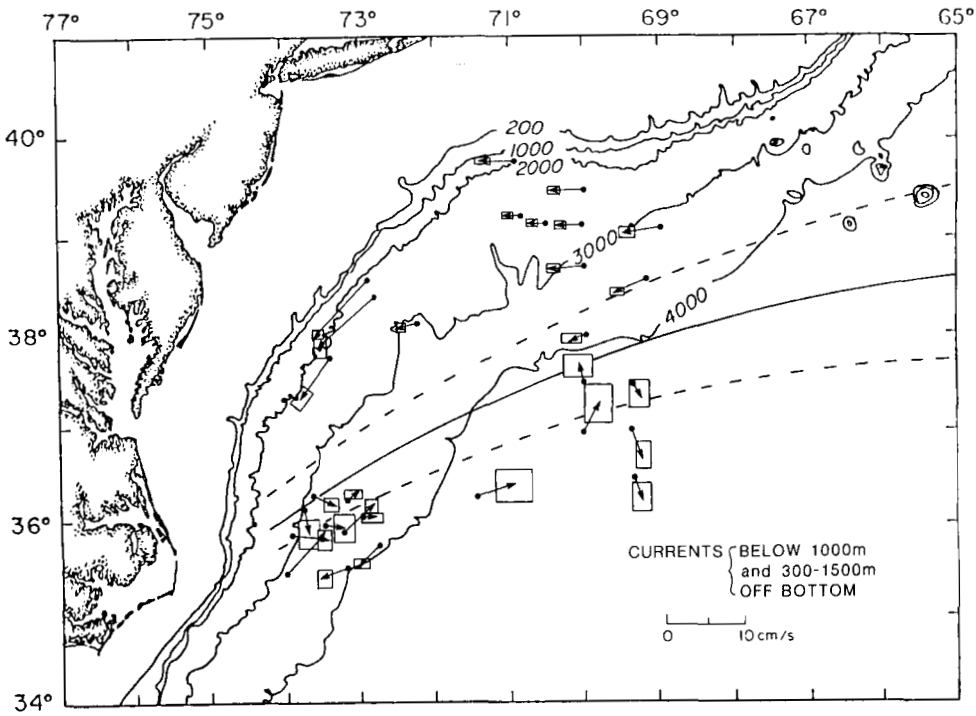

Fig. 2. Mean current vectors 300–1500 m above the ocean bottom, and deeper than 1000 m. Speed key is given at lower right. Boxes indicate standard error of the mean in u,v directions, as described in text.

shifts to follow about 600 m deeper bathymetric contours as it continues southward.

4 CURRENT STRUCTURE AND WATER-TYPE DISCUSSION

4.1 *Current bands categorized by temperature*

Within the equatorward near-bottom flow there is a notable structure in the current speeds, depending upon the water depth and temperature of the current. It is clearest to categorize them by temperature, as shown in Figure 3, in which their *in situ* mean temperatures have been adjusted to approximate potential temperatures, θ, as described earlier.

The speed structure has three peaks of height 6–7 cm s^{-1} in potential temperature bands $\leq 2.0°C$, near 2.9–3.0°C, and $\geq 4.0°C$. The intervening low speeds are around 3 cm s^{-1}, encompassing broader θ bands between approximately 2.1–2.8°C and 3.1–3.9°C.

Could the current peaks in the θ structure have arisen from some non-synoptic sampling problem; for instance could "high-current years" exist such that the records by chance appear to create a peak at 2.9–3.0°C? We can argue against this sampling problem as follows: Two of the points in the 2.9–3.0°C peak are from 1984–85 and one each from 1980 and 1986; most of the points from the low speed bands on either side of the peak were also obtained on experiments that used the same variety

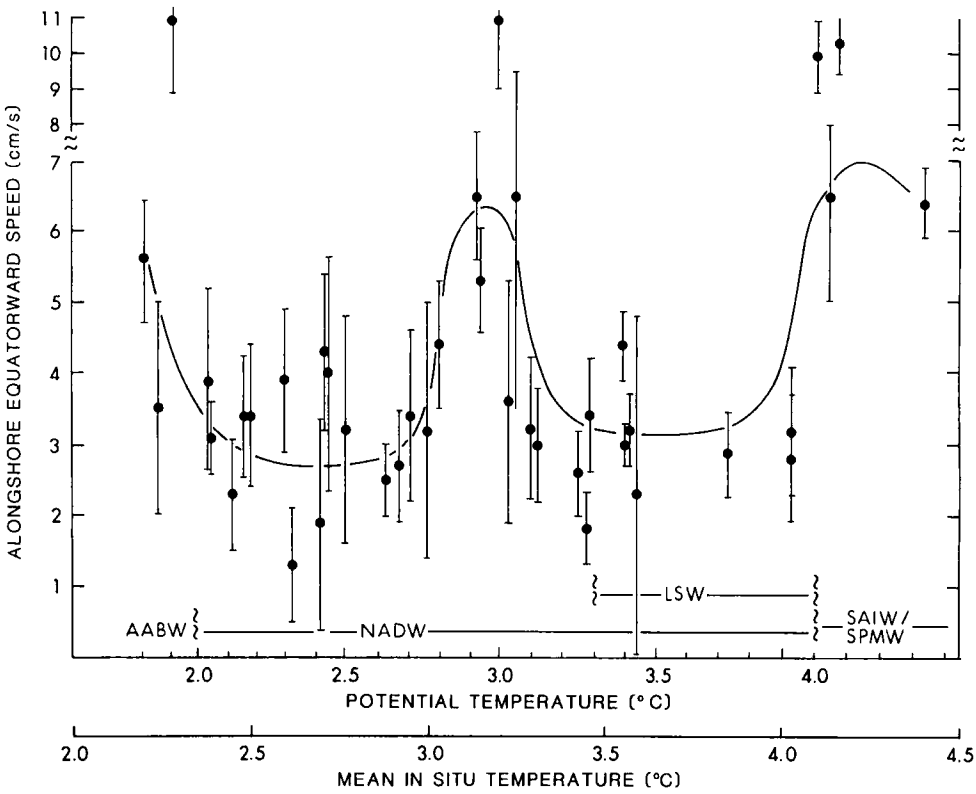

Fig. 3. Mean equatorward alongshore current speed classified according to mean potential temperature, θ, which is derived from mean *in situ* temperature of each current meter record as described in text. Error bars are standard error of the mean.

of moorings and instruments in those same years. The four points in the $\theta \geq 4.0°C$ peak are also from 1984–86 and from the same experiments as points in the neighboring valley. The $\theta \leq 2.0°C$ peak is less certain, resulting from just two high (and one average) data points. The evidence tends to exclude the above mentioned sampling problem, and the equatorward speed peaks appear to be real in the sense that independent sets of measurements within their respective temperature ranges consistently stand above the valleys between them.

4.2 *$\theta \leq 2.0$ and 2.1 to 2.8°C*

Starting our water-type discussion with the coldest waters, Worthington (1976) shows that waters with θ colder than 2.0°C in the North American Basin carry the low salinity and high silicate signature of Antarctic Bottom Water (AABW) and are distinct from deep waters of the Labrador Basin which have Denmark Strait Overflow Water (DSOW) characteristics. The AABW constituency for $\theta \leq 2.0°C$ waters south of New England appears to be well established, consistent with Amos *et al.* (1971) and Weatherly and Kelley (1982), although samples with low silicate DSOW have also

been observed here. This is the first example that we offer of a swifter southward flowing core in the DWBC that does not flow directly from a northern source, nor in this case from a northern source at all!

In Figure 3 the slower moving waters with $2.1 \leq \theta \leq 2.8$°C are probably just North Atlantic Deep Water. Because this article deals primarily with current meter data and because we find no puzzles in this temperature range, the reader is referred to Smethie's article in this volume or to Pickart (1990) for water property discussion for NADW in this sub-band.

4.3 *Freon (CFM-12) content*

The average vertical profile of θ *vs.* freon (specifically CFM-12) will facilitate the continued discussion of warmer water-types. Smethie's article in this volume shows many individual freon profiles and discusses generally how one should interpret this anthropogenic tracer with regard to recent convective renewal processes. The curve in Figure 4 is an average θ *vs.* CFM-12 profile from Pickart (1990) from four sections crossing the DWBC. Waters flowing through our study region with traditional LSW temperatures carry a much weaker freon signature than waters below 2.6°C or above 3.8°C. This freon minimum could result from two main factors: (a) the age since renewal could be greater by a decade or more (*i.e.* formation before the atmospheric freon content was substantial), or (b) the renewal could have been only partial and/or the water may have been diluted with unrenewed water. In either case, the profile clearly suggests that waters in the DWBC south of New England with $\theta = 2.6$–3.8°C have not recently had strong exchange with the atmosphere.

4.4 θ *= 2.9-3.0°C and 3.1 to 3.9°C*

Returning now to Figure 3, the current core at $\theta = 2.9$–3.0°C is clearly colder than traditional LSW. Talley and McCartney (1982) show data from OWS *Bravo* that indicate LSW was not significantly changed or renewed from 1950 through 1971, only slowly warming from 3.2 to 3.7°C and getting slightly saltier while the density remained roughly constant. This period was followed in 1972 by a severe winter that produced 3.4°C water. Clarke and Gascard (1983) reported deep convective overturning in a broad gyre in the central Labrador Sea in strong winter cooling events again in 1976. That newly formed LSW had $\theta = 2.9$°C.

It is not known how long it takes to dissipate a large pool of newly formed LSW, but the above quoted OWS *Bravo* observations suggest punctuated renewal events followed by long decay-time scales. The transit time for northern-source waters to travel at the observed core speed of 6 cm s^{-1} from the Labrador Sea to the Mid-Atlantic Bight (a 4000 km distance) is only about 2 years. One might first think that the current core at $\theta = 2.9$–3.0°C is the new colder LSW, however the CFM-12 profiles across the DWBC (Figure 4), all more recent than 1980, show a freon minimum for this θ range. If waters from the Labrador Sea were contributing to the DWBC, they would likely have a high CFM-12 concentration. I can find no way to rationalize the timing of the current meter records (1980–1986), the CFM-12 sections (> 1980), and the new LSW formation events (1972, 1976) such

that the θ = 2.9–3.0°C core could have come directly from the Labrador Sea.

Altogether, LSW does not appear to be a significant contributor to the DWBC south of New England, neither the traditional θ =3.3–3.8°C type, for which Figure 3 shows relatively slow movement, nor the newly formed θ =2.9–3.0°C type as just discussed. This conclusion is in stark contrast with the idealized model of DWBC constituents, but is completely consistent with the following two studies of the spreading of LSW. Ivers' (1975) interpretation of the deep circulation pattern in the northern North Atlantic, reproduced in McCartney and Talley (1982), indicates LSW flowing only into the eastern North Atlantic. Similarly, Talley and McCartney (1982) map the salinity minimum along the LSW potential vorticity minimum surface. Their map provides substantiating evidence that LSW mainly spreads into the eastern North Atlantic and does not round the Grand Banks to the south.

The best explanation I can offer for the θ = 2.9–3.0°C core is that it should be NADW and that it should have formed sometime prior to 1970, when Smethie (1990) shows the atmospheric CFM-12 content to have begun rising sharply. Interestingly, NADW that is at least one decade old must have come to the region south of New England by some indirect path, because the direct path, *i.e.*, a continuous DWBC ribbon flowing at 6 cm s^{-1} from the northern source regions, would indicate an age of only 2–4 years.

4.5 $\theta \leq 4.0°C$

Our discussion of the current structure ends with the warmest ($\theta \geq$ 4.0°C) peak of equatorward speed observed in Figure 3. These waters are flowing in depths of 600–1100 m, and hydrographic studies find they are sometimes associated with low-salinity and high-oxygen anomalies. One's first expectation is that these water types may originate in the Labrador Basin north of the North Atlantic Current. They have been given a variety of names, as follows.

In a 1971 section off Cape Hatteras, Richardson (1977) found the strongest low-salinity anomalies associated with θ between 3.9–5.0°C, hugging the continental margin in depths from 700–1500 m. He identified this water-type as Labrador Basin Water, distinct from LSW. It has been given other names as well. Sverdrup *et al.* (1942) identified Sub-Arctic Intermediate Water (SAIW) in this temperature range from the Labrador Basin. McCartney and Talley (1982) have a comprehensive discussion of the formation of Subpolar Mode Water (SPMW) in the North Atlantic, which includes high-volume modes with θ = 4–6°C in the Irminger Sea.

The mean CFM-12 profile in Figure 4 showed its strongest maximum for θ = 4–6°C, indicating that the waters have had *recent* vigorous exchange with the atmosphere, whatever their exact source region.

For the source of our observed current-core for $\theta \geq$ 4.0°C water south of New England to be in the Labrador Basin, then it is likely to have traveled by a direct path, rounding the Grand Banks. This behavior would contrast markedly with that of LSW (which flows into the eastern North

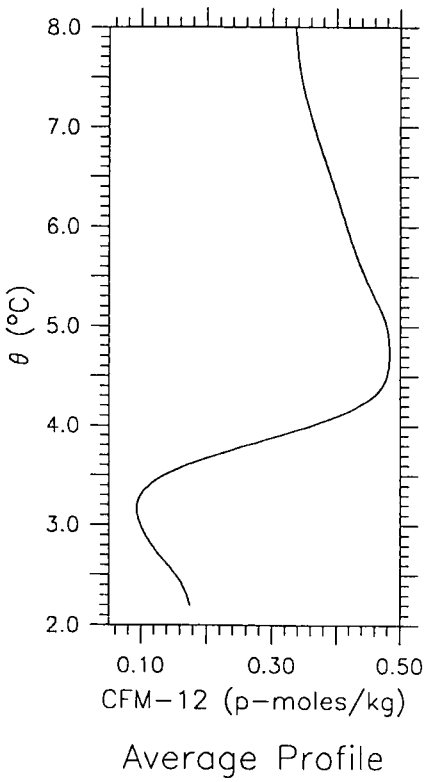

Fig. 4. Average freon CFM-12 profile *vs.* θ from four sections across DWBC in the Mid-Atlantic Bight.

Atlantic), even though these two water types are neighboring in temperature and depth and possibly in formation region. From this viewpoint, it would be surprising if the 4–6°C waters originated in the Labrador Basin. The problem is reminiscent of Worthington's (1976) emphatic claim that water properties above 4°C remain distinct on either side of the tail of the Grand Banks, *i.e.* between the Newfoundland Basin and the Nova Scotian Basin. He presented clear evidence against flow around the Grand Banks and even argued against strong cross-frontal mixing, although Clarke *et al.* (1980) later disputed this claim.

Another possible source region for 4–6°C waters is southwest of the Grand Banks, in the recirculation gyre north of the Gulf Stream. Mann (1967) shows several springtime sections near 50W, south of the Grand Banks, in which a mode of 4–6°C is evident near the surface in the Slope Water; in those sections the Slope Water Current is flowing east, suggestive of a source to the west within the recirculation gyre of Slope Water. Mountain and Shuhy (1980) show another section in which the Slope Water and Gulf Stream northern portions all flow eastward across the Newfoundland Ridge.

Altogether this makes an interesting question for future study: What is the formation region and

process for the relatively swift core of θ = 4–6°C water in the upper DWBC south of New England?

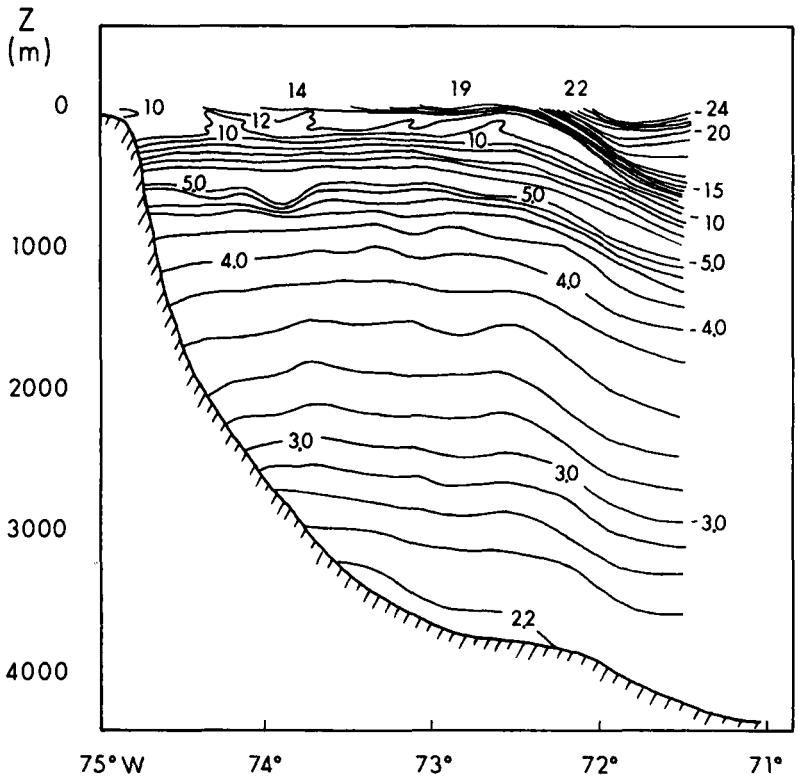

Fig. 5. Vertical section of *in situ* temperature along 36°15′N across the Slope Water out to the Gulf Stream, from Fuglister (1960).

5 TRANSPORT ESTIMATES

In order to construct a representative mean velocity section across the DWBC south of New England, I have projected all the southwestward speeds onto a single cross-section. All along the Mid-Atlantic Bight, cross-sections of the bottom topography retain a relatively similar shape, and the temperature stratification in the Slope Water remains quite similar. A typical *in situ* temperature section is represented by Figure 5, from Fuglister (1960); this section is just north of Cape Hatteras at 36°15′N.

In projecting the set of measured mean current velocities onto this one section, each current measurement was placed at a point with the same *in situ* temperature as its mean and at approximately the same distance above the bottom. The resulting mean current structure with depth may be seen in Figure 6.

Typically south of New England, the Gulf Stream will be found offshore of the 3000–4000 m isobath, and the deep currents under it are more variable, as already discussed. Inshore of the Gulf Stream, general equatorward mean flow occurs along the continental slope and rise, with typical mean velocity approximately 3 cm s^{-1} throughout a large depth range. However, three swifter bands of mean flow can be seen in Figure 6. It is helpful to view Figures 5 and 6 together.

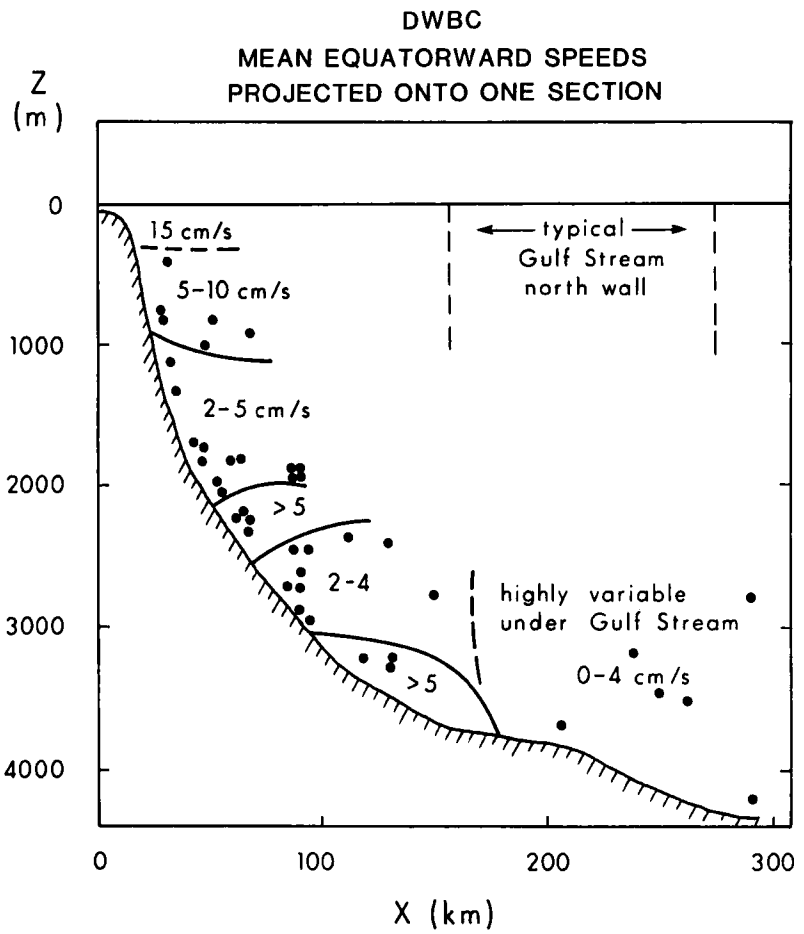

Fig. 6. Structure of the Deep Western Boundary Current constructed by projecting mean equatorward speeds onto single section shown in Figure 5.

In a relatively thin band at the bottom of Figure 5, 100–200 m thick, the coldest waters ($\theta \leq 2.0°C$, $T \leq 2.3°C$) are restricted to depths from 3200–3800 m. (The offshore edge of this feature may range deeper in sections taken farther east.) The corresponding swift band of equatorward flow in

Figure 6 is exemplified by the core near 3500 m depth. Near 2400 m depth is the mid-depth high-current core (≈ 7 cm s^{-1}) for which $\theta = 2.9$–3.0°C ($T \approx 3.1$–3.2°C). In the depth range 500–1100 m is the corresponding high-current core of 4–6°C water. For completeness on Figure 6, the near-surface Slope Water circulation is roughly characterized; it typically has southwestward (alongshore) currents around 15 cm s^{-1} near a front at the shelf break (Csanady and Hamilton, 1988).

One may use Figure 6 to make very approximate transport estimates for the several θ sub-ranges within the DWBC that have been identified in this study. The transport is simply estimated as the product of the mean current speed times the depth range times the width of the current. While the depth range and mean current speed may be reasonably estimated from our data in Figures 5 and 6, we can only infer typical current core widths from historical water property surveys to be in the range 40 to 120 km. Thus the main uncertainty in the following transport estimates comes from the range of estimated current widths. It is possible that more transport could join the DWBC after it has crossed south of the Gulf Stream.

Notwithstanding, it seems useful to attempt to quantify the transport structure of the DWBC, particularly through the Mid-Atlantic Bight where it approaches the Gulf Stream crossover. For $\theta = 4.0$–6.0°C the equatorward transport estimate is 2–6 Sv; this is a substantial transport regardless of whether these waters are from the Labrador Basin (*e.g.* SPMW) or from the northern recirculation gyre of the Gulf Stream west of the Grand Banks. Below 4°C we have tentatively identified the next three bands as NADW constituents. The two low speed bands for which $\theta = 3.2$–3.9°C and respectively $\theta = 2.1$–2.8°C each carry about 1–3 Sv. Interestingly, the swifter but thinner band between them at $\theta = 2.9$–3.0°C also carries 1–3 Sv. Thus the NADW transport for $\theta = 2.1$–3.9°C sums to 3–9 Sv through this mean DWBC section. The southward transport of the small remnant core of AABW ($\theta \leq 2.0$°C) is 0.7–2 Sv. The total transport of all DWBC components below 800 m is estimated to be 5–14 Sv.

6 ACKNOWLEDGMENTS

I would like to thank Jean-Claude Gascard and Curt Collins for organizing the symposium on The Formation of Deep Waters in the Ocean which spurred on the completion of this paper. I want to express my gratitude to Robert Pickart and to Ross Hendry for informative discussions. I am pleased to acknowledge SAIC Inc., Raleigh, North Carolina, through whom I participated in the U.S. Department of the Interior, Minerals Management Service sponsored MASAR contract (14-12-0001-30066), by which much of these data were initially collected. Later portions of this study have been supported by the U.S. Office of Naval Research contract N00014-87K-0235.

7 REFERENCES

Amos, A. F., A. L. Gordon, and E. D. Schneider, 1971. Water masses and circulation patterns in the region of the Blake-Bahama Outer Ridge. Deep-Sea Res., 18: 145–165.

Bendat, J. S. and A. G. Piersol, 1971. Random Data: Analysis and Measurement Techniques. Wiley-Interscience, New York.

Budyko, M. I., 1974. Climate and Life. Academic Press, New York.

Clarke, R. A. and J. C. Gascard, 1983. The Formation of Labrador Sea Water. Part I: Large-Scale Processes. J. Phys. Oceanogr., 13: 1764–1778.

Clarke, R. A., H. Hill, R. F. Reiniger, and B. A. Warren, 1980. Current system south and east of the Grand Banks of Newfoundland. J. Phys. Oceanogr., 10: 25–65.

Csanady, G. T. and P. Hamilton, 1988. Circulation of slopewater. Cont. Shelf Res., 8: 565–624.

Dewar, W. K. and J. M. Bane, 1989. Gulf Stream Dynamics. Part I: Mean Flow Dynamics at 73W. J. Phys. Oceanogr., 19: 1558–1573.

Fuglister, F. C., 1960. Atlantic Ocean Atlas of Temperature and Salinity Profiles and Data from the International Geophysical Year of 1957–1958. Woods Hole Oceanographic Institution Atlas Series 1: 209pp.

Gascard, J. C. and R. A. Clarke, 1983. The Formation of Labrador Sea Water. Part II: Mesoscale and Smaller-Scale Processes. J. Phys. Oceanogr., 13: 1779–1797.

Ivers, W. D., 1975. The deep circulation in the northern North Atlantic, with especial reference to the Labrador Sea. Ph.D. thesis, University of California at San Diego, 179 pp.

Johns, W. E. and D. R. Watts, 1986. Time scales and structure of topographic Rossby waves and meanders in the deep Gulf Stream. J. Mar. Res., 44: 267–290.

Lazier, J. R. N., 1973. The renewal of Labrador Sea Water. Deep-Sea Res., 20: 341–353.

Mann, C. R., 1967. The termination of the Gulf Stream and the beginning of the North Atlantic Current. Deep-Sea Res., 14: 337–359.

McCartney, M. S. and L. D. Talley, 1982. The Subpolar Mode Water of the North Atlantic Ocean. J. Phys. Oceanogr., 12: 1169–1188.

Mountain, D. G. and J. L. Shuhy, 1980. Circulation near the Newfoundland Ridge. J. Mar. Res., 38: 205–213.

Pickart, R. S., 1990. Shallow and Deep components of the North Atlantic Deep Western Boundary Current. Deep-Sea Res., (submitted).

Pickart, R. S. and D. R. Watts, 1990. Deep Western Boundary Current variability at Cape Hatteras. J. Mar. Res. (accepted).

Richardson, P. L., 1977. On the crossover between the Gulf Stream and the Western Boundary Undercurrent. Deep-Sea Res., 24: 139–159.

Schultz, J., 1988. Structure and Propagation of Topographic Rossby Waves northeast of Cape Hatteras, North Carolina. M.S. Thesis, Univ. North Carolina.

Smethie, W. M., 1990. Formation and Spreading of North Atlantic Deep Water in the North Atlantic Ocean: Evidence from transient tracers. (in this volume).

Stommel, H., and A. B. Arons, 1960. On the Abyssal Circulation of the World Ocean–II. An idealized model of the circulation pattern and amplitude in oceanic basins. Deep-Sea Res.,: 217–233.

Sverdrup, H. U., M. W. Johnson and R. H. Fleming, 1942. The Oceans: Their Physics, Chemistry and General Biology. Prentice-Hall, Englewood Cliffs, N.J.

Talley, L. D. and M. S. McCartney, 1982. Distribution and Circulation of Labrador Sea Water. J. Phys. Oceanogr., 12: 1189–1205.

Weatherly, G. L. and E. A. Kelley Jr., 1982. 'Too cold' bottom layers at the base of the Scotian Rise. J. Mar. Res., 40: 985–1012.

Worthington, L.V., 1976. On the North Atlantic Circulation. Johns Hopkins Oceanographic Studies, No. 6: 110 pps.

ENHANCEMENTS TO DEEP TURBULENT ENTRAINMENT

ROLAND W. GARWOOD, JR.
Department of Oceanography, Naval Postgraduate School, Monterey, CA 93943 USA

ABSTRACT

At first glance, one-dimensional mixed layer dynamics do not appear to predict sufficiently deep mixing to explain the formation of the large volumes of deep water observed in the polar and Mediterranean seas. However, two processes have been neglected in the turbulent kinetic energy (TKE) budget that lead to larger vertical turbulent velocities that may enable deep penetrative convection, possibly contributing to the formation of deeper waters. The energetics of deep convection are examined for two asymptotic regimes: (i) free convection with pressure augmentation of buoyancy flux, and (ii) forced convection with vertical mixing assisted by planetary rotational conversion of wind-generated horizontal TKE into vertical TKE.

In the case of free convection, the buoyant production of vertical turbulence may be increased considerably by the increase in the thermal expansion coefficient (α) with pressure. An entrainment model including this nonlinearity in the equation of state predicts greater vertical mixing and penetrative convection into the pycnocline than does a model with the linear equation of state used traditionally for mixed layer predictions. The increase in thermal expansion coefficient with pressure is temperature-dependent and is more significant for cold polar water convection than it is for Mediterranean Sea convection. The significance of pressure enhancement of the buoyancy flux may be expressed in terms of the ratio of depth of mixing (h) to a depth scale $H_\alpha = \alpha / \frac{\partial \alpha}{\partial z}$ that depends mostly on mixed layer temperature. If $h/H_\alpha \sim 1$ or larger, the TKE budget will be dominated by pressure-enhanced free convection. For the Mediterranean Sea, $h/H_\alpha \approx 0.3$ when convection penetrates to the bottom. However, for the coldest polar seas $h/H_\alpha \approx 8$ for penetrative convection to the bottom, and h/H_α is significant for mixing deeper than about a hundred meters.

In the case of forced convection, maximum entrainment rate may be achieved when the wind stress is toward the west. Then the northward component of planetary rotation may transfer horizontal wind-generated turbulence to vertical turbulence. This enhances vertical flux rates in general and entrainment deepening by the mixed layer in particular. Such augmented wind mixing may cause sufficiently deep mixing to "turn on" the pressure-enhancement of buoyancy flux, with substantially increased vertical convection.

INTRODUCTION

One-dimensional mixing arguments have failed in the past to predict sufficiently strong deep convection to explain the large volume of deep water in the oceans (Stommel, 1972). For this reason, perhaps, mixed layer and turbulent entrainment processes have received subsequently little attention in this regard. Although the mixed layer is recognized as having a fundamental climatic role in coupling with the atmosphere in polar regions, model development and applications (Hakkinen, 1987; Lemke et al., 1989; Chu and Garwood, 1988) have not included at least two of the processes necessary for accurate entrainment calculations for mixed layer depths greater than about 100 m.

In this paper, the two previously neglected processes of (i) buoyancy flux-enhancement by

pressure, and (ii) planetary rotational transfer of TKE between components are included in an otherwise conventional one-dimensional model that is applied to very deep oceanic mixing. Both free (buoyancy-driven) convection and forced (wind-driven) convection cases are considered. Although one-dimensional convection may not wholly explain the formation of most deep waters, it will be shown that vertical turbulent mixing forced by local wind stress and surface heat flux may indeed be a major factor. Two important results are revealed that make the TKE budget for deep (greater than 1 km) ocean convection very different from the budget for shallow (order 100 m and less) mixing regimes. The advantage of analyzing the TKE budget in considering these processes is that it leads from first principles to an objective calculation of the energetics of the system including a prediction of the vertical convective velocity scale, $|w'|$.

The first result is attributable to the pressure-dependence of the thermal expansion coefficient $\alpha = -\left(\rho_\theta^{-1}\frac{\partial \rho_\theta}{\partial \theta}\right)$ for seawater where ρ_θ is the potential density and θ is the potential temperature. The dependence of α upon pressure is a nonlinearity in the equation of state that has been recognized as contributing to a reduction in hydrostatic stability in both oceanic (Carmack and Aagaard, 1974; McDougall, 1984 and 1987) and freshwater lake (Eklund, 1965; Bennett, 1976; Carmack and Farmer, 1982; Carmack and Weiss, 1990; and others) environments.

The possible importance of the pressure-enhancement of buoyancy flux is dependent upon how the thermal expansion coefficient changes with depth, or equivalently the magnitude of $\frac{\partial^2 \rho_\theta}{\partial p \partial \theta}$ (Fofonoff, 1956). McDougall (1987) coined the term "thermobaric" in describing processes that depend on this second derivative of the density with respect to potential temperature and pressure. In particular, he uses "thermobaric" to denote vertical advection caused by lateral mixing on neutral surfaces (McDougall, personal communication). In any case, the magnitude of this term is largest for seawater that is near the freezing point. Hence the nonlinear increase in buoyancy flux due to pressure may be most significant in the deep convection "chimneys" of the polar seas (Gordon, 1978; Killworth, 1979) and less significant in deep convection in the warmer Mediterranean waters (Medoc Group, 1970).

In this study, the dependence of α upon pressure is included in the computation of the buoyancy flux term of the budget for the vertical component of the turbulence. Traditional scaling for the convective moist atmosphere is used first to provide a steady-state solution to the non-buoyancy conserving deep oceanic convection problem. In addition, time-dependent effects can be revealed with an unsteady model (Garwood,1977) for the vertically-integrated TKE budget. This will also allow an assessment of the individual terms of the budget and, in particular, the mixed layer average of the vertical turbulence, $\overline{\langle w'^2 \rangle}$,where <> denotes a vertical mean over the mixed layer depth, h.

Also using this same unsteady model, the final result in this paper is a quantification of the possible role of the north component of planetary rotation, $\Omega_y = \Omega\cos\phi$, where Ω is the planetary rotation rate, and ϕ is the latitude. This complement to the Coriolis parameter can cause TKE to be redistributed between eastward $(\overline{u'^2})$ and vertical $(\overline{v'^2})$ components. Wyngaard et al. (1974) have studied this process in the convective atmospheric boundary layer, finding small effects. Garwood et

al.(1985a), Gallacher (1987), and Galperin et al.(1989) have investigated the possible importance of rotation in oceanic turbulent boundary layers. Garwood et al. (1985b) suggested that Ω_y interacts with the westward surface wind stress to help deepen the tropical oceanic mixed layer convectively forced by the zonal wind stress. Although this hypothesis remains unverified for the tropical oceanic mixed layer, it is suggested here that the very deep convective scales in deep water formation may cause significant rotational conversion of horizontal TKE to vertical TKE. This mechanism requires forced convection to be generated by winds having a westward wind stress component, $\tau_x < 0$. Also, this same process can be responsible for limiting the depth of forced-convection mixing whenever winds are toward the east, $\tau_x > 0$. Because Ω_y varies with the cosine of the latitude the rotational conversion of turbulence might be expected to be a mostly low-latitude phenomenon. However, Ω_y is still half as large at latitude 60 as it is at the equator, and the depth of mixing may more than compensate for the reduced Ω_y.

2 TKE BUDGET

The one-dimensional total TKE equation is

$$\frac{\partial}{\partial t}\left(\frac{\bar{E}}{2}\right) = -\left(\overline{u'w'}\frac{\partial \bar{u}}{\partial z} + \overline{v'w'}\frac{\partial \bar{v}}{\partial z}\right) + \alpha g\overline{\theta'w'} - \frac{\partial}{\partial z}\left(\frac{\overline{w'(E+p')}}{\rho}\right) - \varepsilon \qquad (1)$$

where $E = u'^2 + v'^2 + w'^2$ and $\rho\,(\bar{E}/2)$ is the total TKE per unit mass. Here u is the easterly velocity (x-direction), v is the northerly (y-direction) velocity, and w is the upward velocity (z is positive up). Horizontal homogeneity is assumed here to simplify the system of equations in order to focus on the roles of pressure-enhancement of the buoyancy flux and planetary rotation. The four terms on the right-hand side of (1) are: (i) shear production of horizontal turbulence by conversion of mean kinetic energy by the action of the wind stress, (ii) buoyancy flux production or damping of vertical turbulence, depending upon the sign, (iii) vertical diffusion of TKE by turbulent and pressure transport, and (iv) viscous dissipation of all components of turbulence.

Equation (1) is the sum of the individual component equations:

$$\frac{\partial}{\partial t}\left(\frac{\overline{u'^2}}{2}\right) = -2\Omega_y\overline{u'w'} - \overline{u'w'}\frac{\partial \bar{u}}{\partial z} - \frac{\partial}{\partial z}\left(\frac{\overline{w'u'^2}}{2}\right) - \frac{\overline{p'\partial u'}}{\rho\,\partial x} - \frac{\varepsilon}{3} \qquad (2)$$

$$\frac{\partial}{\partial t}\left(\frac{\overline{v'^2}}{2}\right) = -\overline{v'w'}\frac{\partial \bar{v}}{\partial z} - \frac{\partial}{\partial z}\left(\frac{\overline{w'u'^2}}{2}\right) - \frac{\overline{p'\partial v'}}{\rho\,\partial y} - \frac{\varepsilon}{3} \qquad (3)$$

$$\frac{\partial}{\partial t}\left(\frac{\overline{w'^2}}{2}\right) = 2\Omega_y\overline{u'w'} + \alpha g\overline{\theta'w'} - \frac{\partial}{\partial z}\left(\frac{\overline{w'(w'^2+2p')}}{2\rho}\right) - \frac{\overline{p'\partial w'}}{\rho\,\partial z} - \frac{\varepsilon}{3} \qquad (4)$$

In (4) the thermal expansion coefficient α increases with depth, causing pressure-augmentation of the buoyancy flux. The Ω_y terms in (2) and (4) are identical except for sign and represent the transfer of energy between components, depending upon the sign of the Reynolds stress.

2.1 Steady-state free convection

For steady state, horizontal homogeneity and no surface stress, the TKE budget (1) is reduced to

$$0 = \alpha g\overline{\theta'w'} - \frac{\partial}{\partial z}\left(\frac{\overline{w'(E+p')}}{\rho}\right) - \varepsilon \qquad (5)$$

In this condition of free convection, there is a balance between the generation of turbulence by positive buoyancy flux, $\alpha g\overline{\theta'w'} > 0$, the vertical transport of turbulence and its rate of viscous dissipation, ε. Equation (5) may be integrated vertically between the surface, $z=0$, and the bottom of the turbulent boundary layer at $z=-h$:

$$0 = \int_{-h}^{0} \alpha g\overline{\theta'w'}dz - \int_{-h}^{0} \varepsilon dz \qquad (6)$$

The transport term makes no net contribution over the vertical extent of the turbulent region because transport can only redistribute the TKE, making no net contribution to the total TKE within the region.

2.1.1 Shallow, buoyancy-conserving mixing

The vertical flux profiles for conservative properties in well-mixed boundary layers in a steady free convective state are well understood. Potential temperature is conserved for both shallow and deep mixing. However, buoyancy conservation depends upon depth of mixing. For relatively shallow mixed layers, the thermal expansion coefficient α may be considered constant in depth for the whole turbulent boundary layer. Then buoyancy may be considered a conservative property, and the profile of the vertical flux of buoyancy will be linear in z, provided the potential temperature is approximately homogeneous in the mixed layer. Absolute neutrality is not necessary, but approximate homogeneity of $\bar{\theta}$ is invoked, again for the sake of simplicity here. Then, for such shallow mixed layers (6) becomes

$$0 = \alpha g\overline{\theta'w'}\Big|_{0}\frac{h}{2} + \alpha g\overline{\theta'w'}\Big|_{-h}\frac{h}{2} - \int_{-h}^{0} \varepsilon dz \qquad (7)$$

If there is steady state, dissipation will be a fixed fraction of the net production for the free-convective case, and (7) may be written:

$$\overline{\theta'w'}\Big|_{-h} = -A\overline{\theta'w'}\Big|_{0} \qquad (8)$$

Stull (1976) found a consensus estimate for the value of the constant, $A \approx 0.2$. Expression (8) is reasonable for free convection in the case of shallow oceanic mixing, but it will not be appropriate for deep mixing where buoyancy will not be conserved or when steady state is not achieved.

2.1.2 Deep mixing with buoyancy not conserved

Buoyancy is not conserved if the thermal expansion coefficient α is not constant over the vertical extent of turbulent mixing. Figure 1 shows how the thermal expansion coefficient changes with

both potential temperature and depth. For most oceanic mixed layers, the mixing depth is of the order 100 m or less, and α may be considered constant. However, for $h \geq 1$ km, α may increase significantly above the surface value, depending upon mixed layer temperature as illustrated by Figure 1. The effect is most notable for cold water. Going from the surface to a 4000 m depth, with an intermediate salinity of S=32 psu, α increases from 1.81×10^{-4} to 2.42×10^{-4} if $\bar{\theta} = 12$C, an increase of 33%. However, for $\bar{\theta} = -2$C, α increases from 0.15×10^{-4} to 0.28×10^{-4}, an increase of more than 800%.

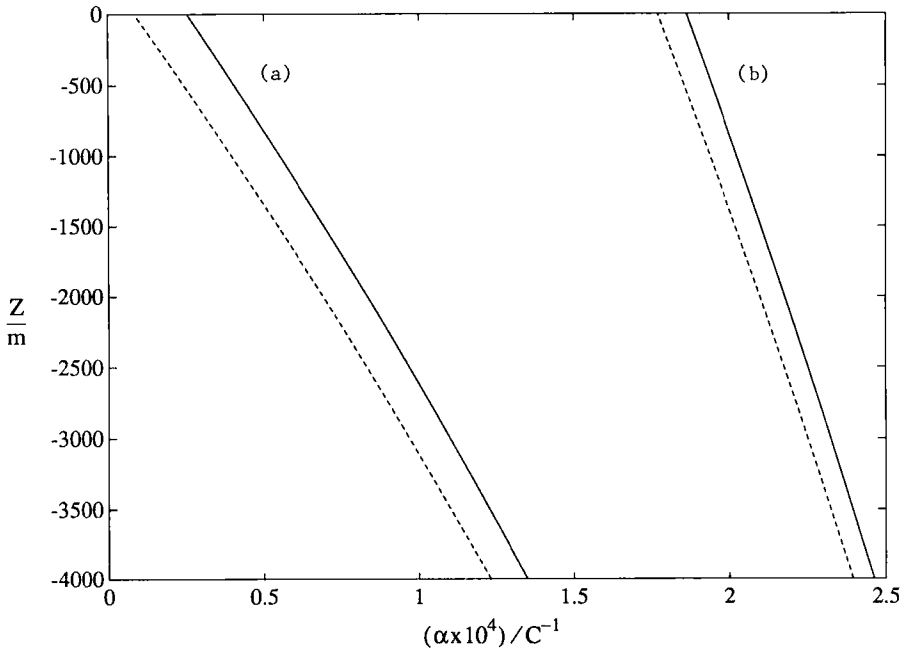

Fig. 1. Dependence of the thermal expansion coefficient upon depth for potential temperatures of (a) -2 C, and (b) 12 C. S=30 psu for dashed curves and S=35 psu for solid curves.

A similar problem with buoyancy not conserved occurs for free convection in a moist atmospheric boundary layer with clouds. Unlike free convection for which buoyancy is conserved, moist atmospheric convection is similar to deep oceanic convection because in both situations the entrainment buoyancy flux can not be expressed as a simple fraction of the upward surface buoyancy flux. Rather, the vertical integral of the buoyancy flux must be calculated. Addressing this problem, Deardorff (1976) expressed the entrainment work rate as a fixed fraction of the net work rate by buoyant forces on the whole boundary layer,

$$-\alpha g \overline{w'\theta'}|_{-h} = \frac{m}{h} \int_{-h}^{0} (\alpha g \overline{w'\theta'})\, dz \qquad (9)$$

Equation (9) is therefore a more universal solution for penetrative convection that is powered by free convection, whether or not buoyancy is conserved. If buoyancy is conserved, (7), (8) and (9) can be used to show that

$$m = \frac{2A}{1-A} \tag{10}$$

Hence Deardorff's value of m=0.5 is equivalent to Stull's value of A=0.2 when buoyancy is conserved. However, the value of A will vary, depending upon the vertical distribution of sources and sinks for buoyancy if buoyancy is not conserved.

Another universal result from (9), with m=0.5, is that 80% of the buoyantly-produced TKE is viscously dissipated and 20% is available for penetrative convection, independent of any requirement for buoyancy conservation.

For an initial investigation into the salient properties of deep free convection, Deardorff's entrainment hypothesis (9), together with a prescribed $\alpha(z)$, is applied to representative oceanic cases. Representative values for surface heat flux and ambient conditions of potential temperature, salinity and mixing depth are provided by observations of the convective chimneys in the arctic, antarctic and Mediterranean Sea.

As is evident in Figure 1, the thermal expansion coefficient varies with temperature, salinity and pressure (depth). The variation with depth is nearly linear, or

$$\alpha \approx \alpha_0(\bar{\theta}, \bar{S}) - a_1(\bar{\theta}, \bar{S})\, z \tag{11}$$

where α_0 is the thermal expansion coefficient at the surface, and a_1 is a coefficient for the pressure-enhancement of buoyancy.

$$a_1 = g\frac{\partial^2 \rho_\theta}{\partial p \partial \theta} \tag{12}$$

Using (11), together with (9), the buoyancy flux profile may be derived as a function of the upward surface heat flux Q_0 and the mixed layer depth (h):

$$\alpha g\overline{w'\theta'}(z) = \frac{(\alpha_0 - a_1 z)\, gQ_0}{\rho C_p}\left[1 + \left(\frac{mK_1}{m+2K_2}\right)\frac{z}{h}\right] \tag{13}$$

where

$$K_1 = \frac{a_1 h}{3\alpha_0} + 1 \tag{14}$$

and

$$K_2 = \frac{2a_1 h}{3\alpha_0} + 1 \tag{15}$$

Figure 2 shows solutions to (13) for two cases that demonstrate the importance of temperature for very deep convection, with $\alpha(z)$ corresponding to the two cases depicted in Figure 1.

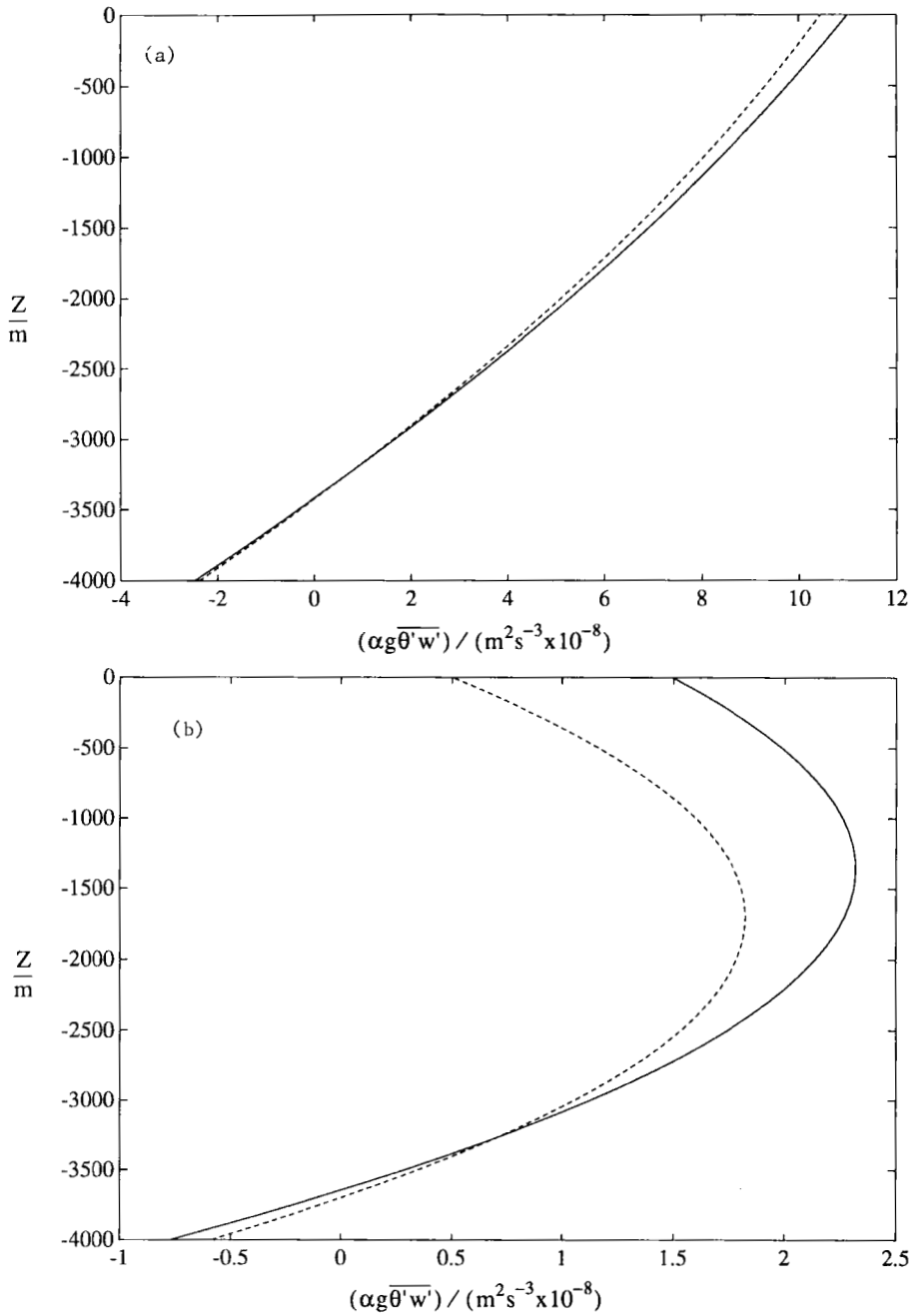

Fig. 2. Steady-state free convection buoyancy flux profiles for potential temperature of (a) 12 C, and (b) -2 C. Solid curves are for S=35 psu, and dashed curves are for S=30 psu. Surface heat flux is 250 watts per square meter in all cases.

The curve in Figure 2a may be representative of the buoyancy flux profile for very deep free convection in the western Mediterranean Sea. Clearly, this buoyancy flux profile departs from a linear shape that would be indicative of buoyancy conservation. Although the degree of nonlinearity is not negligible for the Mediterranean Sea case, it is not as significant as it is for a colder ocean.

The curve in Figure 2b may be representative of the buoyancy flux profile for very deep free convection in a polar sea. In such cold polar waters, buoyancy is very non-conservative, and the deviation from a linear profile is extreme. Also, potential temperature has a more significant role than does salinity in determining the shape of the buoyancy flux profiles. However, it is notable that salinity differences have a potentially greater influence on the buoyancy flux profiles for the cold ocean than they have in warmer seas.

To better generalize the relative importance of depth of mixing and potential temperature, a depth scale for the pressure-enhancement of buoyancy flux is defined:

$$H_\alpha = \frac{\alpha|_{z=0}}{\frac{\partial \alpha}{\partial z}} \approx \frac{\alpha_0}{a_1} \qquad (16)$$

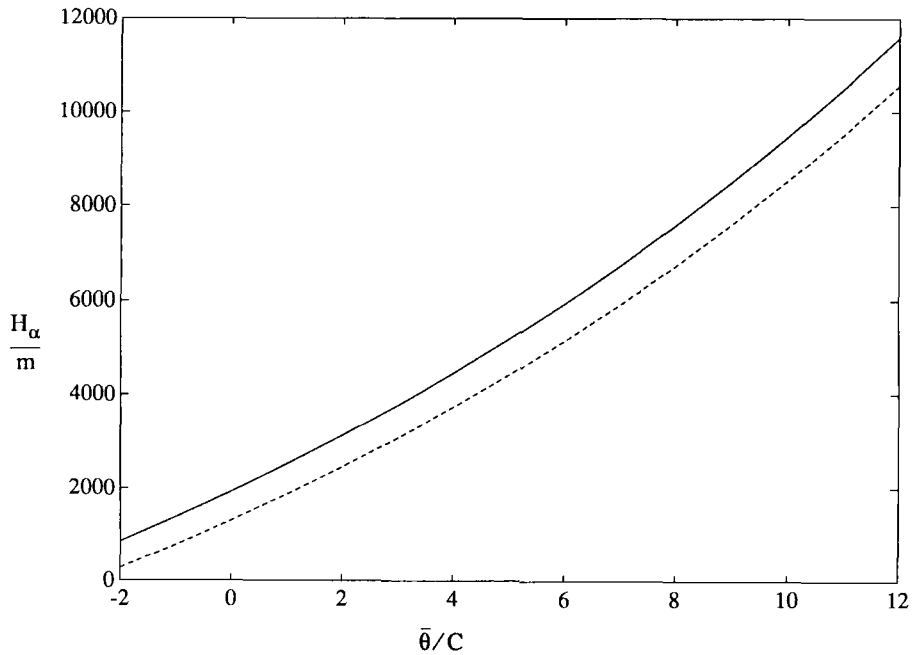

Fig. 3. Dependence of H_α upon potential temperature for S=35 psu (solid) and S=30 psu (dashed).

The size of H_α increases strongly with potential temperature and slightly with salinity (Figure 3). A dimensionless depth of mixing may be defined as h/H_α. For the two cases above, H_α is 11000 m for the Mediterranean Sea and 500 m for the polar sea case. For a mixing depth of 4 km in each case, the dimensionless mixing depths are about 0.36 and 8.0 for the warm and cold-water cases, respec-

tively. Hence The Mediterranean Sea case, with $h/H_\alpha < 1$, is only marginally "deep," but the polar sea case may be considered "deep," with a value for h/H_α that is more than 20 times as large. As a general rule, buoyancy may be assumed to be conserved for $h/H_\alpha \ll 1$. Hence, for the Mediterranean Sea, pressure effects on the buoyancy flux are negligible for mixing depths less than about 1 km. For the coldest ocean waters, however, the dependence of α upon pressure should not be neglected for mixed layer depths greater than about 100 m.

The value for the entrainment mixing factor, A in (8), may be derived in terms of m, α_0, and $a_1 h$:

$$A = \frac{3\alpha_0 + a_1 h}{(3 + \frac{6}{m})\,\alpha_o + (2 + \frac{6}{m})\,(a_1 h)} \qquad (17)$$

This may be written in terms of the dimensionless mixing depth, letting m=0.5:

$$A = \frac{3 + h/H_\alpha}{15 + 14\,(h/H_\alpha)} \qquad (18)$$

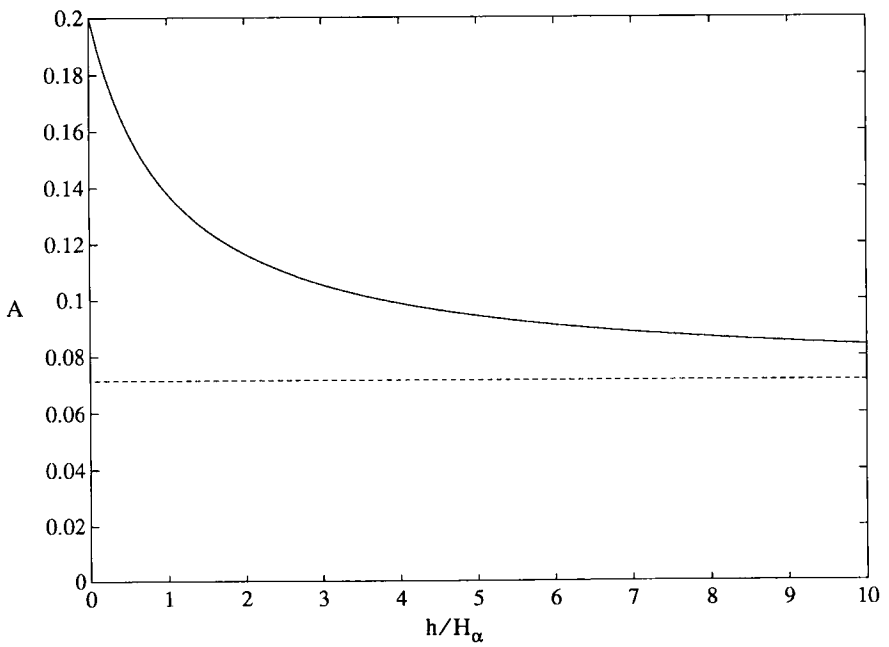

Fig. 4. Dependence of entrainment flux to surface flux ratio, A, upon h/H_α.

Figure 4 illustrates how A is reduced from its maximum value of $A_{max} = (1+\frac{2}{m})^{-1} = 0.2$ for the most shallow free convection when buoyancy is conserved to a value that is asymptotic on $A_{min} = (2+\frac{6}{m})^{-1} = \frac{1}{14}$ for $h/H_\alpha \rightarrow \infty$, for the coldest and deepest mixed layers.

2.2 Enhancement of forced convection by planetary rotation

With zero or negative surface buoyancy flux, turbulence may be produced only by shear production, converting wind-generated mean kinetic energy to horizontal TKE. With entrainment mixing, a buoyancy flux is generated, but it will be negative and consume TKE throughout the turbulent boundary layer. Normally, forced convection cannot mix a stratified water column very deeply because the potential energy increase that is associated with vertical mixing is not efficiently provided by the highly dissipative turbulence. For turbulence generated by free convection, 80% or more of the energy is dissipated. For typical forced convection regimes, the percentage lost to dissipation may be even greater because wind forcing generates horizontal TKE. Before vertical mixing can occur, some of the horizontal turbulence must be converted to the vertical component by pressure redistribution (next-to-last terms in eqs. 2-4).

Provided the Reynolds stress component, $\overline{u'w'}$ is positive, there is an additional mechanism for converting TKE from horizontal to vertical that may increase the efficiency of the conversion of wind energy to oceanic potential energy. The physical explanation for this is that when the wind stress is toward the west, there will be a vertical elongation of the wind-forced convective eddies due to the inertial tendency provided by Ω_y. This is evident in the momentum budgets for the turbulent velocities:

$$\frac{\partial u'}{\partial t} = fv' - 2\Omega_y w' + \ldots. \qquad (19)$$

$$\frac{\partial w'}{\partial t} = 2(\Omega_y w') + \ldots. \qquad (20)$$

The component TKE equations arise from the products of u' with the terms of (19) and of w' with the terms of (20):

$$\frac{\partial}{\partial t}\frac{u'^2}{2} = u'\frac{\partial u'}{\partial t} = fv'u' - 2\Omega_y u'w' + \ldots. \qquad (21)$$

$$\frac{\partial}{\partial t}\frac{w'^2}{2} = w'\frac{\partial w'}{\partial t} = 2\Omega_y u'w' + \ldots. \qquad (22)$$

Hence when $\overline{u'w'}$ is positive (negative) for a westward (eastward) wind stress, the Coriolis force acts to increase (decrease) vertical TKE. Depending upon the sign of the Reynolds stress, TKE is converted from horizontal to vertical or vice versa.

3 MODEL FOR UNSTEADY DEEP CONVECTION: PRELIMINARY DEMONSTRATION

The Naval Postgraduate School second-order closure, vertically-integrated mixed layer model was modified to include both pressure-enhancement of buoyancy flux and rotational redistribution of TKE. Table I summarizes the model equations, configured for solving the unsteady TKE budget for very deep mixing that is forced by upward surface heat flux and wind stress. The results of three simple numerical experiments for forced and predominantly free convection into very weakly stratified water follow. The initial stratification is purposely weak, emulating a water column that was "preconditioned" so as to be readily mixed so that the potential role of unsteadiness can be best evaluated.

3.1 Simulation with free convection dominant

The results in 2.1.2 above for the effect of pressure upon free convection, equations (13) and (17), presume a steady-state condition. However, solving the system of equations (Table I) as an initial-value problem with a constant westward wind stress of 0.2 and an upward surface heat flux Q_0= 250 watts/m^2 demonstrates the importance of unsteadiness during the first couple days after the onset of a surface cooling event that might be representative of the Greenland Sea during winter. For initial conditions, the mixed layer is assumed to be 30 m deep, with an underlying very weak stratification in the potential temperature of $10^{-6}Cm^{-1}$ and a homogeneous salinity of 35 Kg/m^3. The turbulent boundary layer depth (Figure 5a) increases initially with an entrainment velocity of about 1.5 cm/sec, but this increases to a maximum entrainment rate of almost 10 cm/sec after about 7 hours.

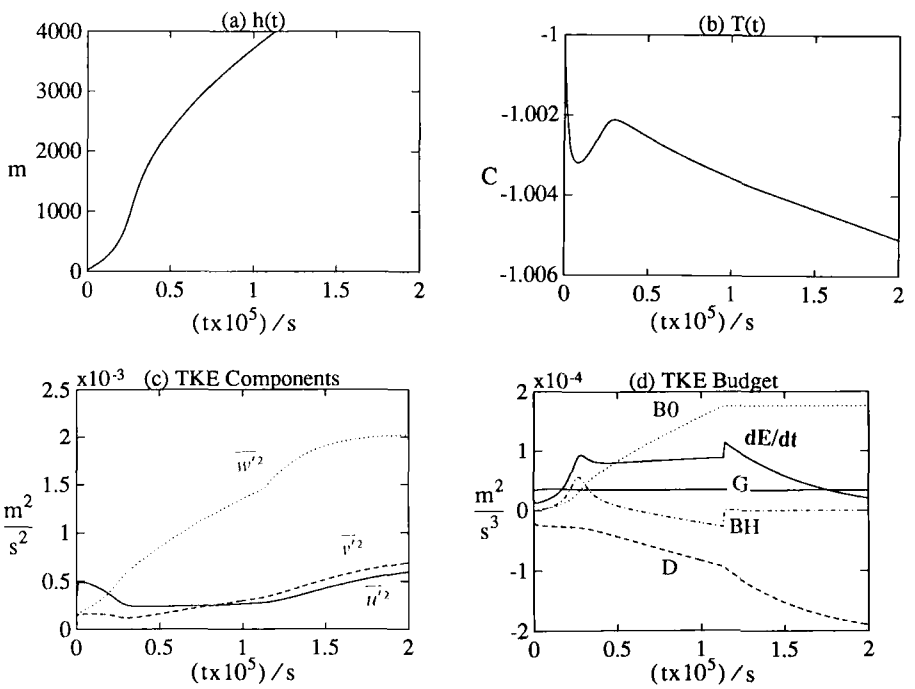

Fig. 5. Model results with strong surface cooling: (a)Turbulent boundary layer depth, (b) Mixed layer temperature, (c) TKE components, (d) Shear production, G, dissipation, D, entrainment buoyancy flux, BH, surface buoyancy flux, B0, and storage, dE/dt.

At time t=1.12x10^{5}sec (31 hours after the start), the turbulent boundary layer reaches the bottom at z = -4000 m. The mixed layer temperature (Figure 5b) cools most rapidly at the outset because the heat is taken out of a relatively shallow layer. It cools so rapidly that the mixed layer actually becomes somewhat cooler than the underlying water, and the entrainment zone is hydrostatically unstable. Because the entrainment model realistically limits the entrainment velocity so that it cannot exceed the vertical velocity of the turbulence (Figure 5c), the deepening rate is accelerated as indicated, but the top-to-bottom mixing requires 31 hours to be achieved.

Figure 5c also provides evidence of when the production of vertical TKE by buoyancy flux begins to dominate over the shear production of horizontal TKE. This occurs at time t=2x10^4 sec when the turbulent boundary layer is about 500 m deep. Soon after this time the surface wind stress becomes less and less significant, and the regime becomes predominantly free convective.

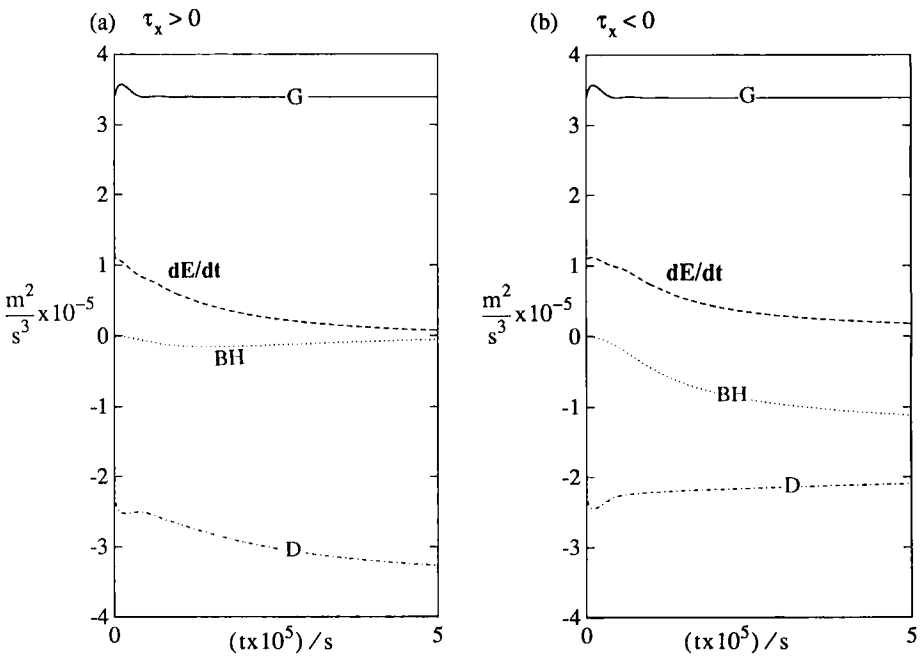

Fig. 6. Forced convection TKE budgets for (a) Eastward wind stress, and (b) Westward wind stress. Shear production is G, Dissipation is D, Entrainment buoyancy flux is BH, and Storage is dE/dt.

The magnitudes of the terms of the TKE budget are displayed in Figure 5d. Initially, the balance is mostly between dissipation (D) and shear production (G). The size of G remains almost constant throughout the experiment, reflecting the constant value of wind-shear production (near the surface) and a varying but much smaller entrainment shear production. At time t=2x10^4 sec, the net buoyant production (surface plus entrainment components), B0+BH, exceeds G, and hence the regime changes from predominantly forced convection to predominantly free convection. Unlike the steady-state solutions for free convection, yielding predictions of a negative entrainment buoyancy flux or

A > 0 in (18), the entrainment buoyancy flux in this unsteady experiment is positive from the outset until shortly after time t=6x10^4 sec when the mixed layer temperature is no longer cooler than the underlying water, even though it is still cooling (Figure 5b). The unsteadiness or storage term for the TKE budget is a relatively large term for most of the experiment, falling to lesser value only after the turbulent boundary layer has expanded to its limiting thickness when the bottom is reached. Even then the component values of the turbulence continue to rise (Figure 5c), and equilibrium state is approached only after an additional day model integration. A major conclusion here is that steady-state solutions for free convection are probably not appropriate for surface cooling events that are limited to a few days or less in duration.

3.2 Forced convection experiments

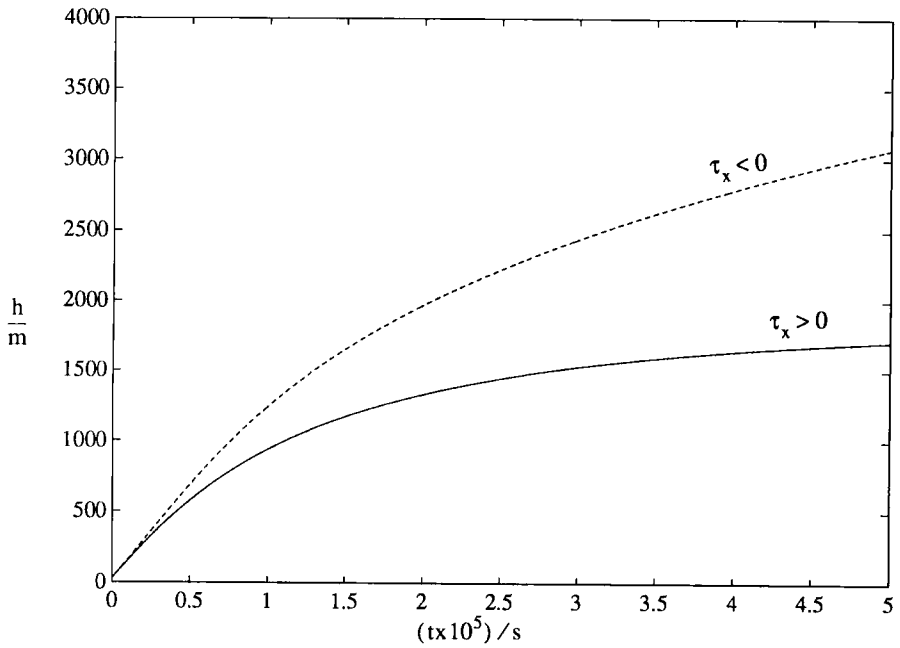

Fig. 7. Mixed layer depth for forced convection experiments. Eastward wind stress curve is solid, and westward wind stress curve is dashed.

Starting with the same initial conditions as above, but with no surface buoyancy flux, the model is solved for two cases of purely forced convection: (i) with the wind stress toward the west, and (ii) with the wind stress toward the east. The TKE budgets for these cases are displayed in Figures 6a and 6b, respectively. With the wind toward the west, the mixed layer continues to deepen throughout the integration period of 10^5 sec (Figure 7). However, for the wind in the opposite direction, mixed layer deepening ceases half way through the period. The reason for the difference is the rotational redistribution of TKE between horizontal and vertical components. When the wind stress is toward the west, planetary rotation acts to convert horizontal TKE to vertical TKE. When the wind is in the opposite

direction, vertical turbulence is converted to horizontal turbulence. The plot of mixed layer depth (Figure 7 solid curve) and Figure 8a show that the cessation of entrainment for the second case coincides with the loss of vertical turbulence to horizontal turbulence by rotational redistribution.

A quasi-steady state is nearly achieved by the end of the period of model integration for the easterly wind stress case. Figures 6a and 7 show that the mixed layer almost stops deepening by the end of the period when the TKE budget is almost entirely between shear production, G, and dissipation, D. Figure 8a shows that the vertical turbulence is much smaller than either of the horizontal components after the first couple days because of the rotational conversion of vertical to horizontal turbulence. For the westerly wind stress case, however, the entrainment buoyancy flux, BH, is a significant loss term throughout the period of integration, and a balance is achieved between G, D, and BH (Figure 6b). The growing intensity of vertical turbulence (Figure 8b) causes continued strong deepening and hence strong buoyant damping by entrainment, BH. For both wind directions, it is evident that unsteadiness is not as significant as it was for the case with surface cooling and much more rapid deepening. A principal conclusion for this set of forced convection experiments is that the turbulence is not as energetic as it is for free convection, but the rotational mechanism may help achieve a sufficiently deep surface layer to "turn on" the free convection that has buoyancy flux enhanced by the pressure dependence for the thermal expansion coefficient.

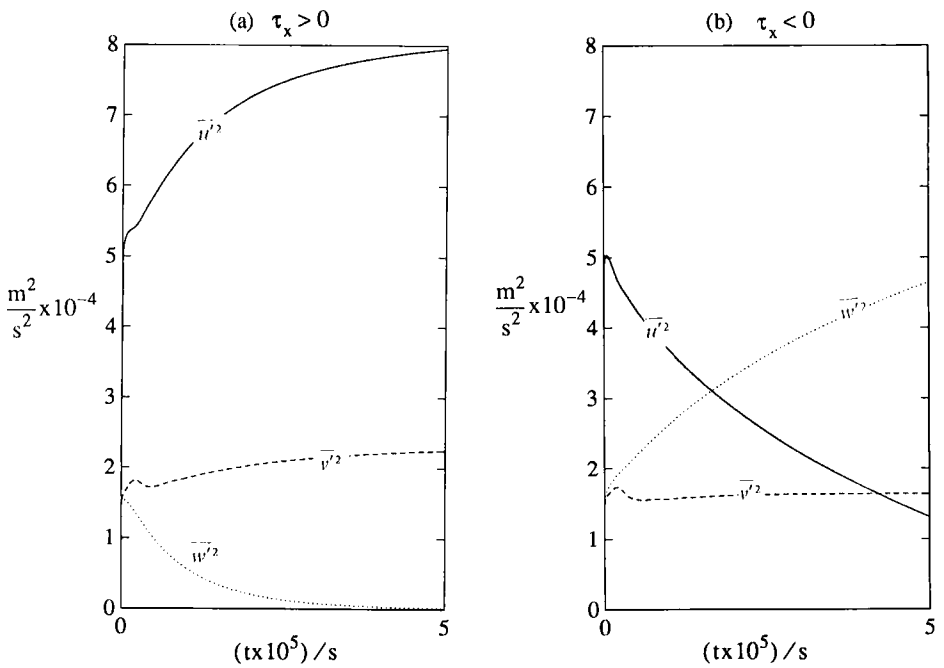

Fig. 8. Forced convection TKE components for (a) Eastward wind stress, and (b) Westward wind stress.

TABLE 1 NPS Mixed Layer Model For Deep Convection

The vertically-integrated (bulk) turbulent kinetic energy equations:

$$\partial(h\overline{u'^2})/\partial t = 2m_3(\tau_x/\rho)^2/u_* + (\Delta U)^2 w_e + R_x + R_\Omega - D/3 \tag{I.1}$$

$$\partial(h\overline{v'^2})/\partial t = 2m_3(\tau_y/\rho)^2/u_* + (\Delta V)^2 w_e + R_y - D/3 \tag{I.2}$$

$$\partial(h\overline{w'^2})/\partial t = B_o - B_H + R_z - R_\Omega - D/3 \tag{I.3}$$

The mixed layer depth equation:

$$\partial h/\partial t = w_e - W_{-h} \tag{I.4}$$

The mixed layer temperature, salinity and momentum budgets:

$$\partial T/\partial t = -Q_o/(\rho c_p h) - \Delta T w_e/h \tag{I.5}$$

$$\partial S/\partial t = S(\text{e-p} + \text{r})/h - \Delta S w_e/h \tag{I.6}$$

$$\partial(hU)/\partial t = f(hV) + \tau_x/\rho \tag{I.7}$$

$$\partial(hV)/\partial t = -f(hU) + \tau_y/\rho \tag{I.8}$$

Functions

Entrainment velocity: $w_e = E(\overline{w'^2})^{1/2}/\{gh[(\alpha_o + a_1 h)\Delta T - \beta\Delta S] + E\}$

Depth-dependent thermal expansion coefficient: $\alpha(z) = \alpha_o - a_1 z$

Jumps: $\Delta U = (hU)/h$; $\Delta V = (hV)/h$; $\Delta T = T - (T_o - h\Gamma_T)$; $\Delta S = S - (S_o - h\Gamma_S)$

TKE components: $\overline{u'^2} = (h\overline{u'^2})/h$; $\overline{v'^2} = (h\overline{v'^2})/h$; $\overline{w'^2} = (h\overline{w'^2})/h$; Total, $E = \overline{u'^2} + \overline{v'^2} + \overline{w'^2}$

Entrainment buoyancy flux: $B_H = gh[(\alpha_o + a_1 h/1.5)\Delta T - \beta\Delta S]w_e$

Surface buoyancy flux: $B_o = (\alpha_o + a_1 h/3)ghQ_o/\rho c_p + \beta ghS(\text{e-p} + \text{r})$

Rotational redistribution: $R_\Omega = 2\Omega_y h\tau_x/\rho$

Press. redis.: $R_x = 2m_2(E - 3\overline{u'^2})E^{1/2}$; $R_y = 2m_2(E - 3\overline{v'^2})E^{1/2}$; $R_z = 2m_2(E - 3\overline{w'^2})E^{1/2}$

Viscous dissipation: $D = 2m_1(E)^{3/2}$

Model constants

Dimensionless constants: $m_1 = 1$; $m_2 = 0.5$; $m_3 = 6$

Dimensional constants have c.g.s units:

$\alpha_o = 4x10^{-5}$; $a_1 = .26x10^{-5}$; $\beta = 8x10^{-3}$; $g = 980$; $\rho = 1$; $f = 2\Omega\sin(\phi)$; $\Omega_y = \Omega\cos(\phi)$; $c_p = 1$

Initial $T(z)$ and $S(z)$: sfc. intercepts, T_o, S_o ; $\Gamma_T = \partial T/\partial z_{(z<-h)}$; $\Gamma_S = \partial S/\partial z_{(z<-h)}$

Time-dependent boundary conditions to be prescribed

Wind stress components: τ_x, τ_y, where friction velocity, $u_* = \{(\tau_x/\rho)^2 + (\tau_y/\rho)^2\}^{1/4}$

Net upward surface heat flux: $Q_o = Q_B + Q_H + Q_E - Q_S$

Net evaporation minus precipitation plus freezing in cm/sec: (e-p+r)

Mean vertical velocity at base of mixed layer: W_{-h}

4 CONCLUSIONS

- The significance of the pressure enhancement of buoyancy flux for free convection in deep oceanic mixed layers may be expressed in terms of the ratio of mixed layer depth (h) to a depth scale H_α that depends mostly upon the potential temperature. The value of H_α can be as low as 500 m for the coldest polar waters, but it is greater than 10 km for the Mediterranean Sea.
- For all cold (potential temperature of 0 C or less), deep (h greater than 100 m) mixed layers, pressure enhancement of the buoyancy flux should be explicitly included in entrainment calculations.
- In the Mediterranean Sea, the pressure enhancement of the buoyancy flux becomes important only for convection that penetrates to the bottom.
- Because of the effect of planetary rotation on the vertical convection motion of deep wind-driven eddies, wind direction may be important in determining the efficiency of wind-mixing. Forced convection by westward wind stress may be most efficient in deepening the mixed layer. This process may help initiate deep convection that is at first wind-driven and later buoyancy-driven.
- Unsteadiness cannot be neglected for the wind-forced convection events that deepen the mixed layer by more than 1 km within a few days time.

ACKNOWLEDGMENTS. This study was prepared for the Office of Naval Research with funding by the Naval Postgraduate School. I thank Ms. Arlene Bird for comments on this paper.

5 REFERENCES

Bennett, E. B., 1978. Characteristics of the thermal regime of Lake Superior. J. Great Lakes Res., 4, 310-319.

Carmack, E. C., and K. Aagaard, 1974. The formation of bottom water in the Greenland Sea, in Processus de Formation des Eaux Oceaniques Profondes en Particulier en Mediterranee Occidentale, vol. 215, p 65, Centre National de la Recherche Scientifique, Paris.

Carmack, E. C., and D. M. Farmer, 1982. Cooling processes in deep, temperate lakes: A review with examples from two lakes in British Columbia. J. Mar. Res., 40, Supp., 85-111.

Chu, P. C. and R. W. Garwood, Jr., 1988. Comment on 'A coupled dynamic-thermodynamic model of an ice-ocean system in the marginal ice zone.' J. Geophys. Res., 93, 5155-5156.

Eklund, H., 1965. Stability of lakes near the temperature of maximum density. Science, 149, 632-633.

Fofonoff, N. P., 1962. Physical properties of seawater, in The Sea, vol. 1, ed. by M. N. Hill, pp. 3-30, Wiley-Interscience, New York.

Gallacher, P. C., 1987. Importance of rotation shear stress for entrainment in the oceanic mixed layer. Ph. D. Thesis, Naval Postgraduate School, 136 pp.

Galperin, B., A. Rosati, L. H. Kantha, and G. L. Mellor, 1989: Modeling rotating stratified turbulent flows with application to oceanic mixed layers. J. Phys. Oceanogr., 19, 901-916.

Garwood, R. W., Jr., 1977: An oceanic mixed layer model capable of simulating cyclic states. J. Phys. Oceanogr., 7, 455-468.

Garwood, R. W., Jr., P. C. Gallacher, and P. Muller, 1985a: Wind direction and equilibrium mixed layer depth: General theory. J. Phys. Oceanogr., 15, 1325-1331.

Garwood, R. W., Jr., P. Muller, and P. C. Gallacher, 1985b: Wind direction and equilibrium mixed layer depth in the tropical Pacific Ocean. J. Phys. Oceanogr., 15, 1332-1338.

Gordon, A. L., 1978: Deep Antarctic convection west of Maud Rise. J. Phys. Oceanogr., 8, 600-612.

Hakkinen, S., 1987. A coupled dynamic-thermodynamic model of an ice-ocean system in the marginal ice zone. J. Geophys. Res., 92, 9469-9478.

Killworth, P. D., 1979. On "chimney" formations in the deep ocean. J. Phys. Oceanogr., 9, 531-554.

Lemke, P., W. B. Owens, and W. D. Hibler III, 1990. A coupled sea ice-mixed layer-pycnocline model for the Weddell Sea. J. Geophys. Res., 95, 9513-9526.

McDougall, T. J., 1984. The relative roles of diapycnal and isopycnal mixing on subsurface water-mass conversion. J. Phys. Oceanogr., 14, 1577-1589.

McDougall, T. J., 1987. Thermobaricity, cabbeling, and water-mass conversion. J. Geophys. Res., 92, 5448-5464.

Medoc Group, 1970. Observation of formation of deep water in the Mediterranean Sea. Nature, 227, 1037-1040.

Saint Guily, B., 1972. On the response of the ocean to impulse. Tellus, 24, 344.

Stommel, H., 1972. Deep winter-time convection in the western Mediterranean Sea. Studies in Physical Oceanography, A Tribute to George Wust on His 80th Birthday, Vol. 2, ed. by A. L. Gordon, pp. 207-218, Gordon and Breach, New York.

Wyngaard, J. C., S. P. S. Arya, and O. R. Cote, 1974. Some aspects of the structure of convective planetary boundary layers. J. Atmos. Sci., 31, 747-754.

This Page Intentionally Left Blank

Convection in Lake Baikal: An Example of Thermobaric Instability

Eddy C. Carmack[1] and Ray F. Weiss[2]

[1]Institute of Ocean Sciences
P.O. Box 6000, Sidney B.C., V8L 4B2, Canada

[2]Scripps Institution of Oceanography
University of California, San Diego
La Jolla, CA, 92093-0220, USA

ABSTRACT

Observations from Lake Baikal (maximum depth, 1632 m) are used to study the mechanism and rate of deep water renewal. The physical mechanism governing convection is the "thermobaric" instability; because the temperature of maximum density decreases with depth, a reversely stratified lake (surface temperature, T_s < bottom temperature, T_b) becomes unstable if the base of the cold mixed-layer is displaced downwards to a depth where its temperature matches that of maximum density. An important consequence of this mechanism is that Lake Baikal does not completely mix or "turn over" twice yearly. Instead, deep water renewal is episodic, and takes place only when sufficiently cold, surface-layer water is mixed downwards by wind forcing to the depth where convection can ensue. Profiles of temperature taken in early summer show three distinct layers culminating from this ventilation process: a 200 - 300 m thick upper layer of actively mixing water from which the thermobaric instability is initiated; a mid-depth layer of older vintage water marked by an exponential decrease in temperature; and a near-bottom layer of relatively new water distinguished by an abrupt change in temperature gradient. Temperature profiles from the northern and central basins show numerous inversions relative to the temperature of maximum density, indicating that convection was still active in these regions at the time of our survey. Profiles of chemical parameters (i.e. oxygen, nutrients, and dissolved atmospheric chlorofluorocarbon-12) are qualitatively consistent with the conclusions drawn from temperature measurements. Because renewal events are dependent upon mechanical displacement of cold water downwards, an asymmetry between the efficiency of deep water renewal in spring (ice covered and wind shielded) and autumn (ice free and wind mixed) is predicted.

1. Introduction

Lake Baikal is the deepest (1632 m) lake in the world. Of key importance to any deep lake system is the time scale of deep water renewal, for it is the deep convection process that most strongly controls the internal redistribution of biogeochemical properties such as dissolved oxygen, nutrients, and pollutants (see Wüest, et al., 1988). Baikal is a "temperate" lake; i.e. one in which the surface water passes through the temperature of maximum density ($T_{\rho max}$) in autumn and spring (Hutchinson, 1957; Carmack and Farmer, 1982). It does not necessarily follow, however, that such lakes "turn over" or mix completely twice yearly. This is because the temperature of maximum density ($T_{\rho max}$) decreases with increasing pressure (about 0.021 $^{\circ}C \cdot bar^{-1}$), so that while water near 4 °C is at maximum density at the surface, it is less dense than slightly colder waters at depth, and thus cannot possibly displace by free convection any colder underlying waters that may lie closer to the $T_{\rho max}$ versus depth curve; hence a additional physical mechanism is required to allow displacement of older deep water.

It has long been known that bottom temperatures in many deep lakes remain below 4 °C throughout the year (Vereshchagin, 1927, 1933; Wright, 1931; Yoshimura, 1936; Johnson, 1964). Strom (1945) showed that many deep lakes also exhibit a slope change in their temperature versus depth during winter; temperatures increase from 0°C at the surface to a maximum at mid-depth, and then decrease towards the bottom. Strom thought the slope of the temperature profile below the temperature maximum represented, in fact, the curve of $T_{\rho max}$ versus depth. On this point he was incorrect, but we must acknowledge his observations and synthesis. Eklund (1963, 1965) obtained an expression for the $T_{\rho max}$ versus depth curve based on a simplified equation of state for fresh water, and further suggested that maximum static stability is obtained when the in situ temperature gradient is midway between isothermal and the $T_{\rho max}$ versus depth curve. Bennett (1976) derived a similar expression for stability taking into account both compressibility and contraction on mixing in evaluating the net work required for mixing (cf. Eckel, 1949; Fofonoff; 1961). While these thermodynamic theories illustrate the importance of non-linear processes, and demonstrate the existence of a unique temperature profile yielding maximum stability, they do not explain the dynamical processes actually leading to ventilation.

Farmer and Carmack (1981) emphasized two ways that the unique properties of fresh water can influence convection at temperatures near that of maximum density. First, because of the quadratic dependence of density on temperature, the magnitude and sign of the buoyancy flux depends on the mixed-layer temperature and well as the rate of cooling. More importantly, since the

temperature of maximum density decreases with depth, a reversely stratified lake can be made conditionally unstable if the base of the mixed layer is lowered to a depth where its temperature matches that of maximum density. The arguments below start from the theory of Farmer and Carmack (1981) and lead to an intuitive model of convection in deep, temperate, freshwater lakes based on the differential compressibility of water. We will ignore for simplicity any density driven convection due to dissolved and suspended solids. This assumption is valid for Baikal, but must be verified by observations in other lakes (Weiss, et al., 1991).

2. Phenomenology

Terminology - Non-linearities in the equation of state for natural waters are due mainly to temperature, and are most pronounced in cold waters. Non-linear effects fall into two main types: the **thermostoltic** effects (from the Greek word "systole" meaning contraction), which arise from contraction on mixing of waters of different temperatures (Eckel, 1949; Mamayev, 1972), and the **thermobaric** effects, which arise from the differential compressibility of water (Ekman, 1934; Fofonoff, 1956; McDougall, 1987). In thermodynamic terms, thermostaltic effects are irreversible, while thermobaric effects are reversible. Both non-linear effects have associated instabilities: the **cabbeling instability**, which occurs when the mixture of two water masses is denser than either parent water mass (Witte, 1902; Foster, 1972), and the **thermobaric instability**, which results when an interface is displaced to a depth (pressure) at which it is no longer statically stable. Such instabilities arising from non-linear effects depend on an interaction between two or more different water masses of equal or near equal density. In sea water, a difference in salinity allows two waters of different temperature to have near-equal densities; in fresh water, the occurrence of a density maximum at temperatures above freezing plays an analogous role. Our focus here is on thermobaric effects; we emphasize that the mechanism we discuss is **not** the "thermal bar" circulation, which is related to thermostoltic effects (cf. Carmack, 1979).

Thermobaric Instability - To see how the differential compressibility of water can lead to a convective instability, consider the following scenario. Suppose a layer of cold water overlies a layer of slightly warmer water, both colder than 4 °C (Figure 1a). At all depths the lower water is nearer the $T_{\rho max}$ curve than the upper water, and so the interface is stable. Suppose now that the interface is moved downwards, so that the interface between the two layers crosses the $T_{\rho max}$ curve and the densities of the two layers at the interface are equal (Figure 1b). The interface is then neutrally stable. We will refer to the depth at which two parcels of water of different temperature have equal densities as the local compensation depth, h_c.

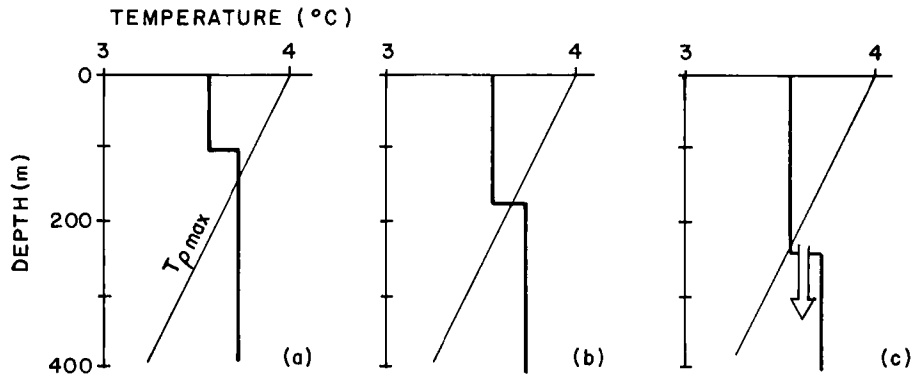

Figure 1. Schema illustrating conditions leading to the onset of the conditional instability.

With further deepening the interface becomes unstable, and convection ensues (Figure 1c). Once this mechanism is triggered, the convecting elements will start to sink and, in the absence of mixing with ambient waters, can reach the bottom unless colder (denser) waters are encountered at some greater depth.

Consider, now, the annual cycle beginning with a typical temperature profile for late summer (Figure 2a). Initially, when surface temperatures are above 4 °C, surface heat loss and wind mixing simply cool and deepen the mixed layer. As surface temperatures fall below 4 °C, however, the sign of the buoyancy flux (relative to surface pressure) changes. Between 4 °C and T_c the temperature profile tends to advance along $T_{\rho max}$ (Figure 2b). As surface temperatures drop below bottom temperatures, the lake becomes reversely stratified, with colder water overlying warmer water. However, the potential for the thermobaric instability is now established. For example, suppose that strong winds mix or displace the surface layer downward such that the interface reaches its local compensation depth; this will trigger the conditional instability and allow deep water ventilation (Figure 2c).

To understand spring convection we start with typical winter conditions in a frozen lake; i.e. temperature increases with depth from 0°C at the ice/water interface down to the depth, h_c, at which it crosses the $T_{\rho max}$ curve, and is constant below (Figure 3a). For deep ventilation to occur, clearly the renewal water must be colder (i.e. closer to the $T_{\rho max}$ curve) than existing deep water; this means that renewal can occur only if cold surface water is mechanically driven below the local compensation depth. But, in the presence of an ice cover the main warming in spring is by solar radiation penetrating the ice cover. The resulting radiation-induced convection forms a deepening mixed layer that advances into the stable

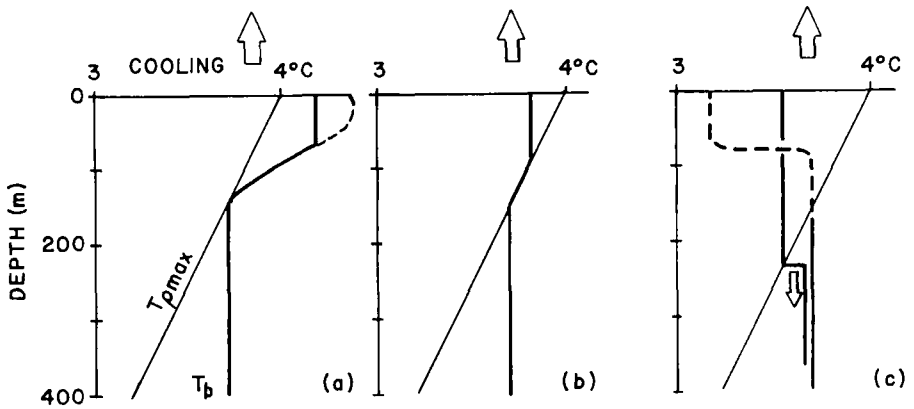

Figure 2. Schema illustrating the sequence of events leading to deep convection in autumn.

temperature profile below (Farmer, 1975). If the lake remains ice covered throughout this part of the temperature cycle, there may be no wind forcing to drive cold surface water below the depth h_c, and hence there would be little chance that deep ventilation could occur. Only if penetrative convection occurs such that cold plumes overshoot the interface to depths below their local compensation depth, will finite elements of water sink, but this is probably not an efficient ventilation mechanism. When the surface temperature warms above that of the bottom water, the potential for ventilation of deep water ends. Subsequent warming toward 4 °C would tend to a temperature curve above h_c that simply followed the $T_{\rho max}$ profile

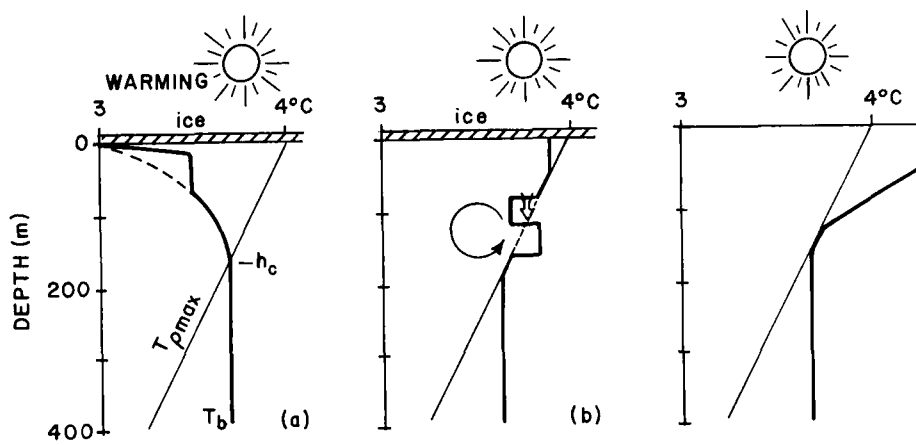

Figure 3. Schema illustrating the sequence of events leading to deep convection in spring.

up to the surface (Figure 3c), since convecting elements are only drawn to their local compensation depth. Warmer water that is forced below the $T_{\rho max}$ curve by wind mixing forms a stable base for the onset of stratification. When the surface temperature rises past 4 °C, heating begins to stabilize the surface layer, and the seasonal thermocline forms as a balance between wind mixing and buoyancy flux.

The above scenario of deep renewal involves three convective regimes: the upper convective regime which lies above the compensation depth of deep water; the deep regime in which convection can only be triggered by conditional instabilities at the compensation depth; and the near-bottom layer which is intended to represent new deep water. We admit, however, that the sequence of events by which surface water is first cooled and then displaced below its compensation depth has not been observed. It is likely that the one-dimensional process of mixed-layer deepening discussed above is enhanced by two-dimensional effects such as local wind convergence, internal seiche generation, or downwelling along lake boundaries (Figure 4). The amount of new deep water formed this way will depend on the frequency and severity of storms; hence, the autumn formation rate will probably exceed that of spring when ice cover can inhibit wind forcing.

Thermobaric Flow - The differential compressibility of water leads not only to the instability discussed above, but also to a mechanism for lateral flow through gravitational adjustment (Carmack and Hamblin, in preparation). This mechanism may explain a second feature of many deep temperate lakes in winter; namely, the mid-depth maximum in temperature. Large lakes do not cool or warm uniformly across their entire surface, nor are isotherms everywhere level. Instead, horizontal

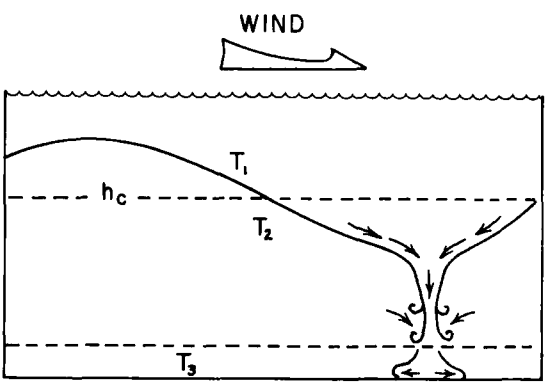

Figure 4. Schema illustrating how internal deformations such as local wind convergence, internal seiche generation, or downwelling can displace cold surface water below its local compensation depth and trigger the thermobaric instability. T_1 is the temperature of the upper layer, T_2 of the mid-depth layer, and T_3 of the near-bottom layer.

temperature gradients develop during convective episodes, which subsequently lead to gravity-driven currents. To see how this leads to the formation of a mid-depth temperature maximum layer in winter, consider two columns of water, each with uniform but different temperature temperatures, $T_1 < T_2 < 4°C$, are juxtaposed (Figure 5a). The colder column is lighter than the warmer at the surface, and thus will spread as a density current across the surface; at the same time, due to differential compressibility, the colder column is denser than the warmer at depth, and will thus spread as a density current along the bottom (Figure 5b). Hence, the cold column bifurcates, with the warm column intruding at mid-depth, thus forming the mid-depth temperature maximum (Figure 5c).

An estimate of the adjustment time scale for thermobaric flow can be obtained from the spreading rate for a density current $U = (g'H)^{1/2}$ where g' is the reduced gravity (see, Turner, 1973). As an example, for two columns of water at 3 and 4 °C, in a 1000 m deep lake, the density anomaly at 500 m is zero, while at the surface and bottom is 8×10^{-6} kg m^{-3}; thus a mean value for the upper and lower layers is 4×10^{-6} kg m^{-3}. Taking H = 250 m for the surface and bottom density flows, this yields a horizontal spreading speed of about 0.1 m s^{-1}. This estimate, however, does not take into account the modifications to the flow due to the Coriolis effect, which one would expect intuitively to produce a circulation similar to that seen in buoyancy boundary flow, with currents following their rightward boundaries in the northern hemisphere.

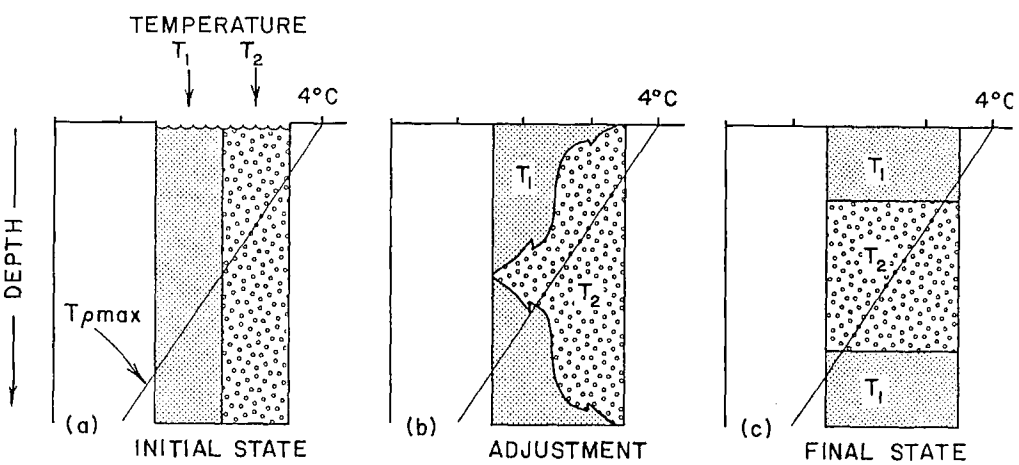

Figure 5. Schema illustrating the mechanism of thermobaric flow. Adjacent homogeneous columns of water of different temperature and equal density at mid-depth are allowed to collapse to form a temperature maximum around the compensation depth.

3. Observations in Lake Baikal

Data reported here were collected 15 - 24 July, 1988, aboard the *R.V. Vereshchagin* at twenty-six stations along sections crossing the three main basins of the lake (Figure 6). Two internally recording temperature/ conductivity/depth (CTD) systems were employed: an NBIS ("Smart") CTD, and an AML (Model 12) CTD. Both systems were paired to SeaTech Trans-missometers (0.25 m pathlength). The NBIS system gave greater temperature accuracy and finer depth resolution; the AML, however, was fitted with custom circuitry to measure the low values of conductivity extant in Baikal (ca. 0.100 mS cm^{-1}). Discrete water samples were collected at three stations in each of the basins using 5-litre Niskin bottles. Measurements of temperature and pressure for the discrete samples were taken using protected and unprotected thermometers. Shipboard analyses were made for oxygen, nutrients, and dissolved atmospheric chlorofluorocarbon-12 (CFC-12). Samples were also collected for shorebased measurements of major ions, trace elements, suspended particulate material, tritium, and helium isotopes; the results of these measurements will be reported elsewhere.

Temperature profiles from the southern, central, and northern basins of Lake Baikal illustrate some consequences of the above convective mechanism (Figure 7a-c). Plotted here are temperature data from our expedition as well as wintertime data from the southern basin reported by Vereschagin (1937). At the time of our expedition the central and northern basins had surface temperatures that were still below 4 °C while the southern basin had temperatures above 4 °C and was entering summer stratification. Hence, while convection was actively occurring in the upper layers of the north and central basins, the potential for deep water renewal was no longer extant, so that evidence for ventilation must be based on the inferred characteristics of the thermobaric mechanism. The most conspicuous feature of all three temperature profiles is the division into three layers. The upper layer roughly follows the $T_{\rho max}$ versus depth curve; the base of this layer is marked by the distinct "knee" in the temperature profile near the $T_{\rho max}$ curve at about 250 m. The north and central basin profiles show numerous temperature inversions, indicating that convection is still active within the upper layer. The mid-depth layer is marked by a gradual decrease in temperature from the knee downwards. Finally, the near-bottom layer is distinguished by the abrupt increase in temperature gradient approximately 100 m above the bottom. Near-bottom temperatures of 3.2 to 3.1 °C correspond to compensation depths of 400 to 450 m. The wintertime profile, obtained from the south basin, shows a temperature maximum layer near 200 m depth; it would thus appear that the summer knee is a remnant of winter temperature structure and represents the depth to which the thermobaric

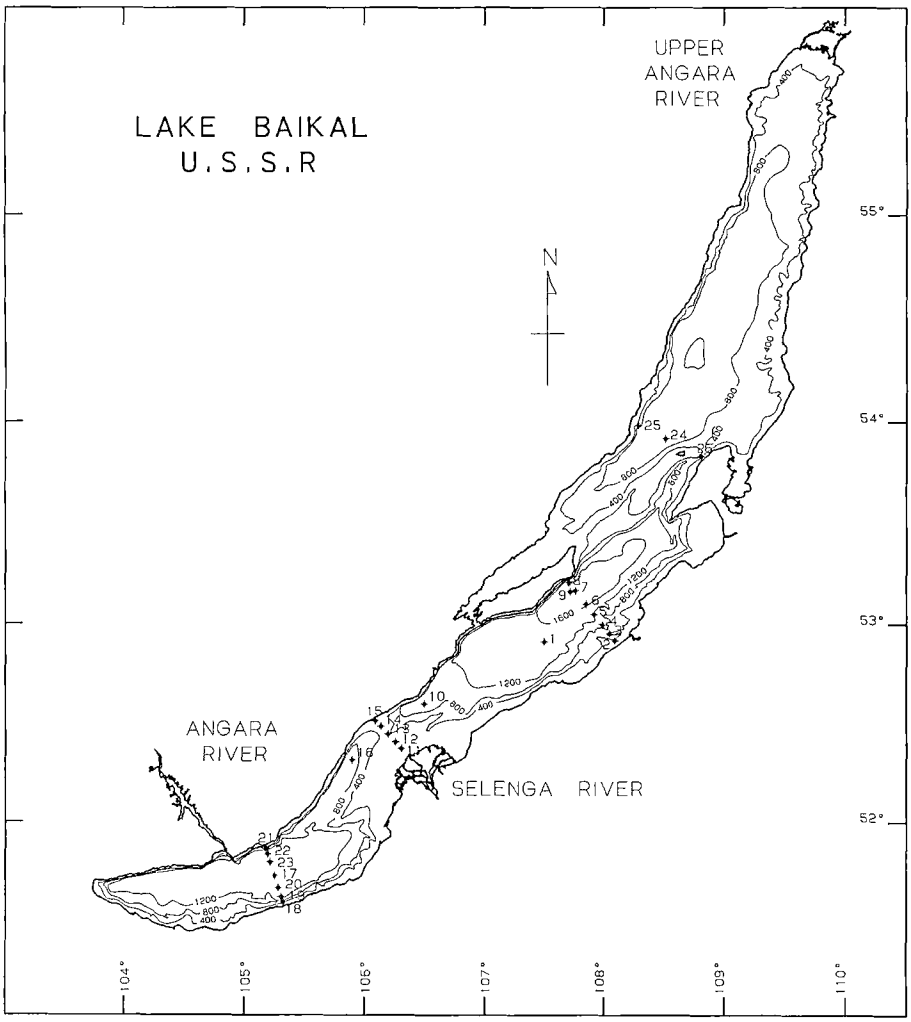

Figure 6. Map showing the bathymetry of Lake Baikal and the location of stations occupied by us during July, 1988.

instability and adjustment occurred.

Temperature fine-structure was evident at all stations where surface temperatures were below 4 °C (see insert, Figure 7b). Inversions near the $T_{\rho max}$ versus depth curve are especially interesting in that the static stability of a given intrusion may be stable or unstable depending on its depth relative to the $T_{\rho max}$ versus depth curve. The three-layer structure noted above is also evident in the distribution of chemical properties. Figure 8 shows vertical profiles of oxygen, silicate, and CFC-12 at Station 7 in the central basin. The upper layer displays high oxygen values (near 99 % saturation) and relatively low silicate values, both indicative of well-ventilated, biologically

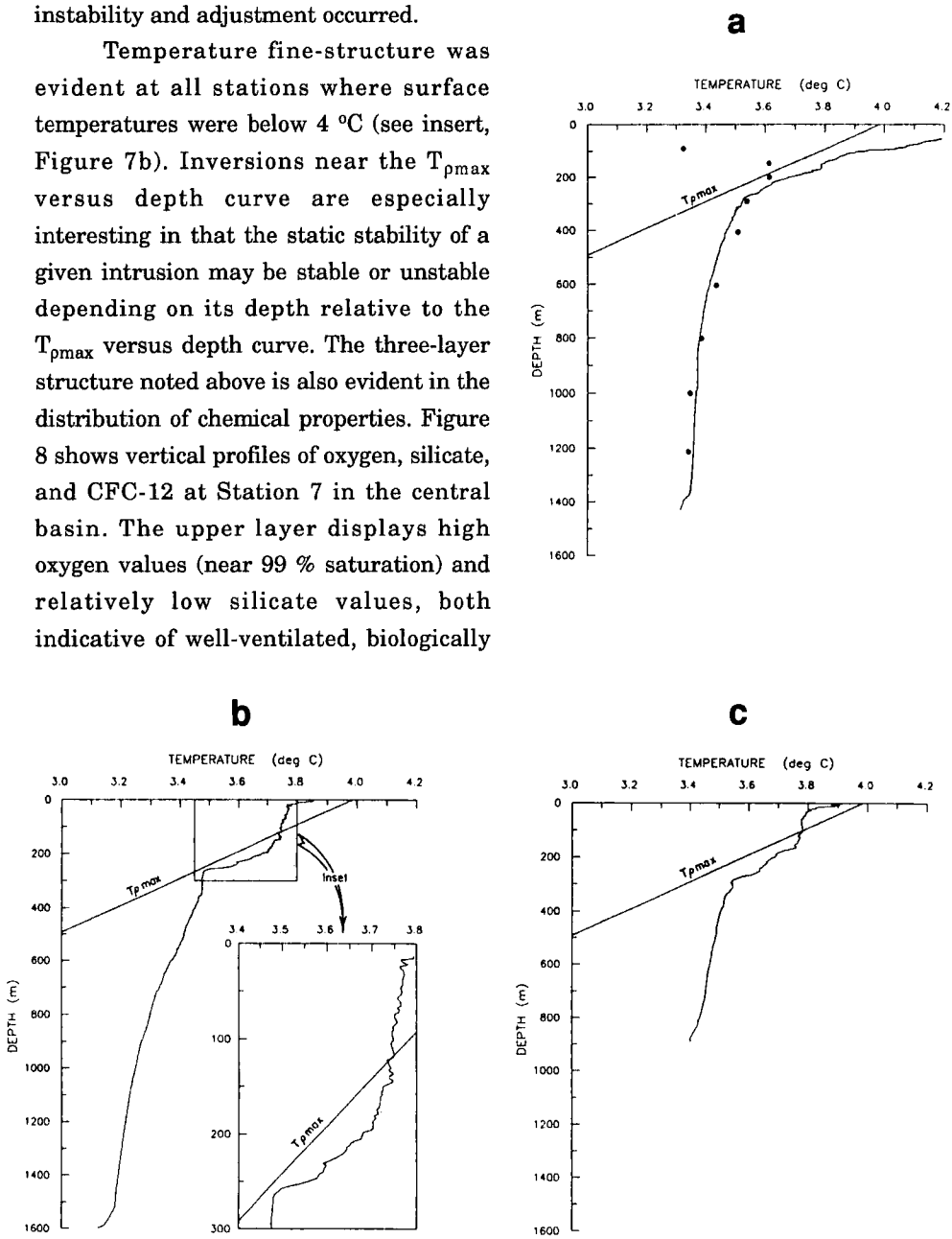

Figure 7. Vertical temperature profiles from the (a) southern, (b) central, and (c) northern basins of Lake Baikal obtained in July, 1988. Solid line denote our July, 1988 NBIS CTD data; solid circles in (a) are reversing thermometer data from the south basin obtained in April, 1934 (Vereshchagin, 1937).

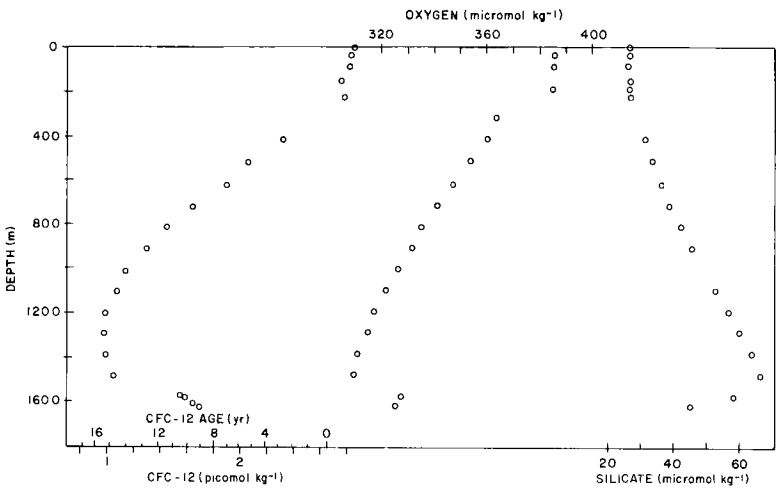

Figure 8. Vertical profiles of CFC-12, oxygen, and silicate from the central basin of Lake Baikal in July, 1988.

active surface water. The mid-depth layer shows decreased oxygen and enriched silicate, suggesting older water and nutrient regeneration. The near-bottom layer displays intermediate levels of oxygen and silicate, indicating that it is more actively ventilated than water at mid-depth.

Of special interest to the question of deep water renewal is the vertical distribution of CFC-12, a conservative, time-dependent chemical tracer. The profile of CFC-12 is qualitatively consistent with the conclusions drawn from the temperature measurements: the upper layer shows the highest concentration, and thus the greatest degree of ventilation; the mid-depth layer shows decreasing concentrations and degree of ventilation with depth; and the near-bottom layer shows an increase in concentration, indicating the presence of relatively new water near the bottom. Because the atmospheric source function for CFC-12 is relatively well-known, its concentration within the water column can be used to estimate an "age" of formation (Weiss, et al., 1991); when applied to the profiles in the deep basins, this yields a mean age of the deep water in Lake Baikal below 250 m of 8.0 years, or about 12.5 % renewal each year.

Temperature sections across central basin is shown in Figure 9. Also shown are the approximate boundaries of the three layers, as given by the temperature "knee", and by the depth at which the near-bottom temperature gradient increases. This representation shows that the depth of the upper convecting layer is relatively constant. The 4 °C isotherm intersects the surface at both sides of the lake,

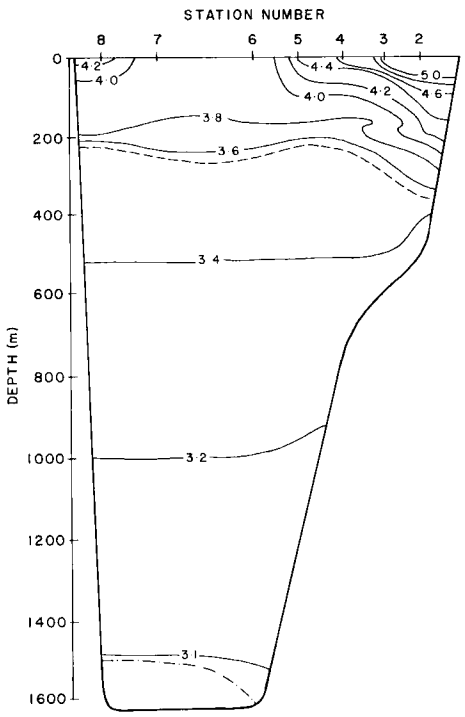

Figure 9. Transverse sections of temperature across the central basin of Lake Baikal in July, 1988. Boundaries between the upper layer and the mid-depth layer, and between the mid-depth layer and the near-bottom layer, are shown by dashed and dash-dotted lines, respectively.

suggesting that a "thermal bar" circulation is active in the upper layer.

4. Final Remarks

Thermobaric effects have been largely overlooked until now, but they are significant. One reason that non-linear effects have been ignored is that the resulting density anomalies are small, and hence require a somewhat quiescent environment in order to dominate. Such an environment, however, is found in deep lakes and the abyssal ocean where even small negative density perturbations acted upon by gravity lead, inexorably, to convective flow and large-scale re-adjustment of water masses.

5. Acknowledgements

This work was carried out under the auspices of the US/USSR Working

Group VIII Bilateral Agreement for Protection of the Environment, under the leadership in the Soviet Union of V. Koropalov, and with the support of the Institute of Limnology at Irkutsk, under the direction of M. Grachev. We acknowledge the field efforts of R. Williams, R. Van Woy, N. Williams, C, Lange, Y. Kushner, V. Verhozina, and the officers and crew of the research vessel *R.V. Vereshchagin*, and the data processing efforts of D. Richards, D. Macdonald, and P. Salameh.

6. References

Bennett, E. B., 1978. Characteristics of the thermal regime of Lake Superior. J. Great Lakes Res., 4: 310-319.

Carmack, E. C., 1979. Combined influence of inflow and lake temperatures on spring circulation in a riverine lake. J. Phys. Oceanogr., 9: 422-434.

Carmack E. C., and D. M. Farmer, 1982. Cooling processes in deep, temperate lakes: A review with examples from two lakes in British Columbia. J. Mar. Res., 40, Supp.: 85-111.

Carmack, E.C., and P.F. Hamblin. Thermobaric flow in deep lakes near the temperature of maximum density, in preparation.

Chen, C.-T., and F. Millero, 1986. Precise thermodynamic properties for natural waters covering only the limnological range. Limnol. Oceanogr., 31: 657-662.

Eckel, O., 1949. Uber die Mischungsarbeit von stabil geschichteten Wassermassen. Arch. Meteorol. Geophys. Bioklimatol., 1: 264- 269.

Eklund, H., 1963. Fresh water: temperature of maximum density calculated from compressibility. Science, 142: 1457-1458.

Eklund, H., 1965. Stability of lakes near the temperature of maximum density. Science, 149: 632-633.

Farmer, D. M., 1975. Penetrative convection in the absence of mean shear. Q. J. R. Meteorol. Soc., 101: 869-891.

Farmer, D. M., and E. C. Carmack, 1981. Wind mixing and restratification in a lake near the temperature of maximum density. J. Phys. Oceanogr., 11: 1516-1533.

Foster, T. D., 1972. An analysis of the cabbeling instability in sea water. J. Phys. Oceanogr., 2: 294-301.

Fofonoff, N. P., 1961. Energy transformations in the sea. Fish. Res. Board Can., Ms. Rep. Ser., 109, 82 pp.

Hutchinson, G. E., 1957. A Treatise on Limnology, I Wiley, New York, 1015pp.

Imboden, D. M., R. F. Weiss, H. Craig, R. L. Michel, and C. R. Goldman, 1977. Lake Tahoe geochemical study. I Lake Chemistry and tritium mixing study. Limnol. Oceanogr., 22: 1039-1051.

Johnson, L., 1964. Temperature regime of deep lakes. Science, 144: 1336-1337.

Kozhov, M., 1963. Monographiae biol. 11: 1-344, Junk, The Hague.

Mamayev, O. I., 1975. Temperature-Salinity Analysis of World Ocean Waters. Elsevier, New York, 374 pp.

Maddox, J., 1987. Baikal a symbol of Soviet Intent. Nature, 329: 802.

McDougall, T. J., 1987. Thermobaricity, cabbeling, and water mass conversion. J. Geophys. Res., 92: 5448-5464.

Strom, K. M., 1945. The temperature of maximum density for fresh waters. Geofys. Publ.,16: 1-14.

Turner, J. S., 1973. Buoyancy Effects in Fluids. Cambridge University Press, Cambridge, 367 pp.

Vereŝcagin, G. Y., 1937. Etudes du lac Baikal, Quelques problems limnologiques (in French). Verh. int. Ver. Limnol., 8: 189-207.

Vereshchagin, G. Y., 1927. Some data on the regime of the deep waters of Baikal in the area of Maritui (In Russian). Trudy Comm. for the Study of Baikal, II: 77-138.

Vereshchagin, G. Y., 1933. Basic features of the vertical distribution of dynamics of the water masses in Baikal. Coll. of art. Dedic. to the 50th anniv. of the scient. and pedag. activities of Acad. V. I. Vernadsky, 2: 1207-1230.

Weiss, R.F., E.C. Carmack, and V.M. Koropalov, 1991. Deep water renewal and biological production in Lake Baikal. Nature, in press.

Witte, E., 1902. Zur Theorie der Strom-kabbelung. Gaea, Klon, 484-487.

Wright, S., 1931. Bottom temperatures in deep lakes. Science, 74: 413.

Wüest, A., D.M. Imboden, and M. Schurter, 1988. Origin and size of hypo-limnic mixing in Urnersee, the southern basin of Vierwaldstättersee (Lake Lucerne). Schweiz. Z. Hydrol., 50: 40-70.

Yoshimura, S., 1936. A contribution to the knowledge of deep water temperatures of Japanese lakes. Part II. Winter temperatures, Jap. J. Astron. Geophys., 14: 57-83.

THE NORTHERN ADRIATIC SEA AS A PROTOTYPE OF CONVECTION AND WATER MASS FORMATION ON THE CONTINENTAL SHELF

PAOLA MALANOTTE-RIZZOLI
Department of Earth, Atmospheric and Planetary Sciences, Center for Meteorology and Physical Oceanography, Massachusetts Institute of Technology, Cambridge, MA 02139

ABSTRACT

The Northern Adriatic Sea can be taken as a prototype example of convection and water mass formation near an ocean boundary, i.e. on the continental shelf. The observational evidence indicates that three ingredients are necessary for the process. First, the Northern Adriatic wide shelf acts as a reservoir for the dense water formed in wintertime. Second, the dominant winter meteorological conditions provide a surface buoyancy flux strong enough to mix the water column to the shelf bottom. Third, the existence of a steady cyclonic circulation provides the mechanism for the dense water to cross isobath contours and replenish the depths of the mid-Adriatic pit, where it remains stored in the bottom layer until renewal during a successive winter. Modeling simulations under realistic meteorological conditions for the Northern Adriatic agree quite well with the observational evidence and show the crucial role played by topography for the spreading of the dense water tongue. Even though not recent, the modeling results here summarized are the only ones existing for the convection, water mass formation and winter circulation of the Northern Adriatic sea.

INTRODUCTION

Two main types of convection processes with very different physics were distinguished by Killworth (1983). One is the open-ocean deep convection, that occurs far from land and is predominantly vertical. The other is convection near an ocean boundary, usually involving a shallow continental shelf, the continental slope and the deep ocean in mutual interaction. A dense water mass is formed in the convection which reaches the bottom of the ocean by sinking along the continental slope. Killworth (1983) proposes a "five-ingredients recipe" for the production of deep water near oceanic boundaries. The first is a reservoir in which dense water can be formed. This is provided in the greatest majority of examples by a wide continental shelf or by a combination of shelf and sill enabling the dense water to be stored.

The second ingredient is a source capable of producing the dense water itself. In the case of Arctic and Antarctic shelves, among which the Weddell and Ross Seas are the most known examples, this source is given by ice formation in wintertime. The freezing of

seawater induces a drainage of brine from the ice to the water below. If the shelf is sufficiently shallow, the resulting vertical convection mixes the entire water column to the shelf bottom and provides very dense water (cold and salty) at depth on the shelf. For the shelves not in polar regions but at midlatitudes this source of dense water is usually given by the atmospheric conditions prevailing in the winter season. The latter ones in many instances make the convection and dense water formation process to occur during every winter, even though with different degrees of intensity.

The third ingredient is a dynamical reason for the dense water to descend the continental slope down to the deep ocean. Simple downslope buoyancy forces are not sufficient as, through geostrophic adjustment, the dense water after descending over the distance of a deformation radius (~10 km is the typical value for vertically well mixed regions) will flow horizontally along isobath contours. Thus the dynamical ingredient is the existence of a circulation capable of driving the dense water at depth off the shelf. Killworth (1983) discusses such circulation for the Weddell and Ross sea examples.

The last two of Killworth's ingredients are more empirical and, in a sense, subjective. The fourth seems to require that more than one water mass be involved in the dense water formation process. Indeed, Foster and Carmack (1976) propose a rather complicated mixing T/S diagram for the production of Antarctic Bottom Water in the Weddell Sea. Other examples exist, however, in which basically only one water mass is involved, i.e. the one originally produced in the convection that reaches and fills the depth of the nearby deep sea. The Northern Adriatic Sea is such an example. The fifth ingredient is the "strategic" combination of all the previous ones to allow the dense water mass first to be formed by a sufficiently strong source, and second to be driven to the deep reservoir crossing the isobath contours by some dynamics, such as bottom friction or a preexisting deep circulation. This "strategic" combination might induce one to think that the dense water formation process near ocean boundaries is indeed a rare occurrence. It is instead quite common. In Antarctica, for instance, after the two major shelves of the Weddell and Ross sea were studied, it has been found that dense water formation occurs all around Antarctica at the boundary with the local shelf (Killworth,1983).

Apart from these last two "empirical" ingredients, and contradicting the fourth one, the Northern Adriatic Sea can be considered a "prototype" of dense water formation near an ocean boundary. It has a wide continental shelf, ~300 km long, gently sloping from a depth of ~25 m in the northern extremity to ~100 m at the shelf break. Here dense water can be formed and stored through convection in wintertime. During this season, the prevailing atmospheric conditions provide regularly every winter air-sea thermal and evaporation fluxes sufficiently strong to mix the water column down to the shelf depth and

beyond. Regular bathymetric contours allow the dense water to flow southward along the Italian coastline and a steady, year-long cyclonic circulation drives the dense water off the coastal layer down to the deep (250 m) mid-Adriatic (Jabuka) pit, south of the shelf break, where the dense water is stored until renewal in the successive winter season. The geometry of the Adriatic is shown in Fig. 1, throughout its entire length to the southern Strait of Otranto that communicates to the Ionian Sea in the Eastern Mediterranean.

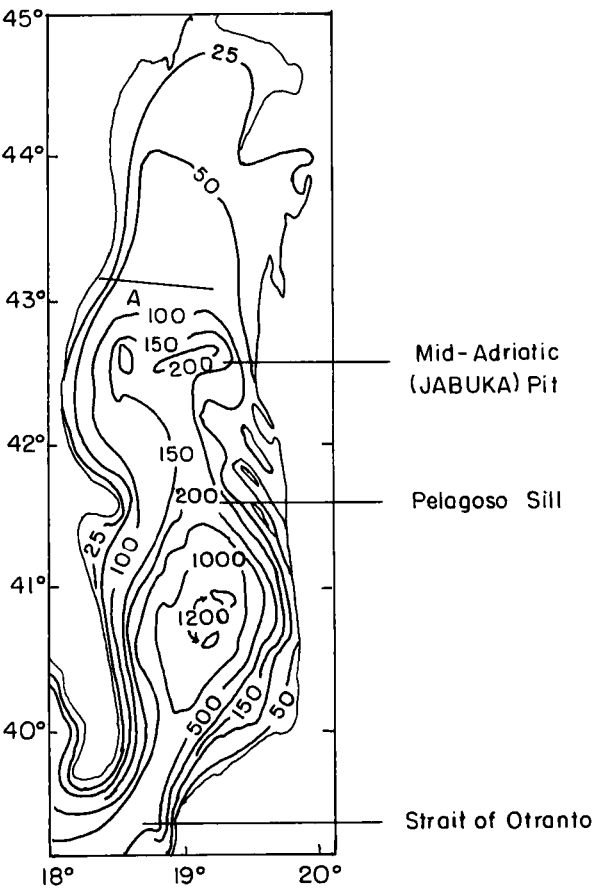

Fig. 1. Adriatic Sea map of bottom topography on the scale 1:2,000,000 cm. A is the location of the hydrographic section shown in Fig. 2. Isobath contours are in meters.

2. PHENOMENOLOGY OF THE NORTHERN ADRIATIC SEA

A more detailed discussion is now given of the Northern Adriatic phenomenology. The Northern Adriatic Sea itself is constituted first by the northernmost continental shelf, ~25 m deep in the Gulf of Venice and ~100 m at the shelf break. A steep continental slope then leads to the Mid-Adriatic, or Jabuka pit, down to 250 m. The relief then rises to ~120 m in the Pelagosa sill that separates the Northern Adriatic from the deeper southern part of the basin. The Northern Adriatic itself is a closed circulation basin, characterized by a cyclonic gyre with a northward broad flow along the Yugoslavian coast and a southward more intense current concentrated in a boundary along the Italian coast. The gyre closes in cross-basin direction at the latitude of the mid-Adriatic Pit (Zore-Armanda, 1963, 1968; Mosetti and Lavenia, 1969; Franco et al., 1982). Thus the Pelagosa sill dynamically isolates the Northern Adriatic from the Southern one. Geostrophic computations show an almost neglibible transport across the sill (Mosetti and Lavenia, 1969). Also dynamical considerations (Hendershott and Malanotte-Rizzoli, 1976) show that the Pelagosa sill is indeed a dynamical barrier that prevents the flow of the Southern Adriatic from penetrating significantly into the Northern basin. Thus, the circulation of the Northern Adriatic can be studied almost independently from the communication with the southern, deep region.

Two extreme average situations can be distinguished in the northern Adriatic (Malanotte-Rizzoli and Bergamasco, 1983). One is the late spring-summer phenomenology and will not be discussed here. The second one is the late autumn-winter phenomenology, the one relevant to the dense water formation process. In late autumn-winter, hydrographic properties (temperature, salinity, density) are vertically well mixed down to the bottom in all the northern Adriatic. This is evident in all the hydrographic data collected in the region (Trotti, 1970; Mosetti and Lavenia, 1969; Malanotte-Rizzoli, 1977). The vertical homogeneitiy is complete to depths of ~200 m, characteristic of the mid-Adriatic pit. Figs. 2a,b,c show vertical distribution of temperature, salinity, density along the cross-section A marked in Fig. 1, for Winter 1972 (from Malanotte-Rizzoli, 1977). The preconditioning of the water column begins in late autumn, through progressive surface cooling that reduces the static stability of the water mass.

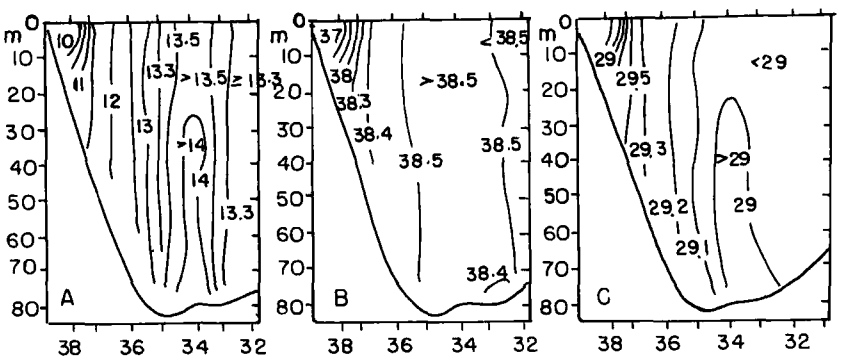

Fig. 2. Vertical distributions along section A of Fig. 1 of a) temperature in °C; b) salinities in ‰; c) density anomaly (from Malanotte-Rizzoli, 1977).

In wintertime, mostly during the months of January and February, the meteorological average pattern is constituted by an anticyclone centered in North-Eastern Europe. (See Hendershott and Malanotte-Rizzoli, 1976 for one such example). This meteorological pattern produces episodes of outbreaks of very cold and dry air of Euro-Asiatic origin blowing directly onto the Mediterranean Sea and typically lasting 10-15 days. This Euro-Asiatic flow is broken by the Alps. One branch is deflected to flow onto the Gulf of Lyons and Ligurian basin, is called Mistral and is responsible for the formation of the deep water mass of the Western Mediterranean studied during the MEDOC experiment (Sankey, 1973). Another branch called Bora flows directly onto the entire Northern Adriatic. During these outbreaks, evaporation and cooling fluxes are intense enough to induce convection and rapid mixing of the water column down to the bottom of the shelf. The result is the production of a water mass of very high density anomaly ($29.4 \leq \sigma_t \leq 29.9$) that occupies the entire northern basin interior (Hendershott and Malanotte-Rizzoli, 1976; Malanotte-Rizzoli, 1977). As an example, in Figs. 3a,b,c we show the density anomaly pattern for Winter 1972, in which the outbreak of cold-dry flow was particularly intense (from Malanotte-Rizzoli, 1977). Fig. 3a shows the surface density anomaly, 3b the 20 m depth anomaly and 3c the deepest bottle density anomaly (not at constant depth).

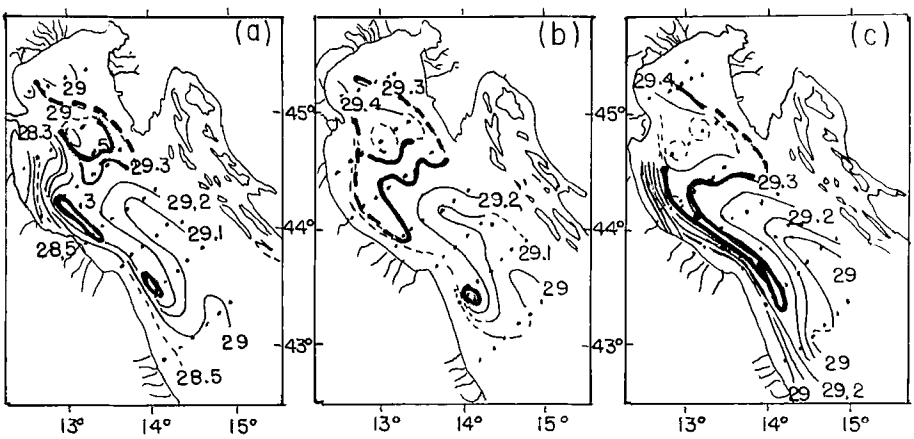

Fig. 3. Contours of density anomaly for the cruise Winter 1972. a) surface field; b) 20 m depth; c) bottom anomaly (not at constant depth) (from Malanotte-Rizzoli, 1977).

Fig. 3a,b,c show quite clearly the pool of dense water spreading over the whole interior of the basin. This dense water flows southward in a characteristic "tongue" along the isobath contours that run mostly parallel to the Italian coastline. This is particularly evident in Figs. 3a,b,c. In 3a, the surface density anomaly, the major pool with $\sigma_t \geq 29.3$ is centered in the northern interior and is separated from a secondary, more southward pool stretching along the Italian coastline and from a southern small dense water center almost at the latitude of the mid-Adriatic pit. The two northern pools are joined at 20 m depth, as clear in Fig. 2b, and they successively join the southernmost center in the bottom map of Fig. 3c. Fig. 3 illustrates pictorially the process of geostrophic adjustment. After formation, the dense water mass does not simply "slide" in the basin interior towards the shelf break, thus crossing isobath contours that in the interior run in cross-basin direction. Rather, the stretching in southward direction is accomplished in the narrow coastal layer adjacent to the Italian side where isobaths run in north-south direction and where the movement of the dense water can occur in geostrophic equilibrium. Here, it is moreover intensified by the advetion from the intense southward flowing coastal current that constitutes the western branch of the general cyclonic gyre.

In wintertime, this gyre affects the entire depth of the Northern basin. The southward current detaches from the Italian coast at the height of the mid-Adriatic pit, then flowing in a cross-basin direction on the northern side of the Pelagosa sill, the dynamical southern

boundary of the circulation. The gyre is thermally driven by the horizontal density gradients between the interior water mass and the light water of the coastal Italian boundary layer where the outflows of the major rivers of the Italian northern side are concentrated. In winter, the coastal water is lighter than the interior one being fresher, in summer being warmer. In winter, the cyclonic gyre occupies the entire depth of the northern basin. Thus, when the coastal southward flowing current detaches from the Italian coastline it advects the dense water mass across the isobaths and drives it at depth directly into the mid-Adriatic pit where it mixes with the water mass formed in the preceeding winter and there stored. In summer, the cyclonic gyre affects only the surface layer, ~100 m deep, thus occupying the continental shelf but leaving the deepest layer of the pit isolated from the above circulation. Here the winter dense water remains stored until renewal during the successive winter (Franco et al., 1982).

The dense water formation process in the northern Adriatic occurs basically every winter, due to the predominance of the favorable meteorological pattern above discussed in January-February. The differences are mainly in the intensity of the formation process, leading to masses more or less dense, with σ_t in the range 29.4-29.9, and to different volumes of the total new water produced. But basically only one water mass is involved in the process. This dense water affects very little the depth of the Southernmost Adriatic. Only a very narrow communication channel exists in fact between the mid-Adriatic pit and the Southern Adriatic and the volume that can be exchanged through it is insignificant.

The winter phenomenology discussed above shows that the Northern Adriatic can be indeed considered as a mid-latitude prototype example of convection on the shelf and dense water formation near an ocean boundary.

3. MODELING

The basic model of convection on the Northern Adriatic shelf, dense water formation and wintertime circulation in the Northern Adriatic sea is the one proposed by Hendershott and Malanotte-Rizzoli (1976). One of the important results of the model was to show that the significant alongshore transport along the Italian coastline is induced by the bottom torque term (or Jebar effect) $\frac{\partial h}{\partial x} \bullet \frac{\partial \sigma}{\partial y}$, if h is the local depth and σ the density anomaly. If no alongshore density variations are present (i.e. $\sigma \equiv \sigma(x)$ only), then no net alongshore transport can be produced, as it had been shown by Csanady (1978). Successive analytical computations showed that the reversal from Winter to Summer observed in the boundary current along the Italian coastaline can be attributed to the winter-to-summer reversal of the meridional density gradient $\partial\sigma/\partial y$ (Malanotte-Rizzoli and Bergamasco, 1983). To my

knowledge, the two above quoted references are the only modeling studies carried out thus far for the Adriatic sea, for the winter and summer seasons respectively.

The Hendershott and Malanotte-Rizzoli (1976) model of the wintertime circulation is depth integrated upon the assumption that vertical mixing occurs on a very fast time scale (is instantaneous on the average circulation time scale) and that the density anomaly is vertically homogeneous, $\sigma \equiv \sigma(x,y)$ only. The seasonal circulation occurs on time scales $T \geq 20$ days, and is therefore assumed steady. Over this scale, however, order-of-magnitude density variations are induced by the air-sea thermal and evaporation fluxes. Thus a time-dependent advection/diffusion equation is assumed for σ. The model is thus reduced to two nonlinear, coupled equations for the transport streamfunction Ψ and the density anomaly σ. Numerical integration of the model equations under the source function given by the real air-sea fluxes for cooling and evaporation for the months of January and February 1966, related to the winter cruise carried out during that year by Trotti (1970), produced the density anomaly and streamfunction field reproduced in Fig. 4. Real bottom bathymetry was used as well as real daily averages of the river water runoff on the Italian northwestern corner for the two above months.

The left panel of Fig. 4 shows the (dimensionless) transport streamfunction after ~40 days of numerical integration. The development is observed of a well defined cyclonic gyre over the entire Northern Adriatic, that is completely separated from the inflow at the southern open mouth. This latter inflow remains confined there and does not penetrate significantly northward. The gyre induces a strong southward transport all along the Italian coast and detaches from it at the latitude of the mid-Adriatic pit, thus closing the cyclonic circulation. The right panel of Fig. 4 shows the corresponding (dimensionless) density anomaly field, to be compared with Fig. 3. Notice the pool of very dense water formed in the northern half of the basin. This pool stretches southward along the isobath contours and is advected out over and into the mid-Adriatic pit by the gyre circulation. Notice in fact that the dense water tongue detaches from the coast and protrudes onto the pit in the southwestern corner. Even though idealized, the pattern of Fig. 4 is in excellent agreement with the observational evidence of Fig. 3.

Of particular interest is the model equation for the density anomaly σ:

$$\delta \frac{\partial \sigma}{\partial t} + J(\Psi,\sigma) = Q + \delta \Gamma \nabla^2 \sigma \qquad (1)$$

All quantities are dimensionless; Ψ is the transport streamfunction; $\delta(x,y)$ is the depth, Γ is the diffusivity coefficient; J is the Jacobian operator and ∇^2 the Laplacian one. Q(t) is the source function for buoyancy that includes the (realistic) daily average values for the two above months of sensible and latent heat and evaporation rate.

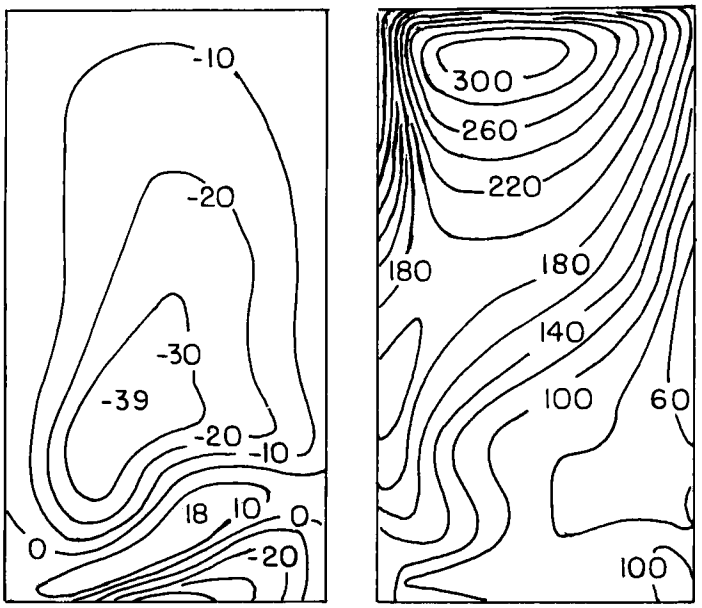

Fig. 4. Left panel: dimensionless mass transport streamfunction after 38.10 days of model integration. The stream function contour can be interpreted as dimensional transports in units of 10^{-4} m^2 sec^{-1}. Right panel: dimensionless density anomaly field. Density contours are increments of 2σ in units of 10^{-2} (from Hendershott and Malanotte-Rizzoli, 1976).

If Q(t) changes rapidly (i.e. increases in wintertime) over a time significantly shorter than the advective and diffusive time scales, then diffusion can be ignored at zero order and (1) admits the simple solution:

$$\Psi = \Psi(\delta)$$

$$\sigma = \frac{1}{\delta}\int_o^\tau Q(t)dt \qquad (2)$$

Advection vanishes because fluid columns flow parallel to isobaths that are also isopycnals. Density changes only due to the cumulative time history of the surface source function Q and the density anomaly total change over the water mass formation period T is inversely proportional to the local depth δ. (2) was tested by plotting σ versus δ^{-1} for the 1966 Winter cruise and a linear relationship was found. Successively, (2) was again tested using data collected in the 1972 Winter cruise carried out by Malanotte-Rizzoli. Fig. 5 (from Malanotte-Rizzoli, 1977) shows this later test. The linear relationship of σ versus δ^{-1} predicted by (2) is indeed satisfied extremely well. This test further illustrates the crucial role played by topography upon the spreading of a dense water mass formed upon the shelf.

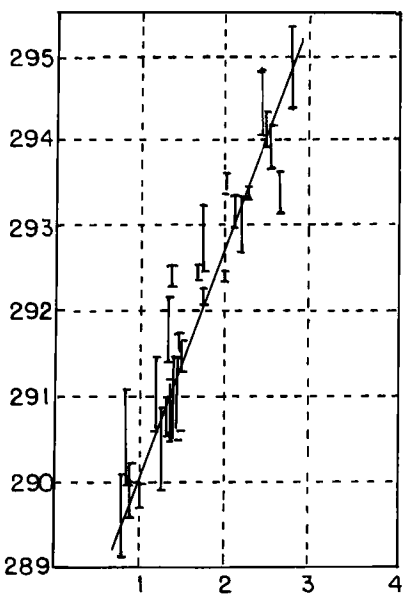

Fig. 5. Density anomaly σ plotted against the inverse dimensionless depth δ^{-1} (= 100 m/depth) for the hydrographic stations collected during the winter cruise 1972. The total range of σ values at each station is shown by the vertical bars (from Malanotte-Rizzoli, 1977).

4. CONCLUSION

The Northern Adriatic Sea has been discussed as a prototype example of convection and water mass formation near an ocean boundary, i.e. on the continental shelf. Both the existing observational evidence and modeling results comply quite well with Killworth's first three ingredients of his recipe for water mass formation near an ocean boundary. These three ingredients are of dynamical nature and embody the necessary physical processes to explain the formation of a water mass on a shelf and its subsequent spreading to the open ocean depths. Models similar to the one here discussed for the Northern Adriatic might be constructed for other shelves of the world ocean, such as the Weddell and Ross Sea shelves. Even though more than a decade old, the Hendershott and Malanotte-Rizzoli model is still valid. To our knowledge no other model with similar features and equally successful has been since proposed for water mass formation and wintertime circulation on a continental shelf.

REFERENCES

Foster, T.D. and E.C. Carmack, 1976, Frontal zone mixing and Antarctic bottom water formation in the Southern Weddell Sea, Deep-Sea Res., 23, 301-317.

Franco, P., L. Jeftic, P. Malanotte-Rizzoli, A. Michelato and M. Orlic, 1982, Descriptive model of the Northern Adriatic, Oceanol. Acta, 5, 3-15.

Hendershott, M.C. and P. Malanotte-Rizzoli, 1976, The winter circulation of the Adriatic Sea, Deep-Sea Res., 23, 353-370.

Killworth, P.D., 1983, Deep convection in the world ocean, Rev. Geophysics Space Phys., 21, 1-26.

Malanotte-Rizzoli, P., 1977, Winter oceanographic properties of northern Adriatic Sea, Cruise January-February 1972, Archivio Oceanogr. Limnol., 19, 1-45.

Malanotte-Rizzoli, P. and A. Bergamasco, 1983, The dynamics of the Coastal Region of the Northern Adriatic Sea, J. Phys. Oceanogr., 13, 1105-1130.

Mosetti, F. and A. Lavenia, 1969, Richerche oceanografiche in Adriatico nel periodo 1966-68, Boll. Geofis. Teor. Appl., 9, 1-28.

Sankey, T., The formation of deep water in the Southwestern Mediterranean, 1973, Progr. Oceanogr., 6, 159-179.

Trotti, L., 1970, Crociere Mare Adriatico, Consiglio Nazionale Richerche, Raccolte dati oceanografici, Serie A, no. 29.

Zoré-Armanda, M., 1963, Les masses d'eau de le mer Adriatique, Acta Adriatica, 10, 5-88.

Zoré-Armanda, M., 1968, The system of currents in the Adriatic Sea, Etud. Rev., 34, 1-42.

This Page Intentionally Left Blank

THERMOHALINE-DRIVEN DEEP WATER FORMATION IN THE NORTHWESTERN MEDITERRANEAN SEA

GURVAN MADEC and MICHEL CREPON
Laboratoire d'Océanographie DYnamique et de Climatologie, université Pierre et Marie Curie, 75252 Paris (France)

ABSTRACT

Deep water formation (DWF) occuring in the Northwestern Mediterranean Sea in winter is investigated using an analytical model and a 3D primitive equation numerical model forced by a simplified thermohaline forcing. It is found that the longshore forcing variations excite Kelvin wave fronts which contribute to detachment off the coast of the deep convective area. Dealing with a realistic values of surface cooling and evaporation, the numerical model reproduces the main features of DWF observed in nature, and the convection penetrates down to the ocean bottom after 3 months. The importance of the *convective* process versus the *baroclinic adjustment* process is discussed. The thermohaline forcing is found to be a major component of the horizontal circulation of the Northwestern Mediterranean Sea.

1. INTRODUCTION

Surface cooling and evaporation can be as efficient as wind-stress to drive ocean motion at basin scale as well as at mesoscale. A first attempt to consider the role played by the buoyancy fluxes on the global ocean circulation was done by Stommel *et al.* (1958) and Stommel and Arons (1960), who considered the abysall circulation forced by a source-sink distribution of mass. They gave a possible explanation for deep ocean motions. Recently, several studies have focused on the role played by thermohaline forcing in the driving of basin scale ocean motions. In a series of publications dealing with the circulation of the North Atlantic Ocean, Worthington (1972 a,b, 1976, 1977) was able to demonstrate from many observations that the Gulf stream south of New England is generally more intense in winter. He postulated that the strong surface cooling occuring in winter was the cause of this intensification, i.e. that a thermal mechanism is partially responsible for driving the Gulf stream. Csanady (1982) examined this hypothesis from a theoritical point of view and found that the argument for the existence of the thermohaline circulation is fairly conclusive. Luyten and Stommel (1986) in an analytical study and Colin de Verdière (1988) with a numerical model showed that the subtropical and the subpolar gyres in the Northern Hemisphere can be driven by heating and cooling respectively. Similar results have been obtain by Cox and Bryan (1984) and by Wajsowicz and Gill (1986) using an Ocean General Circulation Model (OGCM).

Strong mesoscale motions can also be generated by surface thermohaline fluxes. This has been investigated in the past decade by several authors. Gill *et al.* (1979) analysed the results of a tank experiment on a rotating platform, Crépon and Boukthir (1987) and Crépon *et al.* (1989) used an analytical model and Barnier *et al.* (1989) performed numerical quasi-geostrophic experiments. These

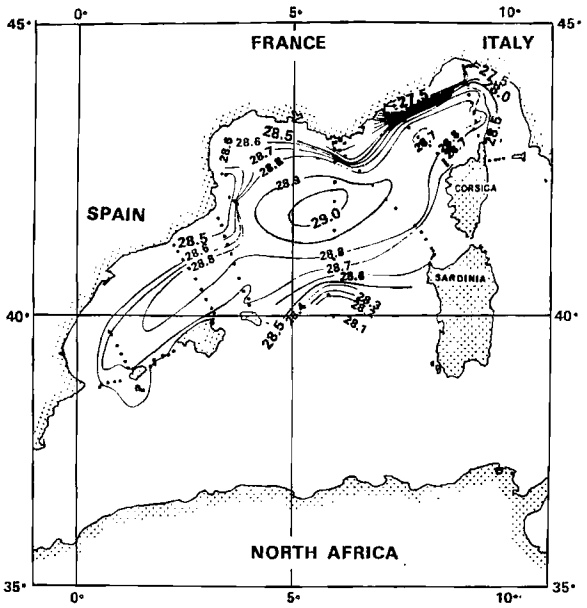

Fig. 1. Sea surface density ($\sigma\theta$ units) in winter obtained from the Elie Monier cruise (February-March 1969). The 28.9-isopycnal delimits the cyclonic vortex area where DWF occurs.

authors showed that deep water formation (DWF) occuring in winter in the Northwestern Mediterranean Sea (NM) can be responsible for the regional cyclonic circulation observed in that region (Crépon *et al.* 1982, Millot 1987). For the Labrador Sea, Seung (1987) showed that thermohaline forcing driven by regional variations in the air-sea fluxes is a likely driving mechanism for the development of the large cyclonic gyre observed by Clarke and Gascard (1983). The sinking of surface waters induced by surface cooling is also thought to play an important role in driving the cyclonic circulation of the Norvegian Sea (Carmack and Aagaard 1973) and the circulation of the Weddell Sea (Gordon 1978, Killworth 1979, 1983).

In the above areas, the thermohaline-driven mesoscale horizontal circulation is linked to DWF occuring in winter when air-sea interactions are at their apogee. In order to have a good understanding of the main characteristics of this circulation, it is necessary to study carefully the mechanisms which drive DWF. Deep water results from interactions between oceanic circulation and atmospheric forcing. Its formation involves complex and intricate phenomena which operate over a large spectrum in both time and space, and which include deep convection, mixing processes, internal waves, baroclinic instabilities, topographic effects, wind and thermohaline driven currents. In the NM, the area of interest in this paper, the DWF process has been divided into three phases : a *preconditioning* phase, a *violent mixing* phase and a *sinking and spreading* phase (MEDOC Group 1970).

The *preconditioning* phase consists in the generation of a cyclonic vortex inscribed in the regional cyclonic circulation where the main thermocline is progressively eroded (Fig.1). This

vortex, ~ 100 km in diameter, defines the specific area for DWF (Gascard 1978). Two mechanisms have been advanced to account for the vortex formation. Swallow and Caston (1973) and Hogg (1973) suggest the cause of the vortex is the cone-like topography of the Rhône Deep Sea Fan. Sankey (1973) and Gascard (1978) ascribe the *preconditioning* to both the localization of the atmospheric forcing and the pre-existing regional cyclonic circulation. As winter progresses, surface waters trapped by the vortex lose heat and water vapor to the atmosphere. They become more dense and mix with the warmer, saltier subsurface waters. A neutrally stable column of water is formed in the vortex centre. It extends from the surface to depths which sometimes reach the ocean bottom (the local depth is ~2400 m). This phase of intense deepening of the column is called the *violent mixing* phase since it involves strong vertical motions. This deepening is generally explained by two kinds of processes that occur alternatively or together : a *convective* process and a *baroclinic adjustment* process (Gascard 1978). They are linked to non-hydrostatic motions (Voorhis and Webb 1970, Gascard 1973) and baroclinic instability (Killworth 1976, Gascard 1978, Madec *et al.* 1990a), respectively. The final phase of the process is a breakup, or *sinking and spreading* of the neutrally stable column of water, with a rapid restratification of the surface waters (Stommel 1972). This phase is also attributed to a baroclinic instability process (Killworth 1976, Madec *et al.* 1990a).

Theoretical studies such as those of Crépon *et al.* (1989) give valuable arguments to explain the generation of meso-scale circulation linked to a buoyancy forcing but are unable to describe the detail of DWF. Therefore a three-dimensional primitive equation model was used by Madec *et al.* (1990a,b) to study DWF and the subsequent horizontal circulation in the NM. These authors deal with a schematic forcing having an oval shape in order to generate the cyclonic circulation linked to the *preconditioning* phase. The model simulates the main features of DWF that are found from *in situ* measurements during the *violent mixing* and the *sinking and spreading* phases of DWF.

In the present paper, we investigate the ocean response to a slightly different thermohaline forcing than those considered by Madec *et al.* (1990a, b). This forcing has a tongue like shape which approximatively fits the NM region where cooling and evaporation are maximum in winter (Meteorological Office 1962). In particular, it intercepts the coast at right angle and reaches its maximum value over the coastal area. The problem is studied using an analytical two layer model and a 3D numerical model. Emphasis is given on the *preconditioning* and the *violent mixing* phases of DWF, with special attention on the inhibition of deep convection along the coast which causes the detachment from the northern coast of the convective area where DWF occurs.

The paper is structured as follows. In section 2, an analytical two layer model is used to investigate the coastal ocean response to a buoyancy forcing applied over a strip perpendicular to the coast. In section 3, the results of a 3D numerical experiment are presented and analysed. In the conclusion, the oceanic relevance of the results is discussed.

2. ANALYTICAL STUDY

In this section we use an analytical model to investigate the main characteristics of the ocean response to a buoyancy forcing. We deal with the equations presented in Crépon *et al.* (1989). A semi-infinite ocean is considered which density variation is idealized in terms of a homogeneous two-

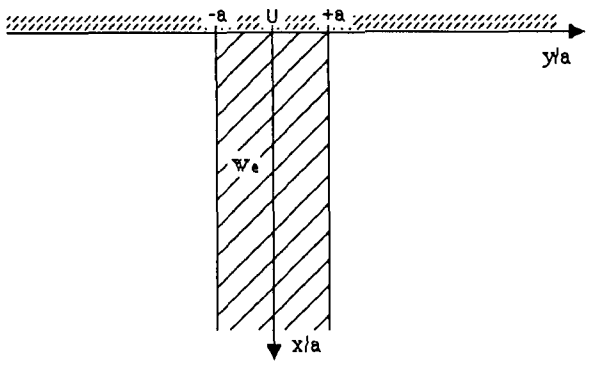

Fig. 2. Horizontal pattern of the forcing w_e (dashed area) for the analytical model.

layer fluid of fixed density ρ_1 and ρ_2. A coordinate system with x positive southward and y positive eastward is used and the coast is fixed at x = 0 (Fig. 2). Since we consider small perturbations from rest, the equations can be linearized. We model the convection by saying that the upper fluid is converted into the lower fluid at a rate of $\rho_2 w_e$. Following Crépon *et al.* (1989) the problem can be reduced to two equivalent one-layer models by the standard decomposition into normal modes. The surface and interface elevations, as well as the upper and lower layer velocities, can be expressed in terms of the barotropic (n=1) and baroclinic (n=2) normal mode elevation η_n and velocity $\mathbf{u}_n$. The momentum and continuity equations can be written :

$$\begin{aligned} &\partial_t \mathbf{u}_n + f\,\mathbf{z} \times \mathbf{u}_n = - g_n \nabla \eta_n \\ &\partial_t \eta_n + \nabla . H_n \mathbf{u}_n = \alpha_n w_e \end{aligned} \tag{2.1}$$

where $H_1 = h_1 + h_2$, $H_2 = h_1$, $\mathbf{z}$ is the upward vertical unit vector, $g_1 = g$, $g_2 = g\,\varepsilon\, h_2/H_1$ with ε the density ratio, h_1 (h_2) is the thickness of the upper (lower) layer at rest, and α_n is the projection of the forcing onto the modes such that $\alpha_1 = \varepsilon\, h_2/H_1$ and $\alpha_2 = - H_1/h_2$.

Using the f-plane approximation, $\mathbf{u}_n$ can be eliminated from (2.1) to obtain the following equation for η_n :

$$\partial_t \left[c_n^2 \nabla^2 \eta_n - \left(\partial_t^2 + f^2\right) \eta_n \right] = - \alpha_n \left(\partial_t^2 + f^2\right) w_e \tag{2.2}$$

where c_n is the speed of long barotropic (n=1) or baroclinic (n=2) gravity waves ($c_n = g_n H_n$). The corresponding velocity $\mathbf{u}_n$ is a solution of :

$$\left(\partial_t^2 + f^2\right) \mathbf{u}_n = - \frac{1}{H_n} c_n^2 \left[\partial_t \nabla \eta_n + \nabla \eta_n \times f\,\mathbf{z} \right] \tag{2.3}$$

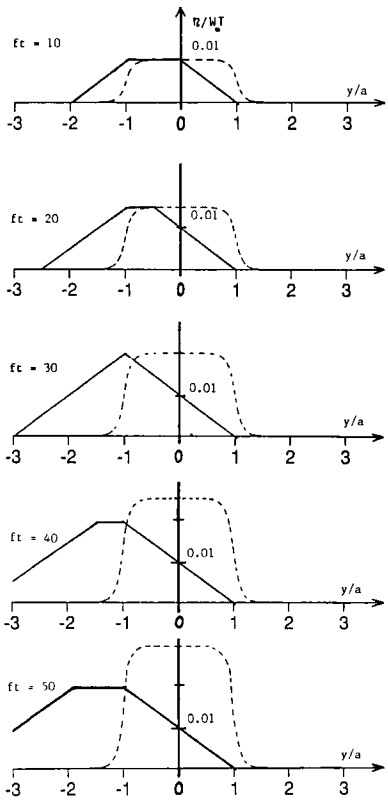

Fig. 3. Dimensionless interface elevation at different dimensionless times ft for a forcing defined by $w_e T$ = 100m (where T is the total duration of the forcing) and for r_2/a = 0.2. The dotted line shows the offshore interface elevation (large x/r_2) : it increases linearly with respect to time, generating a dome of the interface. The solid line shows the interface elevation at the coast : two the Kelvin wave fronts are excited at y = -a and at y = +a. The front excited at y = +a stops the rise of the interface at the coast.

Let us now assume that $\rho_2 w_e$ is constant with respect to time and takes a non zero value in a strip perpendicular to the coast defined by $|y| < a$ (Fig. 2). This forcing can be viewed as the result of strong cooling and evaporation induced by a southward gust of wind (the Mistral) confined to a strip.

Equation (2.2) is solved by applying a Fourier transformation on y and a Laplace transformation on t. For simplicity, the indices are omitted in the equations. The Fourier-Laplace transform (FLT hereafter) of (2.2) is :

$$c^2 \partial_x^2 \overline{Z} - [p^2 + f^2 + (2\pi kc)^2] \overline{Z} = - \alpha \frac{p^2 + f^2}{p} \overline{W(k)} \qquad (2.4)$$

where $\overline{Z(p,k,x)}$ and $\overline{W(p,k,x)}$ are the FLT of η and w_e respectively, and p and k are the FLT variables with respect to t and y as they are defined in Crépon *et al.* (1984, 1989).

Using the FLT of (2.3) and the coastal boundary condition (u=0 at x=0) the following solution of (2.4) is obtained :

$$\overline{Z} = i2\pi kf \ \alpha \frac{p^2 + f^2}{p^2} \overline{W(k)} \ \frac{1}{p^2 + f^2 + (2\pi kc)^2} \left(1 + \frac{i2\pi kf}{p\gamma - i2\pi kf} e^{-\gamma x}\right) \tag{2.5}$$

where $\gamma^2 = \left[p^2 + f^2 + (2\pi kc)^2\right]/c^2$.

A Laplace inversion of $\overline{Z}$ is difficult. Nevertheless, we can obtain an asymptotic expansion as (ft) tends to infinite when using Sutton's algorithm (1934), which is based on an algebraic expansion around the Laplace transform singularities which have the largest real values. The leading terms of the asymptotic expansion of Z, the Fourier transform of η, are given by :

$$Z(t,x,k)_{ft \to \infty} = \frac{\alpha W}{f} \left\{ \underbrace{\frac{1 - e^{-x/r\sqrt{1 + (2\pi kr)^2}}}{1 + (2\pi kr)^2} ft}_{(1)} + \underbrace{\frac{i}{2\pi kr}\left[\frac{e^{-x/r\sqrt{1 + (2\pi kr)^2}}}{1 + (2\pi kr)^2} - e^{-x/r}\right]}_{(2)} \right. \tag{2.6}$$

$$\left. + \underbrace{\frac{i\, e^{-x/r}}{2\pi kr}\left[1 - e^{i2\pi k\, r\, ft}\right]}_{(3)} \right\}$$

where r = c/f is the radius of deformation

The modal elevation is obtained by a Fourier inversion of Z(t,x,k). The first term of (2.6) corresponds to a direct response to the forcing. It leads to a zero elevation at the coast and to a linear increase of the elevation far from the coast (far with respect to the radius of deformation). The offshore elevation within the forcing strip forms a dome (Fig.3). It is given by (Crépon *et al.* (1989) :

$$\eta(1)_{ft,\, x/r \to \infty} \approx \alpha\, t\, w_e \left\{1 - \frac{1}{2}\left(e^{-(y+a)/r} + e^{-(y-a)/r}\right)\right\} \qquad \text{for } |y| < a \tag{2.7}$$

The second term represents Poincaré waves of the second kind and zero frequency which are excited at the coast in order to satisfy the boundary condition (u=0 at x=0).

The third term of (2.7) leads to the following elevation :

$$\eta(3) = \alpha\ w_e\, e^{-x/r} \left\{ \left[t + \frac{y-a}{c}\right] S\left(t + \frac{y-a}{c}\right) - \left[t + \frac{y+a}{c}\right] S\left(t + \frac{y+a}{c}\right) \right\} \tag{2.8}$$

where S(.) is the step function. This elevation is a combination of two elementary elevations of opposite sign whose amplitude increases linearly with respect to time in the region y >a and y>-a respectively and whose extremity propagates westward as a Kelvin wave front excited at y = ± a . The resulting interface displacement is presented in Fig. 3. For t > (a - y)/c, $\eta(3)$ becomes steady and equal to :

$$\begin{aligned} \eta(3.1) &= \alpha\ w_e \frac{a-y}{r} e^{-x/r} && \text{for } |y| < a \text{ (in the strip)} \\ \eta(3.2) &= \alpha\ w_e \frac{2a}{r} e^{-x/r} && \text{for } y < -a \text{ (west of the strip)} \end{aligned} \tag{2.9}$$

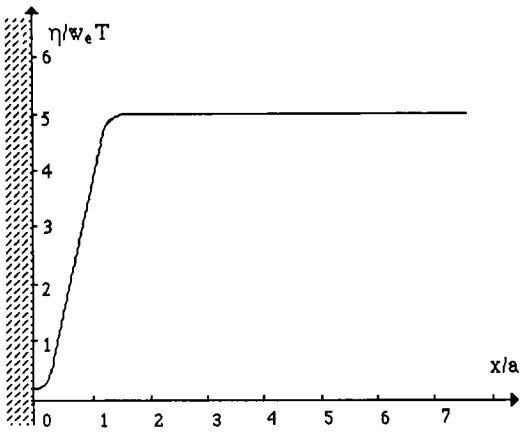

Fig. 4. Dimensionless interface elevation along the x axis (y=0) at ft = 1000 (100 days) for the same parameters as Fig.3. The increase of interface elevation is stop along the coast (x=0) and allows the offshore detachment of the interface dome.

The passage of the Kelvin wave front generated at y = a stops the increase with time of the coastal elevation. Hence at large t (t > (a - y)/c) the coastal elevation within the strip becomes steady and a Kelvin wave front of constant amplitude given by η(3.2) continues to propagate westward outside the strip. Since the offshore elevation which depends only on η(1) continues to increase, an offshore gradient of the elevation is generated (Fig. 4). It results in a detachment from the coast of the dome of the elevation induced by the forcing.

The corresponding velocities can be obtained from (2.3). As an example, far from the coast, the velocity v(1) which is in geostrophic balance with η(1) is given by :

$$v(1)_{ft,\, x/r \to \infty} \approx -\frac{1}{2}\,\alpha\,\frac{r}{H}\,ft\,w_e\,sgn(y)\left(e^{-|y+a|/r} - e^{-|y-a|/r}\right) \qquad (2.10)$$

As long as the forcing acts this velocity increases with time.

Surface and interface elevations as well as the upper and the lower layer velocities can be obtained in terms of normal modes. As an example, if we consider the NM, we use h_1 = 400 m, H_1 = 2400 m and $\varepsilon = 2.\ 10^{-4}$ (Crépon *et al.* 1982), which yields $r_1 = 55.\ 10^6$ m , $r_2 = 9.\ 10^3$ m, $\alpha_1 = 1.7\ 10^{-4}$, $\alpha_2 = -\ 1.2$. Owing to the values of α and ε, the interface elevation and the velocities are found to depend on the baroclinic mode only : the ocean response is baroclinic.

Far from the coast, the solution given by Crépon *et al.* 1989 is retrieved. As long as the forcing acts the upper layer thickness diminishes with time and the interface forms a dome which can be related to the dome of the isopycnal surfaces observed in nature. In the upper layer, an inshore (offshore) current of ~$2r_2$ width flows along the forcing discontinuity y = a (y = - a). At the coast, these two currents are deviated toward y < 0 and generate two Kelvin wave fronts of opposite sign whose associated elevations are given by the first term and the second term of (2.9) respectively. At large t (t > (a - y)/c_2) a surface cyclonic circulation is then generated around the dome while a weak

circulation of opposite direction is obtained in the lower layer. The coastal part of these circulation insures the mass continuity between the inshore and offshore currents. As a result, the interface rise is stopped in the coastal area of the forcing strip and the interface dome is detached from the coast. In order to explain this detachment several mechanisms such as the space variations of the atmospheric boundary layer (Seung, 1987) or the existence of a background coastal regional circulation (Gascard, 1978) have been invoked. In the present work the detachment is driven by the hydrodynamic ocean response to longshore forcing discontinuities. Should the forcing be constant in the ocean, an homogeneous interface elevation would result. The longshore variation of the forcing includes a self consistant mechanism explaining the detachment of the dome from the coast.

3. NUMERICAL EXPERIMENT

3.1 Model description

The numerical study has been performed with the OGCM developed at LODYC under the direction of P. Delecluse (Chartier 1985, Andrich *et al.* 1988b). The model solves the primitive equations, i.e. the three-dimensional Navier-Stokes equations slightly simplified by assuming the Boussinesq approximation and the hydrostatic equilibrium. The rigid lid approximation is used to remove the barotropic gravity waves (Bryan, 1969). The finite difference form of these equations is solved on a Arakawa type "C" grid (Arakawa, 1972) with a curvilinear formulation in the three space directions. Time stepping is achieved by a leapfrog scheme, with the spurious time splitting being removed by an Asselin (1972) time filter. The potential enstrophy-conserving finite difference formulation given by Sadourny (1975) is fitted to the non-linear terms of the momentum equation. The prognostic variables are the horizontal velocity $\mathbf{U_h}$=(u,v), the temperature T and the salinity S. The vertical velocity w, the density ρ and the hydrostatic pressure p are diagnostic variables computed at each time step from the prognostic variables using the continuity, state and hydrostatic equations, respectively. The model runs on a CRAY2 in a multitasked version (Andrich *et al.* 1988a).

Let $\mathbf{k}$ be the unit upward vertical vector. The model equations on a rotating sphere are :

$$\partial_t \mathbf{U_h} + (\mathrm{rot_z}\, \mathbf{U_h} + f)\, \mathbf{k} \times \mathbf{U_h} + w\, \partial_z \mathbf{U_h} = - \frac{1}{\rho_o} \mathrm{grad} \left(p + \frac{1}{2} \rho_o \mathbf{U_h}^2 \right) + F^U(\mathbf{U})$$

$$\partial_z p = - \rho\, g$$

$$\mathrm{div}\ \mathbf{U_h} + \partial_z w = 0 \qquad (3.1)$$

$$\partial_t T + \mathrm{div}(T\, \mathbf{U_h}) + \partial_z (T\, w) = F^T(T)$$

$$\partial_t S + \mathrm{div}(S\, \mathbf{U_h}) + \partial_z (S\, w) = F^S(S)$$

where F^U, F^T and F^S parameterize the effects of sub-grid scale physics, i.e. eddy viscosity and eddy diffusivity. They are assumed to be second order operators of the following form :

$$F^U(\mathbf{U}) = \upsilon_h[\,\mathrm{grad}_h(\,\mathrm{div}\,\mathbf{U}_h) - \mathrm{rot}(\,\mathrm{rot}\,\mathbf{U}_h)\,] + \partial_z(\,\upsilon_v\,\partial_z\mathbf{U}_h\,)$$

$$F^T(T) = \kappa_{hT}\,\mathrm{div}(\,\mathrm{grad}_h\,T) + \partial_z(\,\kappa_{vT}\,\partial_z T\,) \qquad (3.2)$$

$$F^S(S) = \kappa_{hS}\,\mathrm{div}(\,\mathrm{grad}_h\,S) + \partial_z(\,\kappa_{vS}\,\partial_z S\,)$$

The density is calculated from temperature and salinity fields by a simplified non-linear equation of state (Eckart 1958).

The numerical integration may lead to static instabilities at particular gridpoints. In nature, convective processes re-establish the static stability of the water column. These processes have been removed from the model via the hydrostatic approximation. They are parameterized by a non-penetrative convective adjustment algorithm which restores instantaneously and at each time step the static stability by mixing downwards the statically unstable portion of the water column, but only until the density structure becomes neutrally stable (i.e. until the mixed portion of the water column has exactly the density of the water just below). The algorithm used converges for any profile in a smaller number of iterations than the number of vertical levels of the model. This property is of paramount importance for our simulations as was pointed out by Killworth (1989) : it avoids the existence of permanent and unrealistic static instabilities at the sea surface. Such a non-penetrative convective algorithm is consistent with winter observations in the MEDOC area (Anati 1971) and has proved successful in previous studies (Madec *et al.* 1990a, b).

The surface boundary conditions are :

$$w = 0$$

$$\upsilon_v\,\partial_z U_h = 0 \qquad (3.3)$$

$$\kappa_{vT}\,\partial_z T = \frac{Q}{\rho_o\,C_p}$$

$$\kappa_{vS}\,\partial_z S = S\,E$$

where Q is the surface heat flux (latent and sensible heat flux and net radiatif flux) in W m^{-2}, E is the surface water flux (evaporation minus precipitation) in mm d^{-1}, and Cp is the specific heat.

"No slip" boundary conditions and zero fluxes of heat and salt are applied at the solid boundaries. The ocean starts from rest with a horizontally homogeneous density field computed from temperature and salinity profiles given in Fig.5. Vertical temperature and salinity gradients are typical of the NM in early winter. The cold and relatively fresh surface water with a subsurface temperature minimum at 100 m overlies the warm and salty Levantine Intermediate Water (LIW) between 200 and 600 m, and a typical thick layer of deep water (Nielsen 1912). The complexity of the vertical profiles of both temperature and salinity leads us to refine the mesh with up to 20 vertical levels whose separation varies from 10 m to 25 m in the upper 200 m, and is no more than 400 m at the bottom.

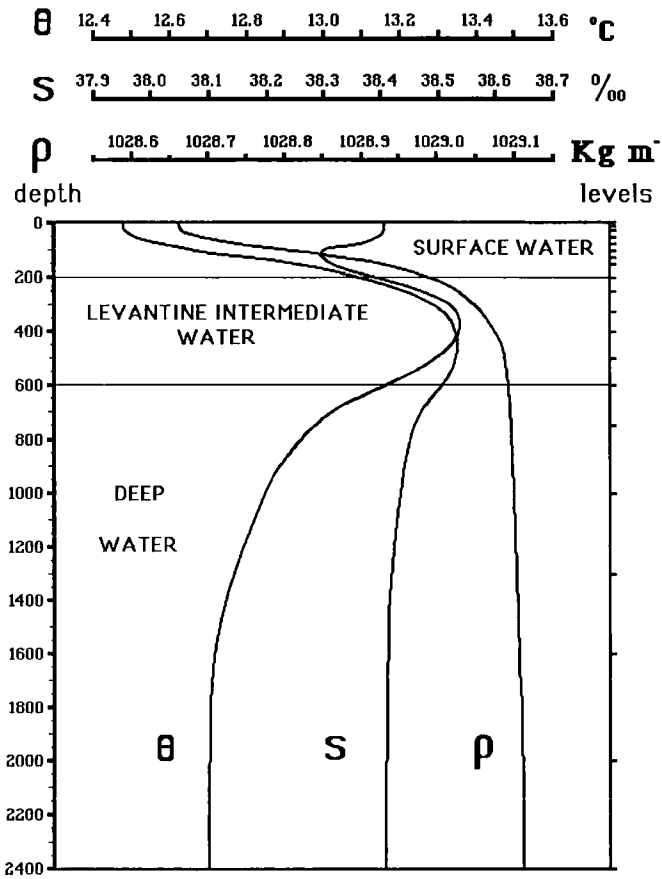

Fig. 5. Initial vertical structure for potential temperature, salinity and potential density (σ_θ units) for the numerical 3D simulation. The depth of the 20 vertical grid levels is indicated on the right of the frame.

Such an initial stratification presents a small first baroclinic radius of deformation (6.53 km) which imposes a small horizontal grid spacing : 4.5 km. The timestep is 30 min and the horizontal eddy mixing coefficients are 80 $m^2\ s^{-1}$ for momentum, salinity and temperature. The vertical eddy viscosity and diffusivity coefficients (υ_v and κ_v) are assumed to vary as a function of the local Richardson number Ri, according to the following formula (Pacanowski and Philander 1981) :

$$\upsilon_v = \upsilon_o/(1 + 5\ Ri)^2 + \upsilon_b$$

$$\kappa_v = \upsilon_v/(1 + 5\ Ri) + \kappa_b \qquad (3.4)$$

with $\upsilon_o = 10^2\ cm^2\ s^{-1}$ and $\upsilon_b = \kappa_b = 1.34\ 10^{-2}\ cm^2\ s^{-1}$. They vary from the molecular diffusivity to a maximum value of $10^2\ cm^2\ s^{-1}$ when Ri is zero.

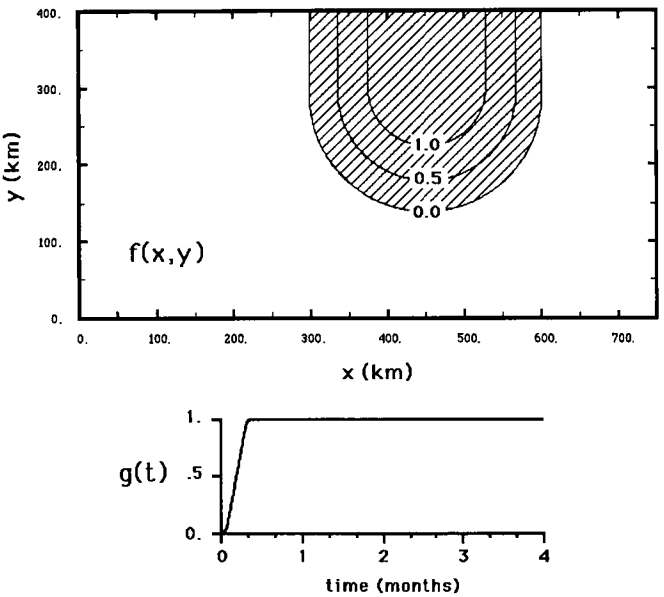

Fig. 6. Basin geometry and pattern of the thermohaline forcing for the numerical 3D simulation : the space forcing function f(x,y) and the time forcing function g(t). The total heat flux Q and the evaporation E are given by $Q = Q_o\ g(t)\ f(x,y)$ and $E = E_o\ g(t)\ f(x,y)$ where $Q_o = -170$ W m^{-2} and $E_o = 6.3$ mm d^{-1}.

The above governing equations are solved in a closed, flat rectangular basin of 750 km x 400 km x 2.4 km centered at 42°N, which accounts for the so-called MEDOC area. The thermohaline forcing is applied over a tongue like area (200 kmx 300 km) (Fig.6) which approximatively fits the observed area where strong cooling and evaporation associated with the Mistral and the Tramontane are the most common in winter (Meteorological Office 1962). The forcing is assumed to be constant during the four months of integration with a rise time of 10 days (Fig.6). It consists of an ocean heat loss of 170 W m^{-2} and an evaporation of 6.3 millimeters of water per day. These are the mean winter values deduced from the monthly mean estimations given by Bunker (1972) for the MEDOC area.

3.2 Numerical results

(i) the *preconditioning* phase of DWF : the vortex formation (first 2 months). Under the effect of the thermohaline forcing, surface water within the forcing area becomes colder, saltier and thus more dense than the surrounding water. Static instabilities are generated which cause surface waters to mix with subsurface waters. This mixing is done through the non-penetrative convective adjustment algorithm which is a vertical process parameterizing the convection found in nature. It yields to the formation of a neutrally stable column of water in the surface layers whose horizontal pattern is linked to the forcing geometry (Fig.7-a). During this phase the convection involves the well stratified surface waters : the column deepening rate is slow (~ 4 m d^{-1}) and its density increase rate is relatively fast.

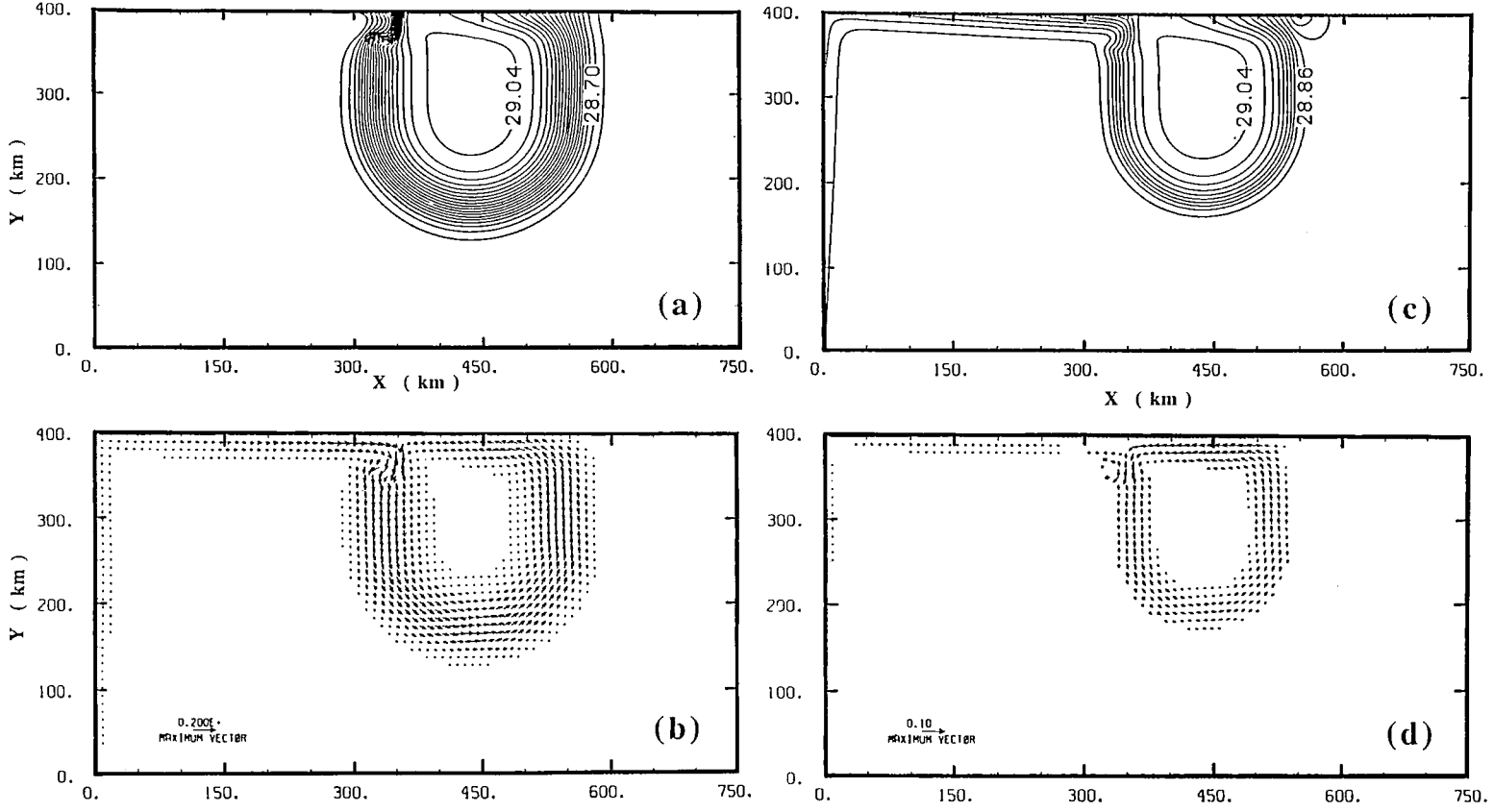

Fig. 7. Horizontal section of density (σ_θ units) and horizontal velocity at the surface (a and b) and at 112m (c and d) at month 2. Note the Kelvin wave front propagating along the coast whose signature is well marked on the density field at 112m and the offshore detachment of the neutrally stable column associated with a cyclonic vortex in the surface layers.
Figure Caption

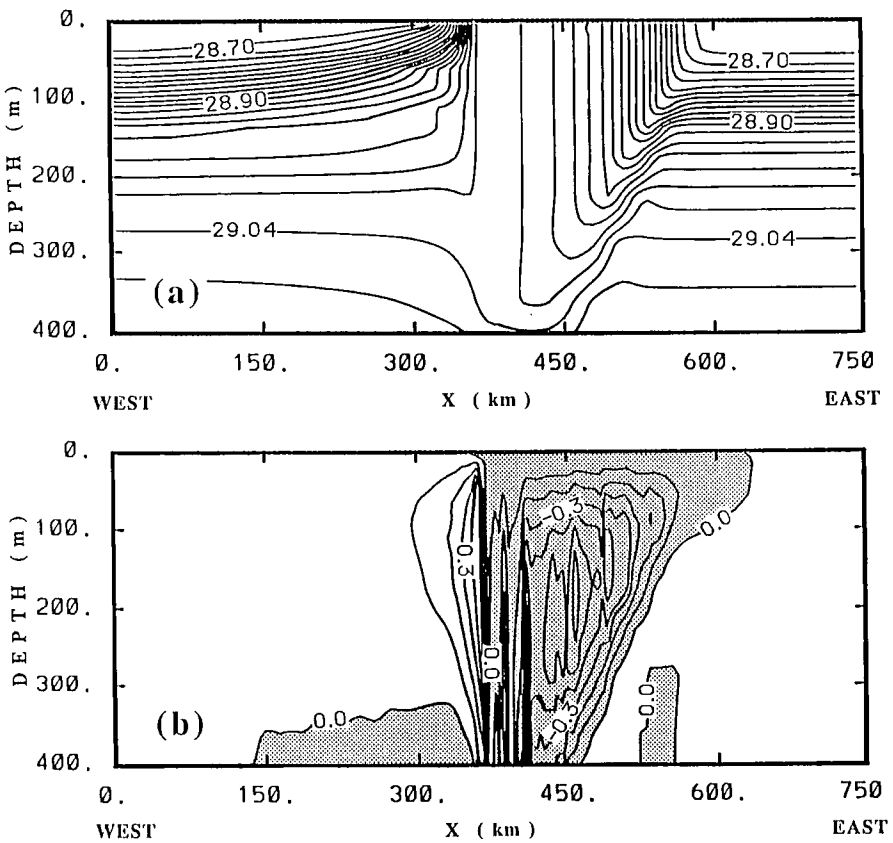

Fig. 8. West-East vertical coastal section (y=400 km) of (a) density (σ_θ units) and (b) vertical velocity at month 2 in the top 400 m. Contour intervals equal 0.02 kg m^{-3} and 0.1 mm s^{-1}, respectively.

In the off-shore region, the dynamical response is similar to that obtained by Madec *et al.* (1990a) and fits the linear theory developed in section 2. The convective area is surrounded by a horizontal density gradient (Fig. 7) which drives a geostrophic horizontal baroclinic circulation formed by an upper layer cyclonic circulation of ~10 cm s^{-1} mean velocity (Fig. 7-b and d) and overlying a weaker (some mm s^{-1}) and vertically quasi-uniform anticyclonic circulation. Both circulations have the same magnitude in term of volumetric transport as predicted by the analytical model.

At some distance from the coast (some radii of deformation), geostrophic currents perpendicular to the coast are generated at the west and east sides of the forcing area. These currents are deviated by the coast and their streamlines bend westwards for an observer facing the coast (Fig.7-b and d). They generate two coastal baroclinic Kelvin wave fronts of opposite signs which propagate westwards (Fig. 7-c) in agreement with the linear theory presented in section 2. Indeed, the contribution of the Coriolis acceleration in the zonal momentum equation vanishes in the vicinity

of the coast, owing to the boundary condition v=0 at y=0. Thus the longshore pressure gradient linked to the longshore density gradient balances the inertial term ∂_t u and drives the dynamics of the Kelvin wave fronts. These Kelvin wave fronts have phase speed of 25 cm s^{-1} and their propagation along the coast is followed by an upwelling or a downwelling of isopycnal surfaces depending on their generation zone (west or east side of the forcing) (Fig. 7-c). This response is conceptually the same as the Kelvin wave front generation induced by a longshore discontinuity of a wind stress field parallel to the coast (Crépon and Richez 1982, Hua and Thomasset 1983).

Nevertheless, strong departures from the theory appear in the coastal dynamics of the numerical results. In the linear analytical theory, the eastside Kelvin wave front (i.e. generated at the east side of the forcing) first stops the interface elevation (which parameterizes the convection) along the coastal region of the forcing area and then blocks the upwelling induced by the westside Kelvin wave front. In the numerical model, the eastside Kelvin wave front is followed by a westward surface coastal jet which advects light offshore peripheral surface waters between the centre of the convective area and the northern coast. As they progress along the coast, these light waters feel the effect of the thermohaline forcing and become denser. The interaction of this advection with the vertical convection generated by the thermohaline forcing imposes a longshore non linear density gradient. The strongest density gradients (and thus the strongest pressure gradients) are located at the east side of the forcing area (Fig.8-a). This longshore variation of pressure gradients implies a westward decrease of horizontal acceleration which induces a coastal accumulation of surface waters due to the mass conservation. This accumulation generates strong downward vertical velocities of several tenth of a millimeter (i.e. one order of magnitude greater than the vertical velocity associated with coastal upwelling west of the forcing area) (Fig.8-b). This yields to a progressive damping of the eastside Kelvin wave front which cannot compensate the upwelling linked to the westside Kelvin wave front as in the linear theory. Therefore the westside Kelvin wave front continues to increase with respect to time.

In the surface layers, the coastal dynamics described above allows to close the cyclonic circulation generated off-shore. It results in the formation of a broad surface cyclonic gyre, ~200 km in diameter. This vortex surrounds the convective region where DWF will occur during the months to come. This region is thus partly detached from the northern coast, by some ten kilometers, a distance which corresponds to the off-shore extension of a Kelvin wave for an internal radius of deformation of some kilometers. In the deep layers, the arrival of the Kelvin wave fronts is also followed by the generation of a coastal circulation, but it is weaker than the surface circulation (by an order of magnitude) and in opposite direction. Its vertical extention is more important, so that the vertically averaged current is zero, in agreement with the analytical theory. As for surface layers, the deep anticyclonic circulation initiated offshore is closed after the passage of the eastside Kelvin wave front.

After 2 months, the ocean state is consistent with the end of the *preconditioning* phase of DWF. A vortex has been formed in the center of which winter surface cooling has reduced the stability of the surface layers, leaving very little reserve of buoyancy in the water column, but the ocean still remains a three layered system. The maximum near-surface density within the vortex reaches σ_θ=29.04, as the well mixed surface water is 300 m thick.

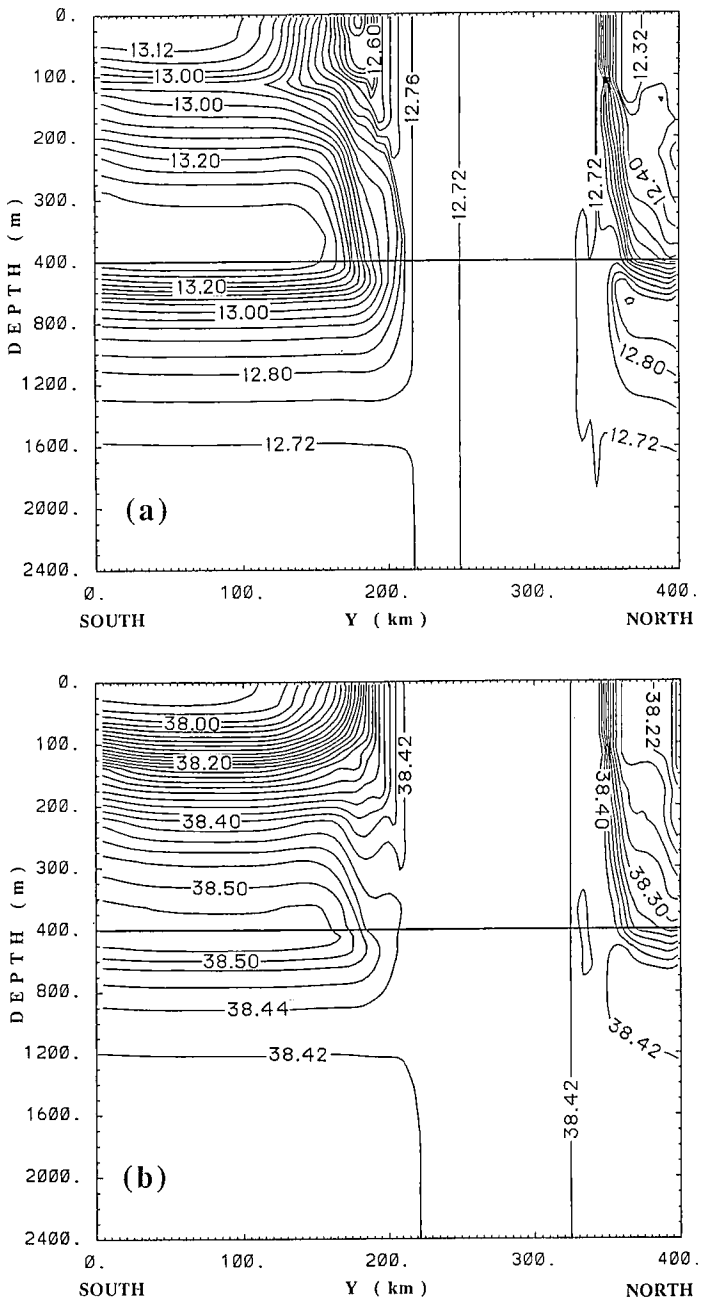

Fig. 9. North-South vertical section of (a) potential temperature and (b) salinity in the centre of the forcing area at month 4. Note that the vertical scale is different between 0-400m and 400-2400m. A broad neutrally stable column has been formed which reaches the ocean bottom and is detached from the northern coast by ~ 50 km. Contour intervals equal 0.04 °C and 0.02 °/oo, respectively.

(ii) The *violent mixing* phase of DWF : deep convection (last two months). After the first two months, the pycnocline has been removed from the vortex centre so that further surface cooling and evaporation lead to deep convection. As in observations, the convection occurs through both a *convective* process and a *baroclinic adjustment* process. Depending on the location with respect to the vortex, one process predominates over the other.

In the centre of the vortex, the thermohaline forcing creates surface static instabilities which induce vertical mixing with the underneath weakly stratified waters. The neutrally stable column density increase rate slightly weakens while its deepening rate strongly increases from ~10 m d^{-1} at 2 months to more than 90 m d^{-1} after 3 months. The convection reaches the ocean bottom in the vortex centre at 3.5 months, i.e. only one week later than in the vertical one dimensional model presented in Madec *et al.* (1990a) which describes the time evolution of the water column depending only on the convective adjustment algorithm. Therefore, in the vortex centre, the horizontal dynamics are negligible and the convection occurs through the *convective* process. After 3.5 months, the column density continues to increase, but at a constant rate which only depends on the ratio between the ocean depth and the buoyancy removal induced by the forcing.

Note that the simple convective adjustment algorithm used to parameterize the *convective* process is able to form a very thick patch of dense water and to restore the static stability of the water column, but can introduce a bias in the simulation. Indeed, a surface density anomaly is redistributed in the vertical in one time step only, which can be too fast with respect to certain phenomena occuring in nature. For example, this sometimes means an overturning of the whole water column in one time step (30 min), which implies an implicit vertical velocity of 1 m s^{-1} ! Nevertheless, this bias does not seem to be dynamically significant. Experiments have been performed with artificial delays introduced in the algorithm to decrease the implicit vertical velocity down to the observed valuesn (i.e. less than 10 cm s^{-1}). They did not produce any significant departures in the ocean response nor changes in the depth of convection.

At the end of the forcing period (month 4) a vertical section given by the numerical model (Fig. 9) is consistent with the observations obtained during the MEDOC 69 cruise (Tchérnia and Fieux 1971). For both measurements and model results the neutrally stable column has nearly the same T-S characteristics (12.7 °C ; 38.4 ‰). Surface waters present a relative temperature and salinity maximum in the center of the column. In both the observations and the simulation a surface temperature minimum is found at the outer edge of the column where convection induced by the forcing is not strong enough to involve the source of heat that constitutes the LIW.

Note that coastal advection of light peripheral water between the vortex centre and the northern coast is sufficient to allow the off coast detachment of the neutrally stable column of water, but not enough to prevent deep convection (down to 400 m) (Fig. 9). The LIW has nearly disappeared in the coasteal area, which is not in agreement with hydrological sections of MEDOC cruises (Tchérnia and Fieux 1971). Other advective mechanisms such as the wind driven circulation or the pre-existing regional cyclonic circulation must be taken into account to explain the persitance of coastal LIW during the *violent mixing* phase of DWF.

At the vortex periphery, the dynamics depart from the linear theory after 2.5 months. Meanders

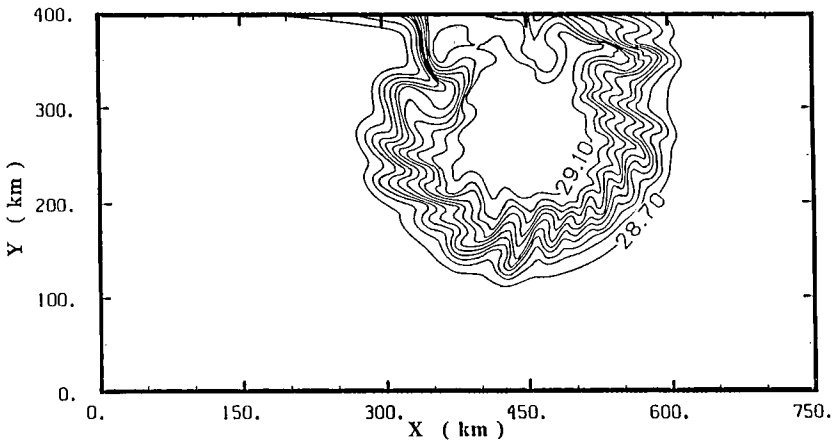

Fig. 10. Sea surface density (σ_θ units) at month 4. Meanders have developed along the front that defined the deep convective area.

start to develop along the front that defines the neutrally stable column (Fig. 10). They are a signature of the *baroclinic adjustment* process. Their wavelength λ ranges between 35 and 40 km which corresponds to a first baroclinic mode oscillation. Such meanders have been observed in early winter satellite pictures (Crépon *et al.* 1982) and during the *violent mixing* phase of DWF by *in situ* measurements (Gascard 1978). Meander crests lean backwards in relation to the direction of the moving current. This is due to the fact that disturbances drift downstream with the mean current. Those near the jet maximum move faster than disturbances away from the jet axis. These meanders propagate in the cyclonic direction with a speed of ~1.8 cm s^{-1}. This phase speed is about 1/5 of the mean surface velocity, as was found by Gascard (1978) when he applied Tang's (1975) analytical model of baroclinic instabilities to this specific problem. The meander development occurs throughout the water column and their amplitude decreases with depth. The phase deflects in the upstream direction as the depth increases (Fig. 11-a) : the surface crests lag the deep crests by $\lambda/4$, as was observed during the MEDOC cruises (Gascard 1978). Since the vertical shear of the density current is positive (from the thermal wind relationship), this vertical phase structure is characteristic of a baroclinic instability process (Pedlosky 1987). It is thus inferred that the development of the meanders occurs through such a process, i.e. through a transfer from the potential energy of the density current to the eddy kinetic energy of the meanders. Further support for this expectation can be found in Madec *et al.* (1990a) through detailed energy considerations concerning the dynamics of similar meanders in a periodic channel.

Associated with the meanders, cells of downward velocity (downward cells) appear centred on the surface density crests of meanders while cells of upward velocity (upward cells) appear between the density crests (Fig. 11). These cells extend throughout the water column without a vertical phase lag so that in the deep layers a downward (upward) cell is on the upstream (downstream) side of the meander. These cells are small : ~10 km (~20 km) in diameter for a downward (upward) cell. Maximum vertical velocities are found between 200 and 300 m (i.e. in the pycnocline) where their

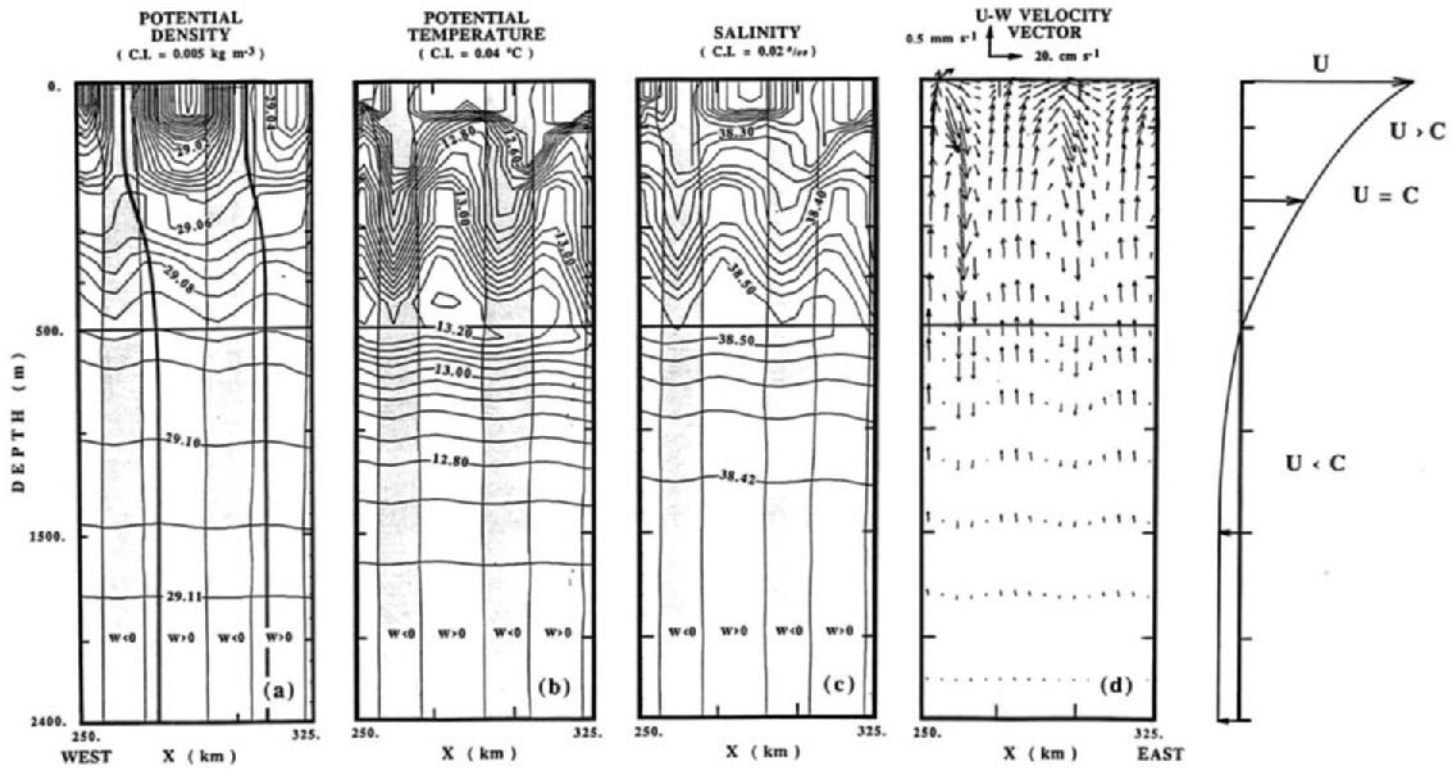

Fig. 11. West-east vertical section in the southern part of the forcing area (x=400 to 475 km ; y= 200 km) at the end of month 4. (a) potential density (σ_θ units), (b) potential temperature, (c) salinity and (d) velocity, which is a combination of the zonal and vertical components of the velocity (maximum vertical velocity is 0.7 mm $s^{-1} \approx 60$ m d^{-1}). Shaded areas are cells of downward velocity. A schematic view of the vertical profile of the along-meander componant U of the horizontal velocity is given on the right. U is compared to the meander phase speed C.

typical value is ± 0.5 mm s^{-1} (Fig. 8-d), but can sometimes exceed - 2. mm s^{-1} (i.e. ~170 m d^{-1}) in downward cells. At a given location, strong vertical motion acts over large periods of several days. Both magnitude and duration of such vertical motions are in good agreement with the low frequency motions observed during the MEDOC cruises (Gascard 1978).

Isothermal and isohaline surfaces are tilted upward and downward within the cells (Fig. 11) with an amplitude of a few hundred meters. Contrary to isopycnal surfaces, the maximum upward displacement of isothermal and isohaline surfaces (i.e. the crests of temperature and salinity) is shifted downstream as the depth decreases. This shift is a result of the relative magnitude of the phase speed C of meanders and the along-meander component U of the horizontal velocity. Below 300 m C is greater than U : a particle of water advected by the current sees the meander passing by from upstream to downstream (i.e. from west to east in Fig. 11). So, the crests of temperature and salinity are on the upstream side of the upward cell. Between 300 m and 200 m C and U are nearly equal. The crests are in the center of the upward cell. Above 200 m C is less than U : the crests are shifted to the downstream side of the upward cell. Note that above 100 m the vertical velocity is very small in comparison to the horizontal component, and pockets of relatively warm and fresh water advected from the periphery of the homogeneous column appear on the top of upward cell (Fig.11).

In the horizontal, such vertical displacements cause phase lags that vary with depth, between extrema of temperature, salinity and density in the meander development area. In the top 100 m both the vertical velocity and the vertical gradient of the characteristics of the sea water are weak. The crests of the density and salinity maxima are in phase with the crest of the temperature minimum. But, between 100 m and 400 m, strong vertical velocities are associated with maximum vertical gradients of both temperature and salinity (Fig.5). Upward motions advect the warm and salty LIW, while downward motions advect cold and fresh surface water (Fig.11). The crests of both the temperature and salinity maxima are deflected in the downstream direction with respect to density crests, while the crests of the temperature and salinity minima are deflected in the upstream direction. This results in a phase lag between temperature and salinity at these depths in the meandering region causing the thermal and haline crests to be in quadrature (Fig.12). Such a phase lag between thermal and haline fronts has been observed in the MEDOC area during the *violent mixing* phase of DWF (Gascard 1978). In some cases, the observations indicated a phase lag up to the surface, which shows that the vertical motion can be strong enough to advect the LIW up to the surface.

The *baroclinic adjustment* process is the result of the meander development which induces a redistribution of water masses and relaxes the mean horizontal density gradient. The vertical redistibution of water masses occurs at scales of some radii of deformation, in cells of upward and downward velocities. These convective events do not induce large displacements of isopycnal surfaces, as might be expected from both their magnitude and their duration. In fact, vertical motions are part of a complex three dimensional motion : strong downward motion is always associated with a horizontal velocity component oriented from the vortex centre to its periphery, and conversely for strong upward motion. Relatively dense water masses within the vortex and which are involved in cells of downward motion, first sink rapidly while being advected outside of the vortex. Then, they continue to sink, but with smaller vertical velocities (by an order of magnitude), and they spread horizontally at a depth where they are nearly in density equilibrium with surrounding water. The

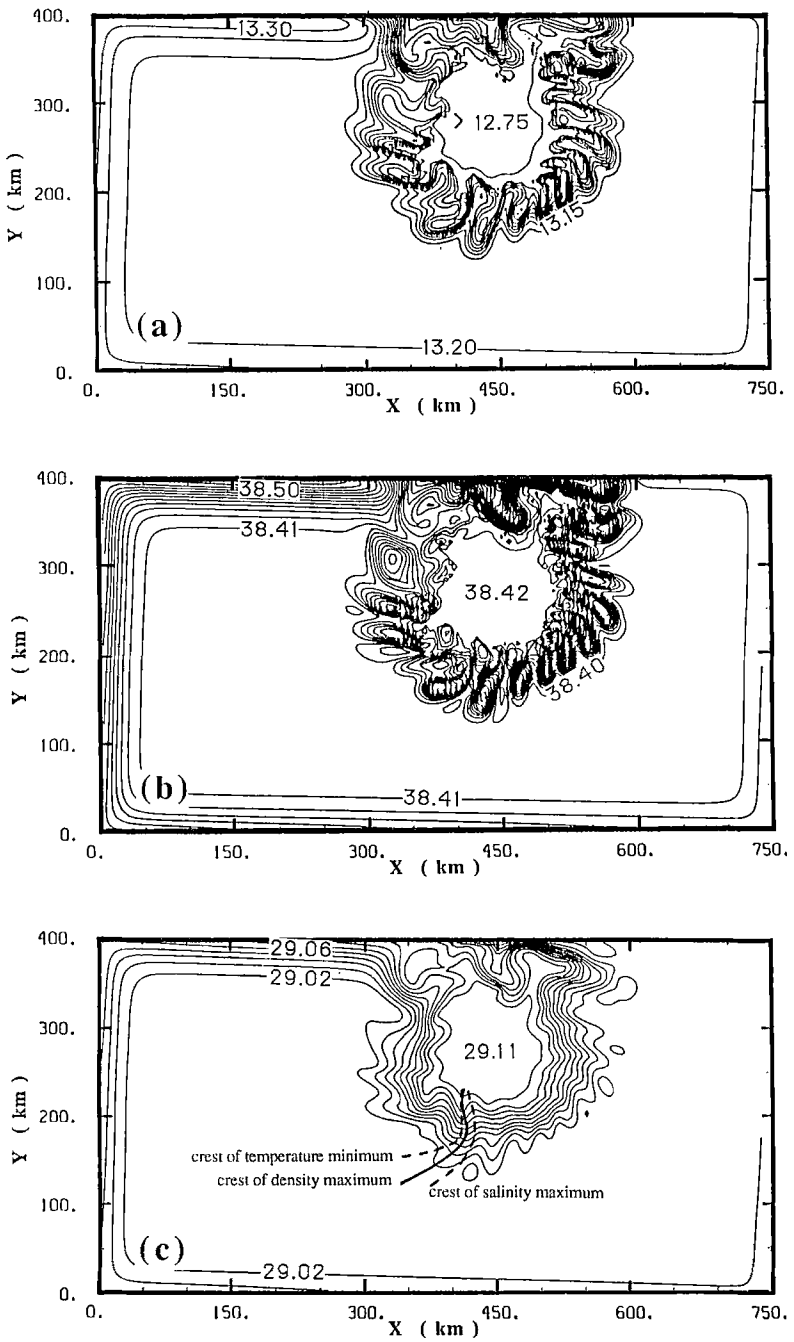

Fig. 12. Horizontal section at 225 m (i.e. just above the LIW) and after 4 months : (a) potential temperature, (b) salinity and (c) potential density (σ_θ units). The contour intervals equal 0.05 °C, 0.01 °/oo and 0.01 kg m^{-3}, respectively. Crests of salinity maximum (temperature minimum) are displaced downstream (upstream) when approaching the cells of upward (downward) motion on the downstream (upstream) side of the meanders. This is due to the upward advection of the warmer and saltier Levantine Intermediate Water and to the downward advection of relatively cold and fresh water originating from the surface.

depth of convection which results from this process is rather small, between 100 and 500 m, as can be expected from the range of density of these sinking waters : $28.96 \leq \sigma_\theta \leq 29.10$.

Both processes of convection are strongly linked, but competitors. The *baroclinic adjustment* process can only develop at the periphery of the column of dense water formed by the *convective* process. The depth to which convection can penetrate through the former process depends on the density of the water mass formed by the latter. The denser the water, the stronger and the deeper the convection. But, the *baroclinic adjustment* process advects light peripheral water into the vortex where it is involved in the *convective* process. It therefore tends to diminish the density of the water mass the *convective* process forms, and thus to restrain the depth of convection. In the present experiment, the vortex horizontal extention is large with respect to the meander amplitude (~50 km). Meander activity is not strong enough to significantly modify the stratification in the vortex centre : the convection penetrates there down to the bottom. This was not the case in Madec *et al.* (1990a) experiment where the smaller size of the vortex (200 km x 100 km) allowed the meanders to block very deep convection.

(iii) Coastal volumetric transport. The westward volumetric transport along the northern coast is given in Fig.12 for the top 800 m (with a zero motion level taken at 800 m) and for the whole water column. The thermohaline forcing induces a large westward transport in the top 800 m : ~1.5 Sv after 3.5 months, a value which is in good agrement with the winter increase of the Liguro-Provencal current transport as computed from observations with a reference level at 800 m (Béthoux et al 1982). The total westward transport (i.e. vertically integrated over the whole water column) is first smaller that those referenced at 800 m, due to both the baroclinic nature of the response and the fact that the zero-current level is above 800 m. After 3.5 months, it becomes slightly larger, reaching 2.2 Sv at month 4 due to the vertical tranfer of momentum induced by the meander development (Madec *et al.* 1990a). This intensification of the coastal weastward total transport is weak : the thermohaline forcing is ineffective to move the deep ocean layers in the cyclonic direction as observed in nature (Millot, 1988).

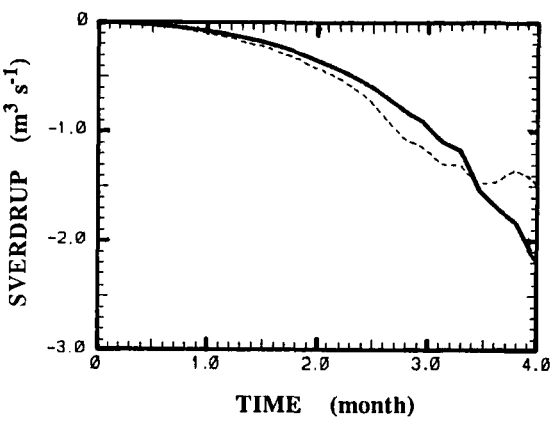

Fig. 13. Time evolution of the westward horizontal volumetric transport (in Sverdrup) between the centre of the deep convective area (x=450 km, y=300 km) and the northern coast (x=450 km, y= 400 km) referenced at 800 m (dashed line) and for the whole water column (thick solid line).

4. DISCUSSION AND CONCLUSION

The present paper is an extension of Crépon *et al.* (1989) and Madec *et al.* (1990a,b). A simple analytical model and then a three-dimensional primitive equation model have been used to investigate the ocean response to a thermohaline forcing which intersepts the coast, referring to what occurs in the NM in winter. Attention was focused on the *preconditioning* phase and *violent mixing* phase of DWF.

In the linear analytical model, two coastal Kelvin wave frons are excited by the longshore forcing discontinuities. The eastside front first stops the interface elevation (which parameterizes the convection) along the coast in the forcing area and then blocks the upwelling induced by the westside front. This yields to an offshore detachment of the interface dome whose length scale of the order of a few internal radii of deformation. Such Kelvin wave fronts are also found in the 3D numerical model, but strong departures from the linear model occurs in the numerical experiment, showing the limits of the linear approach. As the eastside front progresses westwards its intensity is damped through non-linear interactions with the thermohaline forcing. Therefore, the coastal detachment of the convective region is less efficient than in the analytical model and, when the eastside front reaches the forcing western side, its magnitude is not sufficient to cancel the increase of the upwelling which follows the westside Kelvin wave front. The coastal dynamics allow the offshore circulation to be closed in the coastal region. A surface cyclonic vortex is generated in the centre of which DWF occurs during the following months. Interactions between the coast and the ocean circulation associated with spacial variation of the thermohaline forcing inhibit deep convection in the coastal area and thus, contribute to the detachment from the coast of the deep convective area. Nevertheless, other advective mechanisms, such as the wind-driven circulation, topography induced circulation or the pre-existing regional circulation must be considered to explain the full detachment from the coast of the convective area..

In the model as well as in the observations, DWF occurs through two processes (a *convective* process and a *baroclinic adjustment* process) depending on the convective motion magnitude and on its space and time scales. The *baroclinic adjustment* process consists of a water mass redistribution in both vertical and horizontal directions. It is linked to meanders of some 40 km in wavelength which develop around the neutrally stable column. Energy considerations presented in Madec *et al.* (1990a) for similar experiments show that the physical mechanism of meander amplification is a release of potential energy through baroclinic instability. Meander development induces strong horizontal and vertical mixing. It causes dense surface waters within the vortex to sink and spread at its periphery, while light peripheral waters flow into the vortex area. The *baroclinic adjustment* process is associated with strong vertical velocities of some millimeters per second which occur in small cells (~10 km in diameter) and last several days. The depth of convection reached by this process is a function of the sinking water density. Water masses sink down to the level where the ambient density is equal to their own density, and then spread horizontally at this level. Since the water masses formed at the edge of the patch are less dense because of the horizontal mixing induced by meanders, the depth they reach by this process is rather small (some 100 m). The *baroclinic adjustment* process is thus a non penetrative process which does not entail very deep convection, but tends to relax the

patch of dense water and restratify surface waters. The occurrence of these meanders and their associated structure are in good agreement with the observations of the *violent mixing* phase of DWF. In particular, the density maximum exhibits a phase lag between the surface and the bottom, and similarly, phase lags appear between the extrema of temperature and salinity versus depth. These phase lags are a consequence of the cells of intense vertical motion.

The second process of convection (the *convective* process) is directly triggered by surface thermohaline fluxes. It is modeled by a non penetrative convective adjustment algorithm which accounts for the very small time and space scale motions of large magnitude which occur in the ocean to restore the water column static stability. Although rather crude, this parameterization reproduces the effect of the vertical mixing this motion induces. The process is purely vertical and yields to the formation of a broad, neutrally stable column of water whose T-S characteristics are in good agreement with MEDOC cruise observations. As the convection reaches the ocean bottom, the whole water column becomes neutrally stable towards the end of the forcing period.

As in Madec *et al.* (1990a,b) we are able to reproduce the *violent mixing* phase of DWF with its two associated processes of convection but the relative effect of these two processes is quite different from the previous studies. In the present paper the neutrally stable column of water has a broad extension so that the convection mainly occurs through the *convective* process in its centre while the *baroclinic adjustment* process becomes predominant at its periphery. As already mentionned in Madec *et al.* (1990a) it is difficult to extend this conclusion to the real ocean because of the over simplification of the forcing function. Space and time variabilities of the thermohaline forcing play an important role on the enhancement of one or the other process of convection (Madec et al. 1990b).

The surface horizontal circulation induced by the thermohaline forcing has a volumetric transport of 1.5 Sv for the top 800 m, a value which is of the order of magnitude of typical transport estimates for the Mediterranean Sea. The thermohaline forcing, induced by winter wind events, is clearly a major component of the local dynamics in the NM, although it is most likely not the only mechanism responsible for the observed circulation. The local wind stress field as well as the existence of the Rhône Deep Sea Fan may significantly influence the local dynamics. They will be take into account in forthcoming papers (Madec *et al.* 1991, Lott and Madec 1991).

5. ACKNOWLEDGEMENTS

This work is a contribution of EUROMODEL and MEDMODEL Programs. We particularly thank P. Delecluse, M. Chartier, J.-C. Gascard, M.-N. Houssais and C. Millot for stimulating discussions. Funding has been provided by the CEE under the MAST program and by the following French governmental agencies : Direction des Recherches Etudes et Techniques (N° 871073 and 891394) and Centre National de la Recherche Scientifique. Support for computations has been provided be the Conseil Scientifique de Centre de Calcul Vectoriel pour la Recherche.

6. REFERENCES

Anati, D. A., 1971. On the mechanism of the deep mixed layer formation during MEDOC 69. *Cah. Océanogr., 23*, 4, 427-443.

Andrich, P., G. Madec and D. L'Hostis, 1988. Performance evaluation for an ocean general circulation model : vectorization and multitasking. *Conference Proceeding of the International Conference on Supercomputing*, July 4-8, St-Malo, France, AMC press, 295-303.

Arakawa, A., 1972. Design of the UCLA general circulation model. *Numerical Simulation of Weather and Climate*, Dept. of meterology, University of California, Tech. Rep. 7, 116 pp.

Asselin, R., 1972. Frequency filter for time integrations. *Mon. Wea. Rev., 100*, 487-490.

Béthoux, J. P., L. Prieur and F. Nyffeler, 1982. The water circulation in the north-western Mediterranean Sea, its relations with wind and atmospheric pressure. *Hydrodynamics of Semi-Inclosed Seas*. J. Nihoul, Ed. Elsevier, 129-142.

Bryan, K., 1969. A numerical method for the study of the circulation of the world ocean. *J. Comput. Phys., 4*, 347-379.

Bunker, A. F., 1972. Wintertime interactions of the atmosphere with the Mediterranean Sea. *J. Phys. Oceanogr., 2*, 225-238.

Carmack, E. C., and K. Aagaard, 1973. On the deep water of the Greenland Sea. *Deep Sea Res., 20*, 687-715.

Chartier, M., 1985. Un modèle numérique tridimensionnel aux équations primitives de circulation générale de l'océan. *Thèse de Doctorat*, univertité Paris 6, France, 111 pp.

Clarke, R. A., and J. C. Gascard, 1983. The formation of Labrador Sea water. Part I : large-scale processes. *J. Phys. Oceanogr., 13*, 1764-1778.

Colin de Verdière, A., 1988: Buoyancy driven planetary flows. *J. Mar. Res., 46*, 215-265.

Cox, M. D. and K. Bryan, 1984. A numerical model of the ventilated thermocline. *J. Phys. Oceanogr., 14*, 674-687.

Crépon, M. and C. Richez, 1982: Transient upwelling generated by two-dimensional atmospheric forcing and variability in the coastline. *J. Phys. Oceanogr., 12*, 1437-1457.

Crépon, M., L. Wald and J. M. Monget, 1982a. Low-frequency waves in the Ligurian Sea during December 1977. *J. Geophys. Res., 87*, C1, 595-600.

Crépon, M., C. Richez and M. Chartier,1982b. Effect of coast line geometry on upwelling. *J. Phys. Oceanogr., 14*, 1365-1382.

Crépon, M., and M. Boukthir, 1987. Effect of deep water formation on the circulation of the Ligurian Sea. *Ann. Geophysicae, 5B*, (1), 43-48.

Crépon, M., M. Boukthir, B. Barnier and F. Aikman III, 1989. Horizontal ocean circulation forced by deep water formation. Part I : an analytical study. *J. Phys. Oceanogr., 19*, 1781-1792.

Csanady, G. T., 1982. The thermohaline driving mechanism of oceanic jet streams. *J. Mar. Res.* 40 (Suppl), 113-112.

Eckart, C., 1958. Properties of water. Part II. the equation of state of water and sea water at low temperatures and pressures. *Am. J. Sci., 256*, 225-240.

Gascard, J. C., 1973. Vertical motions in a region of deep water formation. *Deep Sea Res., 20*, 1011-1027.

Gascard, J. C., 1978. Mediterranean deep water formation, baroclinic instability and oceanic eddies. *Oceanol. Acta, 1*, (3), 315-330.

Gill, A. E., J. M. Smith, R. P. Cleaver, R. Hide and P. R. Jonas, 1979: The vortex created by mass tranfer between layers of a rotationg fluid. *Geophys. Astrophys. Fluid Dynamics., 12*, 195-220.

Gordon, A. L., 1978. Deep Antarctic convection west of Maud Rise. *J. Phys. Oceanogr., 8*, 600-612.

Hogg, N. G., 1973. The preconditioning phase of MEDOC 1969 - II. Topogrophic effects. *Deep Sea Res., 20*, 449-459.

Hua, B. L., 1988: The internal barotropic instability of surface-intensified eddies. Part I: generalized theory for isolated eddies. *J. Phys. Oceanogr.,18*, 40-55.

Hua, B. L. and F. Thomasset 1983: A numerical study of the effects of coastline geometry on wind-induced upwelling in the Gulf of Lions. *J. Phys. Oceanogr., 13*, 678-694.

Killworth, P. D., 1976. The mixing and spreading phases of MEDOC. I. *Prog. Oceanogr., 7*, 59-90.

Killworth, P. D., 1979: On "chimney" formation in the ocean. *J. Phys. Oceanogr., 19*, 531-554.

Killworth, P. D., 1983. Deep convection in the world ocean. *Rev. of Geophys. Space Phys., 21*, (1), 1-26.

Killworth, P. D., 1989: On the parameterization of deep convection in ocean models. *Proceedings Hawaiian Winter Workshop on parameterization of small scale processes*, January 17-20, University of Hawaii at Manoa, 59-74.

Lacombe, H., 1974. Deep effects of energy transfers across the sea surface : the formation of deep waters. The Western Mediterranean, as an example. *Presidential Adress*, Int. Assoc. for Phys. Sci. of the Oceans, January 15-26, Melbourne.

Lott, F. and G. Madec, 1991. Bottom topographic effect on deep water formation in the Northwestern Mediterranean Sea. In preparation.

Luyten and Stommel 1986. Gyres driven by combined wind and buoyancy flux. *J. Phys. Oceanogr., 16*, 1551-1560.

Madec, G., M. Chartier, P. Delecluse and M. Crépon, 1990a. A three-dimensional numerical study of deep-water formation in the western Mediterranean sea. *J. Phys. Oceanogr*, in press.

Madec, G., M. Chartier and M. Crépon, 1990b. Effect of thermohaline forcing variability on deep-water formation in the western Mediterranean sea : a high resolution 3D numerical study. *Dyn. Atmos. oceans*, in press.

Madec, G., M. Crépon, P. Delecluse and M. Chartier, 1991. Buoyancy- and wind-driven circulation in the Northwestern Mediterranean Sea. Submitted.

MEDOC Group, 1970. Observation of formation of deep water in the Mediterranean Sea, 1969. *Nature, 227*, 1037-1040.

Millot, C., 1987. Circulation in the Western Mediterranean Sea. *Oceanol. Acta, 10*, (2), 143-149.

Nielsen, J. H., 1912. Hydrography of the Mediterranean and adjacent waters. *Rep. Dan. Oceanogr. Exp.* 1908-1910, Rep. I: 72-191.

Pacanowski, R. C. and S. G. H. Philander, 1981. Parameterization of vertical mixing in numerical models of tropical oceans. *J. Phys. Oceanogr., 11*, 1443-1451.

Pedlosky, J., 1987. *Geophysical Fluid Dynamics.* 2nd Edition. Springer-Verlag, New-York: 710pp.

Sadourny, R., 1975. The dynamics of finite-difference models of the shallow-water equations. *J. Atmos. Sci., 32*, 680-689.

Sankey, T., 1973. The formation of deep water in the northwestern Mediterranean. *Prog. Oceanogr., 6*, 159-179.

Seung, Y. H., 1987. A buoyancy flux-driven cyclonic gyre in the Labrodor Sea. *J. Phys. Oceanogr., 17*, 134-146.

Schott, F., K. D. Leaman and R. G. Zika, 1988. Deep mixing in the Gulf of Lions, revisited. *Geophys. Res. Lett., 15,* (8), 800-803.

Stommel, H., A. B. Arons and J. Faller, 1958. Some examples of stationary planetary flow patterns in bounded basins. *Tellus, 10*, 179-187.

Stommel, H., and A. B. Arons, 1960: On the abyssal circulation of the world ocean. - II. An idealized model of the circulation pattern and amplitude in oceanic basins. *Deep sea Res., 6*, 217-233.

Stommel, H., 1972. Deep winter-time convection in the Western Mediterranean Sea. *Studies in Physical Oceanography ; A Tribute to Georg Wüst on his 80th Birthday.* Ed. Gordon and Breach, New-York, 2, 207-218.

Sutton, W., G., 1934. The asymptotic expansion of a function whose operational equivalent is known. *J. London Math. Soc.*, **9**, 131-137.

Swallow, J. C., and G. F. Caston, 1973. The preconditioning phase of MEDOC 1969 - I. Observations. *Deep Sea Res., 20*, 429-448.

Tang, C. M., 1975. Baroclinic instability of stratified shear flows in the ocean and atmosphere. *J. Geophys. Res., 80*, 9, 1168-1175.

Tchernia, P., and M. Fieux, 1971. Résultats des observations hydrologiques exécutées à bord du N/O "Jean Charcot" pendant la campagne MEDOC 69 (30 janvier-28 février), (18-31 mars). *Cah. Océanogr., 23*, suppl. n°1, 1-91.

Voorhis, A., and D. C. Webb, 1970. Large vertical currents observed in a western sinking region of the northwestern Mediterranean. *Cah. Océanogr., 22*, 571-580.

Wajsowicz, R. C. and A. E. Gill, 1986. Adjustment of the ocean under buoyancy forces. Part I : the role of Kelvin waves. *J. Phys. Oceanogr., 16*, 2097-2114.

Worthington, L. V., 1972a. Anticyclogenesis in the ocean as a result of outbreaks of continental polar air. *Tribute to George Wust on his 80th birthday*, A. L. Gordon, Ed. Gordon and Breech, 169-178.

Worthington, L. V., 1972b. Negative heat flux as a cause of water mass formation. *J. Phys. Oceanogr.*, **12**, 205-211.

Worthington, L. V., 1976. On the north Atlantic circulation. *The Johns Hopkins Oceanographic Studies 6*, 110pp.

Worthington, L. V., 1977. Intensification of the Gulf Stream after the winter 1976-77. *Nature, 270*, 415-417.

This Page Intentionally Left Blank

VERTICAL CELLS DRIVEN BY VORTICES - A POSSIBLE MECHANISM FOR THE PRECONDITIONING OF OPEN-OCEAN DEEP CONVECTION

P.C. CHU
Department of Oceanography, U.S. Naval Postgraduate School, Monterey, California 93943 (U.S.A.)

ABSTRACT

The occurrence of open-ocean deep convection requires a background cyclonic circulation and a preconditioning. Both conditions reduce the stratification of the water column within the cyclonic gyre, which will then become eligible for convection if the surface forcing is sufficiently intense. Therefore, for open-ocean deep convection the generation of vertical cells inside the vortex by any mechanism (not necessary by pure thermodynamical processes) is ultimately important. There are two dynamical mechanisms for inducing vertical cells inside a stably stratified vortex: baroclinic and centrifugal instabilities. The combination of the two is called symmetric instability. In order to verify the importance of symmetric instability on the generation of vertical cells inside the vortex, a tangential velocity field with Gaussian distribution in both radial and vertical under stable stratification is taken as a mean flow field. The disturbances produced from this mean flow are assumed to be two dimensional (no azimuthal dependency) and described by a streamfunction in the radial-vertical sections. This streamfunction satisfies a second-order partial differential equation. The numerical solutions show the generation of vertical cells inside the vortex. The strength and structure of these cells largely depend on the four parameters: Burger number $Bu = (NH/fR)^2$, Rossby number $Ro = V/fR$, barotropic index m_r, and baroclinic index m_z. The larger the values of Ro, m_r, and m_z, , or the smaller the value of Bu (weaker stratification for a given size of vortex), the stronger the vertical circulation. The time rate change of density (density redistribution) generated by a vortex and horizontally averaged inside the vortex, indicates the decrease of density in the lower part of the vortex, and the increase of density in the upper part of the vortex. This process, on the time scale of weeks, decreases the static stability and serves as one contributor to preconditioning for the open ocean deep convection.

INTRODUCTION

The association of deep convection with strong vortices has long been observed. Gordon (1978) reported the occurrence of deep convection in February 1977 within the central region of the Weddell Gyre west of Maud Rise. A column of water (14 km radius) was observed in which the normal Antarctic stratification of temperature was absent. The column appeared as a warm, low-salinity surface layer occupying approximately the upper 190 m above a cold nearly homogeneous water column, with a cyclonic eddy (surface velocity greater than 50 cm/s) extending to at least 4000 m.

One may ask such questions: is there any relation between the vortex and the deep convection? and what is the relation? The main task of this paper is to answer these questions and to present a possible mechanism for generating vertical cells by a vortex. In a general sense, convection can be defined as vertical overturning (Chu, 1991), no matter whether the process that generated it is thermodynamical or dynamical.

Vortices represent the most energetic components of the meso-scale eddy field in the world oceans. Their large azimuthal swirl speeds, compared with the rate at which they translate, allows them to carry substantial volumes of fluid with them over long periods of time. Rayleigh (1880, 1916) first investigated the instability of rotating structures in non-rotating fluids. He considered a basic swirling flow of an inviscid fluid which moves with angular velocity $\Omega(r)$, an arbitrary function of the distance r from the axis of rotation. By a simple physical argument Rayleigh then derived his celebrated criterion for stability. Rayleigh's circulation criterion states that a necessary and sufficient condition for stability to axisymmetric disturbances is that the square of the angular momentum does not decrease radially anywhere,

$$C(r) = \frac{1}{r^3}\frac{d}{dr}(r^2\Omega)^2 \tag{1}$$

where the function, $C(r)$, is called the Rayleigh Discriminant. The vortex can be either centrifugally stable or unstable, depending upon the sign of the Rayleigh Discriminant, C. Rayleigh further observed that there is an analogy between the stability of rotating flows and the stability of a stratified fluid at rest in a gravitational field, the analogue of C in fact being the square of the Brunt-Vaisaila frequency.

In subsequent sections a dynamical system is established to discuss the generation of vertical cells inside vortices. The sea water is assumed to be Boussinesq and inviscid. Therefore, the system excludes the damping effect of frictional forces on the vortex. Furthermore, for the sake of simplicity, we also assume no vertical velocity at the top and the bottom of the vortex and no interaction between the vortex and the ambient flow.

2. DYNAMICAL SYSTEM

2.1 Total Flow

A cylindrical coordinate system (r, λ, z) is used in this study with the rotating axis of the vortex as the center of the system (Fig.1). The vertical coordinate is positive upward and zero at the bottom of the vortex.

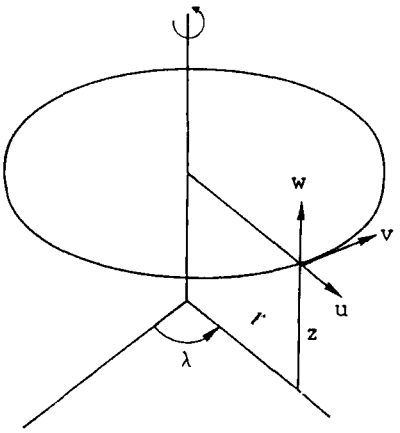

Fig. 1. The cylindrical coordinates (r, λ, z) with the vertical axis at the center of the vortex.

The Boussinesq approximation is assumed for our system. ρ_0 is the characteristic density of the sea water. The total density and pressure can be decomposed into

$$\rho = \rho_0 + \rho_* \tag{2a}$$

$$p = (p_a - \rho_0 g z) + p_* \tag{2b}$$

where p_a is the air pressure at the ocean surface, p_* is the dynamical pressure, and ρ_* is the density deviation from the characteristic value. Under the assumption that the motion is axisymmetric and inviscid, the governing equations are written in the cylindrical coordinates as

$$\frac{du}{dt} - (f + \frac{v}{r})v = -\frac{1}{\rho_0}\frac{\partial p_*}{\partial r} \tag{3a}$$

$$\frac{dv}{dt} + (f + \frac{v}{r})u = 0 \tag{3b}$$

$$\frac{dw}{dt} = -\frac{\rho_*}{\rho_0} g - \frac{1}{\rho_0} \frac{\partial p_*}{\partial z} \tag{3c}$$

$$\frac{\partial (ru)}{\partial r} + \frac{\partial (rw)}{\partial z} = 0 \tag{3d}$$

$$\frac{d\rho_*}{dt} = Q \tag{3e}$$

where u, v, w are radial, tangential, and vertical components of the flow field, respectively. Q is the thermally induced rate of change of density. However, the dynamically driven vertical cells and their contribution to the deep convection are the main items; therefore, Q is set to be zero in this research. The operator d/dt is defined by

$$\frac{d}{dt} = \frac{\partial}{\partial t} + u \frac{\partial}{\partial r} + v \frac{\partial}{\partial \theta} + w \frac{\partial}{\partial z} \tag{4}$$

2.2 Basic Flow

A steady axisymmetric and gradiently balanced circular vortex with depth H and radius R, is taken to be the basic flow, i.e.,

$$\bar{u} = 0, \quad \bar{v} = \bar{v}(r, z), \quad \bar{w} = 0, \quad \text{for } 0 < r < R, \quad 0 < z < H \tag{5}$$

The momentum equations are

$$\left(f + \frac{\bar{v}}{r}\right)\bar{v} = \frac{1}{\rho_0} \frac{\partial \bar{p}}{\partial r} \tag{6a}$$

$$-\frac{\bar{\rho}}{\rho_0} g - \frac{1}{\rho_0} \frac{\partial \bar{p}}{\partial z} = 0 \tag{6b}$$

where $\bar{v}$ is the mean tangential current. f is the Coriolis parameter. The differentiation of (6a) with respect to z minus the differentiation of (6b) with respect to r, leads to the thermal wind relation for the basic flow

$$\left(f + \frac{2\bar{v}}{r}\right) \frac{\partial \bar{v}}{\partial z} = -\frac{g}{\rho_0} \frac{\partial \bar{\rho}}{\partial r} \tag{7a}$$

Therefore, the basic flow is the gradient balanced flow. Including the earth rotation, the angular velocity of water parcels at a radius of r is

$$\Omega = \frac{f}{2} + \frac{\bar{v}}{r}$$

The square of the angular momentum is

$$M = (\Omega r^2)^2 = (\frac{f}{2} + \frac{\bar{v}}{r})^2 r^4$$

The thermal wind relation (7a) becomes

$$\frac{1}{r^3}\frac{\partial M}{\partial z} = \frac{g}{\rho_0}\frac{\partial \bar{\rho}}{\partial r} \tag{7b}$$

2.3 Disturbances

Suppose that axisymmetric disturbances are generated from the basic flow. The total flow field is then a combination of the two parts: basic flow and disturbances.

$$u = u', \quad v = \bar{v} + v', \quad w = w', \quad \rho_* = \bar{\rho} + \rho', \quad p_* = \bar{p} + p' \tag{8}$$

Substituting (8) into (3a-e) and taking into account (6a,b), and assuming small amplitudes of disturbances, a set of equations for the disturbances is then obtained

$$\frac{\partial u'}{\partial t} - (f + \frac{2\bar{v}}{r})v' = -\frac{1}{\rho_0}\frac{\partial p'}{\partial r} \tag{9a}$$

$$\frac{\partial v'}{\partial t} + (f + \frac{\bar{v}}{r} + \frac{\partial \bar{v}}{\partial r})u' + \frac{\partial \bar{v}}{\partial z}w' = 0 \tag{9b}$$

$$\frac{\partial w'}{\partial t} = -\frac{\rho'}{\rho_0}g - \frac{1}{\rho_0}\frac{\partial p'}{\partial z} \tag{9c}$$

$$\frac{\partial (ru')}{\partial r} + \frac{\partial (rw')}{\partial z} = 0 \tag{9d}$$

$$\frac{\partial \rho'}{\partial t} + \frac{\partial \bar{\rho}}{\partial r}u' + \frac{\partial \bar{\rho}}{\partial z}w' = 0 \tag{9e}$$

The vertical circulation generated inside the vortex can be depicted by the streamfunction

$$u' = \frac{1}{r}\frac{\partial \psi}{\partial z}, \quad w' = -\frac{1}{r}\frac{\partial \psi}{\partial r} \tag{10}$$

Eliminating v', p', ρ' from (9a-e), we obtain an equation for the streamfunction ψ,

$$\frac{\partial^2}{\partial t^2}\left[\frac{\partial}{\partial r}\left(\frac{1}{r}\frac{\partial \psi}{\partial r}\right)+\frac{1}{r}\frac{\partial^2 \psi}{\partial z^2}\right]+\frac{\partial}{\partial r}\left(\frac{A}{r}\frac{\partial \psi}{\partial r}+\frac{B}{r}\frac{\partial \psi}{\partial z}\right)+\frac{\partial}{\partial z}\left(\frac{C}{r}\frac{\partial \psi}{\partial z}+\frac{B}{r}\frac{\partial \psi}{\partial r}\right)=0 \tag{11}$$

which is the same equation used by Ooyama (1966) and Charney (1973), and where

$$A \equiv -\frac{g}{\rho_0}\frac{\partial \bar{\rho}}{\partial z} \tag{12a}$$

$$B \equiv -\frac{1}{r^3}\frac{\partial M}{\partial z} = -\left(f+\frac{2\bar{v}}{r}\right)\frac{\partial \bar{v}}{\partial z} = \frac{g}{\rho_0}\frac{\partial \bar{\rho}}{\partial r} \tag{12b}$$

$$C \equiv \frac{1}{r^3}\frac{\partial M}{\partial r} = \left(f+\frac{2\bar{v}}{r}\right)\left(f+\frac{\bar{v}}{r}+\frac{\partial \bar{v}}{\partial r}\right) \tag{12c}$$

represent three different frequencies: $\sqrt{A}$ is the buoyancy frequency, $\sqrt{B}$ is the baroclinic frequency, and $\sqrt{C}$ is the generalized inertial frequency. Here, the mean density $\bar{\rho}$ is a function of r and z. From (12a) and (12b) we can get the relationship between A and B:

$$\frac{\partial A}{\partial r} = -\frac{\partial B}{\partial z} = \frac{1}{r^3}\frac{\partial^2 M}{\partial z^2} \tag{12d}$$

If the ocean has constant stratification outside the vortex, the integration of (12d) with respect to r leads to

$$A = N^2 + D \tag{13a}$$

$$D = \int_r^R \frac{\partial B}{\partial z}\,dr = -\int_r^R \left[\left(f+\frac{2\bar{v}}{r}\right)\frac{\partial^2 \bar{v}}{\partial z^2}+\frac{2}{r}\left(\frac{\partial \bar{v}}{\partial z}\right)^2\right]dr \tag{13b}$$

where N is the characteristic value of the Brunt-Vaisala frequency, which is a constant in this research. The time scale for deep convection is generally much longer than N^{-1} and f^{-1}, i.e.,

$$|\frac{\partial^2}{\partial t^2}| \ll N^2, \quad |\frac{\partial^2}{\partial t^2}| \ll f^2$$

The time rate of change should be neglected against both the buoyancy frequency and the inertial frequency. Therefore, the equation for streamfunction (11) is simplified into

$$\frac{\partial}{\partial r}(\frac{A}{r}\frac{\partial \psi}{\partial r} + \frac{B}{r}\frac{\partial \psi}{\partial z}) + \frac{\partial}{\partial z}(\frac{C}{r}\frac{\partial \psi}{\partial z} + \frac{B}{r}\frac{\partial \psi}{\partial r}) = 0 \tag{14}$$

which shows the vertical cells in (r, z) section generated by the combined effect of buoyancy, baroclinicity, and inertia of a vortex, which is called the symmetric instability. Here, we are interested in the intrinsic physical mechanisms generating vertical cells inside a vortex. Interaction between the vortex and the ambient flow is beyond the scope of this research. Therefore, it is reasonable to assume that no flow can across the edge of the vortex. The radial velocity at the center of the vortex should be zero. Furthermore, we also assume no vertical velocity at the top and the bottom of the vortex for the sake of simplicity. Thus, the boundary conditions for (14) are

$$\psi = 0, \quad \text{at } r = 0, \ r = R, \ z = 0, \ z = H \tag{15}$$

3. NONDIMENSIONALIZATION

If the independent variables (r, z), mean tangential velocity, squares of the three frequencies (B, C, D), and the streamfunction are nondimensionalized by

$$(r, z, \bar{v}) = (R\tilde{r}, H\tilde{z}, V\tilde{v}), \quad (B, C, D) = f^2(Ro\frac{R}{H}\tilde{B}, \tilde{C}, Ro\frac{R^2}{H^2}\tilde{D}), \quad \psi = VH^2\tilde{\psi} \tag{16}$$

where V is the characteristic tangential velocity of the vortex, and

$$\tilde{B} = -(1 + 2Ro\frac{\tilde{v}}{\tilde{r}})\frac{\partial \tilde{v}}{\partial \tilde{z}} \tag{17a}$$

$$\tilde{C} = (1 + 2Ro\frac{\tilde{v}}{\tilde{r}})(1 + Ro\frac{\tilde{v}}{\tilde{r}} + Ro\frac{\partial \tilde{v}}{\partial \tilde{r}}) \tag{17b}$$

$$\tilde{D} = -\int_{\tilde{r}}^{1}[(1 + 2Ro\frac{\tilde{v}}{\tilde{r}})\frac{\partial^2 \tilde{v}}{\partial \tilde{z}^2} + 2\frac{Ro}{\tilde{r}}(\frac{\partial \tilde{v}}{\partial \tilde{z}})^2]d\tilde{r} \tag{17c}$$

where $Ro = V/fR$ is the Rossby number. The nondimensional form of the equation (14) is

$$(Bu + Ro\tilde{D})\frac{\partial^2\tilde{\psi}}{\partial\tilde{r}^2} + 2Ro\tilde{B}\frac{\partial^2\tilde{\psi}}{\partial\tilde{r}\partial\tilde{z}} + \tilde{C}\frac{\partial^2\tilde{\psi}}{\partial\tilde{z}^2}$$

$$-(Bu + Ro\tilde{D})\frac{1}{\tilde{r}}\frac{\partial\tilde{\psi}}{\partial\tilde{r}} + \left(\frac{\partial\tilde{C}}{\partial\tilde{z}} + Ro\frac{\partial\tilde{B}}{\partial\tilde{r}} - Ro\frac{\tilde{B}}{\tilde{r}}\right)\frac{\partial\tilde{\psi}}{\partial\tilde{z}} = 0 \tag{18}$$

where $Bu = (NH/fR)^2$, is the Burger number, which is the square of the ratio of the Rossby radius of deformation to the radius of the vortex. For a given vortex, the magnitude of Bu indicates the stratification. The smaller the Bu, the weaker the stratification. The nondimensional form of the boundary conditions (15) is

$$\psi = 0, \quad \text{at } \tilde{r} = 0, \ \tilde{r} = 1, \ \tilde{z} = 0, \ \tilde{z} = 1 \tag{19}$$

4. VERTICAL CELLS DRIVEN BY A GAUSSIAN VORTEX

A cyclonic vortex with Gaussian distribution in both radial and vertical

$$\tilde{v}(\tilde{r}, \tilde{z}) = \exp\left[-m_r(\tilde{r} - \frac{1}{2})^2 - m_z(\tilde{z} - \frac{1}{2})^2\right] \tag{20}$$

is chosen as a basic flow in this study, where m_r, m_z are parameters indicating the strength of the shear in radial and vertical directions. Equation (18) with the boundary condition (19) and mean flow (20) is integrated numerically. The successive over-relaxation method is used for the integration. The solutions show the generation of vertical cells inside the vortex even in the relatively strong stratification case ($Bu = 1$). The other three model parameters Ro, m_r, m_z are found to be important in affecting the structure of the vertical cells inside the vortex. For a given vortex size, each parameter, taking only two different values, represents the two different physical conditions, such as, $Ro = 0.1$, for a relatively weak vortex, and $Ro = 0.2$, for a relatively strong vortex; $m_r = 0$, for the absence of radial shear, and $m_r = 4$, for a relatively strong radial shear; and $m_z = 0$, for the absence of vertical shear, and $m_z = 4$, for a relatively strong vertical shear.

Fig.2 shows the streamfunction in a radial-vertical section for $Bu = 1$ and $Ro = 0.1$: (*a*) $m_r = 0$, $m_z = 0$, (*b*) $m_r = 4$, $m_z = 0$, (*c*) $m_r = 0$, $m_z = 4$, (*d*) $m_r = 4$, $m_z = 4$. These cases refer to a relatively strong stratification and a relatively weak vortex.

Several results can be easily drawn from Fig.2:

(a) The vertical cells do exist inside the vortex for all cases, even in the case without radial and vertical shears of the mean tangential velocity as shown in Fig.2a. This strongly suggests that the square of the generalized inertial frequency, $C(r)$, is a fundamental factor in generating vertical circulation inside the vortex (since $B = 0$ and $D = 0$).

(b) Comparison of Fig.2a with Fig.2b shows that without the vertical shear on the mean tangential velocity, the effect of the radial shear ($m_r \neq 0$) on the vertical cells is very small.

(c) Comparison of Fig.2b with Fig.2d indicates that with vertical shear on the mean tangential velocity, the effect of the radial shear on the vertical cells becomes evident. The upper cell penetrates to the base of the vortex, and the two-cell structure becomes a three-cell structure.

(d) Comparison of Fig.2c with Fig.2a leads to the result that the baroclinity always intensifies the strength of the vertical cells.

Fig.3 shows the streamfunction in a radial-vertical section for $Bu = 1$ and $Ro = 0.2$: (*a*) $m_r = 0$, $m_z = 0$, (*b*) $m_r = 4$, $m_z = 0$, (*c*) $m_r = 0$, $m_z = 4$, (*d*) $m_r = 4$, $m_z = 4$. These cases refer to a relatively strong stratification and a relatively strong vortex. Comparison of Fig.3 with Fig.2 shows that the increase of the Rossby number will generally strengthen the vertical cells. Therefore, for a given size of the vortex, the faster the rotation of the vortex, the stronger the vertical cells inside the vortex.

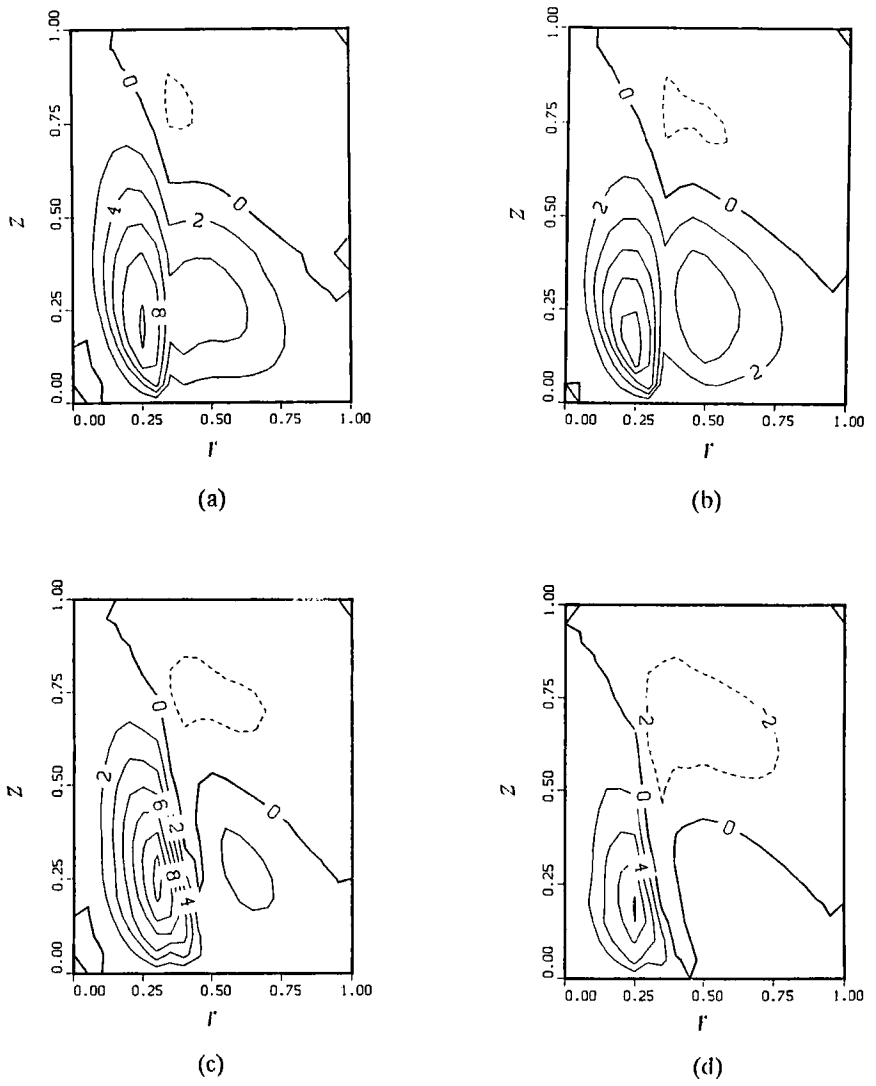

Fig. 2. The streamfunction in radial-vertical section for $Bu = 1$ and $Ro = 0.1$: (*a*) $m_r = 0$, $m_z = 0$, (*b*) $m_r = 4$, $m_z = 0$, (*c*) $m_r = 0$, $m_z = 4$, (*d*) $m_r = 4$, $m_z = 4$.

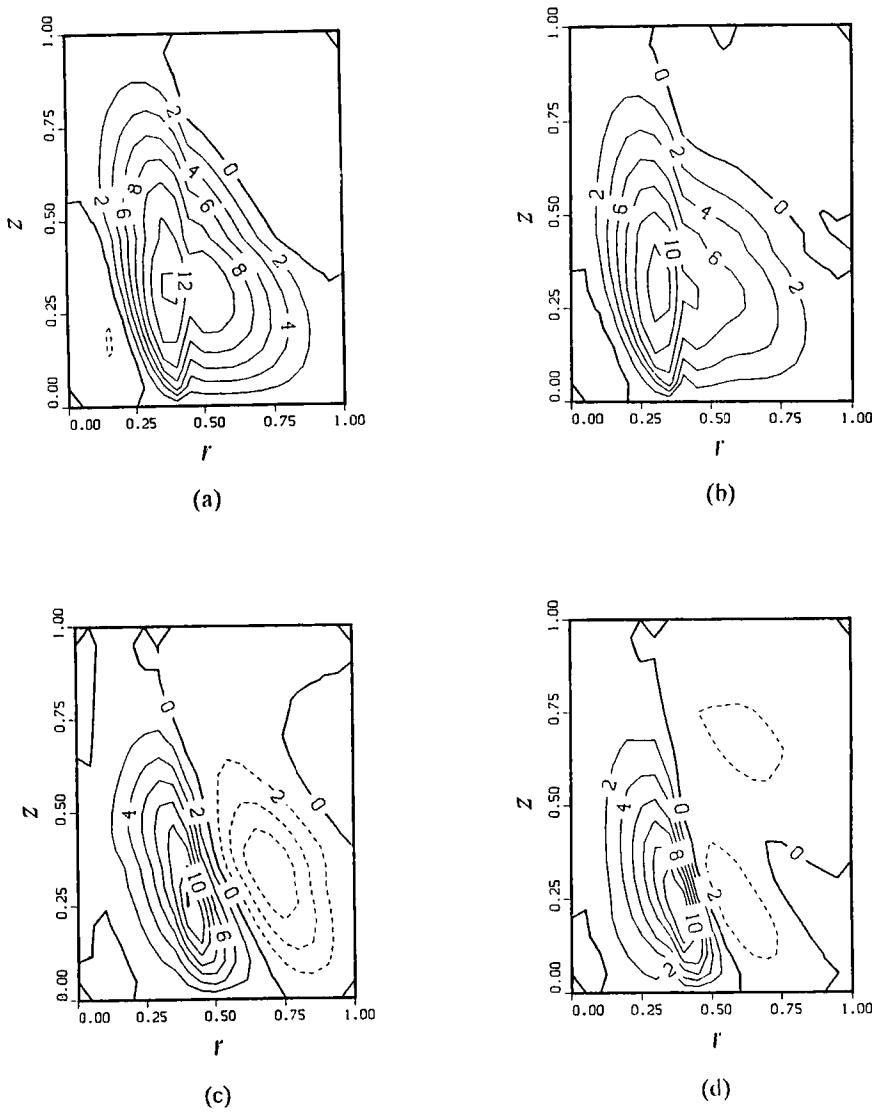

Fig. 3. The streamfunction in radial-vertical section for $Bu = 1$ and $Ro = 0.2$: (*a*) $m_r = 0$, $m_z = 0$, (*b*) $m_r = 4$, $m_z = 0$, (*c*) $m_r = 0$, $m_z = 4$, (*d*) $m_r = 4$, $m_z = 4$.

5. TIME RATE OF DENSITY INSIDE THE VORTEX

Define a nondimensional density perturbation averaged over the horizontal plane inside the vortex as follows:

$$\sigma = \frac{1}{\pi R^2}\int_0^R 2\pi \frac{\rho'}{\rho_0} r dr = 2\int_0^1 \frac{\rho'}{\rho_0}\tilde{r}\, d\tilde{r} \tag{21}$$

Time t is nondimensionalized by

$$t = (f^{-1})\frac{1}{2Fr^2\delta}\tilde{t} \tag{22}$$

where $Fr = V^2/gH$, is the Froude number, and $\delta = R/H$, is the aspect ratio. Integrating the density equation (9e) over the horizontal plane within the vortex, and using the nondimensional forms of parameters (17a,c), a nondimensional equation of time rate of change of horizontally averaged density is obtained

$$\frac{\partial\sigma}{\partial\tilde{t}} = -\int_0^1 (\tilde{B}\frac{\partial\tilde{\psi}}{\partial\tilde{z}} + \tilde{D}\frac{\partial\tilde{\psi}}{\partial\tilde{r}})d\tilde{r} \tag{23}$$

The derivative, $\partial\sigma/\partial\tilde{t}$, is computed for the case: $Bu = 1$, $Ro = 0.1$, $m_r = 4$, $m_z = 4$ (Fig.2d). The effect of the vortical motion on the density redistribution inside the vortex is shown in Fig.4, where the density decreases in the lower part ($\tilde{z} < 0.27$) of the vortex, and increases in the upper part ($\tilde{z} > 0.27$) of the vortex. This process reduces the stratification and tends to make the density vertically uniform inside the vortex. We view this process as one contribution to the preconditioning of the open ocean deep convection.

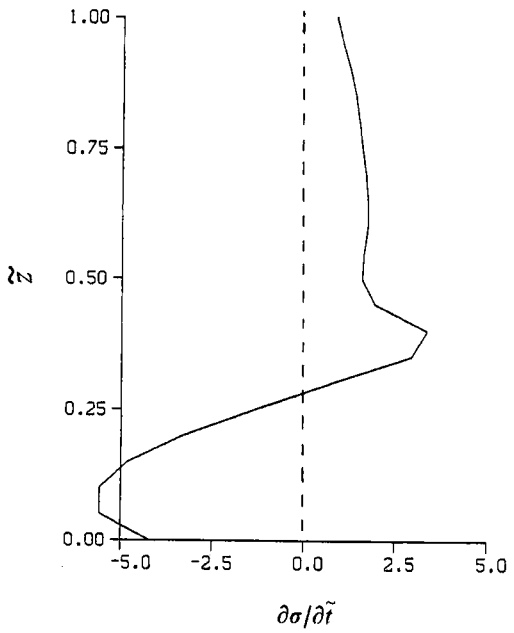

Fig. 4. Vertical dependency of $\partial\sigma/\partial\tilde{t}$ for the vortex with $Bu = 1$, $Ro = 0.1$, $m_r = 4$, and $m_z = 4$.

The time scale for the density redistribution process inside the vortex can be roughly estimated as follows. If the tangential velocity for the vortex V is 50 cm/s, and if the thickness of the vortex H is on the order of 1 km, the square of the Froude number (Fr^2) will be 0.25×10^{-4}. The aspect ratio δ is on the order of 0.1, and the change of the non-dimensional density perturbation $\Delta\sigma$ is on the order of 10^{-3}, and the integration, $I = \int_0^1 (\tilde{B}\partial\tilde{\psi}/\partial\tilde{z} + \tilde{D}\partial\tilde{\psi}/\partial\tilde{r})d\tilde{r}$, is on the order of 5 (Fig. 4). Therefore, the time scale for this density redistribution process is

$$T \sim f^{-1} \frac{\Delta\sigma}{2Fr^2\delta O(I)} \sim 40 f^{-1}, \tag{24}$$

which is on the order of few weeks. This scale is coincident with the time period (few weeks) needed for the preconditioning which creates a region of very weak static stability within the vortex (Killworth, 1983).

6. CONCLUSIONS

(a) This research is intended to bring to the attention of the oceanographic community the importance of symmetric instability in vortex dynamics, and in generating convection. Solutions show generation of a variety of convective cells inside the vortex by this mechanism.

(b) The vertical cells can be generated in the vortex with relatively strong stratification and without any radial or vertical shear. The rotation itself will induce the vertical circulation.

(c) The baroclinicity always intensifies the vertical circulation. However, the effect of the radial shear on the vertical cells becomes important only when it is associated with vertical shear.

(d) The stronger the rotation of the vortex, the stronger the vertical cells inside the vortex.

(e) The time scale for the density redistribution by this dynamically driven overturning is inversely proportional to the square of the Froude number. For numerous observations of vortices in the ocean, this time scale is several weeks. This scale is coincident with the time period needed for the preconditioning.

(f) The solution here refers to the Gaussian type cyclonic vortex. For other kinds of vortices, the solution may vary.

(g) The solution is obtained from assuming rigid boundaries both at the top and the bottom of the vortex. If free boundary conditions or other kinds of boundary conditions are used, the shape of the vertical cells will change, especially near the boundaries, but the basic physics will remain.

7. ACKNOWLEDGEMENTS

The author is grateful to Prof. R.W. Garwood, Jr. and Ms. A. Bird of the Naval Postgraduate School for invaluable discussion and comments.

Funding for this study was provided by the Office of Naval Research, and the Naval Postgraduate School. Computational support was provided by the W.R. Church Computer Center of the Naval Postgraduate School.

8. REFERENCES

Charney, J.G., 1973. Planetary fluid dynamics. In: P. Morel (Editor), Dynamical Meteorology. Reidel, Dordrecht, pp. 99-351.

Chu, P.C., 1991. Geophysics of deep convection and deep water formation in oceans. (in this volume).

Killworth, P.D., 1983. Deep convection in the world ocean. Rev. Geophys. & Space Phys., 21: 1-26.

Ooyama, K., 1966. On the stability of the baroclinic circular vortex: a sufficient criterion for instability. J. Atmos. Sci., 23: 43-53.

Rayleigh, Lord, 1880. On the stability, or instability, of certain fluid motion. Scientific Papers, Cambridge University Press, 1: 474-487.

Rayleigh, Lord, 1916. On the dynamics of revolving fluids. Scientific Papers, Cambridge University Press, 6: 432-446.

This Page Intentionally Left Blank

MODELING THE GEOSTROPHIC ADJUSTMENT AND SPREADING OF WATERS FORMED BY DEEP CONVECTION

A. J. HERMANN and W. B. OWENS
Department of Physical Oceanography, Woods Hole Oceanographic Institution, Woods Hole, Massachusetts 02543 USA

ABSTRACT

The rate and the manner in which newly formed patches of dense oceanic waters may sink and spread is examined as a function of patch size and buoyancy input. The mass of dense fluid resulting from a rapid deep convective process comprises a large reservoir of potential energy, which may be carried away by two different means, broadly classed here as "radiative" (near-inertial waves) vs. "advective" (baroclinic instability). Both numerical and analytical methods are employed to investigate the relative amounts of potential energy radiated to the far field by either class of motion. We also consider the possible interactions between the radiative and advective motions for strong buoyancy forcing.

INTRODUCTION

While past modeling efforts have addressed the process of deep convection and the subsequent evolution of localized dense waters in the ocean, few have attempted to do so in three dimensions, and with sufficient vertical or horizontal resolution to capture the mesoscale dynamics involved. In this study, we employ a three-dimensional, hydrostatic-primitive equation model to address the mechanisms by which recently formed columns of dense water (e.g. "chimneys") geostrophically adjust through radiation of near-inertial waves, while simultaneously sinking and spreading. A determination of the nature of these potential energy and mass fluxes ultimately provides insight into which types of buoyancy forcing will be optimal for deep water formation and spreading in the open ocean.

By focussing on the adjustment of nearly circular columns of dense fluid which are initially at rest, we temporarily set aside the issue of how these patches are formed: the so-called "preconditioning" and "violent mixing" phases as described by Killworth (1976) in his study of deep convection in the northwestern Mediterranean. In effect we are presuming here that the deep convection has taken place on a time scale which is short relative to the

time necessary for full geostrophic adjustment; as shown in the modeling results, this period can be very long indeed. The wave adjustment and, when it occurs, advective instability take place over the same period, necessitating the use of a primitive equation model to capture both super- and subinertial dynamics.

Our motivation for considering the eventual adjustment of an initially quiescent density field is as follows. As outlined by Killworth (1976), preconditioning of the density field creates a situation where buoyancy flux can easily penetrate the main thermocline. While surface buoyancy fluxes are frequently aggregated as monthly or seasonal averages, in fact they more typically consist of a series of powerful events involving both super- and subinertial time scales. This is especially true when atmospheric fronts are a primary feature of the local weather. As an idealization, we consider a single, sudden, powerful storm (a delta function in time), which produces a large buoyancy flux out of a subdomain of the preconditioned area, and leads to a gravitationally unbalanced density field. Note that by considering a delta function buoyancy source, we are in fact exploring the oceanic response to a white spectrum of buoyancy forcing, which includes all time scales.

For the present study, we ignore the latitudinal variations of the Coriolis parameter, f. While this excludes Rossby waves, it should not radically alter our conclusions here, which pertain to time scales of days to weeks. Rossby wave radiation can be dynamically important when very low frequency or constant buoyancy forcing is applied, however (Davey and Killworth, 1989).

We begin with a general discussion of the radiative and advective motions, and an overview of previous research focussing on each class in circular and noncircular geometries. This is followed by a description of the numerical model, and the results of several numerical experiments exploring: (1) the evolution of chimneys as a function of size, and (2) the dynamical impact of the superinertial transients. Finally, we focus on the energetics of gravitational adjustment for circular geometries in a rotating fluid. A scaling law is suggested, for comparing the rates of energy loss by radiative to those by advective means.

2 RADIATIVE AND ADVECTIVE DYNAMICS

Geostrophic adjustment, as classically defined, involves potential energy loss and conversion to kinetic energy through radiation of superinertial transients during the collapse of some gravitationally unbalanced density or pressure field. While locally producing some slumping of fluid, this wavelike gravitational collapse cannot by itself carry a column of

dense fluid any significant distance away from its formation site in a rotating system. For a rotating fluid, the end state of superinertial wave adjustment will consist of a balance between the outward directed pressure gradient and the azimuthal velocity; radial spreading of dense waters by this means alone must eventually cease when no boundaries are nearby to support ageostrophic motions. The small advective component of this wave adjustment phase depends mainly upon the magnitude of the initial disturbance, the width of the initial fluid column, and the Rossby radius scale. Even in the nonrotating case, where all of the available potential energy will be released through wave radiation, the evolution to a final state with no radial velocity will generally involve only small spreading of the fluid.

A second means of spreading dense fluid is available, with no intrinsic limit on the distance it may carry such fluid away from its source region. This advective mechanism in its initial stages is essentially a type of baroclinic instability. At first, as with geostrophic adjustment, it entails a local conversion of available potential energy into kinetic energy. No radiation of wave energy to the far field is involved for the case of constant f. However, the evolving unstable structure may deform in such a manner as to ultimately advect fluid far from the source region. It will be argued here that the rate at which this happens depends essentially upon the available potential energy remaining after superinertial wave adjustment has taken place (although in fact the two processes overlap). Hence the two means of adjustment are intimately linked, and either may dominate in removing potential energy from the dense water source region. The instability phase must ultimately predominate in removing dense fluid itself from its formation site, but the rate at which this happens depends upon the potential energy available to drive it, and hence should also be influenced by the radiative phase.

Previous research on linear adjustment to step discontinuities in pressure and density is extensive for two-dimensional geometries, but less so for the three-dimensional axisymmetric case of interest here. Gill (1982) described the linear gravitational adjustment of a rotating fluid to a step discontinuity in surface height. His solution includes both the radiation of superinertial transients and a steady, geostrophically adjusted state. Middleton (1987) considered the energetics of gravitational adjustment for more complicated initial conditions, in particular those of a nearly monochromatic nature (i.e. a single wavenumber component). He found that more of the initially available potential energy was released when the dominant wavelength was small relative to the Rossby radius scale. McWilliams (1988) calculated the loss of potential energy during gravitational collapse of initially

quiescent submesoscale lenses of fluid embedded in a continuously stratified background. While the loss of energy during collapse was only a weak function of the initial height of the lens, it was strongly dependent upon its width, increasing markedly for the narrowest lenses. Dewar and Killworth (1990) determined the geostrophically adjusted states resulting from the collapse of homogeneous columns of dense fluid embedded in a less dense, homogeneous, ambient fluid. The spatial and temporal nature of the transients necessary to achieve these adjusted states were not addressed, however.

Baroclinic instability problems have been considered extensively for both two- and three-dimensional (e.g. quasi-circular) geometries. The earliest work on such instabilities dates to Eady (1949) and Charney (1947), who described the slow release of potential energy through quasigeostrophic means from density-stratified, geostrophically balanced fluids. Pedlosky's (1964a,b) work elaborated the conditions necessary for such instabilities to occur, and set limits on their growth rates. Ikeda (1981) described several modes of quasigeostrophic instability for a two-layer system with an axisymmetric distribution of potential vorticity. In work especially relevant to our considerations here, Hogg and Stommel (1985) described the breakup of a cloud of discrete baroclinic point vortices in terms of "hetons", dipolar structures which transported fluid away from its initial location. Helfrich and Send (1988) studied the equivalent continuous problem of a circular baroclinic vortex of finite area, using the method of contour dynamics.

3 THE PRIMITIVE EQUATION MODEL

Many of the pertinent features of the gravitational collapse and spreading of dense chimneys can be illustrated with a suitable numerical model. The hydrostatic-primitive equation model employed for this purpose is that of Haidvogel et al. (1990). Their model includes an orthogonal-curvilinear coordinate system, which allows variable grid spacing in the horizontal dimensions. This feature has been exploited here to obtain a "telescoping grid", with broader grid spacing near the edges of our (square) model domain. The boundaries themselves are treated as rigid walls, with a free-slip condition for tangential velocities. A semispectral technique, which employs a modified Chebyshev polynomial basis set, is utilized for the vertical coordinate. The model domain for all experiments reported here was 400 km $\times$ 400 km $\times$ 1000 m depth. Within the interior 200 km $\times$ 200 km portion of the domain, grid spacing was constant at 2.5 km. The background density field outside of the mixed region was linearly stratified, with much stronger stratification in the top half of

the water column:

$$\rho = 1000. - 0.10\ (z + 500)/500\ \text{ kg m}^{-3} \qquad 0 \geq z > -500\ \text{m}$$

$$\rho = 1000. - 0.02\ (z + 500)/500\ \text{ kg m}^{-3} \quad -500 \geq z > -1000\ \text{m} \tag{1}$$

This density field corresponds very roughly to that observed in the upper 1000 m of the water column in the northwestern Mediterranean prior to the onset of localized deep convection there (Anati and Stommel, 1970). Within a patch of specified mean radius, density was set constant at the abyssal value of 1000.02 kg m^{-3}. Beyond this mixed patch, density was tapered off to the stratified background level in a Gaussian manner, with an e-folding scale of 10 km (4 gridpoints). Given a spatially invariant value of $f = 10^{-4}$ s^{-1}, the Rossby radii for the first two internal modes corresponding to the background stratification are 3 km and 1.5 km, respectively. While greater model resolution for these modes would be desirable, considerations of computational economy, coupled with the need for a broad domain so that near-inertial transients may radiate freely in the vicinity of the mixed patch, set the given spacing as a lower bound. Seven vertical levels were used in the model runs; e.g vertical structure was represented with the first seven Chebyshev polynomials. This provided reasonable accuracy for resolving at least the first two internal modes. The time step was 350 seconds. Vertical mixing was effected by a standard Laplacian term, with the identical, constant value of $K_\rho = K_u = 10^{-4}$ m^2 s^{-1} for both momentum and density. Horizontal mixing of density and momentum was achieved through biharmonic friction terms, which effectively dissipate only the smallest scales of each quantity while ensuring numerical stability:

$$A_u \nabla \cdot \nabla (\nabla \cdot \nabla) u$$

$$A_\rho \nabla \cdot \nabla (\nabla \cdot \nabla) \rho$$

Each quantity was diffused in this manner with identical values of the biharmonic coefficient, $A_\rho = A_u = 0.32 \times 10^9$ m^4 s^{-1}. A "generic" passive tracer field, linearly stratified in the vertical and uniform horizontally, was advected by the model to help illustrate vertical motions. This tracer field was subject to the same mixing terms as the momentum and density fields.

4 BEHAVIOR OF A SMALL MIXED PATCH

Initial density and tracer fields for a very small (~1 Rossby radius) mixed patch embedded in the stratified fluid are shown in Figs. 1–2. Although essentially circular, this patch contains a small, sinusoidal (as a function of azimuth), mode 3 perturbation of the radius of the completely mixed area. Over several inertial periods (one inertial day ~17.5 hrs), the initial patch was observed to slump and spread (Fig. 1). After eight inertial periods, the essential vertical structure of the velocity field in the small mixed patch is evident; "stacked" vortices, with cyclonic circulation near the surface and anticyclonic circulation at mid-depth and below (Fig. 3). The magnitudes of the azimuthal velocities are as great as 0.15 m s^{-1}. This yields a Rossby number of approximately 0.2, a range common to many numerical studies which utilize only the quasigeostrophic equations. Near-inertial transients radiate outwards from the point disturbance in a splash-like pattern (Figs. 2–3). The central patch rotates with time, but does not deform in any significant manner. Despite the wave radiation, oscillations at near-inertial frequency are evident in the center of the patch even after eight inertial periods (Fig. 2). Apparently the very slow group velocities for those waves associated with the largest scale density variations in the initial conditions, prevent the rapid escape of a significant portion of the transients. It is worth noting that these oscillations would be even more persistent in a very weakly stratified background, as the group velocities of all radiating transients would then be slower. Gascard (1973) and Gascard and Clarke (1983) observed such superinertial oscillations in regions subject to deep convective events.

5 BEHAVIOR OF A LARGE MIXED PATCH

While the small patch did not to deform in any dramatic way, a larger patch (~8.5 Rossby radii in diameter) exhibited such behavior, consistent with the laboratory experiments of Saunders (1973) and Griffiths and Linden (1981), as well as several of the quasigeostrophic numerical studies (e.g. Hogg and Stommel, 1985; Helfrich and Send, 1988). Again we perturbed the radius of the initial cylinder of constant density with a sinusoid of mode 3. The initial density and tracer fields deform quite significantly with time (Figs. 4–6); as with the smaller patch, ultimately none of the densest fluid remains at the surface. The tracer field reveals strong vertical motions, with amplitudes of greater than 50 m after eight inertial periods. The nearly circular patch of mixed water gradually pinches off at the middle, forming three smaller eddies whose scales are closer to that of the

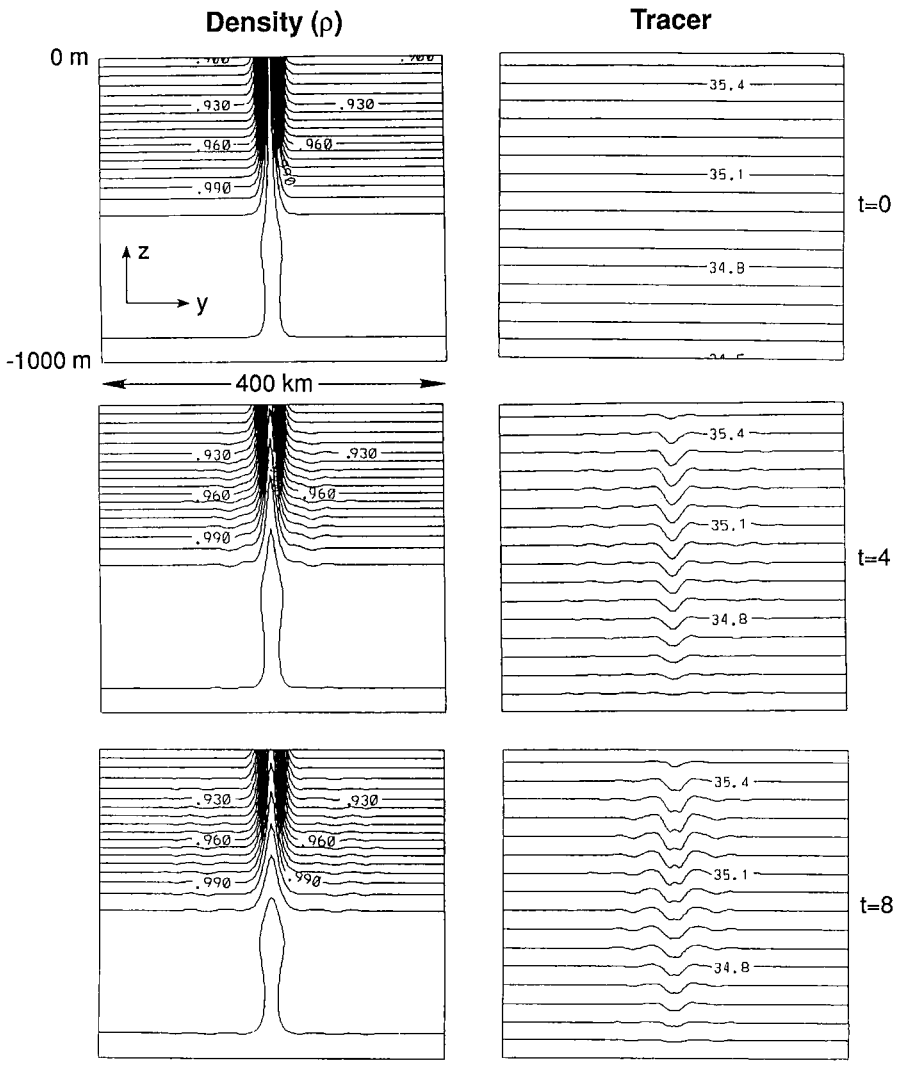

Figure 1: The initial density and tracer fields (y–z plane through the center of the model domain) for the small mixed patch experiment, and their subsequent evolution. t is in inertial days.

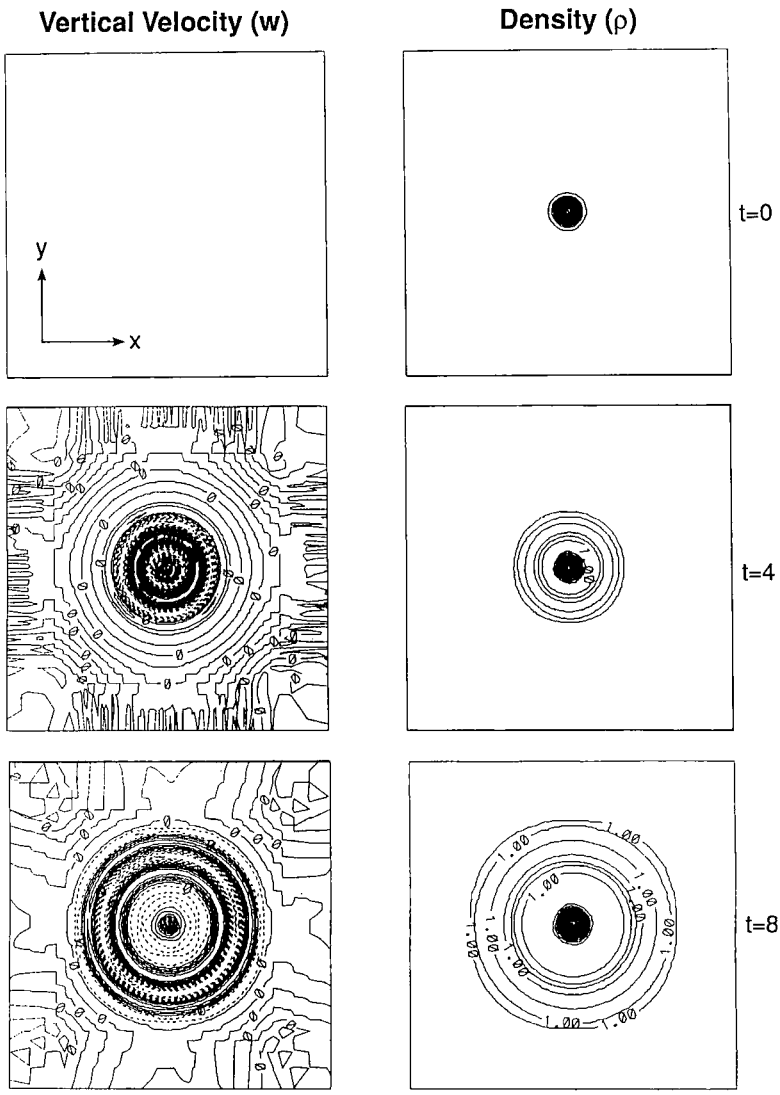

Figure 2: Evolution of density and vertical velocity fields (x–y plane) for the small mixed patch at mid-depth. In this and other plots, the multiple, sometimes irregular, zero crossings near the boundaries indicate a slight (dynamically insignificant) degree of computational noise, resulting especially from: (1) the telescoping grid being used in conjunction with the biharmonic friction term; and (2) the initially unbalanced density field extending out to the boundary, causing reflection of very small amplitude gravity waves there. Contour intervals are: 1×10^{-4} (w), 6×10^{-4} $(\rho, t = 4)$, 5×10^{-4} $(\rho, t = 8)$.

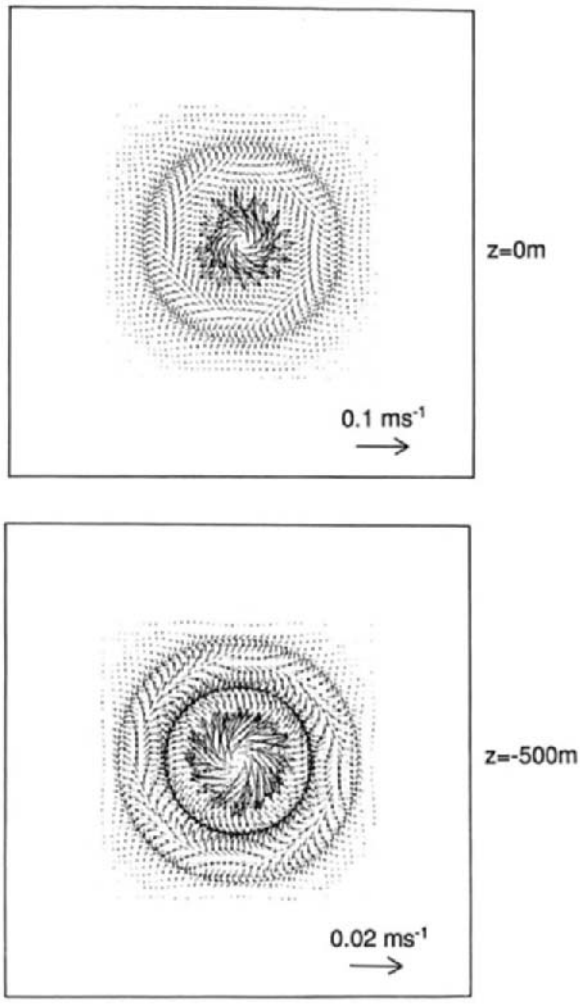

Figure 3: Horizontal velocity vectors, at the surface and at mid-depth, for the small mixed patch after 8 inertial periods. Note vectors are scaled differently in each frame.

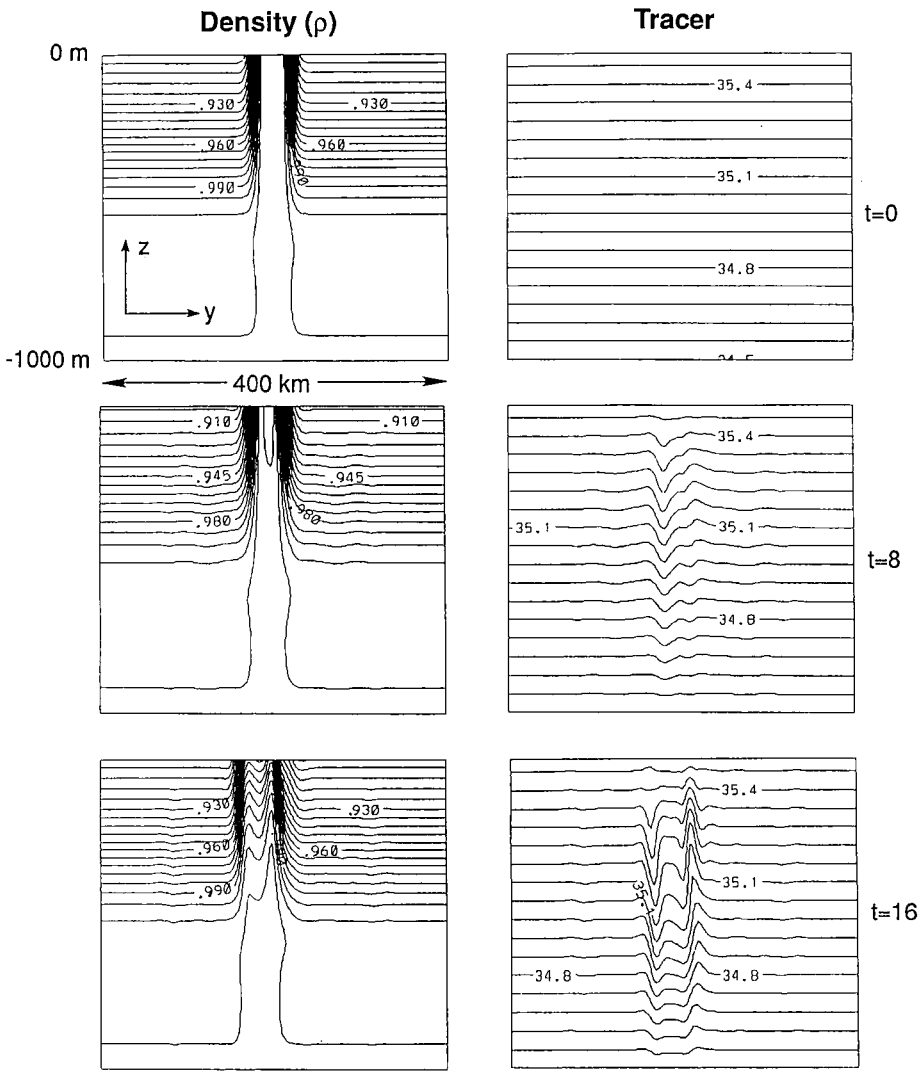

Figure 4: The initial density and tracer fields (x-z plane through the center of the model domain) for the large mixed patch experiment, and their subsequent evolution.

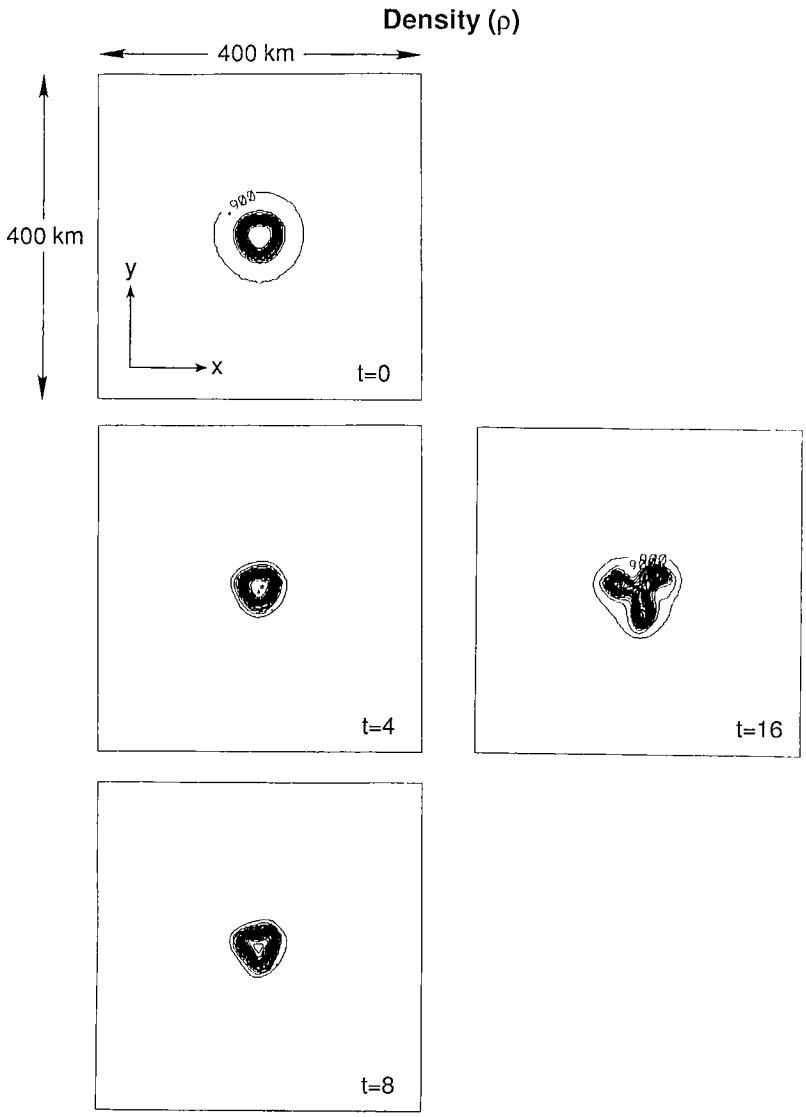

Figure 5: Evolution of the large mixed patch of high density at the surface. Contour intervals are: 6×10^{-2} ($t = 0$), 7×10^{-2} ($t = 4, 8$), 5×10^{-2} ($t = 16$).

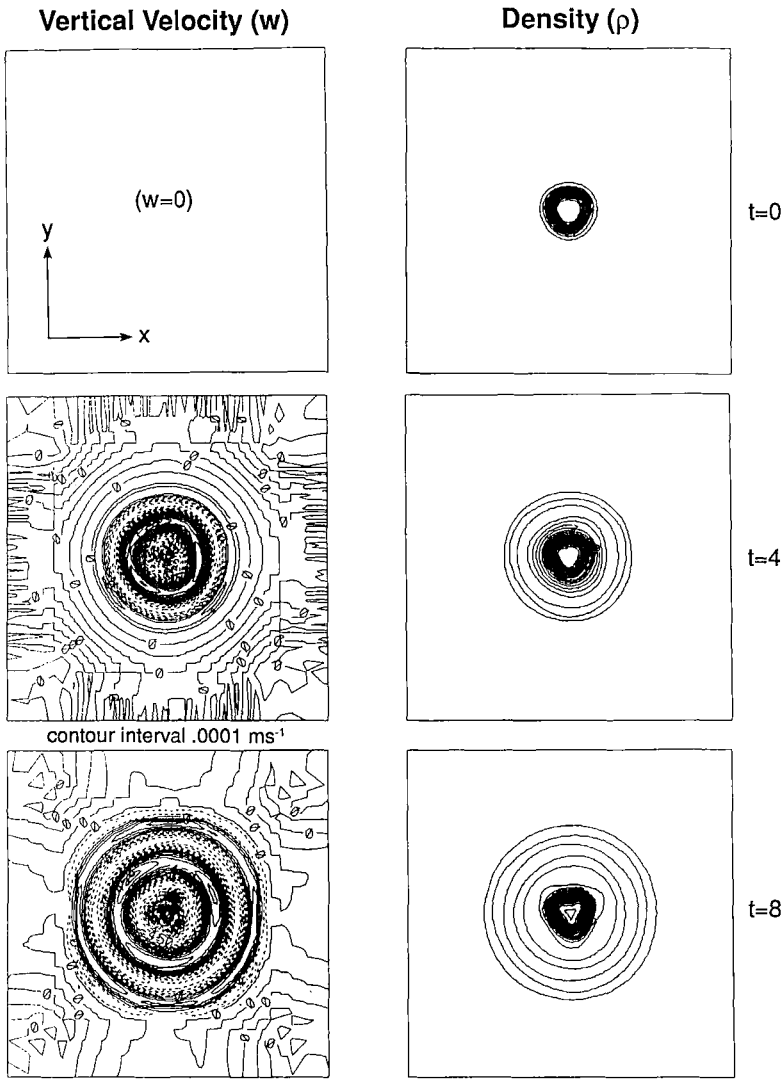

Figure 6: Evolution of density and vertical velocity fields for the large mixed patch at mid-depth. Contour intervals are: 1×10^{-4} $(w, t = 4)$, 9×10^{-5} $(w, t = 8)$, 6×10^{-3} (ρ).

Rossby radius (Fig. 5). Persistent near-inertial radiation is observed as in the smaller patch case, especially within the mixed region. The tracer field illustrates the strong vertical motions within the three developing eddies (Fig. 7). A comparison of Figs. 5 and 7 also helps reveal the vertical structure of the density field, which is most strongly "pinched" at the surface. The circulation remains predominantly cyclonic at the surface and anticyclonic at depth, both for the slightly deformed patch (Fig. 8) and the pinched-off eddies (Fig. 9). The latter exhibit shifting of the rotational axis with depth after 16 inertial periods, although this is not evident in the density field itself. The barotropic streamfunction at this time (Fig. 10) is tri-lobed, and suggests depth-averaged velocities on the order of 0.1 m s^{-1}. Ultimately these eddy pairs would probably drift apart, as in laboratory and numerical studies for analogous two-layer systems. Qualitatively, these several features are strongly suggestive of a baroclinic instability process.

Several of the limitations of our model affect the validity of these experimental results. First, the scale of the grid spacing is close to that of the first internal Rossby radius. This is especially worrisome for the small mixed patch experiment. However, preliminary results using a wide (in absolute distance) patch, but decreasing the value of f, do confirm the tendency against baroclinic instability for those patches small relative to the Rossby radius. Second, our hydrostatic model by definition excludes any nonhydrostatic (small-scale, high frequency) motions which might be important when very small patches ($\sim$ a few kilometers) are considered. Such dynamics will certainly affect the details of gravitational adjustment, but probably not the essential, final state of gradient wind balance. Bugge et al. (1991) have addressed the problem of small scale plume formation using such a nonhydrostatic model. Finally, the limited time span of the numerical results shown here for the wide patch do not *conclusively* prove that the three lobes will drift apart with time, as opposed to merely spinning down from finite amplitude. Given large values of horizontal and/or vertical diffusivity, we might expect the latter to be the case; ultimately such mixing will produce a complete state of rest in a closed system such as this. Even the laboratory results at hand indicate some dense fluid is left at the initial location after the lobes have drifted apart; that is, the lobes remain "connected" as in our numerical results.

Overall, the continuously stratified case examined numerically differs little from the two-fluid (homogeneous column and homogeneous surroundings) laboratory experiments. To the extent that the first internal vertical wave mode accomplishes the major part of geostrophic adjustment, and the first internal vertical mode for the baroclinic instability is

the most unstable one, we should expect our results to be similar to those of quasigeostrophic, two-layer systems (e.g., point vortex or contour dynamics approaches). However, the higher mode dynamics possible in the continuous case could affect the outcome in unpredictable ways, as the basic state of the flow evolves over long times.

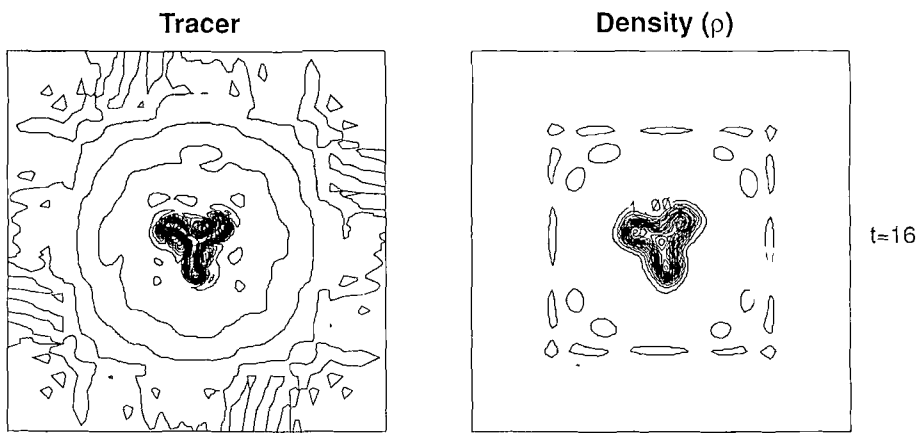

Figure 7. Density and tracer fields at mid-depth for the large mixed patch after 8 inertial periods. Contour intervals are 1×10^{-2} (Tracer), 7×10^{-3} (ρ).

6 A NUMERICAL TEST FOR NONLINEAR INTERACTIONS

The possible interaction of the near-inertial transients with the advective instability process may be examined with a simple model experiment. Here we compare the results obtained by initializing the model of the large patch from a state of complete rest, with those obtained when the initial state is in geostrophic balance. In reality, the properly adjusted state is one of gradient wind balance, which includes the centrifugal forces represented by the nonlinear terms in the full equations of motion. However, for the large patch at least, the difference between a gradient wind balance and a purely geostrophic one is only of the order of ten percent. The geostrophically adjusted initial state should eliminate most of the near-inertial transients, and hence any significant interaction of such oscillations with the advective dynamics.

A comparison of vertical velocity and density at mid-depth for the unadjusted vs. adjusted initial conditions (Figs. 6 and 11) illustrates the near-absence of superinertial transients for the latter. Nonetheless, for the given density stratification and Coriolis

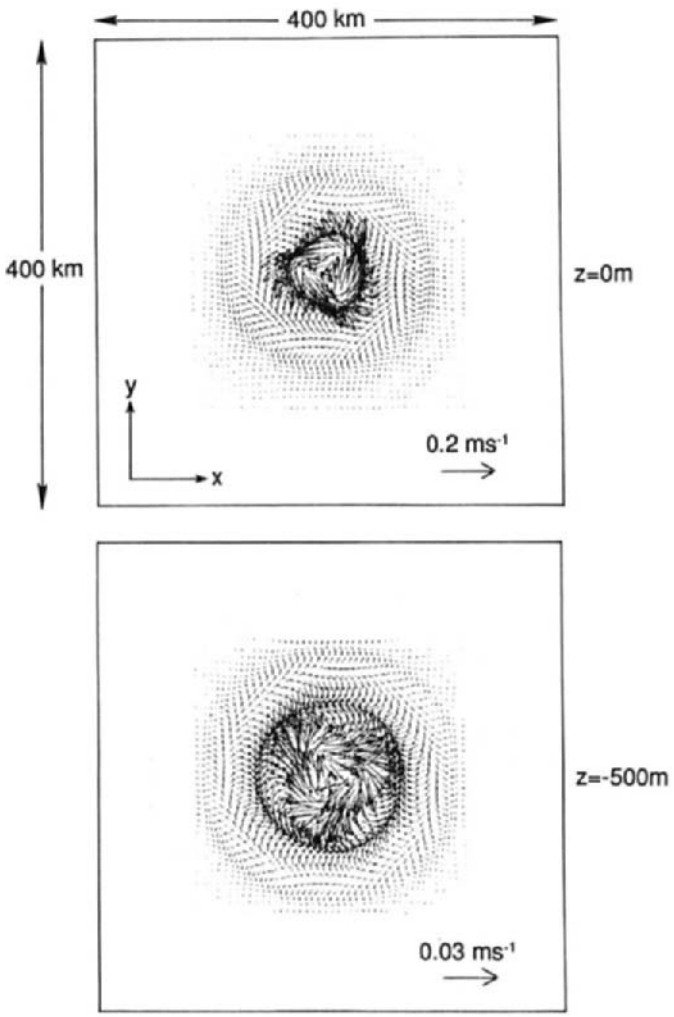

Figure 8: Horizontal velocity vectors, at the surface and at mid-depth, for the large mixed patch after 8 inertial periods. Note vectors are scaled differently in each frame.

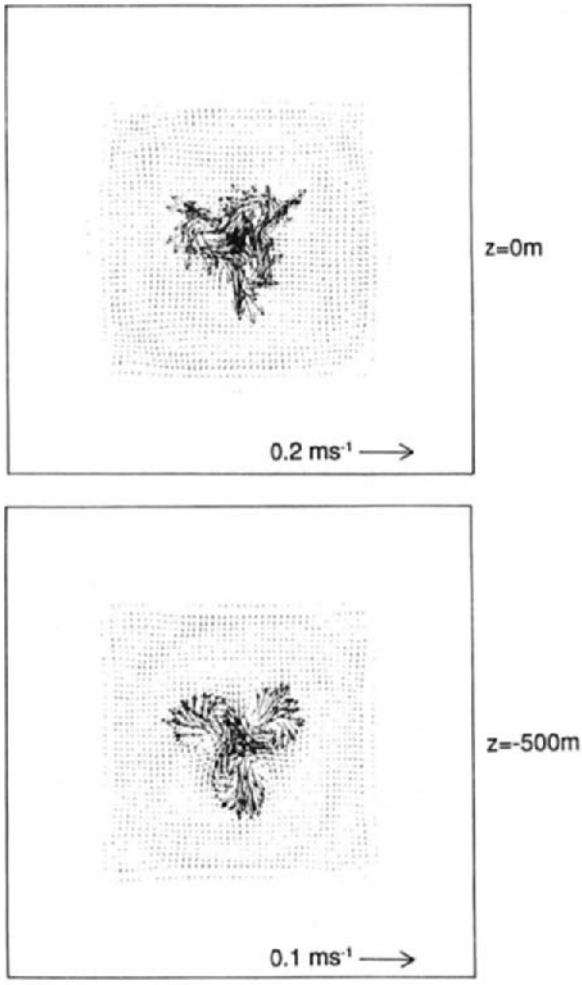

Figure 9: Horizontal velocity vectors, at the surface and at mid-depth, for the large mixed patch after 16 inertial periods. Note vectors are scaled differently in each frame.

parameter, no significant interaction between wave and advective dynamics was evident; that is, the splitting apart of the initial cylinder of dense fluid by the mode 3 instability took place over the same time scale, and to the same extent, when starting with a geostrophically adjusted state as it did when starting from a state of rest. This leaves open the possibility of significant interaction at higher Rossby number (e.g. for a denser chimney), where the radiative and advective time scales are more closely matched. The appropriate time scales will be considered more fully in the next section.

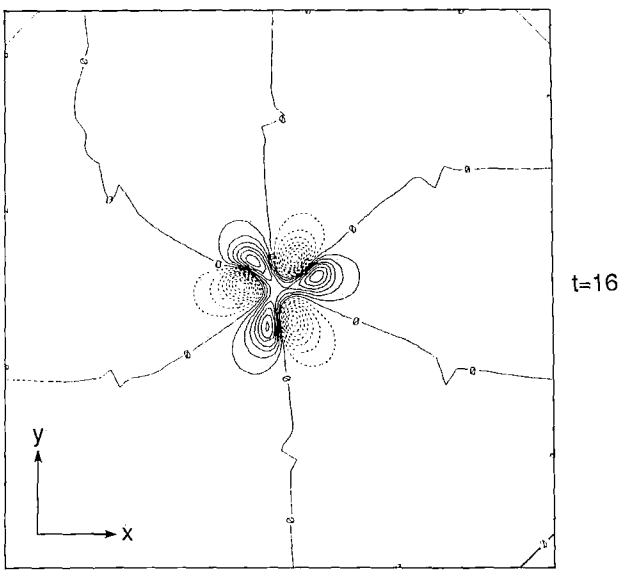

Figure 10. The barotropic streamfunction for depth-integrated flow in the large mixed patch experiment after 16 inertial periods. Contour interval is 7×10^4.

7 DISCUSSION: ENERGETICS OF RADIATION VS. ADVECTION

As illustrated so far, two general mechanisms exist for the release of potential energy from the initially quiescent density configuration; geostrophic adjustment (the radiative phase) and baroclinic instability (the advective phase). Although the difference between these two processes is indistinct for large amplitude perturbations (in our case, for very dense chimneys), it is instructive to consider the amounts of potential energy released by these two means acting separately. As in other nonlinear adjustment problems, we consider

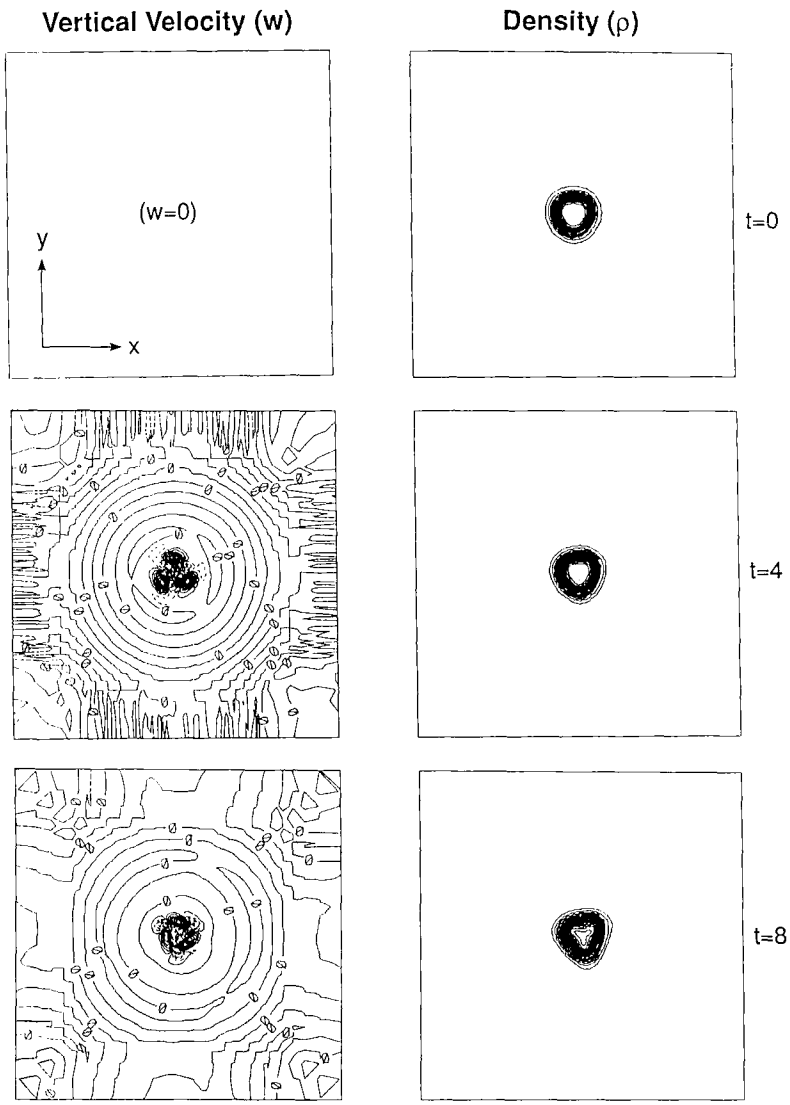

Figure 11: Evolution of density and vertical velocity fields for the geostrophically adjusted large mixed patch at mid-depth. Contour intervals are 2×10^{-5} $(w, t = 4)$, 5×10^{-5} $(w, t = 8)$, 6×10^{-4} (ρ).

the initial state undergoing a linear adjustment process, which is assumed to go to completion, followed by an advective adjustment process, and compare the rates at which each must proceed. When a very slowly rotating system is considered (small f, or equivalently, a very narrow column of fluid), it is clear that significant slumping can take place in the linear adjustment phase, that is, without significant advection of fluid. For the rapidly rotating case (large f or a very wide column of fluid), the advective instability must transfer most of the available potential energy into kinetic energy if the column is to sink. Energy considerations, coupled with the requirement of potential vorticity conservation, limit the amount of purely axisymmetric slumping which can occur (Stern, 1975); this ultimately leads to the Rossby radius-sized structures evident in our numerical results.

Analytically, we can see some indication of the rate at which potential energy is lost by wave radiation through use of the dispersion relation for inertia-gravity waves, derived from the linearized shallow water equations. As described in Gill (1982), the appropriate dispersion relation for superinertial plane waves in a rotating fluid is:

$$\omega^2 = f^2 + c^2 k^2 \tag{2}$$

where c is the phase velocity of the shortest waves. From this we may obtain the group velocity:

$$c_g = c^2 \frac{k}{\omega} \tag{3}$$

or, for small k:

$$c_g \sim c^2 \frac{k}{f} = c\lambda k \tag{4}$$

where λ is the Rossby radius. For the circular patches of dense water considered here, the dominant wavelength will be $2L$, where L is the width of the newly-dense patch. Hence $k \sim \pi/L$, and so

$$c_g \sim \pi c \frac{\lambda}{L} \tag{5}$$

demonstrating that geostrophic adjustment (in the sense of superinertial energy radiation away from the patch) will take longer for larger than for small patches. Gill (1982) also calculated the release of energy per unit length for a step discontinuity in surface height of a barotropic system. This may be directly applied to the baroclinic mode of a two layer system:

$$\text{energy released} = \frac{3}{2}\rho g' \eta_0^2 \lambda \tag{6}$$

where ρ is the density, g' is the reduced gravity of the two-layer system ($= g\Delta\rho/\rho$), and η_0 is one-half the magnitude of the step discontinuity in interface height. Now, for a large circular region of elevated interface height, the ratio of total PE released to total APE of the cylinder is approximately:

$$\frac{\text{PE released}}{\text{APE of cylinder}} = \frac{\frac{3}{2}\rho g' \eta_0^2 \lambda \pi L}{\frac{1}{2}\rho g' \eta_0^2 \pi L^2} = 3\frac{\lambda}{L} \tag{7}$$

Ultimately, only a small fraction of potential energy will be lost from a large cylinder of dense fluid as the system radiates near-inertial waves and comes into a state of geostrophic adjustment. However, this leaves more potential energy to drive the baroclinic instability dynamics, and hence we expect this process to occur more rapidly in the quickly rotating case.

For a continuously stratified system, we can gain some indication of the growth rate of the advective instability using the result of Pedlosky (1982). He specified a maximal growth rate for such instabilities in a strictly zonal flow, based on the maximum vertical and horizontal shear present in the domain. The constraint of "purely zonal" flow is superfluous for the case of constant f and an infinite domain; however, the presumption of a unidirectional basic flow is not, and is most applicable to a column of large radius, where the curvature is small. As stated earlier, the centrifugal terms due to the curvature of the large patch case are, in fact, small relative to the basic geostrophic balance which evolves during gravitational adjustment (centrifugal term $U^2/L \sim 10\%$ of Coriolis term fU), yielding a small Rossby number, U/fL. Generally, we may expect the limit of very small Rossby number to conform most closely to the results for purely zonal flows. Note, however, that certain additional effects, unique to the circular geometry of the problem, may persist for very strong curvature (small L) even at low Rossby number (small U).

In dimensional terms Pedlosky's result is:

$$\alpha \leq \frac{1}{2}\left[\frac{f^2}{N^2}\left(\frac{\partial U}{\partial z}\right)^2 + \left(\frac{\partial U}{\partial y}\right)^2\right]^{1/2} \tag{8}$$

where α is the exponential rate of growth for the instability, U is the basic state velocity, and N is the buoyancy frequency. The crucial point here, insofar as baroclinic instability is concerned, is the dependence on f and N. Specific cases of purely baroclinic instability, where horizontal shear is absent, likewise exhibit this dependence. For example, Eady's

(1949) result for an unsheared purely zonal flow in a continuously stratified fluid indicates the maximal growth rate of quasigeostrophic perturbations on that basic state to be:

$$\alpha \sim \frac{f}{N}\frac{\partial U}{\partial z} \tag{9}$$

Note that for the wave-adjusted basic state, the gradient wind balance yields

$$\frac{\partial U}{\partial z} = \frac{g\frac{\partial \rho}{\partial y}}{\rho f} \tag{10}$$

Hence the growth rate is really independent of rotation per se, depending instead on the geostrophically adjusted density field (and hence its potential energy):

$$\alpha \sim \frac{g\frac{\partial \rho}{\partial y}}{\rho N} \tag{11}$$

Consider a horizontal step discontinuity $\delta\rho$ in stratification. After superinertial wave adjustment has gone to completion, the length scale for horizontal density variations is just the appropriate Rossby radius:

$$\lambda = \frac{NH_T}{f} \tag{12}$$

where H_T is the fluid depth. Hence for the geostrophically adjusted column:

$$\alpha \sim \frac{f}{H_T}\frac{g\delta\rho}{\rho N^2} = \frac{f}{H_T}\frac{\delta\rho}{\partial\rho/\partial z} \tag{13}$$

An equivalent expression may be derived for a two-layer system. We apply the maximal growth rate for a two-layer system as defined by Pedlosky (1982), to the specific instance of a system which has undergone geostrophic adjustment to a step discontinuity in interface height. The result is:

$$\alpha \sim \frac{f\eta_0}{H} \tag{14}$$

where η_0 is again one-half the magnitude of the initial step discontinuity on the interface between the two layers, each of depth H. In other words, $\alpha \sim q$, the perturbation potential vorticity. This general result also appears in the contour dynamical approach to the quasigeostrophic problem of baroclinic vortex evolution (Helfrich and Send, 1988).

While the detailed structure of the instability is not discussed here, clearly for a two-layer system there is a direct dependence on both the magnitude of the initial step size and the Coriolis parameter. We may think of this as a dependence on the available potential energy remaining after geostrophic adjustment; with larger f, a larger store of

available potential energy remains to drive the advective conversion to kinetic energy. It is nonetheless curious to note that, for a given step size, the growth rate α is the same for all values of f when time is expressed in inertial days — just as the rate of geostrophic adjustment is typically assigned a time scale of f^{-1}. A dimensional argument naturally follows. For a two-layer system with specified mean layer depths, and with length scaled by λ and time scaled by f^{-1}, there are only two free parameters affecting the qualitative behavior of the combined radiative plus advective problem: the width of the initial cylinder, and the strength of the perturbation. This gives a posteriori justification for the choice of numerical experiments reported in the previous section.

Only a few studies have addressed the evolution of baroclinically unstable structures for extended time periods. Hogg and Stommel (1985) studied the deformation of a cloud of quasigeostrophic, baroclinic point vortices. Initially these stacked vortices (positive vorticity in the upper layer and negative in the lower) separated horizontally, forming pairs which were self-propelled. These pairs were dubbed "hetons" for their ability to transport mass and the associated heat (or cold, in the present instance). Paired aggregates of the positive and negative vortices, with length scales of $O(\lambda)$, were observed to drift apart, such that the mean radius of the cloud increased. Potential energy is released via this process, which is essentially analogous to the breakup of the chimneys reported in our numerical results. In a series of numerical experiments, Hogg and Stommel (1985) observed the rate of spreading of their clouds to be:

$$v^* = 1.65\lambda q \tag{15}$$

where λ is the Rossby radius for the two-layer system represented by the point vortices and q is the potential vorticity of the vortices. This empirical formula reflects the self-propulsion of the paired vortex aggregates, with the positive and negative members separated a distance of $O(2\lambda)$. This basic configuration appears likewise in the quasilinear solutions of baroclinic instability problems, where 4λ is found to be the wavelength of the fastest growing disturbance on the basic state. In this two-layer system, the value of q may be imagined to derive initially from a displacement of the fluid interface, η_0. Then, as above:

$$q \sim \frac{\eta_0 f}{H} \tag{16}$$

where H is the unperturbed depth of each layer in the two-layer system. Substituting into (15), we find the spreading rate to be independent of rotation per se:

$$v^* \sim \frac{c\eta_0}{H} \tag{17}$$

Assuming that all of the dense fluid breaks into hetonic structures and spreads away from the site of buoyancy input, we may use this semi-empirical formula to compare the rate of potential energy loss by advective means to the rate of potential energy loss by radiative means for our initially quiescent chimney. Combining (5), (7) and (17) yields:

$$\frac{\text{advective PE loss rate}}{\text{radiative PE loss rate}} \sim \frac{1}{3\pi}\frac{\eta_0}{H}\left(\frac{L}{\lambda}\right)^2 \tag{18}$$

Note that this relation is strictly valid only for large patches. Nonetheless, two general points emerge. First is the dependence on the strength of the initial perturbation η_0/H, which frequently appears in problems involving quasigeostrophic evolution. Second, and more intriguing, is the quadratic dependence on L. This suggests a rapidly decreasing contribution of superinertial waves as the scale of the buoyancy forcing increases, or, conversely, their importance when the spatial scale is small.

Preliminary energy flux estimates have been obtained for the large mixed patch ($L \sim 8\lambda$) case. Energy flux decomposition into the "advective" vs. "radiative" components was effected by filtering of the appropriate time series into subinertial and superinertial parts, and utilizing each part separately in a total energy flux equation:

$$F = pu + \rho u\Phi + \rho u\frac{1}{2}\bar{u}^2 \tag{19}$$

where p is pressure and Φ is the potential energy. Total depth-integrated energy flux F out of a box 16λ wide surrounding the large mixed patch was calculated for 20 inertial periods. These calculations revealed the near-inertial flux was $\sim \frac{1}{10}$ as large as the subinertial in the first five inertial days of the numerical experiment. Using $L/\lambda \sim 8$ and $\eta_0/H \sim 1$ in (18) yields a ratio of $O(\frac{1}{10})$, in general conformance with our experimental result. Future numerical and analytical efforts will examine this ratio in more detail, and extend its range of validity to very small patches.

8 CONCLUSIONS

The above numerical and analytical results for localized regions subject to rapid, deep convection have demonstrated:

1) Near-inertial energy can be very persistent within evolving patches of dense water. Although these oscillations may interact with the subinertial dynamics in a manner which affects the spreading of dense waters, no significant interaction was found in this study.

Quasigeostrophic models may be suitable for large patches with moderately greater density than their surroundings.

2) Small (~1 Rossby radius) patches of dense water in a continuously stratified background gradually sink but are relatively stable, whereas large (~8.5 Rossby radii) patches of dense water have a tendency to break apart into smaller patches. The nature of this breakup merits further investigation, but appears to be essentially due to baroclinic instabilities as in related studies. While quasigeostrophic theory has traditionally offered much guidance here, primitive equation modeling permits a more thorough investigation of the relevant fluxes over a wide range of spatial and temporal scales.

3) Scaling arguments, combined with Hogg and Stommel's (1985) results, suggest a ratio for comparing the rates of potential energy loss by advective (baroclinic instability) to those for radiative (superinertial waves) processes. The derived ratio is linearly dependent upon the strength of the density perturbation and quadratically dependent upon the radial dimensions of the dense patch. Larger chimneys must lose the bulk of their energy, and all of their mass, through advective processes, whereas small chimneys may lose much of their energy by radiation of the near-inertial transients.

ACKNOWLEDGEMENTS

The authors wish to thank Jim Price for helpful discussions, and Mary Ann Lucas for preparation of the manuscript. Support was provided under grant N00014-86-K-0751 from the Office of Naval Research. This is contribution number 7549 from the Woods Hole Oceanographic Institution.

REFERENCES

Anati, D. and Stommel, H., 1970. The initial phase of deep water formation in the Northwest Mediterranean, during MEDOC '69, on the basis of observations made by "Atlantis II" January 25–February 12 1969. Cah. Oceanogr., 22: 343–351.

Bugge, R., Jones, H. L. and Marshall, J. C., 1991. Non-hydrostatic ocean modelling for studies of open-ocean deep convection. This volume.

Charney, J. G., 1947. The dynamics of long waves in a baroclinic westerly current. J. Meteorol., 4: 135–163.

Davey, M. K. and Killworth, P. D., 1989. Flows produced by discrete sources of buoyancy. J. Phys. Oceanogr., 19: 1279–1290.

Dewar, W. K. and Killworth, P. D., 1990. On the cyclinder collapse problem, mixing and merger of isolated eddies. J. Phys. Oceanogr., 20: 1563–1575.

Eady, E. T., 1949. Long waves and cyclone waves. Tellus, 1: 33–52.

Gascard, J.-C., 1973. Vertical motions in a region of deep water formation. Deep-Sea Res., 20: 1011–1027.

Gascard, J.-C. and Clarke, R. A., 1983. The formation of Labrador Sea Water. Part III: mesoscale and smaller-scale processes. J. Phys. Oceanogr., 13: 1779–1797.

Gill, A. E., 1982. Atmosphere-Ocean Dynamics. Chapter 7. Academic Press.

Griffiths, R. W. and Linden, P. F., 1981. The stability of vortices in a rotating, stratified fluid. J. Fluid Mech., 105: 283–316.

Haidvogel, D. B., Wilkin, J. L. and Young, R., 1990. A semi-spectral primitive equation ocean circulation model using vertical sigma and orthogonal curvilinear horizontal coordinates. J. Comput. Phys., in press.

Helfrich, K. R. and Send, U., 1988. Finite-amplitude evolution of two-layer geostrophic vortices. J. Fluid Mech., 197: 331–348.

Hogg, N. G. and Stommel, H. M., 1985. Hetonic explosions: the breakup and spread of warm pools as explained by baroclinic point vortices. J. Atmos. Sci., 42: 1465–1476.

Ikeda, M., 1981. Instability and splitting of mesoscale rings using a two-layer quasi-geostrophic model on an f-plane. J. Phys. Oceanogr., 11: 987–998.

Killworth, P. D., 1976. The mixing and spreading phases of MEDOC.I. Prog. Oceanogr., 7: 59–90.

McWilliams, J. C., 1988. Vortex generation through balanced adjustment. J. Phys. Oceanogr., 18: 1178–1192.

Middleton, J. F., 1987. Energetics of linear geostrophic adjustment. J. Phys. Oceanogr., 17: 735–740.

Pedlosky, J., 1964a. The stability of currents in the atmosphere and the ocean: Part I. J. Atmos. Sci., 21: 201–219.

Pedlosky, J., 1964b. The stability of currents in the atmosphere and the ocean: Part II. J. Atmos. Sci., 21: 342–353.

Pedlosky, J., 1982. Geophysical Fluid Dynamics. Chapter 7. Springer-Verlag.

Saunders, P. M., 1973. The instability of a baroclinic vortex. J. Fluid Mech., 3: 61–65.

Stern, M. E., 1975. Ocean circulation physics. Chapter 3. Academic Press.

A BUOYANCY-DRIVEN THERMOCLINE MODEL

W.K. DEWAR
Department of Oceanography, Florida State University, Tallahassee, Florida (USA)

ABSTRACT

A simple analytical model of stratified circulation with application to the global consequences of convection is reviewed. The model is driven by buoyancy and mechanical forcing and buoyancy diffusion is parameterized in terms of diapycnal mass fluxes. The interior responds in typical Sverdrup fashion and the requirements of balanced heat and energy budgets are invoked to calculate the eastern boundary stratification parameters.

This effort differs from past attempts to calculate stratification in that buoyancy flux boundary conditions are explicitly considered in the calculation of diapycnal fluxes. A major feature of the solutions is the interplay of planetary dynamics and buoyancy diffusion. This results in the most important components of the thermocline structure, namely density outcrops and interior "pinchoffs". These are, in turn, essential to the production of thermodynamically balanced states. Some aspects of the present model resemble features found in previous numerical models.

INTRODUCTION

The state of the climate at any one time is determined by the coupled interaction of the ocean and the atmosphere. The ocean is set in motion by solar radiation, momentum, heat and salt exchanges with the atmosphere and (less importantly) by buoyancy sources at solid ocean boundaries. The atmosphere is in turn driven at least in part by heat exchange with the ocean. Thus, it is in the great capacity of the ocean to store and redistribute heat that perhaps its most important connection to climate dynamics is found. A problem of major importance then to the study of the climate (and which also serves as the primary motivation for the present study) is the determination of the mechanics responsible for the large scale ocean stratification, as this is the expression of oceanic heat storage.

Recently, stratified ocean circulation models forced both mechanically and thermodynamically have been proposed (Luyten et al., 1983). The focus of many of these "ventilated thermocline" papers has been the determination of the interior density and velocity fields by the "subduction" process. Buoyancy forcing appears through specified isopycnal outcrops and subsurface fluids away from outcrops are assumed to be purely conservative. Explicit western boundary layer dynamics are generally not considered. Rather, it is tacitly assumed that the western boundaries respond to the interior dynamics however necessary to provide a global mass balance. Calculation of the so-called ventilated thermocline requires knowledge of the conditions on the eastern boundary. While these are generally assumed, it is freely admitted by the authors that calculation of the eastern boundary conditions constitutes part of the complete problem. Indeed, it is here that a connection between the thermocline circulation (which can respond on time scales of 10 years) and the true thermohaline circulation (which responds on the 1000 year time scale) arises. It is the purpose of this paper to address the latter.

The above connection has been studied previously in layered models by Tziperman (1986), Kawase (1987), Huang and Bryan (1987) and Huang (1990). In contrast to pure ventilated thermocline theory, nonconservative processes are central to all these studies. Nonconservative processes are parameterized in layered models as cross interfacial mass fluxes and mass conservation

were worked out analytically (including boundary layers) in the linear model of Kawase (1987), numerically in Tziperman (1986) and integrated numerically to steady state in the studies of Huang and Bryan (1987) and Huang (1990). The latter two studies are distinguished most notably by the inclusion of a functioning mixed layer.

This paper reviews the formulation of heat diffusive parameterizations in layered models and discusses a simple model illustrating some consequences in the global ocean of water mass production. A more detailed and mathematically complete discussion of these points is given in Dewar (1990). This study differs from those of Tziperman and Kawase by explicitly considering surface heat fluxes, and is closest in spirit to the numerical results presented in Huang and Bryan (1987), who did consider explicit surface buoyancy fluxes. In some sense, the present paper considers what must be the simplest possible analytical model relevant to the above study. Certain of the calculated features are reminiscent of the experiments of Huang and Bryan, and hopefully provide a simple framework for understanding those more complex calculations.

The equations of motion are introduced in the next section and a discussion of fluxes consistent with the layered framework is given. The most succinct example of thermodynamically balanced circulation is found in the absence of wind forcing, and such a model is discussed in Section 3. The effects of wind and parameter variations are discussed and a summary is presented in the final section.

2 EQUATIONS OF MOTION AND BUOYANCY FLUXES

A flat bottomed, rectangular ocean basin of total depth H is considered (see Fig. 1). The fluid is Boussinesq and stratification is included by means of three constant density layers. The fluid in these layers will at times be referred to as cold, warm and hot, for layers 3, 2 and 1, respectively. Forcing enters the problem by means of a wind stress field $\underset{\sim}{\tau}$ and a heat flux field F applied at the ocean surface. Fluid velocities are governed by geostrophy augmented with turbulent mixing and incompressibility:

$$-fv_{iT} = -\,p_{ix} + \tau_z^{(x)} = -fv_i - fv_{if} \tag{1}$$

$$fu_{iT} = -p_{iy} + \tau_z^{(y)} = fu_i + fu_{if} \tag{2}$$

$$h_i(u_{ix}+v_{iy}) + \nabla x\{[\underset{\sim}{\tau}(z_{i-1}) - \underset{\sim}{\tau}(z_i)]/f\} + w_i(z_{i-1}) - w_i(z_i) = 0 \tag{3}$$

where the subscript i denotes the i^{th} layer, the subscript T on the velocities denotes total velocities, u_i and v_i denote the geostrophically balanced part of the velocity and u_{if} and v_{if} denote the stress driven part of the velocity. Layer thicknesses and pressures are related by the hydrostatic balance and for simplicity it will be assumed that the density change between layers 1 and 2 is the same as that between layers 2 and 3. The quantity z_i denotes the depth of the interface between the i^{th} and $(i+1)^{th}$ layer, $h_i = z_{i-1}-z_i$ and the quantity $\underset{\sim}{\tau}(z_i)$ denotes the turbulent stress evaluated at z_i.

Thermodynamic considerations and diapycnal fluxes enter the problem through the determination of w_i at the interfaces. The behavior of buoyancy in this system will be modeled after that in a continuous fluid. We will also study a fluid stratified in temperature only, thus "heat" and

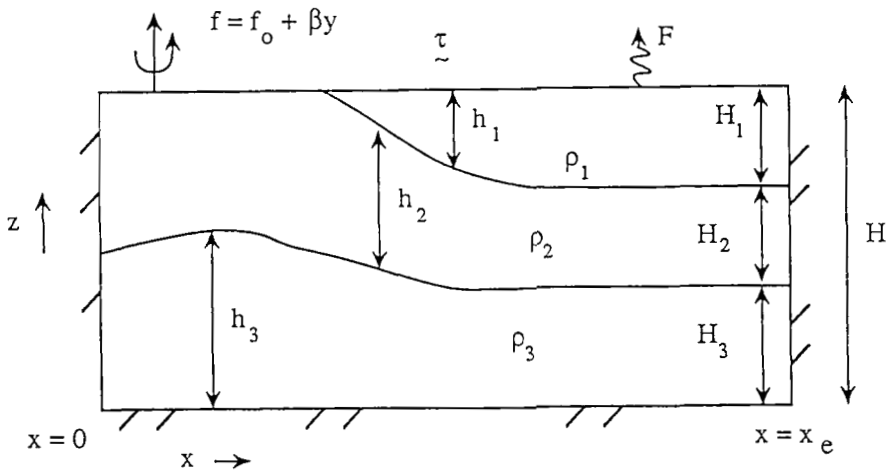

Fig. 1 Model Schematic. A three layer flat bottom model is considered. The fluid is Boussinesq, and the density jumps at the two interfaces are assumed to be the same. Heat fluxes are specified at the surface.

"buoyancy" will be essentially interchangeable terms in this paper. We begin with the equation for the conservation of heat:

$$T_t + (uT)_x + (vT)_y + (wT)_z = - (\overline{w'T'})_z \tag{4}$$

where the heat source on the right hand side is the divergence of the Reynolds averaged turbulent heat flux. Horizontal turbulent heat transports are not considered, in keeping with other studies.

Clearly, the turbulent heat fluxes must be consistent with the layered formalism. One requirement noted immediately is that within a constant density layer, $\overline{w'T'}$ must be independent of z. Heat flux divergences can only occur at interfaces, and they can be related to interface evolution by integrating (4) across an interface. The result is:

$$-\Delta T_i \, (z_{it} + u_{iT} \, z_{ix} + v_{iT} \, z_{iy} - w_i(z_i)) =$$

$$= -\Delta T_i (z_{it} + u_{i+1T} \, z_{ix} + v_{i+1T} \, z_{iy} - w_{i+1}(z_i)) = - \overline{w'T'} \Big]_{z_i+\varepsilon} - (- \overline{w'T'} \,) \Big]_{z_i-\varepsilon} \tag{5}$$

where ε is a small number, $\Delta T_i = T_i - T_{i+1}$ denotes the temperature jump across the i^{th} interface and $\underset{\sim}{u}_{iT} = \underset{\sim}{u}_i + \underset{\sim}{u}_f$. Substituting (5) in (3) yields:

$$h_{it} + (u_i h_i)_x + (v_i h_i)_y = w_i^*{}_{-1} - w_i^* + \nabla x[(\underset{\sim}{\tau}(z_i) - \underset{\sim}{\tau}(z_{i-1}))/f] \tag{6}$$

where

$$w_i^* = \left(\overline{w'T'} \right]_{z_i+\varepsilon} - \left(\overline{w'T'} \right]_{z_i-\varepsilon} \right) \Big/ \Delta T_i \tag{7}$$

denotes the diapycnal mass flux at the i^{th} interface. The content of (5) is that the heat release associated with a heat flux divergence is balanced by an appropriate conversion of cool water (at T_{i+1}) to warm water (at T_i). This diapycnal flux also need not be vertical.

Clearly, boundary conditions on heat flux are required. The conditions that will be used here are a specification of surface heat flux and a no heat flux condition at the bottom, i.e.

$$\overline{w'T'} = F \quad \text{at } z = 0 \tag{8}$$

$$\overline{w'T'} = 0 \quad \text{at } z = -H. \tag{9}$$

The sign convention on F is such that a cooling atmosphere produces an upward heat flux at $z = 0$, and hence a positive F. These conditions, coupled with the independence of heat flux on z, are sufficient to specify the fluxes just above the first interface and just below the second interface.

The second layer heat flux must be specified by a closure theory. The one frequently employed in past literature (Tziperman, 1986; Huang, 1990) is based on a discretization of the vertical diffusion operator expressed in density coordinates. Heat flux is proportional to $1/z_\rho$ (where ρ = density), which in the second layer here yields a simple finite difference operator inversely proportional to thickness:

$$\overline{w'T'}_{\text{layer 2}} = -\mu/h_2 \tag{10}$$

where the diffusion coefficient μ is positive. Note that the diffusive heat flux is always negative, i.e., downward toward colder waters. Combining (8), (9) and (10) with (7) yields diapycnal velocities at the interfaces:

$$w_1^* = \frac{F}{\Delta T_1} + \frac{\mu}{\Delta T_1 h_2} \tag{11}$$

$$w_2^* = -\frac{\mu}{\Delta T_2 h_2} \tag{12}$$

These are different from the diapycnal parameterizations employed elsewhere in that the surface forcing F appears explicitly and the no heat flux condition at the bottom constrains (12). Consider, for example, the parameterization employed by Huang and Bryan (1987) and contained in their Eq. (30). This is the diapycnal flux at the interface between layers 3 and 4, and it has been assumed that no heat flux occurs through the base of layer 4. Thus their Eq. (30) should be compared to (12) here, as both express diapycnal fluxes at interfaces directly above the no heat flux boundary. Their formula includes a contribution inversely proportional to the thickness of layer 4 which represents a nonzero diffusive flux in that layer. The view taken here is that a no heat flux condition removes the need for a flux parameterization in the layer directly affected by the condition. Thus, in the present model, for example, a term inversely proportional to h_3 does not appear. (It should also be noted that for a two layer fluid with one interface, the current formalism shows that the diapycnal flux is unambiguously determined by the surface condition and the parameter μ does not appear.) The complete set of equations to be considered then are geostrophy [(1) and (2)] and mass conservation [(6)] in each layer, along with heat and momentum flux boundary conditions.

3 A BUOYANTLY FORCED MODEL

The model to be discussed here entirely neglects wind stress. It can be viewed either as a purely GFD model, or in some crude way as a stratified model of the deep thermally driven circulation under the wind-driven circulation. In keeping with this idea, diabatic functions F will be chosen which cool in the north and heat in the south. Regions of cooling will be called subpolar zones and regions of heating will be called subtropical zones. The problem to be solved, simply stated, is given the heat fluxes at the surface, insulating boundaries elsewhere and no normal flux conditions at the sides and the bottom, calculate the resulting steady circulation.

First, volume integrating (4) demonstrates, for a steady solution to exist, that heat conservation requires:

$$\iint F \, dA = 0 \tag{13}$$

where the area integral is taken over the entire domain. The function F will always be chosen to satisfy this condition. Frictional stress $\underset{\sim}{\tau}$ will be neglected in (1) and (2), because wind forcing is set to zero. Finally, in order to demonstrate the connection between the buoyant forcing and the circulation as simply as possible, the parameter μ in (11) and (12) will be set to zero. The aptness of this assumption will be discussed shortly.

Under the above assumptions, the lowest layer conserves potential vorticity when it is covered by layers 1 and 2. It is therefore required on the eastern boundary that all motion be trapped in the upper two layers (i.e., that a "shadow zone" exists in the lower layer near the eastern boundary).

Manipulating geostrophy and continuity eventually yields a relation between the upper two layer thicknesses, namely:

$$h_2 = -h_1 + [2H_1^2 + 2H_1 H_2 + H_2^2 - h_1^2]^{1/2} \tag{14}$$

where H_1 and H_2 are the values of the first and second layer thicknesses on the eastern boundary. Eq. (14) is equivalent to a Sverdrup constraint in that it assures that no net meridional transport occurs at any location. Using (14) in the upper layer equations eventually yields one equation in h_1 which can be solved to yield an algebraic equation involving h_1 and x:

$$\frac{h_1^2}{2} + \frac{h_1}{2}\,(2H_1^2+2H_1H_2+H_2^2-h_1^2)^{1/2} - \frac{2H_1^2+2H_1H_2+H_2^2}{2}\,\sin^{-1}\left(\frac{h_1}{\sqrt{2H_1^2+2H_1H_2+H_2^2}}\right) =$$

$$= \frac{f^2}{\beta g'}\, w_1^*(x-x_e) + \frac{H_1^2}{2} + \frac{H_1}{2}\,(H_1+H_2) - \frac{(2H_1^2+2H_1H_2+H_2^2)}{2}\,\sin^{-1}\left(\frac{H_1}{\sqrt{2H_1^2+2H_1H_2+H_2^2}}\right) \tag{15}$$

where $w_1^* = F/(T_1 - T_2)$ and F is assumed to be a function of y only.

Note, (13) requires F = 0 somewhere, which we will here take as the constant latitude line f_o. Eq. (15) demonstrates $h_1 = H_1$ at f_o. Second, from the upper layer equation:

$$\frac{\beta g'}{f^2}\, h_1 \left(1 - \frac{h_1}{(2H_1^2+2H_1H_2+H_2^2-h_1^2)^{1/2}}\right) h_{1x} \;=\; w_1^* = F/(T_1 - T_2) \tag{16}$$

and (14), it is seen that $h_{1x} < 0$ for negative F (i.e., heating) and $h_{1x} > 0$ for positive F (i.e., cooling). This information can be coupled with (14) to show that $h = h_1 + h_2$ decreases to the west for negative F and increases to the west for positive F.

The thermocline tendencies noted in (16) suggest that the first interface will outcrop in regions of cooling and that the second layer thickness will vanish in regions of heating, provided that the diabatic forcing is sufficiently strong. (For convenience, we will denote the condition $h_2=0$ as "incropping".) Indeed, in certain parameter ranges these events occur and the locus of such points is simple to calculate. The conditions on h_1 for $h_2=0$ can be obtained from (14) and used in (15). The result is:

$$\frac{\beta g'}{f^2}\left(\frac{H_1H_2}{2} + \frac{H_2^2}{2} - (H_1^2+H_1H_2+\frac{H_2^2}{2})(\pi/4 - \sin^{-1}\left\{\frac{H_1}{[2H_1^2 + 2H_1H_2 + H_2^2]^{1/2}}\right\})\right) =$$

$$= \frac{F}{T_1-T_2}\,(x_2^* - x_e) \tag{17}$$

Interior pinchoff, or incropping, of h_2 occurs within the basin as long as the x_2^* calculated from (17) lies within the model domain. [Note, pinchoff was also found in a buoyant and wind-driven model of the subtropical gyre discussed by Pedlosky (1986)]. Similarly, the first interface outcrops when $h_1 = 0$, which leads to:

$$\frac{-\beta g'}{f^2}\left(H_1^2+\frac{H_1H_2}{2}-(H_1^2+H_1H_2+H_2^2/2)\sin^{-1}\left\{\frac{H_1}{\sqrt{2H_1^2+2H_1H_2+H_2^2}}\right\}\right) =$$

$$= \frac{F}{T_1-T_2}(x_1^*-x_e) \qquad (18)$$

where x_1^* is the outcrop curve. The formulas (17) and (18) indicate a strong dependence of oceanic thermal structure on H_1 and H_2, which are as yet free parameters. The above structure is illustrated in Fig. 2.

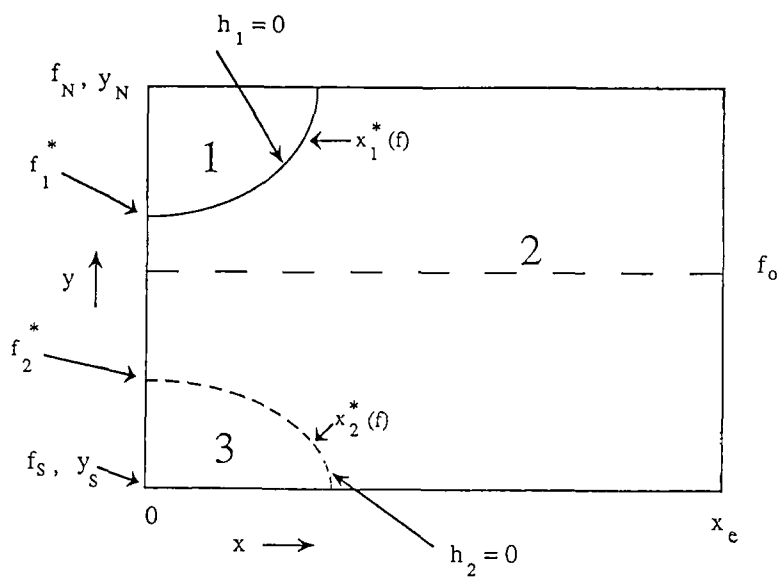

Fig. 2 Solution Schematic. The domain is bounded by latitude f_s to the south and f_N to the north. The upper layer outcrops in the subpolar zone and is denoted by the solid line marked $x_1^*(f)$. The region bounded on the east by the outcrop and on the west by the sidewalls is called region 1. The second layer vanishes in the subtropical domain, and the curve (named $x_2^*(f)$) is denoted by the dotted line. The region enclosed on the east by this curve and on the west by the sidewalls is called region 3. The remainder of the domain consists of 3 layers and is called region 2.

West of the curve x_1^* in the subpolar zone, the stratification has been reduced to two layers (i.e., layers 2 and 3). According to (11), the third layer is now directly forced and therefore in motion. The circulation in this area is straightforward to calculate, being subject to the Sverdrup constraint:

$$p_3 = \frac{g'h_2^2}{2H}\,(x_1^*) - \frac{g'h_2^2}{2H}\,. \tag{19}$$

Second layer thickness is determined by:

$$\frac{h_2^3}{3H}\,\frac{-h_2^2}{2} = \frac{-f^2}{\beta g'}\,\frac{F}{(T_2-T_3)}\,(x - x_1^*) + \left(\frac{h_2^3(x_1^*)}{3H}\,\frac{-h_2^2(x_1^*)}{2}\right) \tag{20}$$

where $h_2(x_1^*)$ denotes the h_2 values along the first layer outcrop.

West of x_2^* in the subtropical basin, the density jump is increased by the disappearance of layer 2. This region nonetheless constitutes a two layer circulation problem with the deepest layer forced and in motion. The formulas for the structure west of x_2^* are similar to (19) and (20), viz:

$$p_3 = \frac{g''h_1^2}{2H}\,(x_2^*)\,\frac{-g''h_1^2}{2H} \tag{21}$$

$$\frac{h_1^3}{3H}\,\frac{-h_1^2}{2} = \frac{-f^2}{\beta g''}\,\frac{F}{(T_1-T_3)}\,(x - x_2^*) + \left(\frac{h_1^3(x_2^*)}{3H}\,\frac{-h_1^2(x_2^*)}{2}\right) \tag{22}$$

where $g'' = \dfrac{g(\rho_3 - \rho_1)}{\rho_o} = 2g'$ and $h_1(x_2^*)$ denotes the upper layer thickness at the location of the interior pinchoff.

3.1 Layer Heat Budgets

The statement of mass conservation, (6), is independent of the momentum equations, and therefore applies even in boundary layers. Integrating the form of (6) appropriate to layer 3 over the basin eventually yields:

$$0 = \int_{f_1^*}^{f_N}\int_{0}^{x_1^*} \frac{F}{(T_2-T_3)}\,dx\,dy + \int_{fs}^{f_2^*}\int_{0}^{x_2^*} \frac{F}{(T_1-T_3)}\,dx\,dy \tag{23}$$

where f_1^* denotes the latitude where $x_1^* = 0$, and f_2^* is where $x_2^* = 0$ (see Fig. 2). Eq. (23) expresses the requirement on the steady thermocline structure that the net production of cold water is zero. In principle, equations similar to (23) expressing the balanced production of layer 1 and layer 2 water can be written down. However, it turns out that these equations add no more information and do not constrain the problem further. This occurs for two reasons. First, the total volume of

fluid in the basin is conserved, independent of diabatic processes and time dependence; therefore, the net production of any one of the three water types in this model can be calculated from knowledge of the other two. There are then at most two independent constraints available from water mass production arguments. Second, the solvability requirement (13) removes a degree of freedom by coupling the remaining budgets.

Because there are two unknowns in this system (i.e. H_1 and H_2), it is necessary to impose an independent constraint to get a unique solution. One possible additional constraint is the requirement of global energy balance. Diabatic forcing at the surface of an initially still fluid alters the total fluid energy and sets it into motion. It is expected on intuitive grounds that a steady state will be realized when the internal frictional dissipation of energy balances the net work performed by the forcing.

A more formal statement is found by forming an integrated energy equation from (1). The result is:

$$0 = -g'' \iint_{A_3} h_1 w_1^* \, dA - g' \iint_{A_2} h_1 w_1^* \, dA - g' \iint_{A_1} h_2 w_2^* \, dA + \iiint \underset{\sim}{u} \cdot \underset{\sim}{\tau_z} \, dV \tag{24}$$

where the areas A_1, A_2 and A_3 are indicated in Fig. 2 and the latter integral is over the entire volume of the basin. It will be assumed when evaluating (24) that the primary contributions to potential energy come from the basin interior where stress is neglected. Frictional dissipation, however, most likely involves western boundary layers. Thus, the explicit evaluation of (24) requires detailed boundary layer models, which are beyond the scope of this paper. In the next subsection, however, a simple example is discussed which demonstrates the foregoing concepts. An ad-hoc form of (24) is thus presented here in order to demonstrate the plausibility of the energetic closure. The idea behind this form is that despite the detailed structure of the boundary layers, the frictional dissipation within them increases with increasing transport. Thus the net dissipation in the final integral in (24) is replaced by:

$$\iiint \underset{\sim}{\tau_z} \cdot \underset{\sim}{u} \, dV = -r \sum_{i=1}^{3} |Q_i| \tag{25}$$

where "r" represents a drag coefficient and Q_i denotes the maximum western boundary current transport in the i^{th} layer.

The transport in the upper layer, Q_1, can be calculated by integrating continuity over the subpolar zone, which yields:

$$Q_1 = \iint_{2p} \frac{F}{T_1 - T_2} \, dA > 0 \tag{26}$$

where the notation "2p" denotes that the integral is taken over the subdomain of A_2 where $F > 0$. The quantity Q_1 is positive, indicating a northward flux. This is consistent with the fact that the sources for hot water occur to the south where $F < 0$ (i.e., where cold and warm water is converted to hot) and the hot water sinks are to the north. Since no interior mass flux crosses $f = f_o$ in this model, the hot water for the subpolar zone is fed northward entirely in the western boundary current.

Integrating continuity over the 3 layers demonstrates that the vertically integrated flow is nondivergent. It is further seen that the sources for warm and cold water are found only in the subpolar zone, so the western boundary currents in those layers transport fluid south across latitude f_o. Thus, $|Q_2| = -Q_2$ and $|Q_3| = -Q_3$, which demonstrates that $|Q_2| + |Q_3| = Q_1$.

Therefore, $\sum_{i=1}^{3} |Q_i| = 2Q_1$, which can also be demonstrated directly by integration of (6) in the bottom layers over the subpolar zone. Eq. (24) becomes:

$$2r \iint_{2p} \frac{F}{T_1 - T_2} = -g'' \iint_{A_3} h_1 w_1^* \, dA - g' \iint_{A_2} h_1 w_1^* \, dA - g' \iint_{A_1} h_2 w_2^* \, dA \qquad (27)$$

and acts as a second independent constraint on H_1 and H_2.

3.2 An Analytical Example

For the special case of heat fluxes inversely proportional to f^2, the outcrop and incrop structures may be analytically determined. The particular flux law to be used here is:

$$F = \frac{F_c}{f^2} \quad f_N > f > f_o$$

$$F = \frac{-F_c}{3f^2} \quad f_s < f < f_o \qquad (28)$$

where $f_o = 2f_s$ and $f_N = 3f_s$. The above form with the indicated coefficients satisfies (14). Inserting (28) in (17) and (18) demonstrates that both x_1^* and x_2^* are lines of constant longitude (see Fig. 3). The constraint implied by (23) is after some algebra found to be:

$$2x_1^* = x_2^* \cdot \qquad (29)$$

where the fact that $T_1 - T_2 = T_2 - T_3 = (T_1 - T_3)/2$ has been used. Any (H_1, H_2) combination resulting in (29) produces a balanced heat budget.

Evaluating the energy constraint (27) yields:

$$r (x_e - x_1^*) = \frac{g'}{2} \left[\int_3 h_1 dx + \int_{2t} h_1 dx - \int_{2p} h_1 dx - \int_1 h_2 dx \right] . \qquad (30)$$

The subscript 2t and 2p denotes zonal integrations in the subtropical and subpolar zones of area 2, respectively and the subscripts 1 and 3 denote zonal integrations in areas 1 and 3, respectively. The fact that h_1 is independent of f in these zones has been used to simplify the right hand side of (30). The left hand side of (30) is positive. The positivity of the right hand side of (30) (and hence the existence of a unique solution) is demonstrated by simply noting that h_1 in the subtropical zone is greater than h_1 in the subpolar zone for all x. Therefore the sum of the first three integrals on the right hand side of (30) is positive. Further, for the special case $x_2^* = x_1^* = 0$, the final integral on the right hand side of (30) vanishes, leaving a positive residual. Thus there exists some positive value of r which satisfies (30) in this extreme case. For small nonzero values of x_1^*, the right hand side of (30) will still be positive (assuming a smooth dependence of the right hand side on x_1^*) and can thus be associated with a positive r value.

An example of a balanced solution which meets all the above constraints is given in Fig. 3. The basin in this example is 5,000 km wide, 5,000 m deep and extends from a southern latitudewhere $f_S = 5 \times 10^{-5}$ sec^{-1} to a northern latitude where $f_N = 1.5 \times 10^{-4}$ sec^{-1}. The value of the imposed heat flux varies with latitude according to (28), but is always of 0(100 W/m^2). Thermocline structure in both zones is also shown. The subpolar outcrop of interface 1 occurs 1,000 km east of the western margin and the second layer pinchoff occurs 2,000 km east of the margin. The eastern boundary thickness values are $H_1 = 2{,}500$ m and $H_2 = 1{,}500$ m. The value of r is 6×10^4 cm^2/sec^2.

In short, to achieve thermodynamic equilibrium, the circulation must internally move fluid from diabatic source to diabatic sink with a combination of geostrophic and western boundary currents. A result of this is the structured permanent thermocline, whose features and variations are intimately connected with that balance.

4 DISCUSSION

4.1 Parameter Sensitivity

It is interesting to determine if the thermocline structure at the heart of the model, i.e., the upper interfacial outcrop and the vanishing of the second layer thickness, are robust. This was tested in three ways (the details are available in Dewar (1990)). First, the heat flux law was changed from that in (28) to:

$$F = F_0(f-f_0) \tag{31}$$

with F_0 positive. Also, some details pertaining to the third layer potential vorticity structure were altered. The formulas for the layer thicknesses are modified versions of those quoted in the previous section and, although analytical tractability is lost, outcrop and incrop conditions can be numerically calculated. An example of such a thermally balanced solution with $H_1 = 3000$m and $H_2 = 967.5$m is shown in Fig. 4. The main thermocline features persist in this test .

An interesting variation is the inclusion of weak, but nonzero μ (i.e., weak buoyancy diffusion). This also appears to induce no important changes in the thermocline structure from that

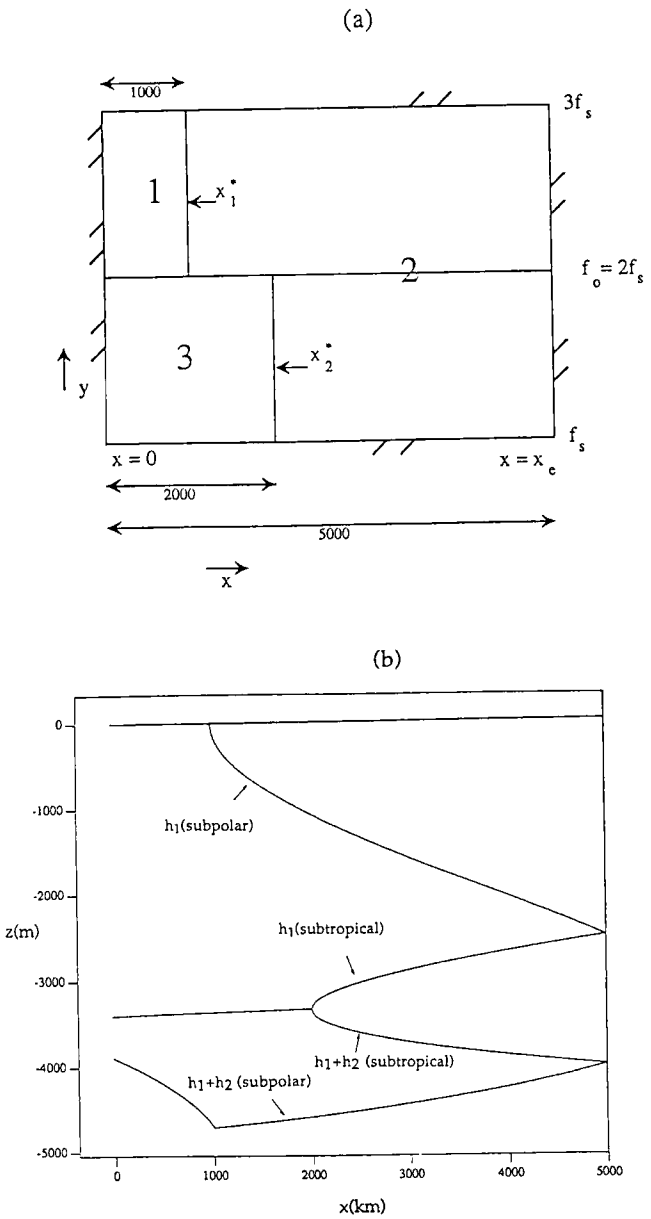

Fig. 3 Analytical Solution. The surface heat fluxes are inversely proportional to f^2, therefore the upper layer outcrop, denoted in (a) by x_1^*, and the second layer incrop, denoted by x_2^*, are simply lines of constant longitude. These critical lines are related by $2x_1^* = x_2^*$, according to the heat balance. Upper and second layer thicknesses for the subtropical and subpolar zones are shown in (b).

calculated for $\mu = 0$. Note, the importance of diffusive fluxes relative to forcing fluxes is expressed by the nondimensional parameter $\frac{\mu}{F_0 H}$, which must be small for diffusion to be weak. The quantity $\mu/\Delta T_1$ has the units of a diffusion coefficient, and the order typically assumed for diapycnal diffusion coefficients is 1 cm^2/sec. Assuming H~5,000 m, heat fluxes of ~100 W/m^2 and ΔT~5°C, the above parameter is seen to be $0(10^{-2})$, suggesting ocean diffusion is properly modeled as weak. The lowest order results turn out to be precisely those for $\mu = 0$ discussed in the previous section. These are expected to be valid everywhere in the subpolar zone and until h_2~$0(\mu)$ in the eastern part

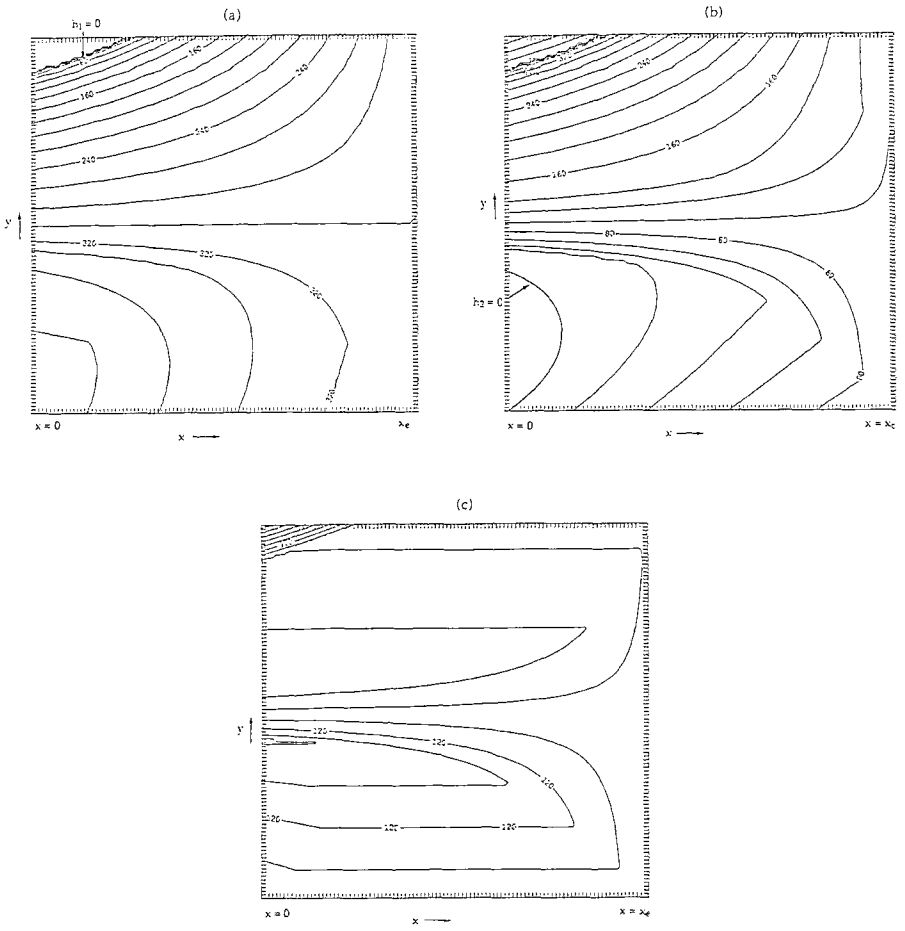

Fig. 4 Thermocline Solutions. The layer 3 potential vorticities west of the $\hat{x}(f)$ trajectories are taken as constants in regions where the third layer is not directly forced, and the heat flux is given by $F = F_0(f-f_0)$. The panels (a), (b) and (c) are of thickness (measured in 10's of meters) in layers 1, 2 and 3, respectively.

of the subtropical zone. It is then possible to demonstrate that the system retains $h_2 = 0(\mu)$ to the western boundary. The intermediate layer, while nonvanishing, becomes thin and essentially passive. Nonetheless, this suggests in observations that evidence of incroppings will come in the form of areas where isopycnals come closer together in the western half of the basin.

Lastly, it can be demonstrated that wind-driving does not qualitatively change the basic model results; i.e., isopycnal outcrops and interior pinchoffs still appear, and are central to the production of acceptable, balanced steady states.

4.2 Summary

Some simple models of stratified circulation have been presented with the primary novel feature being that eastern boundary conditions are calculated, rather than imposed. In contrast to earlier efforts in this direction (i.e., Tziperman, 1986; Kawase, 1987), the relation between the surface forcing and the density structure is illustrated. It is further argued that the constraint of no net water mass production must be augmented with additional constraints to produce a unique solution. Here the additional constraint was taken to be the requirement of a global energy balance and, by means of a simple frictional parameterization, a unique solution was determined.

A point of distinction between this calculation and many ventilated thermocline models lies in the imposition of surface buoyancy flux rather than surface density [not withstanding Pedlosky et al. (1984) who discussed outcrop formation in a subtropical gyre subject to buoyancy fluxes]. As a result, the thermocline develops outcrops, and these critically affect the stratification. An important feature of the model is the strong geographical variation of the stratification. This is due ultimately to planetary dynamics. A somewhat unexpected result is the interplay between the effects of beta and buoyancy forcing, which results in the incrops and the outcrops that are crucial to the development of a balanced solution.

This work is perhaps closest in spirit to (although much simpler than) that of Huang and Bryan (1987) and Huang (1990). Their work focussed on a numerical multilevel model with a relatively active surface mixed layer. The present calculation serves in some sense as a much simpler analytical complement to those very interesting numerical experiments, and some interesting comparisons can be made between the present model and the model runs discussed in Huang and Bryan (1987). One notes in their Fig. 5b map of third layer thickness a reduction in thickness in the subtropical gyre from 500m in the east to 300m in the west. It is also clear from this diagram that fourth layer water is being produced in the subpolar gyre. The model presented in this paper argues that the net fourth layer subpolar production must be recycled to warmer layers, and that a preferred location for this recycling is the southwestern quadrant of the basin where the third layer is the thinnest. Although the thickness change in the Huang and Bryan model is less than that predicted here, it is encouraging to see the trend. Interestingly, their Fig. 11 also shows a southward western boundary transport in the fourth layer and there is a persistent tendency for deeper layers to be exposed to the atmosphere in the north western corners of the subpolar gyre. Both features have analogues in the present calculation.

Lastly, it is worth pointing out explicitly that flow in the deepest layer in the present model is critical to the overall heat budget. Although the velocities in this layer can be small because of its

thickness, the transports can be sizeable, and result in basin scale source-sink flows. Indeed, it is this horizontal advection which ultimately provides local balances in the heat equations. In some sense, the governing deep layer heat equation is more like $\underset{\sim}{u}_H \cdot \nabla_H T = \overline{-w'T'_z}$ than $wT_z = \overline{-w'T'_z}$.

5 ACKNOWLEDGEMENTS

My research is sponsored by ONR contract # N00014-89-J-1577 and NSF grant # OCE-8711030. It is a pleasure to acknowledge the assistance of Ms. S. Heseltine in the preparation of this manuscript.

6 REFERENCES

Dewar, W.K., 1990. Simple models of stratification, J. Phys. Oceanogr., submitted.

Huang, R.X., 1990. Sensitivity of a multilayered oceanic general circulation model to the sea surface thermal boundary condition, J. Geophys. Res., 94, 18011-18022.

Huang, R.X. and K. Bryan, 1987. A multilayer model of the thermocline and wind-driven ocean circulation, J. Phys. Oceanogr., 17, 1909-1924.

Kawase, M., 1987. Establishment of deep ocean circulation driven by deep-water production, J. Phys. Oceanogr., 17, 2294-2317.

Luyten, J.R., J. Pedlosky and H. Stommel, 1983. The ventilated thermocline, J. Phys. Oceanogr., 13, 292-309.

Pedlosky, J., 1986. The buoyancy and wind-driven ventilated thermocline, J. Phys. Oceanogr., 16, 1077-1087.

Pedlosky, J., W. Smith and J.R. Luyten, 1984. On the dynamics of the coupled mixed layer-thermocline system and the determination of the oceanic surface density, J. Phys. Oceanogr., 14, 1159-1171.

Tziperman, E., 1986. On the role of interior mixing and air-sea fluxes in determining the stratification and circulation of the oceans, J. Phys. Oceanogr., 16, 680-693.

This Page Intentionally Left Blank

NON-HYDROSTATIC OCEAN MODELLING FOR STUDIES OF OPEN-OCEAN DEEP CONVECTION

R. BRUGGE, H.L. JONES AND J.C. MARSHALL
Space and Atmospheric Physics Group, Department of Physics, Imperial College, London SW7 2BZ (England)

ABSTRACT

It is argued that non-hydrostatic effects are important in the dynamics of open-ocean deep convection on horizontal scales $\sim$ 1 km, typical of sinking plumes. The formulation and numerical implementation of a non-hydrostatic ocean model appropriate for the explicit representation of plume-scale dynamics is described. The model is used to study the spin-up, through convective overturning induced by surface cooling, and subsequent geostrophic adjustment of a baroclinic vortex with a horizontal scale of the order of the Rossby radius of deformation.

INTRODUCTION

We describe here a non-hydrostatic primitive equation numerical model which is appropriate for the study of oceanic convection from scales of metres upwards. The model has its origins in an atmospheric model developed by M.J. Miller at Imperial College (see Miller, 1974 and Miller and Pearce, 1974) used to study moist convection in a compressible atmosphere; recently it has been adapted to study the overturning of an incompressible fluid such as sea-water.

The model is highly novel in its formulation; in its compressible form acoustic filtering is achieved by transforming the equations of motion, continuity, thermodynamics and state (for the free adiabatic flow of a compressible perfect gas) to pressure coordinates and neglecting various small terms by exploiting knowledge that the flow remains quasi- (but importantly *not* strictly) hydrostatic. Detailed reviews of the scaling assumptions can be found in Miller and White (1984) and White (1989). The resulting quasi-hydrostatic equations in pressure coordinates are isomorphic to the incompressible fluid equations in height coordinates (which guarantees the desired acoustic filtering). In view of this isomorphism it occurred to the authors that the model would be ideally suited to the study of the overturning of an incompressible fluid such as the ocean. Accordingly, Miller's convection model has been adapted to simulate an incompressible fluid with an equation of state appropriate to sea-water.

Below we present the formulation of the resulting non-hydrostatic ocean model. Although many of the details of our model are common to Miller's original convection model, we believe it to be worthwhile to draw them together here because a comprehensive account does not exist in the literature at present. We focus attention particularly on Miller's model adapted for applications in ocean modelling, especially its use in problems of deep convection.

In section 2 we show, by scale analysis of the vertical momentum equation, that non-hydrostatic effects cannot be neglected in oceanic convective overturning events having an observed scale of less than 1 km — the "plume-scale". In section 3 we review the formulation of Miller's quasi-hydrostatic compressible model in pressure coordinates drawing attention to its isomorphism with the incompressible equations in height coordinates. A non-hydrostatic ocean model suitable for studying plume-scale dynamics, based on Miller's model, is described in section 4. In section 5 we illustrate the model's capabilities by using it to study the spin-up and geostrophic adjustment of a 'chimney' with a horizontal scale of the order of the local Rossby radius of deformation; the chimney is a baroclinic vortex driven by the surface cooling of an initially stably stratified fluid in the presence of rotation. The processes resolved by the model may be important in the generation of submesoscale coherent vortices, as reviewed by McWilliams (1985).

2 SCALE ANALYSIS OF THE VERTICAL MOMENTUM EQUATION

Conventional primitive equation ocean models assume precise hydrostatic balance between the pressure and the density fields. Thus if, in standard notation,

$$\frac{Dw}{Dt} + g + \frac{1}{\rho}\frac{\partial p}{\partial z} = 0 \tag{1}$$

is the vertical momentum equation with the height z as the vertical coordinate and $w = Dz/Dt$, then the term Dw/Dt is omitted. But the condition for the validity of the hydrostatic approximation is much more stringent than $Dw/Dt \ll g$, the acceleration due to gravity, because almost all of g is balanced by the inert hydrostatic pressure gradient associated with the resting reference state.

More helpfully, we can isolate this hydrostatically balanced and dynamically inactive pressure gradient by writing the Boussinesq form of eqn. (1) as

$$\frac{Dw}{Dt} + g\frac{\rho'}{\rho_o} + \frac{1}{\rho_o}\frac{\partial p'}{\partial z} = 0 \tag{2}$$

where the primes denote a deviation from the hydrostatically balanced reference state and ρ_o is a standard (constant) value of density. Now it can be clearly seen that the condition for the neglect of Dw/Dt is that it should be much smaller than $g(\rho'/\rho_o)$ rather than g. Let us now try and estimate typical space and velocity scales and stratifications for which the hydrostatic approximation is valid, according to this more stringent condition.

Consider a convective event which has a characteristic horizontal scale L and vertical scale H with horizontal and vertical velocity scales U and W respectively. The time-scale of a particle of fluid moving through the convective system is of order L/U and a typical W will be (making use of the thermodynamic equation)

$$W \sim \frac{gU}{LN^2}\frac{\rho'}{\rho_o}$$

where N^2 $(= -(g/\rho_o)\partial\rho/\partial z)$ is the Brunt-Väisälä frequency of the ambient fluid in which the convection is occurring.

So

$$\frac{Dw}{Dt} \sim \frac{gU^2}{L^2N^2}\frac{\rho'}{\rho_o}$$

and hence $Dw/Dt \ll g\rho'/\rho_o$ if

$$\frac{U^2}{N^2L^2} \ll 1 \tag{3}$$

If the condition (3) is not satisfied then the full vertical momentum equation, eqn. (2), must be used. In other words if the horizontal scale of the motion is such that

$$L \leq U/N$$

then non-hydrostatic effects are important. This contrasts with $L \leq H$, the usual criterion. The scale U/N is the distance travelled by a particle of fluid in a buoyancy period. We now appraise the significance of this condition for the Mistral in the Gulf of Lyons.

2.1 *Scaling for open-ocean deep convection*

Deep convection sites are characterized by anomalously weak stratifications. For example Leaman and Schott (1990) publish σ_o cross-sections during a period of intense vertical mixing in the Gulf of Lyons, which illustrate the striking degree of homogeneity within the well-mixed column. This data suggests that N^2 can fall below 10^{-8} s^{-2}. Accompanying such stratifications, horizontal velocities of the order of tens of centimetres per second were observed. The value U/N for a range of stratifications and horizontal currents are set out in Table 1 below. This ratio should be interpreted as an estimate of the upper limit of the length scale, L, below which non-hydrostatic effects become important.

TABLE 1

The ratio U/N (km) for a range of U (m s $^{-1}$) and N (10^{-4} s $^{-1}$). Typical values for open-ocean convection are enclosed within the box.

		increasing currents →		
	U/N	U (m s $^{-1}$)		
	(km)	0.1	0.2	0.4
N (10^{-4} s^{-1})	0.1	10	20	40
↓ increasing	1	1	2	4
↓ stratification	10	0.1	0.2	0.4

We see that in the deep convection regime, characterised by very weak stratifications and relatively strong currents, non-hydrostatic effects become important on scales on or below about a kilometre. It would seem important, then, that in attempting to explicitly model convection on the plume- scale, non-hydrostatic effects should be adequately represented.

The simulations of deep convection reported in section 5 of the present study occur in an ambient stratification of $N^2 = 5 \times 10^{-8}$ s $^{-2}$, not untypical of those observed in the Gulf of Lyons. The horizontal resolution of the non-hydrostatic model is 250m.

3 QUASI-HYDROSTATIC CONVECTION MODELS

3.1 *The equations*

The quasi-hydrostatic equations (written with pressure (p) as the vertical coordinate) describing the free adiabatic flow of a perfect gas which form the basis of Miller's dry compressible atmospheric model are (see Miller and White (1984) and White (1989)):
horizontal momentum:

$$\frac{Du}{Dt} + g\frac{\partial h'}{\partial x} = 0 \tag{4}$$

$$\frac{Dv}{Dt} + g\frac{\partial h'}{\partial y} = 0 \tag{5}$$

vertical momentum:

$$\frac{D\tilde{w}}{Dt} - g\frac{\theta'}{\theta_s} - g^2\rho_s\frac{\partial h'}{\partial p} = 0 \tag{6}$$

continuity:

$$\frac{\partial u}{\partial x} + \frac{\partial v}{\partial y} + \frac{\partial \omega}{\partial p} = 0 \tag{7}$$

thermodynamics:

$$\frac{D\theta}{Dt} = 0 \tag{8}$$

where

$$\frac{D}{Dt} = \frac{\partial}{\partial t} + u\frac{\partial}{\partial x} + v\frac{\partial}{\partial y} + \omega\frac{\partial}{\partial p} \tag{9}$$

is the substantial derivative and

$$\tilde{w} = -\frac{\omega}{g\rho_s} \tag{10}$$

Here, all differentials with respect to x and y are formed at constant pressure. The vertical velocity in pressure coordinates is $\omega = Dp/Dt$. The velocity components in the x- and y-directions are u and v, respectively. The potential temperature is θ and h' is the deviation of the height of a pressure surface from its reference height. Forcing and dissipation on the r.h.s. of eqns. (4) - (6) and (8) have, for the moment, been omitted, as have the Coriolis terms.

Primed quantities denote deviations from an (initial) reference state (subscripted s),

$$\rho = \rho_s(p) + \rho'(x, y, p, t) \tag{11}$$

$$h = h_s(p) + h'(x, y, p, t) \tag{12}$$

where ρ_s and h_s are in hydrostatic balance:

$$g\frac{\partial h_s}{\partial p} + \frac{1}{\rho_s} = 0 \tag{13}$$

Note that in eqn. (6) the true vertical velocity w $(= Dz/Dt)$ is *approximated* by

$$w \simeq \tilde{w} = -\frac{\omega}{g\rho_s}$$

This, together with the form adopted for the continuity equation, is the crucial filtering approximation which ensures the absence of acoustic modes in the compressible equations; buoyancy modes remain undistorted and the treatment of gravity modes is more accurate than in the hydrostatic formulation. The compressible formulation in pressure coordinates, eqns. (4) – (10), above, can be justified by scale analysis (see Miller and White, 1984).

However, it occurred to the authors that if we *interpret* $\tilde{w}$ in eqn. (6) as the vertical velocity in height coordinates, then eqns. (4) – (7) are exact statements of the momentum and continuity equations governing the evolution of an incompressible Boussinesq fluid. This important step is now made explicit by noting the isomorphism of Miller's compressible model in pressure coordinates with the incompressible equations written in height coordinates.

3.2 *The incompressible fluid isomorphism*

If we introduce the vertical coordinate $h_s(p)$, the hydrostatic height, then making use of eqn. (13)

$$\frac{\partial}{\partial h_s} = -g\rho_s\frac{\partial}{\partial p}, \tag{14}$$

and so

$$\omega\frac{\partial}{\partial p} = \tilde{w}\frac{\partial}{\partial h_s}. \tag{15}$$

Eqs. (4) – (7) can now be written with h_s as the vertical coordinate thus:

$$\left(\frac{\partial}{\partial t} + \underline{u}.\nabla\right)\underline{u} - g\frac{\theta'}{\theta_s}\underline{k} + g\nabla h' = 0 \tag{16}$$

$$\frac{\partial u}{\partial x} + \frac{\partial v}{\partial y} + \frac{1}{\rho_s}\frac{\partial}{\partial h_s}\rho_s\tilde{w} = 0 \tag{17}$$

where

$$\underline{u} = (u, v, \tilde{w})$$

and

$$\nabla = \underline{i}\frac{\partial}{\partial x} + \underline{j}\frac{\partial}{\partial y} + \underline{k}\frac{\partial}{\partial h_s}$$

Eqns. (16) and (17) have the same form as the Boussinesq equations describing an incompressible fluid written in height coordinates. It is this isomorphism that lies at the heart of the 'clever' filtering approximation of the quasi-hydrostatic compressible model. But in the present context it enables us to employ Miller's model as a Navier-Stokes model describing the evolution of an incompressible fluid: we simply *reinterpret* $\tilde{w}$ as the vertical velocity in height coordinates ($\tilde{w} \longrightarrow w$) and *reinterpret* the vertical coordinate p (divided by $\rho_s g$) as the hydrostatic height ($p \longrightarrow \rho_s g h_s$).

4 A NON-HYDROSTATIC OCEAN CIRCULATION MODEL

4.1 *The continuous equations*

The non-hydrostatic equations for a Boussinesq incompressible fluid with an equation of state appropriate to sea-water that form the basis of our model are, in height coordinates (replacing ρ_s by ρ_o, a standard value of density and, to standardize our notation, using z in place of h_s in eqns. (16) and (17))

$$\left.\begin{aligned} \frac{Du}{Dt} + \frac{1}{\rho_o}\frac{\partial p'}{\partial x} - fv &= F_u - D_u \\ \frac{Dv}{Dt} + \frac{1}{\rho_o}\frac{\partial p'}{\partial y} + fu &= F_v - D_v \end{aligned}\right\} \tag{18}$$

$$\frac{Dw}{Dt} + g\frac{\rho'}{\rho_o} + \frac{1}{\rho_o}\frac{\partial p'}{\partial z} = F_w - D_w \tag{19}$$

$$\frac{\partial u}{\partial x} + \frac{\partial v}{\partial y} + \frac{\partial w}{\partial z} = 0 \tag{20}$$

$$\frac{DT}{Dt} = F_T - D_T \tag{21}$$

$$\frac{DS}{Dt} = F_s - D_s \tag{22}$$

where

$$\frac{D}{Dt} = \frac{\partial}{\partial t} + u\frac{\partial}{\partial x} + v\frac{\partial}{\partial y} + w\frac{\partial}{\partial z} \tag{23}$$

and

$$\rho = \rho(T, S, z) \tag{24}$$

Here S is the salinity, T is the temperature and p' is the deviation of the pressure from its reference (hydrostatic) value. Note that now we have included Coriolis terms in the momentum equations and represented forcing and dissipation terms symbolically by F and D respectively.

Eqns. (18) – (20) are identical to those of Miller's compressible model (except for an appropriate modification of the buoyancy terms in eqn. (19)), *when viewed isomorphically.* The density perturbation is obtained from the evolving temperature and salinity fields using an equation of state written symbolically in eqn. (24).

The prognostic variables of the model are u, v, w, T and S; the pressure field is diagnosed. The model can be used in two or three dimensions with or without Coriolis terms, and with or without salt. In two dimensions, v and all derivatives with respect to y are set to zero and the Coriolis term in eqn. (18) is omitted.

(i) *Diagnosing the pressure field.* Time integration of eqns. (18) – (24) requires the inversion of an elliptic equation for p' which is formed by taking the divergence of the momentum equations exploiting the continuity eqn. (20):

$$\frac{\partial^2 p'}{\partial x^2} + \frac{\partial^2 p'}{\partial y^2} + \frac{\partial^2 p'}{\partial z^2} = \frac{\partial}{\partial x} G_1 + \frac{\partial}{\partial y} G_2 + \frac{\partial}{\partial z} G_3 \tag{25}$$

where

$$\frac{1}{\rho_o} G_1 = -\frac{\partial u^2}{\partial x} - \frac{\partial uv}{\partial y} - \frac{\partial uw}{\partial z} + fv + F_u - D_u$$

$$\frac{1}{\rho_o} G_2 = -\frac{\partial uv}{\partial x} - \frac{\partial v^2}{\partial y} - \frac{\partial vw}{\partial z} - fu + F_v - D_v$$

$$\frac{1}{\rho_o} G_3 = -\frac{\partial uw}{\partial x} - \frac{\partial vw}{\partial y} - \frac{\partial w^2}{\partial z} + g\frac{\rho'}{\rho_o} + F_w - D_w$$

Appropriate boundary conditions for eqn. (25) are discussed in section 4.2 below. The method of solution of eqn. (25) is described in section 4.3(iii).

(ii) *Forcing and dissipation.* The choice of representation of forcing and dissipation depends on the use to which the model is to be put but also, particularly where parametrisation of dissipation processes is concerned, on one's tastes and prejudices. Various more or less sophisticated dissipative parametrisations have been used, but the standard 'Fickian' form will be described here.

Diffusion of Φ is adopted, relaxing the field back to a specified standard background state Φ_s where Φ may be T, S, u, v or w:

$$F_\Phi = K_\Phi^h \left(\frac{\partial^2 (\Phi - \Phi_s)}{\partial x^2} + \frac{\partial^2 (\Phi - \Phi_s)}{\partial y^2} \right) + K_\Phi^v \frac{\partial^2 (\Phi - \Phi_s)}{\partial z^2} \tag{26}$$

Here K_Φ^h and K_Φ^v are horizontal and vertical 'eddy' diffusion coefficients respectively for the quantity Φ. The K's are assumed to be positive and are normally held constant in time and space. The magnitude of the diffusion coefficent for each velocity component is assumed to be the same. As in all numerical models these diffusion terms are to some extent adhoc and multi-purpose, being used partly as a computational device to suppress spurious noise, but also to represent the mean effects of poorly understood physical processes which cannot be resolved in the model.

Thermal forcing is represented by adding a warming or cooling function $F_T(x, y, z, t)$ to the body of the fluid on the r.h.s. of eqn. (21). Such a device will be used in the deep convection experiments described in section 5 to cool the water column in the near-surface

layers. Similarly the process of brine ejection during ice formation can be represented by a forcing function in the salt eqn. (22).

4.2 *Boundary conditions*

The equations are integrated in a Cartesian 'box' with rigid boundaries at the top and bottom. At the lateral boundaries doubly periodic conditions can be employed or, if we are modelling a limited area, radiation conditions and/or sponge layers can be used. The model can be run in two or three dimensions with or without rotation.

(i) *Upper and lower boundary conditions.* To eliminate fast-moving surface gravity waves at the upper boundary of the model we apply the condition

$$w = 0 \quad \text{at } z = 0 \tag{27}$$

Likewise, we assume that the lower boundary of the model, at a depth H, is flat and apply

$$w = 0 \quad \text{at } z = -H \tag{28}$$

These imply, through the vertical momentum eqn. (19) that

$$\frac{\partial p'}{\partial z} + g\rho' = 0 \quad \text{at } z = 0, -H \tag{29}$$

providing Neumann boundary conditions for the inversion of eqn. (25) to find the height field.

The Fickian diffusion terms necessitate the use of additional conditions at the top and bottom of the model. Choosing to set the vertical flux of horizontal momentum, heat and salt to zero, we impose:

$$\left.\begin{aligned} \frac{\partial u}{\partial z} &= \frac{\partial u_s}{\partial z} = 0 \\ \frac{\partial v}{\partial z} &= \frac{\partial v_s}{\partial z} = 0 \\ \frac{\partial T}{\partial z} &= \frac{\partial T_s}{\partial z} = 0 \\ \frac{\partial S}{\partial z} &= \frac{\partial S_s}{\partial z} = 0 \end{aligned}\right\} \quad \text{at } z = 0, -H \tag{30}$$

These ensure that, *intoto*, momentum, heat and salt are conserved in the periodic model in the absense of imposed sources and sinks.

(ii) *Lateral boundary conditions.* In the limited area model radiation boundary conditions (Miller and Thorpe, 1981) are employed at the open boundaries to determine the time-evolution of the p', T and S fields and the velocity components normal to the boundary:

$$\frac{\partial \phi}{\partial t} = \hat{c}\frac{\partial \phi}{\partial x} \tag{31}$$

where $\hat{c}$ is the velocity (a combination of wave propagation and advection) at which the property is to be transported across the boundary. Knowledge of the height field around the boundary provided by (31) supply the lateral boundary conditions for the elliptic equation (25). In addition stress-free velocity boundary conditions, $\partial V_t/\partial n = 0$, are applied on all lateral boundaries, where V_t is the velocity tangential to the boundary (this includes the vertical velocity).

In certain problems, when extended integrations of the model have been carried out, we have found it necessary to incorporate a 'sponge' layer around the edge of the limited area model; in this layer all model fields are relaxed back to their background values on a chosen time-scale.

The periodic model uses neither radiation nor tangential boundary conditions; fluid leaving the domain through the western boundary re-enters through the eastern boundary while that leaving through the northern boundary re-enters via the southern boundary and vice-versa.

4.3 *Numerical implementation*

The advective terms in the model equations are discretised using quadratic-conserving finite-difference approximations of eqns. (18), (19), (21) and (22), and written in the form:

$$\frac{\partial \phi}{\partial t} = -\frac{\partial u\phi}{\partial x} - \frac{\partial v\phi}{\partial y} - \frac{\partial w\phi}{\partial z} + \ldots . \tag{32}$$

where ϕ is either u, v, w, T or S.

At each timestep, given u, v, w, T and S, p' is obtained diagnostically by solving eqn. (25).

(i)*Spatial discretisation.* Fig. 1 shows the staggered 'C'-grid used by the model. The velocity fields are located at the centre of the face lying perpendicular to the direction of the velocity component, while the height, temperature and salt variables are to be found at the centre of the 'grid box'.

The model equations of the generic form (32) are, in the main, centre-differenced and the r.h.s. for a given variable ϕ is evaluated at the ϕ point itself. The horizontal grid is square, $\Delta x = \Delta y$, and the vertical gridspacing, Δz, is constant. Typically the model is run, in three dimensions, with 65 gridpoints in each horizontal direction, and 19 gridpoints in the vertical.

(ii) *Time-stepping scheme.* The prognostic variables are u, v, w, T and S. The time-differencing scheme consists of alternate Euler-backward and Euler-forward steps. If the superscripts n, $n+1$ and $n+2$ refer to successive timesteps, and $*$ refers to a temporary (intermediate field), then the following equations are used to step the variable ϕ forward in time in eqn. (32).

Odd timestep:

$$\phi^{*n+1} = \phi^n + \Delta t \frac{\partial \phi^n}{\partial t} \tag{33}$$

$$\phi^{n+1} = \phi^n + \Delta t \frac{\partial \phi^{*n+1}}{\partial t} \tag{34}$$

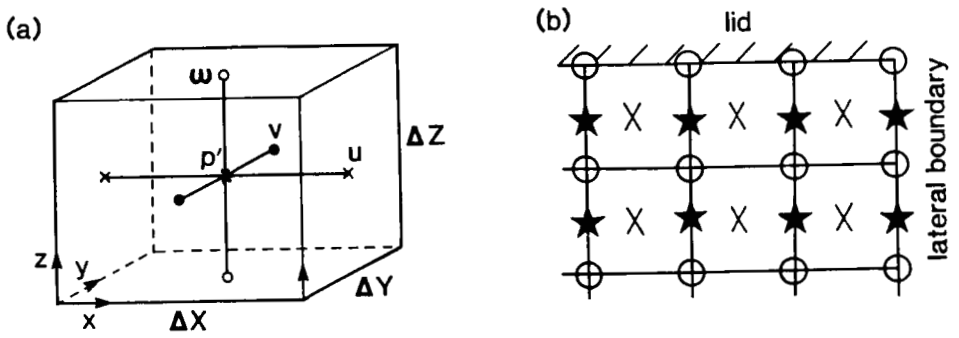

Fig. 1. (a) Model 'C'-grid configuration. u is located at points marked $\times$, v at points marked $\bullet$, w at points marked $\circ$ while the height field, temperature and salt variables are located at points marked $\star$. (b) The location of model gridpoints at the upper and eastern boundaries of the model. Note that the v gridpoints are located in west-east planes $\Delta y/2$ in front of, and behind, the plane containing the height field; they are not shown in fig. (b).

Even timestep:

$$\phi^{n+2} = \phi^{n+1} + \Delta t \frac{\partial \phi^{n+1}}{\partial t} \tag{35}$$

where Δt is the timestep. Note that the tendency in eqn. (33) is evaluated setting the forcing and dissipation terms to zero. The scheme is negligibly unstable for the linearized system when $\Delta t \leq \Delta x/c$, where c is the speed of the fastest waves. The quadratic-conserving space-difference scheme, together with the application of a highly selective two-gridlength filter at regular intervals, results in a model which is highly robust numerically.

(iii) *Inversion of the elliptic equation for the pressure field*

At each timestep eqn. (25) must be inverted for the pressure field (p'). It will be recalled from section 4.1(i) that eqn. (25) is derived by taking the divergence of the momentum eqns. (18) and (19). This leads to a term

$$-\frac{\partial}{\partial t}\left(\frac{\partial u}{\partial x} + \frac{\partial v}{\partial y} + \frac{\partial w}{\partial z}\right)$$

Exploiting the continuity equation (20), this term should be identically zero, giving the height equation (25) as quoted. However, in any finite difference approximation, the time tendency of the divergence, as a result of (small) rounding errors, will be non-zero. To overcome this problem, the source term in our numerical representation of eqn. (25) includes a term 'divergence $/\Delta t$', where

$$\frac{\partial}{\partial t}\text{divergence} = -\text{divergence}/\Delta t$$

In this way the 'new' divergence is relaxed toward zero when inverting eqn. (25) controlling numerical noise in the divergence field. This is similar to the method of Harlow and Welch (1965); see also Williams (1969).

The elliptic equation is solved, employing a mixture of Fourier transform techniques (in the horizontal) and the recursive 'method-of-no-name' (in the vertical), exploiting the appropriate boundary conditions.

5 MODEL SIMULATION OF THE SPIN-UP OF A BAROCLINIC VORTEX BY CONVECTIVE OVERTURNING

To illustrate the capabilities of the model we now describe one of a series of numerical experiments designed to study the way in which a balanced vortex can be spun-up through convective overturning in the presence of rotation.

Consider the following scenario. Suppose that an initially weakly statically stable ocean is subjected to vigorous cooling at the surface, as for example might happen in the Gulf of Lyons during the late winter Mistral. Strong cooling will produce a density inversion leading to the possibility of overturning. The fluid cannot be expected to overturn on the scale of the cooling (some hundreds of kilometres), rather the qualitative description must be that the response to widespread cooling is one in which relatively small cells develop. The detailed physics that sets the scale of the overturning is uncertain at present (and is under active investigation by the authors). The preferred scale may depend on the (assumed) coefficients of eddy viscosity and thermal diffusivity but it is likely that variations in the local stratification on the scale of the Rossby radius of deformation will be more influential.

Whatever the precise details, the dynamics of the plumes will be profoundly affected by rotation if their horizontal scale is a significant fraction of the Rossby radius. In the weakly stratified waters typical of open-ocean deep convection sites, the Rossby radius may be only a few kilometres. The observations quoted in section 2.1 suggest that in the well-mixed interior of a Medoc convection site, N is about 10^{-4} s^{-1} giving a local Rossby radius of deformation, NH/f, of 2 km where the fluid depth is 2 km. In the numerical experiment described below, we study the overturning of a stably stratified fluid on the scale of the Rossby radius of deformation.

5.1 *Model set-up*

The limited-area three-dimensional version of the model was employed in a domain measuring 25km square by 2km deep, with radiation lateral boundary conditions. The horizontal and vertical gridlengths were chosen to be 250m and 100m respectively. The time step used was 60 seconds. The simulation was initialised with a stably stratified fluid at rest governed by an equation of state given by

$$\rho = \rho_O(1 - \varepsilon(T - T_O))$$

where ε is the coefficient of thermal expansion of water taken to have a value of 2×10^{-4} K^{-1}, and ρ_O and T_O are appropriately chosen constants. There is no salt. A linear temperature

profile was set up with a top-to-bottom temperature difference of 0.05 K giving a static stability corresponding to $N^2 = 5 \times 10^{-8}$ and a Rossby radius of deformation in the ambient fluid of $NH/f = 2\sqrt{5}$ km. To mimic the effect of pre-conditioning of the stratification on this scale a forcing function F_T of Gaussian form with an e-folding scale of 2km was chosen. This applied a steady decrement of temperature to eqn. (21) over a 200m deep surface layer equivalent to a peak surface heat flux of 800 Wm^{-2} for two days, consistent with meteorological observations taken at the height of the Mistral in the Gulf of Lyons (Leaman and Schott, 1990). After this two-day period the cooling was switched off and the fluid allowed to adjust under gravity and rotation.

The following eddy viscosity and thermal diffusivity coefficients were used: $K^h = 5$ m^2 s^{-1} and $K^v = 0.2$ m^2 s^{-1} for the temperature field and all components of the velocity fields. These coefficients were chosen to be as small as possible whilst ensuring reasonably smooth fields on the grid-scale of the model.

5.2 *Results*

Temperature sections through the centre of the cooling at days 1, 2 and 3, Fig. 2, vividly chart the development of a "chimney" on the scale of the forcing (Rossby radius). Fluid exposed to the cooling is constrained by the earth's rotation and trapped in the vorticular motion that is set up. Cooled at the surface, it eventually becomes sufficiently dense to sink within the chimney to its neutrally buoyant level. For example on day 2, fluid of a similar temperature to that existing in the deepest layers of the model can be seen riding in the upper two to three hundred metres of the chimney. Notice how, at the end of the forcing period, the sides of the chimney are vertical. By day three, however, the dense water has slumped under gravity; as expected from geostrophic adjustment theory the walls of the chimney slope horizontally by a distance close to the deformation scale; rotation prevents the isopycnals from returning to the horizontal.

Sinking fluid shows up in the vertical velocity fields (not shown) where speeds reaching a maximum of 10 cm s^{-1} downwards, over an area roughly corresponding to the cooling patch, have developed by day 2. Once the cooling ceases, however, vertical velocities decline to a small fraction of their values under actively forced conditions; within twelve hours the vortex geostrophically adjusts and becomes more closely horizontally non-divergent. An estimate of the Rossby number can be made from an inspection of the horizontal currents.

Fig. 3 shows the horizontal velocity field at days 1 and 3 at two levels in the model corresponding to depths of 200 and 1500m. On day 1 we see that the imposed cooling has spun-up a cyclonic vortex near the surface but with significant radial inflow. Deeper down, where fluid is spreading radially outward — compensating for the horizontal convergence nearer the surface — the sense of circulation is anticyclonic. This is in accord with angular momentum considerations. Horizontal speeds of order 10 cms^{-1} have developed. By day three the vortex has come into geostrophic adjustment with cyclonic flow in the near-surface layers and anticyclonic flow beneath. The currents are in geostrophic balance; we estimate

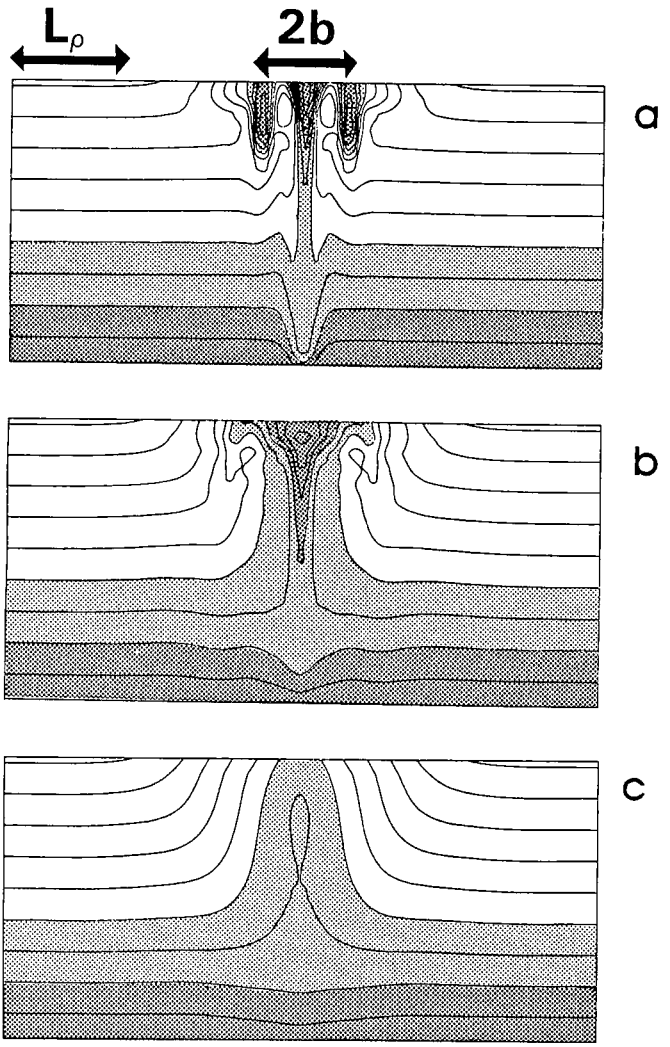

Fig. 2. West-east cross-sections through the centre of the chimney, showing the density after (a) 1 day, (b) 2 days and (c) 3 days. The most dense fluid in the domain has been shaded to highlight the chimney formation. The density difference between top and bottom in the ambient fluid is 0.01 kg m^{-3}, consistent with the observations of Leaman and Schott (1990). Also shown is the horizontal e-folding scale of the imposed initial cooling (b) and the Rossby radius (L_ρ).

that the Rossby number is about 0.2. The lack of radial symmetry evident in these horizontal sections is believed to be of numerical origin, arising from inadequacies inherent in attempts to represent an axisymmetric structure on a cartesian grid.

The net result of the overturning induced by surface cooling has been, therefore, to create a baroclinic vortex with an almost vertically homogeneous core — a mini-chimney —

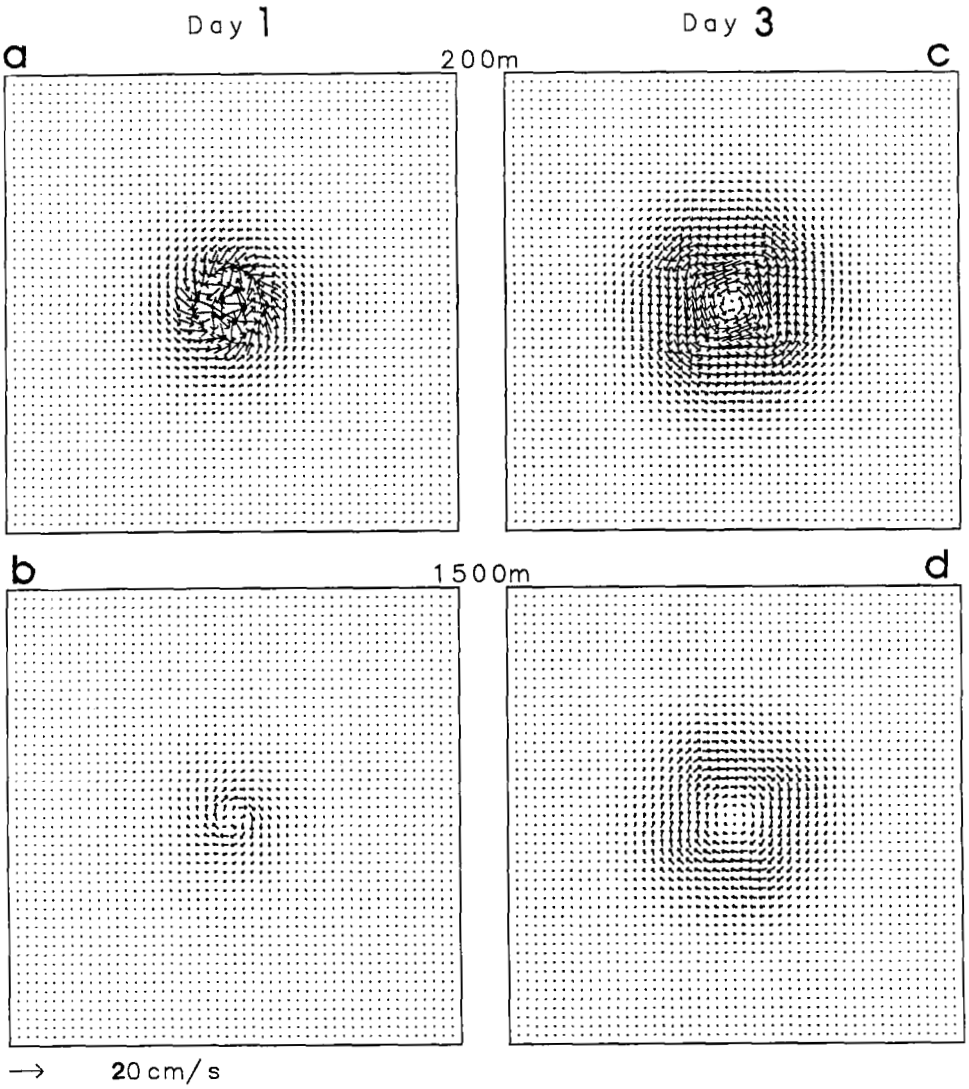

Fig. 3. Plan views of the horizontal velocity fields after 1 day at (a) 200 m and (b) 1500 m,and after 3 days at (c) 200 m and (d) 1500 m. The same velocity scale is used in all figures, as shown by the annotated arrow.

with cyclonic azimuthal circulation in the upper layers and anticyclonic circulation below in balance with the radial pressure gradient. Over the column, net cyclonic vorticity has been generated. The initial vertical mixing occurs rapidly to generate an almost neutrally buoyant column which then undergoes geostrophic adjustment.

It should be emphasised that there is no constraint on Kelvin circulation integrals eval-

uated on isopycnal surfaces because, as can readily be seen from Fig. 2, they outcrop at the free surface. A rather more appropriate diagnostic method would be to monitor the angular momentum surfaces $M = rv + fr^2/2$ of the axi-symmetric vortex, where v is the azimuthal velocity; as noted by Dewar (1987), these are material surfaces even in a non-hydrostatic dynamical framework in the presence of diabatic forcing. What is clear from such considerations is that we would expect to see a concentration of cyclonic vorticity in upper levels whereas deeper down, at the base of the chimney, there is anticyclonic vorticity; this is readily seen in our numerical experiments.

6 CONCLUSIONS

Terms in the vertical momentum equation which can be justifiably neglected in large-scale models of the ocean circulation become important on scales smaller than U/N. In particular, in regions of weak stratification and swift currents, non-hydrostatic terms such as Dw/Dt will be important on the plume-scale. Inclusion of such terms obviates the need for a parametric representation of convective overturning such as convective adjustment since, given sufficient spatial resolution, the dynamics of the sinking plumes can be modelled explicitly .

It should be mentioned that other non-hydrostatic terms, conventionally neglected in the vertical momentum equation, can be included. Coriolis terms involving $2\Omega \cos(latitude)$ are likely to be important on the plume-scale but have not been considered here; for energetic consistency they must be included in both zonal and vertical momentum equations.

We have described the formulation and numerical implementation of a non-hydrostatic incompressible model suitable for the study of dynamical processes down to, and including, the plume-scale of order 500m to 1km. Rather than build a new model we modified an existing atmospheric convection model developed by Miller (1974). This is a highly flexible, tried and tested code, known to be numerically robust, which has been successfully used to simulate a variety of atmospheric phenomena. We have exploited the isomorphism between the quasi-hydrostatic compressible equations in pressure coordinates and the non-hydrostatic incompressible fluid equations written in height coordinates, to study oceanic convection.

A corollary of this isomorphism is that any conventional Navier-Stokes model can, with minor modifications, be used to represent the evolution of a compressible atmosphere in the quasi-hydrostatic regime identified by Miller and White (1984). This does not seem to be widely appreciated.

The numerical experiment briefly described in section 5 has been included here primarily to demonstrate the capabilities of our ocean model, but is of interest in its own right. It articulates a mechanism that may be important in the dynamics of the plume-scale at open-ocean deep convection sites: the rapid overturning induced by cooling at the surface, and subsequent geostrophic adjustment of the well-mixed column. A key aspect which is not yet fully understood are those factors which control the scale of the plume. This is presently under investigation by the authors using the non-hydrostatic model in a doubly periodic domain.

7 ACKNOWLEDGEMENTS

We acknowledge, in particular, Dr A.A. White, who clarified many of the subtleties of the compressible-incompressible fluid isomorphism.

The present study is part of the FRAM community modelling effort supported by the Natural Environment Research Council of the United Kingdom.

8 REFERENCES

Dewar, W.K., 1987. Ventilating warm rings: theory and energetics. J. Phys. Oceanogr., 17, 2219-2231.

Harlow, R.H. and Welch, J.E., 1965. Time dependent viscous flow. Phys. Fluids, , 8, 2182-2193.

Leaman, K.D. and Schott, F.A., 1990. Hydrographic structure of the convection regime in the Gulf of Lions: winter 1987. (accepted for publication in J. Phys. Oceanogr.).

McWilliams, J.C., 1985. Submesoscale coherent vortices in the ocean. Rev. Geophysics, 23, No. 2, 165-182.

Miller, M.J., 1974. On the use of pressure as vertical co-ordinate in modelling. Quart. J. R. Meteorol. Soc., 100, 155-162.

Miller, M.J. and Pearce, R.P., 1974. A three-dimensional primitive equation model of cumulonimbus convection. Quart. J. R. Meteorol. Soc., 100, 133-154.

Miller, M.J. and Thorpe, A.J., 1981. Radiation conditions for the lateral boundaries of limited-area numerical models. Quart. J. R. Meteorol. Soc., 107, 615-628.

Miller, M.J. and White, A.A., 1984. On the non-hydrostatic equations in pressure and sigma coordinates. Quart. J. R. Meteorol. Soc., 110, 515-553.

White, A.A., 1989. An extended version of a non-hydrostatic, pressure coordinate model. Quart. J. R. Meteorol. Soc., 115, 1243-1251.

Williams G.P., 1969. Numerical integration of the three-dimensional Navier-Stokes equations for incompressible flow. J. Fluid Mech., 37(4), 727-750.

CONVECTION IN THE LABRADOR SEA: COMMUNITY MODELING EFFORT (CME) RESULTS

E.D. SKYLLINGSTAD, D.W. DENBO and JOHN DOWNING
Battelle - Pacific Northwest Laboratory / Marine Science Laboratory, P. O. Box 999, Richland, Washington (USA)

ABSTRACT

Results from the World Ocean Circulation Experiment Community Modeling Effort are compared with observations to study the effects of convective parameterization in the Labrador Sea. The results show that the model boundary conditions have a strong influence on the relative intensity of convection in the northern part of the Labrador Sea, producing an anomalous cross current at about 60° N. Cross sections from the coast of Labrador and south of Greenland show overall agreement, but are considerably different in some areas. In particular, the cold, North Atlantic Bottom Water is not modeled correctly and the model exhibits overly warm, salty surface water south of Cape Farewell. Convection in the model is in general too widespread and does not extend to the proper depth.

INTRODUCTION

Accurate representations of convection in ocean general circulation models (OGCM) are important for many reasons. Convection transfers heat from the deep ocean to the atmosphere and transports surface waters to depths of 2000 m or more in the high latitude Greenland, Labrador, and Norwegian Seas. Convection produces North Atlantic Deep Water (NADW), which is a primary water mass in the oceanic meridional circulation (Killworth, 1983), and influences the global distribution of sources and sinks of carbon dioxide in the ocean (Tans, et al., 1990). Most recent large scale models and some regional ocean process models use a convective adjustment scheme where adjacent unstable grid points are averaged to restore static stability (Semtner and Chervin, 1989 and Medec, et al., 1990, for example). The first World Ocean Circulation Experiment (WOCE) Community Modeling Effort (CME) model calculation for the North Atlantic provides an excellent data set for examining the performance of an ocean-scale circulation model with this adjustment scheme.

We report in this paper a descriptive analysis of the CME model data from the subdomain including the Labrador Sea and western North Atlantic Ocean (Fig. 1). Our interest in the Labrador Sea evolved from research we are conducting to better understand deep convection in high-latitude regions, away from the sea ice edge, and to develop improved techniques for modeling this process. Our specific objectives were to: 1) describe differences between model results and the available observations, 2) determine, so far as possible, whether

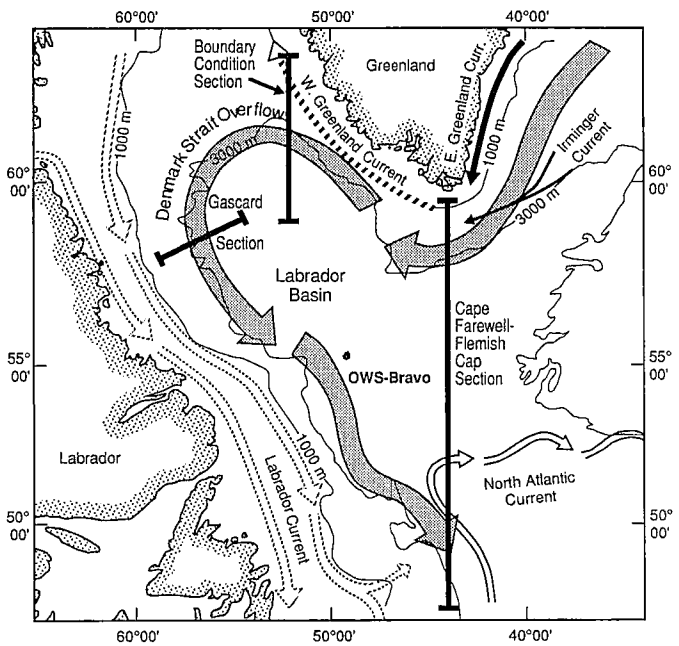

Fig. 1. Schematic representation of the currents in the Labrador Sea. Cross section positions are also shown (from Clarke, 1984).

problems we identified in the CME data were the result of inaccurate initial or boundary conditions, the climatological relaxation, or the convective adjustment scheme, and 3) estimate the magnitude of errors in calculated model fields and their time evolution. We chose the Labrador Sea because observations from the region provide a reasonably complete picture of the density field, the general circulation, and deep convection in action.

We begin with a description of the CME model and model data from the 5-yr period after the 25-year model spinup. Next, we compare model results and observations with emphasis on the possible influences of the convective adjustment, climatological relaxation, and the boundary conditions. We conclude the paper by summarizing the deviations between calculated fields and observations and suggest explanations for these differences.

2 CME MODEL DESCRIPTION

The CME model is a variant of the Cox-Bryan OGCM (Bryan and Cox, 1967) adapted for simulations of the North Atlantic Ocean (Bryan and Holland, 1989). The model domain extends from 15° S to 65° N latitude and 100° W to 14° E longitude with a grid resolution of 1/3° and 2/5° respectively. With this grid spacing, the CME model is almost eddy resolving at the latitude of the Labrador

Sea where the Rossby radius of deformation is of the order - 15 to 25 km. The vertical grid has 30 layers with resolution decreasing from 35 m at the surface to 250 m below 1000 m. The initial conditions were derived from the climatology of Levitus (1982). The surface forcing is position-dependent, monthly average heat flux from Han (1984), with surface salinity restored to climatology using a 50-day damping period, and surface wind stress based on Hellerman and Rosenstein (1983). Model boundaries that are not part of a land surface are treated as closed boundaries without normal flow. The effects of inter-basin exchange are parameterized by restoring model temperature and salinity fields back to climatology using Newtonian damping over the five grid points adjacent to inter-basin boundaries. Because the CME model does not have a sea ice parameterization, damping is also applied in coastal regions when subfreezing temperatures are forced by the surface heat flux.

The CME model was started at rest and integrated for 20 years before storing model fields of temperature, salinity, u,v, and w components of velocity, an age tracer and convective adjustment indicator (CAI), every 3 days. For each time step, the age tracer parameter is transported and diffused as a conserved quantity and incremented with the fractional year, except at the top grid point where it is set to zero. The convective adjustment indicator is 1 or 0 depending on whether or not convection occurred in the preceding time step. We will examine monthly average values of potential temperature, salinity, potential density, and velocity from the five year simulation, representing the current velocity and density structure along cross sections where hydrographic observations have been made.

3 RESULTS

3.1 Comparisons to observations

As in most of the high latitude ocean, observations from the Labrador Sea are non-synoptic and sparse in the winter. We selected three data sets for our descriptive analysis; the study locations are shown in Fig. 1. The first one (Gascard Section, Clarke and Gascard, 1983) consists of conductivity-temperature-depth (CTD) profiles in the western Labrador Sea. These CTD data indicate mesoscale motions resolvable by the CME model. The second data set is a hydrographic section from Cape Farewell, Greenland to Flemish Cap off Newfoundland (Cape Farewell - Flemish Cap Section, Clarke, 1984). The third data set is the ten-year time series of temperature and salinity profiles from Ocean Weather Ship (OWS) Bravo located at 56°30' N, 51°00' W (Lazier, 1980). This paper reports our initial results and provides a qualitative description of large scale features along cross sections from the above mentioned studies. A more quantitative analysis of these and other observations is being conducted for a future publication.

(i) Currents. A schematic of the Labrador Sea circulation derived from a composite of current observations by Clarke (1984), is shown in Fig. 1. In Fig. 2, plots of the average model surface currents (17.5 m) and interior flow (462 m) are shown for the month of May, representing circulation in the model Labrador Sea during late spring. The most obvious difference between observed and model circulations is the strong jet-like flow across the Labrador Sea at

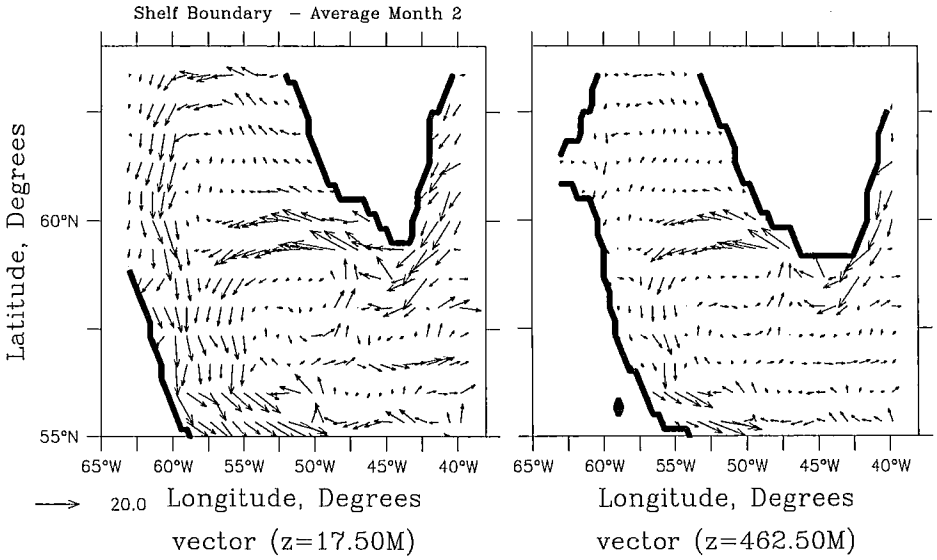

Fig. 2. Vectors of horizontal motion (cm^{-1}) from CME month 5 at 17.5 m and 462.5 m depth.

mid-depth from the southern end of Greenland to the Canadian coast. This prominent model current has not been observed. Instead, the West Greenland Current flows along the coast of Greenland following the bottom topography until reaching the Davis Strait, and then turns southward at 65° N (Fig. 1).

Strong zonal flow at 60° N in the model appears to result in part from the northern boundary condition and the climatological damping of temperature and salinity in areas of subfreezing temperatures along the west coast of Greenland. A model cross section along 52° W of potential temperature, salinity, and potential density (boundary condition section, Fig. 3) reveals that, during the month of February, the surface water along the Greenland coast is too fresh for convection to occur north of the cross current, even though the temperature is below freezing. Lack of convection in the northern area of the section is revealed by relatively "old" values of the age tracer (Fig. 4). Restoration to climatology of seawater with below freezing temperatures is the

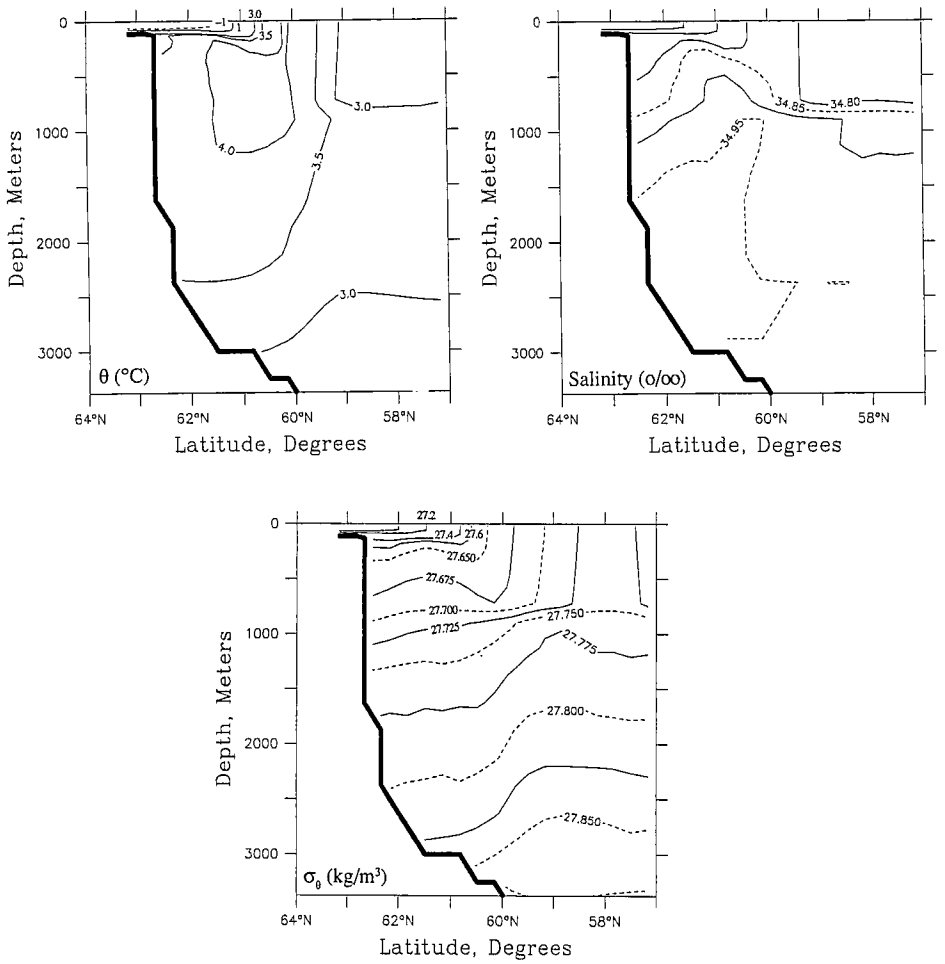

Fig. 3. CME simulation cross section of monthly average potential temperature, salinity, and potential density at 52° W for the month of february.

likely cause for the relatively fresh water (probably a result of a summer bias in the observed climatology). This prevents significant convection along the west coast of Greenland even though active cooling and convection occurs south of 60° N and in the middle of the Labrador Sea. The Boundary-condition section of the CAI during February (Fig. 4) clearly shows the lack of convection north of the cross current.

The net effect of suppressed convection is a strong horizontal density gradient that extends to the bottom at 60° N. Calculation of the current shear using the model density gradient with the thermal wind equation (Pedlosky, 1987) gives a shear of about 0.04 ms^{-1} per 1000 m. This agrees with the vertical shear in the zonal velocity component (u) calculated by the CME

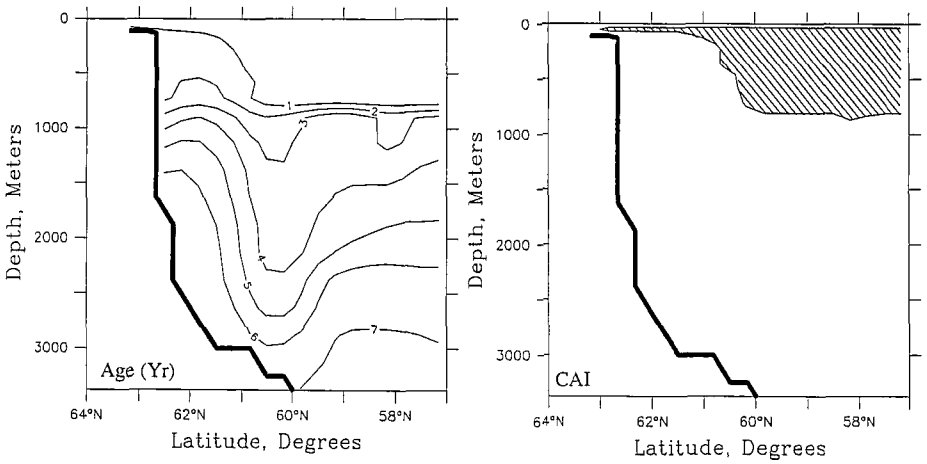

Fig. 4. Monthly average age tracer and Convective Adjustment Indicator (CAI) from the CME model along 52° W for February.

model. However, it seems unlikely that relaxation to climatology in the shallow northeast corner of the Labrador Sea could produce such a large density anomaly, particularly in the deep water. Although further analysis is required, we suspect that the anomaly is a result of the accumulation of "climatological water" during spinup and/or too much low salinity, ~4°C, water being advected into the region from outside the Labrador Sea. We intend to further examine the effects of the boundary conditions in a more quantitative analysis now in progress.

ii) Eddies. Mesoscale eddies are pervasive in the model Labrador Sea and they have substantial time variability. Model Labrador Sea eddies are most stable in strength and position where convective adjustment is frequent, as determined by the CAI. Clarke and Gascard (1983) proposed that a dynamic link may exist between mesoscale eddies and convection. They describe a 200 km mesoscale cyclonic circulation observed in March, 1976 near 56° N, 56° W, which appeared to result from cooling at the sea ice edge in the western Labrador Sea, and say it is analogous to cyclonic eddy production in the Medoc region of the Mediterranean Sea. Eddies north of approximately 55° N and south of the strong zonal flow at 60° N are numerous in the model, persist in the same position for long periods, and maintain nearly constant current speeds, suggesting a connection to the convection process as proposed by Clarke and Gascard (1983).

In contrast, eddies south of 55° N in non-convective waters propagate northwestward from near the Gulf Stream and dissipate rapidly as they penetrate the Labrador Sea. The existence of such eddies in the southern Labrador Sea is questionable. The limited hydrographic observations do not show mesoscale

variability in this area to the extent exhibited by the CME model. For example, observed sections of temperature and salinity do not show significant mesoscale structure north of about 50° N. However, because of limited observations we cannot conclude that the model eddy structure is totally in error. In addition to the large-scale currents, the model eddy heat and momentum transport appears to be a crucial component of the overall energy budget of the Labrador Sea and should therefore not be discounted.

iii) Hydrography (water masses). The Gascard and Cape Farewell-Flemish Cap Sections (Clarke and Gascard, 1983) (Clarke, 1984) are compared with model sections in the same regions to assess the water mass representation by the model. The major features of model Gascard section of potential temperature, salinity and potential density (Fig. 5) for March agree with the sections from

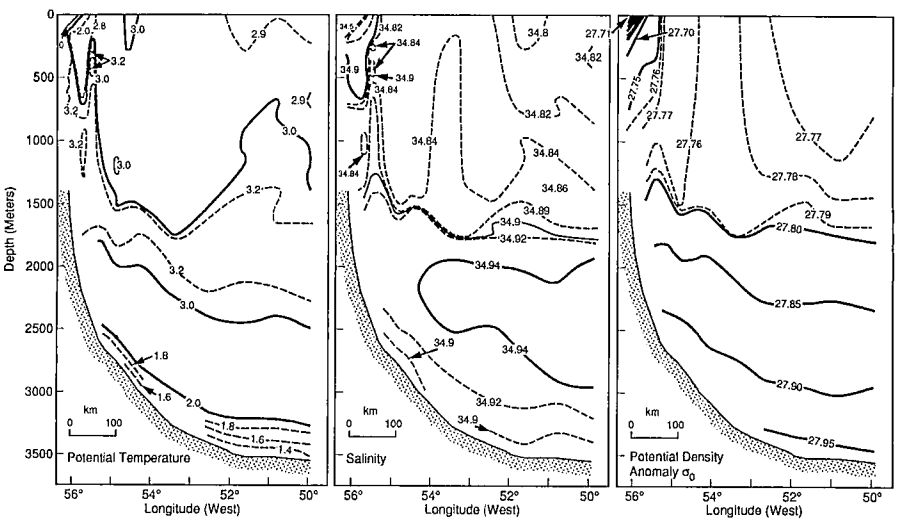

Fig. 5. Potential temperature, salinity and potential density from March, 1976 along the Labrador Coast near 56° N, 56° W (from Clarke and Gascard, 1983).

March 1976 shown in Fig. 6. Above 1000 m, both model and observed sections show 3.0° C water and salinities of about 34.85, identifying newly formed Labrador Sea Water (LSW) (Clarke, 1984). However, between 1000 and 1500 m, the observed temperature and salinity profiles show more mixing from 53° W to 56° W than does the CME model, as indicated by the more vertically uniform density. This discrepancy seems to indicate that the model does not produce deep enough mixing, at least in limited areas, to produce realistic water masses. Another

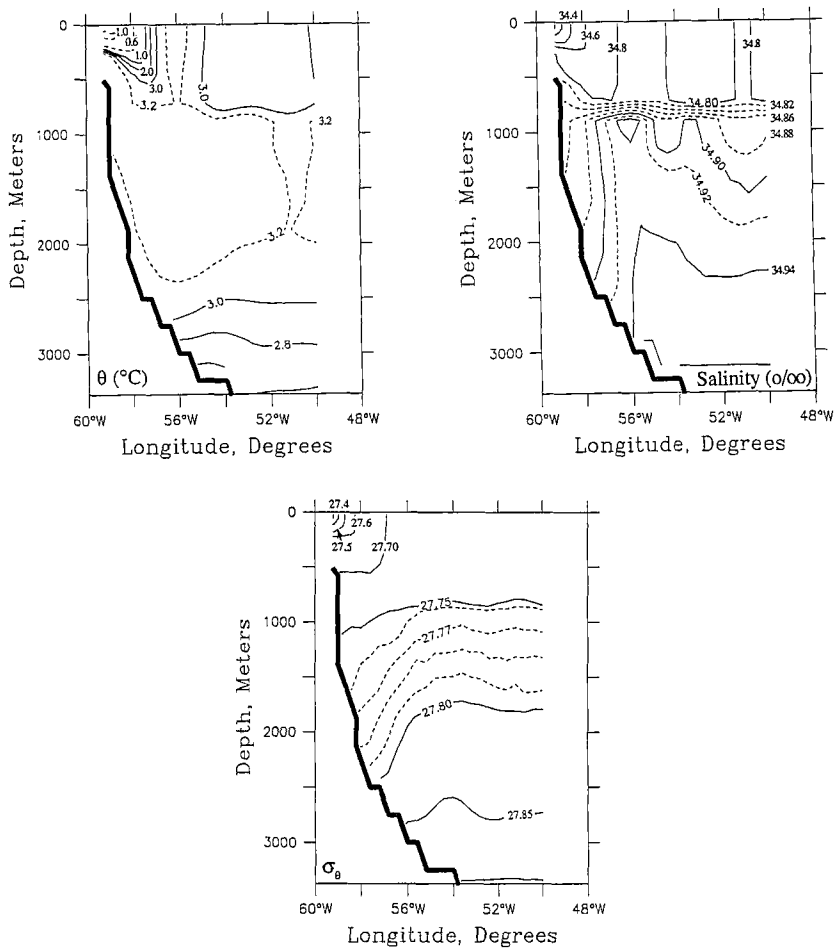

Fig. 6. Average potential temperature, salinity and potential density from CME results at 57.16 latitude for March.

problem in the model is indicated by warmer (by 0.3° to 0.5° C) bottom water below 2500 m. In the observations, this water represents North Atlantic Bottom Water (NABW). The discrepancy is probably linked to the coarse vertical grid resolution in the CME model (250 m at the bottom), the smoothed initial conditions of Levitus, or possible errors in the Labrador Sea deep inflow currents discussed below.

In the second comparison (Fig. 7), the model Cape Farewell - Flemish Cap section, between 55° N and 57° N, is too saline and warm near the surface indicating a more northerly transport of atlantic waters then is observed in

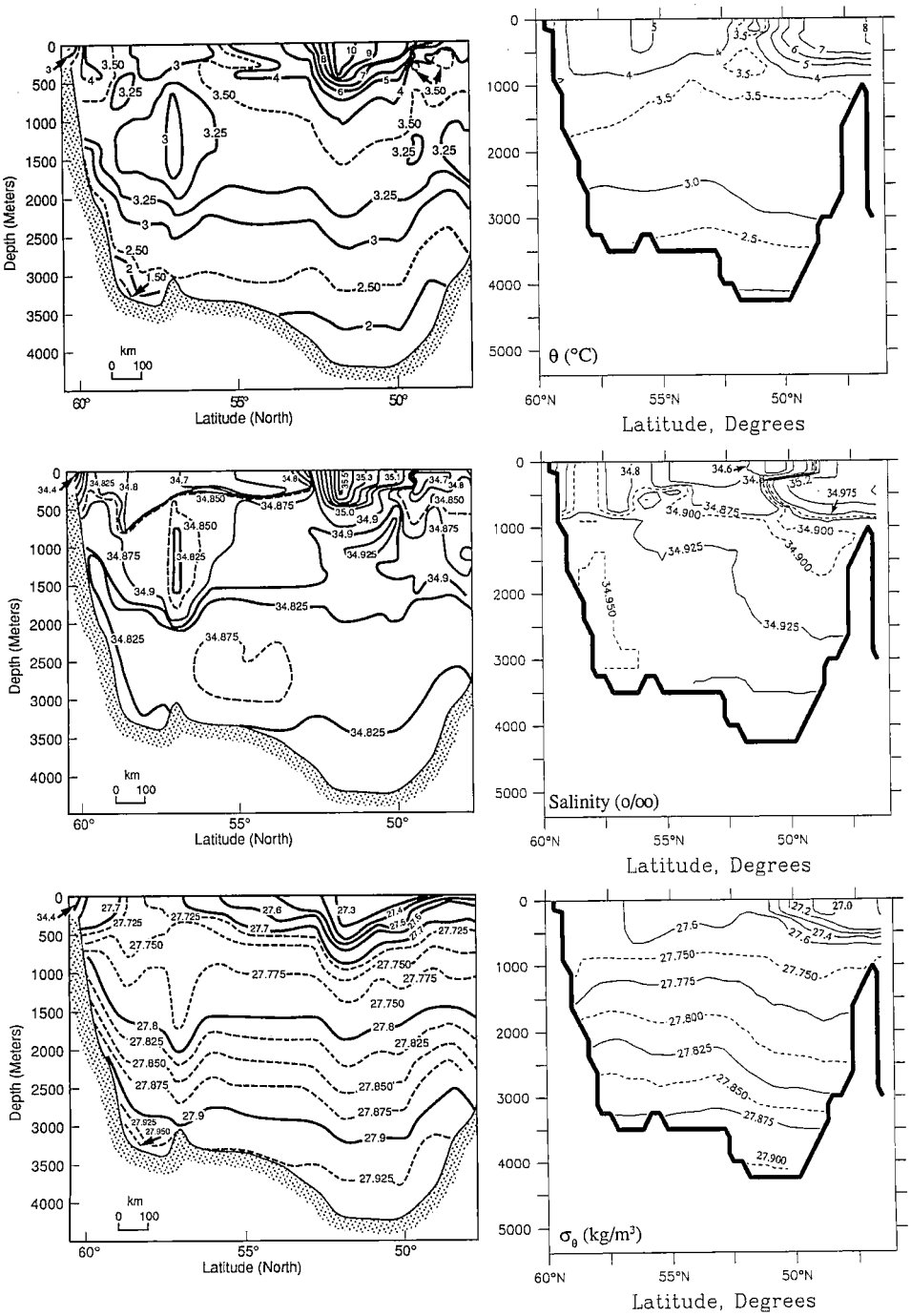

Fig. 7. Potential temperature, salinity, and potential density fields along the Cape Farewell to Flemish Cap Section shown in Fig. 1 from Clarke (1984) (left) and April average from the CME model along 43.2° W (right).

the Labrador Sea. The warm, salty water may also be a signature of the central Labrador Sea mesoscale eddies discussed above, providing further evidence that eddy transport of warm water is not a real phenomena in the Labrador Sea South of 55° N. The model upper ocean results agree more favorably with the observations showing temperatures rising rapidly where the cross section intersects the northern edge of the Gulf Stream. In the deep water, the model does not accurately simulate the inflow of NABW, which is identified by the relatively cold, fresh water along the coast of Greenland at 2500-3000 m. Observed current speeds in this water are approximately 20 cms^{-1} as compared to modeled values of about 6 cms^{-1}. Errors in the Labrador Sea bottom water structure noted in the Gascard Section could be a result of this inaccurate NABW inflow.

3.2 Convective Effects

The effects of the CME convective adjustment scheme were evaluated by combined analysis of the CAI and the age tracer model data. Plots of the CAI and age tracer at cross sections along 52° W shown previously in Fig. 4 for February demonstrate that a significant problem with the adjustment scheme is the large number of time steps required to mix water from the top of the convective layer to the bottom and that, in a nearly uniform water mass, tracer age increases with depth. As shown in Fig. 4, the age of water at the bottom of the convective surface layer is about 1 year and tracer age in the layer increases with depth. Observations in the Labrador Sea have shown that convective plumes can transport surface water to 1500 m depth in a matter of days and that vertical hydrographic gradient are destroyed in the process (Gascard and Clarke, 1983). With the CME convective adjustment, this process is not possible because the degree of convective mixing in the model is limited by the number of grid points and convective iterations.

The Bryan-Cox model scans a vertical profile with two passes, mixing adjacent grid levels 1 and 2, 3 and 4, ..., n and n+1 on the first pass, 2 and 3, 4 and 5, ..., n-1 and n on the second pass. If the model is initialized with the top grid point most dense, then mixing is confined to the top three points for each timestep, assuming one iteration of the scheme. Increasing the number of convective iterations causes the effects of convection to propagate to greater depths in a given timestep. However, this is usually not performed for computational efficiency (Bryan and Cox, 1967). In any case, it is nearly impossible for the direct transport of surface water to great depths without significant vertical and horizontal mixing in the intermediate waters. Also, the slow convergence of the adjustment scheme can lead to unrealistic areas of active mixing even when the surface layer is stratified.

In regions where the convective adjustment scheme produces deep seasonal mixing, anomalous water characteristics are produced. A good example is the mixing profiles near OWS Bravo. Fig. 8 shows stacked time series plots of isopycnal surfaces for OWS Bravo (1964 - 1973) and CME model years 20-24. Although the seasonal cycle of mixing is well simulated, the CME produces a persistent layer of water with a strong vertical density gradient between approximately 700 and 900 meters. The OWS Bravo hydrographic profiles do not

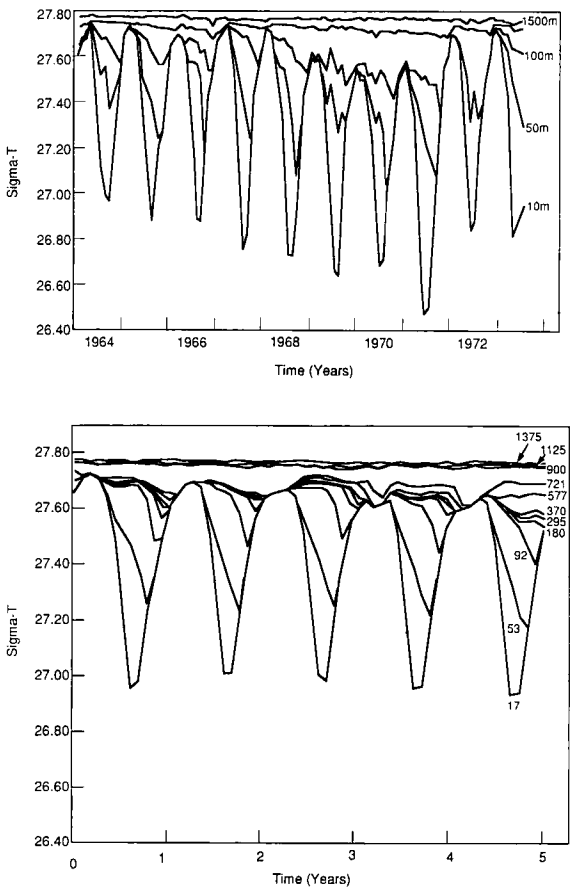

Fig. 8. Potential density as a function of time at various depths from OWS Bravo (top) and the CME model at 51.2° W, 56.5° N (bottom).

show this feature. Also, analysis of the CAI field at 462 m depth (Fig. 9) shows convective adjustment occuring over a wide area in the CME model, which is in disagreement with measurements showing isolated patches of convection in primarily the western half of the Labrador sea (Clarke and Gascard, 1983).

Although the dynamic implications of the convective adjustment scheme require further investigation, it is our initial assessment that the scheme is physically unrealistic for regions of open ocean deep convection such as the Labrador Sea.

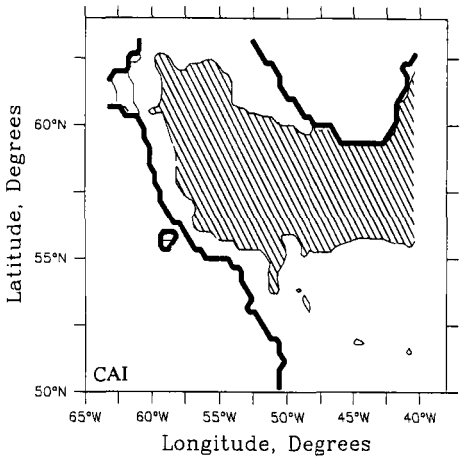

Fig. 9. CME monthly average CAI at 462 m from February.

4 SUMMARY AND CONCLUSIONS

The following points summarize our comparison of the CME model to observations in the Labrador Sea.

(1) Strong zonal flow at 60° N in the model appears to result from the combined effects, in unknown proportions, of the northern boundary condition, climatological damping to avoid sea ice formation along the west coast of Greenland, advection of atlantic water into the Labrador Sea, and/or accumulation of "climatological water" during model spinup.

(2) The existence of eddies as produced in the southern Labrador Sea is inconsistent with the limited hydrographic observations.

(3) The major features of the model Gascard hydrographic section for March are similar to the section from March 1976 obtained by Clarke and Gascard (1983). The CTD profiles show more mixing between 1000 and 1500 m than the CME model. This seems to indicate that the model does not mix deep enough, in areas analyzed, to produce realistic water masses.

(4) The model does not accurately simulate the influx of NABW around the southern tip of Greenland. The absence of this water inflow may be the cause of relatively warmer water (by 0.3° to 0.5° C) below 2500 m in the central Labrador basin.

Finally, in our examination of the CME convective adjustment we show that modeled convection occurs over an unrealistically large region of the Labrador Sea, persists through the summer, and does not penetrate below 700 m. The seasonal cycle of mixing is well simulated, but the CME model produces a persistent layer of water with strong density gradient between 700 and 900 m that is not observed. A possible explanation for this behavior is that the model convective adjustment scheme and coarse vertical resolution make it nearly impossible for direct transport of surface water to great depths.

5 ACKNOWLEDGMENT

This work was supported at the Pacific Northwest Laboratory and at Battelle/Marine Sciences Laboratory by the U.S. Department of Energy (DOE). The laboratories are operated for DOE under contract DE-AC06-76RLO-1830 by Battelle Memorial Institute.

6 REFERENCES

Bryan, F.O. and Holland, W.R., 1989. A high resolution simulation of the wind and thermohaline-driven circulation of the North Atlantic Ocean, Paper presented at Hawaiian Winter Workshop: Parameterizations of small scale processes, Univ. of Hawaii, Jan 17-20, 1989. Sponsored by U.S. Office of Naval Research, Hawaiian Inst. of Geophysics, and Dept. of Oceanogr. Univ. of Hawaii.

Bryan, K. and Cox M.D., 1967. A numerical investigation of the oceanic general circulation, Tellus, 19:54-80.

Clarke, R.A., and Gascard, J.C., 1983. The formation of Labrador Sea water: Part I: Large scale processes. J. Phys. Oceanogr. 13: 1764-1778.

Clarke, R.A., 1984. Transport through the Cape Farewell-Flemish Cap section. Rapp. P.-v. Reun. Cons. int. Explor. Mer., 185:120-130.

Gascard, J.C. and Clarke, R.A., 1983. The formation of Labrador Sea water: Part II: Mesoscale and smaller-scale processes. J. Phys. Oceanogr.,13: 1779-1797.

Han, Y.J., 1984. A numerical world ocean general circulation model. Part II, a baroclinic experiment, Dyn. Atmos. Oceans.,8:141-172.

Hellerman, S. and Rosenstein, M., 1983. Normal monthly wind stress over the world ocean with error estimates, J. Phys. Oceanogr., 13: 1093-1104.

Lazier, J.R.N. 1980. Oceanographic Conditions at O.W.S. Bravo 1964-1974. Atmos. Oceans. 18:227-238.

Levitus, S., 1982. Climatological atlas of the world ocean. NOAA Prof. Pap., 13, 173 pp.

Killworth, P.D., 1983. Deep convection in the world ocean. J. Geophys. Res., 21:1-26.

Madec, G., Chartier, M. Delecluse, P., and Crepon, M., 1990. A three-dimensional numerical model study of deep water formation in the Northwestern Mediterranean Sea. Submitted to J. Phys. Oceanogr.

Pedlosky, J., 1987. Thermocline Theories. In: General Circulation of the Oceans, Abarbanel, H.D.I. and W.R. Young eds., Springer-Verlag, New York, 291 pp.

Semtner, A.J., and Chervin, R.M., 1988. A simulation of the global ocean circulation with resolved eddies. J. Geophys. Res., 93: 15502-15522.

Tans, P.T., Fung, I.Y., and Takahashi, T., 1990. Observational constraints on the global atmospheric CO_2 budget. Science, 247:1431-1438.

SMALL AND MESOSCALE CONVECTION AS OBSERVED IN THE LABORATORY

J. A. WHITEHEAD
Department of Physical Oceanography, Woods Hole Oceanographic Institution, Woods Hole, Massachusetts 02543, USA

ABSTRACT

Whitehead, J. A., 1990. Small and mesoscale convection as observed in the laboratory. Elsevier.

Some laboratory studies of convectively driven flows in a rotating fluid are reviewed. Sugimoto and Whitehead investigated a model of a shallow sea of constant depth bounded by a deep ocean through a uniformly sloping continental rise. The experiment was cooled from above and heated at the deep ocean wall. There was a region that exhibited sinking convection cells which formed the coldest water. This water then spilled off the right-hand side of the shallow sea as a density current (looking downstream for counterclockwise rotation) and formed bottom water in the deep experimental ocean. There were three flow regimes: for very slow rotations there was one big gyre in the shallow sea, and the sinking (convection) region was near the coast; for faster rotations, there were two or three gyres, and for even faster rotations, there were many gyres. In this latter case, the sinking regions were very patchy and sporadic. Comparison with theoretical estimates of temperature difference between the coldest shelf water and the offshore water (based upon the assumption that the density current removes all the cold water) was good but yielded somewhat low predictions.

Next, a study by Speer and Whitehead of convection in a rotating square laboratory basin is reviewed. The convection was driven by non-uniform heating from below, in a manner thought to be analogous to large-scale convection in the ocean. Like a previous non-rotating experiment by Rossby, the upper fluid showed little temperature variation. There was a thermal boundary layer near the warm bottom and fluid moved from the cool to the warm end. At a given location, convection cells were observed and as the water continued to move toward the warm end, the penetration depth of these cells increased. At the hottest point, the cells penetrated all the way to the surface. The scaling advanced by Rossby for the non-rotating experiment is reviewed and the difficulty in applying it to this experiment and to the ocean is discussed. Another scaling based upon both the Sugimoto and Whitehead results and upon arguments in other papers is put forth.

Next, a review is given of the behavior of baroclinic eddies in a rotating fluid that are produced by the turbulent sinking of dense fluid. When there was a sloping bottom, and for certain parameters, a coherent lense of dense bottom water formed on the sloping bottom and propagated west (to the left looking upslope) with an overlying cyclonic vortex. The circulation in the bottom lense was relatively weak. Finally, recent experiments by Helfrich with a turbulent dense plume sinking into a rotating stratified fluid are reviewed. The analogy with various Heton generation processes is discussed.

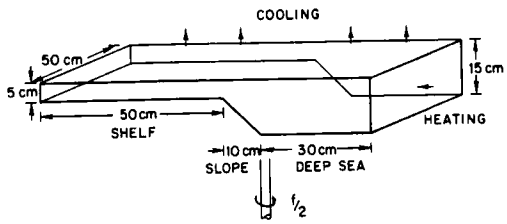

Figure 1: Experimental apparatus to observe flow from cooling over a shallow sea next to a heated deep basin.

INTRODUCTION

Although direct observations of deep water formation in oceans are relatively scarce (a majority are reviewed by Killworth, 1983), observations of corresponding processes in laboratory experiments are even rarer, in spite of the ease and economy of laboratory studies. We review some experiments producing dense water formation in rotating multilayer systems. All studies were conducted by the author and colleagues, so this is not a comprehensive review. The intent is to present some data that illuminate a form of convection that may be found in the ocean. First a study of a shallow rotating pan cooled from above, but connected to a warm deep tank will be reviewed. Next a study of a rectangular rotating pan differentially heated along the bottom will be reviewed. Last, studies of rotating plumes of dense water will be described.

2 A MODEL OF A COOLED SHALLOW SEA

If waters in a shallow sea are subjected to high levels of surface cooling and evaporation for a sufficiently long period, it is reasonable to expect them to be denser than water in the neighboring deep ocean. Sugimoto and Whitehead (1983) constructed a rotating, rectangular basin which consisted of a square shelf (50 cm x 50 cm x 5 cm deep) connected by a narrow (10 cm wide) slope to a deeper basin (30 cm x 50 cm x 15 cm deep) mounted on a turntable as is shown in Figure 1. The enclosed fluid was cooled through a top lid and bath and was also heated through an offshore metal sidewall in contact with a second heated bath.

Photographs of the current pattern were taken by a 35 mm camera and a 16 mm movie camera located above the basin. For visualization of the flow, the test fluid was buffered to be close to the transition pH for the pH-sensitive indicator "thymol blue." A voltage was applied between 0.01-mm diameter wires which were stretched at 1 and 4 cm depths. This resulted in the fluid near the wires changing from a yellow color to a dark blue. It was possible

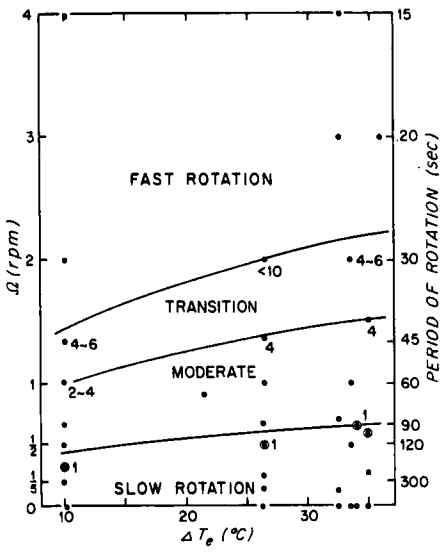

Figure 2: Location of the experimental parameters in the space of externally controlled variable rotation Ω ($= 2\pi/\text{period}$, p) and external temperature difference ΔT_e. Also delineated are boundaries between the slow (S), moderate (M), transition (T) and fast (F) rotation limits. The numbers in the graph indicate the visually estimated number of eddies in the large scale circulation.

to trace the movement of this fluid for a number of minutes thereafter. Temperature in the basin was measured by thermistors lowered through small holes in the top. Figure 2 shows the distribution of large-scale structures of the flows on the shelf as a function of the angular rotation rate of the tank Ω and the temperature difference between cooling bath and heated bath ΔT_e.

At zero rotation, vertical circulation was predominant, like a Hadley cell. The sinking region was limited to a narrow inner coastal zone region 2 cm in width. In cases with slight rotation, warm surface water steadily flowed toward the inner coastal zone but was more concentrated on the right looking onshore and circled to the left. The sinking region was concentrated to the left. Cold bottom water from the inner shelf twisted slightly to the right looking offshore. The net circulation consisted of a slightly cyclonic gyre in the upper fluid and a slightly anticyclonic gyre in the lower fluid. At greater rotation, smaller and more numerous gyres were observed on the shelf. The convection region broke into numerous patches that would spontaneously emerge and vanish in an apparently random manner, although they tended to be located primarily inshore.

Vertical temperature sections in the longitudinal direction (17.5 cm from the right sidewall) from the inner coast of the shelf to the offshore sidewall and lateral sections at the

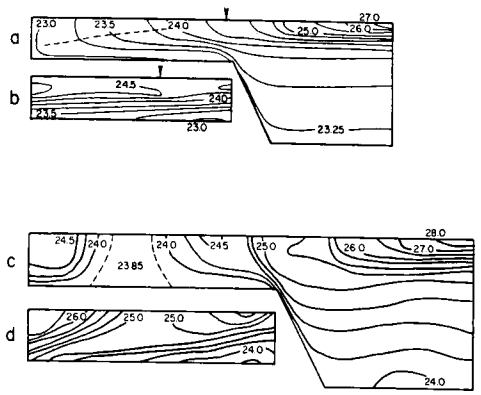

Figure 3: Temperature section from coast to offshore sidewall *a*, *c*, and across the shelfbreak, *b*, *d*. The upper pair are for a case of slow rotation and the lower for faster rotation. In *c*, the dashed region at 23.85°C may be the experimental equivalent of deep ocean convection. Arrows show section locations.

shelfbreak of the temperature were drawn. Thermal structures corresponding to the previous groups of current patterns are as follows (see Figure 3).

For slow rotation, thermal effluents of about 2.5 cm thick extended from the offshore sidewall towards the shelf. They were cooled down fairly rapidly but intruded close to the coast. Regions which were probably well-mixed in the vertical exhibited small-scale convection rolls whose axes were aligned with the flow direction.

For moderate rotation, corresponding to the typical single gyre on the shelf, the temperature fields showed cold domes in the central region and a thermal front at the shelfbreak. For a little faster rotation rate, the cold domes and the front retreated toward the inner part of the shelf. Warm offshore water came into the shelf along both the right-hand and the left-hand sidewalls and then circulated cyclonically on the shelf. The width of the front associated with inflow and outflow through the shelfbreak was reduced as the rotation rate increased, as is shown in the lateral section at the shelfbreak. The density fields are stratified on the average, except at some spots where there are a few convection cells penetrating to the lower layer in the central regions and the inner left-hand-side corner. Cold bottom water made by the sinking (and swirling) cells came out from the inner coastal region, generating anticyclonic circulation. A strong jet in the lower layer flowed along the shelfbreak toward the right-hand side in the lower layer, hit the right wall and cascaded down the slope along the right wall.

The regions where convection cells conveyed the coldest water from the top lid to the floor of the shelf could be made visible by injecting a minute amount of acid into the bottom.

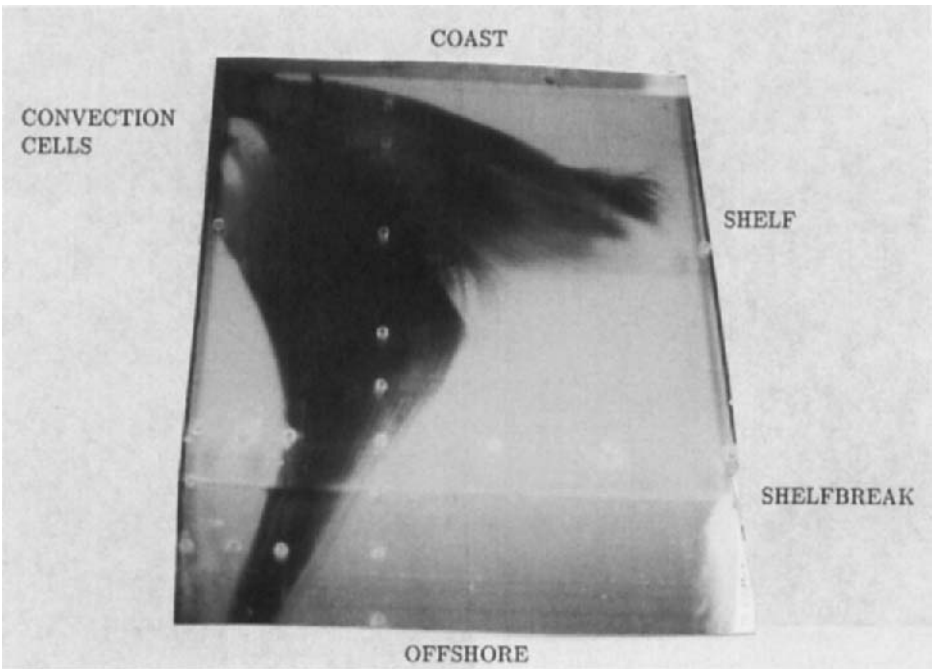

Figure 4: A plume of dyed fluid spreading over the bottom of the shelf. This is looking down at the model shelf from above and offshore. To the left are two clear spots caused by convection cells. Near the bottom the plume is swept off the shelfbreak by a density current.

Figure 4 shows a photograph of a plume of such dyed water spreading over the floor of the shelf. Two convection cells produced two clear bare spots in the lower left.

Temperature varied significantly at each spot due to turbulent eddies, and each vertical profile thereby differed. However, these figures still showed eddies and, in addition, a distinct thermal front was formed at the shelfbreak, although the front wandered around and varied in association with turbulent eddies.

Assuming a geostrophic current removes the cold water from the shelf with volume flux $g\alpha\Delta T d^2/f$, the temperature difference between shelf and offshore was predicted to be

$$\Delta T = \left(\frac{2f\ H}{\rho\ C_p\ g\alpha d^2} \right)^{\frac{1}{2}} \tag{2.1}$$

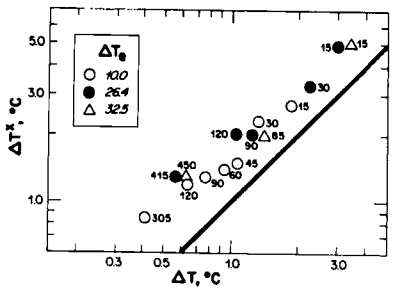

Figure 5: Relation between the temperature difference between the shelf and offshore ΔT^x and theoretical prediction ΔT from equation (2.1). The correlation coefficient is 0.86, but there is a systematic offset.

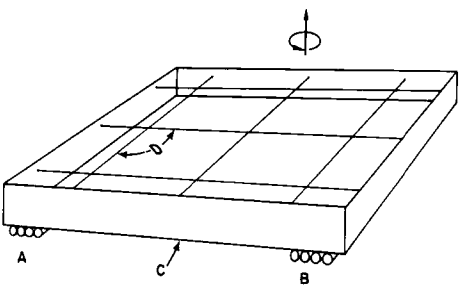

Figure 6: Layout of the apparatus (A) warm water pipes, (B) cool water pipes, (C) copper bottom, (D) Thymol blue flow visualization wires.

where f is the Coriolis parameter, H is heat flux out of the entire basin through the lid, ρ is density, C_p is specific heat, and d is depth of the shelf. The exponent of the formula had systematic agreement with the data (Figure 5) for all parameters (that varied over about one order of magnitude). However, the data were consistently warmer than the prediction. Since the formula is based only on scaling considerations, agreement was expected to be off by some unknown constant.

3 A NON-UNIFORMLY HEATED ROTATING FLUID

Speer and Whitehead (1988) constructed a square basin with a flat copper bottom, (90 cm x 60 cm x 12 cm deep) (Figure 6). The configuration was similar to an earlier one by Rossby (1965). The bottom was heated at one end and cooled at the opposite end by water flowing in pipes soldered to the copper. The high thermal conductivity of the copper helped to

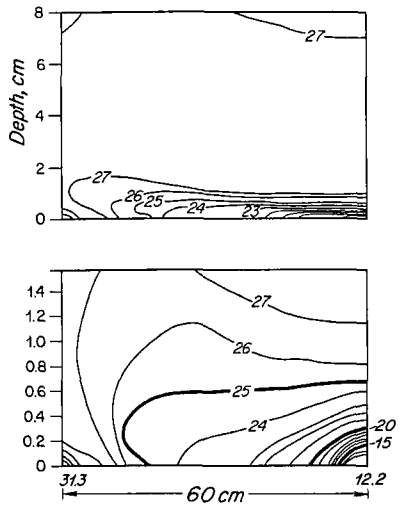

Figure 7: Vertical sections of temperature from the hot to the cold end, for an experiment with $R = 6 \times 10^{10}$, zero rotation. The lower plot is an exploded view of the upper plot.

maintain a uniform temperature gradient. The sidewalls were 0.65-cm-thick Plexiglas with 1-inch thick styrofoam on the outside. An insulated lid was placed on the top, although this was temporarily removed for photography. The basin was gridded with thin wires, three in each direction, for thymol blue flow visualization. Cold and warm water reservoirs, with submersible pumps, supplied the pipes on the bottom of the basin. The experiment is analogous to an oceanic situation which is differentially heated from above. To transform the experiment to the ocean, the sense of hot and cold and also the sign of gravity must be reversed. With rotation, this means that the direction of gravity is reversed compared to the rotation vector. Thus, if this experiment is viewed upside-down, the gyre would circulate in a clockwise direction. It would, of course, still be cyclonic, but analogous to one in the southern hemisphere.

Three regimes of flow were identified; two steady regimes for fast and slow rotation and an unsteady regime for intermediate rotation. These appear to be in qualitative agreement with the early results of Fultz (1961) for his annulus experiments. For no rotation, there was a pure Hadley cell. There was a rising at the hot end in a relatively narrow region, 1–2 cm, and a broad outflow at the top and inflow at the bottom to this narrow updraft. Over the heated end there was cellular convection of width about 1 cm. Figure 7 shows a vertical temperature section from a run with the parameters $T_{\text{hot}} = 30°\text{C}$, $T_{\text{cold}} = 5°\text{C}$, $R = 6$

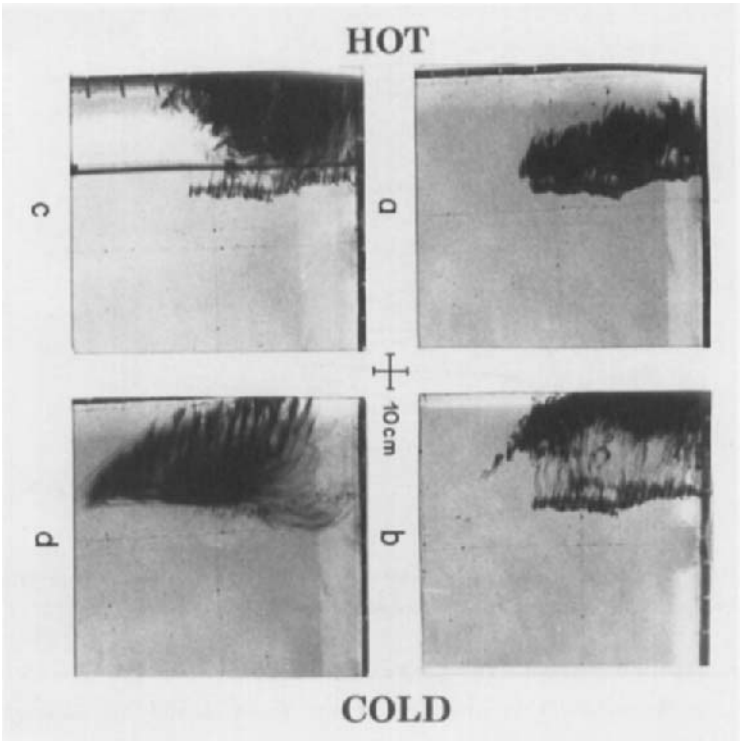

Figure 8: Close-up of dye injected in the heated rising region of the rotating experiment, viewed from above. Immediately above the hot bottom, convection rolls are aligned in the direction of flow. (a) Dye immediately after injection. (b) At 56 s, the dye approaches the hot end and rises. Lineations in the dye extending left to right reveal convection rolls. (c) At 96 s the leading edge of the dye patch sinks. The vertical stripe is the shadow of the top edge of the side wall. (d) At 200 s, the dye moves along the bottom where convection rolls form again.

x 10^{10} where $R = \frac{g\alpha L^3 \Delta T}{\kappa\nu}$. Here R is the Rayleigh number, g is acceleration from gravity, α is thermal expansion coefficient, L is lateral length of the box, ΔT is external temperature difference, κ is thermal diffusivity, and ν is viscous diffusivity. Results closely resemble both the numerical calculation of Beardsley and Festa (1972) and a section from Rossby's (1965) experiment. Two striking features are a nearly isothermal upper fluid and the well-known marked asymmetry in temperature distribution between the hot and cold end.

For slow rotation (period typically 200 s), the flow in the thermal boundary layer near the bottom was from the cold end toward the hot end and was not visibly different from the flow near the bottom without rotation. However, the convection region was now about 10-cm-wide and adopted a more complicated three-dimensional structure (Figure 8). The circulation in the convection region appeared to possess a helical spiral produced by a miniature convective

cell superimposed on a translation to the right (looking from the hot end to the cool end). In the upper layer, the warm fluid moved away from the hot end and moved to the right. If then circulated about the upper portion of the fluid in a counter-clockwise (cyclonic) gyre.

For faster rotation, the flow broke down into a number of eddies. The convection region broke into patches that appeared to randomly emerge and vanish. The qualitative structure of the flow was very similar to the flow in the previous section.

4 MAGNITUDE OF THE THERMAL FIELD, THE BOUNDARY LAYER, AND OCEAN SCALING

In this study of a rectangular box, heated differentially from below and insulated on the top and sides, Rossby (1965) presented scaling laws for the bottom boundary layer, and the velocity potential scale was given in his equation 10 as

$$\delta_B = L\, R^{-\frac{1}{5}}, \quad \psi = \kappa\, R^{-\frac{1}{5}} \tag{4.1}$$

The scale of the vertical velocity was thus $w = \frac{\kappa}{\delta_b}$, and the horizontal velocity was $u = \frac{wd}{L}$.

This scaling was confirmed by Rossby (1965) and Beardsley and Festa (1972). It was also tested in the considerably larger apparatus used by Speer and Whitehead (1988) for one value of the external parameters: $g = 10^3$ cm^2/s, $\alpha = 2 \times 10^{-4}$°C, $L = 60$ cm, $\Delta T = 10$°C, $\kappa = 0.0014$ cm^2/s. These gave $\delta_b = 0.48$ cm. A map of the isotherms (Figure 7) shows that this prediction is within range of the observed depth of the bottom boundary layer. The values are also given in Table 1.

If one tries to naively apply the above scaling to the ocean, one finds that the above scaling laws are deficient in a fundamental sense. To illustrate this, let us try to calculate a depth of a boundary layer from equation (4.1) in hopes of equating this depth to the depth of the thermocline. Using "ocean" length $L = 10^7$ m, $g = 10^3$ cm /s^2, coefficient of expansion $\alpha = 2 \times 10^{-4}$°C^{-1}, $\Delta T = 20$°C, kinematic viscosity $\nu = 10^{-2}$ cm^2/s and thermal diffusivity $\kappa = 0.0014$ cm^2/s, we get $\delta_b = 3.0$ m. This is, of course, too small. The width of the sinking region (which is analogous to the rising region in the heated box) can also be calculated and is $\delta_s = h\, \frac{\delta_b}{\gamma L}$ from continuity. Unfortunately, h and γ are not defined in the text, but presumably h is the depth of the ocean = 5000 m and γ is an order one constant which we will put arbitrarily at $\frac{1}{2}$. These give a value of $\delta_s = 3 \times 10^{-3}$ m, which is also too small.

One obvious explanation for the discrepancy between the above results and the depth of the true thermocline is that one should use turbulent values for the viscosity and thermal diffusivity. Let us determine a value of turbulent diffusivity and viscosity to produce a realistic thermocline depth. Take $\delta_b = 1000$ m and calculate ν and κ assuming they are

equal. Using equation (4.1) above, we find $\nu = \kappa = 6.3 \times 10^3$ cm^2/s. These numbers are significantly bigger than those thought to exist in the ocean. For instance, Munk (1966) came up with κ of order 1.3 cm^2/s. In addition, vertical velocity is then predicted to be equal to $\frac{\nu}{\delta_b} = 6.3 \times 10^{-2}$ cm/s, which is 19.7×10^3 m/year or 49 m/day, a value which is also far too big for the ocean. To see this, note that 10 Sv [a magnitude somewhat greater than the Norwegian Sea overflows into the North Atlantic (Worthington, 1970)] divided by an area of 10^{14} m^2 gives 10^{-7} m/s, a widely accepted number [Munk, 1966 calculated 1.2 cm/day ($= 1.4 \times 10^{-7}$ m s^{-1}) for the interior Pacific]. Finally, using this realistic thermocline depth of 10^3 m, we still only increase δ_s by a factor of 1000, so it would be about 1 m. A one-meter sheet of water descending into the depths of the oceans is ridiculous, but possibly that small number might explain why the deep water formation events in our oceans are so rare. The results from all three cases are summarized in Table 1.

TABLE 1

Numbers for the Laboratory and the Ocean Based Upon the Scaling for a Non-Rotating Box

	Laboratory	Ocean (mol)	Ocean (turb)
h (m)	0.08	5000	5000
L (m)	0.6	10^7	10^7
ΔT (°C)	10	20	20
R_a	3×10^{10}	4×10^{32}	10^{25}
δ_b (m)	0.005	3	1000
δ_s (m)	0.001	0.003	1
w (m/s)	3×10^{-5}	3×10^{-8}	6×10^{-4}

A better ocean model needs to "throttle" velocities and heat transports down so that smaller numbers are predicted.

It is not difficult to imagine that earth rotation can provide such a "throttle." A rotational constraint for a laboratory experiment was, in fact, considered by Sugimoto and Whitehead (1983) for a model of a shallow sea cooled uniformly from above and bordered on one side by a shelfbreak and a deep ocean. The outside of the deep basin was a metal sidewall kept at a constant warm temperature. Their scaling ws governed by the fact that volume flux onto or off the shelf obeyed a rotating "lock exchange" relation

$$Q = \frac{g\alpha\Delta T\, d^2}{2f} \tag{4.2}$$

where ΔT is the temperature difference between the deep ocean water and the shelf water. In that case, heat flux H off the shelf is given by

$$H = \rho C_p Q \Delta T = \frac{\rho C_p g \alpha \Delta T^2 d^2}{2f} \tag{4.3}$$

where C_p is specific heat. Since heat flux H and rotation f are external variables in this experiment, we must solve for the temperature scale

$$\Delta T = \left(\frac{2fH}{\rho C_p g \alpha d^2} \right)^{\frac{1}{2}} . \tag{4.4}$$

In the shelf experiment the depth d is set to the depth of the shelf, but for purposes of the deep ocean, we set $d = \frac{\kappa}{w}$, the depth for a thermal boundary layer thermocline. Here $w = \frac{Q}{A}$ is the vertical velocity in response to deep water formation where A is the area of the ocean. Using the above formulas for Q and ΔT, we generate a formula for thermal boundary layer depth

$$d = (\kappa A)^{\frac{1}{2}} \left(\frac{2f \rho C_p}{g \alpha H} \right)^{\frac{1}{4}} . \tag{4.5}$$

This is equivalent to the depth scale of Bryan and Cox (1968) except they used a relation between d and ΔT instead of H, which can be found by combining (4.4) and (4.5).

We will use representative numbers to determine whether this predicts an ocean thermocline depth of roughly the right order of magnitude. Take $H = 10^{15}$ watts from Bryden and Hall's (1980) estimate for the North Atlantic at 25°N, $A = 4 \times 10^{14}$ m^2 (roughly 40% of the earth's surface), $\kappa = 1.3 \times 10^{-4}$ m^2 s^{-1} (Munk, 1966 — the molecular value of 1.4×10^{-7} m^2 s^{-1} will not be used, although we will comment on what number it would lead to later), $g = 10$ m s^{-2}, $\alpha = 2 \times 10^{-4}$°C, $f = 10^{-4}$ s^{-1}, and $\rho C_p = 4 \times 10^6$ J m^{-3}°C^{-1}, we find $d = 721$ m. The accompanying $\Delta T = 6.9$°C. These results are clearly the right order of magnitude even though the numbers were from different sources and apply in detail to various parts of the oceans. H, for instance, is too small for all the world oceans, A is much too large for the North Atlantic, and κ was taken for the deep Pacific. If we used a molecular value for κ, d would have been increased by that factor. Also, some sort of areal average should be used for f. Using better numbers and applying them in detail to the real oceans are all possible subjects for future work.

This scaling consideration is developed here to indicate that the rotating box experiments that were investigated by Speer and Whitehead may be of fundamental interest to the large-scale structure of the ocean. That the thermal driving rather than the wind driving dominates the greatest vertical motions can be deduced from the results of Levitus (1988), who showed that Ekman volume fluxes of the world oceans are less than the fluxes associated

with the vertical motions. The important dynamical balance that is responsible for the areal and temporal distribution of deep convection events remains unsolved in this new framework and is an important subject for future work.

5 EDDIES FROM A TURBULENT JET

Laboratory experiments in which a source of dense fluid is introduced at the top of a rotating fluid exhibit eddies that may be crude models of cells. Whitehead, Stern, Flierl, and Klinger (1990) (see also Whitehead, 1989) observed the formation of eddies when salty water flowed down a sloping bottom. Turbulence from the density current generated a cyclonic circulation of the upper ambient fluid. The accompanying low pressure in the ambient fluid appeared support a relatively circulationless lens of the denser fluid. The cyclonic eddy and the underlying lens translated to the left (looking onshore) for counterclockwise turntable rotation. This is equivalent to traveling west on a topographic β-plane. Various theoretical considerations, including an integral constraint were discussed in the paper. The integral constraint dictates that flow is cyclonic in the upper fluid and motionless in the lens over the sloping bottom.

Other experimental methods can also generate eddies like these. For instance, the removal of a known volume of ambient water above a reservoir of static denser water makes very similar eddies. Also a plume of dense water released at the water surface but located over a sloping bottom make excellent eddies. In this case it is believed that cyclogenesis in the upper fluid arises from the entrainment of fresh water by the turbulent plume as it sinks. A final method is to place an ice cube in a rotating fluid over a sloping bottom (Figure 9). The cold fluid not only sinks to the bottom, but it also causes ambient surface fluid to sink by becoming cold thereby dense through conductive cooling. In all cases the bottom dense fluid appeared to lack an anticyclonic circulation, a result in agreement with the integral constraint.

The study of eddies over a sloping bottom were intended to illuminate a process likely to take place over "cataracts" or turbulent density currents that are located over shelfbreaks. The Mediterranean or Denmark Straits overflow are two well documented examples of ocean cataracts. There have been measurements of unsteadiness in both that could correspond to eddies similar to those reported here.

6 CONCLUSION

Laboratory experiments can cover a large variety of problems related to deep ocean convection, from the local scale of the individual convection cells to the global scale of sinking regions within the large differentially heated ocean. They can uncover the importance of poorly understood processes, such as the role of turbulence in the upper regions and its

ICE CUBE

MIRROR

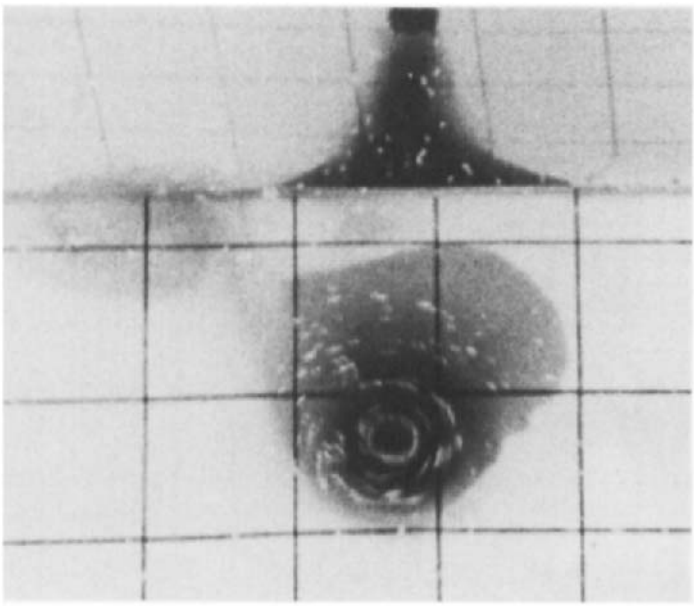

COAST

Figure 9: Elevation view (above) and plan view (below) of an eddy produced by a dyed ice cube in rotating water. Cyclonic circulation is revealed by the streaks. This circulation is found in the clear water over the lens of dense, cold dyed water, and is generated by convergence produced by sinking of water next to the ice cube that is cooled by thermal conduction.

This Page Intentionally Left Blank

METEOROLOGICAL TRIGGERS FOR DEEP CONVECTION IN THE GREENLAND SEA

P.S. GUEST and K.L. DAVIDSON
Dept. of Meteorology
Naval Postgraduate School
Monterey, CA 93943-5000

ABSTRACT

We postulate that a favorable condition for deep convection just seaward of a pack ice edge within a marginal ice zone (MIZ) occurs when the direction of a cold, strong, off-ice wind is at an angle of less than 45 degrees from the ice edge, with the edge to the right looking downwind. In this situation, the Ekman transport of the ice formed in the outer MIZ will be toward the pack ice, keeping the outer MIZ clear of thick ice. Sustained rapid freezing and brine rejection will occur in the outer MIZ as the cold air blowing off the ice removes heat from the ice-free ocean surface.

In the East Greenland Sea MIZ (EGSMIZ), a favorable situation for cold strong winds at the correct angle occurs when there is high pressure in the region between NE Greenland and the pole and unoccluded lows south of the EGSMIZ. This pattern occurs regularly in the EGSMIZ.

On horizontal scales less than 20 km, MIZ wind stress and heat flux have large variability due to changes in surface roughness, wind speed and sea surface temperature. The pack ice edge orientation is also highly variable on small scales. Thus, dynamic and thermodynamic forcing of the ocean and the induced vertical motions vary at the small scales and may contribute to confining deep convection to very small (5 to 10 km diameter) chimneys.

INTRODUCTION

Several processes have been proposed for the deep water formation in the Arctic Mediterranean Seas (Arctic Ocean, Greenland Sea, Norwegian Sea and Iceland Sea). These include brine formation in shelf waters (Aagaard *et al.*, 1981), double-diffusive exchange (Carmack and Aagaard, 1973; McDougall, 1983) and chimney convection (Killworth, 1979). None of these processes have been directly observed in the Greenland Sea because the deep convection necessary for deep water formation occurs rarely. The atmosphere may provide the final "trigger" which initiates a deep convection event. The purpose of this paper will be to examine the types of meteorological phenomena which could trigger the deep convection. The experimental oceanographer will have a greater chance of directly observing deep convection in the Greenland Sea by choosing the right location and time based on oceanographic and meteorological conditions.

DEEP CONVECTION NEAR AN ICE EDGE

If the ocean has already been pre-conditioned for deep convection, what events may provide the final "trigger", and where will it occur? The most likely scenario is a situation where intense cooling and freezing is occurring at the surface of the ocean during winter or early spring. Because ice formation will effectively insulate the atmosphere from the ocean

there must be a mechanism to remove the ice as it is formed. Aagaard *et al.*, (1981) proposed that a cold off-shore wind could maintain intense freezing in coastal waters by removing the ice as it is formed. The salty water left behind could trigger a deep water formation event.

Ice in the MIZ is free to move, and an off-ice wind normal to the ice edge cannot sustain deep convection due to advection of ice and fresh water over the potential convection region. However, if the wind direction is between 0 and 45 degrees from the ice edge, with the ice to the right looking downwind, newly formed ice is transported with a component toward the main pack ice body (Fig. 1). The atmosphere is very cold near the edge due to its over-ice origin, but it warms rapidly from contact with the ocean. (During these conditions, the authors have observed atmospheric heating which reduced the air-sea temperature difference and heat flux by a factor of four between an ice-free ocean region just off the ice edge and a region 100 km away from the edge.) The ocean surface temperature is usually at the freezing point within the MIZ near the pack ice edge, but becomes warmer away from the ice regions. New ice forms near the edge where the air and surface water are coldest and the Ekman transport moves it toward the pack ice. The warm water and/or decreased heat loss prevent ice formation further away from the edge. The brine left behind in the region of rapid freezing could provide the trigger for deep convection.

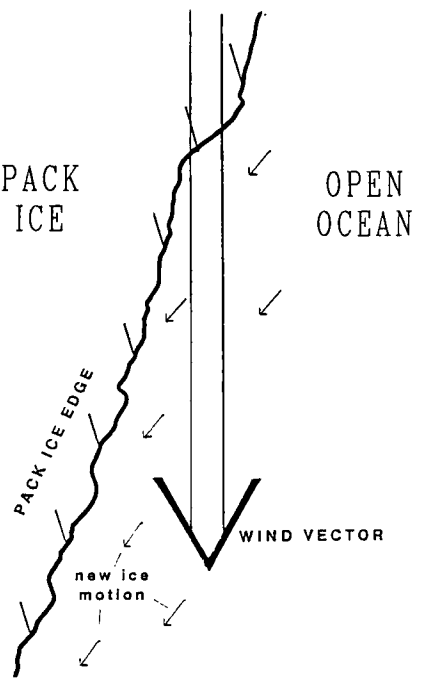

Fig. 1. A diagram showing a downwind vector (double arrow) with respect to a hypothetical ice edge. The cold air blows off-ice but Ekman transport moves newly-formed ice back toward the edge (small arrows), thus preventing formation of an insulating ice cover. This situation maximizes surface cooling and brine formation.

The center of a mesoscale cyclonic eddy is a location which is particularly susceptible to chimney convection (Killworth, 1979). The Greenland Sea MIZ is a region where many cyclonic eddies are known to occur (MIZEX Group, 1986; Johannessen *et al.*, 1987; Bourke *et al.*, 1987; MIZEX87 Group, 1989). The centers of the cyclonic eddies are composed of relatively spicy and dense upwelled Atlantic water surrounded by less spicy and less dense Arctic water. Therefore, the water column within the eddy is less stable than the surrounding water. The eddy rotation also inhibits advection of ice from surrounding areas during light wind periods, enhancing surface cooling and brine formation.

Aagaard *et al.* (1985) argued that water from the Greenland Gyre must be a major source of deep water in the Arctic Mediterranean. The water within the cyclonic eddies in the MIZ has similar properties as the water in the central Greenland Gyre and may be an alternative source region for the Greenland Sea deep waters.

SYNOPTIC METEOROLOGICAL CONDITIONS

The type of large scale meteorological conditions which would produce favorable conditions for deep convection in the Greenland Sea MIZ will be examined with three examples from the Coordinated Eastern Arctic Experiment, CEAREX. The near-surface air parcels must be cold and their trajectories must cross the edge at the correct angle. When the surface isobars are parallel to the ice edge with higher pressure over the ice, surface winds will blow at a 15 to 45 degree off-ice angle, a favorable direction for the deep convection mechanism described above. The central ice pack and northern Asia provide a potential source of cold air for the Greenland Sea MIZ region.

The first example occurred 18 - 22 January, 1989, when wind and temperature measurements were obtained from the research vessel *Polarbjoern*, operating in the MIZ. Strong winds in the favorable direction were maintained by a series of low pressure systems to the south (Fig. 2). The air was from the central Arctic or Siberia which caused cold air temperatures over the MIZ. Low pressure systems in the Arctic usually are associated with warm air. For deep convection-favorable winds, a cold air source must be tapped and the warm air from the south must be prevented from looping east-north-west around the low center.

The period 12 - 16 March 1989 was another example of favorable winds for several days (Fig. 3). During this period, there was not a single deep low, but rather a general region of low pressure over the southern Greenland Sea and Norwegian Sea. This, in combination with a ridge extending over Greenland, caused a tight pressure gradient and high winds over the MIZ. Notice that the large region of low pressure and the high in the central arctic

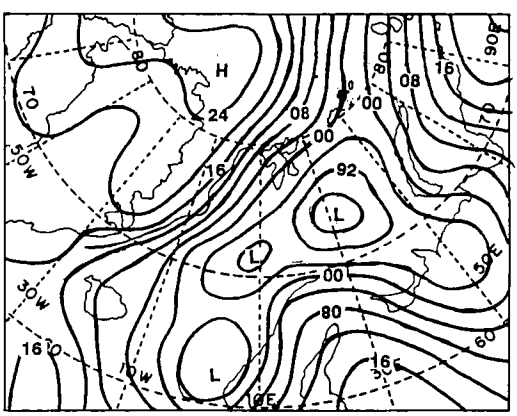

Fig. 2. A re-drawn Fleet Numerical Oceanography Center sea level pressure analysis which shows a pattern typical of the 18 - 22 January, 1989 period. The approximate ice edge in the East Greenland Sea is shown as a thin solid line between Svalbard (upper center) and Greenland (right).

caused the air parcels to come from Siberia instead of further south, which would have been the case for a smaller stationary low pressure system. Ship measurements in the MIZ confirmed the relatively cold temperatures (-15 to -20 °C) and strong winds (10 to 15 m/s) which existed over the MIZ during this time period.

The final example was another situation with a persistent low pressure region off the northern Norwegian coast and a ridge over Greenland which occurred 20 - 23 April 1989 (Fig. 4). A ridge to the east of Spitzbergen caused the air to dip south prior to reaching the ship in the MIZ. However, further upwind, the Siberian origin of the air resulted in cold temperatures (approx. -18 °C) throughout the period, accompanied by strong winds (10 - 15 m/s) in the favorable direction.

All these examples had a high pressure or ridge near the NE coast of Greenland and low pressure in the ice free areas of the Greenland Sea. This situation is quite common. The average pressure field for winter and early spring has a ridge extending over northern Greenland from the north and a trough between Norway and the MIZ (Figs. 5 and 6). The average pressure gradient produces favorable winds over much of the MIZ. The authors'

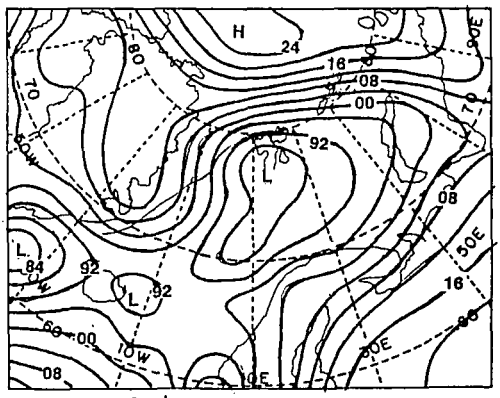

Fig. 3. Same as Figure 2 but for the 12 - 16 March 1989 period.

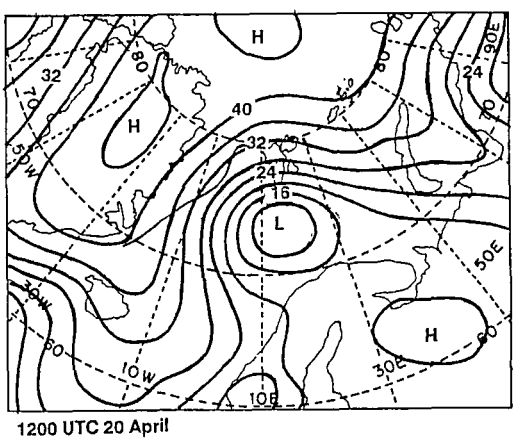

Fig. 4. Same as Figure 2 but for the 20 - 23 April 1989 period.

ship measurements of winds in the MIZ during the months of December, January and February, 1988 - 1989 revealed that a favorable wind direction existed 25% of the time.

A Greenland high is a semi-permanent feature in the winter. A favorable situation occurs when the center of the high is near the NE coast of Greenland. This causes a tight gradient in the MIZ and taps the sources of very cold air to the north and in Siberia. Another favorable situation is when there is a high near the pole with a ridge extending toward Greenland. This also creates a Siberian source for the air mass over the MIZ.

The climatological low pressure area to the south of the MIZ, Figs. 5 and 6, indicates the region of a storm track, where storms frequently move from near Iceland to south of Spitzbergen. In order for these storms to trigger a deep convection event they must advect cold air in the favorable direction over the ice edge. If they are rapidly moving to the NE, the warm air in front of the low will not be able to wrap around, and the air to the west will remain cold. This means the storms must maintain surface fronts; they cannot become occluded.

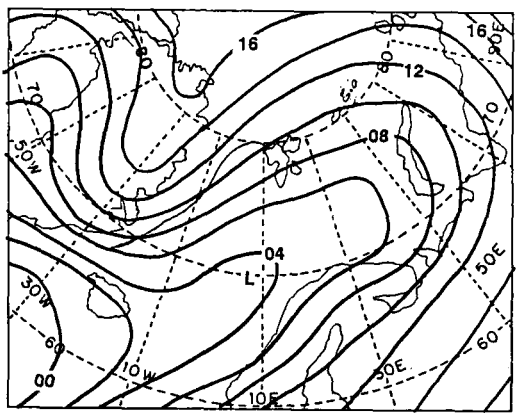

Fig. 5. January mean (1952-86) sea level pressures based on NCAR analyses. The contour interval for this figure is 2 mb instead of 4 mb as above (from Walsh and Chapman, 1990).

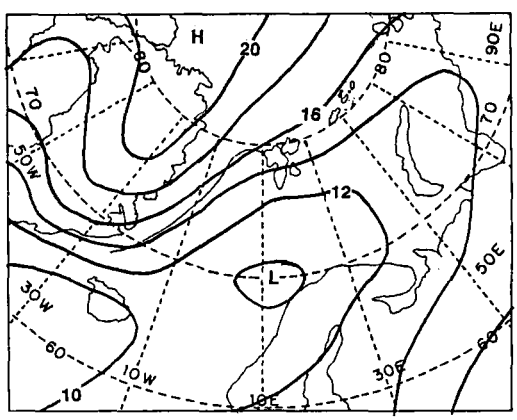

Fig. 6. Same as Figure 5 but for the month of April (from Walsh and Chapman, 1990).

MESOSCALE ATMOSPHERIC FORCING

By using a "yo-yo" CTD technique, the Nansen Remote Sensing group was able to obtain high horizontal resolution measurements of the upper ocean in and near the MIZ (MIZEX87 Group, 1989). They found structures of nearly constant sigma-t extending down hundreds of meters. These were similar to the chimney described by Killworth, but were smaller in horizontal scale, 5-10 km diameter. These features have an even smaller scale than the eddies within which they are embedded. Variations in wind stress and heat flux may be factors in determining the location and size of the chimneys. This section will examine these variations in the MIZ.

Measurements of wind stress and heat flux in the MIZ by the authors have revealed large variations in wind stress and heat flux on scales much smaller (5 to 200 km) than the resolution of standard surface pressure analyses. Large variations in wind stress and heat flux are due to changes in surface roughness, temperature distribution and wind speed.

Surface roughness variations caused by different types and concentrations of sea ice can cause the wind stress to vary by at least a factor of three (Guest and Davidson, 1987). The surface wind vector can also be highly variable; an extreme example is shown in Fig. 7. The ice edge shape, pressure field and ocean surface features also affect stress and heat flux fields. The dynamic (wind stress curl) and thermodynamic forcing of the ocean which can generate vertical motions are very complex in the MIZ and cannot be described by a simple model or observation.

The ice edge can be diffuse or curved and convoluted. Small areas may experience the favorable wind direction (0 to 45 degrees from the edge) while other, nearby regions do not, due to a different ice edge orientation. The variations in surface forcing described in the above paragraphs can confine the most favorable conditions for surface triggering of deep convection to horizontal regions on the scales of the size of the observed chimney structures.

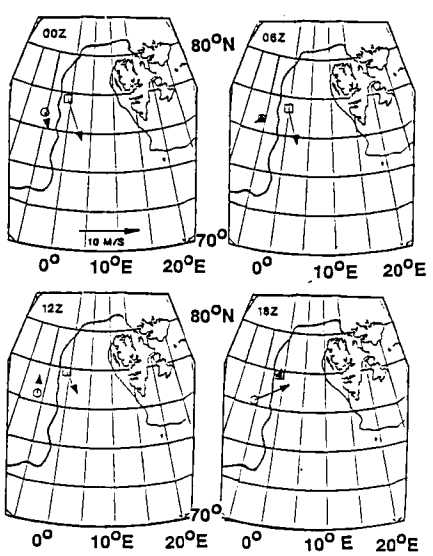

Fig. 7. Average downwind vectors from the R/V *Polar Circle* (circle) and the R/V *Haakon Mosby* (square) for four six-hour periods on 8 April during the 1987 Marginal Ice Zone Experiment. The line of 50% ice concentration is shown. Note the large variability between the two ships.

CONCLUSIONS

This paper examined certain events which may initiate deep convection. A cold wind blowing off-ice

at an angle of less than 45 degrees to the ice edge in a MIZ will cause rapid heat loss from the surface in some regions. The examples from the Greenland Sea showed that a favorable situation for deep convection exists when the MIZ is squeezed between a high to the NE of Greenland and a rapidly moving series of lows (or a permanent large low pressure area) south of the ice edge.

The most favorable regions, with respect to surface forcing, can have horizontal scales as small as 5-10 km. This is the size of observed chimney features and is close to the internal Rossby radius of the ocean for this region. Understanding the small scale interactions between ocean features such as chimneys and surface forcing fields on these small scales may help us understand the nature and location of deep convection events.

REFERENCES

Aagaard, K.L., Coachman, L.K. and Carmack, E.C., 1981. On the halocline of the Arctic Ocean. *Deep Sea Research, 28*: 529-545.

Aagaard, K.L., Swift, J.H., and Carmack, E.C., 1985. Thermohaline circulation in the arctic mediterranean seas. *J. Geophys. Res., 90*: 4833-4846.

Bourke, R.H., Newton, J.L., Paquette, R.G. and Tunnicliffe M.D., 1987. Eddy near the Molloy Deep revisited. *J. Geophys. Res., 92*: 6773-6776.

Carmack E.C. and Aagaard, K.L., 1973. On the deep water of the Greenland Sea. *Deep Sea Research, 20*: 687-715.

Guest, P.S. and Davidson, K.L., 1987. The effect of observed ice conditions on the drag coefficient in the summer East Greenland Sea marginal ice zone. *J. Geophys. Res., 92*: 6943-6954.

Johannessen, J.A., Johannessen, O.M., Svendsen, E., Shuchman, R., Manley, T., Campbell, W., Josberger, E., Sandven, S., Gascard, J., Olaussen, T., Davidson, K. and Van Leer, J., 1987. Mesoscale eddies in the Fram Strait marginal ice zone during MIZEX 1983 and 1984. *J. Geophys. Res., 92*: 6754-6772.

Killworth, P.D., 1979. On "chimney" formations in the ocean. *J. Phys. Oceanogr., 9*: 531-554.

McDougall, T.J., 1983. Greenland Sea bottom water formation: A balance between advection and double-diffusion. *Deep Sea Research, 30*: 1109-1117.

MIZEX Group, 1986. MIZEX East 83/84: the summer marginal ice zone program in the Fram Strait/Greenland Sea. *EOS, 27*, No. 33, June.

MIZEX '87 Group, 1989. MIZEX East 1987 - Winter marginal ice zone program in the Fram Strait and the Greenland Sea. *EOS, 70,* No. 17, April 25.

Walsh, J.W. and Chapman, W.L., 1990. Short-term climatic variability of the arctic. *J. Climate, 3*: 237-250.

This Page Intentionally Left Blank

SOME EARLY RESULTS OF THE HUMIDITY EXCHANGE OVER THE SEA MAIN EXPERIMENT

STUART D. SMITH
Department of Fisheries and Oceans, Bedford Institute of Oceanography,
P.O. Box 1006, Dartmouth, Nova Scotia, Canada B2Y 4A2

ABSTRACT

Deep convection events are a result of formation of dense water at the surface by cooling and evaporation. The Main Experiment (HEXMAX) of the Humidity Exchange over the Sea (HEXOS) program has shown that, contrary to predictions, the evaporation coefficient C_E does not increase significantly with wind speed, at least up to a speed of 20 m/s. The flow distorton formula of Wyngaard (1981) for correction of turbulent wind stress has been verified. The wind drag coefficient is seen to depend on wave age.

1 INTRODUCTION

Surface processes of evaporation and cooling are mainly responsible for the initial formation of dense water masses, and wind stress at the sea surface drives local circulation. Parameterization describing surface fluxes in stormy conditions (e.g. Smith, 1980, 1988, 1989) is needed to model water mass formation and local and regional circulation in response to surface and air temperatures, humidity and wind speed. The HEXOS program (Katsaros *et al.*, 1987; Smith *et al.*, 1990) is a coordinated series of field, laboratory and modeling studies of evaporation from the sea surface at moderate to high wind speeds and of the influence of spray droplets. Prior to this program there were no direct eddy flux measurements of evaporation from the sea surface in conditions relevant to dense water mass formation: all were at low wind speeds and/or at near-shore sites. This was not due to a lack of attempts, but to failures in operating fast-response humidity sensors, which are easily damaged by contact with salty droplets. The HEXOS Main Experiment (HEXMAX) was a comprehensive air-sea interaction experiment carried out by participants from 15 institutions in 7 countries in October and November 1986 at the Dutch offshore research platform Meetpost Noordwijk (MPN) and from ship, aircraft and shore stations in the vicinity. Evaporation, heat flux and wind stress were determined at all stations using combinations of eddy flux, dissipation and profile methods. Favorable winds during most of HEXMAX resulted in collection of an extensive and unique data set. Although deep convection does not occur in this area, we were able to measure surface fluxes in relevant (windy) conditions. This chapter presents some of the results of the Bedford Institute of Oceanography (BIO) group, one of several groups which made eddy

flux measurements at a boom extending 17 m upwind from the west side of MPN.

2 EVAPORATION FROM THE SEA SURFACE

Using an aspirated "refinery" to remove droplets from airflow to a Lyman-alpha ultraviolet humidiometer, we were able to measure turbulent fluctuations of humidity at higher wind speeds than previously possible. Several theoretical analyses (Ling and Kao, 1976; Bortkovskii, 1987; Stramska, 1987) had predicted rapid increase in the evaporation coefficient

$$C_E = E/[\rho U_{10}(Q_s - Q_{10})]$$

at wind speeds above 14 - 15 m/s (the upper limit of available data) due to evaporation of spray droplets ejected from bubbles formed by breaking waves. Here E is the evaporation rate (g/m^2s), ρ is the density of air (g/m^3), U_{10} is the mean wind speed (m/s) at a 10 m reference level, Q_{10} is the specific humidity at 10 m and Q_s is the saturation humidity of air in contact with the surface water at temperature T_s. Surprisingly, we found no such increase, at least for wind speeds up to 20 m/s (Fig. 1), and this was corroborated by two other groups with independent sensors. It appears instead that the evaporation coefficient of Smith (1989) based on a survey of pre-HEXOS results, $C_{EN} = 0.0012$, can be extended to a wind speed of 20 m/s. Beyond that wind speed we still have no direct measurements and it is possible that the evaporation coefficient may increase significantly. Winds above 20 m/s are relatively infrequent and although their contribution to the total water flux is relatively small, they may be very important in regional processes such as the formation of dense water masses.

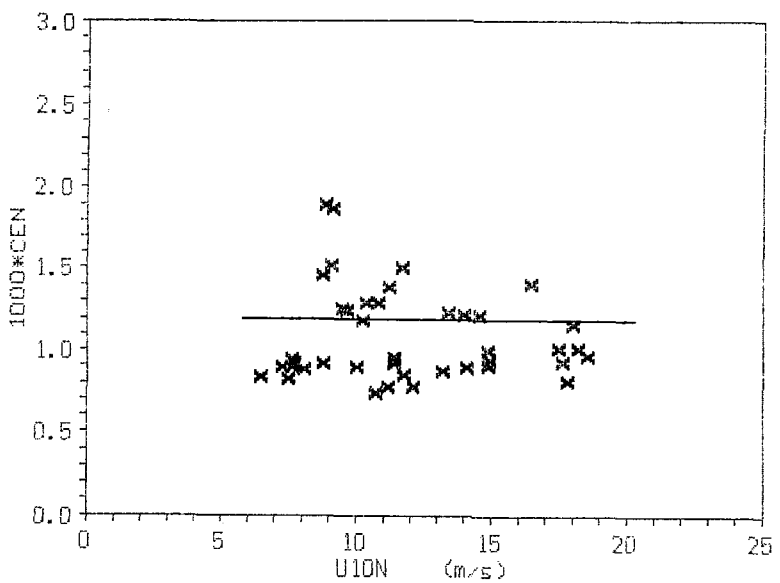

Fig.1. Evaporation coefficients from HEXMAX, adjusted to neutral stability.

We are working on two explanations of this negative result. One is that the modellers may have overestimated the quantity of spray droplets present at a given wind speed. All three cited a lack of data on droplet density as a major source of uncertainty. Subsequently a series of laboratory experiments was undertaken by other HEXOS participants to determine the source density of droplets generated by the bursting of bubbles at the surface (see Smith *et al.*, 1990). Another explanation is a negative feedback whereby evaporating droplets increase the humidity of the air immediately above the surface and inhibit or reduce the turbulent flux of vapor in this layer, so that some of the droplet evaporation replaces rather than adds to the vapor flux at the surface. HEXOS models will include the interaction of turbulent fluxes and droplets and their influence on humidity and temperature profiles.

3 WIND STRESS RESULTS

3.1 Correcting for flow distortion

Wind stresses and drag coefficients at the MPN boom measured with a sonic anemometer operated by the host group from the Royal Netherlands Meteorological Institute (KNMI) were found to be significantly (20 - 30%) larger than those recently reported at other comparable sites (e.g. Geernaert *et al.*, 1986). We discovered that part of this difference was due to flow distortion by the boom tip and instrument supports. Because space was needed at the tip of the boom for a number of sensors, the sonic anemometer probe was suspended below the boom tip in an inverted position. A few runs were taken with the sonic anemometer above the boom in an upright position and all of these had lower drag coefficients and mean updrafts (positive mean wind tilt angles). All of the data runs with the sonic anemometer in the inverted position had negative mean wind tilt angles, ranging from -1.5 to -3.5°. Our routine analysis includes coordinate rotation to align the coordinates with the indicated mean wind direction; this is called a "tilt correction". Wyngaard (1981) proposed that the error in wind stress, τ, can be estimated byassuming that the flow distortion is due to potential flow around a horizontal cylinder which is nearby in relation to the measuring height but far from the anemometer in relation to its diameter:

$$\tau/\rho = u_*^2 = u_{*_t}^2 + 2\langle u_3^2 \rangle \sin \theta_v$$

where u_* is the friction velocity, u_{*_t} is the friction velocity with only the tilt correction applied, $\langle u_3^2 \rangle$ is the variance of the vertical component of wind turbulence, and θ_v is the mean wind tilt. This formula is easy to apply because it does not depend on the size and location of the distorting object, only on its influence on the tilt angle. It was intended originally only to demonstrate that local flow distortion could cause serious errors in measured

Table 1. Test of flow distortion correction for wind stress.

BIO run	Sonic	U m/s	u_{*t}^2 $(m/s)^2$	$\langle u_3^2 \rangle^{1/2}$ m/s	θ_v deg	$10^3 C_{Dt}$	u_*^2 $(m/s)^2$	$10^3 C_D$
168	up	10.88	0.163	0.494	3.37	1.38	0.192	1.62
175	up	5.61	0.039	0.263	4.06	1.24	0.049	1.55
176	up	6.06	0.046	0.273	3.80	1.24	0.055	1.51
331	up	8.81	0.117	0.455	3.63	1.50	0.143	1.84
332	up	8.60	0.116	0.441	3.79	1.57	0.142	1.91
Mean	up	7.99			3.73	1.39		1.69
167	down	7.75	0.124	0.419	-3.10	2.07	0.105	1.76
174	down	6.27	0.074	0.308	-2.36	1.87	0.066	1.68
177	down	6.14	0.068	0.300	-2.35	1.81	0.061	1.62
333	down	10.69	0.204	0.531	-1.99	1.79	0.185	1.62
334	down	11.92	0.269	0.589	-1.88	1.90	0.246	1.74
Mean	down	8.55			-2.36	1.89		1.68

wind stress (*pers. comm.*, J.C. Wyngaard). The potential flow theory also shows that no correction beyond the coordinate rotation to remove tilt is required for scalar fluxes such as those of heat and water vapor.

We have five BIO data runs with the anemometer upright. Since we do not have simultaneous runs with two sonic anemometers, we selected for each run the nearest run in time with the anemometer in its usual inverted position. Flow distortion is reversed when the anemometer is inverted and this doubles its influence, making it easier to resolve in the statistical scatter which is inherent in analysis of finite samples (typically 40 minute runs) of an ongoing time series process. Drag coefficients $C_D = u_*^2/U^2$ are not adjusted for height or stability. The mean drag coefficients C_{Dt} with only the tilt correction are 0.00139 for the 5 runs with the sonic anemometer upright and 0.00189 for the 5 comparison runs in similar conditions but with the anemometer inverted. After the correction we have mean C_D values of 0.00169 and 0.00168, respectively (Table 1); this formula removes differences in wind stress caused by local flow distortion, at least for our small data set. This is based on only a few runs and a more thorough test will be needed. For 45 HEXMAX data runs analysed by BIO with the sonic anemometer inverted the average indicated wind tilt was -2.38° and the flow distortion formula reduced the wind stress by an average of 11 %. To our knowledge this is the first use of this formula as a correction. A colleague (W.A. Oost) is extending the potential flow formula to ellipsoidal objects with the intention of using a more realistic representation of the distorting objects such as the boom tip and a rotor used to align the sonic anemometer into the wind.

3.2 Influence of wave age

It has long been recognized that the drag coefficient of the sea surface is higher during transient events (such as may accompany the final stages of formation of dense water) than in steady-state conditions (e.g. Large and Pond, 1981). This suggests that waves must be aerodynamically rougher during early stages of growth than in fully-developed conditions. To examine the influence of wave age on the wind drag coefficient we first calculate the drag coefficient "anomaly" ΔC_{10}, i.e. the excess of the HEXOS drag coefficients adjusted to neutral stability, C_{10N}, over values proposed by Smith (1988) for open ocean conditions, C_{10S}. The "wave age" is the ratio $(c_p/U_{10N}\cos\theta)$ of the wave phase velocity to the component of wind velocity in the direction of wave propagation. The phase velocity c_p is calculated for the peak frequency of the one-dimensional wave spectrum, taking account of the 18 m depth at MPN. θ is the difference between wind and wave directions. Wave direction is based on visual analysis of video tapes of the surface (*pers. comm.*, E.C. Monahan). For about half of the runs multiple wave trains were seen and the drag coefficient "anomalies" were scattered. For runs with a single (visually observed) wave train, ΔC_{10N} decreases with increasing wave age (Fig. 2). A "neutral" linear regression (average of regression lines with each variable in turn independent) for wave ages from 0.4 to 0.9 is

$$10^3 \Delta C_{10N} = 1.85 - 2.24\ c_p/(U_{10N}\cos\theta)$$

with squared correlation $r^2 = 0.59$. This line gives zero drag coefficient "anomaly" at a wave age of 0.83, a typical value for open ocean situations.

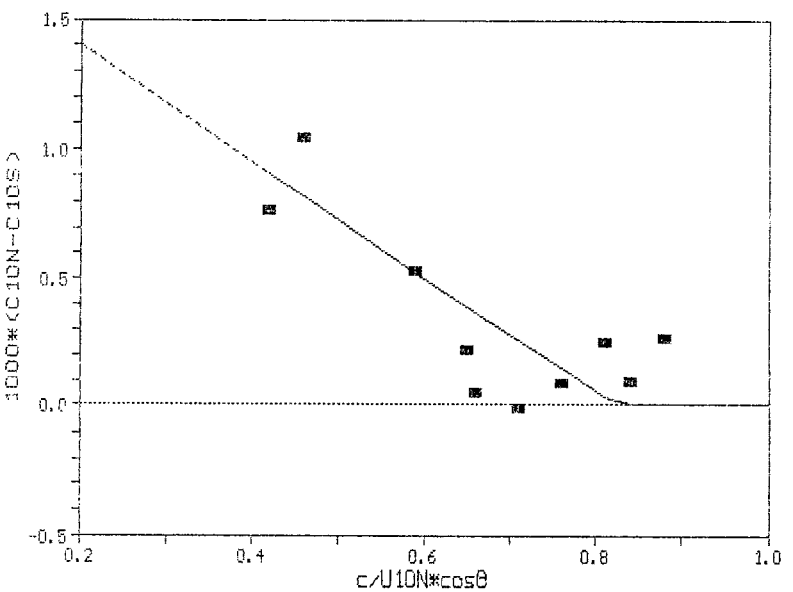

Fig. 2. Variation of drag coefficient anomaly with wave age.

This preliminary result will be modified as other groups analyse and interpret their HEXMAX data. This is one of the first experiments to directly demonstrate a long-anticipated influence of wave age on the drag coefficient in addition to its dependence on wind speed.

4 SUMMARY

HEXMAX has expanded knowledge of evaporation from the sea surface in conditions relevant to the modeling of formation of dense water masses conducive to deep convection events, making it necessary to reduce estimates of the influence of spray. A neutral evaporation coefficient $C_{EN} = 0.0012$ is found to apply at wind speeds up to 20 m/s. The influence of flow distortion on wind stress measured by eddy correlation was detected by comparing data from a sonic anemometer operated above and below a supporting boom. The presence of relatively "young" waves at the experimental site has made it possible to detect the influence of wave age on the sea surface drag coefficient in transient conditions.

ACKNOWLEDGEMENTS

The contributions and cooperation of many colleagues and particularly of Dr. W.A. Oost and the team from KNMI made HEXMAX a success. C.W. Fairall and J.B. Edson pointed out the applicability of the Wyngaard flow distortion correction to wind stress. R.J. Anderson analysed the BIO data, and I thank him and D.L. Hendsbee for their participation in the field project.

REFERENCES

Bortkovskii, R.S., 1987. Air-Sea exchange of Heat and Moisture during Storms. Reidel, Dordrecht, 194 pp.

Geernaert, G. L., K. B. Katsaros and K. Richter, 1986. Variation of the drag coefficient and its dependence on sea state. *J.Geophys. Res.*,**91**: 7667-7679.

Katsaros, K.B., S.D. Smith and W.A. Oost, 1987: HEXOS - Humidity Exchange over the Sea, a program for research on vater-vapor and droplet fluxes from sea *to air* at moderate to high wind speeds. *Bull. Amer. Meteor. Soc.*, **68**: 466-476.

Ling, S. C. and T. W. Kao, 1976. Parameterization of the moisture and heat transfer process over the ocean under whitecap sea states. *J. Phys. Oceanogr.*, **6**: 306-315.

Smith, S. D., 1980. Wind stress and heat flux over the ocean in gale force winds. *J. Phys. Oceanogr.*, **10**: 709-726.

Smith, S. D., 1988. Coefficients for sea surface wind stress, heat flux and wind profiles as a function of wind and temp[erature. *J. Geophys. Res.*, **93**: 15467-15472.

Smith, S.D.,1989. Water vapor flux at the sea surface. *Boundary-Layer Meteor.*, **47**: 277-293.

Smith, S. D., K. B. Katsaros, W. A. Oost and P. G. Mestayer, 1990. Two major experiments in the Humidity Exchange over the Sea (HEXOS) program. *Bull. Amer. Meteor. Soc.*, **71**: 161-172.

Stramska, M., 1987. Vertical profiles of sea salt aerosol in the atmospheric surface layer: A numerical model. *Acta Geophysica Polonica*, **35**: 87-100.

Wyngaard, J. C., 1981. The effects of probe-induced flow distortion on atmospheric turbulence measurements. *J. Appl. Meteor.*, **20**: 784-794.